DEPARTMENT OF MECHANICAL,AEROSPACE
AND MANUFACTURING ENGINEERING
Thermodynamics and Fluid Mechanics Division

Development and Application of a New Wall Function for Complex Turbulent Flows

by

Simon Gant

University of Manchester
Institute of Science and Technology
P.O. Box 88, Manchester M60 1QD, UK

November 2002

Development and Application of a New Wall Function for Complex Turbulent Flows

by

Simon E. Gant

Department of Mechanical,
Aerospace and Manufacturing Engineering

A thesis submitted to
the University of Manchester Institute of Science and Technology
for the degree of Doctor of Philosophy

November 2002

Declaration

No portion of the work referred to in this thesis has been submitted in support of an application for another degree or qualification of this or any other university, or other institution of learning.

Acknowledgements

I would like to express my sincere thanks to Professor Brian Launder, my supervisor, for his guidance and support throughout the course of this research. I would also like to thank Dr Tim Craft and Dr Hector Iacovides for their advice and patience in answering my numerous questions. The many discussions I have had with them have benefitted considerably my understanding of turbulent flows and turbulence modelling.

Funding for this project was provided by the UK Engineering and Physical Sciences Research Council (EPSRC), through the ROPA scheme (grant ref: GR/M99170), and from the European Union Project: "Models for Vehicle Aerodynamics (MOVA)" (BRITE/EURAM BE-97-4043). I would like to thank all the members of the MOVA project group for their helpful discussions. In particular I would like to thank: Professor D. Laurence (UMIST & Electricité de France), Professor K. Hanjalić (TU Delft), Dr H. Lienhart (LSTM, Erlangen), Dr L. Elena (PSA, Peugeot-Citroën) and Dr B. Basara (AVL, Graz). There are a number of researchers in other institutions whom I would like to thank for their assistance in providing papers and in giving advice: Dr Marshall Richmond (IIHR), Dr Andreas Abdon (Alstom Power) and Dr Eric Goncalves (ONERA).

I have greatly enjoyed the last four and a bit years studying in the Thermofluids Division at UMIST. My thanks go to all the regulars of the Thermofluids Coffee Club, both past and present, for their daily insights and discussions: Dr Chris Robinson, Dr Rob Prosser, Dr Valerie Guimet, Yacine Addad, Ante Soda, Mark Richardson, Michael Deevy and Melinda Curtis. Special thanks go to Yusuf Al-Suleimani and Dr Ghassan Abu-Orf for their culinary skills with the roof-top barbecues and to Aleksey Gerasimov with whom I have had the pleasure of sharing an office for the last three years. Last, but by no means least, I would like to my wife, Helen, for her love and support.

Abstract

Wall functions are widely used in commercial CFD software and offer significant savings in computational expense compared to low-Reynolds-number formulations. However, existing wall functions are based on assumed near-wall profiles of velocity, turbulence parameters and temperature which are inapplicable in complex, non-equilibrium flows. A new wall function is developed in this thesis which, instead of assuming profiles of the dependent variables, determines these quantities by solving boundary-layer-type transport equations across a locally-defined subgrid.

The new wall function, called UMIST-*N*, is applied to three test cases: an axisymmetric impinging jet, a spinning "free" disc and a three-dimensional simplified car body. The impinging jet flow ($H/D = 4$; $Re = 70,000$) is studied using linear and non-linear $k-\varepsilon$ models with the UMIST-*N* wall function, four "standard" log-law-based wall functions and full low-*Re* treatments. It is demonstrated that heat transfer predictions with the UMIST-*N* wall function are in excellent agreement with low-*Re* model results, in contrast to standard log-law-based wall functions. The new wall function also shows less sensitivity to the size of the near-wall cell than standard wall functions.

Spinning-disc calculations are carried out at rotational Reynolds numbers up to $Re_\phi = 3.3 \times 10^6$ using a similar array of turbulence models and wall treatments. The UMIST-*N* wall function and low-*Re* model results are again in excellent agreement, in contrast to standard wall functions which are unable to predict correctly the radial velocity profile. The location of the predicted transition point from laminar to turbulent flow on the spinning-disc shows some slight sensitivity to the near-wall grid arrangement with the UMIST-*N* wall function, although the results are close to those obtained with the low-*Re* models.

Simulation of the simplified "Ahmed" body flow demonstrates that the UMIST-*N* wall function can be applied to complex geometry using a non-orthogonal multiblock grid. Flow predictions over the 25° rear slant of the car using UMIST-*N* with linear $k-\varepsilon$ model are shown to be similar to those obtained using a log-law-based wall function.

In the three test-cases considered, computing times with the new wall function are up to twice as high as for standard wall functions, but they are still an order-of-magnitude less than low-Reynolds-number calculations.

Contents

Nomenclature

Symbols	Definition
$a_{E,W,N,S,T,B,P}$	East, west, north etc. coefficients in the discretized equations
a_{ij}	Anisotropic stress, $a_{ij} = \overline{u_i u_j}/k - 2\delta_{ij}/3$
$A_{e,w,n,s,t,b}$	Areas of the east, west, north etc. cell faces
A_2	Second invariant of anisotropic stress, $A_2 = a_{ij}a_{ij}$
$A_x^\xi, A_x^\eta, A_x^\zeta$	Components of the area vector, $A_x^\xi = J\partial\xi/\partial x$; $A_x^\eta = J\partial\eta/\partial x$; $A_x^\zeta = J\partial\zeta/\partial x$
c_h	Constant of integration in the temperature log-law
c_i, d_i, e_i	Subgrid interpolation functions
c_l	Constant in near-wall length-scale definition
c_m	Integral moment (in the spinning disc flow, $c_m = M/0.5\rho\Omega^2 r^5$)
c_p	Constant-pressure specific heat
c_w	"Constant" in the differential Yap correction
$c_{\varepsilon 1}, c_{\varepsilon 2}$	Constants in the modelled ε transport equation (Equation 2.15)
c_μ	Coefficient or function in eddy-viscosity formula (Equation 2.9)
$c_1 - c_7$	Constants in non-linear $k-\varepsilon$ model (Equation 2.27)
C	Constant of integration
C_D	Coefficient of drag
C_F	Coefficient of friction
C_P	Coefficient of pressure, $C_P = (P - P_0)/0.5\rho U_0^2$

C_B^*, C_K^*, C_S^*	Components of pressure drag on Ahmed body, due to the base, nose cone and rear slant, respectively
C_R^*	Friction drag on Ahmed body
C_W	Total drag on Ahmed body
d_{ij}	Diffusion term in the $\overline{u_i u_j}$ transport equation
$dl_e dy$	Equilibrium length-scale gradient in the differential Yap correction
D	Diameter (in the impinging jet flow, the diameter of the inlet pipe)
$D_{e,w,n,s,t,b}$	Diffusion coefficients for the east, west, north etc. cell faces
$\mathbf{e}_i, \mathbf{e}^i$	Cartesian covariant and contravariant unit vectors, respectively (N.B. these are equivalent, $\mathbf{e}_i \equiv \mathbf{e}^i$)
E	Integration "constant" used in wall functions ($E \approx 9.79$ for smooth walls)
f_{RS}	Damping term in the differential Yap correction
f_1, f_2, f_μ	Damping functions used in the low-Reynolds-number $k-\varepsilon$ model
F	Difference between the predicted and equilibrium length-scale gradients in the differential Yap correction
$F_{e,w,n,s,t,b}$	Convective mass flux through the east, west, north etc. cell faces
F_{wall}	Wall force, $F_{wall} = -\tau_{wall} A$
g	Determinant of the g_{ij} matrix
$\mathbf{g}_i, \mathbf{g}^i$	Curvilinear covariant and contravariant base vectors, respectively
g_{ij}, g^{ij}	Covariant and contravariant metric tensors, respectively
G	Production rate of turbulent kinetic energy, sometimes denoted P_k
G_{ij}	Adjoint of the g_{ij} matrix
h	Heat transfer coefficient, $h = q_{wall}/(T_{wall} - T)$
H	Height (in the impinging jet flow, the height from the inlet pipe to the wall)
J	Jacobian of transform matrix for curvilinear coordinate system
J_ϕ^j	Contravariant components of the scalar flux vector, $\mathbf{q}$

k	Turbulent kinetic energy, $k = \frac{1}{2}(\overline{uu} + \overline{vv} + \overline{ww})$
L	Reference length (in the Ahmed body flow, L is the height of the Ahmed body)
l	Length scale
l_m	Mixing length
M	Moment, defined in the spinning disc flow as $M = -2\pi \int_0^r r^2 \tau_\phi dr$
n	Displacement in the wall-normal direction
$\hat{\mathbf{n}}$	Wall-normal unit vector
$\hat{n}_x, \hat{n}_y, \hat{n}_z$	Cartesian components of the wall-normal unit vector, $\hat{\mathbf{n}}$
Nu	Nusselt number (Equation 5.1)
P	Mean pressure
$P(\sigma/\sigma_t)$	Jayatilleke P-function in the temperature log-law
$P^{'}$	Pressure correction (in the SIMPLE algorithm) or mean pressure plus the isotropic Reynolds stress component $\left(P^{'} = P + 2\rho k/3\right)$ in the momentum equation
Pe	Cell Peclet number, $Pe = F/D$
P_{ij}	Production term in the $\overline{u_i u_j}$ transport equation
P_k	Production rate of turbulent kinetic energy, sometimes denoted G (Equation 2.13)
$\overline{P_k}$	Total average production rate of turbulent kinetic energy in near-wall cell
P_{kuv}	Production rate of turbulent kinetic energy due to shear stress
$P_{\varepsilon 3}$	Gradient production term in low-Re model $\tilde{\varepsilon}$-equation, sometimes denoted E (Equation 2.24)
P_0	Reference pressure
$\mathbf{q}$	Scalar flux vector
q_{wall}	Wall heat flux
r	Radius
r_b	Outside disc radius

R_v	Viscous sublayer Reynolds number, $R_v = k_v^{1/2} y_v/\nu$
R_ϕ	Residual for discretized ϕ-equation
Re	Reynolds number, $Re = Ul/\nu$
$R_t, \tilde{R}_t$	Turbulent Reynolds number, $R_t = k^2/\nu\varepsilon$; $\tilde{R}_t = k^2/\nu\tilde{\varepsilon}$
Re_τ	Reynolds number based on the wall friction, $R_\tau = U_\tau L/\nu$
Re_ϕ	Rotational Reynolds number, $Re_\phi = \Omega r^2/\nu$
s	Physical distance parallel to the curvilinear ζ-axis
s_P	Contributions to linearized source term which are a function of the dependent variable
s_U	Source term in discretized transport equation
$S, \tilde{S}$	Dimensionless strain invariants (Equation 2.32) or source term
S_I	Dimensionless third invariant of the strain-rate tensor
S_{ij}	Strain-rate tensor, $S_{ij} = \partial U_i/\partial x_j + \partial U_j/\partial x_i$
$\hat{\mathbf{t}}$	Tangential, or wall-parallel, unit vector
$\hat{t}_x, \hat{t}_y, \hat{t}_z$	Cartesian components of the wall-parallel unit vector, $\hat{\mathbf{t}}$
T	Temperature
T_{wall}	Wall temperature
T_τ	Friction temperature, $T_\tau = q_{wall}/\rho c_p U_\tau$
T^+	Dimensionless temperature, $T^+ = (T_{wall} - T)/T_\tau$
$u_i = u, v, w$	Turbulent velocities (i.e. instantaneous minus mean velocities)
$\overline{uu}, \overline{vv}, \overline{ww}$ $\overline{uv}, \overline{uw}, \overline{vw}$ $\overline{u_i u_j}$	Reynolds (turbulent) stresses
$\widehat{\overline{u_i u_j}}$	Non-linear components of the Reynolds stress
$\overline{u_n^2}$	Reynolds stress in the wall-normal direction
$\mathbf{U}$	Velocity vector
U, V, W	Mean velocity components

U_{ref}	Reference velocity used to non-dimensionalize variables in STREAM
U_x, U_y, U_z	Cartesian components of the velocity vector, $\mathbf{U}$
U_0	Free-stream velocity
U_τ	Friction velocity, $U_\tau = \sqrt{\tau_w/\rho}$
U^+	Dimensionless velocity, $U^+ = U/U_\tau$
W	Tangential velocity in cylindrical-polar coordinates
x, y, z, x_i	Cartesian coordinate directions
y^+	Dimensionless distance to the wall, $y^+ = yU_\tau/\nu$
y^*	Dimensionless distance to the wall, $y^* = y\sqrt{k}/\nu$
Y_c	Yap correction
Y_{dc}	Differential Yap correction

Greek Symbols

α	Under-relaxation factor or scaling factor used in the UMIST-*N* wall function calculation of wall-normal velocity
β	Rear-slant angle of the Ahmed body (to the horizontal)
β^i_j	Elements of the inverse Jacobian matrix which are used to obtain curvilinear components from Cartesian components, $\beta^i_j \equiv \partial\xi^i/\partial x_j$
Γ_ϕ	Diffusion coefficient for parameter ϕ
Γ_{ijk}	Christoffel symbol of the first kind
Γ^k_{ij}	Christoffel symbol of the second kind
$\delta_{ij}, \delta^{ij}, \delta^j_i$	The Kronecker delta (if $i = j$ then $\delta_{ij} = \delta^{ij} = \delta^j_i = 1$, otherwise, if $i \neq j$ then $\delta_{ij} = \delta^{ij} = \delta^j_i = 0$)
Δ	Denotes change in given variable
$\Delta x, \Delta y, \Delta z$	Physical cell dimensions (i.e. distance between cell-faces) in Cartesian coordinates
$\Delta\xi, \Delta\eta, \Delta\zeta$	Computational cell dimensions (i.e. distance between cell-faces) in curvilinear coordinates

ΔVol	Cell volume
ε	Rate of dissipation of turbulent kinetic energy
$\overline{\varepsilon}$	Average rate of dissipation of turbulent kinetic energy in near-wall cell
$\tilde{\varepsilon}$	Isotropic part of turbulence energy dissipation (where, by definition, $\tilde{\varepsilon} = 0$ at the surface of a solid boundary)
ε_{ij}	Dissipation term in the $\overline{u_i u_j}$ transport equation
η	Maximum of the strain and vorticity invariants,$\eta = \max(S, \Omega)$, or wall-parallel curvilinear coordinate in the UMIST-*N* wall function
θ	Momentum thickness ($\theta = \int_0^\infty \lvert W/\Omega r\,(1 - W/\Omega r)\rvert \,\mathrm{d}y$) or angle between two vectors
κ	von Kármán constant in the velocity log-law, $\kappa \approx 0.42$
κ_h	von Kármán constant in the temperature log-law, $\kappa_h = \kappa/\sigma_t$
λ	Function used in Johnson & Launder wall function, thermal conductivity ($\lambda = \mu c_p/\sigma$) or Taylor microscale
λ_t	Turbulent thermal conductivity
μ	Molecular or dynamic viscosity
μ_{eff}	Effective viscosity, $\mu_{eff} = \mu + \mu_t$
μ_t	Turbulent (eddy) viscosity
ν	Kinematic viscosity, $\nu = \mu/\rho$
ν_t	Kinematic turbulent (eddy) viscosity
$\xi_i = (\xi, \eta, \zeta)$	Curvilinear coordinate directions. In the UMIST-*N* wall function, the ξ- and η-axes are parallel to the wall and the ζ-axis intersects the wall.
ρ	Density
ρ'	Reference density used to non-dimensionalize variables in STREAM
σ	Molecular Prandtl number, $\sigma = \mu c_p/\lambda$
$\sigma_k, \sigma_\varepsilon$	Empirical constants in k and ε transport equations
σ_t	Turbulent Prandtl number, $\sigma_t = \mu_t c_p/\lambda_t$

τ	Shear stress
τ_{wall}	Wall shear stress
ϕ	General variable or scalar parameter
ϕ_{ij}	Redistribution or pressure-strain correlation
φ	Ahmed body rear slant angle (to the horizontal) as used by Ahmed *et al*. (equivalent to β, see above)
ω	Specific rate of dissipation of turbulent kinetic energy, $\omega = k/\varepsilon$
Ω	Angular velocity
$\Omega, \tilde{\Omega}$	Dimensionless vorticity invariants (Equation 2.35)
Ω_{ij}	Vorticity tensor, $\Omega_{ij} = \partial U_i/\partial x_j - \partial U_j/\partial x_i$

Subscripts

b	Bulk value
body	Pertaining to the Ahmed body without the stilts
$E, W, N, S, T, B,$ $EE, WW, NN, SS,$ $TT, BB,$ e, w, n, s, t, b	Node and face values of variables
i	Covariant components, $i = 1, 2, 3$
in	Inlet value
(i)	Physical covariant components
nb	Neighbouring nodes
NL	Non-linear
P	Value at the near-wall node or current node
tot	Total
v	Value at the edge of the viscous sublayer
wall	Wall value
x, y, z	Derivative with respect to the Cartesian coordinate components

ξ, η, ζ	Derivative with respect to the curvilinear coordinate components
τ	"Friction" value (as in the friction velocity, U_τ)

Superscripts

calc	Calculated value at present iteration
i	Contravariant components, $i = 1, 2, 3$
(i)	Physical contravariant components
n	Wall-normal
new	Final or new value at present iteration
old	Value at previous iteration
t	Tangential or wall-parallel
T	Transpose of the matrix
$+$	Non-dimensional near-wall value scaled by U_τ
$*$	Non-dimensional near-wall value scaled by $\sqrt{k}$, guessed values in SIMPLE algorithm or assigned boundary value
$()^*$	In the UMIST-*N* wall function, $()^*$ denotes that the upstream value of the gradient inside parenthesis is transformed from the coordinate system in upstream cell into the coordinate system of the current cell, so that both upstream and current cells use the same base vectors
$'$	Characteristic variables used in STREAM to non-dimensionalize variables, or correction values in SIMPLE algorithm

Acronyms

AIAA	American Institute of Aeronautics and Astronautics
AGARD	Advisory Group for Aerospace Research & Development
ASM	Algebraic Stress Model
ASME	American Society of Mechanical Engineers
CFD	Computational Fluid Dynamics
CHF	Constant Heat Flux

CL	Chieng & Launder wall function
CPU	Central Processing Unit
CWT	Constant Wall Temperature
DGLR	Deutsche Gesellschaft für Luft- und Raumfahrt
DIA	Direct Interaction Approximation
DNS	Direct Numerical Simulation
EPSRC	Engineering and Physical Sciences Research Council
ERCOFTAC	European Research Community on Flow, Turbulence and Combustion
EVM	Eddy-Viscosity Model
IUTAM	International Union of Theoretical and Applied Mathematics
JL	Johnson & Launder wall function
LEVM	Linear Eddy-Viscosity Model
LES	Large Eddy Simulation
LSTM	Lehrstuhl für Strömungsmechanik
MOVA	Models for Vehicle Aerodynamics
NLEVM	Non-Linear Eddy-Viscosity Model
N-S	Navier-Stokes
PLDS	Power Law Differencing Scheme
PSL	Parabolic Sub-Layer
QDNS	Quasi-Direct Numerical Simulation
QUICK	Quadratic Upwind Interpolation for Convection Kinematics
RANS	Reynolds-Averaged Navier-Stokes
RDT	Rapid Distortion Theory
RMS	Root Mean Square, $\left(\sqrt{\overline{\phi^2}}\right)$
RNG	Re-Normalization Group

SAE	Society of Automotive Engineers
SCL	Simplified Chieng & Launder wall function
SIMPLE	Semi-Implicit Method for Pressure-Linked Equations
SSG	Speziale, Sarkar & Gatski differential stress model
SST	Shear Stress Transport turbulence model
STREAM	Simulation of Turbulent Reynolds-averaged Equations for All Mach numbers
TDMA	Tri-Diagonal Matrix Algorithm
TEAM	Turbulent Elliptic Algorithm – Manchester
T-S	Tollmien-Schlichting
TVD	Total Variation Diminishing
UMIST	University of Manchester Institute of Science and Technology or Upstream Monotonic Interpolation for Scalar Transport
UMIST-*A*	Unified Modelling through Integrated Sublayer Treatment - an *Analytical* approach
UMIST-*N*	Unified Modelling through Integrated Sublayer Treatment - a *Numerical* approach
URANS	Unsteady Reynolds-Averaged Navier-Stokes
VLES	Very Large Eddy Simulation

Chapter 1

Introduction & Literature Survey

1.1 Background

Understanding and predicting turbulent flow is vital for a wide range of applications, from weather prediction to car design. The phenomena that are observed in turbulent flows, such as the beautiful and intricate eddy structures, are also fascinating. Turbulence is characterized by its disorder or apparent unpredictability. It typically has a large range of length and time scales: in atmospheric turbulence the eddies may range in size from centimetres up to hundreds of kilometres. The rapidly changing velocity field in turbulent flows encourages rapid mixing which enhances diffusion of momentum, mass and heat. This feature can be advantageous if one wants to remove heat or mix fluids, or it can be disadvantageous if, for instance, one wants to minimize friction drag. Turbulence is also dissipative, meaning that energy must be constantly supplied to the flow in order for turbulence to be maintained or else it will decay (a commonly cited example being the motion of stirred liquid in a cup, where the fluid eventually ceases moving). This dissipation of turbulent kinetic energy is linked to an "energy cascade", where energy is supplied to the largest eddies by shearing motions in the bulk flow, which interact with and transfer energy to smaller eddies. In the smallest eddies the velocity gradients are largest and viscous action converts kinetic energy into heat. Whilst it is influenced by the fluid viscosity and density, turbulence is not a material property of the fluid but a continuum flow phenomena (continuum in the sense that the minimum length scale in a turbulent flow is always much greater than the mean free path of its constituent molecules). The turbulence considered in this thesis is also three-dimensional. Turbulence can occur in 2-D but it exhibits behaviour unlike 3-D turbulence, in particular the energy cascade seems to work in reverse, leading to larger and larger eddies.

Turbulent flow predictions have evolved significantly during the last half-century, largely due to the appearance of digital computers in the 1950's and 60's, and their exponential increase in processing power over the following decades. Before the advent of computing, predictions were made using either empirical correlations or integral methods. The latter approach involves the solution of ordinary differential equations (in 2-D flows) through the use of integral parameters such as momentum thickness and skin-friction coefficient (by assuming profiles or shape functions, see for example [1]).

This approach is limited to fairly simple flows which do not involve boundary-layer separation or recirculation, but is still commonly used in industry [2].

At present, there are five main approaches to predicting turbulent flow. The first and conceptually the simplest approach is to solve directly the equations governing fluid flow, the Navier-Stokes equations. This so-called "Direct Numerical Simulation" (DNS) has the advantages of not needing any assumptions of the turbulence behaviour and hence data from DNS is often used in a similar manner to experimental results (the bonus being that quantities that cannot be determined experimentally can easily be examined, as all flow parameters are calculated). In fact it has even been used to estimate the measurement errors in experiments (see, for example, Moin & Mahesh [3]). DNS is also proving useful for examining the internal mechanisms of turbulence and transition from laminar to turbulent flow. The disadvantage of DNS is the computational expense: massively parallel computers have to be used and computations are limited to relatively low-Reynolds-number flows with a small ratio of large to small eddies. This high cost is due to the nature of turbulence itself. In order for turbulence to be represented accurately it is necessary to resolve *all* the length and time scales of the flow. Tennekes & Lumley [4] showed that the computational cost scales with the cube of the integral-scale Reynolds number, Re_l^3. It is therefore unlikely that DNS will be used routinely in engineering calculations for the foreseeable future, although it is invaluable as a tool for providing very detailed data which may be used to help develop or to validate turbulence models.

The second approach, Large Eddy Simulation (LES), uses a coarser grid than that employed in DNS and applies the filtered Navier-Stokes equations (effectively N-S equations averaged over a small region of space). Since the grid cannot discern the smallest scales of turbulence, a sub-grid-scale model is used to account for the dissipation of energy at the smallest scales and any "backscatter" of energy from the small to the large scales. The large-scale motions, which are responsible for most of the transport of momentum and turbulence energy, are computed explicitly and do not require modelling. Therefore, it is anticipated that this method should be more accurate than the RANS approach discussed below, in which all turbulent scales are modelled. LES was first developed for application to weather prediction, but is increasingly being used throughout the engineering and scientific communities. However, the relatively high computational expense still limits LES to analysis and trouble-shooting rather than as an aid to engineering design[1].

The third approach uses Reynolds-Averaged Navier-Stokes (RANS) equations. Here the turbulent flow is considered as consisting of two components: a fluctuating part and a mean or average part. The mean flow is calculated using RANS equations which are obtained by averaging the Navier-Stokes equations over time, space or using ensemble averaging. The equations look very similar to the unaveraged (instantaneous) Navier-Stokes equations but for an additional non-linear term involving the Reynolds stress, $\overline{u_i u_j}$ (where u_i is the fluctuating velocity and the overbar denotes Reynolds averaging). A transport equation can also be derived for the unknown Reynolds stress, but this involves

[1]For example, at present in UMIST an opposed wall-jet flow is being examined using both LES and RANS approaches. The RANS simulations (using a two-equation model) take approximately 6 hours whereas the LES simulations take between 1 and 2 weeks, on the same platform, depending on grid resolution.

additional unknown third-order terms ($\overline{u_i u_j u_k}$). Likewise, the expression for $\overline{u_i u_j u_k}$ involves unknown fourth moments and so on. This issue of specifying the Reynolds stress is known as the turbulence modelling "closure problem". The closure problem is also complicated by the fact that the Reynolds stress may depend upon non-local events. In the exact equation for $\overline{u_i u_j}$ there are terms involving the fluctuation pressure, p, for which one can derive a Poisson equation. This equation can be solved, using Green's functions, but the value of p at any point in the flow is found to be a function of the velocity at all points throughout the whole flow domain. "Single-point" closures assume that the Reynolds stress can be calculated in terms of local parameters. Various single-point turbulence models exist which attempt to approximate $\overline{u_i u_j}$, ranging from simple algebraic expressions to additional transport equations for each of the six independent Reynolds stresses. These models are discussed below (Section 1.2).

Solving the RANS equations with a single-point linear eddy-viscosity model (discussed below) can be thought of as solving the Navier-Stokes equations for a laminar flow (i.e. the mean velocity) but with a modified fluid viscosity which is a function of the local turbulence behaviour. If the flow is stationary (i.e. if the averaged velocity field does not change over time) it is not necessary to compute the time-dependent flow behaviour with a RANS scheme, unlike DNS or LES where the flow must always be considered as unsteady. Symmetry can also be used to reduce the computational demands where appropriate so, for example, the axisymmetric impinging jet studied in this thesis was treated as essentially a 2-*D* problem. DNS and LES on the other hand require full 3-*D* solutions in order to model 3-*D* turbulence. The RANS approach using single-point closure is therefore economical and flexible and is widely used in industry for both design and analysis.

The fourth method of analyzing turbulent flows involves "multi-point" or in most cases simply "two-point" correlations. Here the turbulent statistics at two separate points in space are used. The analysis is complex and the resulting equations are sometimes intractable. Research is principally being undertaken by two groups, L'Ecole Centrale de Lyon and the Los Alamos National Laboratories. Complex turbulent flows have been examined using two-point closures, but only in relatively simple geometries. Whilst this approach is unlikely to be used in practical engineering applications in the near future, the theories developed in two-point closures give insight into some of the physics of turbulent interactions and provide guidance for the development of single-point turbulence models.

The fifth and final approach to predicting turbulent flow uses Probability Density Functions (PDFs). A PDF expresses the likelihood of an event taking place per unit sample space[2]. The mean velocity and Reynolds stress are the first and second moments of the Eulerian PDF of velocity. Therefore, if the shape of the PDF can be determined then the closure problem can be solved. An equation for the velocity PDF can be derived from the Navier-Stokes equations. In this equation the convective transport and the mean pressure gradient term are in closed form but the remaining fluctuating pressure and viscous terms require modelling. Various models for the PDF equation are detailed by Pope

[2]For example, if there is a uniform probability of velocity, V, being greater than one and less than three metres per second (i.e. an equal chance that V will take any value between 1 and 3 m/s), then the PDF will be a constant value of $1/2$ between $V = 1$ and $V = 3$.

[5]. This method has mostly been applied to reactive flows because it avoids the need for additional closure approximations in the chemical reaction equations. For simpler non-reactive flows, the current PDF models involving particle methods lead to increased computing times compared to single-point Reynolds-stress models. As yet, there have not been sufficient comparative studies between PDF and Reynolds-stress models to draw any firm conclusions as to their relative accuracy.

For simplicity, the above discussion has been limited to the five main approaches to predicting turbulent flow. There are numerous other hybrid methods in which, for example, an unsteady RANS calculation is used near solid boundaries while LES is applied in the bulk of the flow (an approach dubbed "Detached Eddy Simulation", DES). An interesting discussion of hybrid methods (including DES, VLES and URANS) is provided by Spalart [6].

The objective of the work presented in this thesis is to develop a new wall boundary condition suitable for simulations using RANS equations and single-point Reynolds-stress models (the third of the above five approaches). The following sections review single-point Reynolds-stress models, near-wall flow phenomena and current approaches used in modelling the near-wall flow behaviour.

1.2 Turbulence modelling

The Reynolds-averaged continuity and momentum equations can be written in Cartesian coordinates as follows:

$$\frac{\partial \rho}{\partial t} + \frac{\partial}{\partial x_j}(\rho U_j) = 0 \tag{1.1}$$

$$\frac{\partial}{\partial t}(\rho U_i) + \frac{\partial}{\partial x_j}(\rho U_i U_j) = -\frac{\partial P}{\partial x_i} + \frac{\partial}{\partial x_j}\left[\mu\left(\frac{\partial U_i}{\partial x_j} + \frac{\partial U_j}{\partial x_i}\right) + \lambda\delta_{ij}\frac{\partial U_m}{\partial x_m} - \rho\overline{u_i u_j}\right] \tag{1.2}$$

where upper-case U_i and P denote Reynolds-averaged velocity and pressure, ρ is the density, μ is the molecular viscosity, λ is the bulk viscosity and δ_{ij} is the Kronecker delta. Expanding the above expressions in three-dimensions gives 4 equations (continuity and three momentum equations) and 10 variables: three velocity components (U, V and W), pressure and six independent Reynolds stress components[3]. To close this system of equations, an expression for the Reynolds stress needs to be found. Boussinesq, in the late nineteenth century, approached the turbulence closure problem by assuming the turbulent stress to be proportional to the strain rate, introducing an apparent or "eddy" viscosity as the scalar proportionality term. The turbulence closure problem therefore changed from calculating six Reynolds stresses to finding one eddy-viscosity. One of the simplest approaches to calculating this eddy-viscosity has been the mixing length model which was derived independently by G. I. Taylor [7] and L. Prandtl [8]. Here, the following expression is obtained for the eddy-viscosity in a simple shear flow in which $\partial U/\partial y$ is the only strain-rate:

$$\nu_t = l_m^2 \left|\frac{\partial U}{\partial y}\right| \tag{1.3}$$

[3]There are only six independent components, since $\overline{u_i u_j}$ is a symmetric tensor ($\overline{u_i u_j} = \overline{u_j u_i}$).

The mixing length, l_m, is a characteristic of the local flow and is prescribed algebraically. There are no additional transport equations to solve and so the mixing length model is referred to as an algebraic or zero-equation model. The problem is now a question of how to prescribe the mixing length, l_m. In the fully-turbulent region of equilibrium boundary layers, l_m can be described by a simple linear expression, $l_m = \kappa y$, where y is the distance from the wall and κ the von Kármán constant. However, in more complex flows l_m must be varied considerably to obtain good experimental agreement. Another limitation of the simple mixing length model is that it predicts that the turbulent viscosity vanishes when the strain rate $(\partial U/\partial y)$ is zero, as may occur for example in separated boundary layers, whereas in reality the effects of turbulence can be significant in such regions.

A slightly more sophisticated class of models involves the solution of a transport equation for a turbulence parameter. Prandtl's one-equation model [9] solves a transport equation for the turbulent kinetic energy, k, so that the eddy-viscosity is given by:

$$\nu_t = c_\mu k^{1/2} l \tag{1.4}$$

where c_μ is a constant and l is a prescribed length scale. In this model, the problem associated with turbulent viscosity becoming zero where the velocity takes a maximum or minimum value is overcome by using $k^{1/2}$ as a velocity scale. However, as with the zero-equation models, its weakness is the algebraic length scale prescription: a different algebraic expression needs to be applied for different flow geometry. A more recent one-equation model by Spalart & Allmaras [10] which solves a transport equation directly for ν_t has been quite successful in predicting attached flow around airfoils [11]. However, it performs less well in separated flows and the model requires the prescription of a wall-distance which can be difficult to specify around a body of complex geometry.

Two-equation eddy-viscosity models involve the solution of transport equations for two turbulence parameters (usually turbulent kinetic energy and a second independent variable). This enables the calculation of the velocity and length scales which are used to calculate the eddy-viscosity. There have been many two-equation models using a variety of different choices for the second variable (e.g. ε, kl, ω, ω^2, τ). The most popular scheme for the last 20 years has been the $k-\varepsilon$ model. The "standard" version of the model was presented by Jones & Launder [12] with improved values for constants and damping functions given later by Launder & Sharma [13]. In the $k-\varepsilon$ model the eddy-viscosity is calculated from:

$$\nu_t = c_\mu \frac{k^2}{\varepsilon} \tag{1.5}$$

where c_μ is a constant of proportionality, which is normally defined empirically by considering flow under local equilibrium. The quantity ε is the rate of dissipation of turbulent kinetic energy per unit mass, which appears directly in the k-equation as a sink term. The dissipation rate can be thought of physically as the speed at which turbulent kinetic energy is transferred from large scale eddy-motion to smaller scales (since the rate of dissipation by the small eddies is equal to the rate of energy transfer from the large eddies). An exact equation for the transport of ε can be derived from

the definition of the dissipation rate[4] but the expression includes many unknown terms, including double and triple correlations of fluctuating velocity, pressure and velocity gradients (see, for example [14]). The modelled ε-equation of Launder & Sharma was therefore devised more by intuition and empirical reasoning, following the earlier work of Chou [15], Davidov [16] and Harlow & Nakayama [17]. Reasonably accurate solutions have been obtained using the $k-\varepsilon$ model for a wide range of industrially relevant flows.

Another popular two-equation model solves a transport equation for the "turbulence frequency" or, more correctly, the dissipation rate per unit turbulent kinetic energy, ω, as the second parameter[5]. This approach was first suggested by Kolmogorov [18] and in more recent times the major proponent of the $k-\omega$ model has been Wilcox. In his book [14], Wilcox discusses the performance of $k-\varepsilon$ and $k-\omega$ models with reference to free shear flows, boundary layers and separated flows and reports that the $k-\omega$ model performs well in 2-*D* boundary layers with adverse or favourable pressure gradients and in recirculating flows, but suffers from increased sensitivity to freestream boundary conditions in free shear flows. Since the dissipation rate, ε, tends to a finite value at the wall and k falls to zero, ω $(=\varepsilon/k)$ tends to infinity. To overcome this problem, wall boundaries are handled by prescribing the value of ω at the first node adjacent to the wall. For a review of one and two-equation models see, for example, Pope [5] or Patel *et al*. [19].

Menter [20] adopted a pragmatic approach to two-equation modelling, taking the best aspects of both $k-\varepsilon$ and $k-\omega$ models and blending the two. In the Shear Stress Transport (SST) model, the $k-\omega$ model is applied in the inner region of the boundary layer (near the wall) whilst the $k-\varepsilon$ model is used in the outer region and in free shear flows, to remove the $k-\omega$ model's dependence upon freestream turbulence levels. The expression for eddy-viscosity is also modified to make the shear stress proportional to the kinetic energy in the boundary layer. Two blending functions, which employ the distance from the wall, are used to switch between the turbulence models and to modify μ_t. The SST model has been demonstrated to perform well in a variety of flows including adverse pressure-gradient boundary layers and transonic flows.

Whilst linear eddy-viscosity models are, in general, relatively easy to implement and give reasonable predictions of attached boundary layer flows, they have a number of limitations. In simple shear flows where the velocity $U=U(y)$, the normal Reynolds stresses predicted by a linear EVM are isotropic (i.e. $\overline{u^2}=\overline{v^2}=\overline{w^2}=2k/3$) whereas experiments and DNS studies [21] indicate that there is normal stress anisotropy with $0.5\overline{u^2}\approx\overline{v^2}\approx\overline{w^2}$. Whilst this may not be influential in correctly predicting the dynamic field in a simple shear flow, Brundrett & Baines [22] showed that the correct prediction of normal stress anisotropy is vital in predicting secondary flow in non-circular ducts. In impinging flows, linear models which have the turbulent kinetic energy production proportional to the strain-rate squared $\left(P_k\propto S^2\right)$ overpredict the turbulent kinetic energy near the stagnation point and

[4]The dissipation rate of turbulent kinetic energy is defined as: $\varepsilon=\nu\overline{\frac{\partial u_i}{\partial x_k}\frac{\partial u_i}{\partial x_k}}$.

[5]One can transform the modelled ε-equation into the ω-equation by re-tuning the constants and introducing an additional cross-diffusion term. This source term can be derived from the definition $(\omega=\varepsilon/k)$ and expanding $(D\varepsilon/Dt=\omega Dk/Dt+kD\omega/dt)$ using the transport equations for k and ω.

therefore predict far higher heat transfer rates than occur experimentally (see discussion in Chapter 5). In addition, a linear model predicts a linear variation in swirl velocity with radius in a fully-developed swirling shear flow in a pipe, although experiments [23] indicate that the profile is non-linear. Likewise, the asymmetric velocity profile that is observed in a fully-developed curved channel flow cannot be predicted with a linear EVM without curvature corrections [24].

More sophisticated Differential Stress Models (DSMs), also called Second-Moment Closures or Stress-Transport Models, are able to overcome this inability to account properly for rotational strains and the inaccurate prediction of normal stress anisotropy. These models involve the solution of transport equations for each of the independent Reynolds stress components. The transport equations for the Reynolds stress are of the following form:

$$\frac{D\overline{u_i u_j}}{Dt} = P_{ij} + d_{ij} + \varepsilon_{ij} + \phi_{ij} \tag{1.6}$$

where terms on the right-hand-side are respectively: production, P_{ij}, diffusion, d_{ij}, dissipation, ε_{ij}, and a term known as the "pressure-strain" or "redistribution", ϕ_{ij}. The production term is calculated in its exact form and does not require modelling. The effect of the pressure-strain term is to redistribute energy among the normal stresses whilst usually acting as a sink for the shear stresses. Because ϕ_{ij} has zero trace, it does not appear in the turbulent kinetic energy equation used in simpler two-equation models (which is derived from the transport equation for $\overline{u_i u_j}$). In addition to improved modelling of flow curvature and Reynolds stress anisotropy, DSM's are able to account for the history of the Reynolds stresses, which is important in rapidly developing flows. For example, in an initially anisotropic turbulence field which has its mean strain-rate suddenly set to zero, two-equation models predict an instantaneous return to isotropy whereas experiments (and differential stress models) predict a more gradual change. A review of recent developments in differential stress models is given by leading researchers in [25]. Whilst these models offer the greatest sophistication of current one-point closures, they are costly to use, requiring the solution in 3-D of 11 transport equations rather than the 6 used by two-equation models. Moreover, the models are complex to implement and computations can sometimes suffer from numerical instability.

Non-linear Eddy-Viscosity Models (NLEVMs) have been developed as a compromise between the simple low-cost linear schemes and the more accurate but expensive DSMs. In a NLEVM, the Reynolds stress is calculated from an algebraic expression which includes linear, quadratic and sometimes higher-order combinations of strain-rate (S) and vorticity (Ω). A number of approaches have been adopted in developing NLEVMs. The first method takes a Differential Stress Model and simplifies the transport equations for the Reynolds stress using the "weak equilibrium assumption" [26]:

$$\frac{D}{Dt}\overline{u_i u_j} = \frac{\overline{u_i u_j}}{k}\frac{Dk}{Dt} + \underbrace{k\frac{D}{Dt}\left(\frac{\overline{u_i u_j}}{k}\right)} \tag{1.7}$$

where D/Dt represents combined convection and diffusion and the underbraced term is assumed zero.

This results in an implicit Algebraic Stress Model (ASM) in which the Reynolds stress appears on both sides of an expression involving non-linear functions of strain and vorticity. Different methods have been used to obtain an explicit formula (in the form $\overline{u_i u_j} = f(S, \Omega)$), see for example Gatski & Speziale [27] or Apsley & Leschziner [28]. An alternative more pragmatic approach to developing NLEVMs is simply to introduce higher-order combinations of S and Ω into the eddy-viscosity model and then tune the constants for a wide range of flows. This approach was formalised by Pope [29] and has been used by, among others, Craft *et al*. [30] and Speziale [31]. Some further approaches to deriving NLEVM's have involved Renormalization-Group (RNG) theory [32] and Direct Interaction Approximation (DIA) methods [33]. Quadratic combinations of S and Ω are necessary in NLEVMs to account for Reynolds stress anisotropy while swirl and curvature effects are only accounted for by cubic terms (for details, see Suga [34]). Some models have also incorporated constraints such as realizability, for instance Speziale's quadratic model [31] which ensures that turbulent kinetic energy is always positive. In general, NLEVM's solve transport equations for two or three turbulence parameters and so, in terms of computing costs, these models are marginally more expensive than linear two-equation EVMs but far less than DSMs. NLEVMs are unable to account accurately for history effects (since convection and diffusion of the individual Reynolds stress components are not modelled directly) but nevertheless these models have been shown to perform reasonably well in a wide variety of complex flows [34, 35].

Finally, it should be mentioned that different RANS turbulence models can be combined to make two-layer or zonal schemes. Typically a two-equation or higher-order model is used in the bulk of the flow while the near-wall region is treated with a simpler, usually algebraic or one-equation, low-Reynolds-number model. For example, the zonal model of Iacovides & Launder [36] employed a $k-\varepsilon$ model in the high-*Re* region and a van Driest mixing-length model close to walls to study the flow around pipe bends. The two-layer approach can offer savings in computing times compared to integrating a high-order model all the way to the wall surface, but there can be problems coupling the two layers in complex flows and results depend upon the location of the boundary.

1.3 Near-Wall Flow Phenomena

There is a vast amount of literature on the statistics and structure of turbulence near solid boundaries (see, for example, the review article of Moin & Mahesh [3]). The object of the present discussion is not to review this literature but merely to identify what it is about turbulent flow in the near-wall region that causes problems for turbulence modelling and to introduce some basic terminology describing the near-wall flow. The section begins by deriving the universal "laws of the wall", which describe the near-wall velocity and temperature profiles for flows close to equilibrium, after which some analytical and DNS results for the behaviour of Reynolds stresses near walls are discussed. The distance from the wall in these discussions is specified in terms of wall units or y^+ values. This is defined for simple

shear flows, where $U = U(y)$, as follows:

$$y^+ = \frac{U_\tau y}{\nu} \qquad\qquad U_\tau = \sqrt{\frac{\tau_{wall}}{\rho}} \tag{1.8}$$

where U_τ is the "friction velocity", τ_{wall} is the wall shear stress and y is the distance from the wall.

Law of the Wall for Velocity

In a zero-pressure-gradient fully-developed Couette flow in which there are no streamwise gradients of velocity or stress, the wall-normal velocity is zero from continuity and the equation for the streamwise mean U-velocity simplifies to:

$$\frac{\partial}{\partial y}\left(\mu\frac{\partial U}{\partial y} - \rho\overline{uv}\right) = 0 \tag{1.9}$$

Integrating this using the wall boundary conditions $-\rho\overline{uv} = 0$ and $\tau = \mu\partial U/\partial y = \tau_{wall}$ at $y = 0$, one obtains:

$$\mu\frac{\partial U}{\partial y} - \rho\overline{uv} = \tau_{wall} \tag{1.10}$$

In the thin region immediately adjacent to the wall ($y^+ < 5$), termed the "viscous sublayer", the Reynolds stress ($\rho\overline{uv}$) is negligible in comparison to the viscous stress ($\mu\partial U/\partial y$). Integrating Equation (1.10) with ($\rho\overline{uv} = 0$) leads to an expression in which the U-velocity is a linear function of the wall-normal distance. This is often written:

$$U^+ = y^+ \tag{1.11}$$

where U^+ is the dimensionless streamwise velocity given by $U^+ = U/U_\tau$. As one moves further away from the wall, viscous effects diminish and the turbulent stress dominates. In the fully turbulent region, from $y^+ \approx 30$ to $y/\delta \approx 0.1$ (where δ is the boundary layer thickness), viscous stresses are negligible in comparison to the turbulent stresses and Equation (1.10) simplifies to:

$$-\rho\overline{uv} = \tau_{wall} \tag{1.12}$$

Applying the mixing length hypothesis:

$$-\rho\overline{uv} = \rho l_m^2\left(\frac{\partial U}{\partial y}\right)^2 \tag{1.13}$$

assuming an equilibrium length scale, $l_m = \kappa y$, and integrating, leads to the following expression:

$$U^+ = \frac{1}{\kappa}\ln y^+ + C \tag{1.14}$$

The above formula is known as the "log-law". The two constants κ and C are usually assigned the following values for a smooth wall:

$$\kappa = 0.41 \qquad\qquad C = 5.0$$

However, values of κ and C given in turbulence modelling literature vary by approximately $\pm 8\%$. The linear and log-layers described by Equations (1.11) and (1.14) are shown in Figure 1.1 on semi-logarithmic axes. Between the two regions is a buffer zone (from approximately $y^+ = 5$ to 30) where the turbulence levels increase and viscous effects diminish with wall-distance. The combined linear and log-laws are often collectively termed the "law of the wall" and the whole region from the wall up to the outer edge of the log-law is called the "inner-layer". Beyond this region, further from the wall, is the "outer layer". Here the velocity-defect law is held to apply. This states that the difference between the mean velocity and the free-stream velocity normalized by the friction velocity, $(U_\infty - U)/U_\tau$, is a function only of dimensionless wall-distance (y/δ) and is independent of the fluid properties. However, unlike the linear and log-laws, the velocity in the outer region is flow dependent and a "universal" defect law does not exist.

Millikan [37] used an alternative approach to derive the law of the wall where the velocity profile in the viscous sublayer was assumed to be solely a function of the wall-distance (y), the wall shear stress (τ_{wall}) and fluid properties (ρ and μ), and not directly dependent upon the boundary layer thickness (δ) or the free-stream velocity, (U_∞). Dimensional arguments were then used to arrive at Equation (1.11). A similar approach can be taken in the log-layer, where the flow is considered to be independent of fluid properties, U_∞ and δ. The log-law has also recently been derived using Rapid Distortion Theory (RDT) [38].

The existence of the law of the wall has been confirmed by numerous experiments and by DNS simulations of zero pressure-gradient boundary layers [21] and channel flows [39, 40]. The discrepancy in the values of the constants used in the log-law may be because of low-Reynolds-number effects, experimental "noise" or perhaps because the log-law is being assumed to apply over too wide a portion of the flow. Both Spalart [21] and Moser *et al*. [40] when presenting their DNS data discuss the stringent criteria for a true log-law region. Moser *et al*. also assess some claims [41] that in fact the log-law is more correctly a power-law profile. Bradshaw & Huang [42] discuss in some detail the performance of the log-law in boundary layers in which there are strong streamwise pressure gradients. They argue that simply modifying the constants to be functions of the local shear stress (τ) or its gradient $(\partial\tau/\partial y)$ is unlikely to produce a generally-applicable wall model, although they also note that the log-law appears "tenacious" in providing reasonable results for non-equilibrium flows in which its underlying assumptions are no longer valid. Some authors have employed a more sophisticated characterization of the various regions than the simple approach presented above. For example Pope [5] identifies in total seven overlapping regions.

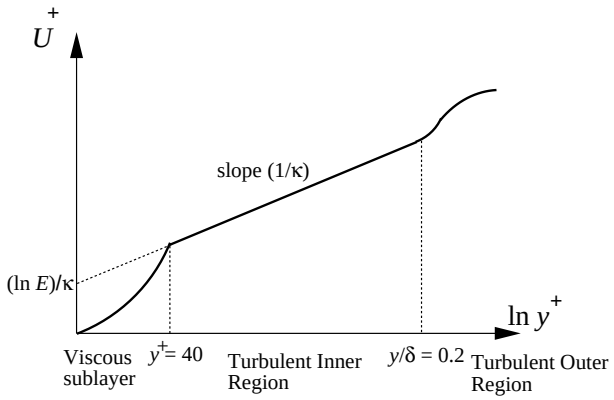

Figure 1.1: Schematic "universal" velocity distribution for a smooth wall (boundary values shown are approximate).

Law of the Wall for Temperature

Following on from the law of the wall for velocity there is a similar law for temperature. The temperature, T, is made dimensionless by the "friction" temperature, T_τ, and wall temperature, T_{wall}:

$$T^+ = \frac{(T_{wall} - T)}{T_\tau} \qquad\qquad T_\tau = \frac{q_{wall}}{\rho c_p U_\tau} \tag{1.15}$$

In the viscous-dominated sublayer, the relationship between T^+ and y^+ is given by Fourier's heat-conduction law:

$$q_{wall} = -\lambda \frac{\partial T}{\partial y} \tag{1.16}$$

which can be reformulated as:

$$T^+ = y^+ \sigma \tag{1.17}$$

where σ is the molecular Prandtl number ($\sigma = \mu c_p/\lambda$) – the ratio of a fluid's ability to diffuse momentum to its ability to diffuse heat. Further from the wall a log-law for temperature can be derived of the following form (see Cebeci & Bradshaw[43]):

$$T^+ = \frac{1}{\kappa_h} \ln\left(y^+\right) + c_h \tag{1.18}$$

where the constants are given by:

$$\kappa_h = \kappa/\sigma_t \qquad\qquad c_h = \frac{1}{\kappa_h} \ln(E) + P\left(\frac{\sigma}{\sigma_t}\right) \tag{1.19}$$

and the Jayatilleke [44] P-function is given by:

$$P\left(\frac{\sigma}{\sigma_t}\right) = 9.24\left[\left(\frac{\sigma}{\sigma_t}\right)^{3/4} - 1\right]\left\{1 + 0.28\exp\left[-0.007\left(\frac{\sigma}{\sigma_t}\right)\right]\right\} \tag{1.20}$$

The quantity σ_t is the turbulent Prandtl number (defined in analogy to the molecular Prandtl number with $\sigma_t = \mu_t c_p/\lambda_t$). Usually, the log-law for temperature is expressed:

$$T^+ = \sigma_t\left[U^+ + P\left(\frac{\sigma}{\sigma_t}\right)\right] \tag{1.21}$$

The temperature log-law is applicable in near-equilibrium flows from $y^+\sigma \approx 50$ to $y/\delta_t \approx 0.1$, where δ_t is the thickness of the thermal boundary layer. Compared to the velocity-law, the log-law for temperature appears more sensitive to streamwise pressure gradients [42].

Near-Wall Reynolds Stress Behaviour

Immediately adjacent to the wall, the behaviour of the Reynolds stresses, k and ε can be obtained from the asymptotic behaviour of the fluctuating velocity components, as follows:

$$\overline{u^2} = \overline{a_1^2}y^2 + 2\overline{a_1 a_2}y^3 + \left(\overline{a_2^2} + 2\overline{a_1 a_3}\right)y^4 + \ldots \tag{1.22}$$

$$\overline{v^2} = \overline{b_2^2}y^4 + \ldots \tag{1.23}$$

$$\overline{w^2} = \overline{c_1^2}y^2 + 2\overline{c_1 c_2}y^3 + \left(\overline{c_2^2} + 2\overline{c_1 c_3}\right)y^4 + \ldots \tag{1.24}$$

$$\overline{uv} = \overline{a_1 b_2}y^3 + \left(\overline{a_1 b_3} + \overline{a_2 b_2}\right)y^4 + \ldots \tag{1.25}$$

where the a's, b's and c's are functions of x, z and time but not of y. Due to continuity, the wall-normal fluctuating velocity component, v, dies out faster than the wall-parallel components, u and w, hence the wall-normal stress $\overline{v^2}$ increases with y^4 whilst the two wall-parallel components $\overline{u^2}$ and $\overline{w^2}$ increase as y^2. The turbulent kinetic energy, k, is given by:

$$\begin{aligned} k &= \frac{1}{2}\left(\overline{u^2} + \overline{v^2} + \overline{w^2}\right) \\ &= \frac{1}{2}\left[\left(\overline{a_1^2} + \overline{c_1^2}\right)y^2 + 2\left(\overline{a_1 a_2} + \overline{c_1 c_2}\right)y^3 + \ldots\right] \end{aligned} \tag{1.26}$$

and the dissipation rate, ε:

$$\begin{aligned} \varepsilon &= \nu\overline{\left(\frac{\partial u}{\partial y}\right)^2} + \nu\overline{\left(\frac{\partial v}{\partial y}\right)^2} + \nu\overline{\left(\frac{\partial w}{\partial y}\right)^2} \\ &= \nu\left[\left(\overline{a_1^2} + \overline{c_1^2}\right) + 4\left(\overline{a_1 a_2} + \overline{c_1 c_2}\right)y + \ldots\right] \end{aligned} \tag{1.27}$$

The dissipation rate is therefore finite at the wall ($\varepsilon = \nu\left(\overline{a_1^2} + \overline{c_1^2}\right)$ when $y = 0$). Referring back to the expression for k at the wall (Equation 1.26), the first-order terms result in the following expression for ε in terms of k:

$$\varepsilon = \nu\left(\overline{a_1^2} + \overline{c_1^2}\right) = \frac{2\nu k}{y^2} \tag{1.28}$$

At the wall surface, the dissipation rate of turbulence energy is balanced by viscous diffusion of kinetic energy towards the wall, which can be expressed:

$$\nu\frac{\partial^2 k}{\partial y^2} = \nu\frac{\partial^2\left[\left(\overline{a_1^2} + \overline{c_1^2}\right)y^2/2\right]}{\partial y^2} = \frac{2\nu k}{y^2} \tag{1.29}$$

An approximate profile for the near-wall turbulent kinetic energy production, P_k, in a zero pressure-gradient boundary layer can also be identified, as follows: in the log-layer, the shear stress is approximately constant across the near-wall region and since the strain-rate decreases as $\partial U/\partial y \propto y^{-1}$, the production-rate of kinetic energy ($P_k = \rho\overline{uv}\partial U/\partial y$) must be decreasing as the distance from the wall increases. Since $\overline{uv}$ is zero at the wall surface this means that the production-rate must reach a maximum value at some location between the wall and the log-layer. This inflection point occurs when:

$$\frac{\partial}{\partial y}\left(\rho\overline{uv}\frac{\partial U}{\partial y}\right) = 0 \tag{1.30}$$

Expanding this and substituting in Equation (1.10) it is possible to show that P_k reaches a maximum value when:

$$\mu\frac{\partial U}{\partial y} = -\rho\overline{uv} \tag{1.31}$$

i.e. when the viscous and turbulent stresses are equal. This point occurs in the buffer zone, between the linear and logarithmic regions identified above.

Detailed near-wall profiles of the Reynolds stresses, k and ε, have been obtained by DNS studies [21, 39, 40]. Profiles of the turbulence intensities, u', v' and w' from Moser *et al.* [40] for a channel flow at three different Reynolds numbers are reproduced in Figure 1.2. The largest component, the streamwise u', reaches a peak at approximately $y^+ = 13$ before decreasing sharply towards the wall. The anisotropy between the three normal Reynolds stresses is also shown. Figure 1.3, taken from Mansour *et al.* [45], shows the budget of the turbulent kinetic energy equation in a channel flow for $y^+ < 150$. Away from the wall ($y^+ > 30$) the turbulence is well approximated by the assumption of local equilbrium ($P_k = \rho\varepsilon$). As the wall is approached ($y^+ < 30$), viscous and turbulent diffusion terms increase and finally at the wall surface there is a balance between dissipation and viscous diffusion of k (as expressed above by Equations 1.28 and 1.29).

In order to discern the rapid changes in turbulence parameters across the near-wall region, as shown by the DNS results, it is clearly necessary to have a refined near-wall grid with a number of nodes within the viscous sublayer. The alternative would be to use empirically-based shape functions to represent the changes in velocity, temperature and turbulence parameters near the wall. In the

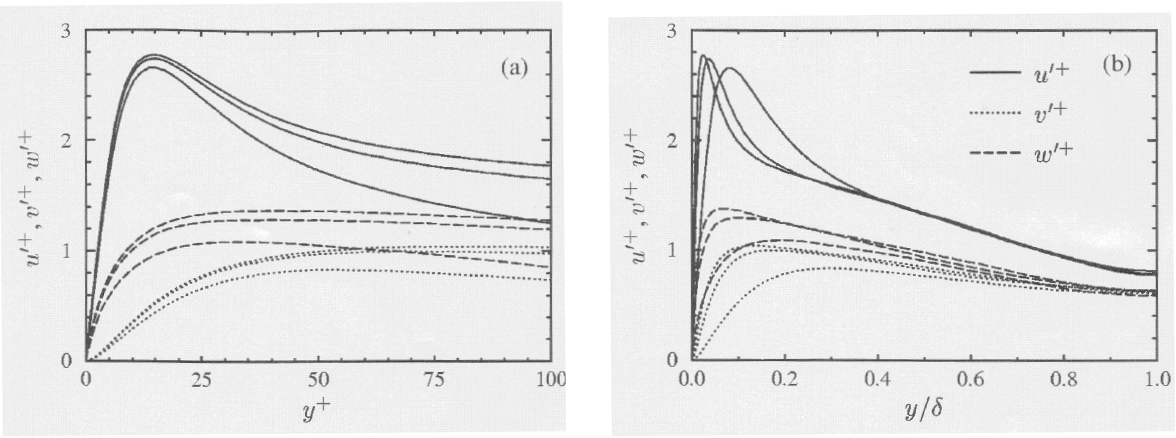

Figure 1.2: DNS predictions of the turbulence intensity across a fully-developed channel flow from Moser *et al*. [40] in wall coordinates (left) and global coordinates (right). Profiles for three Reynolds numbers are shown: $Re_\tau = U_\tau \delta/\nu = 590$, 395 and 180 (where U_τ is the friction velocity and δ the channel half-width). The peak RMS velocities generally increase with Reynolds number.

following section the implications of near-wall grid refinement are discussed along with the issue of computational costs and the need for effective wall functions.

1.4 Wall Functions vs. Low-*Re* Models

In RANS simulations of turbulent flows, there are two main approaches to the treatment of the near-wall region: the low-Reynolds-number approach and the wall-function approach. In the low-*Re* approach, specially formulated low-Reynolds-number turbulence transport equations are solved across the near-wall region. These incorporate damping functions that account for the increasing influence of molecular viscosity and the preferential damping of wall-normal fluctuating velocity components as the wall is approached. A very fine grid has to be employed[6] in order to track the rapid changes in the turbulence parameters near the wall, with typically 10 nodes within $y^+ = 10$ and the near-wall node below $y^+ = 1$. Provided that the turbulence model accounts correctly for the flow behaviour, this approach offers the greater accuracy of the two methods. However, the highly elongated cells in the near-wall region slow numerical convergence, CPU costs are high and computer storage requirements are large. The low-*Re* approach is therefore not routinely used for large and complex industrially-relevant CFD simulations.

The popular alternative is the high-*Re* approach which uses a coarse near-wall mesh so that the cell adjacent to the wall includes all of the viscous sublayer and part of the fully-turbulent region of the boundary layer (typically at the near-wall node $30 < y^+ < 300$). Transport equations solved in the main (high-*Re*) region of the flow domain therefore neglect the effects of molecular viscosity.

[6]To obtain an idea of the physical thickness of the viscous sublayer: for flow over a flat plate at a distance of one metre from the leading edge with a flow speed of 10ms^{-1} (21mph) the friction velocity is $u_\tau \approx 0.44$ms^{-1} and the physical wall-normal height corresponding to $y^+ = 5$ is: $y_n = 0.17$mm. (c.f. Rautaheimo & Siikonen [46]).

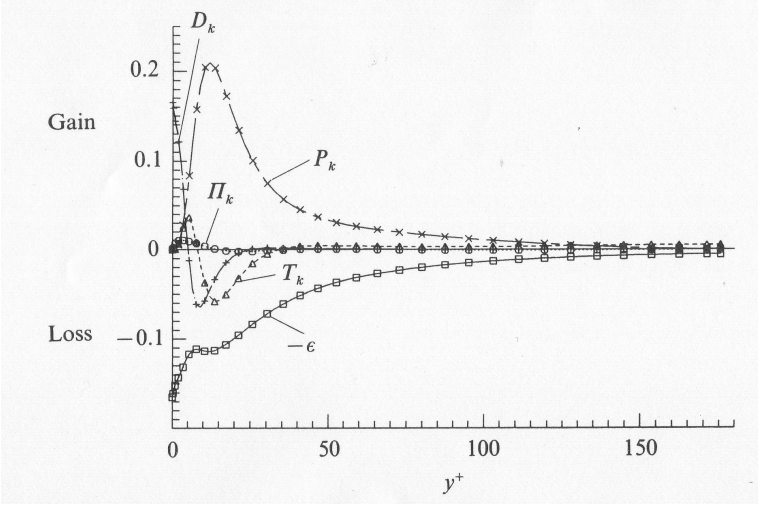

Figure 1.3: Channel flow turbulent kinetic energy equation budget taken from the DNS of Mansour *et al*. [45] for a Reynolds number, $Re = U_c\delta/\nu = 3,300$ (where U_c is the centreline velocity and δ the channel half-width). P_k = production; T_k = turbulent transport; D_k = viscous diffusion; ε_k = dissipation rate; Π_k = velocity pressure-gradient term.

In the cells adjacent to solid boundaries, empirically-based expressions (so-called "wall functions") are employed to obtain quantities such as wall shear stress which account for the influence of low-Reynolds-number effects on the flow near the wall. This approach is economical, both in computer storage and CPU time, with computations at least an order-of-magnitude faster than with the low-*Re* approach. However, the empirical profiles of velocity, turbulence parameters and temperature which are used in standard wall functions are only applicable in very simple near-wall flows and can lead to major errors in complex, non-equilibrium flows. In addition, the near-wall grid cannot be successively refined, since it is usually required to keep the near-wall node within the log-law region, and results can be sensitive to the size of the wall-adjacent cell.

A number of attempts have been made over the last 30 years to generalize wall functions for non-equilibrium flows. In the most basic wall function, the "universal" log-laws described in Section 1.3 are adopted for the wall-parallel velocity and temperature. Values of the turbulence parameters are specified at the near-wall node, based on local-equilibrium assumptions[7]. One of the first improvements upon this treatment, proposed by Launder & Spalding [48], was to replace the wall shear stress, τ_{wall}, in the velocity log-law with the turbulent kinetic energy, k (scaling the velocity with $k^{1/2}$ instead of the "friction velocity", $(\tau_{wall}/\rho)^{1/2}$, is crucial in flows involving separation, stagnation and reattachment, where the wall shear stress vanishes). The turbulent kinetic energy equation in the near-wall cell was solved using cell-averaged production and dissipation rates which were calculated by assuming constant shear stress and a linear turbulent length scale variation $\left(k^{3/2}/\varepsilon \propto y\right)$ across the near-wall

[7]For instance: $k = U_\tau^2/c_\mu^{1/2}$ and $\varepsilon = U_\tau^3/\kappa y$, based on an assumed constant shear stress $\left(\tau = -\rho\overline{uv} = c_\mu^{1/2}k\right)$ and equilibrium length scale $l = k^{3/2}/\varepsilon = c_l y$ (c.f. Grotjans & Menter [47]).

cell. However, even in fairly simple flows (fully-developed channel or pipe flow) the shear stress is not constant. Chieng & Launder [49] therefore proposed a wall function in which the near-wall cell was divided into two layers: the viscous sublayer and the fully turbulent region. In the viscous sublayer the shear stress, $\rho\overline{uv}$, was assumed to be zero and the turbulent kinetic energy to vary quadratically with wall distance, whilst in the fully turbulent region both $\rho\overline{uv}$ and k were assumed to vary linearly. Since at the wall the dissipation rate is given by $\varepsilon = 2\nu\left(\partial k^{1/2}/\partial y\right)^2$ and k varies quadratically, ε was assumed to take a uniform value in the viscous sublayer. In the fully turbulent region, ε was obtained from assuming an equilibrium turbulence length scale variation, $k^{3/2}/\varepsilon = c_l y$ (these profiles are discussed in detail in Chapter 2, see in particular Figures 2.2 and 2.3). The k-equation was solved in the near-wall cell using cell-averaged production and dissipation rates, and the dissipation rate, ε, was specified at the near-wall node. In order to locate the boundary of the viscous sublayer, the Chieng & Launder wall function assumed that the turbulence Reynolds number at the edge of the sublayer was $R_v = y_v k^{1/2}/\nu = 20$. For flows involving strong pressure gradients where the shear stress falls rapidly with wall distance, a constant value of $R_v = 20$ under-predicts the actual width of the sublayer. Johnson & Launder [50] therefore introduced a variable viscous sublayer thickness, based on the ratio of the diffusion of k towards the wall to the rate of dissipation within the sublayer. More recently, Ciofalo & Collins [51] proposed making the sublayer thickness a function of the local turbulence intensity. A review of the Launder & Spalding, Chieng & Launder and Johnson & Launder wall functions can be found in Acharya *et al*. [52] for flow past a surface-mounted 2-*D* rib. Performance characteristics of the three treatments were mixed and depended upon the turbulence model used ($k-\varepsilon$, algebraic stress or non-linear $k-\varepsilon$).

Two wall functions were proposed by Amano [53]. In the first, similar assumptions were adopted to the earlier treatments, but instead of solving only the k-equation in the near wall cell and prescribing the nodal value of ε based on local-equilibrium assumptions, Amano suggested solving transport equations for both k and ε in the near-wall cell using cell-averaged source and sink terms. The second wall function proposed by Amano used a three-layer model, in which different profiles for k and shear stress were used in the viscous sublayer, buffer layer and fully turbulent region. Better results were obtained using the three-layer model in an abrupt pipe expansion at various Reynolds numbers. A further proposal by Grotjans & Menter [47] assumed that the location of the wall, as specified by the user, was treated as the edge of the viscous sublayer. This enabled unlimited near-wall grid refinement. Wilcox [14, 54] presented two wall functions for the $k-\omega$ model. The first was analogous to a simple $k-\varepsilon$ wall function but the second included pressure-gradient terms which Wilcox suggested were necessary in order to obtain grid-independent results for flows with non-zero pressure gradients. Viegas & Rubesin [55] extended the Chieng & Launder wall function for compressible flow problems and, later, Viegas *et al*. [56] extended the treatment to enable greater flexibility of the near-wall node location: an approximate solution of the energy equation was obtained in the near-wall cell to determine the local temperature and density profiles and an additional power-law term was added into the logarithmic velocity profile expression to account for wake effects. Results using Viegas *et al*. wall

function were, for the most part, in good agreement with low-*Re* model solutions in a number of transonic and supersonic flows involving boundary-layer separation and reattachment.

All of the above-mentioned treatments rely upon an assumed semi-logarithmic velocity and temperature distribution in the near-wall cell. To avoid these limitations, Smith [57] developed a novel wall function in conjunction with a two-equation $k-kl$ model. The wall function used simplified boundary-layer transport equations for momentum, turbulent kinetic energy and internal energy, neglecting convection and assuming a parabolic turbulent length scale profile. These transport equations were solved numerically with two or three iterations per main iteration of the solution process. The approach was shown to perform well in a flat-plate flow, transonic and supersonic flows, and a hypersonic boundary layer flow involving separation and heat transfer. Boyer & Laurence [58] also developed a wall function which avoided assumptions of local equilibrium. Their approach used shape functions to represent the velocity, k and ε distribution across the near-wall cell. These shape functions consisted of the Reichard law for velocity and profiles to match channel-flow DNS data for turbulence parameters, combined with four wall scaling factors. The scaling factors were evaluated by solving equations for the mean-flow energy and turbulent kinetic energy, incorporating terms for pressure gradient, production, destruction, diffusion and convection. The wall function was shown to reproduce channel flow profiles for a range of near-wall cell sizes ($2.5 < y^+ < 100$) but the approach has yet to be applied in more complex flows.

A rather different scheme to traditional wall functions was developed in the mid-eighties at UMIST. The Parabolic SubLayer (PSL) approach [59, 60], employed a low-Reynolds-number model using a fine near-wall grid but assumed the static pressure distribution to remain constant in a thin layer adjacent to the wall. The pressure-correction algorithm was not solved in the near-wall cells and instead the wall-normal velocity was calculated from continuity. Significant savings were reported in computing times compared to full low-*Re* solutions and results were encouraging but the approach encountered difficulties in complex geometries with the calculation of velocity in corner cells.

Efforts at UMIST have recently been focussed on two new and independent wall treatments. These share some features of the numerical wall function of Smith, described above, and the LES wall function of Balaras *et al.* (see below). The first treatment is based on the analytical integration of the momentum and energy equations, accounting for the effects of convection, pressure gradient and buoyancy forces [61]. Inevitably, fairly simple prescriptions of turbulent viscosity have to be made to allow an analytical integration, but encouraging results have been obtained for forced and mixed convection flows in pipes and an opposed-jet flow involving buoyancy effects. The second treatment is the subject of this thesis and is based on the efficient one-dimensional numerical integration of simplified low-*Re* model equations across an embedded grid within the near-wall cell.

LES Wall Functions

In LES, as in RANS, there have been different approaches to modelling the near-wall flow. The most accurate approach (which Spalart [6] refers to as “Quasi-DNS”) uses fine grid-spacing in all three

coordinate directions to resolve the near-wall turbulent streaks. This involves huge computational costs and cannot be used routinely in LES calculations. Most calculations therefore employ a coarser grid and calculate the wall shear stress for the near wall cell using a variant of the log-law (see for example [62]). A notable exception is the wall function of Balaras *et al*. [63] which is mentioned here as it shares some similarities to the RANS treatment presented in this thesis. In the Balaras *et al*. wall function, an embedded grid is defined between the near-wall node and the wall. Simplified boundary-layer-type transport equations for the wall-parallel momentum are solved numerically across the embedded grid, using a mixing-length model for the eddy-viscosity, with modified van Driest damping. The velocity profiles obtained across the embedded grid are used to provide the main LES calculation with values of the instantaneous wall shear stress. Promising results were obtained by Balaras *et al*. using this treatment for plane channel, square duct and rotating channel flows with a modest computational overhead of 10-15% compared to existing log-law treatments.

1.5 Study Objectives

The objective of the work presented in this thesis is to develop and test a new wall function for flow calculations using RANS turbulence models. The ideal properties of the wall function are as follows:

- **Accuracy**: the wall function should be practically as accurate as a low-Reynolds-number model. One cannot expect it to improve upon low-*Re* model predictions without embodying more physics or empiricism.

- **Computational Speed**: current wall functions decrease the computing time by roughly an order-of-magnitude compared to low-*Re* calculations[8]. There needs to be a significant time advantage in using the new wall function over low-*Re* treatments although probably the best one could hope for would be to equal the current status quo.

- **Robustness**: the wall function should not impair the numerical stability of the calculation.

- **Flexibility**: bearing in mind the wide variety of flows in which industrial users are interested, the wall function should be able to be adapted easily to work with different turbulence models, to include heat and mass transfer effects and to work in complex geometry.

- **Ease of Use**: it should be conceptually easy to understand and simple to implement. It should also follow as closely as possible the format of existing wall functions to make it straightforward to switch from standard wall functions to the new treatment.

[8]The saving in computing time one can achieve in switching from a low-*Re* model approach to using wall functions depends upon many factors. The most significant of these is the number of walls compared to the domain size. The stated figure of an "order-of-magnitude" decrease in computing time is based on a flow involving a single wall, such as the impinging jet flow, discussed later. In flows involving a larger number of walls for the same domain size one would expect to see a greater decrease in computing time.

- **Validation**: It is easy to make coding mistakes and, if possible, there should be simple routes to validating the wall function code.

In order to test the performance of the new wall function, a variety of flows are studied: channel, impinging jet, spinning disc and simplified car-body flows. The final flow around the "Ahmed" car body is a demanding test-case both in terms of implementation and performance: the wall function has to be coded to suit a three-dimensional non-orthogonal multiblock grid arrangement while the flow involves impingement, strong streamline curvature, separation and possibly reattachment. The Ahmed body flow is recognized as an important test-case and has been the subject of two ERCOFTAC workshops[9].

In each of the flows examined, the performance of the new wall function is compared to that of standard wall functions and low-*Re* model treatments (with the exception that the Ahmed body is not considered using low-*Re* models because the computing resources for such a calculation are currently unavailable). Computing times are also compared for each of the treatments in each of the flows.

A secondary objective of the current work is to examine the performance of the two-equation NLEVM of Craft *et al*. [30]. This has previously been tested in impinging flows by Suga [34] but for slightly different geometry. Robinson [35] also tested the NLEVM in a variety of complex flows, including the Ahmed body flow, although his study did not employ the new wall function.

1.6 Outline of Thesis

The RANS equations and "standard" wall functions used in the numerical simulations are first presented in Chapter 2. Following this, in Chapter 3, the main features of the two CFD codes used in the current study, TEAM and STREAM, are presented. Chapter 4 introduces the new subgrid-based wall function. The assumptions used in its derivations are first presented, followed by an overview of the transport equations, its implementation and finally some comments on the validation of the wall function in a simple channel flow. The following three chapters then present the test cases to which the new wall function has been applied: the impinging jet, the spinning disc and the Ahmed body flows. Each of these chapters begins with an introduction and a review of previous simulations, before going on to present results and comparisons of the new wall function's performance. The main findings of the thesis are summarized in Chapter 8.

A significant proportion of this thesis consists of appendices. The first appendix presents the full set of transport equations used in axisymmetric swirling flow. This is followed by an appendix giving a general introduction to non-orthogonal curvilinear coordinates. This introduction has been included since most undergraduate and even post-graduate courses in fluid mechanics avoid the complexity of covariant and contravariant tensor analysis, which is used to derive the RANS equations in

[9] the 9th ERCOFTAC-IAHR-COST Workshop on Refined Turbulence Modelling, Darmstadt, Germany, October 4-5, 2001 and 10th ERCOFTAC-IAHR-QNET/CFD Workshop on Refined Turbulence Modelling, Poitiers, France, October 10-11, 2002.

non-orthogonal curvilinear coordinates. It is the author's experience that textbooks on the subject are also not, in general, accessible and different notation is often used in different texts. After this introduction, Appendix C presents the RANS equations in curvilinear coordinates, where velocity vectors are aligned to the curvilinear coordinate axes. The UMIST-*N* wall function transport equations in curvilinear coordinates are then presented in Appendix D. Appendix E describes the implementation of the UMIST-*N* wall function in the STREAM code. Appendix F presents the main-grid transport equations solved in STREAM. Finally, Appendix G discusses a number of routes which have been investigated in the course of developing the new wall function which, for one reason or another, have been found not to work. This information has been included in order to fully document the work, to help explain the current choice of options used in the wall function and to serve as a guide to its future development.

Figures have been included in amongst the text where possible so that the reader does not have to continually flick between pages. However, most computational grids and results have been placed in a *Figures* section at the end of the thesis to avoid the text being split over many pages.

Chapter 2

Mathematical Models

The following sections present the equations which are used in the numerical simulations documented in this thesis. For clarity, equations have been presented in Cartesian tensor notation. Equivalent expressions for axisymmetric swirling flow and for a more general non-orthogonal coordinate system are provided in Appendices A and C.

2.1 Reynolds-Averaged Navier-Stokes Equations

The Reynolds-averaged expression for the conservation of mass, or as it is commonly termed the continuity equation, is expressed in Cartesian tensors as follows:

$$\frac{\partial \rho}{\partial t} + \frac{\partial}{\partial x_j}(\rho U_j) = 0 \tag{2.1}$$

where upper-case U_j is the mean velocity vector which has components (U,V,W) in the Cartesian (x,y,z) directions. Summation is implied by repeated indices and so the above expression can be expanded:

$$\frac{\partial \rho}{\partial t} + \frac{\partial}{\partial x}(\rho U) + \frac{\partial}{\partial y}(\rho V) + \frac{\partial}{\partial z}(\rho W) = 0 \tag{2.2}$$

Equation (2.1) can also be expanded, using the product rule:

$$\underbrace{\frac{\partial \rho}{\partial t}} + \rho\frac{\partial U_j}{\partial x_j} + \underbrace{U_j\frac{\partial \rho}{\partial x_j}} = 0 \tag{2.3}$$

For steady flows that do not involve compressibility effects, the two underbraced terms in the above expression are zero and continuity is written simply:

$$\frac{\partial U_j}{\partial x_j} = 0 \tag{2.4}$$

The above expression can also be employed for steady buoyancy-affected flows (provided they do not involve shock-waves) where it is assumed that density-gradients $(\partial\rho/\partial x_j)$ are small in comparison with strain-rates $(\partial U_j/\partial x_j)$.

The RANS equation for transport of momentum can be written in Cartesian tensors as follows:

$$\frac{\partial}{\partial t}(\rho U_i) + \frac{\partial}{\partial x_j}(\rho U_i U_j) = -\frac{\partial P}{\partial x_i} + \frac{\partial \tau_{ij}}{\partial x_j} \tag{2.5}$$

where P is the mean pressure and the stress tensor, τ_{ij}, is given by:

$$\tau_{ij} = \mu\left(\frac{\partial U_i}{\partial x_j} + \frac{\partial U_j}{\partial x_i} - \underbrace{\frac{2}{3}\delta_{ij}\frac{\partial U_k}{\partial x_k}}\right) - \rho\overline{u_i u_j} \tag{2.6}$$

The term $\overline{u_i u_j}$ is the Reynolds stress tensor and δ_{ij} the Kronecker delta which is zero if $i \neq j$ and unity if $i = j$. The underbraced term in Equation (2.6) makes the trace[1] of the viscous stress tensor zero. In its most general form, the Boussinesq Eddy-Viscosity Model (EVM) can be written in Cartesian tensors:

$$-\rho\overline{u_i u_j} = \mu_t\left(\frac{\partial U_i}{\partial x_j} + \frac{\partial U_j}{\partial x_i} - \underbrace{\frac{2}{3}\delta_{ij}\frac{\partial U_k}{\partial x_k}}\right) - \underbrace{\frac{2}{3}\delta_{ij}\rho k} \tag{2.8}$$

where k is the turbulent kinetic energy and the two underbraced terms are included to satisfy the trace condition, $\overline{u_i u_i} = 2k$.

2.2 Linear $k-\varepsilon$ Model

In the low-Reynolds-number linear $k-\varepsilon$ model of Launder & Sharma, the eddy-viscosity is calculated from:

$$\mu_t = \rho c_\mu f_\mu \frac{k^2}{\tilde{\varepsilon}} \tag{2.9}$$

where c_μ is assumed constant $(c_\mu = 0.09)$, the damping function f_μ is given by:

$$f_\mu = \exp\left[\frac{-3.4}{\left(1+\tilde{R}_t/50\right)^2}\right] \tag{2.10}$$

[1]The trace of the expression is obtained by setting $i = j$ and summing over repeated indices. The trace of the viscous part of the stress tensor is given by:

$$\mu\left(\frac{\partial U_i}{\partial x_i} + \frac{\partial U_i}{\partial x_i} - 2\frac{\partial U_k}{\partial x_k}\right) = 0 \tag{2.7}$$

Tensors with zero trace are also called “deviatoric”. If the flow is incompressible the underbraced term in Equation (2.6) is zero.

and the turbulence Reynolds number, $\tilde{R}_t$, is defined by:

$$\tilde{R}_t = \frac{k^{1/2} l}{\nu} = \frac{k^2}{\nu \tilde{\varepsilon}} \tag{2.11}$$

The function f_μ accounts for both the true viscous damping at low Reynolds number and the preferential damping of the wall-normal fluctuations as the wall is approached.

Transport equations are solved for the turbulent kinetic energy, k, and isotropic dissipation rate, $\tilde{\varepsilon}$. The exact transport equation for k can be derived from its definition $(k = \overline{u_i u_i}/2)$, using the transport equation for the Reynolds stress tensor, $\overline{u_i u_j}$ and approximating diffusion terms in the resulting expression by an eddy-diffusivity model. This gives the following expression:

$$\frac{\partial}{\partial t}(\rho k) + \frac{\partial}{\partial x_j}(\rho U_j k) = \frac{\partial}{\partial x_j}\left[\left(\mu + \frac{\mu_t}{\sigma_k}\right)\frac{\partial k}{\partial x_j}\right] + P_k - \rho\varepsilon \tag{2.12}$$

The terms on the left-hand side represent convection and those on the right are diffusion, production and dissipation, respectively (reading left to right). The constant σ_k is the effective Prandtl number for the diffusion of kinetic energy (taken as $\sigma_k = 1.0$ in the Launder-Sharma model) and the production rate of kinetic energy, P_k, is calculated from:

$$P_k = -\rho\overline{u_i u_j}\frac{\partial U_i}{\partial x_j} \tag{2.13}$$

Unlike turbulent kinetic energy, the dissipation rate does not fall to zero at the wall. Instead ε takes a value at the wall which balances the rate of diffusion of turbulent kinetic energy towards the wall (as discussed in Section 1.3). For numerical convenience, rather than solve an equation for ε, a transport equation is solved for the isotropic dissipation rate $(\tilde{\varepsilon})$ which, by definition, falls to zero on the wall surface (see Jones & Launder [12]). The dissipation rate term appearing in the k-equation is the total dissipation rate, defined as:

$$\varepsilon = \tilde{\varepsilon} + 2\nu\left(\frac{\partial k^{1/2}}{\partial x_j}\right)^2 \tag{2.14}$$

The modelled equation for the isotropic dissipation rate follows a similar format to the k-equation, being composed of convection, diffusion, production and dissipation components:

$$\frac{\partial}{\partial t}(\rho\tilde{\varepsilon}) + \frac{\partial}{\partial x_j}(\rho U_j \tilde{\varepsilon}) = \frac{\partial}{\partial x_j}\left[\left(\mu + \frac{\mu_t}{\sigma_\varepsilon}\right)\frac{\partial \tilde{\varepsilon}}{\partial x_j}\right] + c_{\varepsilon 1} f_1 P_k \frac{\tilde{\varepsilon}}{k} - c_{\varepsilon 2} f_2 \rho \frac{\tilde{\varepsilon}^2}{k} + \rho Y_c + P_{\varepsilon 3} \tag{2.15}$$

The final two terms on the right-hand-side of the above equation are the Yap correction, Y_c, and a low-Reynolds-number turbulence damping term, $P_{\varepsilon 3}$ (sometimes denoted E). The Yap correction [64] is used to reduce the departure of the turbulence length scale $\left(l = k^{3/2}/\varepsilon\right)$ from the local equilibrium length scale $(l_e = 2.55y)$. It was developed initially in response to studies of impinging jets and pipe expansions that showed that the linear $k-\varepsilon$ model overpredicted heat transfer near the stagnation and

reattachment points (see, for example, [65]). The standard Yap correction is given by:

$$Y_c = \max\left\{\left[0.83\left(\frac{k^{3/2}/\tilde{\varepsilon}}{2.55y}-1\right)\left(\frac{k^{3/2}/\tilde{\varepsilon}}{2.55y}\right)^2\frac{\tilde{\varepsilon}^2}{k}\right],0\right\} \tag{2.16}$$

where y is the wall-normal distance. The above expression can introduce problems in certain flows with complex geometry where it is difficult to define a wall-normal distance. For this reason, Iacovides & Raisee [66] introduced an alternative correction based on the gradient of the length scale (a so-called differential Yap correction, Y_{dc}) which is independent of wall distance. This takes the following form:

$$Y_{dc} = c_w\frac{\tilde{\varepsilon}^2}{k}\max\left[F\left(F+1\right)^2,0\right] \tag{2.17}$$

where:

$$F = \frac{1}{c_l}\left[\left(\frac{\partial l}{\partial x_j}\frac{\partial l}{\partial x_j}\right)^{1/2} - dl_e dy\right] \tag{2.18}$$

$$dl_e dy = c_l\left[1-\exp\left(-B_\varepsilon\tilde{R}_t\right)\right] + B_\varepsilon c_l\tilde{R}_t\exp\left(-B_\varepsilon\tilde{R}_t\right) \tag{2.19}$$

c_l	B_ε	c_w
2.55	0.1069	0.83

The c_w constant was later modified by Craft *et al*. [67] to reduce the degree of correction in regions of high straining and to improve numerical stability. In this more recent form, c_w is made a function of the strain-rate and vorticity invariants and turbulence Reynolds number, as follows:

$$c_w = \frac{0.83\min(1,\tilde{R}_t/5)}{\left[0.8+0.7\left(\eta'/3.33\right)^4\exp(-\tilde{R}_t/12.5)\right]} \tag{2.20}$$

where:

$$\eta' = \max\left(\tilde{S}',\tilde{\Omega}'\right) \tag{2.21}$$

$$\tilde{S}' = \max\left(\frac{k}{\tilde{\varepsilon}},\sqrt{\frac{\nu}{\varepsilon}}\right)\sqrt{\frac{1}{2}S_{ij}S_{ij}} \tag{2.22}$$

$$\tilde{\Omega}' = \max\left(\frac{k}{\tilde{\varepsilon}},\sqrt{\frac{\nu}{\varepsilon}}\right)\sqrt{\frac{1}{2}\Omega_{ij}\Omega_{ij}} \tag{2.23}$$

The effect of the Yap correction is far greater with low-Reynolds-number formulations than with standard wall functions formulations, but the effect is still measurable with the latter (see discussion in Chapter 5, in particular Figures 5.31 and 5.32). Both "standard" and differential Yap corrections are tested in this thesis, the latter using the variable c_w of Craft *et al*. (Equation 2.20).

The gradient production source term, $P_{\varepsilon 3}$, is included in the $\tilde{\varepsilon}$-equation to obtain the correct near-wall distribution of k [12]. The expression for $P_{\varepsilon 3}$ and the remaining constants and damping functions

used in the $\tilde{\varepsilon}$-equation are as follows:

$$P_{\varepsilon 3} = 2\mu\nu_t \left(\frac{\partial^2 U_i}{\partial x_j \partial x_k} \right)^2 \tag{2.24}$$

$$f_1 = 1.0 \tag{2.25}$$

$$f_2 = 1.0 - 0.3\exp\left(\tilde{R}_t^2\right) \tag{2.26}$$

$c_{\varepsilon 1}$	$c_{\varepsilon 2}$	σ_ε
1.44	1.92	1.3

2.3 Non-Linear $k-\varepsilon$ Model

In the non-linear eddy-viscosity model (NLEVM) of Craft *et al*. [30], additional quadratic and cubic functions of strain and vorticity are introduced into the equation for the Reynolds stress. The constitutive equation for the Reynolds stress anisotropy, a_{ij}, defined as the ratio of the deviatoric Reynolds stress to the turbulent kinetic energy, is as follows:

$$\begin{aligned} a_{ij} \equiv \frac{\overline{u_i u_j}}{k} - \frac{2}{3}\delta_{ij} = & -\frac{\nu_t}{k} S_{ij} \\ & + c_1 \frac{\nu_t}{\tilde{\varepsilon}} \left(S_{ik}S_{kj} - \frac{1}{3} S_{kl}S_{kl}\delta_{ij} \right) \\ & + c_2 \frac{\nu_t}{\tilde{\varepsilon}} \left(\Omega_{ik}S_{kj} + \Omega_{jk}S_{ki} \right) \\ & + c_3 \frac{\nu_t}{\tilde{\varepsilon}} \left(\Omega_{ik}\Omega_{jk} - \frac{1}{3}\Omega_{lk}\Omega_{lk}\delta_{ij} \right) \\ & + c_4 \frac{\nu_t k}{\tilde{\varepsilon}^2} \left(S_{ki}\Omega_{lj} + S_{kj}\Omega_{li} \right) S_{kl} \\ & + c_5 \frac{\nu_t k}{\tilde{\varepsilon}^2} \left(\Omega_{il}\Omega_{lm}S_{mj} + S_{il}\Omega_{lm}\Omega_{mj} - \frac{2}{3} S_{lm}\Omega_{mn}\Omega_{nl}\delta_{ij} \right) \\ & + c_6 \frac{\nu_t k}{\tilde{\varepsilon}^2} S_{ij}S_{kl}S_{kl} \\ & + c_7 \frac{\nu_t k}{\tilde{\varepsilon}^2} S_{ij}\Omega_{kl}\Omega_{kl} \end{aligned} \tag{2.27}$$

where the strain-rate and vorticity tensors are given by:

$$S_{ij} = \frac{\partial U_i}{\partial x_j} + \frac{\partial U_j}{\partial x_i} \qquad \Omega_{ij} = \frac{\partial U_i}{\partial x_j} - \frac{\partial U_j}{\partial x_i} \tag{2.28}$$

Quadratic combinations of S and Ω are necessary in order to capture the Reynolds stress anisotropy in simple shear flows, whilst cubic terms are necessary to correct for streamline curvature and swirl (for details see [34]).

The eddy-viscosity is calculated as previously in the linear EVM:

$$\nu_t = c_\mu f_\mu \frac{k^2}{\tilde{\varepsilon}} \tag{2.29}$$

and the near-wall damping function, f_μ, and the $\tilde{\varepsilon}$-equation source term, $P_{\varepsilon 3}$, are re-optimized:

$$f_\mu = 1 - \exp\left[\left(-\frac{\tilde{R}_t}{90}\right)^{1/2} - \left(-\frac{\tilde{R}_t}{400}\right)^2\right] \tag{2.30}$$

$$\begin{aligned} P_{\varepsilon 3} &= 0.0022\frac{\tilde{S}\mu_t k^2}{\tilde{\varepsilon}}\left(\frac{\partial^2 U_i}{\partial x_j \partial x_k}\right)^2 \quad \text{for} \quad \tilde{R}_t \leq 250 \\ &= 0 \qquad\qquad\qquad\qquad\qquad\quad \text{for} \quad \tilde{R}_t > 250 \end{aligned} \tag{2.31}$$

where $\tilde{S}$ is the dimensionless strain invariant, calculated from:

$$\tilde{S} = \frac{k}{\tilde{\varepsilon}}\sqrt{\frac{1}{2}S_{ij}S_{ij}} \tag{2.32}$$

The constant value of c_μ used in the Launder & Sharma $k-\varepsilon$ model was derived by considering simple shear flows where production and dissipation of turbulence energy are in balance and hence the ratio of shear stress to kinetic energy is approximately constant ($c_\mu = (\overline{uv}/k)^2 \approx 0.09$). In the Craft *et al*. model, c_μ is made a function of the strain-rate and vorticity invariants. The original formulation for c_μ, developed by Suga [34], is as follows:

$$c_\mu = \min\left(0.09, \frac{0.3}{1+0.35\eta^{1.5}}\left\{1-\exp\left[-0.36\exp\left(0.75\eta\right)\right]\right\}\right) \tag{2.33}$$

where:

$$\eta = \max\left(\tilde{S}, \tilde{\Omega}\right) \tag{2.34}$$

and the dimensionless vorticity invariant, $\tilde{\Omega}$, is given by:

$$\tilde{\Omega} = \frac{k}{\tilde{\varepsilon}}\sqrt{\frac{1}{2}\Omega_{ij}\Omega_{ij}} \tag{2.35}$$

More recently, Craft *et al*. [67] introduced a c_μ function with a slightly weaker dependence on the strain and vorticity invariants which was found to suffer less from unstable feedback[2]:

$$c_\mu = \min\left(0.09, \frac{1.2}{1+3.5\eta+f_{RS}}\right) \tag{2.36}$$

with:

$$f_{RS} = 0.235\left[\max\left(0, \eta - 3.333\right)\right]^2\left[\exp\left(-\tilde{R}_t/400\right) + \sqrt{S_I^2}\right] \tag{2.37}$$

where the third invariant of the strain-rate tensor, S_I, is given by:

$$S_I = \frac{S_{ij}S_{jk}S_{ki}}{\left(S_{nl}S_{nl}/2\right)^{3/2}} \tag{2.38}$$

[2] As discussed in Craft *et al*. [67], a c_μ function based on strain and vorticity invariants can lead to numerical instabilities where an overpredicted strain-rate leads to a reduced c_μ, which in turn reduces the eddy-viscosity and leads to an increased strain-rate, which then reduces c_μ etc.

Both of the above c_μ functions have been tested in this thesis. The recent Craft *et al*. paper also described a number of methods for improving the stability of the NLEVM. The last two cubic terms in the NLEVM expression, Equation (2.27), with coefficients c_6 and c_7 are tensorially linear, being composed of a product of the strain-rate, S_{ij}, and a scalar parameter. The linear term and these two cubic terms can thus be combined as follows:

$$\begin{aligned} a_{ij} \equiv \frac{\overline{u_i u_j}}{k} - \frac{2}{3}\delta_{ij} = \; & - \left(\frac{\nu_t}{k} - c_6 \frac{\nu_t k}{\tilde{\varepsilon}^2} S_{kl} S_{kl} - c_7 \frac{\nu_t k}{\tilde{\varepsilon}^2} \Omega_{kl} \Omega_{kl} \right) S_{ij} \\ & + c_1 \frac{\nu_t}{\tilde{\varepsilon}} \left(S_{ik} S_{kj} - \frac{1}{3} S_{kl} S_{kl} \delta_{ij} \right) \\ & + c_2 \frac{\nu_t}{\tilde{\varepsilon}} \left(\Omega_{ik} S_{kj} + \Omega_{jk} S_{ki} \right) \\ & + c_3 \frac{\nu_t}{\tilde{\varepsilon}} \left(\Omega_{ik} \Omega_{jk} - \frac{1}{3} \Omega_{lk} \Omega_{lk} \delta_{ij} \right) \\ & + c_4 \frac{\nu_t k}{\tilde{\varepsilon}^2} \left(S_{ki} \Omega_{lj} + S_{kj} \Omega_{li} \right) S_{kl} \\ & + c_5 \frac{\nu_t k}{\tilde{\varepsilon}^2} \left(\Omega_{il} \Omega_{lm} S_{mj} + S_{il} \Omega_{lm} \Omega_{mj} - \frac{2}{3} S_{lm} \Omega_{mn} \Omega_{nl} \delta_{ij} \right) \end{aligned} \tag{2.39}$$

When the sum of the c_6 and c_7 terms in the first line of Equation (2.39) is negative, their contribution to the coefficient of S_{ij} will be positive, in effect increasing the magnitude of the eddy-viscosity, which improves numerical stability. The momentum equation can therefore be rewritten, following the same sign convention used in Craft *et al*. [67]:

$$\rho U_j \frac{\partial U_i}{\partial x_j} = \frac{\partial P}{\partial x_i} + \frac{\partial}{\partial x_j} \left(\left(\mu + \mu_t' \right) S_{ij} - \rho \widehat{\overline{u_i u_j}} \right) \tag{2.40}$$

where the modified eddy-viscosity, μ_t', includes any positive contribution from the last two cubic terms in Equation (2.27), and $\widehat{\overline{u_i u_j}}$ contains the remaining higher-order components of the Reynolds stress, i.e.:

$$\mu_t' = \mu_t - \mu_t \frac{k^2}{\tilde{\varepsilon}^2} \min \left[\left(c_6 S_{kl} S_{kl} + c_7 \Omega_{kl} \Omega_{kl} \right), 0 \right] \tag{2.41}$$

$$\begin{aligned}
\rho\widehat{\overline{u_i u_j}} &= c_1\frac{\mu_t k}{\tilde{\varepsilon}}\left(S_{ik}S_{kj}-\frac{1}{3}S_{kl}S_{kl}\delta_{ij}\right)\\
&+c_2\frac{\mu_t k}{\tilde{\varepsilon}}\left(\Omega_{ik}S_{kj}+\Omega_{jk}S_{ki}\right)\\
&+c_3\frac{\mu_t k}{\tilde{\varepsilon}}\left(\Omega_{ik}\Omega_{jk}-\frac{1}{3}\Omega_{lk}\Omega_{lk}\delta_{ij}\right)\\
&+c_4\frac{\mu_t k^2}{\tilde{\varepsilon}^2}\left(S_{ki}\Omega_{lj}+S_{kj}\Omega_{li}\right)S_{kl}\\
&+c_5\frac{\mu_t k^2}{\tilde{\varepsilon}^2}\left(\Omega_{il}\Omega_{lm}S_{mj}+S_{il}\Omega_{lm}\Omega_{mj}-\frac{2}{3}S_{lm}\Omega_{mn}\Omega_{nl}\delta_{ij}\right)\\
&+\frac{\mu_t k^2}{\tilde{\varepsilon}^2}\max\left[\left(c_6S_{kl}S_{kl}+c_7\Omega_{kl}\Omega_{kl}\right),0\right] \qquad (2.42)
\end{aligned}$$

Following this treatment, the turbulence energy production can be written:

$$\begin{aligned}
P_k &= -\rho\overline{u_i u_j}\frac{\partial U_i}{\partial x_j}\\
&= \left(\mu_t' S_{ij}-\rho\widehat{\overline{u_i u_j}}\right)\frac{\partial U_i}{\partial x_j} \qquad (2.43)
\end{aligned}$$

The Craft *et al*. model was developed with reference to flow in curved channels, through a rotating pipe, transitional flow over a flat plate, impinging jet flow and flow over a turbine blade [34]. The model has since been applied to abrupt pipe expansions [67], flow through ribbed passages [68], flow over a square cylinder adjacent to a wall, through a 10° plane diffuser, through a square-section U-bend and over a three-dimensional simplified car body [35]. The recent studies by Robinson in a plane diffuser concluded that the model was able to predict smooth wall separation and reattachment in an adverse pressure gradient. For flow through the U-bend which involves strong flow curvature and streamwise vorticity, the predicted velocity profiles were in good agreement with experiments (in fact, as good as the more sophisticated cubic differential stress model of Craft *et al*. [69]). However, for flow over the "Ahmed" car body, the model predicted boundary layer separation over the 25° rear slant whereas experiments (and a linear $k-\varepsilon$ model) indicated that the flow was attached. This discrepancy is discussed in greater detail in Chapter 7.

2.4 "Standard" Wall Functions

In the following section and in later discussions it is necessary to distinguish between the relatively simple log-law based wall functions and the new numerical wall function. To make this distinction clear, all the wall functions which prescribe log-law velocity and temperature profiles within the near-wall cell are called "standard" treatments. The section begins by identifying some common features of the standard wall functions which are tested in the current work, before proceeding to discuss each wall function in more detail. Implementation of the wall functions into the two codes, TEAM and STREAM, are discussed in more detail in Chapter 3.

2.4.1 Common Features

All of the standard wall functions presented below (Sections 2.4.2 to 2.4.5) follow the same functional form. Each involves the modification of the discretized transport equations for momentum, kinetic energy and dissipation rate in the near-wall cell to account for the presence of the wall. For a description of the near-wall cell notation (e.g. locations of nodes P and N) see Figure 2.1.

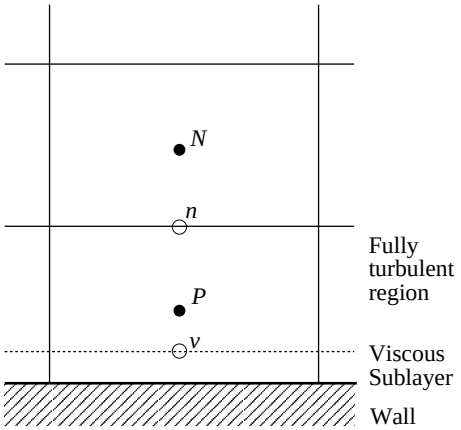

Figure 2.1: Cell notation used by standard wall functions.

Momentum

All of the standard wall functions make use of the log-law for determining the wall shear stress, τ_{wall}, using the velocity scale $\left(c_\mu^{1/4}k^{1/2}\right)$:

$$\begin{aligned} U^+ &= \frac{1}{\kappa}\ln(Ey^+) \\ \frac{c_\mu^{1/4}k^{1/2}U}{\tau_{wall}/\rho} &= \frac{1}{\kappa}\ln\left(\frac{Ec_\mu^{1/4}k^{1/2}y}{\nu}\right) \end{aligned} \tag{2.44}$$

which can be rearranged as:

$$\tau_{wall} = \frac{\rho\kappa c_\mu^{1/4}k^{1/2}U}{\ln\left(Ec_\mu^{1/4}k^{1/2}y/\nu\right)} \tag{2.45}$$

In some wall functions k is evaluated at the near-wall node, denoted k_P, and in others, at the edge of the viscous sublayer, k_v. The above conditions apply if the near-wall node is within the fully-turbulent region, which is defined as $y^+ > 11.6$. If the viscous sublayer is large in comparison to the width of the near-wall cell and $y^+ < 11.6$, the linear-law should be used:

$$U^+ = y^+ \tag{2.46}$$

which gives the following expression for the wall shear stress:

$$\tau_{wall} = \mu \frac{U}{y} \tag{2.47}$$

In the spinning-disc case examined later, the wall is rotating at an angular velocity $W_{wall} = \Omega r$. Using a stationary reference frame, the dimensionless tangential velocity is therefore given by:

$$W^+ = \frac{W - W_{wall}}{W_\tau} \tag{2.48}$$

Analogous expressions to Equations (2.45) and (2.47) can be defined for the wall shear stress in the tangential direction.

Turbulent Kinetic Energy

The transport equation for k is solved for the near-wall nodes (node P in Figure 2.1) but since production, P_k, and dissipation, ε, are expected to change rapidly across the near-wall region, it is not suitable to use values of P_k and ε evaluated at the centre of the cell. Instead, values of P_k and ε are substituted with cell-averaged $\overline{P_k}$ and $\overline{\varepsilon}$ terms which take into account the changes in turbulence quantities across the near-wall cell. These averaged quantities are approximated differently in different wall functions and it is principally through changes in the assumed profiles of turbulent stress ($\tau = -\rho\overline{u_i u_j}$) and k, used in $\overline{P_k}$ and $\overline{\varepsilon}$, that improvements in the standard wall functions are achieved.

The wall functions, presented below, all describe an averaged production term due to shear stress which is denoted $\overline{P_{kuv}}$. In impinging, separating or reattaching flows the normal stress contribution to k-production is significant and so it is inadvisable to use only the shear stress contribution. In the impinging jet and spinning disc calculations, described later, a normal stress contribution has therefore been included in $\overline{P_k}$. This has been calculated based on the normal stress at the near-wall node and the strain-rate across the cell (based on the velocity interpolated to the cell boundaries). For a two-dimensional Cartesian grid arrangement the cell-averaged production is therefore given by:

$$\overline{P_k} = \overline{P_{kuv}} - \rho\overline{uu}\frac{\partial U}{\partial x} - \rho\overline{vv}\frac{\partial V}{\partial y} \tag{2.49}$$

In Chapter 5 the effects of neglecting the normal stress contribution to $\overline{P_k}$ on heat transfer predictions for the impinging jet are discussed (see Figures 5.39 and 5.42).

Dissipation Rate

The transport equation for ε is not solved at the near-wall nodes in the standard wall functions considered here, but instead the value of ε_P is prescribed from equilibrium length scale assumptions. The

equilibrium length scale is given by:

$$l_m = c_\mu^{3/4} \frac{k^{3/2}}{\varepsilon} = \kappa y \tag{2.50}$$

and hence the dissipation rate at the near-wall node is prescribed as:

$$\varepsilon_P = \frac{c_\mu^{3/4} k_P^{3/2}}{\kappa y_P} \tag{2.51}$$

Temperature

For calculations involving heat transfer, the wall temperature is calculated using the log-law:

$$T^+ = \frac{1}{\kappa_h} \ln\left(y^+\right) + c_h \tag{2.52}$$

which can be rearranged to give:

$$T^+ = \sigma_t \left(U^+ + P\right) \tag{2.53}$$

where P is the function of Jayatilleke [44], σ_t is the turbulent Prandtl number and the dimensionless temperature, T^+, is given by:

$$T^+ = \frac{(T_{wall} - T)}{T_\tau} \qquad\qquad T_\tau = \frac{q_{wall}}{\rho c_p U_\tau} \tag{2.54}$$

This can be rearranged into an expression for either the wall temperature, T_{wall}:

$$T_{wall} = T_P + \frac{q_{wall} \sigma_t \left(U^+ + P\right)}{\rho c_p c_\mu^{1/4} k_P^{1/2}} \tag{2.55}$$

or the wall heat flux, q_{wall}:

$$q_{wall} = \frac{\rho c_p c_\mu^{1/4} k_p^{1/2} \left(T_{wall} - T_P\right)}{\sigma_t \left(U^+ + P\right)} \tag{2.56}$$

If the near-wall node is within the viscous sublayer, defined as $y^+ < 11.6$, Fourier’s heat conduction law is applied instead of the log-law:

$$T^+ = y^+ \sigma \tag{2.57}$$

where σ is the molecular Prandtl number ($\sigma = \mu c_p / \lambda$). This can be rearranged for wall temperature, T_{wall}:

$$T_{wall} = T + \frac{q_{wall}}{\lambda} y \tag{2.58}$$

or wall heat flux, q_{wall}:

$$q_{wall} = \lambda \frac{(T_{wall} - T)}{y} \tag{2.59}$$

2.4.2 Launder & Spalding (TEAM)

The original TEAM code used the wall function of Launder & Spalding [48] (see also the TEAM manual [70]). This calculates the wall shear stress from the log-law with properties evaluated at the near-wall node P:

$$\frac{c_\mu^{1/4} k_P^{1/2} U_P}{\tau_{wall}/\rho} = \frac{1}{\kappa} \ln\left(\frac{E c_\mu^{1/4} k_P^{1/2} y_P}{\nu}\right) \tag{2.60}$$

with constants $\kappa = 0.42$ and $E = 9.79$. The average production of k due to shear stress is calculated assuming a constant shear stress across the whole of the near-wall cell ($\tau = \tau_{wall}$) including viscous sublayer, and the strain-rate used in the cell-averaged production term is simply taken from the nodal value of velocity ($\partial U/\partial y = U_P/y_P$):

$$\overline{P_{kuv}} = \frac{1}{y_n}\int_0^{y_n} -\rho\overline{uv}\frac{\partial U}{\partial y}\mathrm{d}y = \tau_{wall}\frac{U_P}{y_P} \tag{2.61}$$

Likewise, the average dissipation rate is found from assuming that $-\rho\overline{uv} = \tau_{wall}$ and $\partial U/\partial y = U_P/y_P$:

$$-\rho\overline{uv} = \tau_{wall} = \mu_t \frac{\partial U}{\partial y} \tag{2.62}$$

$$\frac{\tau_{wall}}{\rho} = c_\mu \frac{k^2}{\varepsilon}\frac{U_P}{y_P} \tag{2.63}$$

and substituting in $U^+ = \rho c_\mu^{1/4} k_P^{1/2} U/\tau_{wall}$:

$$\overline{\varepsilon} = \frac{c_\mu^{3/4} k_P^{3/2} U_P^+}{y_P} \tag{2.64}$$

2.4.3 Simplified Chieng & Launder (SCL)

In the Simplified Chieng & Launder (SCL) wall function, the wall shear stress is evaluated as previously with the original TEAM wall function. For the average production, in the fully turbulent region, the turbulent shear stress is assumed to be constant and equal to the wall shear stress while in the viscous sublayer the turbulent stress is assumed to be zero (see Figure 2.2). The strain rate ($\partial U/\partial y$) is determined from differentiating the log-law.

$$\overline{P_{kuv}} = \frac{1}{y_n}\int_{y_v}^{y_n} \tau_{wall}\frac{\tau_{wall}}{\kappa c_\mu^{1/4}\rho k_P^{1/2} y}\mathrm{d}y = \frac{\tau_{wall}^2}{\kappa c_\mu^{1/4}\rho k_P^{1/2} y_n}\ln\left(\frac{y_n}{y_v}\right) \tag{2.65}$$

where the sublayer thickness, y_v, is found from assuming a constant sublayer Reynolds number, ($R_v = k_P^{1/2} y_v/\nu = 20$).

The average dissipation rate is obtained by assuming ε to be constant in the viscous sublayer and equal to its wall limiting value, such that k increases quadratically across the viscous sublayer. In the

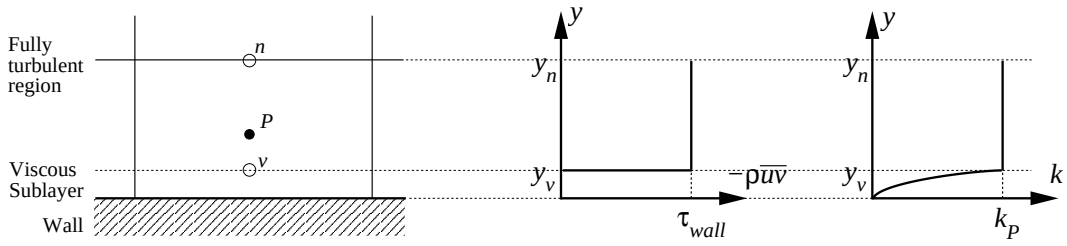

Figure 2.2: Simplified Chieng & Launder wall function: assumed profiles of turbulent shear stress $(-\rho\overline{uv})$ and turbulent kinetic energy (k) across the near-wall cell.

turbulent region ε varies according to the equilibrium length scale $\left(k^{3/2}/\varepsilon = c_l y\right)$ and the turbulent kinetic energy is assumed to be constant outside the sublayer $(k = k_P)$.

$$\overline{\varepsilon} = \frac{1}{y_n}\left(y_v \frac{2\nu k_P}{y_v^2} + \int_{y_v}^{y_n} \frac{k_P^{3/2}}{c_l y}\mathrm{d}y\right) = \frac{1}{y_n}\left[\frac{2k_P^{3/2}}{k_P^{1/2} y_v/\nu} + \frac{k_P^{3/2}}{c_l}\ln\left(\frac{y_n}{y_v}\right)\right] \tag{2.66}$$

2.4.4 Chieng & Launder (CL)

The Chieng & Launder wall function [49] accounts for variations in turbulent stress $(-\rho\overline{uv})$ and kinetic energy across the near-wall cell. The log-law is defined using k extrapolated to the edge of the viscous sublayer (k_v) in order to make the value of τ_{wall} less dependent upon the physical location of the near-wall node y_P:

$$\frac{c_\mu^{1/4} k_v^{1/2} U_P}{\tau_{wall}/\rho} = \frac{1}{\kappa}\ln\left(\frac{E c_\mu^{1/4} k_v^{1/2} y_P}{\nu}\right) \tag{2.67}$$

where the sublayer thickness, y_v, is determined from $y_v k_v^{1/2}/\nu = 20$, the integration constant is given by $E = 9.79$ and k_v is obtained by a fitting a straight-line through values of k at the two near-wall nodes, P and N (shown in Figure 2.1). To calculate $\overline{P_{kuv}}$, the turbulent stress in the viscous sublayer is assumed to be zero and in the fully turbulent region the stress is assumed to vary linearly with wall distance (see Figure 2.3). The velocity gradient $(\partial U/\partial y)$ is calculated from the log-law as previously:

$$\overline{P_{kuv}} = \frac{1}{y_n}\int_{y_v}^{y_n}\left[\tau_{wall} + \frac{(\tau_n - \tau_{wall})}{y_n} y\right]\frac{\tau_{wall}}{\kappa c_\mu^{1/4}\rho k_v^{1/2}}\frac{1}{y}\mathrm{d}y \tag{2.68}$$

$$= \frac{\tau_{wall}^2}{\kappa c_\mu^{1/4}\rho k_v^{1/2} y_n}\ln\left(\frac{y_n}{y_v}\right) + \frac{\tau_{wall}(\tau_n - \tau_{wall})}{\kappa c_\mu^{1/4}\rho k_v^{1/2} y_n^2}(y_n - y_v) \tag{2.69}$$

For the purpose of evaluating ε, k is assumed to vary quadratically in the viscous sublayer and linearly in the fully turbulent region. The cell-averaged dissipation rate is evaluated using the same assumptions as used with the SCL wall function, but with a linear interpolation for k in the fully turbulent

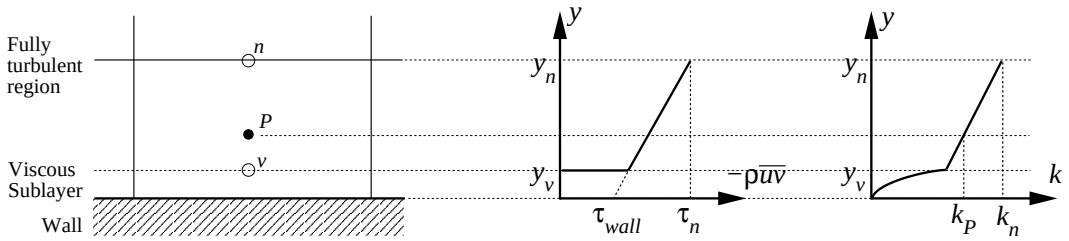

Figure 2.3: Chieng & Launder wall function: assumed profiles of turbulent shear stress $(-\rho\overline{uv})$ and turbulent kinetic energy (k) across the near-wall cell.

region:

$$\overline{\varepsilon} = \frac{1}{y_n}\left(y_v \frac{2\nu k_v}{y_v^2} + \int_{y_v}^{y_n} \frac{1}{c_l y}\left[k_n - \frac{(k_n - k_P)}{y_n - y_P}(y_n - y)\right]^{3/2} \mathrm{d}y\right) \tag{2.70}$$

The above integration is performed numerically. The turbulent kinetic energy evaluated at the northern edge of the cell, k_n, is obtained by linear interpolation between the two neighbouring nodes P and N. Following the expression for wall shear stress, τ_{wall}, the wall temperature is based on k_v rather than k_P to reduce the dependence on the position of node P:

$$T_{wall} = T_P + \frac{q_{wall} T^+}{\rho c_p c_\mu^{1/4} k_v^{1/2}} \tag{2.71}$$

where T^+ is evaluated using U^+ evaluated with k_v as for the wall shear stress expression.

2.4.5 Johnson & Launder (JL)

The Johnson & Launder wall function [50] extends the Chieng & Launder wall function by accounting for variation in the sublayer thickness, y_v. Johnson & Launder noted that if the magnitude of the shear stress falls rapidly with distance from the wall (e.g. in highly accelerated boundary layers) the thickness of the sublayer is increased beyond that which would be predicted from a constant sublayer Reynolds number, R_v. Conversely in the reattachment region of a backward step there is low wall shear stress but high shear stress and turbulence energy a short distance away from the wall. The modification proposed by Johnson & Launder is to make the sublayer Reynolds number a function of the near-wall gradient of k such that, if there is a diffusion of energy towards the wall, then the dimensionless thickness of the sublayer is reduced. This is implemented by introducing a variable sublayer Reynolds number, R_v:

$$R_v = \frac{k_v^{1/2} y_v}{\nu} = \frac{20}{1 + 3.1\lambda} \qquad \lambda = \frac{k_v - k_{wall}}{k_v} \tag{2.72}$$

where k_{wall} and k_v are extrapolated from k_P and k_n. At the edge of the sublayer $(y = y_v)$, both the log-law and the linear relationship between U^+ and y^+ can be applied (Equations 1.11 and 1.14). If

these two expressions are equated it can be shown that the integration “constant”, E, in the log-law is not in fact a constant as it has been assumed up to this point, but a function given by:

$$E = \frac{\exp\left(c_\mu^{1/4}\kappa R_v\right)}{c_\mu^{1/4} R_v} \tag{2.73}$$

The Johnson & Launder wall function therefore consists of two modifications to the CL wall function: variable R_v and E.

2.4.6 Chieng & Launder Modifications

Two modifications to the Chieng & Launder wall function were tested during the course of the current work to try to reduce the sensitivity of the wall function to changes in the near-wall cell size and to improve its overall performance. In the first modification, the normal stresses were assumed to vary linearly across the fully-turbulent region of the near-wall cell when calculating the cell-average production term $\overline{P_k}$. This is a simple continuation of the approach adopted by Chieng & Launder for the shear stress variation across the cell. In the second modification, the Reynolds stresses were no longer assumed to be zero across the viscous sublayer, but instead were assumed to follow their wall-limiting behaviour (see Section 1.3). This introduces additional terms into the expression for $\overline{P_k}$. The performance of these two modifications are discussed with reference to the impinging jet flow in Chapter 5. A further modification, for which results are not shown, assumed that the length scale varies linearly across the two wall-adjacent cells in order to specify the value of the dissipation rate at the near-wall node, ε_P. This was proposed in order to reduce the sensitivity of the wall function to the size of the near-wall control volume in flows where the turbulence length scale does not follow the equilibrium length-scale variation $\left(k^{3/2}/\varepsilon = c_l y\right)$. However, it was found in the impinging jet flow that this modification introduced stability problems.

2.4.7 NLEVM Implementation

The Craft *et al*. NLEVM uses strain-rates evaluated at the near-wall node, P, to calculate the c_μ-function and the additional non-linear stress components, $\mu_t^{'}$ and $\widehat{\overline{u_i u_j}}$ in Equations (2.41) and (2.42). To be entirely consistent with standard wall functions, the strain-rate $(\partial U/\partial y)$ at node P should be obtained by differentiating the log-law:

$$\frac{\partial U}{\partial y} = \frac{\tau_{wall}}{\kappa c_\mu^{1/4} \rho k_P^{1/2} y} \tag{2.74}$$

In practice, however, using the above expression for $\partial U/\partial y$ in the non-linear terms was found to worsen the predictions of the wall functions in the impinging jet flow (see Figure 5.45 for the Chieng & Launder wall function results). All the calculations discussed in Chapters 5 to 7 assume a linear velocity profile across the cell for the strain-rate at the node used in the NLEVM terms.

Chapter 3

Numerical Implementation

Two finite-volume-based CFD codes have been used in the present work: Turbulent Elliptic Algorithm of Manchester (TEAM) [70, 71] and Simulation of Turbulent Reynolds-averaged Equations for All Mach numbers (STREAM) [72, 73]. Only the main elements of the two codes are presented which have direct relevance to the current study. More information on the SIMPLE algorithm, finite-volume discretization etc. can be found in numerous books on CFD techniques (for example, Patankar [74], Versteeg & Malalasekera [75] and Ferziger & Perić [76]).

3.1 The Finite-Volume Method

In the finite-volume method, the governing equations are integrated over each of the finite control volumes in the flow domain and the resulting integrated transport equations are then discretized, using finite-difference-type formulas, to give a set of algebraic equations which are solved using an iterative method (e.g. TDMA). To illustrate this procedure, one can consider a simple one-dimensional convection-diffusion transport equation for steady flow, which is written as follows:

$$\frac{\partial(\rho U\phi)}{\partial x} = \frac{\partial}{\partial x}\left(\Gamma\frac{\partial\phi}{\partial x}\right) + C \tag{3.1}$$

where ϕ is the transport variable, Γ is the diffusion coefficient and C contains the source terms. This is integrated over a finite volume as follows:

$$\int_{\Delta Vol}\frac{\partial(\rho U\phi)}{\partial x}\mathrm{d}Vol = \int_{\Delta Vol}\frac{\partial}{\partial x}\left(\Gamma\frac{\partial\phi}{\partial x}\right)\mathrm{d}Vol + \int_{\Delta Vol} C\mathrm{d}Vol \tag{3.2}$$

where the ΔVol is the cell volume. Considering the cell to have constant cross-sectional area, A, between east and west faces (denoted e and w, respectively), the above equation can be written:

$$(\rho UA\phi)_e - (\rho UA\phi)_w = \left(\Gamma A\frac{\partial\phi}{\partial x}\right)_e - \left(\Gamma A\frac{\partial\phi}{\partial x}\right)_w + C_P\Delta Vol \tag{3.3}$$

The diffusion terms are discretized using central differencing, with quantities evaluated at the cell faces, $()_e$ and $()_w$, being replaced by expressions involving nodal values, as follows:

$$\left(\Gamma A\frac{\partial\phi}{\partial x}\right)_e = (\Gamma A)_e \frac{(\phi_E - \phi_P)}{\Delta x_{PE}} \tag{3.4}$$

$$\left(\Gamma A\frac{\partial\phi}{\partial x}\right)_w = (\Gamma A)_w \frac{(\phi_P - \phi_W)}{\Delta x_{PW}} \tag{3.5}$$

where subscripts P, E and W refer to values at the current node, the neighbouring eastern and western nodes, respectively and Δx_{PW} is the distance between nodes P and W. Substituting these expressions into Equation (3.3), the discretized transport equation becomes:

$$F_e\phi_e - F_w\phi_w = D_e(\phi_E - \phi_P) - D_w(\phi_P - \phi_W) + S \tag{3.6}$$

where $F = \rho UA$ is the convective mass flux, $D = \Gamma A/\Delta x$ is the diffusion coefficient and $S = C_P\Delta Vol$ is the integrated source term.

Central differencing is not used to approximate convective fluxes for reasons of boundedness and transportiveness. A number of different discretization schemes for convection are outlined in Sections 3.2.2 and 3.3.3. For the present purposes of illustration the simplest scheme is adopted: the upwind scheme, which approximates the boundary value as the upstream nodal value. For positive U-velocity (i.e. from west to east) and for negative U-velocity (east to west) the value of ϕ on the eastern cell face is approximated as:

$$\phi_e = \phi_P \quad U > 0 \tag{3.7}$$

$$\phi_e = \phi_E \quad U < 0 \tag{3.8}$$

Similar expressions can be written for the ϕ at the western cell face. The convective flux terms can thus be expressed compactly as follows:

$$F_e\phi_e = \phi_P \max(F_e, 0) + \phi_E \min(F_e, 0) \tag{3.9}$$

$$F_w\phi_w = \phi_W \max(F_w, 0) + \phi_P \min(F_w, 0) \tag{3.10}$$

The discretized 1-D convection-diffusion equation can now be written (substituting Equations 3.9 and 3.10 into 3.6):

$$a_P\phi_P = a_E\phi_E + a_W\phi_W + S \tag{3.11}$$

where:

$$a_E = D_e - \min(F_e, 0) \tag{3.12}$$

$$a_W = D_w + \max(F_w, 0) \tag{3.13}$$

$$a_P = a_E + a_W + (F_e - F_w) \tag{3.14}$$

and $F_e - F_w = 0$, from continuity (Equation 2.1).

The discretized governing equation (Equation 3.11) is typically solved using the Tri-Diagonal Matrix Algorithm (TDMA)[1]. In order to improve the stability of the TDMA, the source term (S) is decomposed into two parts:

$$S = s_U + s_P \phi_P \tag{3.15}$$

In general, if s_P is negative then it is transferred to the left-hand-side of the discretized equation:

$$[a_P - \min(s_P, 0)]\,\phi_P = a_E \phi_E + a_W \phi_W + s_U + \max(s_P, 0)\,\phi_P \tag{3.16}$$

which improves the diagonal dominance of the coefficient matrix and hence the stability.

For those flow variables that, by definition, must always be positive, such as k and ε, slightly different rules are applied: when the source term, S, is negative it is transferred to the left-hand-side of the discretized equation to prevent physically unrealistic negative values:

$$\left[a_P - \frac{\min(S, 0)}{\phi_P}\right] \phi_P = a_E \phi_E + a_W \phi_W + \max(S, 0) \tag{3.17}$$

It is relatively straight-forward to extend the above derivation to two and three-dimensional cases. The resulting discretized transport equations have the following general form:

$$a_P \phi_P = \sum_{nb} a_{nb} \phi_{nb} + S \tag{3.18}$$

where:

$$a_P = \sum_{nb} a_{nb} \tag{3.19}$$

and *nb* indicates the neighbouring nodes (E, W, N, S, T and B).

3.1.1 SIMPLE Pressure-Correction Algorithm

For the RANS equations there is no direct method of specifying an equation for pressure. Instead, pressure is determined indirectly using the continuity equation: if the correct pressure field is used to solve the momentum equations then the continuity equation will be satisfied. In both the TEAM and STREAM codes, the Semi-Implicit Method for Pressure-Linked Equations (SIMPLE) of Patankar & Spalding [78] is used to handle the pressure-velocity coupling.

The discretized U-momentum equation for a two-dimensional geometry can be written:

$$a_P U_P = \sum_{nb} a_{nb} U_{nb} + (P_w - P_e)\,\Delta y \tag{3.20}$$

where *nb* indicates the neighbouring nodes (E, W, N and S). The SIMPLE algorithm starts by assum-

[1] Details of the TDMA (or Thomas' algorithm) are not provided here but can be found in most CFD textbooks, for example Anderson [77].

ing a guessed pressure field, P^*, and guessed velocity field, U^*:

$$a_P U_P^* = \sum_{nb} a_{nb} U_{nb}^* + (P_w^* - P_e^*)\,\Delta y \tag{3.21}$$

It is assumed that to satisfy the continuity equation, one must make a correction to the guessed velocity and pressure fields. The correct velocity and pressure fields are given by:

$$U = U^* + U^{'} \tag{3.22}$$

$$P = P^* + P^{'} \tag{3.23}$$

where $U^{'}$ and $P^{'}$ are the necessary corrections. One can derive an equation for the necessary correction, $U^{'}$, by subtracting Equation (3.21) from (3.20):

$$U_P^{'} = \underbrace{\frac{\sum_{nb} a_{nb} U_{nb}^{'}}{a_P}} + \frac{\Delta y}{a_P}\left(P_w^{'} - P_e^{'}\right) \tag{3.24}$$

The SIMPLE algorithm assumes that the underbraced term in Equation (3.24) is negligible. The correct velocity is thus given by:

$$U_P = U_P^* + \frac{\Delta y}{a_P}\left(P_w^{'} - P_e^{'}\right) \tag{3.25}$$

The discretized continuity equation for a two-dimensional Cartesian grid can be written:

$$(\rho UA)_e - (\rho UA)_w + (\rho VA)_n - (\rho VA)_s = 0 \tag{3.26}$$

where *e*, *w*, *n* and *s* denote values at the east, west, north and south cell faces, respectively. The expressions for the correct velocity through the cell faces (U_e, U_w, V_n and V_s) can be obtained in a similar manner to that described above for U_P, and substituted into the continuity equation. The resulting expression can be rearranged in terms of the pressure-correction, in the form:

$$a_P P_P^{'} = \sum_{nb} a_{nb} P_{nb}^{'} + S \tag{3.27}$$

This equation is solved to find the pressure-correction $P^{'}$ at all points throughout the flow domain. Once the pressure correction is known, it is then possible to update the guessed pressure (P^*) to its correct value (P) and update the velocity field from Equation (3.25).

The steps involved in the SIMPLE algorithm can be summarized as follows:

1. Initially a pressure field is guessed, P^*, which used in the discretized momentum equations to find the guessed velocity field.

2. An equation is solved for the pressure correction, $P^{'}$, which gives the pressure difference between the guessed pressure and pressure necessary to satisfy the continuity condition.

3. The pressure and velocity fields are then updated based on the pressure correction (with some under-relaxation).

4. Other scalar transport equations are solved (e.g. k and ε).

5. Steps 1 – 4 are repeated (using the pressure field from the previous step as the initial guess) until the calculation has converged.

3.1.2 Under-Relaxation

Under-relaxation is a means of slowing down the updating process of the variables and is necessary for convergence of coupled non-linear equations. Variables are updated in the following manner:

$$\phi_P^{new} = \alpha\phi_P^{calc} + (1-\alpha)\phi_P^{old} \tag{3.28}$$

where ϕ_P^{old} is the value of ϕ from the previous iteration and ϕ_P^{calc} is the result of the current calculation. Applying the above formula to the discretized transport equation (Equation 3.18) gives:

$$\frac{a_P}{\alpha}\phi_P^{new} = \sum_{nb} a_{nb}\phi_{nb} + S + (1-\alpha)\frac{a_P}{\alpha}\phi_P^{old} \tag{3.29}$$

In practice, under-relaxation involves the modification of the coefficient a_P and source S:

$$(a_P)_{new} = \frac{a_P}{\alpha} \tag{3.30}$$

$$(S)_{new} = S + (1-\alpha)(a_P)_{new}\phi_P^{old} \tag{3.31}$$

Its effect, therefore, is to increase the diagonal dominance of the coefficient matrix and add in a source term.

Since the pressure is updated by means of a pressure correction, its under-relaxation takes the form:

$$P_P^{new} = P_P^{*} + \alpha P_P^{'} \tag{3.32}$$

where P' is the pressure correction.

If the under-relaxation factor, α, in the above equations is set to unity there is no under-relaxation and the new value is equivalent to the calculated value. Typical values for the under-relaxation factors used in the impinging jet, spinning disc and Ahmed body studies are shown in Tables 5.1, 6.1 and 7.2, respectively (see pages 97, 114 and 136).

3.2 TEAM Code

TEAM is a finite-volume code for the simulation of steady two-dimensional or axisymmetric turbulent elliptic flows. It was used to study the fully-developed channel flow, impinging jet and spinning disc

flows, documented in Chapters 4 to 6.

3.2.1 Storage Arrangement

A staggered Cartesian grid is used with scalars stored at nodal positions and velocities at the cell faces (see Figure 3.1). This arrangement is used to prevent a "checker-board" pressure field being developed, where neighbouring pressure nodes have alternating high-low values but the cell face pressures calculated using linear interpolation are constant across the flow field (so in effect the velocity field "feels" a constant pressure). The grid is specified algebraically by setting the locations of the cell faces, with nodes then being placed in the centre of each cell. Boundary nodes are located along the edges of the flow domain which are used to apply the boundary conditions. Transport equations are solved up to, but not including, the boundary nodes (i.e. in Figure 3.1 transport equations solved from node *P* northwards but not at node *S*).

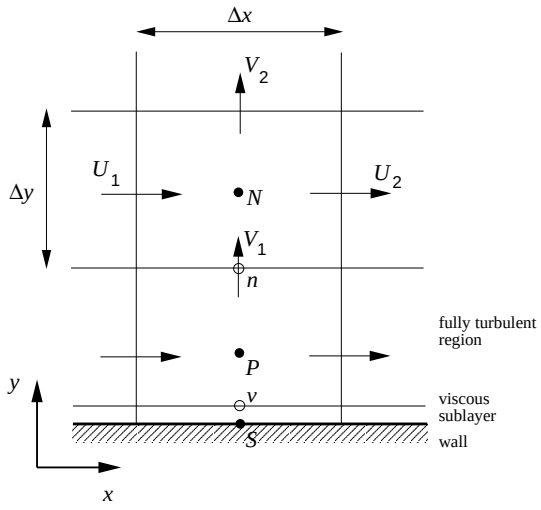

Figure 3.1: Staggered grid arrangement used by TEAM: scalars stored at nodes (e.g. *P* and *N*), velocities stored at cell faces (e.g. V_1 stored at *n*), edge of viscous sublayer located at *v*, boundary node *S* located on wall. In axisymmetric coordinates the *x*-axis becomes the radial *r*-axis.

In the staggered grid arrangement, the wall shear stress is evaluated at cell faces (where the velocity is calculated) whilst the average turbulent scalar source terms ($\overline{P_k}$, $\overline{\varepsilon}$ etc.) and wall heat flux, q_{wall}, are evaluated at the scalar node in the centre of the cell. The UMIST-*N* wall function nodes are positioned in the centre of the subgrid cells, in the equivalent position to the main-grid scalar nodes. The wall shear stress is obtained at the scalar node position and is then linearly interpolated to the cell boundary location. It was found that this gave identical results to those obtained when the wall function was applied twice per cell (at both scalar and velocity nodes).

3.2.2 Differencing Schemes

In the TEAM code, diffusion terms appearing in the transport equations for momentum and turbulence parameters are discretized using second-order central differencing. There are two options for approximating the convection terms: the Power-Law Differencing Scheme (PLDS) of Patankar [74] and the Quadratic Upstream Interpolation for Convective Kinetics (QUICK) scheme of Leonard [79].

PLDS

PLDS is first-order accurate with respect to its Taylor series truncation error and is unconditionally bounded. For a uniform mesh and positive U-velocity (from west to east), the eastern boundary value ϕ_e is approximated as:

$$\begin{aligned} \phi_e &= \phi_P + \frac{\phi_E - \phi_P}{2} \frac{(1-0.1Pe_e)^5}{(1-0.05Pe_e)^5} \quad \text{for} \quad 0 \le Pe \le 10 \\ \phi_e &= \phi_P \qquad\qquad\qquad\qquad\qquad\quad \text{for} \quad Pe > 10 \end{aligned} \tag{3.33}$$

where subscript E refers to the eastern nodal value. Pe is the non-dimensional cell Peclet number, a measure of the relative strength of convection to diffusion:

$$Pe = \frac{F}{D} = \frac{\rho U}{\Gamma/\Delta x} \tag{3.34}$$

For Peclet number greater than 10, the scheme is equivalent to a simple upwind approach (see discussion in Section 3.3.3).

QUICK

QUICK is a third-order accurate unbounded scheme, where the interpolation for the cell face value, ϕ_e or ϕ_w, is based on a quadratic interpolation using three nodal values, one on the downstream side of the cell face and two on the upstream side. For a uniform mesh, if the U-velocity is positive:

$$\phi_e = \frac{1}{2}(\phi_E + \phi_P) - \frac{1}{8}(\phi_E - 2\phi_P + \phi_W) \tag{3.35}$$

$$\phi_w = \frac{1}{2}(\phi_P + \phi_W) - \frac{1}{8}(\phi_P - 2\phi_W + \phi_{WW}) \tag{3.36}$$

where subscript W refers to the western nodal value and WW is the node to the west of the W node. Boundary values, ϕ_e and ϕ_w, obtained by QUICK can be thought of as a combination of linear interpolation and upstream-weighted correction. Since the discretized equations are solved using a TDMA which only treats the near-diagonal terms implicitly (a_P, a_E and a_W), the other terms (a_{EE} and a_{WW}) are included in the source term. Whilst QUICK is a more accurate scheme than PLDS, it is also unbounded and can suffer from over- or under-shoots. In the impinging jet flow, discussed later, values of k and ε are close to zero near the entrainment boundary. As a consequence, small undershoots

can lead to negative values of k and ε which are physically unrealistic and cause stability problems. Therefore PLDS was used for turbulence scalars and QUICK for the velocity field.

3.2.3 Wall-Function Implementation

Wall-Parallel Velocity

The coding of wall functions into TEAM is much simpler than for STREAM owing to the use of a Cartesian grid. To implement the wall-function conditions for the wall-parallel U-velocity, there are two parts. In the first, the diffusional flux to the wall calculated by the near-wall main-grid cell is set to zero, by setting $a_S = 0$ (for a wall on the south face) in the discretized momentum equation. To understand the effect of setting $a_S = 0$, one can consider the diffusion term:

$$\frac{\partial}{\partial y}\left(\mu_{eff}\frac{\partial U}{\partial y}\right) \tag{3.37}$$

This is discretized, using central differences, and integrated over the cell using the finite-volume method to give:

$$\int \frac{\partial}{\partial y}\left(\mu\frac{\partial U}{\partial y}\right)\mathrm{d}Vol = \left(\mu A\frac{\partial U}{\partial y}\right)_n - \underbrace{\left(\mu A\frac{\partial U}{\partial y}\right)_s} \tag{3.38}$$

where A is the area of the cell face parallel to the wall and n and s refer to north and south boundary values. By setting $a_S = 0$, one is setting the underbraced term to zero. This is necessary since the $\partial U/\partial y$ part of the underbraced term would otherwise be calculated assuming there to be a linear change in velocity between the southern node S (on the wall surface) and the near-wall node, P (see Figure 3.1). When a fine near-wall grid is used with a low-Re model, a linear U-velocity profile provides an adequate approximation of the velocity variation between nodes S and P, but when a large near-wall cell is used one needs to assume, or calculate, a more accurate profile. Standard wall functions replace $\partial U/\partial y$ with a value obtained from assuming a logarithmic U-velocity profile whilst the UMIST-N wall function finds $\partial U/\partial y$ from a local solution of the flow field. Once a_S has been set to zero, the second part of the wall-function implementation is to add in a replacement for the underbraced term. The replacement term consists of the wall shear stress (effectively the $\mu_{eff}\partial U/\partial y$ part of Equation 3.38) multiplied by the area of the cell face parallel to the wall:

$$F_{wall} = -\tau_{wall}A \tag{3.39}$$

The negative sign is introduced since the diffusive flux in Equation (3.38) is negative and the complete term is called the "wall force", F_{wall}. This is added into the source term in the discretized wall-parallel momentum equations at the near-wall node. If a log-law wall function is used, the wall force is expressed in terms of the velocity at the near-wall node: for a near-wall node in the fully-turbulent

region of the boundary layer, $y^+ > 11.6$, the wall force is given by:

$$F_{wall} = -\frac{\rho\kappa c_\mu^{1/4} k^{1/2} U_P A}{\ln(Ey^+)} \tag{3.40}$$

or if $y^+ < 11.6$, the wall force becomes:

$$F_{wall} = -\mu\frac{U_P}{y_P}A \tag{3.41}$$

Since U_P appears explicitly in the above expressions and the term (F_{wall}/U_P) is always negative, one can place the wall force into the linearized source term, s_P:

$$s_P = \frac{F_{wall}}{U_P} \tag{3.42}$$

This increases the diagonal dominance of the coefficient matrix for the discretized U-momentum equation, improving stability.

The UMIST-*N* wall function does not calculate τ_{wall} as a function of U_P and therefore one cannot linearize the source term. Instead the wall force calculated by UMIST-*N* wall function $(F_{wall} = -\tau_{wall}A)$ is added into the source term s_U, i.e.:

$$s_U = F_{wall} \tag{3.43}$$

Tangential Velocity

In the spinning-disc case examined in Chapter 6, the wall is rotating at constant tangential velocity, $W_{wall} = \Omega r$. The tangential velocity log-law can be written, for a stationary reference frame:

$$\frac{W - W_{wall}}{W_\tau} = \frac{1}{\kappa}\ln\left(Ey^+\right) \tag{3.44}$$

Using a standard wall function, the wall force in the tangential direction, $F_{wall,\phi}$, is calculated for $y^+ > 11.6$:

$$F_{wall,\phi} = -\frac{\rho\kappa c_\mu^{1/4} k^{1/2}\left(W_P - W_{wall}\right)A}{\ln(Ey^+)} \tag{3.45}$$

The source term is split into the s_U and s_P source terms as follows:

$$s_U = \frac{\rho\kappa c_\mu^{1/4} k^{1/2} W_{wall} A}{\ln(Ey^+)} \tag{3.46}$$

$$s_P = -\frac{\rho\kappa c_\mu^{1/4} k^{1/2} A}{\ln(Ey^+)} \tag{3.47}$$

Similarly, if the near-wall node is within the viscous sublayer ($y^+ < 11.6$):

$$F_{wall,\phi} = -\mu \frac{(W_P - W_{wall})}{y_P} A \tag{3.48}$$

and the source terms become:

$$s_U = \mu \frac{W_{wall}}{y_P} A \tag{3.49}$$

$$s_P = -\frac{\mu}{y_P} A \tag{3.50}$$

The tangential wall shear stress calculated by the UMIST-*N* wall function is not a function tangential velocity at the near-wall node, W_P, and therefore the tangential wall force calculated by UMIST-*N* is added into the source term s_U.

Wall-Normal Velocity

In a staggered-grid arrangement, the wall-normal velocity, V, is calculated at the wall boundary node and at the north face of the control volume (see Figure 3.1). For a non-porous wall, the V-velocity is simply set to zero on the wall surface. One does not need to make any other modifications to the V-momentum equation.

Turbulence Parameters

In the four "standard" wall functions discussed in Chapter 2, the *k*-equation is solved in the near-wall cell with modified source terms ($\overline{P_k}$ and $\overline{\varepsilon}$), whilst the ε-equation is not solved but instead its value is prescribed at the near-wall node. Introducing modified source terms into the *k*-equation is simply a matter of removing the old calculated near-wall cell values of production and dissipation, P_k and ε, from the source term of the *k*-equation and then adding in the wall-function values. Since the standard wall functions involve expressions for the production due purely to shear stress, only the shear stress component of P_k is removed. The wall function values for average production due to shear stress, $\overline{P_{kuv}}$, and average dissipation rate, $\overline{\varepsilon}$, are placed into source terms s_U and s_P as follows:

$$s_U = \max\left[\left(\overline{P_{kuv}} - \overline{\rho\varepsilon}\right), 0\right] \Delta Vol \tag{3.51}$$

$$s_P = \frac{\min\left[\left(\overline{P_{kuv}} - \overline{\rho\varepsilon}\right), 0\right]}{k_P} \Delta Vol \tag{3.52}$$

where ΔVol is the volume of the near-wall cell. To set the value of ε_P, source terms are added to the discretized equation as follows:

$$s_U = 10^{30}\varepsilon_P^* \qquad\qquad s_P = -10^{30} \tag{3.53}$$

where 10^{30} is an arbitrary large number and ε_P^* is the wall function value for ε at the near-wall node. Substituting these source terms into the discretized equation leads to the following expression:

$$\left(a_P + 10^{30}\right)\varepsilon_P = a_N\varepsilon_N + a_S\varepsilon_S + a_E\varepsilon_E + a_W\varepsilon_W + 10^{30}\varepsilon_P^* \tag{3.54}$$

and, since the neighbouring coefficients $a_N\phi_N$, $a_S\phi_S$ are much smaller than 10^{30} , the expression becomes:

$$\varepsilon_P = \varepsilon_P^* \tag{3.55}$$

The UMIST-*N* wall function involves the solution of both k and $\tilde{\varepsilon}$ equations in the near-wall cell with modified source terms. A similar approach to that suggested above for the k-equation (Equations 3.51 and 3.52) is therefore applied for both k and $\tilde{\varepsilon}$ equations. The cell-averaged production term calculated across the subgrid, $\overline{P_k}$, includes both shear and normal components and so the entire production term, P_k, is removed from the near-wall cell prior to adding in the wall function value.

Using both standard and UMIST-*N* treatments, the diffusive fluxes of k and ε to the wall are set to zero, by setting $a_S = 0$.

Temperature

Implementing the temperature wall function is similar to the procedure used for wall-parallel momentum but instead of replacing the wall shear stress one replaces the wall heat flux, and instead of assuming a no-slip condition at the wall one prescribes (or calculates) the wall temperature. The temperature equation is solved at the near-wall node, suppressing the heat flux to the wall calculated using a linear temperature gradient by setting $a_S = 0$. If constant heat flux conditions are prescribed, one knows the heat flux to the wall, q_{wall}, and must calculate the wall temperature T_{wall}. Conversely, if constant temperature conditions are applied, one knows T_{wall} and has to calculate q_{wall}. The expressions for T_{wall} and q_{wall} used by standard wall functions are presented in Section 2.4 and those calculated by the UMIST-*N* wall function in Section 4.3. The temperature at the node on the wall surface is set to T_{wall} and the following source term is added into the discretized temperature equation in the near-wall cell:

$$s_U = -q_{wall}A \tag{3.56}$$

where A is the area of the cell face parallel to the wall.

3.2.4 Convergence Criteria

If the discretized transport equations are solved exactly then the left and the right sides of the discretized transport equation (Equation 3.18) will be exactly equal. However, since the set of non-linear coupled equations requires an iterative solution, an imbalance or residual may exist between the two sides of the discretized equations. The residual for parameter ϕ in a particular cell is calculated from

the imbalance as follows:

$$R_\phi = a_P \phi_P - \sum_{nb} a_{nb} \phi_{nb} - S \tag{3.57}$$

where *nb* indicates the neighbouring nodes (E, W, N and S). If the calculation is completely converged then the R_ϕ value at all nodal positions is zero. In the TEAM code, an overall residual for each variable is determined by summing the absolute values of the residuals over all the main-grid nodes and normalizing with bulk inlet quantities (for definitions, see [70]). A mass imbalance is calculated rather than a pressure-residual. The calculation is said to have converged when the normalized velocity and mass residuals are less than a prescribed value. For the impinging jet flow this was 5×10^{-4} which corresponded to a reduction in the residuals of approximately four orders-of-magnitude from the start to the end of a calculation. It was verified that using more stringent convergence criteria had no effect on results.

3.3 STREAM Code

The STREAM code is significantly more sophisticated than the TEAM code described above. It can be used in either 2-*D*, 3-*D* or axisymmetric modes using a non-orthogonal body-fitted grid if necessary. Both steady and unsteady flows can be analyzed and mass-weighted averaging can be activated if compressibility effects are significant. STREAM was used to model the flow around the Ahmed body, considered in Chapter 7. For the purposes of this work the STREAM code was only used in steady, incompressible mode.

The STREAM code has many similarities to the TEAM code, described above. The significant issues of difference that are important to the present work are discussed below. Transport equations using curvilinear coordinates, which are solved by STREAM, are presented in Appendix F. For a full description of the code, see Lien [73].

3.3.1 Grid Arrangement

The STREAM code uses a fully-collocated storage arrangement with all velocity components and scalar quantities stored at nodal positions. In order to overcome "checker-board" problems with the pressure field, a Rhie-Chow interpolation is used to calculate velocities at cell faces (see below). A structured non-orthogonal curvilinear grid arrangement is used although the velocity vectors (and hence Reynolds stress components) are always aligned to a Cartesian reference frame. Using Cartesian coordinates for velocity is useful since it allows the momentum equations to be written in conservative form. For complex geometry, the flow domain is decomposed into a number of separate blocks where block-to-block communication is achieved using additional halo nodes. Nodes are located in the centre of each control volume and along the edges of blocks there are boundary nodes. Transport equations are only solved for nodes internal to cells; boundary nodes and halo nodes provide boundary conditions.

3.3.2 Dimensionless Parameters

The STREAM code solves transport equations for dimensionless parameters. The momentum, pressure and turbulence scalar parameters are all non-dimensionalized with bulk quantities. Non-dimensional forms of the parameters are as follows:

$$\underline{U_i} = \frac{U_i}{U'};\ \underline{x_j} = \frac{x_j}{L};\ \underline{t} = t\frac{U}{L} \tag{3.58}$$

$$\underline{\rho} = \frac{\rho}{\rho'};\ \underline{P} = \frac{P}{\rho'(U')^2};\ \underline{\overline{u_i u_j}} = \frac{\overline{u_i u_j}}{(U')^2} \tag{3.59}$$

where underlined characters denote dimensionless parameters, ρ', U' and L are characteristic density, velocity and length scales and the pressure P and dimensionless pressure $\underline{P}$ are measured from the same reference pressure. The momentum equation in Cartesian tensors is given by:

$$\begin{aligned}&\frac{\partial}{\partial t}(\rho U_i) + \frac{\partial}{\partial x_j}(\rho U_i U_j) = \\ &-\frac{\partial P}{\partial x_i} + \frac{\partial}{\partial x_j}\left[\mu\left(\frac{\partial U_i}{\partial x_j} + \frac{\partial U_j}{\partial x_i} - \frac{2}{3}\delta_{ij}\frac{\partial U_m}{\partial x_m}\right)\right] + \frac{\partial}{\partial x_j}(-\rho\overline{u_i u_j})\end{aligned} \tag{3.60}$$

Substituting for dimensionless parameters gives:

$$\begin{aligned}&\frac{\rho'(U')^2}{L}\frac{\partial}{\partial \underline{t}}(\rho\underline{U_i}) + \frac{\rho'(U')^2}{L}\frac{\partial}{\partial \underline{x_j}}\left(\rho\underline{U_i}\underline{U_j}\right) = \\ &-\frac{\rho'(U')^2}{L}\frac{\partial \underline{P}}{\partial \underline{x_i}} + \frac{U'}{L^2}\frac{\partial}{\partial \underline{x_j}}\left[\mu\left(\frac{\partial \underline{U_i}}{\partial \underline{x_j}} + \frac{\partial \underline{U_j}}{\partial \underline{x_i}} - \frac{2}{3}\delta_{ij}\frac{\partial \underline{U_m}}{\partial \underline{x_m}}\right)\right] \\ &+\frac{\rho'(U')^2}{L}\frac{\partial}{\partial \underline{x_j}}\left(-\underline{\rho}\,\underline{\overline{u_i u_j}}\right)\end{aligned} \tag{3.61}$$

which can be rearranged as:

$$\begin{aligned}&\frac{\partial}{\partial \underline{t}}(\rho\underline{U_i}) + \frac{\partial}{\partial \underline{x_j}}\left(\rho\underline{U_i}\underline{U_j}\right) = \\ &-\frac{\partial \underline{P}}{\partial \underline{x_i}} + \frac{\partial}{\partial \underline{x_j}}\left[\frac{1}{Re}\left(\frac{\partial \underline{U_i}}{\partial \underline{x_j}} + \frac{\partial \underline{U_j}}{\partial \underline{x_i}} - \frac{2}{3}\delta_{ij}\frac{\partial \underline{U_m}}{\partial \underline{x_m}}\right)\right] + \frac{\partial}{\partial \underline{x_j}}\left(-\underline{\rho}\,\underline{\overline{u_i u_j}}\right)\end{aligned} \tag{3.62}$$

where Re is the Reynolds number given by:

$$Re = \frac{\rho' U' L}{\mu} \tag{3.63}$$

In the STREAM code, the molecular viscosity appearing in the subgrid momentum and scalar equations is therefore given by the inverse of the bulk flow Reynolds number, $\mu \rightarrow (Re)^{-1}$. To simulate the same flow at different Reynolds numbers one simply modifies the molecular viscosity term. For

example, a channel flow with Reynolds number $Re = 100,000$ (based on the wall-to-wall channel height and bulk velocity) has the flow domain set up with a wall-to-wall channel height of unity, an inlet bulk velocity of unity and a molecular viscosity of $\mu = 1/100,000$. To switch to a Reynolds number of $Re = 1000$ one simply sets the molecular viscosity to $\mu = 1/1000$.

3.3.3 Differencing Schemes

The STREAM code uses central differences to approximate diffusion terms. There are two options in the code for approximating convective transport: the upwind scheme [80] and the Upstream Monotonic Interpolation for Scalar Transport (UMIST) scheme [81].

Upwind

The upwind scheme simply approximates the boundary value as the upstream nodal value. For a positive U-velocity (from west to east) the values of ϕ on the eastern and western boundaries are approximated as:

$$\phi_e = \phi_P \tag{3.64}$$

$$\phi_w = \phi_W \tag{3.65}$$

The upwind scheme is unconditionally bounded but is only first-order accurate. The first-order truncation error term in the Taylor series expansion for the gradient $\partial\phi/\partial x$ contains a second-order derivative term, $\partial^2\phi/\partial x^2$. If insufficient grid nodes are employed, the upwind scheme is therefore liable to introduce unacceptable levels of numerical diffusion (or artificial viscosity). This is only a problem if the flow is not aligned to the grid, when the numerical inaccuracy of the upwind scheme can introduce cross-flow diffusion far in excess of the physical value if the cell Peclet number is greater than $Pe = 2$ [73].

UMIST

UMIST is a TVD (Total Variation Diminishing) scheme based on third-order accurate scheme QUICK (described in Section 3.2.2). A limiter is used to diminish oscillations caused by dispersive truncation errors occurring with QUICK. The resulting scheme returns solutions which are close to those of QUICK but without its oscillatory features. Since the scheme is not oscillatory it can be used for convective transport of both mean-flow and turbulence scalars. For details of the scheme see Lien & Leschziner [81].

3.3.4 Wall-Function Implementation

The implementation of wall functions into STREAM follows the same general procedure presented above for TEAM. There are three notable points of difference. Firstly, when a standard wall function is used, such as the simplified Chieng & Launder scheme, the cell averaged production term, $\overline{P_k}$, used

in the near-wall cell k-equation includes only the shear stress component. Secondly, the use of a body-fitted non-orthogonal grid introduces some complications into the calculation of the wall shear stress with standard wall functions and, thirdly, since a collocated grid arrangement is employed one needs to calculate the pressure on the wall surface. Points two and three are examined below in greater detail.

In STREAM, the main-grid velocity vectors are aligned with Cartesian axes. The velocity vector, $\mathbf{U}$, has components:

$$\mathbf{U} = U_x\hat{\mathbf{i}} + U_y\hat{\mathbf{j}} + U_z\hat{\mathbf{k}} \tag{3.66}$$

where $\left(\hat{\mathbf{i}},\hat{\mathbf{j}},\hat{\mathbf{k}}\right)$ are the Cartesian unit vectors and (U_x,U_y,U_z) the velocity components. The wall-normal unit-vector $\hat{\mathbf{n}}$ has Cartesian components:

$$\hat{\mathbf{n}} = \hat{n}_x\hat{\mathbf{i}} + \hat{n}_y\hat{\mathbf{j}} + \hat{n}_z\hat{\mathbf{k}} \tag{3.67}$$

The magnitude of the projection of vector $\mathbf{U}$ in the wall-normal direction, $|\mathbf{U}^n|$, is calculated from the scalar product of $\mathbf{U}$ and $\hat{\mathbf{n}}$:

$$\begin{aligned} |\mathbf{U}^n| = \mathbf{U}\cdot\hat{\mathbf{n}} &= |\mathbf{U}|\cdot|\hat{\mathbf{n}}|\cos\theta \\ &= U_x\hat{n}_x + U_y\hat{n}_y + U_z\hat{n}_z \end{aligned} \tag{3.68}$$

The magnitude of the velocity vector parallel to the wall, $|\mathbf{U}^t|$, can be found from Pythagoras:

$$\begin{aligned} \left|\mathbf{U}^t\right| &= \left(\mathbf{U}^2 - |\mathbf{U}^n|^2\right)^{1/2} \\ &= \left(U_x^2 + U_y^2 + U_z^2 - |\mathbf{U}^n|^2\right)^{1/2} \end{aligned} \tag{3.69}$$

where $\mathbf{U}^2$ is the dot product $(\mathbf{U}\cdot\mathbf{U})$. It is this term, the magnitude of the velocity component which is tangential to the wall $|\mathbf{U}^t|$, which is used by standard log-law wall functions to determine the wall shear stress, τ_{wall}, i.e. in the standard log-law expression:

$$U^+ = \frac{1}{\kappa}\ln\left(Ey^+\right) \tag{3.70}$$

the dimensionless velocity, U^+, is given by:

$$U^+ = \frac{|\mathbf{U}^t|}{U_\tau} \tag{3.71}$$

The dimensionless wall-normal distance $(y^+ = U_\tau y/\nu)$ from the near-wall node to the wall is determined using:

$$y = \frac{1}{2}\frac{\Delta Vol}{A} \tag{3.72}$$

where ΔVol is the near-wall cell volume and A is the area of the cell face in contact with the wall.

The tangential velocity $\mathbf{U}^t$ is aligned to the tangential unit vector, $\hat{\mathbf{t}}$, the direction of which is dependent upon the local velocity field. It is necessary to find an expression for $\hat{\mathbf{t}}$ in terms of the

Cartesian components so that the wall shear force, calculated from ($F_{wall} = \tau_{wall} A$), can be distributed amongst the U, V and W momentum equations. To find $\hat{\mathbf{t}}$ one first obtains an expression for the velocity vector in the wall-normal direction, $\mathbf{U}^n$. This is simply the product of its magnitude, $|\mathbf{U}^n|$, and the wall-normal unit-vector, $\hat{\mathbf{n}}$:

$$\begin{aligned} \mathbf{U}^n &= (\mathbf{U}\cdot\hat{\mathbf{n}})\,\hat{\mathbf{n}} \\ &= (\mathbf{U}\cdot\hat{\mathbf{n}})\,\hat{n}_x\hat{\mathbf{i}} + (\mathbf{U}\cdot\hat{\mathbf{n}})\,\hat{n}_y\hat{\mathbf{j}} + (\mathbf{U}\cdot\hat{\mathbf{n}})\,\hat{n}_z\hat{\mathbf{k}} \end{aligned} \tag{3.73}$$

The resultant velocity vector, $\mathbf{U}$, is the sum of the wall-normal and wall-parallel velocity components, $\mathbf{U}^n$ and $\mathbf{U}^t$. Therefore, the tangential velocity vector, $\mathbf{U}^t$, is given by:

$$\begin{aligned} \mathbf{U}^t &= \mathbf{U} - \mathbf{U}^n \\ &= \left(U_x\hat{\mathbf{i}} + U_y\hat{\mathbf{j}} + U_z\hat{\mathbf{k}}\right) - \left[(\mathbf{U}\cdot\hat{\mathbf{n}})\,\hat{n}_x\hat{\mathbf{i}} + (\mathbf{U}\cdot\hat{\mathbf{n}})\,\hat{n}_y\hat{\mathbf{j}} + (\mathbf{U}\cdot\hat{\mathbf{n}})\,\hat{n}_z\hat{\mathbf{k}}\right] \\ &= \left[U_x - (\mathbf{U}\cdot\hat{\mathbf{n}})\,\hat{n}_x\right]\hat{\mathbf{i}} + \left[U_y - (\mathbf{U}\cdot\hat{\mathbf{n}})\,\hat{n}_y\right]\hat{\mathbf{j}} + \left[U_z - (\mathbf{U}\cdot\hat{\mathbf{n}})\,\hat{n}_z\right]\hat{\mathbf{k}} \\ &= U_x^t\hat{\mathbf{i}} + U_y^t\hat{\mathbf{j}} + U_z^t\hat{\mathbf{k}} \end{aligned} \tag{3.74}$$

This vector, $\mathbf{U}^t$, is equal to the product of its magnitude, $|\mathbf{U}^t|$, and the tangential unit vector, $\hat{\mathbf{t}}$, and so one can derive an expression for $\hat{\mathbf{t}}$ from:

$$\begin{aligned} \hat{\mathbf{t}} &= \frac{\mathbf{U}^t}{|\mathbf{U}^t|} \\ &= \frac{1}{|\mathbf{U}^t|}\left(U_x^t\hat{\mathbf{i}} + U_y^t\hat{\mathbf{j}} + U_z^t\hat{\mathbf{k}}\right) \\ &= \hat{t}_x\hat{\mathbf{i}} + \hat{t}_y\hat{\mathbf{j}} + \hat{t}_z\hat{\mathbf{k}} \end{aligned} \tag{3.75}$$

The wall force calculated by the wall function acts in the direction of the unit vector parallel to the wall, $\hat{\mathbf{t}}$, and hence the wall force vector can be expressed:

$$\mathbf{F}_{wall} = \tau_{wall} A\hat{\mathbf{t}} = (\tau_{wall} A)\,\hat{t}_x\hat{\mathbf{i}} + (\tau_{wall} A)\,\hat{t}_y\hat{\mathbf{j}} + (\tau_{wall} A)\,t_z\hat{\mathbf{k}} \tag{3.76}$$

where the component of this force in the Cartesian x-direction, included as a source term in the U-momentum equation, is as follows:

$$s_u = (\tau_{wall} A)\,\hat{t}_x \tag{3.77}$$

and similarly for the V- and W-momentum equations. The components of the tangential unit vector are calculated from:

$$\hat{t}_x = \frac{U_x^t}{|\mathbf{U}^t|} = \frac{\left[U_x - (\mathbf{U}\cdot\hat{\mathbf{n}})\,\hat{n}_x\right]}{\left(U_x^2 + U_y^2 + U_z^2 - |\mathbf{U}^n|^2\right)^{1/2}} \tag{3.78}$$

$$\hat{t}_y = \frac{U_y^t}{|\mathbf{U}^t|} = \frac{\left[U_y - (\mathbf{U}\cdot\hat{\mathbf{n}})\,\hat{n}_y\right]}{\left(U_x^2 + U_y^2 + U_z^2 - |\mathbf{U}^n|^2\right)^{1/2}} \tag{3.79}$$

$$\hat{t}_z = \frac{U_z^t}{|\mathbf{U}^t|} = \frac{[U_z - (\mathbf{U}\cdot\hat{\mathbf{n}})\,\hat{n}_z]}{\left(U_x^2 + U_y^2 + U_z^2 - |\mathbf{U}^n|^2\right)^{1/2}} \tag{3.80}$$

where the magnitude of the wall-normal velocity vector is:

$$|\mathbf{U}^n| \;=\; \left\{[(\mathbf{U}\cdot\hat{\mathbf{n}})\,\hat{n}_x]^2 + [(\mathbf{U}\cdot\hat{\mathbf{n}})\,\hat{n}_y]^2 + [(\mathbf{U}\cdot\hat{\mathbf{n}})\,\hat{n}_z]^2\right\}^{1/2} \tag{3.81}$$

and the magnitude of the projection of vector $\mathbf{U}$ in the wall-normal direction $(\mathbf{U}\cdot\hat{\mathbf{n}})$ is given by Equation (3.68).

The above approach assumes that the wall-parallel velocity component at the near-wall node acts in the same direction as the wall shear stress. In a three-dimensional flow, it therefore ignores any skewing of the velocity profile between the near-wall node and the wall. In order to account for skewing of the velocity profile one needs to solve for two independent wall-parallel velocity components. This is the approach used by the UMIST-*N* wall function, which solves for velocity components parallel to the grid lines and obtains two wall-parallel wall shear stress components, τ_{wall}^{ξ} and τ_{wall}^{η} (parallel to the ξ and η grid-lines). The Jacobian matrix $[J]$ is used to transform the wall force components from grid-aligned to Cartesian coordinates:

$$\begin{bmatrix} \tau_{wall}^{x} \\ \tau_{wall}^{y} \\ \tau_{wall}^{z} \end{bmatrix} = \underbrace{\begin{bmatrix} x_\xi & x_\eta & x_\zeta \\ y_\xi & y_\eta & y_\zeta \\ z_\xi & z_\eta & z_\zeta \end{bmatrix}}_{[J]} \begin{bmatrix} \tau_{wall}^{\xi} \\ \tau_{wall}^{\eta} \\ 0 \end{bmatrix} \tag{3.82}$$

The use of the Jacobian matrix to transform between coordinate systems is discussed in greater detail in Appendix E. The wall force vector is then simply:

$$\mathbf{F}_{wall} = (\tau_{wall}^{x} A)\,\hat{\mathbf{i}} + (\tau_{wall}^{y} A)\,\hat{\mathbf{j}} + (\tau_{wall}^{z} A)\,\hat{\mathbf{k}} \tag{3.83}$$

If a standard wall function is used, this approach of calculating two wall shear stress components, τ_{wall}^{ξ} and τ_{wall}^{η}, can be shown to be identical the use of a single resultant wall shear stress[2]. However, in more sophisticated wall functions, such as UMIST-*A* [61], the shear stress is dependent not only upon the velocity vector at the near-wall node but also on the pressure gradient and convection. In principle, it should therefore be possible to derive an analytical wall function which accounts for skewing of the near-wall velocity profile.

[2]This is because the wall shear stress vector is only a function of the velocity vector at the near-wall node (all other terms are scalars) so that any directional terms vanish in the dimensionless velocity U^+ where one divides velocity by the shear stress.

3.3.5 Pressure on the Wall Surface

When a collocated storage arrangement is used, as in STREAM, it is necessary to set the pressure on the wall surface. This is required in order to calculate the pressure gradient along the grid line that intersects the wall plane which is used in the solution of the momentum equations at the near-wall node[3]. The value of the pressure on the wall is set as follows. If one examines a fully-developed channel flow using a 2-*D* Cartesian grid with zero V-velocity in the wall-normal y-direction, the V-momentum equation simplifies to the following:

$$\frac{\partial P}{\partial y} + \frac{\partial \left(\rho \overline{v^2}\right)}{\partial y} = 0 \tag{3.84}$$

When a low-Reynolds-number turbulence model approach is used, the near-wall node is well within the viscous sublayer and the Reynolds stress at the node is practically zero $\left(\overline{v_p^2} = 0\right)$. The pressure at the wall in this case can be set equal to the pressure at the near-wall node ($P_{wall} = P_P$ and $\partial P/\partial y = 0$). However, when wall functions are used the Reynolds stress at the wall-adjacent node is no longer zero. If one simply set the pressure on the wall equal to the value at the near-wall node ($\partial P/\partial y = 0$), the large gradient in $\overline{v^2}$ from the node to the wall would lead to a spuriously large source term in the V-momentum equation, which would lead to a non-zero V-velocity (whereas, for channel flow, the V-velocity should be zero). In order to avoid this problem the above expression (Equation 3.84) is used to set the wall value of the pressure when wall functions are used. To implement the above condition using a three-dimensional body-fitted grid, the following expression is used:

$$\nabla P \cdot \hat{\mathbf{n}} + (\nabla \cdot \rho \overline{\mathbf{u} \otimes \mathbf{u}}) \cdot \hat{\mathbf{n}} = 0 \tag{3.85}$$

where $\hat{\mathbf{n}}$ is the unit wall-normal vector, $\overline{\mathbf{u} \otimes \mathbf{u}}$ is the Reynolds stress in vector form and the gradient operator, ∇, can be written for non-orthogonal coordinates as:

$$\nabla = \frac{\partial \xi^j}{\partial x^i} \frac{\partial}{\partial \xi^j} \mathbf{e}_i \tag{3.86}$$

where $\mathbf{e}_i$ is the Cartesian unit vector and $\partial \xi^j / \partial x^i$ is a property of the grid. This expression is identical to that used by the UMIST-*N* wall function to determine the pressure gradient across the subgrid cells, as discussed in Chapter 4. The value of the pressure on the wall surface is calculated from the known wall-parallel pressure gradients ($\partial P/\partial \xi$ and $\partial P/\partial \eta$) and the gradients of Reynolds stresses in all three coordinate directions (for details, see Appendix E).

If the wall-parallel gradients of pressure and Reynolds stress are negligible, the calculation of the

[3] In a staggered grid arrangement the velocity is calculated at cell faces and one does not need to use the pressure at the wall surface, only the pressure at the near-wall node. The first wall-normal velocity that is calculated is therefore at the top face of the wall-adjacent cell.

wall-pressure (Equation 3.85) can be simplified to:

$$\frac{\partial P}{\partial n} + \frac{\partial \left(\rho \overline{u_n^2}\right)}{\partial n} = 0 \tag{3.87}$$

where n is the wall-normal direction and $\overline{u_n^2}$ represents the components of the Reynolds stress tensor in the wall-normal direction. The fluctuating velocity component in the wall normal direction is calculated from the scalar product, $u_n = (\mathbf{u} \cdot \hat{\mathbf{n}})$ and hence the normal stress, $\overline{u_n^2}$, is given by:

$$\begin{aligned} \overline{u_n^2} = \overline{(\mathbf{u} \cdot \hat{\mathbf{n}})^2} &= \overline{(u_x \hat{n}_x + u_y \hat{n}_y + u_z \hat{n}_z)^2} \\ &= \overline{u_x^2} \hat{n}_x^2 + \overline{u_y^2} \hat{n}_y^2 + \overline{u_z^2} \hat{n}_z^2 + 2\left(\overline{u_x u_y} \hat{n}_x \hat{n}_y + \overline{u_x u_z} \hat{n}_x \hat{n}_z + \overline{u_y u_z} \hat{n}_y \hat{n}_z\right) \end{aligned} \tag{3.88}$$

To find the pressure on the wall, if one first discretizes Equation (3.87):

$$\frac{\left(P + \rho \overline{u_n^2}\right)_P - \left(P + \rho \overline{u_n^2}\right)_{wall}}{\Delta n} = 0 \tag{3.89}$$

where subscripts $_P$ and $_{wall}$ refer to values at the near-wall node and at the wall and, since the Reynolds stress $\overline{u_n^2}$ is zero on the wall surface:

$$\begin{aligned} P_{wall} &= \left(P + \rho \overline{u_n^2}\right)_P \\ &= \left(P' + \rho \overline{u_n^2} - \frac{2}{3}\rho k\right)_P \end{aligned} \tag{3.90}$$

where $P' = P + 2\rho k/3$ is the pressure stored by the STREAM code and $P'_{wall} = P_{wall}$ as $k_{wall} = 0$. This simplified calculation of the wall-pressure (Equations 3.87 to 3.90) is the standard formulation coded into STREAM and was used in the calculations performed by Robinson [35] for the Ahmed body flow. It is not used in the present study as it was found to introduce instability with the UMIST-*N* wall function. Instead, Equation (3.85) is used, which is consistent with the pressure calculation employed in the UMIST-*N* wall function (Equation 4.34).

The pressure gradient term appearing in the U-momentum equation, $\partial P/\partial x$, can be written using the chain-rule:

$$\frac{\partial P}{\partial x} = \frac{\partial P}{\partial \xi}\frac{\partial \xi}{\partial x} + \frac{\partial P}{\partial \eta}\frac{\partial \eta}{\partial x} + \frac{\partial P}{\partial \zeta}\frac{\partial \zeta}{\partial x} \tag{3.91}$$

The source term due to the pressure gradient which appears in the integrated U-momentum equation can therefore be written:

$$\begin{aligned} S &= -\int_{\Delta Vol} \frac{\partial P}{\partial x} \mathrm{d}Vol \\ &= -\frac{\partial P}{\partial \xi} A_x^\xi - \frac{\partial P}{\partial \eta} A_x^\eta - \frac{\partial P}{\partial \zeta} A_x^\zeta \\ &= -(P_e - P_w) A_x^\xi - (P_n - P_s) A_x^\eta - (P_t - P_b) A_x^\zeta \end{aligned} \tag{3.92}$$

where ΔVol is the cell volume (equivalent to the Jacobian, J), subscripts e, w, n, s, t, b refer to the cell

faces, the cell dimensions in computational space are unity $(\Delta\xi = \Delta\eta = \Delta\zeta = 1)$ and the area vector components are given by:

$$A_x^\xi = J\frac{\partial\xi}{\partial x}\ ;\ A_x^\eta = J\frac{\partial\eta}{\partial x}\ ;\ A_x^\zeta = J\frac{\partial\zeta}{\partial x} \tag{3.93}$$

Physically, A_j^i components are the fraction of the area of the i face which is in the plane orthogonal to the j-direction. For a Cartesian grid in which the ξ^i- and x^j-axes are aligned, $A_1^1 \equiv A_x^\xi$ would be total area of the east face of the cell (since, for this geometry, the east face is orthogonal to the x-axis). The pressure-gradient source term is treated as a combination of separate fluxes through each of the cell faces, where for example the flux through the western face is $\left(P_w A_x^\xi\right)$. Once the pressure on the wall surface has been calculated, using Equation (3.85), the pressure gradient flux term for the wall face is included in the source term in the momentum equation. For the U-momentum equation, with a wall on the bottom face of a cell this is written simply:

$$S_{wall} = P_{wall} A_x^\zeta \tag{3.94}$$

it can be shown[4] that this is equivalent to:

$$S_{wall} = P_{wall} A \hat{n}_x \tag{3.100}$$

where $\hat{n}_x$ is the Cartesian x-direction component of the unit-vector in the wall-normal direction, $\hat{\mathbf{n}}$.

[4]The unit vector acting in the wall-normal direction, $\hat{\mathbf{n}}$, is calculated from:

$$\hat{\mathbf{n}} = \frac{\nabla\zeta}{|\nabla\zeta|} \tag{3.95}$$

where $\zeta = constant$ defines the wall surface. The gradient, $\nabla\zeta$, and its magnitude are given by:

$$\nabla\zeta = \frac{\partial\zeta}{\partial x^i}\mathbf{e}_i = \frac{\partial\zeta}{\partial x}\hat{\mathbf{i}} + \frac{\partial\zeta}{\partial y}\hat{\mathbf{j}} + \frac{\partial\zeta}{\partial z}\hat{\mathbf{k}} \tag{3.96}$$

$$|\nabla\zeta| = \sqrt{\left(\frac{\partial\zeta}{\partial x}\right)^2 + \left(\frac{\partial\zeta}{\partial y}\right)^2 + \left(\frac{\partial\zeta}{\partial z}\right)^2} = \sqrt{g^{33}} = \frac{A}{J} \tag{3.97}$$

where g^{33} is the contravariant metric tensor component acting in the ζ-direction, A is the area of the cell face in the $\xi-\eta$ plane (i.e. the area of the cell face in contact with the wall) and J is the Jacobian which is equivalent to the cell volume. The wall-normal unit vector is then:

$$\begin{aligned}\hat{\mathbf{n}} &= \hat{n}_x\hat{\mathbf{i}} + \hat{n}_y\hat{\mathbf{j}} + \hat{n}_z\hat{\mathbf{k}} \\ &= \frac{J}{A}\left(\frac{\partial\zeta}{\partial x}\hat{\mathbf{i}} + \frac{\partial\zeta}{\partial y}\hat{\mathbf{j}} + \frac{\partial\zeta}{\partial z}\hat{\mathbf{k}}\right)\end{aligned} \tag{3.98}$$

The expression for the source term can therefore be written:

$$S = P_{wall} J\frac{\partial\zeta}{\partial x} = P_{wall} A \hat{n}_x \tag{3.99}$$

3.3.6 Rhie-Chow Interpolation

If a uniform grid is used with a collocated storage arrangement and a linear interpolation is used to find the pressure on cell boundaries, the pressure gradient across a cell is dependent only upon the pressure at the nodes in the surrounding cells and is independent of the pressure in the current cell. This can lead to a pressure field developing in which neighbouring nodes have alternating high-low values. A contour plot of pressure would reveal a checker-board pattern. To prevent this occurring, Rhie & Chow [82] proposed an interpolation for the cell-face velocity (used by the convective fluxes in the momentum equations) which incorporates a pressure-smoothing term.

The discretized U-momentum transport equation can be written:

$$a_P U_P = \sum_{nb} a_{nb} U_{nb} + S_C - J\frac{\partial P}{\partial x} \tag{3.101}$$

which can be rearranged as:

$$U_P = \underbrace{\frac{\sum_{nb} a_{nb} U_{nb}}{a_P} + S_C}_{H_P} - (P_e - P_w)\underbrace{\frac{J\partial\xi/\partial x}{a_P}}_{D_P^U} \tag{3.102}$$

where S_C includes the cross-diffusion terms and the pressure gradient terms parallel to axes other than the x-axis, the Jacobian, J, is equivalent to the cell volume and $\partial\xi/\partial x$ appears from the chain-rule: $\partial P/\partial x = (\partial\xi/\partial x)(\partial P/\partial\xi)$. This formula may also be written:

$$U_P = H_P - D_P^U (P_e - P_w) \tag{3.103}$$

A corresponding expression can be written for the neighbouring node to the east:

$$U_E = H_E - D_E^U (P_{ee} - P_e) \tag{3.104}$$

where subscript *ee* is the eastern face of the cell which has node E at its centre. The velocity at the eastern cell face can also be written:

$$U_e = H_e - D_e^U (P_E - P_P) \tag{3.105}$$

This final expression for the velocity at the eastern face includes the terms H_e and D_e^U. In the Rhie-Chow interpolation these terms are linearly interpolated from the neighbouring P and E values, taken from Equations (3.103) and (3.104):

$$\begin{aligned} U_e &= \frac{1}{2}(H_P + H_E) - \frac{1}{2}\left(D_P^U + D_E^U\right)(P_E - P_P) \\ &= \frac{1}{2}\left[U_P + D_P^U (P_e - P_w) + U_E + D_E^U (P_{ee} - P_e)\right] \\ &\quad -\frac{1}{2}\left(D_P^U + D_E^U\right)(P_E - P_P) \end{aligned} \tag{3.106}$$

which may also be written:

$$\begin{aligned} U_e &= \underbrace{\frac{1}{2}\left(U_P+U_E\right)}_{linear\,interpolation} \\ &\quad \underbrace{+\frac{1}{2}\left[D_P^U\left(P_e-P_w\right)+D_E^U\left(P_{ee}-P_e\right)-\left(D_P^U+D_E^U\right)\left(P_E-P_P\right)\right]}_{pressure\,smoothing} \end{aligned} \tag{3.107}$$

The U-velocity through the eastern face, U_e, can therefore be considered as consisting of two parts: a straight-forward linear interpolation and a smoothing term which is a function of the pressure at the neighbouring nodes. If the *ee* location coincides with a wall boundary, the pressure is extrapolated to the wall surface[5].

Extension of Rhie & Chow Interpolation to Include Normal Stresses

The steady momentum equation in Cartesian coordinates at high Reynolds numbers can be written as follows:

$$\frac{\partial}{\partial x_j}\left(\rho U_i U_j\right) = -\frac{\partial P}{\partial x_i} - \frac{\partial}{\partial x_j}\left(\rho\overline{u_i u_j}\right) \tag{3.108}$$

Taking the trace of this expression $(i=j)$, the pressure and Reynolds stress terms are both of the same form, i.e. expressing the gradient of a scalar. It is therefore possible to extend the Rhie-Chow interpolation to include gradients of the normal stresses with the pressure gradient. The discretized U-momentum equation is re-written:

$$U_P = \underbrace{\frac{\sum_{nb} a_{nb}U_{nb}}{a_P} + S_C}_{H_P} - \left(P_e-P_w\right)\underbrace{\frac{J\partial\xi/\partial x}{a_P}}_{D_P^U} - \left(\rho\overline{u^2}_e - \rho\overline{u^2}_w\right)\underbrace{\frac{J\partial\xi/\partial x}{a_P}}_{D_P^U} \tag{3.109}$$

where S_C now excludes the gradient parallel to the x-axis of both pressure and the $\overline{u^2}$ stress. The analysis given above, from Equations (3.103) to (3.107) can be repeated, substituting P with $\left(P+\rho\overline{u^2}\right)$. This results in the following expression for the U-velocity through the eastern face of a cell:

$$\begin{aligned} U_e &= \frac{1}{2}\left(U_P+U_E\right) \\ &\quad +\frac{1}{2}\left\{D_P^U\left[\left(P+\rho\overline{u^2}\right)_e - \left(P+\rho\overline{u^2}\right)_w\right]\right. \\ &\quad +D_E^U\left[\left(P+\rho\overline{u^2}\right)_{ee} - \left(P+\rho\overline{u^2}\right)_e\right] \\ &\quad \left.-\left(D_P^U+D_E^U\right)\left[\left(P+\rho\overline{u^2}\right)_E - \left(P+\rho\overline{u^2}\right)_P\right]\right\} \end{aligned} \tag{3.110}$$

[5]The pressure at the wall surface, calculated instead from Equation (3.85), was found to cause instability in some calculations and was therefore not used.

Similarly one can find the V-velocity through the cell faces using $\left(P+\rho\overline{v^2}\right)$, and for the W- velocity $\left(P+\rho\overline{w^2}\right)$. This correction can improve the stability of a calculation in which there are steep gradients in the normal Reynolds stresses.

3.3.7 Convergence Criteria

In STREAM, the dimensionless residual is calculated from:

$$R_\phi = \phi_P - \frac{\sum_{nb} a_{nb}\phi_{nb} + S}{a_P} \tag{3.111}$$

where *nb* indicates the neighbouring nodes (E, W, N, S, T and B) and the velocity component or turbulence scalar, ϕ, is dimensionless (as discussed in Section 3.3.2). A mass imbalance is calculated instead of a pressure residual. The convergence criteria is specified using the RMS residual which is calculated as follows:

$$R_\phi^{RMS} = \sqrt{\frac{1}{n}\sum_n R_\phi^2} \tag{3.112}$$

where n is the total number of nodes. The RMS residual tends to give a smaller value than the expressions used in the TEAM code (Section 3.2.4). The quantity, R_ϕ^{RMS} is also independent of the grid size (i.e. number of nodes) which allows the relative degree of convergence between different calculations to be assessed.

Chapter 4

Subgrid-Based Wall Function: UMIST-*N*

4.1 Assumptions & Methodology

Before going into the details of the new wall function, it is useful to highlight the similarities between standard wall functions and the new wall function. Firstly, the new wall function uses the same grid as would be used with standard wall functions, where there is a large near-wall cell that spans entirely the viscous sublayer[1]. Secondly, like standard wall functions, the new wall function returns values of the wall shear stress and average source terms, such as $\overline{P_k}$ and $\overline{\varepsilon}$, and these terms are employed in the discretized equations in exactly the same way as with standard wall functions (see Chapter 3). Thirdly, the new wall function can be used with any level of turbulence closure and it can be easily modified to be used in any flow geometry or coordinate system (axisymmetric, 3-*D*, non-orthogonal etc.).

The primary difference between the new wall function and standard treatments is that the new wall function does not use any assumed profiles of velocity or length scale. Instead, profiles of the mean flow and turbulence parameters near the wall are obtained by solving simplified boundary-layer-type transport equations using a fine "subgrid" spanning the wall-adjacent control volume (see Figure 4.1). The wall function differs from standard low-*Re* treatments in that it decouples the numerical solution of the near-wall region from that of the main region of the flow domain and also because it does not involve the solution of the pressure-correction equation over the subgrid. The new wall function therefore does not suffer from the slow convergence problems of a full low-*Re* calculation.

The transport equations solved by the wall function across the subgrid account for convection (both parallel and normal to the wall), pressure gradient, diffusion normal to the wall and source terms. In the present study, a linear and a non-linear $k-\varepsilon$ model have been tested and so simplified *k*- and $\tilde{\varepsilon}$-equations have been solved in the wall function in addition to equations for the wall-parallel velocity components and temperature (where a thermal field is solved). The subgrid transport equations are

[1]Typically the y^+ of the near-wall node should be in the range $30 \rightarrow 300$. However, the new wall function is not reliant upon the velocity log-law and low-Reynolds-number model equations are solved throughout the domain so the cell size can be varied above and below these limits.

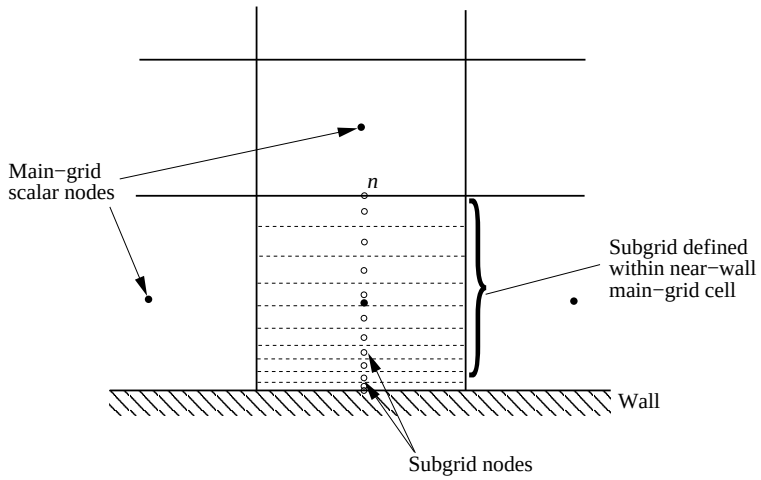

Figure 4.1: Subgrid arrangement within near-wall main-grid control volume

discretized in a similar manner to that used for simple one-dimensional diffusion problems and solved using a Tri-Diagonal Matrix Algorithm (TDMA). The wall-normal V-velocity in the near-wall cell is calculated from continuity within each of the subgrid cells and is scaled to ensure that the subgrid V-velocity at the outer edge of the subgrid (position n in Figure 4.1) is consistent with the main-grid wall-normal velocity at that location. One subgrid iteration is performed for each main-grid iteration so the subgrid solution converges as the main-grid solution converges. After each subgrid iteration, average values of the source terms across the subgrid are calculated (e.g. $\overline{P_k}$, $\overline{\varepsilon}$), along with the wall shear stress and, if the thermal field is being solved, the wall heat flux or wall temperature. These quantities are then applied as modified source terms in the main-grid near-wall cells as would be done in a standard wall-function approach. However, both the k- and ε-equations are solved in the main-grid near-wall cell, unlike the standard wall functions documented earlier which only solved for k and prescribed ε. In addition, low-Reynolds-number damping terms are included in the main-grid transport equations to enable unlimited refinement of the grid near the wall.

As was mentioned in the Introduction, the new wall function has been developed at UMIST as part of a concerted effort to find accurate and efficient alternatives to standard log-law-based wall functions. The new wall function is called UMIST-*N*: Unified Modelling through Integrated Sublayer Treatment - a *N*umerical approach.

4.2 Governing Equations

A number of assumptions are applied within the subgrid in order to obtain a simplified set of transport equations: only the momentum equation(s) parallel to the wall are solved, the diffusion parallel to the wall is assumed to be negligible in comparison to that normal to the wall, and the pressure gradient is assumed to be constant across the near-wall main-grid cell. These assumptions are applied to the Reynolds-averaged Navier-Stokes equations for momentum, energy and appropriate turbulence pa-

rameters. The current version of the wall function uses the low-Reynolds-number Launder & Sharma $k-\varepsilon$ model [13] and the non-linear EVM of Craft *et al*. [30] but in principle any turbulence model that can be integrated all the way to the wall can be used (e.g. one-equation model, $k-\omega$, DSM).

The Navier-Stokes equations are often presented in Cartesian tensor form to express succinctly the physical meaning of the various components (convection, diffusion, pressure gradient etc.) without the complicated and perhaps unfamiliar terms introduced by more general coordinate systems. However, for flows involving curved or complex-shaped walls one is forced to use body-fitted grids and the transport equations must be expressed in curvilinear coordinates. The subgrid wall function was initially developed with reference to flows in fairly simple geometries using a Cartesian grid: the channel flow, impinging jet and spinning disc flows. The governing equations which were used in these test cases are presented below (for simple 2-*D* flow) and in Appendix A for 2-*D*/axisymmetric flows involving swirl. Subgrid transport equations for the more general non-orthogonal curvilinear coordinate system are also summarized below, with a full derivation of these expressions being given in Appendix D.

4.2.1 2-*D* Cartesian Grid

In a simple 2-*D* Cartesian geometry, transport equations are solved across the subgrid for the wall-parallel U-momentum, turbulent kinetic energy, k, isotropic dissipation rate, $\tilde{\varepsilon}$, and for cases in which the thermal field is solved, temperature, T. These four subgrid transport equations are written as follows for steady incompressible flow:

$$\rho U\frac{\partial U}{\partial x}+\rho V\frac{\partial U}{\partial y}=-\frac{\mathrm{d}P}{\mathrm{d}x}+\frac{\partial}{\partial y}\left[\mu\frac{\partial U}{\partial y}-\rho\overline{uv}\right] \tag{4.1}$$

$$\rho U\frac{\partial k}{\partial x}+\rho V\frac{\partial k}{\partial y}=\frac{\partial}{\partial y}\left[\left(\mu+\frac{\mu_t}{\sigma_k}\right)\frac{\partial k}{\partial y}\right]+P_k-\rho\varepsilon \tag{4.2}$$

$$\rho U\frac{\partial \tilde{\varepsilon}}{\partial x}+\rho V\frac{\partial \tilde{\varepsilon}}{\partial y}=\frac{\partial}{\partial y}\left[\left(\mu+\frac{\mu_t}{\sigma_\varepsilon}\right)\frac{\partial \tilde{\varepsilon}}{\partial y}\right]+c_{\varepsilon 1}f_1P_k\frac{\tilde{\varepsilon}}{k}-c_{\varepsilon 2}f_2\rho\frac{\tilde{\varepsilon}^2}{k}+\rho Y_c+P_{\varepsilon 3} \tag{4.3}$$

$$\rho U\frac{\partial T}{\partial x}+\rho V\frac{\partial T}{\partial y}=\frac{\partial}{\partial y}\left[\left(\frac{\mu}{\sigma}+\frac{\mu_t}{\sigma_t}\right)\frac{\partial T}{\partial y}\right] \tag{4.4}$$

Each of the low-Reynolds-number damping terms appearing in the above equations has previously been discussed in Chapter 2. The pressure gradient is intentionally not expressed using partial derivatives since $\mathrm{d}P/\mathrm{d}x$ is assumed constant across the subgrid. Some of the source terms appearing in the above expressions can be simplified using the boundary-layer assumptions. For instance, the total dissipation rate (ε) which appears in the k-equation is given by:

$$\varepsilon=\tilde{\varepsilon}+2\nu\left(\frac{\partial k^{1/2}}{\partial x_j}\right)^2 \tag{4.5}$$

which is approximated in the subgrid by:

$$\varepsilon \approx \tilde{\varepsilon} + 2\nu \left(\frac{\partial k^{1/2}}{\partial y} \right)^2 \tag{4.6}$$

The differential Yap correction (see Equation 2.17) can cause some instability when it is employed in the subgrid wall function. This problem only occurs at the start of a calculation when there are rapid changes in the values of k and $\tilde{\varepsilon}$ between successive iterations. Since the subgrid k- and $\tilde{\varepsilon}$-equations are under-relaxed, they do not respond immediately to changes in the boundary conditions and, if the main-grid k and $\tilde{\varepsilon}$ fields are changing rapidly, this can lead to large length-scale gradients in the subgrid. To overcome this problem, the Yap correction in the outermost subgrid cell (farthest from the wall) is set to zero initially and is re-introduced only once the solution is nearly converged.

Linear $k-\varepsilon$ Model

Using the linear $k-\varepsilon$ EVM, the Reynolds stress is assumed to be a linear function of the mean strain rate:

$$-\overline{u_i u_j} + \frac{2}{3} k \delta_{ij} = \nu_t S_{ij} \tag{4.7}$$

where the strain-rate tensor, S_{ij}, is given by:

$$S_{ij} = \frac{\partial U_i}{\partial x_j} + \frac{\partial U_j}{\partial x_i} \tag{4.8}$$

and the kinematic eddy-viscosity, ν_t:

$$\nu_t = c_\mu f_\mu \frac{k^2}{\tilde{\varepsilon}} \tag{4.9}$$

Substituting these two expressions into the subgrid wall-parallel momentum equation one obtains:

$$\rho U \frac{\partial U}{\partial x} + \rho V \frac{\partial U}{\partial y} = -\frac{\mathrm{d}P}{\mathrm{d}x} - \frac{\mathrm{d}}{\mathrm{d}x}\left(\frac{2}{3}\rho k\right) + \frac{\partial}{\partial y}\left[(\mu + \mu_t)\frac{\partial U}{\partial y}\right] \tag{4.10}$$

Note that the wall-parallel gradient of the isotropic stress component $2/3\rho k$ has been retained, despite the assumption stated earlier that diffusion parallel to the wall is ignored within the subgrid. This term is included for convenience since it is common practice in CFD codes to include the $2/3\rho k$ term with the pressure, so that the "pressure" which is stored in computer memory is in fact $\left(P' = P + 2\rho k/3\right)$. In tests with the impinging jet flow, discussed later, including the $2/3\rho k$ term with the subgrid pressure gradient had negligible effect.

The production of turbulent kinetic energy, P_k, used in the subgrid k and $\tilde{\varepsilon}$ equations, includes

components from all of the stresses:

$$\begin{aligned} P_k &= -\rho\overline{u_i u_j}\frac{\partial U_i}{\partial x_j} \\ &= -\rho\overline{u^2}\frac{\partial U}{\partial x} - \rho\overline{uv}\left(\frac{\partial U}{\partial y}+\frac{\partial V}{\partial x}\right) - \rho\overline{v^2}\frac{\partial V}{\partial y} \end{aligned} \tag{4.11}$$

whilst the gradient production term, $P_{\varepsilon 3}$, is simplified:

$$P_{\varepsilon 3} = 2\mu\nu_t\left(\frac{\partial^2 U_i}{\partial x_j \partial x_k}\right)^2 \approx 2\mu\nu_t\left(\frac{\partial^2 U}{\partial y^2}\right)^2 \tag{4.12}$$

The remaining damping functions in the linear $k-\varepsilon$ model of Launder & Sharma are the same as those presented in Chapter 2.

Non-Linear $k-\varepsilon$ Model

The calculation of the Reynolds stress across the subgrid using the Craft *et al*. two-equation NLEVM involves the same expressions as discussed in Section 2.3 for the main-grid. The recommendations of Craft, Iacovides & Yoon [67] are followed to maximize the numerical stability of the model, which lead to the following expression for the subgrid U-momentum:

$$\rho U\frac{\partial U}{\partial x} + \rho V\frac{\partial U}{\partial y} = -\frac{\mathrm{d}P^{'}}{\mathrm{d}x} + \frac{\partial}{\partial y}\left[\left(\mu+\mu_t'\right)\frac{\partial U}{\partial y} - \rho\widehat{\overline{uv}}\right] \tag{4.13}$$

The modified eddy-viscosity, μ_t', includes any positive contribution from the last two cubic terms in Equation (2.27), and $\widehat{\overline{uv}}$ is the remaining higher-order components of the Reynolds stress, i.e.:

$$\mu_t' = \mu_t - \mu_t\frac{k^2}{\tilde{\varepsilon}^2}\min\left[\left(c_6 S_{kl}S_{kl} + c_7\Omega_{kl}\Omega_{kl}\right),0\right] \tag{4.14}$$

$$\begin{aligned} -\widehat{\overline{uv}} &= \nu_t\frac{k}{\tilde{\varepsilon}}\left[c_1 S_{12}\left(S_{11}+S_{22}\right)\right. \\ &\quad \left. + c_2\Omega_{12}\left(S_{22}-S_{11}\right)\right] \\ &\quad + \nu_t\left(\frac{k}{\tilde{\varepsilon}}\right)^2\left[c_4\Omega_{12}\left(S_{11}^2 - S_{22}^2\right)\right. \\ &\quad \left. + S_{12}\max\left[\left(c_6 S_{kl}S_{kl} + c_7\Omega_{kl}\Omega_{kl}\right),0\right]\right] \end{aligned} \tag{4.15}$$

The only other difference between the subgrid equations and the main-grid equations presented in Section 2.3, is the simplification of the gradient production term, $P_{\varepsilon 3}$, which is approximated as:

$$\begin{aligned} P_{\varepsilon 3} &\approx 0.0022\frac{\tilde{S}\mu_t k^2}{\tilde{\varepsilon}}\left(\frac{\partial^2 U}{\partial y^2}\right)^2 \quad \text{for} \quad \tilde{R}_t \le 250 \\ &= 0 \qquad\qquad\qquad\qquad\quad \text{for} \quad \tilde{R}_t > 250 \end{aligned} \tag{4.16}$$

4.2.2 Non-Orthogonal Curvilinear Grid

There are several types of curvilinear coordinate systems. These can be divided into orthogonal and non-orthogonal curvilinear coordinate systems, which can be further subdivided into systems where the velocity vectors are either aligned with the coordinate system or are aligned to another (usually Cartesian) reference frame. For example, the STREAM code [72, 73] uses a non-orthogonal grid in which velocity vectors are aligned to a Cartesian reference frame. There are advantages to the approach used by STREAM, as discussed in [73], where it is shown that the resulting momentum equations can be expressed in "strong conservation form". However, this approach can also suffer from increased numerical diffusion when there are large skew angles between the velocity components and the faces of the computational cells [83]. In the subgrid wall function, simplified equations are solved for velocity components parallel to the wall within the subgrid region. This requires the use of a coordinate system in which velocity vectors are aligned with the wall (i.e. aligned with the curvilinear coordinate system, assuming a body-fitted grid is adopted).

The Navier-Stokes equations were derived in orthogonal curvilinear coordinates, with velocity vectors aligned to the coordinate system, by Pope [84]. Orthogonal curvilinear coordinates are attractive in that some of the mathematics can be simplified, but this approach relies upon a grid generation algorithm which ensures that grid lines intersect at right-angles throughout the domain, which is difficult to achieve in complex three-dimensional geometries. The alternative formulation of the Navier-Stokes equations in a non-orthogonal curvilinear coordinate system with velocity vectors aligned to the grid has been employed by, among others, Richmond *et al*. [83], Demirdžić *et al*. [85, 86], Gal-Chen & Somerville [87], Mynett *et al*. [88] and Lee & Soni [89].

The transport equations in non-orthogonal curvilinear coordinates are long and fairly complicated. Since it is easy to make typographical errors with such expressions, and due to the relatively unfamiliar nature of the notation to many readers, a comprehensive introduction and background has been provided in Appendix B. This should enable any errors to be traced and allow the reader to follow the derivation without recourse to additional texts. Further analysis can be found in Lien's thesis [73], which describes the fundamentals of the STREAM code. The conventions adopted in this thesis follow those of Farrashkhalvat & Miles [90] whilst, in some cases, conventions used by Demirdžić *et al*. have been used to allow direct comparison with equations given in their paper. For a general introduction to tensors see, for example, Aris [91], Simmonds [92] or McConnell [93].

The three-dimensional non-orthogonal subgrid coordinate system has directional components (ξ,η,ζ). Throughout this thesis, it is assumed that the ξ- and η-components are aligned to grid lines which are parallel to the wall whilst the ζ-axis is usually, but not necessarily, wall-normal (i.e. not wall-parallel), see Figure 4.2. The subgrid transport equations can all be written in the following generic form:

$$\frac{\rho U}{\sqrt{g_{11}}}\left(\frac{\partial\phi}{\partial\xi}\right)^{*}+\frac{\rho V}{\sqrt{g_{22}}}\left(\frac{\partial\phi}{\partial\eta}\right)^{*}+\frac{\rho W}{\sqrt{g_{33}}}\left(\frac{\partial\phi}{\partial\zeta}\right)^{*}=\frac{1}{J}\frac{\partial}{\partial\zeta}\left(Jg^{33}\Gamma\frac{\partial\phi}{\partial\zeta}\right)+C \tag{4.17}$$

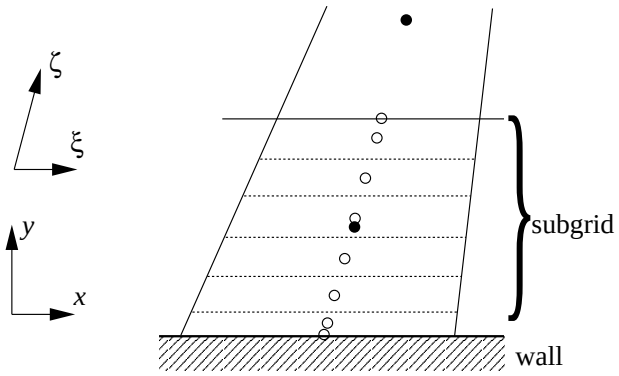

Figure 4.2: Typical non-orthogonal arrangement of subgrid cells showing Cartesian $x-y$ axis and curvilinear $\xi-\zeta$ axes.

where ϕ denotes one of the subgrid parameters: U, V, k or $\tilde{\varepsilon}$, Γ is the diffusivity and the source term, C, includes geometry-related source terms, the pressure gradient in the momentum equations and production and dissipation sources in the k- and $\tilde{\varepsilon}$-equations. The velocity components U, V and W act in the ξ, η and ζ directions respectively and are "physical" velocities, i.e. they have units of (length/time). Gradient terms appearing in the convection are discretized using upwind differencing. The asterisk $(^*)$ denotes the fact that, for some quantities, the upstream values of ϕ appearing in the discretized convection terms are transformed from the coordinate system used in the upstream cell into the current cell coordinate system. This transformation only affects the convection of momentum where the direction of the velocity vectors in the upstream cell may differ from those in the current cell. Since scalar parameters (k and $\tilde{\varepsilon}$) are invariant to the reference frame, the upstream values of scalars do not have to undergo such transformations. The $\sqrt{g_{11}}$, $\sqrt{g_{22}}$ and $\sqrt{g_{33}}$ terms (square-roots of the covariant metric tensor components) are equivalent to the physical widths of the cells in the ξ, η and ζ directions respectively. When the above transport equation is discretized, as discussed later, it is assumed that the widths of the computational cells in the three coordinate directions are unity, i.e. $\Delta\xi = \Delta\eta = \Delta\zeta = 1$. It can be seen, then, that the convection terms in the above expression are equivalent to their counterparts in Cartesian coordinates, i.e.:

$$\frac{\rho U}{\sqrt{g_{11}}}\frac{\partial\phi}{\partial\xi} \rightarrow \rho U\frac{\partial\phi}{\partial x} \tag{4.18}$$

The diffusion term in the above generic transport equation involves two geometric symbols: the Jacobian, J, and the contravariant metric tensor, g^{33}. For cells of unit dimensions ($\Delta\xi = \Delta\eta = \Delta\zeta = 1$), the Jacobian is simply the physical cell volume whilst the g^{33} tensor is equivalent to the square of the area of the face in the wall-parallel $\xi-\eta$ plane (A_{12}) divided by the cell volume squared, i.e.:

$$g^{33} = \left(\frac{A_{12}}{J}\right)^2 \tag{4.19}$$

In a Cartesian system this is simply the inverse of the cell height squared, $g^{33} = (1/\Delta z)^2$, if the wall is in the $x-y$ plane. Substituting this into the diffusion term, we obtain:

$$\frac{1}{J}\frac{\partial}{\partial\zeta}\left[\frac{(A_{12})^2}{J}\Gamma\frac{\partial\phi}{\partial\zeta}\right] \tag{4.20}$$

If this is discretized and integrated over the physical cell volume ($\Delta Vol = J\Delta\xi\Delta\eta\Delta\zeta$), the coefficients associated with the top and bottom nodes in the discretized equation (a_T and a_B) are of the form:

$$\frac{\Gamma A}{L} \tag{4.21}$$

where A is the cell-face area and L is the vertical distance between adjacent nodes. This is identical to the expression obtained when a Cartesian coordinate system is employed. In the linear and non-linear $k-\varepsilon$ models used in the present study, the diffusivity for the wall-parallel momentum equations is:

$$\Gamma = \mu + \mu_t = \mu_{eff} \tag{4.22}$$

and for the k and ε equations:

$$\Gamma_k = \mu + \frac{\mu_t}{\sigma_k} \tag{4.23}$$

$$\Gamma_\varepsilon = \mu + \frac{\mu_t}{\sigma_\varepsilon} \tag{4.24}$$

Wall-Parallel Momentum

The transport equation for the wall-parallel momentum is lengthy and complicated since, on a curved grid, the coordinate axes to which the velocity vectors are aligned change between neighbouring cells. The momentum equation thus has to take into account the fact that the U-velocity in one cell may be pointing in a different direction to the U-velocity in an adjacent cell. The subgrid wall-parallel U- and V-momentum equations are written:

$$\frac{\rho U}{\sqrt{g_{11}}}\left(\frac{\partial U}{\partial\xi}\right)^* + \frac{\rho V}{\sqrt{g_{22}}}\left(\frac{\partial U}{\partial\eta}\right)^* + \frac{\rho W}{\sqrt{g_{33}}}\left(\frac{\partial U}{\partial\zeta}\right)^* = \frac{1}{J}\frac{\partial}{\partial\zeta}\left(Jg^{33}\Gamma\frac{\partial U}{\partial\zeta}\right) + C^1 \tag{4.25}$$

$$\frac{\rho U}{\sqrt{g_{11}}}\left(\frac{\partial V}{\partial\xi}\right)^* + \frac{\rho V}{\sqrt{g_{22}}}\left(\frac{\partial V}{\partial\eta}\right)^* + \frac{\rho W}{\sqrt{g_{33}}}\left(\frac{\partial V}{\partial\zeta}\right)^* = \frac{1}{J}\frac{\partial}{\partial\zeta}\left(Jg^{33}\Gamma\frac{\partial V}{\partial\zeta}\right) + C^2 \tag{4.26}$$

The source term, C^i, can be summarized as follows:

$$\begin{aligned} C^i \quad = \quad & \underbrace{-\tau^{ij}\frac{\Gamma^m_{ij}g_{im}}{\sqrt{g_{ii}}}+\tau^{mj}\Gamma^i_{mj}\sqrt{g_{ii}}}_{diffusion\ I} \\ & \underbrace{+\frac{1}{J}\frac{\partial}{\partial\zeta}\left[J\mu_{eff}g^{33}\left(U^{(m)}\frac{\sqrt{g_{ii}}}{\sqrt{g_{mm}}}\Gamma^i_{m3}-U\frac{g_{im}}{g_{ii}}\Gamma^m_{i3}\right)\right]}_{diffusion\ II} \\ & \underbrace{-g^{ij}\sqrt{g_{ii}}\frac{\partial P'}{\partial\xi^j}}_{pressure\ gradient} \\ & \text{no summation on } i \end{aligned} \tag{4.27}$$

where $i = 1$ and 2 for the U- and V-momentum equations respectively. The velocities, (U,V,W) in the three component directions (ξ,η,ζ) are denoted $U^{(j)}$, where the parenthesis is used to emphasize the fact that the velocities are "physical". The Γ^m_{ij} terms are Christoffel symbols of the second kind which result from having a non-uniform grid distribution. These terms will be non-zero if, for example, the grid cells are clustered together towards the wall or if the wall is curved.

Calculation of the Stress, τ^{ij}

The non-physical stress tensor, τ^{ij}, for incompressible flow is given by:

$$\tau^{ij} = \mu\left(g^{jm}U^i_{,m}+g^{im}U^j_{,m}\right)-\rho\overline{u^iu^j} \tag{4.28}$$

For a linear $k-\varepsilon$ model, the Reynolds stress, $\overline{u^iu^j}$, is given by:

$$\overline{u^iu^j} = -\nu_t S^{ij}+\frac{2}{3}g^{ij}k \tag{4.29}$$

where the strain-rate, S^{ij}, is:

$$S^{ij} = \left(g^{jm}U^i_{,m}+g^{im}U^j_{,m}\right) \tag{4.30}$$

and the velocity gradient, $U^i_{,j}$:

$$U^i_{,j} \quad = \quad \frac{\partial}{\partial\xi^j}\left(\frac{U^{(i)}}{\sqrt{g_{ii}}}\right)+\frac{U^{(m)}}{\sqrt{g_{mm}}}\Gamma^i_{mj} \tag{4.31}$$

For the non-linear $k-\varepsilon$ model of Craft *et al*. the Reynolds stress, $\overline{u^i u^j}$, is given by:

$$\begin{aligned}
\overline{u^i u^j} &= -\nu_t S^{ij} + \frac{2}{3} g^{ij} k \\
&+ c_1 \frac{\nu_t k}{\tilde{\varepsilon}} \left(g_{kl} S^{ik} S^{jl} - \frac{1}{3} g_{km} g_{ln} S^{kl} S^{mn} g^{ij} \right) \\
&+ c_2 \frac{\nu_t k}{\tilde{\varepsilon}} \left(g_{kl} \Omega^{ik} S^{jl} + g_{kl} \Omega^{jk} S^{il} \right) \\
&+ c_3 \frac{\nu_t k}{\tilde{\varepsilon}} \left(g_{kl} \Omega^{ik} \Omega^{jl} - \frac{1}{3} g_{km} g_{ln} \Omega^{kl} \Omega^{mn} g^{ij} \right) \\
&+ c_4 \frac{\nu_t k^2}{\tilde{\varepsilon}^2} \left(S^{ki} \Omega^{lj} + S^{kj} \Omega^{li} \right) g_{lm} g_{kn} S^{mn} \\
&+ c_5 \frac{\nu_t k^2}{\tilde{\varepsilon}^2} \left(g_{kl} g_{mn} \Omega^{ik} \Omega^{ln} S^{mj} + g_{kl} g_{mn} S^{ik} \Omega^{ln} \Omega^{mj} - \frac{2}{3} g_{kl} g_{mo} g_{np} S^{km} \Omega^{on} \Omega^{pl} g^{ij} \right) \\
&+ c_6 \frac{\nu_t k^2}{\tilde{\varepsilon}^2} g_{km} g_{ln} S^{ij} S^{ml} S^{kn} \\
&+ c_7 \frac{\nu_t k^2}{\tilde{\varepsilon}^2} g_{km} g_{ln} S^{ij} \Omega^{ml} \Omega^{kn}
\end{aligned} \tag{4.32}$$

Fortunately the constant c_5 in the Craft *et al*. model is zero so there is no need to expand one line of the above expression. The recommended practice of including the c_6 and c_7 terms with the linear component is used, as for the Cartesian formulation. For details see Appendix D.

Calculation of the Pressure Gradient

Returning to the expression for the source term, C, (Equation 4.27), the final pressure gradient term involves gradients of the effective pressure in all three coordinate directions. For example the U-momentum equation pressure term is given by:

$$g^{ij} \sqrt{g_{ii}} \frac{\partial P'}{\partial \xi^j} = \sqrt{g_{11}} \left(g^{11} \frac{\partial P'}{\partial \xi} + g^{12} \frac{\partial P'}{\partial \eta} + g^{13} \frac{\partial P'}{\partial \zeta} \right) \tag{4.33}$$

where $\left(P' = P + 2\rho k/3 \right)$ is used for convenience as with the Cartesian formulation. If the subgrid cells are arranged such that the ζ-axis is orthogonal to the wall, then the contravariant metric tensor, g^{13}, is zero and there is no contribution from the $\partial P'/\partial \zeta$ term in the above expression. However, if the cells are skewed and the ζ-axis is no longer normal to the wall, g^{13} is finite and the $\partial P'/\partial \zeta$ term may become significant. Effectively, this is saying that when the cells are skewed relative to the wall, the pressure gradient in the ζ-direction has a component that is parallel to the wall. Whilst this may at first seem a relatively simple problem to solve, on closer inspection it becomes apparent that one needs to know how the pressure changes across the near-wall region (even though one does not solve for the pressure across the subgrid). To obtain a truly accurate representation of the pressure distribution across the subgrid for complex flows one would have to solve elliptic equations which would defeat

the purpose of the wall function (since effectively one would be obtaining a full low-Reynolds-number model solution). On the other hand, simply prescribing an arbitrary shape for the $\partial P^{'}/\partial\zeta$ profile is unlikely to be general enough for the wall function to work in a variety of complex flows. Instead, the following expression is solved across the subgrid:

$$\nabla P \cdot \hat{\mathbf{n}} + (\nabla \cdot \rho\overline{\mathbf{u} \otimes \mathbf{u}}) \cdot \hat{\mathbf{n}} = 0 \tag{4.34}$$

where $\hat{\mathbf{n}}$ is the unit wall-normal vector, $\overline{\mathbf{u} \otimes \mathbf{u}}$ is the Reynolds stress in vector form and the gradient operator, ∇, can be written for non-orthogonal coordinates as:

$$\nabla = \frac{\partial \xi^j}{\partial x^i}\frac{\partial}{\partial \xi^j}\mathbf{e}_i \tag{4.35}$$

where $\mathbf{e}_i$ is the Cartesian unit vector and $\partial\xi^j/\partial x^i$ is a property of the grid. This expression is identical to that used in the STREAM code to evaluate the pressure on the wall surface (see Section 3.3.5).

Turbulent Kinetic Energy, k

The subgrid k-equation in curvilinear coordinates is as follows:

$$\frac{\rho U}{\sqrt{g_{11}}}\frac{\partial k}{\partial \xi} + \frac{\rho V}{\sqrt{g_{22}}}\frac{\partial k}{\partial \eta} + \frac{\rho W}{\sqrt{g_{33}}}\frac{\partial k}{\partial \zeta} = \frac{1}{J}\frac{\partial}{\partial \zeta}\left[Jg^{33}\left(\mu + \frac{\mu_t}{\sigma_k}\right)\frac{\partial k}{\partial \zeta}\right] + P_k - \rho\varepsilon \tag{4.36}$$

The production rate source term is given by:

$$P_k = -\rho g_{im}\overline{u^j u^m}U^i_{,j} \tag{4.37}$$

and is expanded fully (including all the shear and normal stress components). The expressions for the Reynolds stresses are given above for the linear and non-linear models (Equations 4.29 and 4.32 respectively) and the velocity gradient, $U^i_{,j}$, is given by Equation (4.31). The expression for the total dissipation rate is simplified by considering only the gradient of $k^{1/2}$ parallel to the ζ-axis:

$$\begin{aligned} \varepsilon &= \tilde{\varepsilon} + 2\nu g^{jm}\left(\frac{\partial k^{1/2}}{\partial \xi^m}\right)\left(\frac{\partial k^{1/2}}{\partial \xi^j}\right) \\ &\approx \tilde{\varepsilon} + 2\nu g^{33}\left(\frac{\partial k^{1/2}}{\partial \zeta}\right)\left(\frac{\partial k^{1/2}}{\partial \zeta}\right) \end{aligned} \tag{4.38}$$

Isotropic Dissipation Rate, $\tilde{\varepsilon}$

The subgrid $\tilde{\varepsilon}$-equation in curvilinear coordinates is as follows:

$$\begin{aligned}\frac{\rho U}{\sqrt{g_{11}}}\frac{\partial\tilde{\varepsilon}}{\partial\xi}+\frac{\rho V}{\sqrt{g_{22}}}\frac{\partial\tilde{\varepsilon}}{\partial\eta}+\frac{\rho W}{\sqrt{g_{33}}}\frac{\partial\tilde{\varepsilon}}{\partial\zeta} &= \frac{1}{J}\frac{\partial}{\partial\zeta}\left[Jg^{33}\left(\mu+\frac{\mu_t}{\sigma_\varepsilon}\right)\frac{\partial\tilde{\varepsilon}}{\partial\zeta}\right] \\ &\quad +c_{\varepsilon1}f_1P_k\frac{\tilde{\varepsilon}}{k}-c_{\varepsilon2}f_2\rho\frac{\tilde{\varepsilon}^2}{k}+\rho Y_c+P_{\varepsilon3} \qquad (4.39)\end{aligned}$$

The source terms appearing in the $\tilde{\varepsilon}$-equation include production $(c_{\varepsilon1}f_1P_k\tilde{\varepsilon}/k)$, dissipation $\left(c_{\varepsilon2}f_2\tilde{\varepsilon}^2/k\right)$, the Yap correction (Y_c) and the near-wall gradient-production source term $(P_{\varepsilon3})$. The production term has already been expanded above for the *k*-equation and the dissipation term does not require further expansion. The standard Yap correction is unchanged in curvilinear coordinates and relies solely upon the wall normal distance and values of *k* and $\tilde{\varepsilon}$. The gradient of the length scale appearing in the differential Yap correction (see Equation 2.17) is simplified as follows:

$$\begin{aligned}F &= \frac{1}{c_l}\left[\left(g^{jk}\frac{\partial l}{\partial\xi^j}\frac{\partial l}{\partial\xi^k}\right)^{1/2}-dl_e dy\right] \qquad (4.40)\\ &\approx \frac{1}{c_l}\left[\left(g^{33}\frac{\partial l}{\partial\zeta}\frac{\partial l}{\partial\zeta}\right)^{1/2}-dl_e dy\right] \qquad (4.41)\end{aligned}$$

where the additional contravariant metric tensor $\left(g^{jk}\right)$ is introduced into Equation (4.40) in order to satisfy the summation convention and it is assumed that the gradient of the length scale parallel to the wall is negligible in comparison with the gradient normal to the wall. The $dl_e dy$ term is identical to that given earlier (see Equation 2.19). The same recommendations apply to the curvilinear version of the UMIST-*N* wall function as with the Cartesian formulation, namely that the differential Yap correction in the outermost subgrid cell (farthest from the wall) is set to zero initially and is re-introduced only once the solution is nearly converged.

The full expansion of the gradient production source term, $P_{\varepsilon3}$, in curvilinear coordinates is given by:

$$P_{\varepsilon3}=2\mu\nu_t g_{im}g_{jn}g^{lp}\left(g^{no}U^m_{,o}\right)_{,p}\left(g^{jk}U^i_{,k}\right)_{,l} \qquad (4.42)$$

where the double-derivative of the velocity component is given by:

$$\left(g^{jk}U^i_{,k}\right)_{,l}=\frac{\partial\left(g^{jk}U^i_{,k}\right)}{\partial\xi^l}+g^{jk}U^m_{,k}\Gamma^i_{ml}+g^{mk}U^i_{,k}\Gamma^j_{ml} \qquad (4.43)$$

To simplify this term, it is assumed that only the gradient of the wall-parallel velocity components in the wall-normal direction are significant (i.e. $k=l=o=p=3$ and $i=m=1,2$):

$$P_{\varepsilon3}=2\mu\nu_t\left[g_{11}g_{jn}g^{33}\left(g^{n3}U_{,3}\right)_{,3}\left(g^{j3}U_{,3}\right)_{,3}+g_{22}g_{jn}g^{33}\left(g^{n3}V_{,3}\right)_{,3}\left(g^{j3}V_{,3}\right)_{,3}\right] \qquad (4.44)$$

where the double-derivative term is obtained from:

$$\left(g^{j3}U^i_{,3}\right)_{,3} = \frac{\partial\left(g^{j3}U^i_{,3}\right)}{\partial\zeta} + g^{j3}\left(U_{,3}\Gamma^i_{13} + V_{,3}\Gamma^i_{23}\right) + U^i_{,3}\left(g^{13}\Gamma^j_{13} + g^{23}\Gamma^j_{23} + g^{33}\Gamma^j_{33}\right) \tag{4.45}$$

It is assumed that the derivative of the W-velocity in the wall-normal ζ-direction is negligible in comparison with the other contributions. The above expressions require the values of strain-rates $U_{,3}$ and $V_{,3}$, the contravariant metric tensor g^{33} and the Jacobian, J to be calculated at the top and bottom subgrid cell boundaries (in the ζ-direction). These are found from linear interpolation of the physical velocity components, U and V, and the Christoffel symbols, between adjacent nodal values.

4.3 Implementation

In the previous section the subgrid transport equations were presented for a simple two-dimensional Cartesian geometry and the more complex non-orthogonal curvilinear coordinate system. The discretization and implementation of these two sets of transport equations is fundamentally the same and so for clarity, the following section describes the implementation of UMIST-*N* in a 2-*D* Cartesian geometry. See Appendix E for details of the non-orthogonal case.

4.3.1 Discretized Equations

The subgrid transport equations for wall-parallel velocity, U, turbulent kinetic energy, k, isotropic dissipation rate, $\tilde{\varepsilon}$, and temperature , T, can all be expressed in the general form:

$$\rho U\frac{\partial\phi}{\partial x} + \rho V\frac{\partial\phi}{\partial y} = \frac{\partial}{\partial y}\left(\Gamma\frac{\partial\phi}{\partial y}\right) + C \tag{4.46}$$

where ϕ is either U, k, $\tilde{\varepsilon}$ or T, Γ is the relevant diffusivity and C includes all the source terms.

1-*D* Diffusion

If one firstly considers only the diffusion and source terms in the above expression:

$$\frac{\partial}{\partial y}\left(\Gamma\frac{\partial\phi}{\partial y}\right) + C = 0 \tag{4.47}$$

where C is assumed constant across each cell. Applying the finite-volume approach (see Section 3.1): integrating the transport equation across a subgrid cell and using central differencing to evaluate gradients, the above equation becomes:

$$\Gamma_n A_n\frac{(\phi_N - \phi_P)}{\Delta y_{NP}} - \Gamma_s A_s\frac{(\phi_P - \phi_S)}{\Delta y_{PS}} + (C)_P\,\Delta Vol = 0 \tag{4.48}$$

where A is the cross-sectional area of the cell, ΔVol is the cell volume, subscripts n and s refer to the north and south boundaries and P, N and S to the current, northern and southern nodes, Δy_{NP} is the distance from node N to node P, and Δy_{PS} the distance from node P to node S, as shown in Figure 4.3. Simplifying this expression one obtains:

$$D_n(\phi_N - \phi_P) - D_s(\phi_P - \phi_S) + (C)_P \Delta Vol = 0 \tag{4.49}$$

where:

$$D_n = \frac{\Gamma_n A_n}{\Delta y_{NP}} \tag{4.50}$$

$$D_s = \frac{\Gamma_s A_s}{\Delta y_{PS}} \tag{4.51}$$

Grouping coefficients of ϕ_P results in:

$$D_n\phi_N + D_s\phi_S + (C)_P \Delta Vol = (D_n + D_s)\phi_P \tag{4.52}$$

which can be expressed as:

$$a_P\phi_P = a_N\phi_N + a_S\phi_S + S \tag{4.53}$$

where:

$$a_N = D_n = \frac{\Gamma_n A_n}{\Delta y_{NP}} \tag{4.54}$$

$$a_S = D_s = \frac{\Gamma_s A_s}{\Delta y_{PS}} \tag{4.55}$$

$$a_P = a_N + a_S \tag{4.56}$$

$$S = (C)_P \Delta Vol \tag{4.57}$$

To maximize the numerical stability of the UMIST-*N* wall function calculation, the source term (S) is linearized, as discussed in Section 3.1.

Convection

There are primarily two different ways in which convection can be modelled: in conservative or non-conservative form. For a steady incompressible 2-*D* flow these can be written:

$$\text{Conservative}: \quad \frac{\partial(\rho U\phi)}{\partial x} + \frac{\partial(\rho V\phi)}{\partial y} \tag{4.58}$$

$$\text{Non}-\text{conservative}: \quad \rho U\frac{\partial\phi}{\partial x} + \rho V\frac{\partial\phi}{\partial y} \tag{4.59}$$

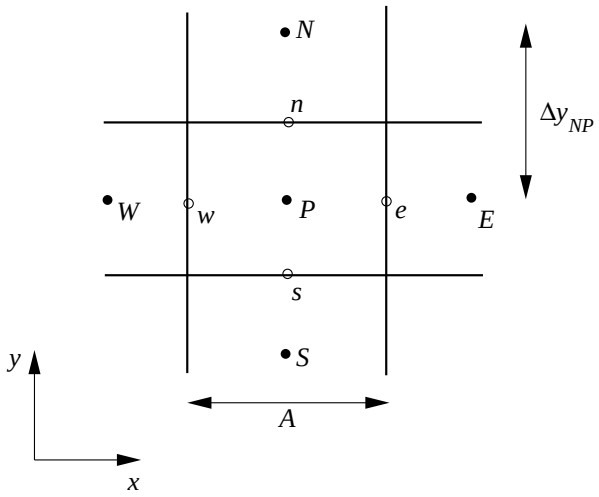

Figure 4.3: Subgrid node and boundary notation

To convert from conservative to non-conservative form one simple expands Equation (4.58) following the product rule and applies the continuity condition:

$$\frac{\partial U}{\partial x} + \frac{\partial V}{\partial y} = 0 \tag{4.60}$$

A conservative form must be used in compressible flows if a shock-capturing method is used, but it also seems to be the more common treatment for convection in incompressible flow [77].

If ϕ represents a homogeneous scalar field (such as a uniform temperature field) then, in the conservative form, any small imbalance in the mass flux though the faces of a cell can lead to finite convection, despite the field being homogeneous (i.e. ϕ is constant but since $\partial U/\partial x + \partial V/\partial y \neq 0$ then the convection is not zero). In a standard incompressible elliptic CFD code (such as the TEAM code), the coupling of velocity and pressure using the SIMPLE algorithm ensures that continuity is observed in each of the grid cells, and so the problem of spurious convection does not occur. However, the subgrid wall function is essentially a parabolic solver and only calculates the momentum parallel to the wall. The pressure gradient is treated as a constant provided by the main-grid solution and hence, within the current framework of the wall function, it is not guaranteed that mass continuity is observed within each of the subgrid cells[2]. It is, therefore, necessary to use a non-conservative convection scheme within the subgrid to avoid the problem referred to above, and to ensure that a homogeneous scalar field will result in zero convection regardless of mass continuity.

Convection parallel to the wall in non-conservative form is written:

$$\rho U \frac{\partial \phi}{\partial x} \tag{4.61}$$

The U-velocity in each of the subgrid cells is known since a transport equation for the subgrid mo-

[2]Continuity is, of course, satisfied over all the main-grid cells, including the near-wall cells.

mentum parallel to the wall is solved. The gradient in ϕ parallel to the wall is found using upwind differencing. Assuming that the velocity is positive, i.e. flowing from west to east:

$$\rho U \frac{\partial \phi}{\partial x} = \rho U_P \frac{(\phi_P - \phi_W)}{\Delta x_{PW}} \tag{4.62}$$

where the subgrid velocity, U_P, is positive and P and W refer to subgrid nodal positions[3] given in Figure 4.4. In order to calculate gradients parallel to the wall it is therefore necessary to store each of the subgrid profiles along the wall. This unfortunately leads to storage requirements of the subgrid wall function approaching those of full low-*Re* model[4]. An alternative scheme was tested during the development of UMIST-*N* which employed scaled main-grid values to calculate $\partial\phi/\partial x$ but this was found to be unstable (see Appendix G).

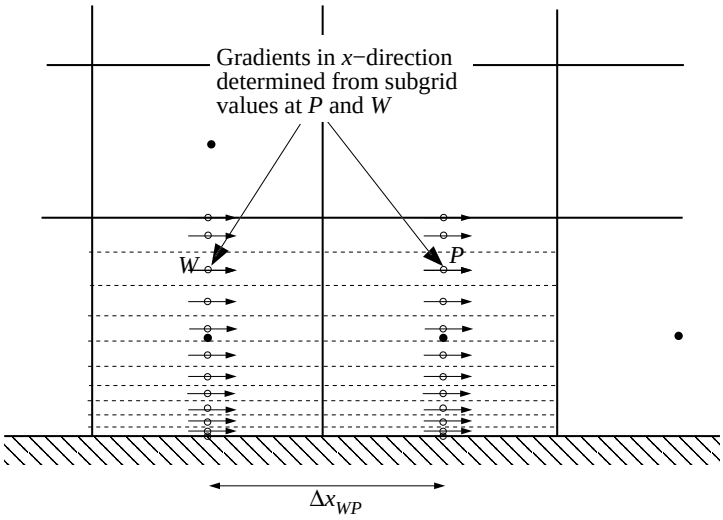

Figure 4.4: Calculation of subgrid convection parallel to the wall

The convection term is added into the source term of the discretized transport equations by first integrating the convection term over the subgrid control volume and introducing a minus sign, since convection appears on the left-hand-side of the transport equation (Equation 4.46):

$$S = -\rho U_P \frac{(\phi_P - \phi_W)}{\Delta x_{PW}} \Delta Vol \qquad \text{for} \quad U_P > 0 \tag{4.63}$$

[3]Since the distance between the upstream node W and current node P is employed, Δx_{PW}, it is the *gradient* that is upwinded rather than just the nodal values. Effectively, one is calculating the gradient in Equation (4.62) using central differencing at the upwind western cell face. In tests with the impinging jet flow, this gave practically identical results to those obtained by upwinding only the values of ϕ, i.e. using:

$$\rho U \frac{\partial \phi}{\partial x} = \rho U_P \frac{(\phi_P - \phi_W)}{\Delta x_{ew}}$$

[4]The storage requirements should be somewhat less than a low-*Re* calculation as pressure is not stored in the subgrid and the number of nodes employed by the wall function approach is likely to be slightly lower.

$$S = -\rho U_P \frac{(\phi_E - \phi_P)}{\Delta x_{EP}} \Delta Vol \qquad \text{for} \quad U_P < 0 \tag{4.64}$$

Rearranging these expression in terms of coefficients of ϕ_P, ϕ_E and ϕ_W:

$$S = -\rho U_P \frac{\phi_P}{\Delta x_{PW}} \Delta Vol + \rho U_P \frac{\phi_W}{\Delta x_{PW}} \Delta Vol \qquad \text{for} \quad U_P > 0 \tag{4.65}$$

$$S = -\rho U_P \frac{\phi_E}{\Delta x_{EP}} \Delta Vol + \rho U_P \frac{\phi_P}{\Delta x_{EP}} \Delta Vol \qquad \text{for} \quad U_P < 0 \tag{4.66}$$

The source S can then be split into s_U and s_P terms as follows:

$$S = s_U + s_P \phi_P \tag{4.67}$$

where the coefficient associated with ϕ_P is included in s_P:

$$\left.\begin{aligned} s_U &= \frac{\rho U_P \phi_W}{\Delta x_{PW}} \Delta Vol \\ s_P &= -\frac{\rho U_P}{\Delta x_{PW}} \Delta Vol \end{aligned}\right\} \quad \text{for} \quad U_P > 0 \tag{4.68}$$

$$\left.\begin{aligned} s_U &= -\frac{\rho U_P \phi_E}{\Delta x_{EP}} \Delta Vol \\ s_P &= \frac{\rho U_P}{\Delta x_{EP}} \Delta Vol \end{aligned}\right\} \quad \text{for} \quad U_P < 0 \tag{4.69}$$

The s_P terms are always negative, and so they always increase the coefficient of ϕ_P and hence the magnitude of the leading diagonal term in the matrix of coefficients, maximizing stability.

Convection perpendicular to the wall in non-conservative form is written:

$$\rho V \frac{\partial \phi}{\partial y} \tag{4.70}$$

A number of different approaches to obtaining the subgrid wall-normal V-velocity profile were explored during the development of the wall function. The most general of these methods relies upon continuity which for a Cartesian arrangement is written:

$$\frac{\partial U}{\partial x} + \frac{\partial V}{\partial y} = 0 \tag{4.71}$$

The process of calculating the wall-normal velocity, V, at each of the nodes across the subgrid is described schematically in Figure 4.5. The process begins in the subgrid cell immediately adjacent to the wall. It is known that the wall-normal velocity at the wall surface is zero, for a non-porous wall, so the mass flux through the south, east and west faces are known. One can then calculate the wall-normal velocity at the northern boundary of the wall-bounded subgrid cell from continuity. This

calculation can be repeated for each subgrid cell from the wall to the outer subgrid boundary.

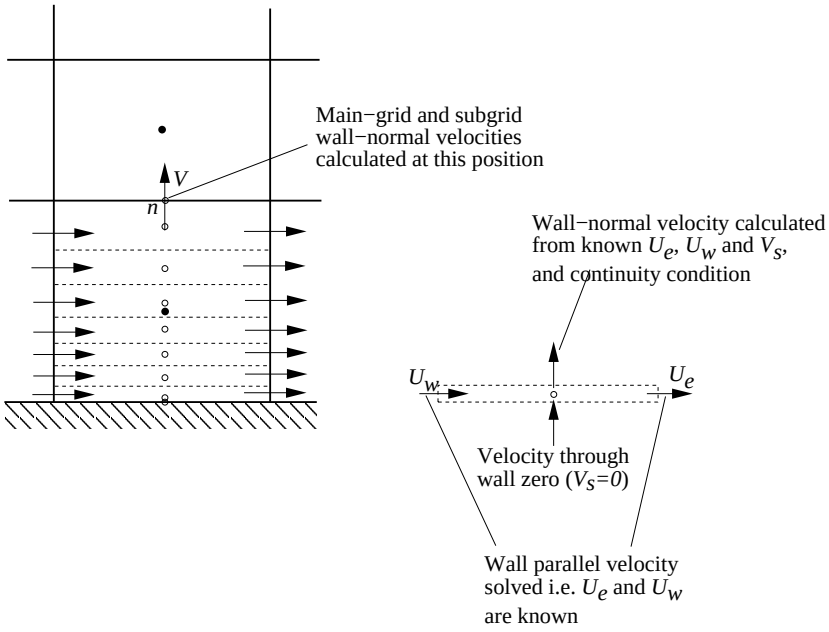

Figure 4.5: Subgrid and main-grid arrangement showing method for calculating the wall-normal velocity from continuity condition in the subgrid cell bounded by the wall

Both subgrid and main-grid wall-normal velocities are calculated at the outer subgrid boundary: the former using the procedure outlined above; the latter from a straightforward interpolation between the nodal values[5]. However, since the integrated subgrid mass fluxes across the east and west faces may not be equal to the corresponding main-grid fluxes parallel to the wall, the subgrid and main-grid wall-normal velocities may not be equal at the outer subgrid boundary (position *n* shown in Figure 4.5). In tests with the impinging jet flow there was, indeed, a mis-match between the main-grid wall-normal velocity at the position *n* and the subgrid value calculated as above (see Figure 4.6). Clearly it is undesirable to have inconsistency between main-grid and subgrid boundary conditions. The subgrid V-velocity profile is therefore scaled with the ratio of the main-grid to the subgrid V-velocity:

$$V_P = \alpha V_P^* \tag{4.72}$$

where the constant, α is given by:

$$\alpha = \frac{V_n'}{(V_n^* \pm tiny)} \quad -3 < \alpha < 3 \tag{4.73}$$

where P denotes the subgrid nodal value, $*$ denotes the subgrid velocities calculated from continuity within the subgrid and the prime ($'$) denotes main-grid value. The constant, α, is evaluated at the outer

[5]The main-grid velocity only needs to be interpolated from main-grid nodal values when a collocated storage arrangement is used. In a staggered grid arrangement, interpolation is unnecessary as the wall-normal V-velocity is calculated at the cell face (position *n*).

subgrid boundary (position n in Figure 4.5). The arbitrary small number *tiny*, which is of the same sign as V_n^*, is included to prevent a singularity occurring as V_n^* approaches zero. In a simple channel flow where the wall-normal velocity is practically zero, the scaling factor can fluctuate between comparatively large positive and negative values as the calculation converges (e.g. $\alpha = \pm 500$) which destabilizes the subgrid solution. To improve the stability the scaling factor α is therefore limited to ± 3. In the impinging jet flow, where there is a significant wall-normal velocity, the maximum calculated value of α was approximately 1.2, and so one would not expect the limit imposed on α to have any adverse affects in other flows. Near-wall V-velocity profiles calculated using the above approach show good agreement with those of low-Reynolds-number models (see Figure 4.6).

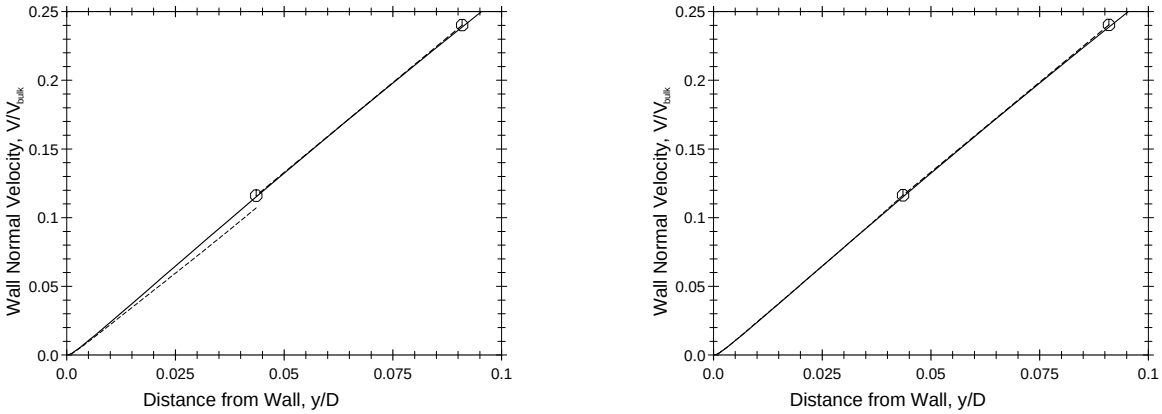

Figure 4.6: Wall normal velocity profiles at the stagnation point of the impinging jet obtained using the linear $k-\varepsilon$ model and standard Yap correction. —-: low-Reynolds-number model; - - -: UMIST-*N* wall function ; $\ominus$: position of main-grid cell faces. The wall-normal subgrid V-velocity is calculated from continuity without scaling on the left-hand plot and with scaling on the right-hand plot (using Equation 4.72). The subgrid profile is shown between the wall (at $y/D = 0$) and the main-grid cell face (at $y/D \approx 0.045$). On the right-hand plot the broken line of the subgrid wall-normal velocity is obscured by the solid line of the low-*Re* model.

Once the V-velocity profile is known, the convection normal to the wall can be calculated. Using an upwind scheme and assuming the V-velocity to be positive (from south to north), convection normal to the wall is discretized as:

$$\rho V \frac{\partial \phi}{\partial y} = \rho V_P \frac{(\phi_P - \phi_S)}{\Delta y_{PS}} \tag{4.74}$$

where ϕ_P and ϕ_S are the subgrid values of U, k, $\tilde{\varepsilon}$ or T evaluated at the current and south subgrid nodes (see Figure 4.3). Integrating convection over the control volume and introducing a negative sign, since the convection term is moved from the left- to the right-hand-side of the Equation (4.46), leads to the following expressions:

$$S = -\rho V_P \frac{(\phi_P - \phi_S)}{\Delta y_{PS}} \Delta Vol \qquad \text{for} \quad V_P > 0 \tag{4.75}$$

$$S = -\rho V_P \frac{(\phi_N - \phi_P)}{\Delta y_{NP}} \Delta Vol \qquad \text{for} \quad V_P < 0 \tag{4.76}$$

The source S can now be split into s_P and a contribution which is introduced into the coefficients a_N and a_S, as follows:

$$\left.\begin{aligned} s_P &= -\frac{\rho V_P}{\Delta y_{PS}}\Delta Vol \\ a_N &= 0 \\ a_S &= \frac{\rho V_P}{\Delta y_{PS}}\Delta Vol \end{aligned}\right\} \quad \text{for} \quad V_P > 0 \tag{4.77}$$

$$\left.\begin{aligned} s_P &= \frac{\rho V_P}{\Delta y_{NP}}\Delta Vol \\ a_N &= -\frac{\rho V_P}{\Delta y_{NP}}\Delta Vol \\ a_S &= 0 \end{aligned}\right\} \quad \text{for} \quad V_P < 0 \tag{4.78}$$

The source term s_P is always negative and hence when s_P is taken over to the left-hand-side of the discretized equation the coefficient a_P (i.e. the leading diagonal elements in the matrix of coefficients) is increased, enhancing stability.

4.3.2 Under-Relaxation

In all of the test-cases considered in this thesis it has been found that no under-relaxation of the wall-parallel momentum or temperature equations is necessary (i.e. $\alpha_U = \alpha_T = 1.0$). A modest amount of under-relaxation of the subgrid k and $\tilde{\varepsilon}$ equations is necessary, typically $\alpha_k = \alpha_\varepsilon = 0.85$. No under-relaxation is required in the subgrid temperature equation since none of the source terms (s_U) appearing in the TDMA are dependent upon the values of ϕ_P. For the momentum equations, there is obviously some feedback through the strain-dependent P_k modifying the eddy-viscosity, and in curvilinear coordinates there are additional geometric source terms which are added into s_U, but these effects do not appear to cause stability problems.

In each iteration of the UMIST-*N* wall function, the subgrid boundary conditions are first updated, the coefficient matrix is assembled and then the matrix is solved with one sweep of the TDMA. Because of the under-relaxation, there may be a small discontinuity in the k and $\tilde{\varepsilon}$ profiles at the northern boundary during the early stages of a calculation, caused by the solution lagging behind the updated boundary conditions. This discontinuity is responsible for the stability problems encountered when using the differential length-scale correction at the start of a new calculation, when k and $\tilde{\varepsilon}$ boundary conditions are changing rapidly (as discussed in Section 4.2).

4.3.3 Boundary Conditions

For each variable, two boundary conditions are required for the one-dimensional subgrid equations. On one side, the subgrid domain is bounded by a wall (node $i = 1$), and on the opposite side it joins the main-grid domain (node $i = n$). The subgrid transport equations are solved from nodes $i = 2$ to $(n-1)$ inclusive. In addition, at the ends of a wall, for example on the axis of symmetry in the impinging jet flow, boundary values need to be supplied in the wall-parallel direction to allow the convection terms to be evaluated.

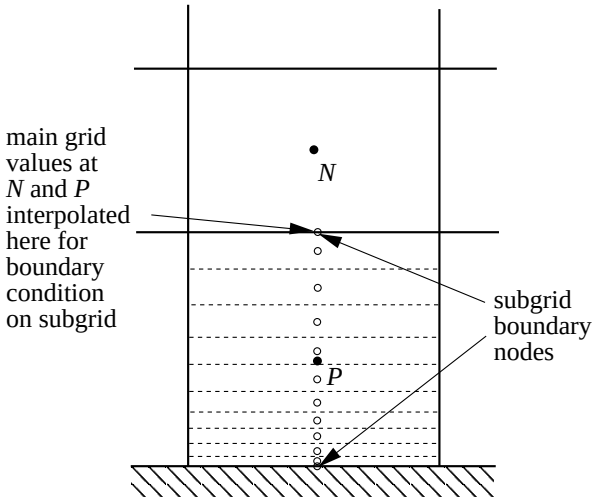

Figure 4.7: Subgrid boundary conditions

Wall Boundary $(i = 1)$

The boundary conditions for the subgrid nodes on the wall are identical to those applied in a low-Reynolds-number solution. U, k and $\tilde{\varepsilon}$ all become zero at the wall (i.e. $U_1 = k_1 = \tilde{\varepsilon}_1 = 0$). There are two common thermal wall boundary conditions: prescribed wall temperature or prescribed wall heat flux. The boundary condition in the former case is trivial since the temperature at the subgrid boundary node is simply set to a prescribed value ($T_1 = T_{wall}$). The wall heat flux can then be calculated from Fourier's law, since the near-wall subgrid cell is within the viscous sublayer. For a wall with constant heat flux, the calculated flux to the boundary is removed (by setting $a_S = 0$ for a wall on the south of the cell) and the given flux is added in as a source term. The wall temperature can then be calculated from Fourier's law.

Free Boundary $(i = n)$

The values of U, k, $\tilde{\varepsilon}$ and T prescribed at the outer (free) boundary, where the subgrid meets the main grid, are interpolated between the two near-wall main-grid nodal values, at P and N, as shown in

Figure 4.7. Although this interpolation may not be desirable in terms of accuracy – assuming a linear variation from node P to node N – the alternative of extending the subgrid only to the main-grid nodal position P (and hence using the calculated values at node P as boundary conditions for the subgrid calculation) introduces significant problems with the calculation of cell-averaged quantities (e.g. $\overline{P_k}$, $\overline{\tilde{\varepsilon}}$). The linear interpolation for the boundary condition does cause a small discrepancy between the main grid and subgrid velocities at P in the log-law plot for a channel flow (see Figure 4.14). Various other interpolation functions were tested but none provided a significant improvement in results whilst maintaining generality. Since k and $\tilde{\varepsilon}$ values are also linearly interpolated, the eddy viscosity $\left(\mu_t = c_\mu f_\mu k^2/\tilde{\varepsilon}\right)$ will not be a linear interpolation of the two near-wall main-grid nodal values. Again, a number of different formulations have been tested, for example, by interpolating the viscosity and obtaining k or $\tilde{\varepsilon}$ from this boundary condition for μ_t, but none of these has been found to provide any improvement upon the simpler practice of interpolating the boundary condition for k and $\tilde{\varepsilon}$ and then calculating μ_t. Assuming a linear variation of U, k, $\tilde{\varepsilon}$ and T between nodes P and N is, moreover, consistent with the assumptions used in the main-grid.

Wall Ends

A typical example of a wall-end boundary is shown in Figure 4.8. In this case, since the boundary coincides with the edge of the domain, additional subgrid nodes are placed on the boundary itself. Subgrid transport equations are not solved for these boundary nodes: their only purpose is to provide boundary values for computing the convection parallel to the wall and for the calculation of the subgrid wall-normal velocity (for which the mass flux through the boundary face needs to be known). Subgrid end-of-wall boundary values are set in exactly the same manner as in the main-grid calculation. For the axisymmetric case shown in Figure 4.8 this would involve zero-gradient conditions for the wall-normal velocity, k, $\tilde{\varepsilon}$ and T and zero wall-parallel (radial) velocity for the nodes on the axis of symmetry.

4.3.4 Subgrid Residuals

The subgrid nodal residual is calculated as follows:

$$R_\phi = a_P\phi_P - (a_N\phi_N + a_S\phi_S + s_U) \tag{4.79}$$

where ϕ is the relevant variable (U, k, $\tilde{\varepsilon}$ or T). The total subgrid residual for each block is calculated by summing $\left|R_\phi\right|$ over each subgrid domain. One could non-dimensionalize the subgrid residuals and place an upper limit on their value so that the calculation would not be considered converged unless residuals fell below that value. In practice, however, if subgrid residuals are not falling, the residuals in the main-grid will be increasing. Monitoring subgrid residuals is useful, however, in a multiblock calculation when one can identify which wall is causing convergence problems. Additionally, subgrid residuals can be useful if, for instance, one wants to freeze the main-grid solution but continue to run

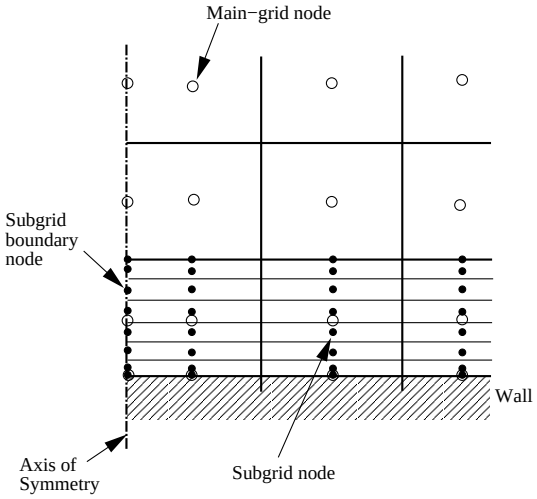

Figure 4.8: Arrangement of subgrid nodes at the end of a wall.

the subgrid calculation to ensure that it converges.

4.3.5 Calculation of Wall-Function Parameters

In standard wall-function treatments, such as that proposed by Chieng & Launder [49], the wall function provides values for:

- wall shear stress, τ_{wall}
- average kinetic energy production, $\overline{P_k}$
- average dissipation rate, $\overline{\varepsilon}$
- nodal dissipation rate, ε_P
- wall temperature, T_{wall}, or wall heat flux, q_{wall}

In such treatments, the momentum equation is solved in the near-wall cell with τ_{wall} included as a source term (having suppressed the internally calculated flux to the wall by setting $a_S = 0$ for a southern wall). The kinetic energy equation is solved in the near-wall cell with production and dissipation terms replaced by $\overline{P_k}$ and $\overline{\varepsilon}$ respectively, and the diffusive flux is set to zero ($a_S = 0$ as before). The dissipation rate equation is not solved in the near-wall cell, but instead the value ε_P is prescribed at the near-wall node.

In the UMIST-*N* wall function, momentum, kinetic energy *and* isotropic dissipation rate equations are solved in the near-wall cells. There is thus no need to prescribe ε_P. Such an approach might lead to instabilities in any case, since the $\tilde{\varepsilon}$-equation solved in the subgrid would be strongly linked to ε_P through the boundary conditions. The new wall function therefore needs to provide values of the following parameters:

- wall shear stress, τ_{wall}
- average kinetic energy production, $\overline{P_k}$
- average total dissipation rate, $\overline{\varepsilon}$
- average production rate of $\tilde{\varepsilon}$, $\overline{(P_k\tilde{\varepsilon}/k)}$
- average dissipation rate of $\tilde{\varepsilon}$, $\overline{(f_2\tilde{\varepsilon}^2/k)}$
- average gradient production $\overline{P_{\varepsilon 3}}$
- average near-wall length scale correction (Yap correction), $\overline{Y_c}$
- wall temperature, T_{wall}, or wall heat flux, q_{wall}

The wall shear stress, τ_{wall}, is calculated by assuming a linear velocity profile between the subgrid node adjacent to the wall and the wall itself (i.e. assuming that the near-wall subgrid cell is well within the viscous sublayer). For a stationary wall in 2-*D* Cartesian coordinates this is simply:

$$\tau_{wall} = \mu\frac{U_P}{y_P} \tag{4.80}$$

where subscript P denotes the value at the subgrid node adjacent to the wall and μ is the molecular viscosity. In a similar manner, the heat flux, q_{wall}, can be calculated from Fourier's heat conduction law:

$$q_{wall} = -\lambda\frac{\partial T}{\partial y} = -\frac{\mu c_p}{\sigma}\frac{\partial T}{\partial y} \tag{4.81}$$

which can be rearranged to give:

$$T_{wall} = T_P + \frac{\sigma q_{wall} y_P}{\mu c_p} \tag{4.82}$$

or:

$$q_{wall} = \frac{\mu c_p (T_{wall} - T_P)}{\sigma y_P} \tag{4.83}$$

As with standard wall functions, the subgrid values of τ_{wall} and q_{wall} replace the diffusive fluxes in the main-grid and so one should set $a_S = 0$ in the momentum and temperature equations.

Average source terms for k and $\tilde{\varepsilon}$ are evaluated by assuming the subgrid values to be constant over the extent of each subgrid cell and equal to the subgrid nodal value. If the subgrid node on the wall surface is $i = 1$ and that on the outer subgrid boundary node $i = n$, then the average production term for a simple 2-*D* Cartesian grid is given by:

$$\overline{P_k} = \frac{\sum_{i=2}^{n-1}(P_k\Delta y)_i}{\sum_{i=2}^{n-1}(\Delta y)_i} \tag{4.84}$$

where $(P_k\Delta y)_i$ is the product of the production rate and the cell thickness for subgrid cell i, and $\sum_{i=2}^{n-1}(\Delta y)_i$ is the total thickness of the subgrid (which is equal to the thickness of the main-grid cell).

The main-grid momentum and heat fluxes to the wall are replaced by values calculated from the subgrid solution (τ_{wall} and q_{wall}). To be entirely consistent with this treatment one should also replace the diffusive fluxes of k and $\tilde{\varepsilon}$ to the wall in the main-grid calculation with values obtained from the subgrid solution. Tests in channel and impinging flows showed that these fluxes are negligible in comparison to other terms in the main-grid k and $\tilde{\varepsilon}$ equations and hence one can just set $a_S = 0$ (for a southern wall) in the main-grid near-wall cell for the k and $\tilde{\varepsilon}$ equations.

When the NLEVM is used, one needs to evaluate strain-rates and vorticity at grid nodes in order to calculate nodal values of the c_μ function and the non-linear stress components, described in Section 2.3. Throughout the main-grid flow domain the nodal strain-rates and vorticity are calculated based on values of velocity at the cell boundaries, assuming a linear velocity profile across the cell. Whilst this practice may be sufficiently accurate across most of the flow domain, the assumption of a linear velocity profile across the near-wall main-grid cell is inappropriate if one is using wall functions. For the near-wall main-grid cell, the subgrid velocity distribution gives a more accurate picture of the strain-rate and vorticity at the main-grid node P. Therefore, the subgrid strain-rates and vorticity are evaluated and interpolated to the main-grid node position. These subgrid values are then used to find the value of c_μ and the non-linear stress components at the main-grid node P.

4.3.6 Generating the Subgrid Mesh

The subgrid transport equations described in Section 4.2 are solved over an algebraically generated grid within the main-grid near-wall cell. In order to obtain sufficient resolution of the peaks of k and $\tilde{\varepsilon}$ it is necessary to cluster subgrid nodes towards the wall. A schematic diagram of a simple 2-D Cartesian subgrid is given in Figure 4.9. The distance from the wall to the face of subgrid cell i is given by y_i and to the subgrid node y_i^p. The locations of the bottom and top of the subgrid (locations y_1 and y_7, respectively) are known from the main-grid coordinates. Between nodes $i = 1$ and $i = 7$ (from the wall to the top edge of the domain), the subgrid is expanded with a given ratio, r, according to:

$$\Delta y_i = r \Delta y_{i-1} \tag{4.85}$$

where Δy_i is the cell width for node i. The distance between the first and last boundary locations consists of the sum of the control volume widths:

$$\begin{aligned} y_n - y_1 &= \Delta y + r\Delta y + r^2 \Delta y + \ldots + r^{(n-3)} \Delta y \\ &= \sum_{m=0}^{n-3} r^m \Delta y \end{aligned} \tag{4.86}$$

where n is the number of nodes, in this case $n = 7$. The width of the smallest control volume $(\Delta y = y_2 - y_1)$ is then given by:

$$\Delta y = \frac{y_n - y_1}{\sum_{m=0}^{n-3} r^m} \tag{4.87}$$

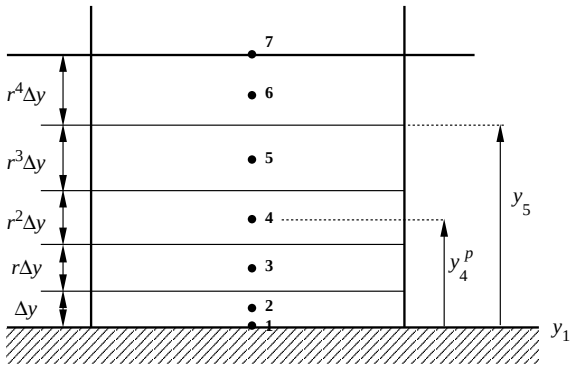

Figure 4.9: Two-dimensional Cartesian subgrid mesh showing node numbers and cell widths.

One can then calculate the position of the cell faces in recursive fashion:

$$y_m = y_{m-1} + r^{(m-2)}\Delta y \quad \text{for} \, m = 2,3,4...(n-2) \tag{4.88}$$

Finally, the subgrid nodes are positioned in the centre of the cells, i.e.:

$$y_m^p = \frac{(y_m + y_{m-1})}{2} \quad \text{for} \, m = 2,3,4...(n-1) \tag{4.89}$$

Following common practice, it should be ensured that the solution is independent of the subgrid mesh. The expansion ratios and number of subgrid nodes should be adjusted until there is no significant difference in computed results. In tests with the impinging jet flow where the main-grid near-wall node y^+ values varied from 230 at the stagnation point to 35 at 6 diameters downstream, a minimum of 30 subgrid cells with an expansion ratio of 1.15 was required to achieve a subgrid-independent solution. However, relatively large expansion ratios were found to introduce stability problems with the NLEVM and, in practice, a maximum ratio of 1.10 was used with a corresponding slight increase in the number of subgrid nodes to maintain the same near-wall y^+values.

4.3.7 Multiblock Implementation

In order to generate structured grids around complex shapes it is sometimes necessary to decompose the grid into a number of blocks. This approach was used in the STREAM code to study the flow around the Ahmed car body (see Figure 7.10). Since the UMIST-*N* wall function uses wall-parallel gradients for convection and for the calculation of the wall-normal velocity from continuity, it is necessary to use a multiblock implementation of the wall function if walls extend over more than one block. In order to implement the multiblock wall function in an efficient manner, it is useful to consider the issues of block addressing, halo nodes and block-to-block swapping of boundary conditions at an early stage in the design of the wall-function code.

Communication of data (i.e. nodal values of U, V, W, k, $\tilde{\varepsilon}$ and T) between blocks is accomplished using halo cells. These are additional nodes tagged on at the end of a block which have physical

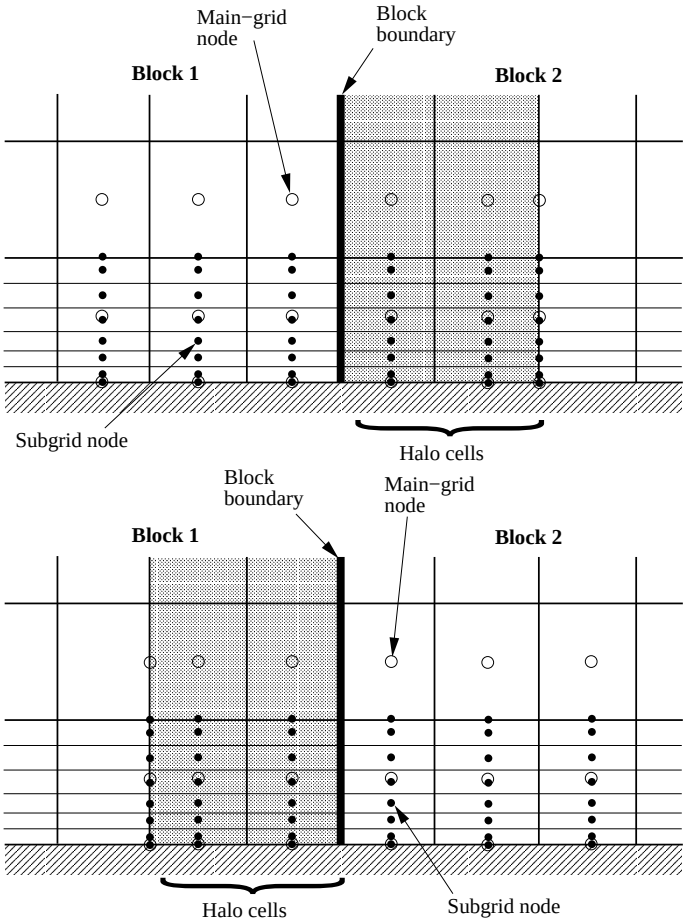

Figure 4.10: Arrangement of subgrid and main-grid nodes at a block interface. The top diagram shows the nodes associated with Block 1, including the halo nodes. The lower diagram shows the nodes associated with Block 2.

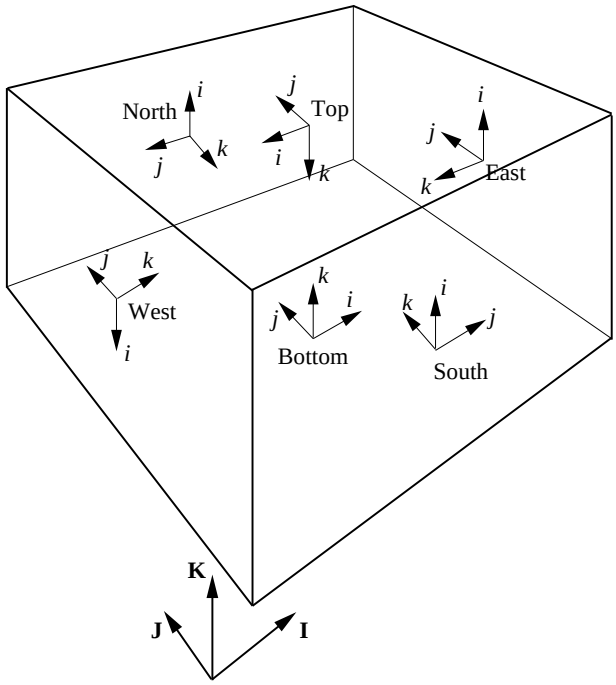

Figure 4.11: Three-dimensional block arrangement showing face labels, main-grid coordinates (in upper-case bold) and subgrid coordinates for each face (lower-case italic).

locations identical to nodes in the neighbouring block (see Figure 4.10). Transport equations are not solved for halo node values. Instead, at the beginning (or end) of each iteration, the values of U, V, W, k, $\tilde{\varepsilon}$ and T at the halo nodes are updated from the neighbouring block's values. Halo nodes therefore provide boundary conditions for the cells internal to a block, for which transport equations are solved. The STREAM code uses a total of three layers of halo nodes, as shown in Figure 4.10. Two layers of nodes are required for the calculation of convection using quadratic differencing. The final layer on the cell boundary is only used to define the edge of the domain. The STREAM code version of the UMIST-*N* wall function was designed with exactly the same halo arrangement as the main-grid code (i.e. three layers of cells). This was not strictly necessary, since the UMIST-*N* wall function only employs upwind differencing, but it was conceptually simpler to keep the same domain size.

Wall functions may be employed on many faces within each block (north, south, east etc.). Rather than code six different versions of the UMIST-*N* wall function, one for each face, a single solution procedure is coded with a local subgrid coordinate frame. This local coordinate frame is specified so that the subgrid ζ-direction is always in the non-wall-parallel direction and increases with distance from the wall (in most cases this means simply that the subgrid ζ-axis is wall-normal and points into the domain from the wall surface). Figure 4.11 shows a single main-grid block with coordinate frame denoted in upper-case bold (**I**, **J**, **K**). Associated with each of the faces of the block are also shown subgrid coordinate frames, denoted in lower-case italic (i, j, k).

To specify fully how two main-grid blocks are joined together, one needs to identify the faces

through which the two blocks are mated and also how the coordinate frames transform between blocks. For instance, the entire south face on Block (1) could be attached to the entire east face on the neighbouring Block (2), with the coordinate frame in Block (1), **(I**, **J**, **K)**, being equivalent to the coordinate frame **(–K**, **I**, **–J)** in Block (2). This specification will be well known to those already using multiblock domain decomposition. In addition to these details, however, one has to be careful when walls continue over two or more neighbouring blocks that the coordinate frames used in the subgrid wall function domains are correctly matched together (bearing in mind that there is a different subgrid coordinate frame according to the face on which the wall is positioned). This is particularly important as the UMIST-*N* wall function uses grid-aligned velocity vectors so that the U-velocity in one block may be equivalent to the V-velocity in a neighbouring block. It is not difficult to work out the permutations of block faces, main-grid coordinate frames and subgrid coordinate frames, and the particular algorithm used will depend on how the multiblock domain decomposition is already coded for the main-grid. In order to provide some assistance to future researchers, a simple cut-out diagram is provided in Figure 4.12 which can be glued together into a cube. The faces of the cube give the subgrid *i*- and *j*-axes and the *k*-axis always acts into the cube. The main-grid (**I**, **J**, **K**) are also provided along with the names of the block faces. In the authors' experience, such cubes are invaluable for examining how to specify the correct transformation between two subgrid coordinate frames.

Finally, it should be mentioned that when coding the subgrid wall function it is inefficient to store values in multi-dimensional arrays and specify a particular subgrid node directly from its wall number[6] and its (i, j, k) coordinates. This approach may lead to excessive storage requirements for the subgrid arrays when, for instance, the *i*-axis on one wall contains twice as many nodes as the *i*-axis on another wall. Instead, an efficient subroutine or function can be written which converts wall number and (i, j, k) coordinates into a single subgrid node number, say (ns), which then increments sequentially from 1 to *nsmax*, where *nsmax* is the total number of subgrid nodes. The subgrid data is then stored as one-dimensional arrays with dimension *nsmax*, rather than as multi-dimensional arrays of size $(imax \times jmax \times kmax)$ times the number of walls.

4.3.8 Solution Sequence

The first step in the subgrid wall function is to define the subgrid mesh and any geometric parameters that are used by the subgrid wall function (a particular consideration if one is using non-orthogonal curvilinear coordinates). This is performed only once, at the beginning of a calculation, just after the main-grid mesh has been defined. In each subsequent main-grid iteration, before the main-grid coefficient matrices are assembled, the following sequence of events is followed:

1. Initialize the one-dimensional subgrid variable arrays from a previous subgrid iteration, previous subgrid solution (used as a starting point) or initial profile.

[6] where each wall face in each block is assigned sequentially a separate wall number.

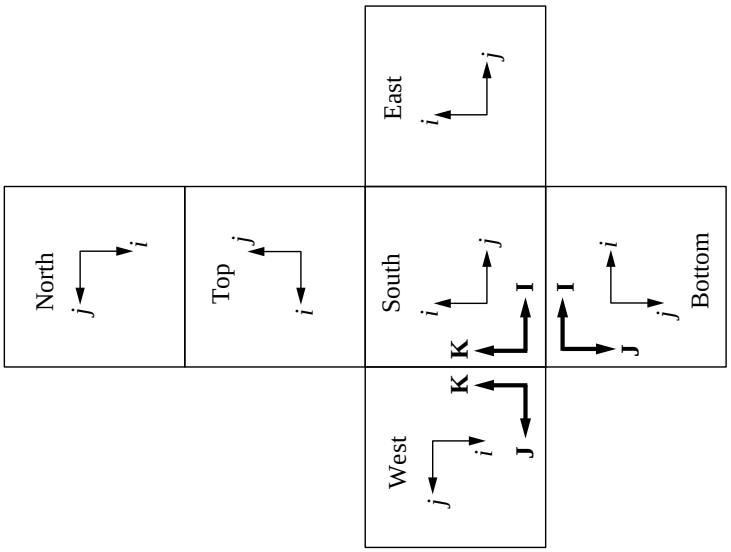

Figure 4.12: Unfolded representation of three-dimensional block arrangement showing face labels, main-grid coordinates (in upper-case bold) and subgrid coordinates for each face (lower-case italic). Once the diagram is cut-out and glued together into a cube with the writing on the outside of the box, the subgrid *k*-axis always acts in the direction into the box

2. Calculate the subgrid eddy-viscosity, μ_t, and source terms for the wall-parallel momentum, k, $\tilde{\varepsilon}$ and temperature equations.

3. Assemble the subgrid coefficient matrices for each of the transport equations and solve each in turn with one sweep of the TDMA.

4. Calculate wall-function parameters to be passed to the main-grid flow solver (τ_{wall}, average source and sink terms in the k and $\tilde{\varepsilon}$ equations, and T_{wall} or q_{wall}).

5. Repeat steps 1 – 4 for each of the main-grid cells along the length of the wall.

It is important, especially when using the strain-dependent c_μ function with the Craft *et al.* NLEVM that boundary conditions are only updated after c_μ and the non-linear stresses have been calculated. Otherwise, the updated velocity boundary value can lead to significant strain-rates across the subgrid cell adjacent to the boundary which may cause instability through the feedback mechanism of $(c_\mu \rightarrow \mu_t \rightarrow S \rightarrow c_\mu)$, as mentioned in Chapter 2.

4.4 Validation: Channel Flow Results

One advantage of the UMIST-*N* wall function is that it is relatively straightforward to reconfigure the code to run as a stand-alone 1-*D* parabolic solver, which can then be tested in simple flows to ensure that it has been coded correctly. The wall-function code was adjusted to run a fully-developed channel flow simulation with the subgrid region extending across the whole flow domain. The Reynolds

number, based on bulk velocity and channel width (wall to wall), was $Re = 100,000$. Results were compared to low-Reynolds-number model results obtained from the 2-*D* elliptic solver, TEAM, using the Launder-Sharma $k-\varepsilon$ model. An identical distribution of subgrid nodes was used as for the low-*Re* model with 110 nodes, clustered towards the wall. The wall function and low-*Re* model results were found to be identical (Figure 4.13).

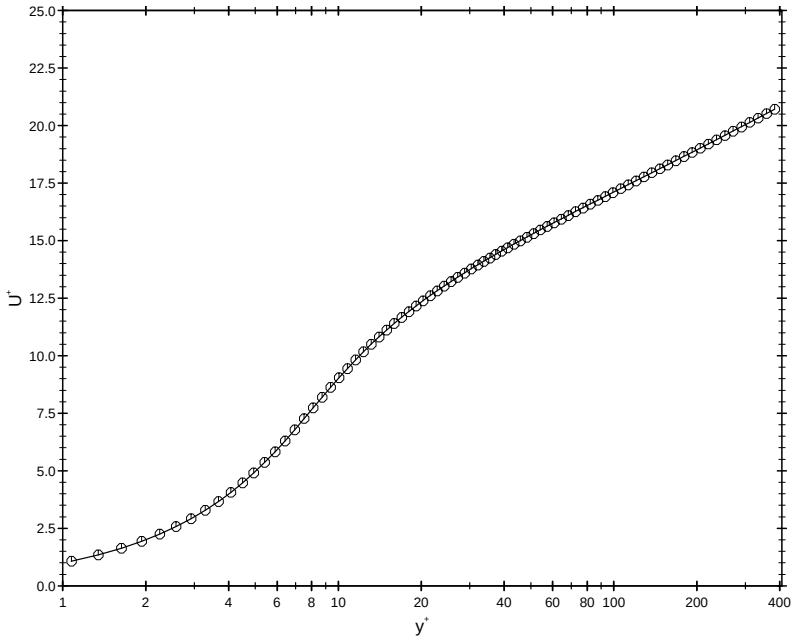

Figure 4.13: Comparison the semi-logarithmic velocity profiles for a fully-developed channel flow at $Re = 100,000$; —-: TEAM 2-*D* elliptic solver; symbols: UMIST-*N* wall function configured as parabolic solver.

Following these tests, the performance of the UMIST-*N* wall function was assessed in a 2-*D* channel flow with periodic inlet and outlet boundaries and a Reynolds number of $Re = 100,000$. Calculations were made using the TEAM code with the linear Launder-Sharma $k-\varepsilon$ model [13]. QUICK differencing was employed for convection of momentum and PLDS for k and $\tilde{\varepsilon}$. A grid with 110 nodes for the half-channel width in the wall-normal direction was used for low-*Re* model simulations and results were tested to ensure that they were fully grid-independent. Two different grid arrangements were used for the wall-function calculations which corresponded to near-wall nodal y^+ values of approximately 30 and 80. Across the subgrid domain, 40 nodes were used with an expansion ratio of 1.1 which was sufficient to obtain a subgrid-independent solution. Figure 4.14 shows the profiles of U^+ versus y^+ obtained using the UMIST-*N* wall function for the two high-*Re* grids against the results obtained from the low-*Re* model and law-of-the-wall profiles.

The UMIST-*N* wall function results for the channel flow, shown in Figure 4.14, are in good agreement with the low-*Re* results for both near-wall cell sizes. A small discrepancy in the near-wall main-grid nodal velocity is due to the linear interpolation between the two near-wall nodes, used to obtain the subgrid boundary condition. Several other methods of interpolating have been tested for

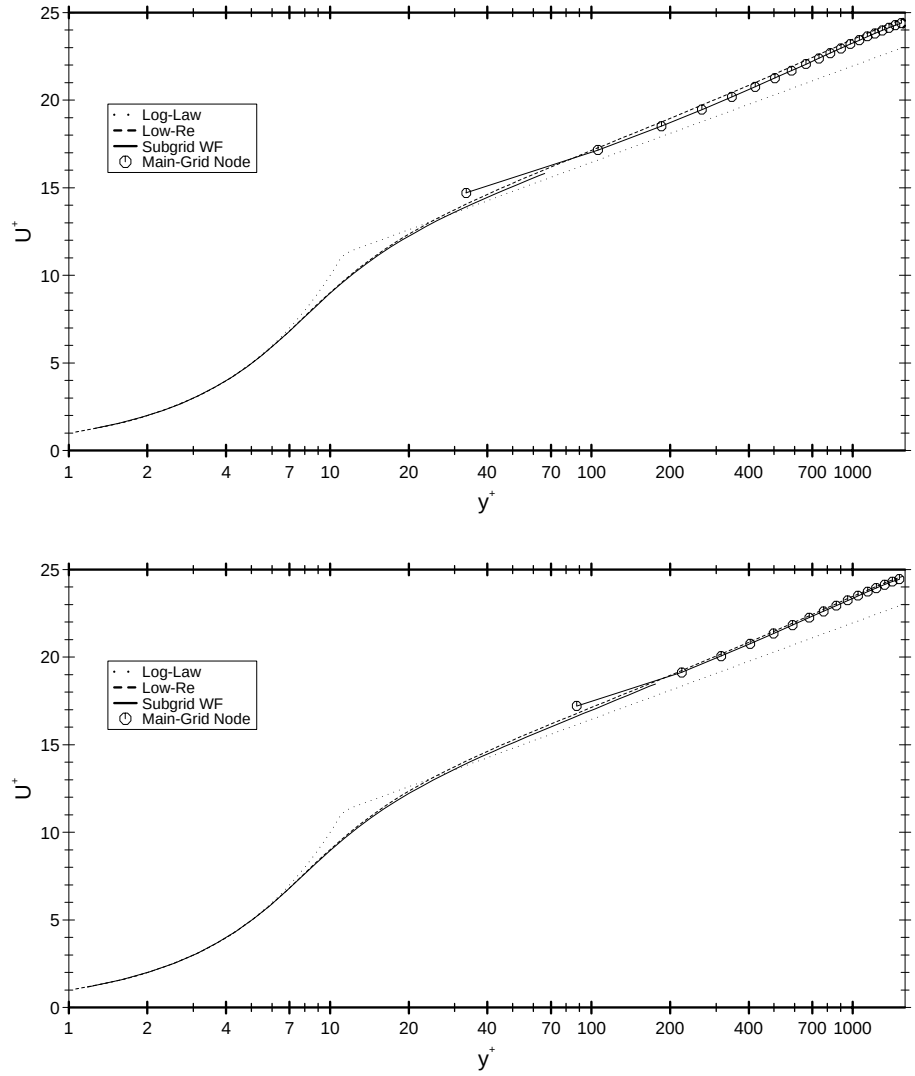

Figure 4.14: UMIST-*N* wall function predictions of the velocity log-law with a near-wall grid arrangement of $y^+ \approx 30$ (top) and $y^+ \approx 80$ (bottom).

the subgrid boundary condition, but none provided any significant improvements without diminishing the generality of the wall function. In any case, within the near-wall cell the subgrid solution provides a more accurate prediction of the velocity profile and this can be used to gain a better picture of the velocity close to the wall if necessary. The results also show little dependence upon the size of the near-wall main-grid cell.

The above tests were carried out using the TEAM code. The UMIST-*N* wall function implementation in the STREAM code was also tested in a fully-developed channel flow before calculations of the Ahmed body were undertaken. The wall function was applied to each of the six possible faces of a block (north, south, east etc.) and results compared to those obtained using a low-*Re* model. Both linear and non-linear $k-\varepsilon$ models were assessed and skewed grids were used to ensure that the calculated subgrid geometric parameters (metric tensors, Jacobians etc.) were correct. The multiblock wall function implementation was also tested by setting up a fully-developed channel flow over two blocks. The relative orientation of the two blocks was then changed to ensure that this had no effect on results.

Chapter 5

Impinging Jet Flow

5.1 Introduction

The axisymmetric impinging jet flow is geometrically simple. Figure 5.1 shows a schematic of the particular arrangement considered in the current work. The fully-developed pipe flow exits the pipe of diameter D at a height of 4 jet diameters from the wall $(H/D = 4)$, impinges onto the wall surface and spreads radially outwards. Figure 5.2 shows a typical velocity vector plot. The Reynolds number of the flow, based on the bulk inlet velocity and pipe diameter, is $Re = 70,000$ and conditions were chosen to match the experimental measurements of Baughn *et al*. [94] and Cooper *et al*. [95].

There have been numerous computational and experimental studies of the impinging jet and this reflects the range of related industrial flows and the usefulness of this particular geometry for testing turbulence models. Jet impingement causes high levels of heat-transfer coefficient near the stagnation point and is used in industrial applications where heating, cooling or drying processes are required. Flow impingement occurs on the upstream face of bluff bodies, such as the simplified car body examined in Chapter 7. As a test case, the impinging jet offers insight into the behaviour of turbulence models in flow regimes far removed from the traditional simple shear flow. In an axisymmetric im-

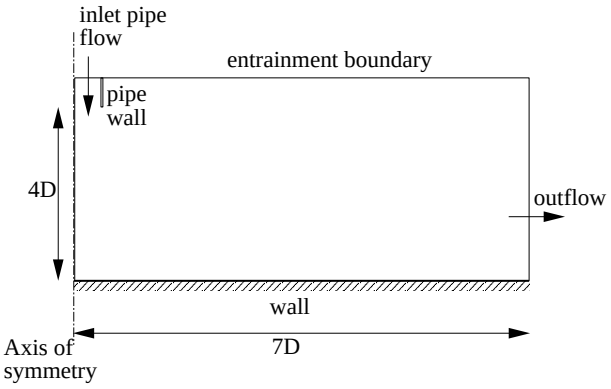

Figure 5.1: Impinging jet flow domain and boundary conditions.

pinging jet, there is significant irrotational straining near the stagnation point and, near the edge of the impinging jet, there is strong streamline curvature. Moving further downstream, the flow tends towards a simple radial wall jet, but one in which the maximum shear stress occurs outside the wall region [95].

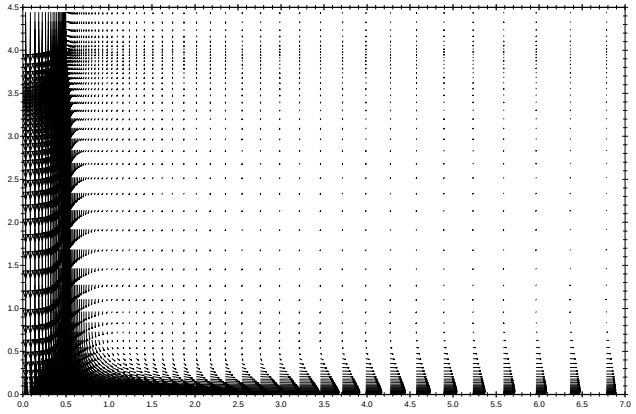

Figure 5.2: Predicted velocity vectors for the impinging jet flow ($Re = 70,000$, $H/D = 4$) using the Craft *et al*. NLEVM

For the purposes of examining the processes involved in the impinging jet flow, the flow domain can be decomposed into three regions. These regions are identified on the plot of experimental Nusselt number[1] shown in Figure 5.3. In the first region, on the axis of symmetry ($r/D = 0$, where r is the radial distance from the axis of symmetry) the mean shear strain is zero and turbulence energy production is from normal straining. The heat transfer rate is greatest at the stagnation point, with Nu at its maximum. Since the jet considered in the current calculations is only four diameters away from the wall, there is insufficient height for significant mixing to occur with the surrounding fluid between the jet inlet and the wall. Therefore the fluid convected into the near-wall region has a low turbulence intensity (similar to that in the fully developed pipe flow) and is at a temperature close to the inlet condition. The thermal boundary layer is confined to the width of the viscous sublayer which is itself thin at this point. In the region between the axis of symmetry and $r/D \approx 1$, the RMS fluctuating velocity component in the wall-normal direction $\left(v^{'}\right)$ exceeds that parallel to the wall $\left(u^{'}\right)$ in contrast to fully-developed channel flows where the $u^{'}$ component is greater than $v^{'}$ (see Figure 1.2). The turbulence length scale $(k^{3/2}/\varepsilon)$ near the wall is strongly affected by length scales of the jet turbulence, retaining a memory of upstream history, whereas in simple shear flows the length scale is a function only of the wall distance. Convective transport of turbulence energy towards the stagnation point is also important (i.e. the flow is not in local equilibrium). The Nusselt number steadily drops

[1]The Nusselt number is a dimensionless heat transfer coefficient proportional to the ratio of the heat transfer by convection to the heat transfer by conduction, which in the impinging jet flow is evaluated as:

$$Nu = \frac{hD}{\lambda} = \frac{q_{wall} D\sigma}{\mu c_p \left(T_{wall} - T_{in}\right)} \tag{5.1}$$

where D is the jet diameter and T_{in} the inlet temperature.

from its maximum at the stagnation point towards a minimum at $r/D \approx 1$. In this region, strong flow curvature has a stabilizing effect on the flow, reducing turbulence energy[2]. In the second region, further downstream $(1 < r/D < 2)$, the Nusselt number rises up to a secondary peak. Here, there is significant acceleration of the fluid away from the stagnation point which in itself might be expected to cause a reduction in turbulence levels. However, as one moves away from the stagnation point (where turbulence levels are low) high near-wall shear strains develop which generate turbulence energy. In addition, the mixing layer around the edge of the jet reaches the wall in this region, bringing with it higher levels of turbulence energy. The fluctuating velocity parallel to the wall also shows an increase relative to the normal component between $r/D = 1$ and 2 (Figure 5.13). In the radial-wall-jet region $(r/D > 2)$, the Nusselt number decreases at a gradually decreasing rate as the thickness of the viscous and thermal boundary layers increase and the radial velocity falls as the wall jet spreads. The near-wall kinetic energy steadily decreases although the maximum turbulent stress levels are more than twice as high as in the corresponding plane wall jet [65, 95].

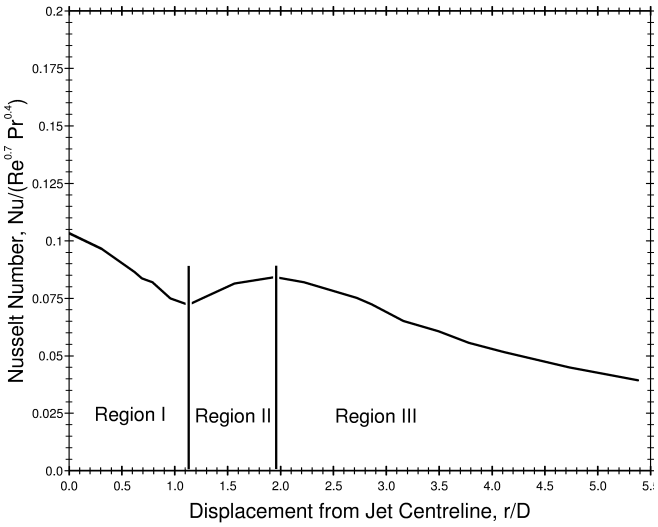

Figure 5.3: Experimental Nusselt number data for the impinging jet ($Re = 70,000$ and $H/D = 4$) from Baughn *et al*. [94] showing the three main flow regions.

5.2 Previous Experimental and Computational Studies

It is well known that the low-*Re* linear $k-\varepsilon$ model overpredicts the level of turbulent kinetic energy at the stagnation point in impinging flows. The Yap correction [64] and the more recent differential

[2]If one considers the kinetic energy production due to shear stress in this region (in 2-*D* Cartesian coordinates), the production of k due to shear stress, $P_{kuv} = -\rho\overline{uv}(\partial U/\partial y + \partial V/\partial x)$, where the shear strain rates $\partial U/\partial y$ and $\partial V/\partial x$ are of opposite sign, tending to reduce P_k and hence k. Normal strain rates $\partial U/\partial x$ and $\partial V/\partial y$ are also of opposite sign and hence kinetic energy production due to normal stresses $\overline{u^2}$ and $\overline{v^2}$ are of the opposite sign, further diminishing P_k (see Bradshaw [96]).

length-scale correction of Iacovides & Raisee [66, 67] improve this behaviour somewhat, although heat transfer rates at the stagnation point are still overpredicted by a factor of nearly two (see results below). An explanation for the behaviour of the linear $k-\varepsilon$ model was provided by Kato & Launder [97] who showed that using this model the production rate of kinetic energy can be written as:

$$P_k = -\rho\overline{u_i u_j}\frac{\partial U_i}{\partial x_j} = \rho c_\mu \varepsilon S^2 \tag{5.2}$$

Near the stagnation point, the irrotational strain field leads to a high value of the dimensionless strain invariant, S, which in turn leads to a large P_k. Kato & Launder suggested a modified production term in which S^2 is replaced with ΩS. Since the vorticity invariant, Ω, is small in irrotational straining, the production term takes a more realistic value. Although the Kato-Launder modification improves the $k-\varepsilon$ model predictions in impinging flows, it was suggested that their correction should not be considered a permanent fix since it would lead to an overly large production in rotating and swirling flows. An alternative remedy of the stagnation-point problem by Durbin [98] imposed a limit on the turbulence time-scale $(T = k/\varepsilon)$ (where T is used to define the eddy-viscosity and appears in the production and dissipation terms of the ε-equation). Abdon & Sundén [99] showed that the Durbin realizability condition improves Nusselt number predictions using a linear $k-\varepsilon$ model in impinging jet flows and Behnia *et al*. [100, 101] demonstrated that the elliptic-relaxation $\left(v^2-f\right)$ model incorporating the correction also performs well. In the NLEVM approach, contributions from the non-linear terms result in a better representation of the normal stresses and hence improve the stagnation-point behaviour. Differential stress models involve the solution of transport equations for the normal stresses which enables more elaborate methods of overcoming the stagnation-point problem to be employed (see [65]).

There have been a number of previous numerical simulations of impinging jet flows using wall functions. Heyerichs & Pollard [102] compared the performance of six low-Reynolds-number models and three wall functions in a 2-*D* impinging jet flow with $Re = 10,000$ and $H/D = 2.6$. No definitive conclusions about the superior performance of any one of the wall functions was made, except for the general comment that wall functions are unsuitable for complex flows where the assumptions used in their derivation are not valid. They also noted that the low-*Re* $k-\omega$ model gave slightly better predictions than the low-*Re* Launder-Sharma $k-\varepsilon$ model, although they also showed that the Yap correction had a negligible effect on the Nusselt number at the stagnation point. Amano & Brandt [103] studied a range of impinging jet nozzle-to-plate distances, ranging from 2 to 40 nozzle diameters, and Reynolds numbers from $50,000$ to $300,000$. They found that good agreement could be obtained between experimental and numerical predictions for the velocity, pressure and skin friction, using a linear $k-\varepsilon$ model with the Chieng & Launder wall function. Further papers by Amano & Jensen [104] and Amano & Sugiyama [105] showed that some small improvements could be made in predicting the stagnation-point heat transfer by solving transport equations for both k and ε in the

near-wall cell[3]. The results of these papers contrast with the more recent findings of Ashforth-Frost & Jambunathan [106] who found that for a confined impinging jet at a Reynolds number of $20,000$ and a nozzle-to-plate spacing of 2 jet diameters, the kinetic energy near the stagnation point was overpredicted by a factor of 9. They used the PHOENICS code with a linear $k-\varepsilon$ model and a wall function based on the velocity log-law and local-equilibrium assumptions. The poor performance of the numerical simulation in the stagnation region was attributed to both the isotropic linear eddy-viscosity model and the wall function. Bouainouche *et al*. [107] evaluated the performance of a simple wall function, based on the velocity log-law and prescribed nodal values for k and ε, and a "generalized" wall function in which a simplified transport equation for k was solved in the near-wall cell with cell-averaged production and dissipation rate source terms. Both approaches were shown to have shortcomings in the prediction of wall shear stress for impinging jet flows, although the latter model showed a lower sensitivity to changes in the near-wall grid spacing. A hybrid wall function was proposed which switched from the generalized wall function, used in the impingement zone, to the simple wall function, used downstream, at an *ad hoc* prescribed radial distance. Vieser *et al*. [108] studied a range of heat transfer problems with the CFX code using the $k-\varepsilon$, $k-\omega$ and SST turbulence models with wall functions. They found that good agreement between computational and experimental results could be obtained for $H/D=2$ and $Re=23,000$ using a linear $k-\varepsilon$ model with the scalable wall function (a reoptimized version of the wall-function proposed by Grotjans & Menter [47]).

In the present study, calculations are compared to the experimental heat transfer data of Baughn *et al*. [94] and the velocity and Reynolds stress data of Cooper *et al*. [95]. Jambunathan *et al*. [109] provide a comprehensive review of experimental heat transfer measurements for the impinging jet flow. The paper by Behnia *et al*. [101], which focuses mainly on the behaviour of the elliptic relaxation turbulence model in impinging flows, noted that there is considerable scatter in experimental measurements of the Nusselt number. They selected five recent sets of experimental Nusselt number data for $H/D=6$ and $Re=23,000$ and found differences of approximately 20-25%. These were attributed to differences in inlet conditions.

5.3 Computational Details

5.3.1 Models Used

Both the linear $k-\varepsilon$ and cubic non-linear $k-\varepsilon$ models presented in Chapter 2 were assessed in the impinging jet flow. For both models, results obtained using a low-Reynolds-number approach were compared to those obtained with four standard wall functions: Launder & Spalding (TEAM), simplified Chieng & Launder (SCL), Chieng & Launder (CL) and Johnson & Launder (JL), and with the new UMIST-*N* wall function. Some modifications to the expression for the cell-averaged

[3]Whereas in the Chieng & Launder approach, a transport equation is solved for k, but ε is specified at the near wall node from local-equilibrium assumptions.

production of turbulent kinetic energy, $\overline{P_k}$, used in the Chieng & Launder wall function, were also tested. The influence of the standard Yap correction and the differential length-scale correction were investigated with both models and two different c_μ functions were tested with the NLEVM. In the wall-function calculations, the sensitivity to changes in the size of the near-wall control volume were also assessed using different near-wall grid arrangements. In all of the results shown for the UMIST-*N* wall function, the same turbulence model was used in the subgrid as in the main-grid.

5.3.2 Numerical Methods

Calculations were made using the TEAM code discussed in Chapter 3. In all calculations, diffusion terms were approximated using central differencing, the QUICK scheme was used for the discretization of convection in the momentum and temperature equations and PLDS was used for k and ε. Near the entrainment boundary, QUICK was found to introduce some instability problems. PLDS was therefore used for all parameters (U, V, T, k and ε) in a region along the entrainment boundary extending roughly $0.5D$ into the flow domain. The dynamic and thermal fields are uncoupled in the impinging jet flow (i.e. the temperature field has negligible effect on fluid density) and therefore the thermal field was solved only once the dynamic field had converged. Typical under-relaxation factors for the main-grid code are shown in Table 5.1 and those for the subgrid solution in the UMIST-*N* wall function in Table 5.2.

U	V	P	k	ε	T	NL
0.35	0.35	0.5	0.45	0.45	0.60	0.4

Table 5.1: Under-relaxation factors used in the impinging jet flow with low-Reynolds-number models, standard wall-function calculations and in the main-grid with UMIST-*N* wall function calculations (*NL* refers to the Non-Linear EVM terms).

U	V	k	$\tilde{\varepsilon}$	NL
1.0	1.0	0.8	0.8	1.0

Table 5.2: Under-relaxation factors used for the subgrid transport equations with the UMIST-*N* wall function in the impinging jet flow.

Calculations involving the NLEVM with the UMIST-*N* wall function were started from an initially quiescent flow field using the linear $k-\varepsilon$ model and Yap correction across the subgrid domain and NLEVM with differential length-scale correction across the main-grid domain. After 500 iterations (approximately one third of the overall calculation time) the NLEVM and differential Yap correction were activated across the subgrid. Convergence was reached when the total non-dimensionalized residuals for the momentum and temperature equations were below 5×10^{-4} . It was confirmed that reducing residuals below this value had no effect on results. Calculations involving the differential Yap correction were, in general, less stable than those with the standard Yap correction and required greater under-relaxation in order to reduce residuals to the required limit. Greater under-relaxation

of the subgrid k and $\tilde{\varepsilon}$ was also required with the differential Yap correction as the near-wall cell size was increased. For the largest cell size ($DX = 500$) the under-relaxation factor for the subgrid k and $\tilde{\varepsilon}$ equations was $\alpha = 0.5$.

5.3.3 Domain and Grid

The flow domain for the impinging jet with a jet discharge height of 4 jet diameters was $4.5D$ in the wall-normal direction, which included $0.5D$ of inlet pipe length. A short length of pipe wall was included in the flow domain to reduce instability arising from the entrainment boundary near the jet inlet. In the radial direction, the domain extended 7 jet diameters.

The low-Reynolds-number grid, which used 90×70 (axial $\times$ radial) nodes, is shown in Figures 5.4 and 5.5. The y^+ values (calculated from $y^+ = c_\mu^{1/4} k^{1/2} y/\nu$) varied according to the turbulence model used, and are summarized in Table 5.3.

Turbulence Model	max. y^+at 5th node from the wall	max. y^+at 10th node from the wall
Linear $k-\varepsilon$	3	13
NLEVM	5	17

Table 5.3: y^+ values for the 90×70 low-Reynolds-number grid

A grid-dependence study was performed with a refined 120×90 grid (see Figure 5.6). This corresponded to an increase in the number of grid nodes of 70%, although the flow domain was also increased from 7 to 10 jet diameters in the wall-parallel direction. A small difference of 2% in the Nusselt number, limited to the region near the stagnation point ($r/D < 0.3$), was observed with the linear $k-\varepsilon$ model (see Figure 5.7). In the refined grid the first 10 cells were within $y^+ \leq 3$.

The high-Reynolds-number grids used with wall functions consisted of 45×70 (axial $\times$ radial) nodes, see Figures 5.8 and 5.9, and used an identical distribution of nodes in the radial direction to the low-*Re* grid. Four different near-wall cell widths were tested, denoted by $DX = 250, 300, 400, 500$, where the low-*Re*-grid near-wall cell width was $DX \approx 1$ (i.e. the near-wall cell size used by the wall functions was between 250 and 500 times larger than that used by the low-*Re* model). The quantity, DX, represents the physical thickness of the wall-adjacent cell in the wall-normal direction. The smallest width ($DX = 250$) corresponds to the lowest recommended size for wall functions based on logarithmic velocity profiles, i.e. $y^+ \geq 30$, and the largest cell ($DX = 500$) had a maximum y^+ of just over 300. The grid specification outside the near-wall cell was unchanged whilst the near-wall cell width was varied. The grid spacing for $DX = 250$ was continuous and so for $DX = 500$ there was a jump in cell size of $2:1$ from the near-wall cell to the adjoining cell (see the right-hand picture in Figure 5.10). The discontinuity in cell size for the large near-wall cells was a consequence of examining the effect of changing one variable only (the near-wall cell size) and not the effect of refining the overall grid. However, steps in cell size can lead to numerical inaccuracies and slow

convergence, particularly with more sophisticated turbulence models (such as the NLEVM tested here). If a continuous grid spacing is used for the largest near-wall cell size, i.e. 1:1 instead of 2:1 grid size ratios, the total number of grid nodes can be reduced from 45 to 41, convergence is improved and results are almost identical using the UMIST-*N* wall function (see Figure 5.11).

5.3.4 Boundary Conditions

Figure 5.1 shows a schematic of the boundary conditions employed in the impinging jet flow.

Inlet Pipe Flow

The inlet conditions at the jet discharge were specified using a fully developed pipe flow with Reynolds number, $Re = 70,000$ (based on bulk inlet velocity, jet diameter and the fluid properties of air at room temperature, $\mu = 1.82 \times 10^{-5} kg/m/s$ and $\sigma = 0.71$). The pipe flow was calculated separately using a parabolic solver (as in Suga [34]). In terms of coding the inlet conditions into TEAM; the velocities, turbulence scalars (k, ε and μ_t) and temperature were simply specified at the domain boundary nodes.

Axis of Symmetry

Along the axis of symmetry, zero-gradient conditions were applied for axial velocity components, turbulence scalars and temperature. To implement zero-gradient conditions in the main-grid, the nodal value on the boundary of the domain was set equal to the neighbouring nodal value (inside the domain) and the flux term associated with the boundary was set to zero in the discretized transport equation (i.e. $a_W = 0$ for the symmetry axis on the west cell face, shown in Figure 5.1). Similarly, in the subgrid, the values of V, k, $\tilde{\varepsilon}$ and T on the boundary were set equal to the neighbouring subgrid values. The radial velocity at the boundary nodes situated on the axis of symmetry was set to zero.

Entrainment

For the entrainment boundary condition at the northern edge of the flow domain, shown in Figure 5.1, different constraints were applied depending upon the local flow direction. If the fluid was entering the domain, Dirichlet conditions were applied: k and ε were given small but finite values ($k = V_N^2 \times 10^{-7}$, where V_N is the axial velocity through the entrainment boundary, and $\varepsilon = k$ so that $\mu_t = c_\mu k^2/\varepsilon = 0.09$), the radial velocity was set to zero and the temperature of the flow entering the domain was set to the ambient temperature. If fluid was leaving through the entrainment boundary, Neumann conditions were applied: values of U, k, ε or T on the boundary were set equal to the neighbouring nodal values just inside the domain and the flux coefficient through the boundary was set to zero ($a_N = 0$).

Irrespective of whether the flow was into or out of the domain, the axial velocity on the boundary of the domain, V_N, was set equal to the neighbouring nodal value and the pressure at the node just inside the entrainment boundary was set to zero.

Outlet

Although in theory the flow through the right-hand face of the domain shown in Figure 5.1 should be leaving the domain, during the iteration process flow may enter or leave through the boundary. For this reason the entrainment conditions described above were also used for the circumferential exit plane. The only difference here was that the radial U-velocity specified on the boundary was determined from:

$$\frac{\partial (rU)}{\partial r} = 0 \tag{5.3}$$

This condition was used to satisfy continuity within the cells adjacent to the exit plane.

Pipe Wall

It was necessary to include a short length of pipe at the jet inlet to improve stability. The surfaces of the pipe wall were treated with TEAM wall functions and the nodes inside the pipe wall had properties set to zero by the source conditions $s_U = 0$ and $s_P = -10^{30}$. The wall function treatment of the inlet pipe wall was not changed throughout the course of the calculations. Only the wall treatment applied to the impingement wall was varied.

Impingement Wall

Either a low-Reynolds-number model approach was used for the impingement wall or wall functions were applied. Heat transfer predictions were made assuming a constant heat flux from the wall surface. In the Nusselt number comparisons shown later, results from the calculations are compared to the experimental data of Baughn *et al*. [94]. In their experiments, Baughn *et al*. employed a transient technique[4] to obtain heat transfer measurements for constant wall temperature conditions. There is a degree of uncertainty in measuring transient phenomena. Baughn *et al*. performed an analysis of this and estimated the uncertainty to be less than 7%.

Figure 5.12 shows the predicted Nusselt number using constant heat flux (CHF) and constant wall temperature (CWT) conditions. The two calculations used the non-linear $k-\varepsilon$ model of Craft *et al*. [67] and the "standard" Yap correction. Prediction of the Nusselt number at the stagnation point was not affected by the choice of thermal boundary condition. However, the trough and peak in the predicted Nu downstream of the stagnation point occurred slightly closer to the jet axis with the CWT treatment than with CHF (CWT gave the min./max. inflexion points at $r/D \approx 1.05/1.65$, respectively, whereas CHF gave them at $r/D \approx 1.2/1.9$). In the radial-wall-jet region $r/D > 2.5$, CWT also gave a lower value of Nusselt number than CHF (a difference of up to 9%).

When using constant wall temperature conditions, there is greater heat transfer at the stagnation point than with constant heat flux boundary conditions. The fluid in the boundary layer adjacent

[4]The impingement plate, which was coated with a layer of liquid crystals, was heated to a set temperature in an oven. The plate was then covered with an insulating plate, taken out of the oven and placed in path of the impinging jet. Video recording equipment was activated, the insulating plate was removed and the coloured fringes on the liquid crystals were recorded.

to the wall in the CWT case is therefore at a higher temperature. Consequently, downstream from the impingement zone the temperature difference between the fluid and the wall is less and the heat transfer coefficient is lower with CWT than with CHF boundary conditions.

5.4 Calculated Flow Results

5.4.1 Linear $k-\varepsilon$

Low-Reynolds-Number Model

The linear $k-\varepsilon$ model is well known to overpredict the levels of turbulence energy, and hence heat transfer, at a stagnation point (see, for example, Craft *et al*. [65]). Profiles of the RMS velocity (Figure 5.13) show that the normal stress at the stagnation point is significantly over-predicted by the low-*Re* $k-\varepsilon$ model: the predicted peak wall-parallel u'-velocity is nearly three times the measured value whilst the wall-normal v'-velocity is approximately twice the size of the u'-component. The large predicted stress anisotropy at the stagnation point falls as one moves radially outwards to $r/D = 1$ and for $r/D \geq 1.5$ the u'- and v'-velocity components are practically identical. This behaviour in the shear flow region of the impinging flow is as would be expected from an isotropic linear model (where the normal stresses tend to $\overline{u_i^2} = 2k/3$ in the absence of any normal strain). Contrary to these predictions, the experimental data of Cooper *et al*. [95] shows the Reynolds stress remaining anisotropic at $r/D \geq 1.5$ with the streamwise (wall-parallel) component exceeding the wall-normal component $\left(v' \approx 2/3u'\right)$. Nusselt number predictions using the low-Reynolds-number $k-\varepsilon$ model (solid line in Figure 5.15) show that heat transfer at the stagnation point is overpredicted by more than 100% even with the Yap correction. The secondary peak in Nusselt number, observed in the experiments of Baughn *et al*. at $r/D \approx 2$, is also entirely missed.

Standard Wall Functions

Resultant velocity profiles are shown for the four standard wall functions: TEAM, SCL, CL, and JL in Figure 5.14. The four wall functions give practically identical results. Overall, the predicted velocity is in fair agreement with the experimental measurements although the near-wall peak in the predicted velocity is too low for $(0.5 \leq r/D \leq 2.5)$ and the velocity profile is too steep for $r/D \geq 1.5$. The poor performance of the wall functions is partly because the experimental maximum velocity occurs between the first nodal position and the wall. The near-wall cell size could not be reduced further without causing problems downstream, where the near-wall node would no longer occupy the log-law region and would fall inside the viscous sublayer[5]. It is impossible to draw conclusions from the velocity profiles about the relative performance of the different wall functions. This is true also of the Reynolds stress profiles (not shown). However, the Nusselt number predictions obtained using

[5]Such problems could be overcome if one used a non-orthogonal grid in which the near-wall cell size increased with distance from the axis of symmetry. This approach was not possible with the TEAM code, employed to study the impinging jet flow, which could only use a Cartesian grid arrangement.

the four standard wall functions are markedly different (Figures 5.15 – 5.18). In general, all of the standard wall functions are in poor agreement with the low-*Re* model predictions although they are in somewhat better agreement with the experimental results. The TEAM, CL and JL wall functions incorrectly predict the maximum heat transfer to occur at a distance of approximately $r/D \approx 0.5$, whilst the SCL wall function has a plateau between $r/D = 0$ and 0.5. All four wall functions predict the correct shape of the Nusselt number profile in the shear flow region $(r/D \geq 2.5)$ although there is significant discrepancy in the actual Nu levels in this region: the TEAM wall function results are lower than the experimental data points, the SCL and JL wall functions are higher and the CL wall function results are in good agreement with the experiments. None of the standard wall functions predict the secondary peak in Nu at $r/D = 2$, although this is due more to the turbulence model employed in the calculations. All of the standard wall functions show some sensitivity to the size of the near-wall cell. This sensitivity is greatest with the TEAM wall function, where a doubling of the cell size (from $DX = 250$ to 500) results in a drop in Nusselt number of approximately 10%. There are a number of features of the TEAM treatment which may be responsible for this behaviour, such as the assumed linear velocity profile used to calculate the strain-rate $(\partial U/\partial y)$ in the expression for average production (Equation 2.61) and the integration of P_k and ε across the whole near-wall cell (rather than just to the edge of the viscous sublayer). The least sensitivity to the cell size is shown by the CL wall function which calculates the wall shear stress using the value of k extrapolated to the edge of the viscous sublayer. Overall, the SCL wall function shows the behaviour closest to the low-*Re* model results of all the standard wall functions. Profiles of y^+ (which changes along the length of the wall) for the different near-wall sizes $(DX = 250, 300, 400, 500)$ are shown in Figure 5.19 using the CL wall function.

UMIST-*N* Wall Function

In comparison to the standard wall function results, the UMIST-*N* wall function shows good agreement with the low-*Re* model predictions of the Nusselt number (Figure 5.20). There is also practically no variation in predicted Nu due to changes in the size of the near-wall main-grid control volume (profiles of y^+ for the different near-wall cell sizes are shown in Figure 5.21). There is, however, a small discrepancy between UMIST-*N* and low-*Re* Nusselt number near the stagnation point ($r/D < 1$). At the stagnation point, the wall-normal velocity profiles across the subgrid are in good agreement with the corresponding low-Reynolds-number model profiles (see the earlier discussion in Section 4.3.1, in particular Figure 4.6). However, near-wall profiles of turbulent kinetic energy, k, (see Figure 5.22) show that the main-grid k values are lower than the low-*Re* model results outside the wall-function region. To investigate whether this discrepancy was due to an insufficient resolution of the peak in kinetic energy, which occurs in the main-grid region, the number of main-grid nodes normal to the wall was increased from 45 to 51, with clustering of nodes near the wall (Figure 5.23). This decreased the y^+ at the stagnation point from approximately 170 to 60 and improved the main-grid resolution of the kinetic energy peak (Figure 5.24). This improved the agreement between the Nusselt number

predicted by the UMIST-*N* wall function and the low-*Re* model (see Figure 5.25). This refinement of the near-wall grid was not applied in other tests since downstream from the stagnation point y^+ decreased to approximately 10, which is below the minimum value recommended in standard wall functions. The minimum size of the near-wall control volume is not restricted with the UMIST-*N* wall function since low-Reynolds-number model equations are solved in the main-grid and no assumed profiles are used across the near-wall cell.

To confirm that the underpredicted Nusselt number shown in Figure 5.20 was a consequence of inadequate main-grid resolution and not some effect introduced by decreasing the size of the subgrid region, the same near-wall cell size was used as in previous cases, with cell sizes in the range $DX = 250 \rightarrow 500$, but the adjoining main-grid cells were made 2.5 times smaller, see Figure 5.26. The predicted *k*-profiles using this grid arrangement and a near-wall cell size of $DX = 250$, shown in Figure 5.27, display a marked improvement in capturing the low-Reynolds-number *k*-profile compared to the earlier case where a coarse main-grid mesh was used. The UMIST-*N* wall function Nusselt number (Figure 5.28) is in good agreement with the result obtained when the main-grid was refined and the near-wall cell size was reduced to $y^+ \approx 60$ (compare to Figure 5.25). Although this test confirms that the original underprediction of the UMIST-*N* Nusselt number shown in Figure 5.20 was caused by insufficient near-wall main-grid resolution, this grid arrangement is not generally recommended, since the discontinuity in main-grid cell sizes, shown in Figure 5.26, may lead to inaccuracies in interpolating and determining gradients at the near-wall cell boundary[6] and will increase convergence times, particularly when more sophisticated turbulence models are applied. Interestingly, though, this same approach of using a relatively fine grid up to the near-wall cell was advocated by Goncalves & Houdeville [110] in their study of transonic flows over airfoils using wall functions. It also has some similarities to the approach of Grotjans & Menter [47] where the edge of the grid is treated as the outer limit of the viscous sublayer, rather than the wall, to enable unlimited grid refinement.

Log-Law Profiles

Profiles of the dimensionless velocity and temperature versus the wall distance, y^+, on semi-logarithmic axes are in Figures 5.29 and 5.30. The low-*Re* model distribution across the near-wall region is compared to the UMIST-*N* and Chieng & Launder wall functions and the "universal" log-law at 8 radial positions. The CL wall function line intercepts the universal log-law line, since the log-law is used to prescribe the velocity and temperature at the near-wall node. It is immediately obvious from these plots that the low-*Re* profiles do not match the law of the wall for velocity or temperature in the stagnation region $(0 < r/D < 1)$. This helps to explain why profiles of the Nusselt number predicted by the standard wall functions are so different from those obtained using low-*Re* model treatments in the vicinity of the stagnation point. Further downstream, $r/D > 1.5$, the velocity log-law is in surprisingly good agreement with the low-*Re* profile. However, the slope of the low-*Re* T^+ profile is

[6] since the gradient defined using central differencing between values at two nodes is more likely to reflect the gradient midway between the two nodes than the gradient in close proximity to one of the nodes.

steeper than the temperature log-law so that the temperature log-law is only valid for a narrow band of $40 < y^+ < 70$.

The UMIST-*N* wall function profiles of U^+ and T^+ are in excellent agreement with the low-*Re* profiles across the entire flow domain, despite the relatively coarse main-grid used in the wall function calculations. In both velocity and temperature plots, the subgrid profile matches that of the low-*Re* model almost exactly. Careful examination of the profiles shows that the subgrid profile does not intersect with the line joining the two near-wall main-grid nodes. This is due to the graph axes being logarithmic whilst a linear interpolation is used for the subgrid velocity and temperature boundary conditions.

Yap Correction

Figure 5.31 compares the performance of the standard and differential Yap corrections (given by Equations 2.16 and 2.17) with the low-*Re* linear $k-\varepsilon$ model. Clearly, either the standard or the differential correction improves significantly upon the heat transfer predictions of the linear $k-\varepsilon$ model without any length-scale correction. The Nusselt number predictions are notably lower overall and closer to the experimental values with the differential Yap correction than with the standard Yap correction. Figure 5.32 shows that the Yap correction has a much smaller influence on the heat transfer predictions when a standard wall function approach is employed than when a low-*Re* model is used. This behaviour is to be expected since standard wall functions fix the turbulence length scale at the near-wall node by specifying ε_P (Equation 2.51) and therefore in effect the Yap correction is not used in the near-wall row of cells[7]. The performance of the UMIST-*N* wall function with the differential Yap correction (Figure 5.33) shows a similar level of agreement with the low-*Re* model to that previously discussed for the standard Yap correction.

5.4.2 NLEVM

Low-Reynolds-Number Model

The impinging jet was one of the flows considered by Suga [34] in developing the non-linear $k-\varepsilon$ model[8] and more recent calculations by Craft *et al.* [67] have confirmed that the model performs well in this flow. Contour plots of the turbulent kinetic energy (Figure 5.34) show that the NLEVM predicts lower values of k at the stagnation point than the linear $k-\varepsilon$ model. Profiles of the RMS axial and radial velocity components in Figure 5.35 also show that the overall level of the predicted normal stress in the vicinity of the stagnation point is much lower and in far better agreement with the experimental measurements than that observed with the linear model (compare to Figure 5.13). At $r/D = 0.5$, the non-linear model correctly predicts the axial stress to be slightly larger than the

[7] The influence of the Yap correction on the predicted Nusselt number when standard wall functions are used is consequently dependent upon the thickness of the wall function region, i.e. the near-wall grid arrangement.

[8] Suga calibrated the model with respect to axisymmetric impinging jet flows with jet heights of $H/D = 2$ and 6, whereas the present study examines a jet height of $H/D = 4$.

radial stress and also the reverse trend at greater radii. However, the degree of anisotropy is slightly overpredicted for $1.0 \leq r/D \leq 1.5$ and underpredicted for $r/D \geq 2$. Craft *et al.* [30] acknowledged that the NLEVM underpredicts the stress anisotropy in plane channel flows but suggested that the correct normal stress behaviour is not a serious problem since it is the shear stress which controls the mean-flow behaviour in such flows, and this is well predicted. Figure 5.36 shows profiles of the shear stress for the impinging jet flow, and these are for the most part predicted accurately, although there is a significant overprediction of the shear stress magnitude at $r/D = 2$.

Nusselt number results for the low-*Re* NLEVM are shown as the solid line in Figure 5.37. The non-linear model predictions are in far better agreement with the experimental measurements than the linear model results shown, for example, in Figure 5.15. The overall shape of the experimental Nu profile is well matched with the secondary peak appearing at the correct location $(r/D = 2)$. However, the level of the predicted Nu is consistently around 10% higher than the experimental value.

Standard Wall Functions

Nusselt number predictions using the four standard wall functions are presented in Figures 5.37 to 5.40. All of the standard wall functions incorrectly predict the maximum heat transfer to occur downstream from the stagnation point, in the range $1 < r/D < 2$, with the TEAM wall function underpredicting the stagnation-point Nusselt number by 50%. All of the standard wall functions also display some sensitivity to the size of the near-wall control volume. Of the four standard wall functions, the Chieng & Launder wall function predicts the best overall shape of the Nusselt number.

Figure 5.42 shows the effect on the predicted Nusselt number of neglecting the normal stress contribution to the cell-averaged production $\overline{P_k}$ in the Chieng & Launder wall function (see discussion in Section 2.4). The stagnation point heat transfer is reduced by 30% compared to the case where normal stress contributions are included and agreement with the experimental data is considerably poorer. Figure 5.43 shows results using the Chieng & Launder wall function which has been modified to calculate the cell-averaged production, $\overline{P_k}$, assuming a linear profile of both shear and normal stresses across the fully-turbulent region of the near-wall cell (in the CL wall function results previously shown in Figure 5.39, the shear stress is assumed to vary linearly and the normal stresses to remain constant). The differences between Figures 5.39 and 5.43 are slight. In a further modification to the CL wall function, discussed in Section 2.4.6, the cell-averaged production is calculated assuming that the Reynolds stresses vary according to their wall-limiting behaviour across the viscous sublayer. This modification introduces a greater sensitivity to the size of the near-wall control volume (Figure 5.44), indicating that the assumed sublayer profiles of the Reynolds stresses are inappropriate.

When using standard wall functions, the strain-rate at the near-wall node $(\partial U/\partial y)_P$ can be calculated by differentiating the log-law, as discussed in Section 2.4.7. This strain-rate is used by the NLEVM to find the value of the strain-dependent c_μ function and the non-linear stress components within the near-wall cell. In fact, since the wall function replaces the production term in the near-wall cell with a cell-averaged value, $\overline{P_k}$, and since the diffusion to the wall is replaced by the wall

shear stress, τ_{wall}, the use of a modified $\partial U/\partial y$ only significantly influences diffusion of momentum through the face of the cell opposite the wall (the north face in Figure 2.1). Figure 5.45 shows the Nusselt number predictions for the impinging jet using the Chieng & Launder wall function with the log-law definition of $\partial U/\partial y$. The use of what could be considered as a more accurate representation of the strain-rate in fact leads to a worsening of the predicted Nusselt number, the log-law $\partial U/\partial y$ predicting entirely the wrong shape of the Nu profile near the stagnation point.

UMIST-*N* Wall Function

In contrast to the standard wall functions, the UMIST-*N* wall function with the NLEVM (Figure 5.46) shows excellent agreement with the low-*Re* model predictions. The wall function and low-*Re* results are practically indistinguishable for $r/D < 1.5$ and $r/D > 3$, with a maximum discrepancy of 8% at $r/D = 2$. The UMIST-*N* results also show negligible sensitivity to changes in the size of the near-wall control volume, whilst the Chieng & Launder wall function showed differences of up to 14% with the NLEVM.

Figure 5.47 shows a similar plot of the Nusselt number predicted by the UMIST-*N* wall function versus the low-*Re* NLEVM model predictions but now using the original c_μ function proposed by Craft *et al*. (Equation 2.33) – the previous results in Figure 5.46 were with the more recent c_μ function of Craft *et al.* [67] (Equation 2.36). The differences between the two c_μ functions are relatively minor. Using Equation (2.33) reduces the secondary peak in the Nu profile by approximately 5% bringing the predicted profile marginally closer to the experimental data. The UMIST-*N* wall function behaves similarly with either c_μ function.

Log-Law Profiles

Figures 5.48 and 5.49 compare the UMIST-*N* and Chieng & Launder wall function predictions of the velocity and temperature with the low-*Re* model predictions and "universal" law of the wall. The dimensionless velocity and temperature predicted by the low-*Re* model in the vicinity of the stagnation point are much lower than those predicted by the universal log-law. The Chieng & Launder wall function is tied to the log-law and consequently is in poor agreement with the low-*Re* profiles, whereas the UMIST-*N* wall function shows good agreement with the low-*Re* profiles across the whole flow domain. The slope of both the low-*Re* velocity and temperature profiles in the fully-turbulent region is somewhat steeper than that predicted by the log-law, even at $r/D = 3.5$, suggesting that agreement between log-law based wall functions and low-*Re* model calculations is only possible for a narrow range of near-wall cell sizes.

Yap Correction

Figure 5.50 compares the predicted Nusselt number using the low-*Re* NLEVM without the Yap correction, with the standard Yap correction (Equation 2.16) and with the differential Yap correction

(Equation 2.17). The purpose of the Yap correction is to suppress turbulence near a stagnation point. It seems therefore remarkable that when the Yap correction is removed, the Nusselt number is *reduced*. This behaviour is contrary to that observed previously with the linear $k-\varepsilon$ model (Figure 5.31).

The causes of this behaviour can be understood by examining the NLEVM expression for the Reynolds stress (Equation 2.27). Along the axis of symmetry, the vorticity tensor, Ω_{ij}, is zero and the expression for the Reynolds stress simplifies to:

$$\begin{aligned} \overline{u_i u_j} - \frac{2}{3}\delta_{ij}k &= \underbrace{-\nu_t S_{ij}}_{linear} \\ &\quad \underbrace{-0.1\nu_t \frac{k}{\tilde{\varepsilon}}\left(S_{ik}S_{kj} - \frac{1}{3}S_{kl}S_{kl}\delta_{ij}\right)}_{quadratic} \\ &\quad \underbrace{-5c_\mu^2\nu_t\left(\frac{k}{\tilde{\varepsilon}}\right)^2 S_{ij}S_{kl}S_{kl}}_{cubic} \end{aligned} \tag{5.4}$$

Assuming the ratio of $(k/\tilde{\varepsilon})$ to be large near the stagnation point, the c_μ function given by Equation (2.36) is approximately proportional to the ratio of $(\tilde{\varepsilon}/k)$:

$$c_\mu \propto \frac{\tilde{\varepsilon}}{k} \tag{5.5}$$

If one also assumes that the strain-rates are approximately equal whether the Yap correction is employed or not, then the cubic non-linear term in Equation (5.4) can be shown to vary in proportion to the eddy-viscosity. The quadratic term, on the other hand, is a function of the eddy-viscosity and the ratio of $(k/\tilde{\varepsilon})$. When the Yap correction is introduced, the turbulent length scale and hence the ratio of $(k/\tilde{\varepsilon})$ are decreased. This then decreases the quadratic term in Equation (5.4) which has the effect of increasing the wall-normal Reynolds stress, $\overline{v^2}$, and hence the production of k. It was found, although results are not shown here, that by making the quadratic coefficient c_1 in the NLEVM a linear function of c_μ, the dependence on $(k/\tilde{\varepsilon})$ is reduced and the NLEVM responds as anticipated to the Yap correction, i.e. heat transfer rates are reduced when the Yap correction is activated.

The difference between the standard and differential Yap correction results are less significant with the NLEVM than those shown previously for the linear model. The differential correction reduces the Nusselt number at the stagnation-point (by around 8% compared to the standard correction) and further downstream $(r/D > 1)$. Results are therefore in marginally better agreement with the experimental data using the differential length-scale correction.

5.5 Computational Costs

Tables 5.4 and 5.5 compare the computing times for the Chieng & Launder wall function, the UMIST-*N* wall function, and low-Reynolds-number treatments for the linear and non-linear $k-\varepsilon$ models. Both wall functions use identical main-grids and the low-Reynolds-number grids only involve refinement normal to the wall (the grid in the radial direction is identical in wall function and low-*Re* model simulations). Main-grid under-relaxation factors are identical for all computations and subgrid under-relaxation factors are those presented in Table 5.2. Calculations were performed on a Silicon Graphics O_2 with the same levels of compiler optimization in each case.

Model Tested	No. of Nodes (axial×radial)	Time per Iter (*s*)	No. of Iterations	Total CPU Time (*s*)	Relative CPU Time
Chieng & Launder WF	45×70	0.147	1523	224	1
UMIST-*N* WF	$(45+[40])\times 70$	0.228	1392	318	1.42
Low-*Re*	90×70	0.270	9698	2616	11.68

Table 5.4: Computing times for the impinging jet flow using the linear $k-\varepsilon$ model

Model Tested	No. of Nodes (axial×radial)	Time per Iter (*s*)	No. of Iterations	Total CPU Time (*s*)	Relative CPU Time
Chieng & Launder WF	45×70	0.158	1426	226	1
UMIST-*N* WF, option 1	$(45+[40])\times 70$	0.224	1392	313	1.38
UMIST-*N* WF, option 2	$(45+[40])\times 70$	0.260	1380	359	1.59
UMIST-*N* WF, option 3	$(41+[45])\times 70$	0.253	1568	398	1.76
Low-*Re*, option 1	90×70	0.318	9346	2971	13.14
Low-*Re*, option 2	90×70	0.324	9116	2955	13.08

Table 5.5: Computing times for the impinging jet flow using the non-linear $k-\varepsilon$ model

All the calculations reported in Table 5.4 employed the "standard" Yap correction. The Chieng & Launder wall function results given in Table 5.5 employed the Craft *et al*. [30] model and "standard" Yap correction. The following options are shown for the subgrid wall function:

1. Craft *et al*. [67] model with "standard" Yap correction and small near-wall cell size ($DX = 250$)
2. Craft *et al*. [67] model with differential Yap correction and small near-wall cell size ($DX = 250$)
3. Craft *et al*. [67] model with differential Yap correction and large near-wall cell size ($DX = 500$)

The large near-wall cell ($DX = 500$) corresponds to a doubling in the size of the smaller ($DX = 250$) near-wall cell. The two cell sizes represent the extremes of recommended near-wall cell sizes for log-law based wall functions: for the small ($DX = 250$) cell the minimum y^+ was around 30 and in the large ($DX = 500$) cell the maximum y^+ was around 300. Two options are shown for the low-Reynolds-number calculations as follows:

1. Craft *et al*. [30] model with "standard" Yap correction
2. Craft *et al*. [67] model with differential Yap correction

5.6 Discussion & Conclusions

The principal aim of examining the impinging jet flow was to assess whether the UMIST-*N* wall function could obtain good agreement with low-Reynolds-number model predictions in a flow far from local equilibrium. Using both linear and non-linear models it has been shown that UMIST-*N* does indeed produce very nearly the same results as with the corresponding low-*Re* model. When used with the linear $k-\varepsilon$ model, the UMIST-*N* wall function slightly underpredicts the low-*Re* model Nusselt number results near the stagnation point. This was shown to be mainly due to insufficient resolution of the peak turbulent kinetic energy in the main-grid. Refinement of the main-grid improved resolution of this peak and consequently improved the Nusselt number prediction, whilst demonstrating that the UMIST-*N* wall-function can be applied in regions where y^+ falls to approximately 10 (below that recommended for standard wall functions based on a log-law velocity profile). When used with the non-linear $k-\varepsilon$ model, there was excellent agreement between the UMIST-*N* wall function and low-*Re* model predictions. Tests with four log-law-based wall functions showed that their performance is poor near the stagnation point. Semi-logarithmic profiles of the dimensionless velocity and temperature (U^+ and T^+ versus y^+) indicated that the flow predicted by the low-*Re* NLEVM in the vicinity of the stagnation point does not follow the law-of-the-wall. The fact that the low-*Re* NLEVM shows good agreement with the experimental Reynolds stress and heat transfer results therefore indicates that wall functions which are based upon the log-law will be unlikely to predict impinging flows with accuracy. Standard log-law wall functions were also shown to be sensitive to the size of the near-wall control volume whereas the UMIST-*N* wall function showed practically no sensitivity. The new wall function leads to a modest increase in computing time of up to 60% compared to a standard wall function. This is, however, an order-of-magnitude less than a standard low-Reynolds-number treatment.

In addition to examining the performance of the new wall function, two different turbulence length-scale corrections were tested: the Yap correction [64], and the differential Yap correction of Craft *et al*. [67]. The latter correction removes the dependence upon the wall-normal distance, which can be difficult to define in flows with complex geometry. The differential Yap correction was shown to have a stronger influence on the turbulence length scale than the standard Yap correction and, with a linear $k-\varepsilon$ model, decreased the predicted Nusselt number at the stagnation point by nearly 25%. Its effect with the non-linear model was shown to be less significant.

Chapter 6

Spinning "Free" Disc Flow

6.1 Introduction

There have been numerous studies of the flow induced by a spinning disc in an infinite quiescent environment, or free-disc flow. The case represents one of the simplest wall-bounded flows involving strong rotational forces. By far the greatest interest in spinning discs comes from simulations of flow through gas turbines, where it is common practice to first validate a CFD code with the free-disc flow, before moving on to study more complex enclosed disc flows which occur inside the turbine. Other practical examples of spinning-disc flows include computer hard disks and wheels on moving vehicles. Experimental studies have shown that approximately one third of the total drag on a typical saloon car is due to the interaction between the flow around the spinning wheels and their associated structures [111], so clearly one would like to predict accurately the flow around the spinning wheel.

In a free-disc flow, the disc of radius r_b rotates with angular velocity Ω and, due to the no-slip condition on the surface of the spinning disc, a tangential velocity $(W = \Omega r)$ is imparted to the fluid in contact with the disc. A radial outflow of fluid from the centre of the disc is also induced due to the centrifugal force. The entrainment of fluid axially into the boundary layer and the exit of the fluid radially is referred to as the "free-disc entrainment rate" or "free-disc pumping effect" [112]. When the disc is spinning sufficiently fast, the boundary layer can become turbulent. The location of transition from laminar to turbulent flow depends upon the local rotational Reynolds number (based on the tangential velocity of the disc and the radius from the disc axis), the surface roughness of the disc and external disturbances to the fluid flow. Experimental studies of the free-disc flow have reported a certain degree of variation in the location of this transition. Gregory *et al.* [113], reported that the transition started at a rotational Reynolds number of approximately $185,000$ which led to fully-developed turbulence at $Re_\phi = 285,000$, whilst Theodorsen & Regier [114] found that transition started at around $Re_\phi = 310,000$ for a highly polished disc and $Re_\phi = 220,000$ for a rough disc. Owen *et al.* [115] even found no sign of transition at all, which was attributed to a 2 degree taper on the disc faces and the presence of a central driving shaft. Once the boundary layer has become fully turbulent, the tangential velocity exhibits a logarithmic velocity profile near the wall whilst the radial velocity

increases from zero at the wall to a peak and then decays with distance from the disc [116].

Mayle [117] describes three modes in which transition occurs from laminar to turbulent flow: natural, bypass and separated-flow transition. In free-disc flows, transition occurs in the "natural" mode, in which a weak instability in the laminar boundary layer leads to the formation of two-dimensional Tollmien-Schlichting waves which are amplified to form hairpin vortices and turbulent spots that grow and are convected downstream until eventually they coalesce to form a fully-turbulent boundary layer. Schlichting [118] noted that the transition mechanism in the free-disc boundary layer is slightly different to that exhibited by classical 2-*D* flat-plate flows. In particular, stationary spiral vortices are formed on the free-disc which show some similarity to Taylor-Görtler vortices [119]. In "bypass" transition, a relatively high free-stream turbulence level diffuses turbulent kinetic energy into the laminar boundary layer. Turbulent spots can appear directly without the preceding stages of T-S waves found in natural transition. In gas turbines, transition on the surface of turbine discs occurs primarily in the bypass mode, while the flow of air over the car wheel is arguably fully turbulent. Although the free-disc flow serves as a useful test-case for validating turbulence models and near-wall treatments for eventual application to gas-turbine flows, or flows around moving vehicle wheels, the mechanism of transition in these cases is different. Therefore, the prediction of transition in the free-disc flow should in many respects be looked at as a separate issue to that of transition prediction in gas turbines or car wheels.

Although the flow is geometrically simple, there are several challenges for the numerical simulation of turbulent free-disc flows using Reynolds-averaged Navier-Stokes equations. Firstly, as already indicated, the flow involves transition from laminar to turbulent flow. This is notoriously difficult to locate accurately and repeatably, and is highly sensitive to the turbulence model, the numerical scheme and the initial turbulence levels [120]. Secondly, the large near-wall cells commonly used with high-Reynolds-number models and wall functions cover the region of the flow where there is a peak in the radial velocity profile. Capturing this type of velocity variation presents an impossible problem for wall functions based on the log-law velocity profile. Moreover, it is usually recommended that, if a wall-function approach is adopted, the near-wall node should be located at a dimensionless wall distance, $y^+ = yU_\tau/\nu$, between 30 and 100 [121]. Since the friction velocity, U_τ, increases with radial distance one may be forced to adopt a non-orthogonal grid to maintain the y^+ value at the near-wall node between these limits. In addition, wall functions are typically developed with reference to simple channel flows in which there is only one Reynolds shear stress, $\overline{uv}$. In the spinning-disc flow, one needs to also account for the $\overline{uw}$ and $\overline{vw}$ shear stresses.

Whilst the free-disc flow is a challenging computational test-case, in terms of predicting transition from laminar to turbulent flow and applying a wall treatment that can capture the near-wall skewing of the velocity profile, quite acceptable results can be achieved using a fairly simple mixing-length turbulence model and a parabolic solver (e.g. Owen *et al*. [115]). Moreover, this method would be considerably faster than the linear and non-linear two-equation models and the elliptic solver used in the present study. However, one would clearly like to have a generally applicable computational

method that can be applied to a wide variety of flows without the need for significant re-optimization. Whilst a mixing-length turbulence model with a parabolic solver may be adequate for the free-disc flow it would be inappropriate for the study of flow around a car body, for example, or even the impinging jet flow considered in Chapter 5.

6.2 Previous Experimental and Computational Studies

There have been numerous computational studies of the turbulent spinning free-disc flow. Owen & Wilson [112] reviewed a number of solutions of the momentum-integral boundary-layer equations using assumed velocity profiles and empirical correlations. Accurate heat transfer predictions of the free-disc have been made using parabolic finite-difference solvers with both mixing-length and two-equation turbulence models (e.g. Owen *et al*. [115] and Launder & Sharma [13], respectively). However, there have been relatively few studies of free-disc flows using high-*Re* turbulence models with wall functions. Chew [122] used the elliptic TEACH code with the high-*Re* $k-\varepsilon$ model previously used by Gosman *et al.* [123] and studied the flow between co-rotating discs, a rotor-stator cavity and the free-disc. The predicted tangential wall shear stress in the free-disc flow was in poor agreement with both experiment and previous integral-momentum solutions. Predictions of the flow between rotating and stationary discs also showed relatively poor agreement with both the experimental radial velocity distribution and the earlier work of Gosman *et al.*, which had shown more encouraging results. It was suggested that the differences with the previous numerical study were due to an insufficient grid density being used by Gosman *et al.*, which was shown to have a significant effect on the moment coefficient. In the third flow considered by Chew, that between co-rotating discs, it was found that the low-*Re* model of Launder & Sharma tended to laminarize much of the cavity which experimentally had been turbulent. This final result was confirmed by Morse [124] in a subsequent study of turbulent flow in rotating cavities. Williams *et al.* [125] studied enclosed spinning-disc flows using a high-*Re* $k-\varepsilon$ model with simple wall functions and the Lam & Bremhorst low-*Re* $k-\varepsilon$ model. The wall-function model outperformed the low-*Re* model in predicting both tangential and radial velocity profiles and the authors concluded that the wall-function approach was to be preferred since it was far more economical in computing time. Virr *et al.* [121] also studied the flow in rotating cavities using the Launder & Spalding $k-\varepsilon$ model with both wall functions and a two-layer near-wall one-equation model. They reported that the wall function returned acceptable results provided that the boundary layer was fully turbulent and that the y^+ was maintained between 30 and 100. A comprehensive comparison of different turbulence models and near-wall treatments for rotating flows was given by Owen & Wilson [112]. They concluded that “at present only low-Reynolds-number $k-\varepsilon$ models have been shown to give good predictions of both flow and heat transfer over the complete range of test cases”.

A number of studies have alluded to convergence difficulties with the free-disc flow. Chew [122] found that, using a high-*Re* model with wall functions, axial grid-refinement led to instability problems. This may have been due to more of the near-wall cells occupying the viscous sublayer region in

which case the wall functions resorted to laminar-type boundary conditions. Chew also encountered problems with the low-*Re* Launder & Sharma model where there was a tendency for the boundary layer to laminarize. In the original calculations by Launder & Sharma [13], transition was triggered by an injection of turbulence energy at a specified radial location. Morse [126] and Ong [127] also reported difficulties in predicting the onset of transition with low-*Re* $k-\varepsilon$ models. To achieve transition, Morse resorted to modifying the eddy-viscosity in the turbulent kinetic energy production term with a proportion of the eddy-viscosity calculated by a mixing-length model. Ong used the Launder & Sharma model with a parabolic semi-implicit Keller-box method and found that if the calculation was started in the laminar boundary-layer region of the free-disc, the solution would remain laminar and never undergo transition to turbulence. To obtain results for the turbulent boundary layer, Ong started the calculation at a radial position corresponding to $Re_\phi = 600,000$, although it was reported that even starting from what should be a fully-developed turbulent region, the boundary layer thickness showed a tendency to decay and laminarize. In contrast to these earlier calculations, Kiliç [128] did not report any difficulties in predicting transition with the same turbulence models using a two-dimensional, elliptic, multigrid solver. Kiliç found that transition occurred naturally at $Re_\phi \approx 150,000$. In the present study, the flow field was initialized with a uniform turbulence level and, as the calculation progressed, turbulence decayed near the axis of the disc to form a laminar boundary layer whilst at a greater radial distance the flow remained fully turbulent. No attempts were made to artificially induce transition and it was found that transition occurred naturally at approximately the same location as Kiliç found (see later discussion).

6.3 Computational Details

6.3.1 Models Used

Two low-Reynolds-number models were tested in the free-disc flow: the Launder & Sharma $k-\varepsilon$ model [13] and the non-linear $k-\varepsilon$ model of Craft *et al.* [30, 67]. Results obtained using the low-*Re* models were compared to those obtained using three "standard" wall functions: Launder & Spalding (TEAM), simplified Chieng & Launder (SCL) and Chieng & Launder (CL) and the new wall function, UMIST-*N*. The standard wall functions all employed a logarithmic profile for both the radial and tangential velocity if the near-wall node was at a dimensionless wall distance of $y^+ \geq 11.6$. If the near-wall node was within the viscous sublayer $(y^+ < 11.6)$ a linear profile was adopted (for details see Chapter 2). The same turbulence model was applied across the subgrid domain of the UMIST-*N* wall function as across the main-grid domain.

6.3.2 Numerical Methods

The free-disc flow was examined using the TEAM code, described in Section 3.2. Diffusion terms appearing in the transport equations were approximated using central differencing. Convective terms

in the momentum and temperature equations adopted the third-order QUICK scheme whilst the power-law differencing scheme, PLDS, was used for turbulence parameters. It was found that the unbounded QUICK scheme led to instability in the initial stages of the calculations and therefore PLDS was used for all quantities in the first 500 or so iterations (approximately $10-25\%$ of the full calculation length of the wall-function calculations). In addition, with the wall-function calculations, PLDS was always used for the wall-adjacent cells. The quadratic interpolation used by QUICK employs two upstream nodes which, if the flow was directed away from the wall, would involve the node on the wall and the wall adjacent node. Since there are abrupt changes in the velocity within the large near-wall cell used with a wall-function approach, the use of these two nodal values could produce unrealistic interpolated velocity profiles which was found to lead to numerical instability (particularly with large near-wall cells). The use of PLDS within the near-wall cells was not considered to be too restrictive on numerical accuracy since one would expect the near-wall flow to be parallel to the wall, in which case PLDS and QUICK would give similar results.

Residuals were summed across all the nodes in the flow domain and non-dimensionalized with a characteristic value for the particular variable. For the momentum equations this was the momentum flux defined using the velocity at the edge of the disc (Ωr_b). The turbulent kinetic energy residual was non-dimensionalized with the flux defined using the velocity scale $(\Omega r_b)^2$, whilst the dissipation rate, ε, was non-dimensionalized using the kinetic energy flux and an assumed length scale $l = r_b$. A mass imbalance was calculated rather than a pressure residual which was also non-dimensionalized using (Ωr_b). Unlike previous studies [124, 128] the factors used to non-dimensionalize the residuals were not linked to the mass flow rate since this varied considerably during the calculation. As a consequence, during a calculation from an initially quiescent flow-field, residuals increased and then decayed. The calculation was stopped when momentum and turbulent kinetic energy residuals fell below 10^{-7}. All the residuals decreased by at least 3 orders of magnitude from their maximum values. It was verified that using more stringent convergence criteria had no effect on results.

Under-relaxation factors were set at a relatively low level for all the calculations performed in the present work, as shown in Table 6.1. Subgrid under-relaxation factors used for the free-disc flow are given in Table 6.2. Previous tests with the UMIST-*N* wall function in the impinging jet found that the under-relaxation of the subgrid turbulence parameters needed to be increased as the size of the near-wall main-grid cell (and hence the number of subgrid nodes) was increased. In the present work, the under-relaxation factors given in Table 6.2 were used throughout.

U	V	W	P	k	ε	T	NL
0.2	0.2	0.2	0.3	0.1	0.1	0.4	0.5

Table 6.1: Under-relaxation factors used for the free-disc flow with low-Reynolds-number models, standard wall-function calculations and in the main-grid with UMIST-*N* wall function calculations (*NL* refers to the Non-Linear EVM terms).

U	W	k	$\tilde{\varepsilon}$	T	NL
1.0	1.0	0.9	0.9	1.0	1.0

Table 6.2: Subgrid under-relaxation factors for the free-disc flow used with the linear and non-linear $k-\varepsilon$ models

6.3.3 Domain and Grid

Figure 6.1 shows the domain size and boundary conditions used for the free-disc study. Following Kiliç [128], a domain height of $0.06D$ was used which corresponds to three times the boundary layer thickness at the outside edge of the disc, where $Re_\phi = 3.3 \times 10^6$, as determined from von Kármán's correlation for turbulent flow over a free-disc [129].

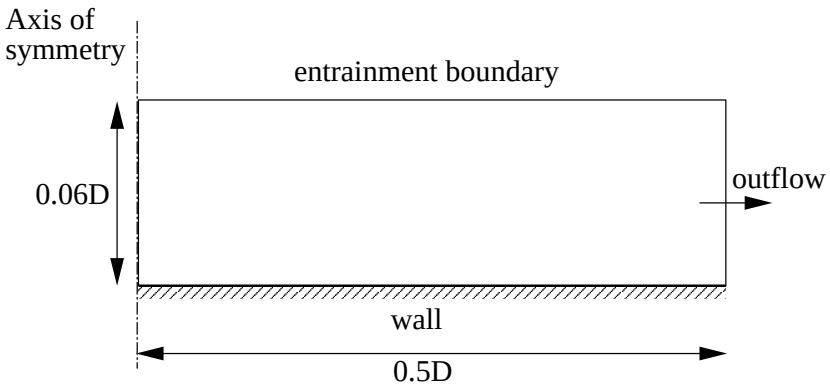

Figure 6.1: Free-disc boundary conditions

A number of previous spinning-disc studies have noted that the placement of grid nodes near the wall is important in obtaining reliable wall shear stress and moment coefficient predictions [112, 128]. Using the same domain size and Reynolds number, Kiliç [128], previously used a low-*Re* grid of 67×67 nodes and checked grid-dependence using a 91×115 (axial $\times$ radial) grid. In the present study, in order to ensure that adequately grid-independent low-*Re* results were obtained, grid refinement was studied separately in the radial and axial directions.

Radial Grid-Refinement

Three different grid densities were tested in the radial direction with 90, 120 and 150 nodes, using 70 nodes in the axial direction (see Figures 6.2, 6.3 and 6.4). Figure 6.5 shows the predicted Nusselt number from these three grid arrangements. The location of transition shifts slightly downstream as one moves to the higher grid density, with approximately the same difference from the 90×70 to the 120×70 grid as from the 120×70 to the 150×70 grid. Clearly the logarithmic plot magnifies the differences in the transition region and, as shown by Figure 6.6, the shift in the transition location achieved by increasing the number of radial nodes by 30% is equivalent to the distance between two or

perhaps three nodes. Following this study, 120 nodes were used in the radial direction for all low-*Re* and wall-function calculations.

Axial Grid-Refinement

Axial refinement of the low-*Re* grid was achieved by increasing the number of nodes from 70 to 120, using 120 nodes in the radial direction in both cases (Figures 6.3 and 6.7). Predicted Nusselt number using the low-*Re* Launder & Sharma $k-\varepsilon$ model are shown in Figures 6.8*a* and 6.8*b*, on semi-logarithmic and linear axes respectively. Corresponding y^+ values for the near-wall node and for the first 10 near-wall nodes are shown in Figures 6.9*a* and 6.9*b*. In order to obtain $y^+ < 0.8$ for the 120×70 grid, an expansion ratio of 1.15 was required for the near-wall cells. The 70 percent increase in the number of nodes in the axial direction shows negligible difference in the predicted Nusselt number on semi-log axes (Figure 6.8*a*), although closer inspection of the Nusselt number distribution on linear axes (Figure 6.8b) shows a maximum difference of just under 2% which occurred at the outside edge of the disc. The use of 70 nodes in the axial direction was therefore considered adequately grid-independent[1].

Four high-Reynolds-number grids were used in the present study to assess the sensitivity of the standard and UMIST-*N* wall functions to changes in the width of the near-wall cell, over which the wall function was applied. In order to avoid sudden increases in cell sizes from the near-wall cell to the adjoining cell, the number of nodes in the axial direction was varied from 22 to 30 (shown in Figures 6.10 to 6.13). With 22 axial cells there was no clustering of cells (i.e. the axial width of the grid cells was constant across the whole flow domain) whilst, with a larger number of radial nodes, there was a small degree of clustering towards the wall. The wall-adjacent cells in the low-*Re* calculations had an average aspect ratio of approximately $2900:1$ whilst the wall-function grid with 28 axial cells cells had an aspect ratio of approximately $5:1$.

The number of subgrid cells used within the wall-adjacent main-grid cell was adjusted for each high-*Re* mesh to ensure that grid-independent results were obtained. Figure 6.14 shows the predicted Nusselt number using the 28×120 high-*Re* mesh with between 30 and 50 subgrid nodes. The expansion ratio used to generate the subgrid mesh was also modified in each case to maintain the size of the wall-adjacent subgrid cell such that $y^+ < 1$ (expansion ratios are shown in parentheses in the key of Figure 6.14). Figure 6.14 shows that there was negligible difference in the predicted Nusselt number due to an increase the number of subgrid nodes from 30 to 50. The total number of subgrid plus main-grid nodes (i.e. 30×120 subgrid and 28×120 main-grid nodes) was thus slightly less than that required by low-Reynolds-number models (70×120 nodes).

[1] Interestingly, the physical width of the wall-adjacent cell with the 70×120 grid is $1.6 \times 10^{-6} D$, where D is the diameter of the disc (the node within this cell has a maximum $y^+ = 0.64$ at the edge of the disc). Using the same rotational speed and viscosity as Cobb & Saunder's experiments [130] (which had an 18-inch disc for a Reynolds number of up to 0.8×10^6), the width of the near-wall cell in the current tests corresponds to 1.5×10^{-6}metres. By comparison, the minimum value of the Kolmogorov microscale $\eta = \left(\nu^3/\varepsilon\right)^{1/4}$, based on the value of ε at the near-wall node at a rotational Reynolds number, $Re_\phi = 3 \times 10^6$, was of the order $\eta = O\left(10^{-4}\right)$ metres.

6.3.4 Boundary Conditions

A schematic of the boundary conditions for the free-disc flow is shown in Figure 6.1.

Axis of Symmetry

The radial (U) and tangential (W) velocity were set to zero on the boundary nodes (in both the main grid and the subgrid) and zero gradient conditions were applied for the wall-normal (axial) velocity, V, turbulent kinetic energy, k, dissipation rate, ε, and temperature, T.

Entrainment Boundary

For the entrainment boundary condition at the northern edge of the flow domain, shown in Figure 6.1, different constraints were applied depending upon the local flow direction. If the flow was entering the domain, k and ε were given small but finite values[2], the radial and tangential velocity were set to zero and the temperature of the flow entering the domain was set to the "ambient" temperature (defined as $T_{amb} = 0$ in the present work). If fluid was leaving through the entrainment boundary then zero-gradient conditions were applied for U, W, k, ε and T. Irrespective of the flow direction, the pressure at the node just inside the entrainment boundary was set to zero and the axial velocity on the boundary of the domain, V_N, was set equal to the neighbouring nodal value.

Circumferential Exit Plane

Although in theory the flow through the east face of the domain should be leaving the domain, during the iteration process flow may enter or leave through the boundary. For this reason the entrainment conditions described above were also used for the circumferential exit plane. The only difference here was that the radial velocity specified on the boundary was determined from:

$$\frac{\partial (rU)}{\partial r} = 0 \tag{6.1}$$

This condition is used so that continuity is satisfied within the cells adjacent to the exit plane.

6.3.5 Initial Turbulence Levels

In order to obtain turbulent flow predictions for the spinning free-disc in a quiescent atmosphere, in which the ambient turbulence levels are practically zero, one must start the calculation from an initially turbulent flow field. If the flow field is initialized with zero turbulence levels then, since turbulence energy does not enter the flow domain through the boundaries of the domain, the flow will remain laminar no matter how high the rotational Reynolds number. Clearly one would like to obtain results that are independent of the chosen initial turbulence levels i.e. one should not obtain a multitude of

[2]Incoming flow turbulence levels were $k = 0.01V_N^2$ and $\varepsilon = \rho c_\mu (k^*)^2 / (0.01\mu)$, where V_N is the axial velocity through the boundary.

fully-converged solutions depending upon the point from which the calculation was started. However, in the present study it was found that the location of the transition from laminar to turbulent flow over the free-disc (or its disappearance altogether) can indeed be affected by the initial turbulence field used in the numerical simulation unless certain precautions are taken. Using these simple precautions, the same location of transition can be calculated, independent of the turbulence initialization.

Morse [126], studied the flow over a spinning disc using two low-Reynolds-number $k-\varepsilon$ models with a parabolic solver and found that an *ad hoc* artificial turbulence viscosity input was required to prevent laminarization of the boundary layer. Morse commented that this was necessary since "it is difficult to effect the transition to turbulent flow with the computation started from reasonable levels of turbulent kinetic energy". Owen & Wilson [112] also mention briefly that the performance of the Morse model and the Launder & Sharma model is sensitive to the initial turbulence field. Kiliç [128] studied the spinning disc flow using the same turbulence models as Morse, with a multigrid solver (in which the turbulence parameters were only solved on the finest mesh) adopting the following initial turbulence levels[3]:

$$k = 10^{-6}\,(\Omega r)^2 \tag{6.2}$$

$$\mu_t = 0.09\mu \tag{6.3}$$

$$\varepsilon = 0.01\rho\frac{k^2}{\mu} \tag{6.4}$$

In contrast to the earlier studies, Kiliç reported that this initial turbulence field was sufficient to cause transition without the need for an artificial production of kinetic energy input.

The following sections describe the initialization of the dynamic field used with low-Reynolds-number models, standard wall functions and the UMIST-*N* wall function.

Low-Reynolds-Number Model

Tests with the low-Reynolds-number models showed that with different starting conditions for k and ε (or μ_t) not only could the flow revert fully to laminar, but that the radial location of transition could be shifted according to the initial turbulence levels chosen. Furthermore, an increase in the under-relaxation moved the transition point to higher rotational Reynolds numbers (i.e. radially outward), particularly for lower initial values of k and μ_t. Table 6.3 shows a matrix with different initial conditions for k on the x-axis and different initial conditions for μ_t on the y-axis. The cells in the table indicate whether the calculation was stable starting from the specified turbulence levels, and if so, a description of the flow: whether the boundary layer was completely laminar or, if transition from laminar to turbulent flow occurred, its location given by the rotational Reynolds number $\left(Re_\phi = \Omega r^2/\nu\right)$. Initial ε values for each entry can be calculated from $\varepsilon = \rho c_\mu k^2/\mu_t$. The calculations described in the Table 6.3 were all obtained using the Launder & Sharma $k-\varepsilon$ model with power-law

[3]There may be an internal inconsistency in Kiliç's values, since typically one would set the levels of two of the variables: k, μ_t and ε, and obtain the third parameter from the definition of the eddy-viscosity, $\mu_t = \rho c_\mu k^2/\varepsilon$. If one accepts the value Kiliç quotes for ε and takes the value of $c_\mu = 0.09$, the initial eddy-viscosity would be $\mu_t = 9\mu$.

differencing (PLDS [74]) for the convective fluxes of momentum and turbulence parameters, and the under-relaxation factors[4] given in Table 6.1.

	$k = 10^{-5}(\Omega r_b)^2$	$k = 10^{-4}(\Omega r_b)^2$	$k = 10^{-3}(\Omega r_b)^2$
$\mu_t = 10\mu$	marginally stable laminar	stable $Re_\phi \approx 4.8 \times 10^5$	stable $Re_\phi \approx 1.0 \times 10^6$
$\mu_t = 100\mu$	marginally stable mostly laminar	stable $Re_\phi \approx 1.3 \times 10^5$	stable $Re_\phi \approx 1.3 \times 10^5$
$\mu_t = 400\mu$	unstable	marginally stable $Re_\phi \approx 1.3 \times 10^5$	stable $Re_\phi \approx 1.3 \times 10^5$

Table 6.3: Predicted transition locations using the low-*Re* Launder & Sharma $k-\varepsilon$ model with different initial turbulence levels

A comparison of the predicted Nusselt number for four of the cases given in Table 6.3 is presented in Figure 6.15. The strong dependence upon the initial turbulence level and the degree of under-relaxation was traced to the initially large magnitude of the near-wall turbulence damping terms and the relatively slow development of the boundary layer with low-*Re* models. In the very first iteration of the numerical simulation, the wall has tangential velocity (Ωr) whilst the neighbouring fluid elements have zero velocity. The large initial near-wall velocity gradient $(\partial W/\partial y)$ led to appreciable damping of the turbulence by the gradient production, $P_{\varepsilon 3}$, in the $\tilde{\varepsilon}$-equation[5]. In cases with low initial turbulence levels, the near-wall turbulence was heavily damped in the initial stages of the calculation and the turbulence level elsewhere had decayed to such an extent that by the time that the boundary layer had developed the whole flow became laminar. If the update of the momentum equations was slowed by increasing the level of under-relaxation, the turbulence had a proportionally greater time to dissipate before the boundary layer developed, and so one saw that the location of transition moved progressively downstream as the level of under-relaxation increased. In contrast to cases of bypass transition, where diffusion of turbulent kinetic energy into the boundary layer from the main flow is responsible for transition, in the free-disc flow the level of turbulence in the surrounding region is zero and so, no matter how long the calculation is run, once the boundary layer has fully laminarized it will never become turbulent[6].

If high initial values of k and μ_t were specified, the turbulence level still decayed as the calculation progressed, but μ_t was sufficiently large by the time that the boundary layer had developed that there

[4]Lower under-relaxation factors were required with $k = 10^{-5}(\Omega r_b)^2$ to obtain converged results ($\alpha_{U,V,W} = 0.1$ and $\alpha_P = 0.2$).

[5]The behaviour of the numerical simulation in the first few iterations is highly complex with large velocity gradients driving both production and destruction terms in the turbulence field. The gradient production term has been singled out here as this term was found to be of particularly large magnitude initially and, as will be discussed with the UMIST-*N* wall function, a temporary switch to remove or clip $P_{\varepsilon 3}$ in the early stages of a calculation was found to lead to a turbulent boundary layer developing with transition in the correct location. This could, however, be attributed to the temporary removal of a turbulence sink, and it may be that a similar outcome could be obtained by reducing other turbulent kinetic energy sink terms.

[6]Once k has fallen to zero, or been clipped to a very small but positive value, the eddy-viscosity, $\mu_t = c_\mu f_\mu k^2/\tilde{\varepsilon}$, is also practically zero, so that no matter how large the strain-rates, the production of turbulent kinetic energy, $P_k = \mu_t S_{ij}\partial U_i/\partial x_j$, is never sufficiently large to increase the turbulence level.

was sufficient production of kinetic energy to sustain the turbulence. The fully turbulent boundary layer then decayed to a laminar boundary layer in regions of low strain-rate, near the axis of the disc. Whilst this approach of specifying a high level of initial turbulence solved the laminarization problem, it was at the expense of the computational time, since one was starting from an initially unrealistic turbulence field.

The alternative to specifying a high initial turbulence field to correctly capture transition was to initialize the dynamic field so that the boundary layer had already partially developed before turbulence parameters were evaluated. The near-wall velocity gradient was then of more moderate magnitude, so that the initial values of the near-wall turbulence damping terms were reasonable. The boundary layer also extended further into the flow domain, so that production of turbulent kinetic energy was not restricted to such a thin layer adjacent to the wall. To initialize the dynamic field, the momentum and pressure-correction equations were solved with frozen μ_t for the first 1000 iterations (approximately 5% of the total number of iterations required for the calculation to converge) before calculation of k and $\tilde{\varepsilon}$ commenced. Using initial turbulence levels of $k = 10^{-5}(\Omega r_b)^2$ and $\mu_t = 10\mu$, which had previously led to a totally laminar boundary layer (see Table 6.3 and Figure 6.15), transition was predicted at precisely the location previously obtained when a much greater initial level of turbulence was specified $\left(Re_\phi \approx 1.3 \times 10^5\right)$. In fact, by initializing the dynamic field using a frozen μ_t before starting to solve for k and $\tilde{\varepsilon}$, the same transition location was predicted, independent of the initial turbulence level or the degree of under-relaxation. This, perhaps, explains the previous findings of Kiliç [128] who studied the spinning disc flow using a multigrid solver, in which the turbulence parameters were only solved on the finest grid. Kiliç did not report any problems obtaining transition to turbulence, unlike previous authors. In effect, the multigrid method initialized the dynamic field before starting to solve for the turbulence parameters.

"Standard" Wall Functions

The simplified Chieng & Launder (SCL) and the Chieng & Launder (CL) wall functions both predicted transition whilst the TEAM wall function treated the boundary layer as fully-turbulent across the whole of the disc. The location of transition with the SCL and CL wall functions was shifted according to the initial turbulence levels specified. Figure 6.16 shows Nusselt number predictions from using two different initial turbulence levels for the SCL and CL wall functions respectively. The initial turbulent kinetic energy level in all cases was $k = 10^{-5}(\Omega r_b)^2$ with the solid lines representing an initial eddy-viscosity $\mu_t = 10\mu$ and dashed lines $\mu_t = 400\mu$.

Figure 6.16 shows that different initialization of the flow field can lead to different predicted transition locations. There are also "spikes" in the Nusselt number predictions with both wall functions near to transition. These spikes were due to the switch within the wall functions which stated that if $y^+ > 11.6$ at the near-wall node, turbulent boundary conditions applied, otherwise the flow was assumed to be laminar. Figure 6.17 shows that changing the level of under-relaxation has a small but measurable effect on the predicted Nusselt number when using the Chieng & Launder wall function.

The approach described above for low-*Re* model calculations to obtain results independent of initial turbulence levels is unlikely to work with standard wall functions. The problems with low-*Re* models are related to the over-damping of turbulence in the initial stages of a calculation when there are very large strain-rates near the wall. Standard wall functions do not include low-Reynolds-number damping terms and hence are not affected in this way. One could investigate using the wall shear stress instead of $k^{1/2}$ as the scaling parameter in the friction velocity, U_τ, used by the wall functions. This may solve the immediate problem of the standard wall functions switching between linear and logarithmic velocity profiles when k falls below a certain level, but in flows involving separation or reattachment the wall shear stress vanishes and one is forced to use $k^{1/2}$ in U_τ.

UMIST-*N* Wall Function

The UMIST-*N* wall function required some attention in order to obtain transition to turbulence that was independent of the specified initial turbulence level. Without any special treatment, solving momentum and turbulence parameters from the start of the calculation, and initializing both the main-grid and the subgrid with a moderate turbulence level (say, $k = 10^{-5}(\Omega r)^2$ and $\mu_t = 10\mu$), the calculation diverged after approximately 100 iterations. The instabilities stemmed from the wall shear stress changing sign, a consequence of the tangential velocity at the near-wall node becoming greater than that at the wall. This was traced to the initial viscosity profile adopted across the subgrid which, during the first few iterations, led to a rapid change in tangential velocity across the wall-adjacent subgrid cell. The large strain-rate across the wall-adjacent subgrid cells led to a very large tangential wall shear stress, $\tau_{wall,\phi}$, and gradient production source term, $P_{\varepsilon 3}$. The overly large $\tau_{wall,\phi}$ caused the main-grid tangential velocity to exceed the wall velocity whilst the subgrid-averaged source term $\overline{P_{\varepsilon 3}}$ was sufficient to suppress the turbulence in the near-wall cell, leading in some cases to laminarization of the boundary layer.

To initialize the subgrid such that predictions were independent of the initial turbulence level, the following steps were taken:

- The main-grid and subgrid velocity fields were initially zero.
- The main-grid and subgrid were initialized with a specified level of turbulence (any of the values given in Table 6.3).
- The value of $\overline{P_{\varepsilon 3}}$ obtained from the first subgrid iteration was set to zero.
- A constant value of μ_t was assumed across all of the subgrid cells (calculated from the initial turbulence level and $\mu_t = \rho c_\mu k^2/\varepsilon$) except for two wall-adjacent subgrid cells in which the subgrid eddy-viscosity was reduced to approximately $\mu_t \approx \mu$ (the solution was insensitive to the actual value, as long as it was in the range $0.5\mu < \mu_t < 3\mu$). This condition was only applied for the first iteration, after which μ_t was calculated from $\mu_t = \rho f_\mu c_\mu k^2/\tilde{\varepsilon}$ as usual[7].

[7]The relation $\mu_t = 0.09k^2/\varepsilon$ did not hold within the two wall-adjacent subgrid cells since initial values for μ_t were

6.3.6 Differential Length-Scale Correction

In tests with the free-disc flow, it was found that the original differential Yap correction developed by Iacovides & Raisee [66], given by Equation (2.17) with constant $c_w = 0.83$, introduced numerical instability arising from a significant turbulent length-scale gradient at the edge of the turbulent boundary layer. This was despite the actual turbulence level being practically zero in this region. Figure 6.18 shows contours of the turbulent length scale gradient $\left(\left|\partial l/\partial x_j\right|\right)$ for the free-disc flow. Near the axis of the disc the flow is laminar; at a radius of approximately $r/D = 0.12$ transition occurs and thereafter one can see in Figure 6.18 the radial growth of the turbulent boundary layer. At the edge of the turbulent boundary layer there are large turbulent length scale gradients related to the difference between the value of the length scale at one node inside the boundary layer and the length scale at the neighbouring node in which the value of k was clipped to a very small but finite value (10^{-15}). Clipping was applied after each successive iteration of the k-equation such that the minimum value of k was 10^{-15}. If this clipping was not applied, small negative values of k could arise during the iteration process, especially in regions where k was naturally very small (i.e. outside the turbulent boundary layer). Additionally, zero values of k introduce singularities into the $\tilde{\varepsilon}$-equation source terms which involve the ratio $\tilde{\varepsilon}/k$. Figure 6.19 shows the magnitude of the differential Yap correction, Y_{dc}, based on the length-scale gradient shown in Figure 6.18. Numerical instability was caused by the significant correction to the $\tilde{\varepsilon}$-equation (with $Y_{dc} \approx 10^7$) at the edge of the turbulent boundary layer.

The Iacovides & Raisee turbulent length scale correction was later modified by Craft *et al.* [67], who introduced a variable c_w term (see Equation 2.20) to reduce the degree of correction in regions of high straining. This correction improved the numerical stability and the resulting Yap correction is shown in Figure 6.20. The differential Yap correction has a small effect on the Nusselt number predictions of the free-disc flow (see Figure 6.21), whereas the "standard" Yap correction returns results practically identical to those obtained using the same model without the Yap correction.

In addition to the above comments on the need for the Craft *et al*. modifications, it was found necessary to activate the differential length-scale correction only once the calculated flow field had settled down and the boundary layer had partially developed. Introducing the differential Yap correction at the start of a calculation led to divergence due to fluctuations in the turbulence length scale.

6.3.7 Code Validation

To show that the code used in the present study produced the correct behaviour in the laminar region of the free-disc flow, the flow up to a rotational Reynolds number of $100,000$ was studied using the same low-Reynolds-number model employed in turbulent flow calculations. Following a similar study undertaken by Kiliç [128], the height of the domain was set to $0.03D$ (where D is the disc diameter) which corresponded to at least three times the boundary layer thickness predicted by Cochran's numerical solution of von Kármán's equations for laminar flow over the free-disc [131]. Calculations

specified in addition to values of k and $\tilde{\varepsilon}$.

were performed on a 60×60 grid (shown in Figure 6.22) with the Launder & Sharma $k-\varepsilon$ model [13].

Figure 6.23 shows the three velocity components in dimensionless form, as suggested by von Kármán [129], compared to the similarity solutions of Owen & Rogers [132]. Symbols show the result of overlaying the predicted velocity at three different Reynolds numbers, $Re_\phi = 9000$, 25000 and 49000. The three results at different Reynolds numbers are indistinguishable and show excellent agreement with the calculations of Owen & Rogers. The predicted moment coefficient, c_m, defined as the dimensionless integral moment on the disc ($c_m = M/0.5\rho\Omega^2 r^5$, where $M = -2\pi \int_0^r r^2 \tau_\phi \mathrm{d}r$), is shown in Figure 6.24. At the outer edge of the disc, the low-*Re* model agreed with Cochran's [131] solution for c_m to within 6 significant figures. However, there is a greater discrepancy between the present predictions and Cochran's values as one approaches the axis of the disc where, at $Re_\phi = 6000$, there is a difference of 15%. This discrepancy may simply be due to any errors in the numerical integration used to calculate the moment coefficient increasing as the radial width of the cell, Δr, increases relative to the radial position, r. These results were considered to show satisfactory validation of the numerical code performance, at least at low Reynolds number.

6.4 Calculated Flow Results

6.4.1 Linear $k-\varepsilon$ Model

Figures 6.25 – 6.28 compare the radial and tangential velocity profiles obtained using the three standard wall functions and the new UMIST-*N* wall function at three radial positions with results obtained from the low-Reynolds-number Launder & Sharma model and the experimental velocity measurements by Cham & Head [116]. In these figures, the distance from the wall, y, is non-dimensionalized with the momentum thickness, $\theta = \int_0^\infty |W/\Omega r\,(1 - W/\Omega r)|\,\mathrm{d}y$. Semi-logarithmic plots of the dimensionless radial and tangential velocity[8], U^* and W^*, are also shown for the different wall functions and compared to the low-*Re* predictions and the "universal" log-law in Figures 6.29 – 6.32. Radial and tangential wall shear stress predictions for the four different wall functions are presented in Figures 6.33 – 6.40, where results using four different main-grid arrangements are compared to low-*Re* model predictions. Similarly, integral and local values of the Nusselt number are presented for the different wall treatments and grid arrangements in Figures 6.41 – 6.49. Although integral Nusselt number comparisons are informative, since experimental data is available (Cobb & Saunders [130]), the integral Nusselt number involves averaging the heat transfer across the whole of the disc and therefore the transition from laminar to turbulent flow is indistinct. To enable a closer examination of transition, plots of the local Nusselt number are also provided. Finally, the y^+ values for the different main-grid arrangements are shown in Figures 6.50 – 6.53.

All of the wall functions show good agreement with the low-*Re* tangential velocity profiles as one

[8]The superscript $*$ refers to the velocity scaling used by Chieng & Launder [49], where $U^* = k^{1/2}U/\left(\tau_{wall,r}/\rho\right)$ and $y^* = k^{1/2}y/\nu$ (i.e. $U^+ = c_\mu^{1/4}U^*$ and $y^+ = c_\mu^{1/4}y^*$) and the local value of k is used, not the value at the near-wall node.

might expect, since the tangential velocity exhibits a log-law profile in the fully-turbulent inner-region of the boundary layer. The radial velocity is under-predicted by both the SCL and the CL treatments (Figures 6.26 and 6.27) but the TEAM wall function, which assumes a fully-turbulent boundary layer across the whole of the disc, shows surprisingly good agreement with the radial velocity predicted by the low-*Re* model (Figure 6.25). However, Figures 6.29, 6.30 and 6.31 show that the logarithmic profile is clearly inapplicable for the radial velocity. Similarly, the wall shear stress predicted by the standard wall functions (Figures 6.33 – 6.38) shows good agreement with the low-*Re* model in the tangential direction but poor agreement with the radial wall shear stress. Here, the use of the log-law to prescribe the radial velocity results in the underprediction of the low-*Re* model radial wall shear stress by up to 50%. Moreover, the TEAM, SCL and CL wall functions all exhibit a strong sensitivity in the predicted radial wall shear stress to the size of the near-wall cell (as indicated by the grid size in Figures 6.34, 6.36 and 6.38).

The predicted velocity using the UMIST-*N* wall function shows excellent agreement with the low-*Re* model results on both linear and semi-log axes (Figures 6.28 and 6.32 respectively). The velocity predictions also show good agreement with the experimental profiles although the near-wall peak in the radial velocity is under-predicted slightly at $Re_\phi = 1 \times 10^6$ and $Re_\phi = 2 \times 10^6$. The main-grid values of the tangential velocity, W^*, are slightly higher than the low-*Re* model predictions shown in Figure 6.32. This may be due to the linear interpolation used to define the boundary conditions at the outer edge of the subgrid. A similar small discrepancy in the log-law was found in the fully-developed channel flow between the near-wall main-grid nodal values and the low-*Re* result. In contrast to the standard wall function predictions, the wall shear stress in both the radial and tangential directions predicted by the UMIST-*N* wall function is in good agreement with the low-*Re* model predictions (Figures 6.39 and 6.40). The UMIST-*N* results also show far less sensitivity to the size of the near-wall cell than the other wall functions. The coarsest main-grid mesh with 22×120 cells gave somewhat lower tangential wall shear stress and slightly higher radial wall shear stress than that predicted by the low-*Re* model and the other UMIST-*N* wall-function grids. The number of subgrid nodes across the wall-adjacent control volume with the 22×120 grid was sufficient to give results independent of the subgrid node density and therefore the disparity between this result and the other UMIST-*N* wall function results must be due to the relative coarseness of the main-grid. In fact, as shown in Figure 6.53, the maximum y^+ with the 22×120 grid was over 300, which is more than three times the recommended maximum cell size suggested by Morse [124] and Virr *et al*. [121] for the spinning free-disc flow.

At rotational Reynolds number, Re_ϕ, above $20,000$ the predicted local Nusselt number using the TEAM wall function (Figure 6.42) increases linearly with rotational Reynolds number and misses altogether the transition from laminar to turbulent flow predicted by the low-Reynolds-number model and observed experimentally. The TEAM wall function exhibits little dependence upon the size of the near-wall cell at high-Re_ϕ. However, at low rotational Reynolds number ($Re_\phi < 20000$) the predicted Nusselt number is sensitive to the grid size, as shown by the integral Nusselt number plot (Figure

6.41). Near the axis of the disc, at low-Re_ϕ, the wall-adjacent node is located within the viscous sublayer and hence a linear velocity profile is assumed. However, since the wall-function grid does not contain sufficient nodes to resolve the near-wall flow, the solution is grid-dependent. The Nusselt number predicted with the SCL and CL wall functions is even more sensitive to the size of the near-wall cell (Figures 6.43 and 6.45). Additionally, the SCL and CL treatments produced spikes in the local Nu profile near transition due to the switch used to select laminar or turbulent wall functions at a specified y^+. As previously noted (see Section 6.3.5) these results are dependent upon the initial turbulence levels chosen.

The UMIST-*N* wall function shows good overall agreement with the low-*Re* Nusselt number (Figures 6.47 and 6.48). The slope of the Nu profile in the laminar and turbulent regions of the flow are close to those observed with the low-*Re* model but there is some sensitivity to the size of the near-wall cell in the predicted transition location. Using different near-wall cell sizes corresponding to maximum y^+ between 70 and 310, the transition point varied from $Re_\phi \approx 0.7 \times 10^5$ to $Re_\phi \approx 2.1 \times 10^5$, whereas the low-*Re* model predicted transition at $Re_\phi \approx 1.2 \times 10^5$. Although this feature is undesirable, it is not entirely surprising since it is well known that the correct prediction of transition is highly sensitive to the numerical scheme. It was shown earlier that transition is sensitive to radial grid density and the use of logarithmic coordinates in Figures 6.47 and 6.48 also magnifies any small differences in the location of transition. The same results to those shown in Figure 6.48 are plotted on linear axes in Figure 6.49 which shows that the local Nusselt number predicted using the coarsest main-grid mesh of 22×120 cells is somewhat lower than that predicted by the finer grids, a consequence of the poor resolution of the flow with so few main-grid nodes.

6.4.2 NLEVM

Figure 6.54 compares the predicted integral and local Nusselt number for the free-disc flow using the low-Reynolds-number linear and non-linear $k-\varepsilon$ models. There is little difference in the heat transfer predictions between the two models with the exception that the NLEVM delays slightly the onset of transition compared to the linear model, from $Re_\phi = 115,000$ to $150,000$. The similarity between the two different models is not entirely unexpected, since the additional terms in the NLEVM are primarily effective in cases of separation and impingement (features which are absent from the spinning free-disc flow). Radial and tangential velocity profiles for the linear and non-linear models are shown in Figure 6.55 and semi-logarithmic U^* and W^* profiles are shown in Figure 6.56. In each case, profiles are shown for three radial positions, corresponding to the rotational Reynolds numbers at which Cham & Head [116] obtained experimental velocity measurements. The two models are practically indistinguishable on the linear axes velocity plots whilst the NLEVM predicts a slightly higher value of U^* and W^* in the fully-turbulent region ($20 \leq y^* \leq 200$). This latter effect was due to a difference in the near-wall turbulent kinetic energy profile predicted by the two models. Figures 6.57 and 6.58 compare normal and shear Reynolds stress profiles at three different rotational Reynolds numbers obtained using the low-*Re* linear $k-\varepsilon$ model and the NLEVM (unfortunately no experimental

data has been found with which comparisons can be drawn). As expected, the linear model produces an isotropic stress field ($\overline{u^2} \approx \overline{v^2} \approx \overline{w^2}$) whilst, with the NLEVM, the tangential component of the normal stress $\left(\overline{w^2}\right)$ is significantly higher than the axial and radial components ($\overline{u^2}$ and $\overline{v^2}$). The shear stresses in planes normal to the wall ($\overline{uv}$ and $\overline{vw}$) are practically identical with the linear and non-linear models. The most striking feature of the Reynolds stress profiles is with the shear stress in the plane parallel to the wall ($\overline{uw}$). The linear $k-\varepsilon$ model predicts this to be practically zero whilst the NLEVM predicts a comparatively large and negative near-wall value that increases towards a positive peak at $y/\theta = 4$ and then decays towards the edge of the boundary layer. In a linear model, the $\overline{uw}$ shear stress is calculated from:

$$-\rho\overline{uw} = \mu_t r \frac{\partial}{\partial r}\left(\frac{W}{r}\right) = \mu_t\left(\frac{\partial W}{\partial r} - \frac{W}{r}\right) \tag{6.5}$$

The wall velocity is a linear function of the radius (i.e. $W_{wall} = \Omega r$) so near the wall at least one would expect $\partial/\partial r\,(W/r) = 0$. Figure 6.59 shows the velocity profiles at three radial positions, also shown in Figure 6.55, overlaid on the same set of axes. The dimensionless tangential velocity $(W/\Omega r)$ shows little change between a rotational Reynolds number of 3.4×10^5 and 2×10^6. The negligible value of $\overline{uw}$ predicted by the linear model is thus a consequence of the radial gradient of (W/r) being close to zero. The shear stress $\overline{uw}$ is not zero with the non-linear $k-\varepsilon$ model since the stress is also affected by quadratic and cubic functions of strain-rate and vorticity.

Previous studies have shown that the Craft *et al*. two-equation NLEVM can produce unrealizable (negative) axial normal stress, $\overline{v^2}$, in flows where there is a strong swirling component of velocity [133]. In a purely swirling flow, the only velocity gradient is $\partial W/\partial r$ and hence the only finite vorticity component is $\Omega_{13} = -\partial W/\partial r - W/r$. Simplifying the expression for turbulence anisotropy, Equation (2.27), the axial normal stress is given by:

$$\overline{v^2} = \frac{2}{3}k - \frac{2}{3}c_3\frac{\nu_t k}{\tilde{\varepsilon}}\left(\Omega_{13}\right)^2 \tag{6.6}$$

The sign of $\overline{v^2}$ is thus dependent upon the value of the constant c_3 which the Craft *et al*. non-linear $k-\varepsilon$ model takes as $c_3 = 0.26$. Gatski & Speziale [27] recommended that coefficient of the quadratic vorticity term (which, in the Craft *et al*. model corresponds to c_3) should be zero in purely swirling flow. The three-equation $k-\varepsilon-A_2$ model Craft *et al.* [134] used invariants of the strain-rate and vorticity tensors to remove the non-linear contribution to $\overline{v^2}$ in purely swirling flow. The free-disc flow is not a purely swirling flow, having significant velocity gradients in the axial (wall-normal) direction and finite radial velocity. In the present study it was found that, using the Craft *et al.* $k-\varepsilon$ model, the normal stress was positive near the wall, as shown in Figure 6.57. Away from the wall, towards the edge of the turbulent boundary layer, the normal stress decreased to zero and in some cases there were small overshoots with negative normal stress levels of approximately -10^{-14}. Since the gradient of the stress is used in the momentum equations, rather than its actual value, the small negative stresses were inconsequential.

Figures 6.60 – 6.63 compare the predicted velocity using four different wall functions with the

low-*Re* NLEVM results and experimental data from Cham & Head [116]. Semi-logarithmic plots of the dimensionless velocity, U^* and W^*, are shown for the different wall functions and compared to the low-*Re* predictions and the "universal" log-law in Figures 6.64 – 6.67. Predicted integral Nusselt number are also shown for the four different wall functions and compared to the low-*Re* NLEVM result and experimental data from Cobb & Saunders [130] in Figures 6.68 – 6.71. The behaviour of the wall functions with the NLEVM is practically identical to that previously observed with the linear $k-\varepsilon$ model (see above). The UMIST-*N* wall function shows superior performance to the other wall functions in predicting the radial and tangential velocity in the fully-turbulent region of the boundary layer and the location of transition predicted by the UMIST-*N* wall function shows a similar degree of dependence upon the size of the near-wall cell to that exhibited by linear model.

6.5 Computational Costs

Tables 6.4 and 6.5 show comparisons of computing times for the free-disc flow using the linear and non-linear $k-\varepsilon$ turbulence models respectively. In all cases the turbulence field was initialized with $k = 10^{-5}(\Omega r)^2$ and $\mu_t = 10\mu$. Under-relaxation factors used in the low-*Re* and standard wall-function calculations and in the main-grid region of the UMIST-*N* wall-function calculations are those given in Section 6.3.2. The QUICK differencing scheme was used for momentum and temperature equations (except for the wall-adjacent cells) and PLDS was used for all other quantities. Calculations were performed on a single processor of a Silicon Graphics *Origin 2000* with the same levels of compiler optimization in each case. The UMIST-*N* wall function required 30 subgrid cells in order to obtain grid-independence.

Model Tested	No. of Nodes	Time per Iter (*s*)	No. of Iterations	Total CPU Time (*s*)	Relative CPU Time
TEAM WF	120×28	0.07	2009	136	1
Chieng & Launder	120×28	0.07	2208	154	1.1
UMIST-*N*	$120 \times 28(+30)$	0.14	2363	339	2.2
Low-*Re*	120×70	0.20	19928	3996	29.4

Table 6.4: Computing times for the free-disc ($Re = 3.3 \times 10^6$) with the linear $k-\varepsilon$ model

Model Tested	No. of Nodes	Time per Iter (*s*)	No. of Iterations	Total CPU Time (*s*)	Relative CPU Time
TEAM WF	120×28	0.11	3917	410	1
Chieng & Launder	120×28	0.10	4181	415	1.0
UMIST-*N*	$120 \times 28(+30)$	0.19	3623	692	1.7
Low-*Re*	120×70	0.25	21390	5272	12.9

Table 6.5: Computing times for the free-disc ($Re = 3.3 \times 10^6$) with the non-linear $k-\varepsilon$ model

In the previous study of an impinging jet using different wall treatments (Chapter 5), the UMIST-*N*

wall function was up to 60% slower than the Chieng & Launder wall function and about 8 times faster than a low-Reynolds-number model. In the present study, with the linear $k-\varepsilon$ model, the UMIST-*N* wall function takes twice as long as a standard wall function but is more than 13 times faster than the low-*Re* model. Using the NLEVM, the difference is slightly less with the UMIST-*N* wall function taking 70% more computing time than the Chieng & Launder wall function but only one eighth of that of the low-Reynolds-number model.

There are several factors which increase the relative computing times for the free-disc flow. Firstly, there are two wall-parallel velocity components in the free-disc flow, whereas the axisymmetric impinging jet tested previously did not have a swirling velocity component. The swirling and radial components of velocity are also strongly coupled in the free-disc flow through the source terms appearing in the U and W momentum equations. The number of nodes in the wall-parallel direction used in the present calculations exceeds that used in the earlier study and if one multiplies the number of transport equations solved per-node by the number of nodes for the impinging jet and the free-disc, one finds that in the impinging jet the number of calculations performed in a low-*Re* iteration was twice that of the standard wall functions whilst in the free-disc the corresponding ratio was 2.5.

6.6 Discussion & Conclusions

It has been shown that “standard” wall-functions have a number of shortcomings in predicting the free-disc flow. The “universal” log-law adequately approximates the near-wall tangential velocity profile but is inappropriate for the radial velocity. Moreover, standard wall functions are unable to account correctly for transition from laminar to turbulent flow. It has been demonstrated that new UMIST-*N* wall-function treatment, based on the integration of simplified transport equations across a near-wall subgrid, is able to capture the skewing of the velocity profile in the near-wall region and shows excellent agreement with velocity predictions obtained using low-Reynolds-number treatments. Nusselt number predictions using the UMIST-*N* wall function are also in good agreement with those of low-*Re* models in contrast to the other standard wall functions tested. The location of transition from laminar to turbulent flow predicted by the UMIST-*N* wall function showed some sensitivity to the size of the near-wall control volume although the results were close to those obtained with low-*Re* models. The UMIST-*N* wall function calculation was also between 8 and 13 times faster than the corresponding low-Reynolds-number calculation in the free-disc flow, similar to the savings observed previously in an impinging jet flow.

The linear $k-\varepsilon$ model of Launder & Sharma [13] and the non-linear $k-\varepsilon$ model of Craft *et al*. [67] were both tested. Results with the two models were broadly similar except for a slight delay in transition with the NLEVM and some differences with the stress profiles. It was found that the more recent Craft *et al*. [67] version of the differential length scale correction was necessary in the free-disc flow calculations to prevent numerical instability arising from significant turbulence length scale gradients at the outer edge of the turbulent boundary layer.

During the course of the present study, some interesting features relating to the initialization of free-disc flow calculations were investigated. "Natural" transition was obtained in the computational model by initializing the flow domain with a uniform level of turbulence; as the calculation progressed, turbulence decayed in regions of low strain-rate leaving a laminar boundary layer near the axis of the disc whilst at higher rotational Reynolds number the boundary layer remained turbulent. However, it was found that the onset of transition from laminar to turbulent flow could be shifted by starting the calculation from a different "guessed" turbulence level. One could even completely laminarize the boundary layer by starting a low-*Re* calculation with relatively low, but finite turbulence levels ($\mu_t = 10\mu$ and $k = 10^{-5}\left(\Omega r_b\right)^2$). This sensitivity to the initial turbulence level was traced to the near-wall turbulence damping terms which, during the initial stages of the calculation, were of considerable magnitude due to the large velocity gradient between the spinning wall and nearby cells. It was found that by freezing the eddy-viscosity and solving initially only the mean-flow equations (i.e. momentum equations and pressure-correction) before commencing the solution of the turbulence parameters, one could obtain low-*Re* model predictions that were independent of the initial turbulence levels. This finding was used retrospectively to explain previous studies of the free-disc flow where, for example, Kiliç [128] was able to capture natural transition (by using a multigrid solver where k and ε were only solved on the finest grid) whilst Morse [126] was forced to apply an *ad hoc* correction to the eddy-viscosity in order to obtain transition.

Chapter 7

Ahmed Body Flow

7.1 Introduction

The "Ahmed" body, shown in Figure 7.1, has the form of a highly simplified car, consisting of a blunt nose with rounded edges fixed onto a box-like middle section and a rear end that has an upper slanted surface (like a "hatch-back" car), the angle of which can be varied. The model is supported on circular-sectioned legs or stilts, rather than wheels. Despite neglecting a number of features of a real car (rotating wheels, rough underside, surface projections etc.) the Ahmed body generates the essential features of flow around a car, namely: flow impingement and displacement around the nose, relatively uniform flow around the middle and flow separation and wake generation at the rear.

The principal aim of studying such a simplified car body is to understand the flow processes involved in drag production. Through understanding the mechanisms involved in generating drag one should be able to design a car to minimize drag and therefore minimize fuel consumption and maximize performance.

The principal contribution to drag experienced by a car is pressure drag. The rear of the vehicle provides the major contribution to pressure drag and, in particular, the angle of the rear slant is critical in determining the mode of the wake flow and hence the drag experienced by the vehicle. Janssen & Hucho [135] found that the maximum drag was obtained for a vehicle with rear slant angle $\beta \approx 30^\circ$ (to the horizontal) where the flow over the slant remained partially attached and longitudinal trailing vortices were formed at the edges of the slant. For steeper slant angles ($\beta > 30^\circ$) the flow over the rear slant became fully-separated and the drag decreased.

7.2 Previous Experimental and Computational Studies

In the original experiments undertaken by Ahmed [136] and Ahmed *et al*. [137], the angle of the rear slant was varied from $\beta = 0^\circ$ to 40°. Visualization techniques were employed to examine the structure of the wake and time-averaged velocity measurements were made on the centreline plane and at transverse planes in the wake. Measurements of the total drag were made at 5° intervals for

slant angles from $\beta = 0^\circ$ to 40°. The total drag was observed to fall from $\beta = 0^\circ$ to 15° and then rise to a maximum at 30°, followed by a sudden decrease, thereafter remaining almost constant between 30° and 40° (see Figure 7.2). A breakdown of the relative contributions to drag from pressure on the nose, base[1] and slant was taken at $\beta = 5^\circ$, 12.5°, 30° (high drag) and 30° (low drag). A vertical splitter plate in the symmetry plane was used in the wake of the 30° slant to encourage the low-drag flow. This indicates that some unsteadiness in the wake may have been instrumental in maintaining the high-drag 30° slant flow.

A physical description of the flow structure over the rear of the Ahmed body was presented in some detail in the Ahmed papers and also in the more recent experiments undertaken by Lienhart *et al*. [138] and Spohn & Gilliéron [139]. Figures 7.3 and 7.4 show sketches of the time-averaged wake structure taken from the Ahmed *et al*. paper for the low drag $\beta \approx 20^\circ$ and high drag $\beta = 30^\circ$ configurations, Figure 7.5 shows oil/soot streakflow visualization of the 25° and 35° slants from Lienhart *et al*. and Figure 7.6 shows a diagrammatic representation of the wake over the 25° rear slant taken from Spohn and Gilliéron. The low-drag configuration of the Ahmed body, with a rear-slant angle of approximately 20°, is characterized by longitudinal vortices which originate along the edges between the side and the rear slant surfaces (vortex *C* in the Ahmed Figure 7.3). The formation of these side-edge vortices is similar to that observed for low aspect-ratio wings where the high pressure on the underside of the wing and low pressure above the wing forces fluid to flow around the edges of the wing-tips. In the case of the Ahmed body, the fast moving air around the side of the body is pulled into a low-pressure region just above the rear slant near the side edge and, in doing so, the flow curls over to create a vortex which has its axis roughly aligned to the slant edge. Tucked just underneath the large side-edge vortex is a smaller vortex which rotates in the opposite direction. The smaller side-edge vortex is shown clearly in the Spohn & Gilliéron diagram (Figure 7.6) and the attachment line which occurs on the surface of the slant between the large and the small side-edge vortices can be seen on the Ahmed diagram (Figure 7.3). The flow over the 20° slant is fully attached, promoting pressure recovery and low drag. Downstream of the base of the Ahmed body there are two horseshoe vortices (marked as *A* and *B* in Figure 7.3) which interact with the flow leaving the slant, the side-edge vortices and the flow from the underside of the body. As the slant angle is increased from 20° to 30° the strength of the side-edge vortices increases and a separation bubble appears at the leading edge of the slant (where the slant meets the top surface of the Ahmed body). On the 25° rear slant, the oil/soot streakflow shows a separated flow region near the leading edge which reattaches roughly half-way down the slant and remains attached until the edge is reached between the slant and the vertical base. The separation bubble appears to be slightly larger in the diagram of Spohn & Gilliéron for the 25° slant which may be a consequence of the lower Reynolds number used in their experiments ($Re \approx 3 \times 10^4$, compared to the Lienhart *et al*. visualization which was carried out at $Re \approx 9 \times 10^4$) or the lower turbulence level in the boundary layer approaching the slant[2]. Spohn & Gilliéron also noted

[1] "base" refers to the vertical plane surface on the rear of the Ahmed body, below the slant.

[2] Lienhart *et al*. employed a trip on the curved part of the front of the Ahmed body to increase turbulence levels in the boundary layer whereas Spohn & Gilliéron did not use a trip.

that whilst the flow near the leading edge of the slant is steady, the flow closer to the downstream end of the slant is highly unsteady. The low pressure induced by the separation bubble and the strong side-edge vortices lead to a high pressure-drag on the slant surface. The Ahmed figures show the separation bubble increasing in size as the slant angle is increased up to 30°. For the high-drag 30° slant, the bubble (shown as vortex *E* in Figure 7.4) reaches practically to the downstream edge of the rear slant before the boundary-layer reattaches.

For the low-drag configuration for the 30° slant, and at higher slant angles, the separation bubble over the rear slant merges with the upper of the two horseshoe vortices behind the base to create a large recirculation region with weaker side-edge vortices. This is indicated by the oil/soot visualization for the 35° rear slant (Figure 7.5).

A possible explanation for the switch from the high-drag mode at slant angles $20^\circ < \beta < 30^\circ$ to the low-drag mode at slant angles greater than 30° was put forward by Menter at the 2002 ERCOFTAC Workshop on Refined Turbulence Modelling[3]. It was suggested that the size of the high-pressure region (linked to the separation bubble located on the leading edge of the slant) grows as the slant angle is increased from 20° to 30°. At the critical slant angle of 30°, the high-pressure region is sufficiently large that it interferes with the low-pressure zone at the corner between the slant and the side of the Ahmed body. As the strength of this low-pressure zone is reduced so the main driving force behind the creation of the strong side-edge vortices is removed, the vortices become weaker and hence exert a reduced force on the flow over the slant which then becomes fully separated. Additionally, as the slant angle is increased up to the critical angle, the recirculation bubble on the rear slant extends beyond the downstream end of the slant and combines with the upper horseshoe vortex downstream of the base. As one tries to visualize this transition from high- to low-drag modes one should keep in mind that in reality the flow is highly unsteady. This was demonstrated clearly by the large-eddy simulation of flow around the 25° Ahmed body, presented by Hinterberger *et al*. at the 2002 ERCOFTAC workshop, which showed an unsteady wake over the rear slant with eddies that were occasionally becoming detached from the slant surface being convected downstream.

Perhaps the earliest simulation of the Ahmed body flow was undertaken by Han [140] who studied a range of different slant angles using a finite-volume code and standard linear $k-\varepsilon$ model with wall functions. Han found that the drag coefficient for slant angles in the range $0^\circ < \beta < 20^\circ$ were consistently predicted around 30% too high. This was attributed to an overly low pressure on the base of the body. At the critical slant angle of $\beta = 30^\circ$ no separation was predicted over the slant and the steep rise in drag reported by Ahmed for slant angles in the range $25^\circ < \beta < 30^\circ$ was not calculated. Wilcox [14] suggested that the poor predictions obtained by Han were due to the linear

[3]Simulations of flow around the Ahmed body were presented at two ERCOFTAC Workshops on Refined Turbulence Modelling: at Darmstadt, Germany, in 2001, and at Poitiers, France, in 2002. Formal proceedings from the 2001 workshop have not been published although the details of the computational methods used by the participants and cross-plots of the data are available from the workshop coordinator, Dr Jakirlic, on the TU-Darmstadt website: http://www.sla.maschinenbau.tu-darmstadt.de/workshop01.html. At the time of writing, proceedings from the 2002 workshop have also not yet been published formally although it is planned to make the results freely available. Details of the 2002 meeting in Poitiers can be obtained from the workshop coordinator: Dr Manceau, Laboratoire d'études aérodynamiques, University of Poitiers, France.

$k-\varepsilon$ model which is known to perform poorly in flows involving strong adverse pressure gradients. It was suggested that the overly low base pressure was caused by a vortex which was too strong, which was itself the result of an overly large wall shear stress being predicted by the $k-\varepsilon$ model. Robinson [35] noted that there are a number of other considerations which may have influenced Han's results. The linear $k-\varepsilon$ model is well known to overpredict the turbulent kinetic energy at a stagnation point and this may have led to an overly large level of turbulence energy in the boundary layer approaching the slant which would encourage the flow to remain attached. A similar effect may have been obtained from specifying too low a level of dissipation rate or too high a level of turbulent kinetic energy at the inlet (the inlet turbulence levels were not specified in Han's paper). Furthermore, it may have been the simple log-law-based wall function employed by Han that was to blame for the overly large wall shear stress which, following Wilcox's analysis, was responsible for the base pressure being too low. At the 2002 ERCOFTAC workshop, Leschziner presented some preliminary results which indicated that the linear $k-\omega$ model of Wilcox was able to predict correctly the location and size of the separation bubble at the leading edge of the slant for the 25° Ahmed body. This would indicate that a model which responds more accurately to adverse pressure gradients is able to account for the complex behaviour on the rear of the Ahmed body.

Authors	**Turbulence Model**	**Slant Flow Mode**
Guilmineau & Queutey (EC Nantes)	low-*Re* SST $k-\omega$ model	fully separated
Braun, Lanfrit & Cokljat (Fluent)	realizable linear $k-\varepsilon$ SST $k-\omega$ model	fully attached separation bubble
Craft, Gant, Iacovides, Launder & Robinson (UMIST)	linear $k-\varepsilon$ with SCL wall function linear $k-\varepsilon$ with UMIST-*N* wall function realizable linear $k-\varepsilon$ with SCL WF realizable linear $k-\varepsilon$ with UMIST-*A* WF cubic non-linear $k-\varepsilon$ with SCL WF cubic non-linear $k-\varepsilon$ with UMIST-*A* WF	fully attached fully attached fully attached fully attached fully separated fully separated
Durand, Kuntz, Menter (EC Nantes/CFX)	linear $k-\varepsilon$ with scalable wall function low-*Re* SST $k-\omega$ model SSG DSM	fully attached fully separated fully attached
Leonard, Hirsch, Kovalev, Elsden, Hillewaert & Patel (Vrije Universiteit, Brussels/NUMECA)	low-*Re* linear $k-\varepsilon$ (Yang-Shih)	fully attached
Leschziner (Imperial College)	low-*Re* linear $k-\omega$ model	separation bubble

Table 7.1: RANS simulations of the 25° Ahmed body flow contributed to the 2001 and 2002 ERCOFTAC Workshops on Refined Turbulence Modelling.

Table 7.1 lists a number of other recent calculations of the Ahmed body which were submitted to the 2001 and 2002 ERCOFTAC Workshops on Refined Turbulence Modelling. In the final column of the table, a brief indication of the flow regime over the rear slant of the 25° Ahmed body is given. Only two simulations correctly predicted the appearance of a separation bubble at the leading edge of the

25° slant: the SST model results from Fluent[4] and the preliminary $k-\omega$ model results of Leschziner. The Fluent results are, however, somewhat in doubt as two other simulations of the same flow using the same SST model (from EC Nantes and CFX) predicted fully separated flow over the rear slant. This apparent conflict in results may be due to differences in the grid, boundary conditions and convection schemes employed. There is insufficient information provided in the description of the computational methods to come to any firm conclusions. There is agreement amongst the numerous simulations which used a linear $k-\varepsilon$ model that the boundary layer remains fully attached for the entire length of the 25° slant. The actual velocity profiles over the slant differ somewhat between different linear $k-\varepsilon$ model calculations which can be attributed to slight differences in the models (realizable, low-*Re* or with wall functions), grid, boundary conditions and convection schemes. The realizable linear $k-\varepsilon$ model results from UMIST, in particular, showed a tendency towards a separated boundary layer at the downstream edge of the rear slant. Both the UMIST non-linear $k-\varepsilon$ model and the EC-Nantes/CFX SST model predicted fully separated boundary layers over the entire rear slant. Interestingly, both groups also found that running the same calculations again with a lower-order upwind convection scheme caused the flow over the rear slant to become fully attached. This remarkably strong effect of the convection scheme was analyzed in detail by Robinson [35] who concluded that the more diffuse side-edge vortex predicted using the lower-order scheme was able to draw a sufficient amount of fluid out of the boundary-layer on the slant to cause the flow to remain attached. Using a less-diffusive, higher-order convection scheme the side-edge vortex predicted by the non-linear model used by Robinson was insufficiently strong to cause the boundary layer to remain attached.

Hinterberger & Rodi submitted LES results for both the 25° and 35° Ahmed bodies to the 2001 ERCOFTAC workshop using a grid with approximately 8.8 million nodes and, the following year, submitted results using a refined grid of 18.5 million nodes. The results from these huge calculations (the more recent ones taking $30,000$ CPU hours) showed no clear improvement in flow prediction compared to the RANS approaches. The time-averaged boundary-layer over the 25° slant was predicted as predominantly separated, in poor agreement with the experiments, although the Reynolds stress profiles over the rear slant showed better agreement with the experiments than any of the RANS models (indicating that the LES may have captured correctly the level of unsteadiness seen in the experiments). These slightly disappointing results may have been due to an averaging time used to generate the mean-flow data which was relatively low (4.5 non-dimensional time-steps[5]).

The above discussion has concentrated on the prediction of flow in the vicinity of the rear slant as this has the greatest contribution to the overall drag experienced by the Ahmed body. One could also examine the flow in the wake downstream from the body although experience from the workshops has shown that accurate prediction of the trailing vortices in the wake is strongly dependent upon predicting the correct mode of flow over the slant.

[4]Fluent did not state explicitly that they used a low-*Re* modelling approach although they did use 2.3 million cells for the half-body (a mixture of tetrahedral and hexahedral cells). This compares to the calculations presented in this thesis which used $331,000$ cells for the half-body using wall functions.

[5]where one time-step is equivalent to the time taken for a packet of fluid to travel the length of the flow domain, from inlet to outlet.

Suga *et al*. [141] studied a related flow, around the car body of Maeda *et al.* [142], using the low-*Re* Launder-Sharma $k-\varepsilon$ model and the three-equation cubic non-linear $k-\varepsilon-A_2$ model of Craft *et al*. [134]. The Maeda car body features a more rounded front section than the Ahmed body and a rear slant which extends from the top to the bottom surfaces (i.e. the vertical "base" surface which occurs on the rear of the Ahmed body is absent). The pressure coefficient distribution predicted by the $k-\varepsilon-A_2$ model was generally in good agreement with the experimental measurements, although a separation bubble was predicted near the leading edge of the 25° rear slant whereas the experiments suggested that there was almost no separation. The drag coefficient predicted by the linear $k-\varepsilon$ model was too high for all slant angles (25° to 55°) which was attributed to excessive turbulence levels generated around the leading edge of the body. The $k-\varepsilon-A_2$ model predicted more reasonable overall levels of drag coefficient, although the predictions were slightly too high at 25° (due to the separation bubble) and too low at 35° and 55°.

7.3 Computational Details

7.3.1 Models Used

The results from two calculations of the flow around the 25° Ahmed body are documented in this thesis. The first calculation used the standard linear $k-\varepsilon$ model of Launder & Spalding [143] in conjunction with the Simplified Chieng & Launder (SCL) wall function, the second used the same turbulence model with the low-*Re* damping functions of Launder & Sharma [13] and the new numerical wall function (UMIST-*N*). Both calculations employed the standard Yap correction. The UMIST-*N* wall function employed 45 subgrid nodes across the near-wall cell, clustered near the wall using an expansion ratio of 1.09. This gave a maximum $y^+ < 0.1$ for the wall-adjacent subgrid node with a minimum of 10 subgrid nodes within $y^+ \approx 13$ (where $y^+ = c_\mu^{1/4} k^{1/2} y/\nu$). Increasing the number of subgrid nodes to 60 had no visible effect on the results of the simulation. It was originally intended that results would be obtained using the non-linear Craft *et al*. model [30] with the UMIST-*N* wall function, to complement the earlier work of Robinson (who used the Craft *et al*. model with two other wall functions). However, the combination of non-linear model and UMIST-*N* wall function was found to cause numerical instability in the calculations. Some suggestions for the possible causes of the stability problems are discussed in Section 8.3. Further investigation and correction of the stability problems was not possible within the framework of this thesis due to time and funding limitations.

7.3.2 Numerical Methods

The STREAM code, described in Section 3.3, was used to study the Ahmed body flow. Convection of both momentum and turbulence parameters was approximated using the UMIST differencing scheme discussed in Section 3.3.3. The flow was considered as steady and the symmetry plane was used so that a grid was constructed only around half of the body. Calculations were converged until residuals

of the momentum, mass and turbulence equations were all below 5×10^{-6}, approximately an order-of-magnitude lower than that achieved in the previous calculations by Robinson [35] for the Ahmed body flow, which were considered to be fully converged. Under-relaxation factors are shown in Table 7.2.

U	V	W	P	k	ε
0.2	0.2	0.2	0.3	0.1	0.1

Table 7.2: Under-relaxation factors used for the Ahmed body flow.

7.3.3 Domain and Grid

Figures 7.7, 7.8 and 7.9 show the computational grid used to study the flow around the 25° Ahmed body. The grid was identical to that used in a previous study of the Ahmed body by Robinson [35] and employed 22 blocks (shown schematically in Figure 7.10) and approximately 331,000 cells. The legs, or stilts, on which the model was supported in the wind tunnel experiments, were not modelled in the computational grid. The effects of ignoring the stilts on the predicted drag and the flow field are discussed later. The near-wall distribution of cells was arranged to maintain main-grid y^+ values of as many as possible near-wall cells around the body to within the limits $30 < y^+ < 300$ (where $y^+ = c_\mu^{1/4} k^{1/2} y/\nu$), but these limits were exceeded in some regions of stagnation and boundary-layer separation or reattachment. The y^+ values of the near-wall cells adjacent to the ground plane were not controlled since to maintain $y^+ < 300$ would have required high-aspect ratio cells which would have compromised the stability of the calculation. Due to the large number of nodes required to model the Ahmed body, it was not possible to refine the grids and establish grid independence. However, Robinson did examine a coarser grid, with $158,000$ cells, to provide some information regarding grid independence. Using a realizable linear $k-\varepsilon$ model, the flow over the entire 25° rear slant was predicted to be fully attached with the coarse grid. In comparison, flow predictions using the finer ($331,000$ cell) grid showed a greater tendency towards separation of the boundary layer at the trailing edge of the slant. It was suggested that the enhanced "artificial diffusion" induced by the coarse grid helped to maintain attached flow over the rear slant.

7.3.4 Boundary Conditions

The computational domain used to study the Ahmed body flow is shown in Figure 7.11. The Simplified Chieng & Launder (SCL) wall function was always used for the floor boundary whereas around the surface of the Ahmed body either the SCL or the UMIST-*N* wall function were applied. The domain boundary along the centreline of the body (at $y = 0$), the opposite boundary at the outside limit of the domain ($y = 1.044$m) and the upper domain boundary ($z = 1.044$m) were all treated as symmetry planes. Ideally the upper and side domain boundaries would be treated with entrainment conditions.

However, symmetry planes were used instead to provide a more stable calculation and were justifiable as there is little deflection of the flow at these boundaries. The downstream outlet was set with zero-gradient for all variables. Flat profiles (i.e. constant values) of velocity and turbulence parameters were set at the inlet plane, one body-length upstream of the Ahmed body. Values of the inlet streamwise velocity and turbulent kinetic energy were calculated by integrating the U- and k-profiles measured by Lienhart *et al*. across the flow domain at $x = -1.444$m. This resulted in an inlet bulk U-velocity which was lower (38.51ms^{-1}) than the stated experimental bulk U-velocity of 40ms^{-1}. The lower inlet bulk velocity corresponded to an inlet Reynolds number of $Re = 7.57 \times 10^5$ (based on the body's height) which compares to the original Ahmed experimental value of $Re = 1.18 \times 10^6$. The Reynolds number is sufficiently high that this minor adjustment should not have significantly influenced the results. The average inlet turbulent kinetic energy was calculated as $k_{in} = 6.58 \times 10^{-3}\text{m}^2\text{s}^{-2}$ and the inlet dissipation rate was calculated from a viscosity ratio of $\nu_t/\nu = 10$. This viscosity ratio was recommended by Lienhart *et al*. following experimental measurements which estimated the Taylor microscale upstream of the body as $\lambda = 2.6$mm, where the dissipation rate is given by:

$$\varepsilon = \frac{2k}{\lambda^2}\nu \tag{7.1}$$

7.4 Calculated Flow Results

Figures 7.13 and 7.14 show profiles of the streamwise mean U-velocity and RMS u-velocity at six measurement locations on the top surface of central portion of the Ahmed body, approximately midway between the nose and the slant (positions shown in Figure 7.12). There is practically no difference in the results obtained using the SCL and the UMIST-*N* wall functions. The predicted boundary layer thickness is slightly greater than that found in the experiments and the freestream velocity is also slightly higher in the calculations due to the blockage effect of the body and the use of symmetry conditions at the far-field boundaries (the body blocked approximately 5% of the cross-sectional area of the calculation flow domain).

If one examines more closely the near-wall region one can discern differences between the two wall function predictions. Figure 7.15 shows profiles of the mean U-velocity, turbulent kinetic energy and eddy-viscosity on the top surface of the Ahmed body (on the centreline) at $x = -831$mm, just downstream of the curved section near the nose. These profiles show nodal values (not interpolated values) and the UMIST-*N* wall function results show the subgrid distribution of U, k and μ_t across the near-wall cell. There are clear differences between the UMIST-*N* and SCL wall function results at this position, notably in the k and μ_t profiles. This can be attributed to the overprediction of k at a stagnation point associated with the linear $k-\varepsilon$ model being more pronounced with a low-*Re* type treatment, as is effectively provided by the UMIST-*N* wall function, than with standard wall functions (as discussed in Chapter 5). In addition, the UMIST-*N* wall function accounts for the effects of pressure gradient and convection which are neglected by the SCL wall function. As one moves further downstream along the top of the Ahmed body to a region where the flow is closer to equilibrium, the

differences between the two wall function treatments becomes less pronounced (see Figure 7.16). Progressing still further along the top (Figures 7.17 and 7.18) one can see differences in the two wall function predictions becoming apparent again (although these differences are less than are observed in Figure 7.15). Towards the leading edge of the slant, situated at $x = -201.2$, the streamwise velocity increases and k decreases everywhere except very near the wall. This trend for k decreasing is what one would expect in an accelerating boundary-layer flow [12]. On the slant surface (Figures 7.19, 7.20 and 7.21) a more pronounced difference in the levels of U, k and μ_t arises between the two wall function predictions although the profiles are of similar general shape.

Figures 7.22 – 7.27 show centreline profiles of the mean-velocity, Reynolds stresses and turbulent kinetic energy over the rear slant. Due to the scales needed in order to fit the multiple profiles into one figure, the differences between the two wall function predictions are barely discernible although differences between the predicted and experimental results can be seen quite clearly. These differences are particularly visible for the Reynolds stress profiles where the experimental values are nearly an order-of-magnitude larger than those predicted by the two wall functions. The significant underprediction of the Reynolds stresses and turbulent kinetic energy was a feature of all the RANS simulations of the Ahmed body which were submitted to the two ERCOFTAC workshops. Only the LES results submitted to the workshops came close to predicting the experimental Reynolds stress profiles.

The U-velocity profiles, Figure 7.22, show that the mean-flow recirculation bubble, observed in the experiments, existed from the leading edge of the slant to around $x = -100$mm. With the linear $k-\varepsilon$ model, both wall functions predicted a fully attached boundary layer for the whole length of the slant. This can be seen more clearly in Figure 7.28 which shows velocity vectors and pressure coefficient contours over the rear slant as viewed from above[6]. The two wall function predictions are similar with the UMIST-*N* wall function showing a minor increase in velocity near the downstream edge of the slant as compared to the SCL wall function.

Figure 7.29 compares the resultant velocity vector at the near-wall main-grid node to that at the wall-adjacent subgrid node over the rear slant of the Ahmed body, using the UMIST-*N* wall function. There is considerable skewing of the velocity vector across the subgrid. Near the side edge of the rear slant the subgrid and main-grid vectors are misaligned by up to 90°. The subgrid results also show that there was a reattachment line parallel to the side edge of the slant surface, similar to that shown in the experimental results of Ahmed *et al*. (see Figure 7.3) and Spohn & Gilliéron (marked "B" in Figure 7.6). Skewing of the velocity profile across the near-wall main-grid cell is ignored by standard log-law-based wall functions (such as the SCL treatment) which assume that the wall-shear stress is aligned to the resultant velocity vector at the near-wall main-grid node position.

Figures 7.30, 7.31 and 7.32 chart the growth of the wake from near the leading edge of the slant to a position approximately one-half of a body length downstream (from $x = -178$mm to $x = 500$mm). Experimental measurements of turbulent kinetic energy and mean velocity are compared to those pre-

[6]The resultant velocity vectors are obtained from the main-grid node values with the UMIST-*N* wall function, not the subgrid values.

dicted by the linear $k-\varepsilon$ model with UMIST-*N* wall function (those obtained with the linear $k-\varepsilon$ model and SCL wall function are similar and are not shown). The underprediction of k near the slant surface, discussed above, is shown clearly on Figures 7.30 and 7.31. In addition, the measured turbulent kinetic energy is significantly higher than that predicted around the bottom of the model, near the wind-tunnel wall. This latter feature is mainly due to the enhanced turbulence levels generated by the stilts on which the body was supported in the wind tunnel, which were neglected in the computational model. Over the rear slant the predicted side-edge vortex has the same location but is weaker than the measured vortex. Further downstream, the predicted and measured trailing vortices are in remarkably good agreement both in terms of position and strength (Figure 7.32). However, contours of turbulent kinetic energy continue to show poor agreement in the wake downstream of the body with measured peak values approximately twice the peak predicted values.

In order to provide a brief comparison of the current computations with those of Robinson [35] (who used the same code and an identical grid but with different turbulence models) Figures 7.33 and 7.34 show contours of the turbulent kinetic energy at the centreline plane around the Ahmed body. As previously discussed, there are some minor differences between the current linear $k-\varepsilon$ model predictions using the UMIST-*N* and SCL wall functions (Figure 7.33). The linear $k-\varepsilon$ model predictions of Robinson using the realizability constraint of May [144], shown in Figure 7.34, have slightly lower levels of k in the impingement region on the nose of the Ahmed body and higher values of k over the slant and in the wake, although the flow over the slant is still fully attached. The Craft *et al*. [30] non-linear $k-\varepsilon$ model also predicted low turbulence levels on the nose of the Ahmed body and a fully separated boundary layer over the rear slant with a larger wake.

Drag Predictions

Tables 7.3 and 7.4 compare drag coefficients for the Ahmed body predicted by the present computations to those of Robinson [35] and the experimental measurements of Ahmed *et al*. [137] and Lienhart *et al*. [138]. The reference pressure used to calculate the pressure coefficient $\left(c_p = (P - P_{ref})/0.5\rho U_{bulk}^2\right)$ in both sets of computational results was taken at $(x,y,z) = (-977\text{mm}, 0\text{mm}, 912\text{mm})$ – vertically above the nose of the body on the centreline plane. The values shown from Ahmed *et al*. have been extracted from Figure 7.2 which plots the breakdown of the drag coefficient for slant angles from 0° to 40° . It should be noted that Ahmed *et al*. only actually measured the components of drag at four slant angle 5°, 12.5°, 30° (high drag) and 30° (low drag). These measurements were then interpolated to produce the continuous distribution shown in Figure 7.2. In addition, Ahmed *et al*. calculated the friction drag by subtracting the three pressure-drag components (on the nose, slant and base) from the total drag force on the car body. Any errors in the pressure-drag measurements would therefore effect the value of the friction drag. There are differences between the pressure coefficients extracted from Ahmed *et al*.'s graph and the more recent Lienhart *et al*. measurements. The Lienhart *et al*. measurements show the pressure coefficient on the slant to be only around 36% higher than that on the base, compared to Ahmed *et al*.'s assumed difference of 100%. In addition, Lienhart *et al*.'s values

are slightly higher overall than those of Ahmed *et al*. It is not possible to identify whether the differences between the two sets of experimental data are due to differences in the location of the reference pressure[7], inaccurate interpolation or experimental error since Lienhart *et al*. did not measure the total drag or the pressure coefficient on the nose.

The total drag coefficient predicted by the current calculations using the linear $k-\varepsilon$ model are close to those obtained previously by Robinson with a realizable linear $k-\varepsilon$ model. There are only slight differences between the linear $k-\varepsilon$ model predictions with the SCL and UMIST-*N* wall function values (9.1% error for the SCL wall function compared to 8.4% with UMIST-*N*). The ratio of pressure coefficient on the slant to that on the base is slightly higher with the linear model than the realizable model although it is difficult to make conclusions about the accuracy of the two models due the discrepancies in the experimental measurements mentioned above.

Table 7.3 shows that Robinson's calculations using the non-linear model with the SCL wall function gave the total drag coefficient in best agreement with Ahmed *et al*.'s measurements. However, it would be misleading to conclude from this that the model provided the best predictions of the flow since it also predicted a fully-separated boundary layer over the rear slant, whereas in fact the flow was predominantly attached. The difference in the predicted mode of the flow over the rear slant is indicated by the balance between the slant and base pressure coefficients, shown in Table 7.4. The non-linear model predicted the pressure coefficient on the base to be greater than that on the slant whilst the linear models (and the experiments) predicted the opposite. This shows the importance of looking at the breakdown of drag and not just the total value.

Case	**No Stilt**	**With Stilt**	**% Error**
Ahmed *et al.* [137]	-	0.285	-
linear $k-\varepsilon$, SCL	0.294	0.311	**9.1**
linear $k-\varepsilon$, UMIST-*N*	0.292	0.309	**8.4**
realizable $k-\varepsilon$, SCL (*)	0.294	0.311	**9.1**
realizable $k-\varepsilon$, UMIST-*A* (*)	0.293	0.310	**8.8**
non-linear $k-\varepsilon$, SCL (*)	0.267	0.286	**0.4**
non-linear $k-\varepsilon$, UMIST-*A* (*)	0.251	0.270	**-5.3**

Table 7.3: Total drag for the 25° Ahmed body. Realizable and non-linear $k-\varepsilon$ model results, marked with an asterisk (*), are taken from Robinson [35]. Allowance for the drag due to the stilts (on which the body is supported in the wind-tunnel) is based on the drag on a circular cylinder (see [35]).

Influence of $\partial P/\partial\zeta$ in the UMIST-*N* Wall Function

In Chapter 4 it was noted that the pressure-gradient term appearing in the non-orthogonal UMIST-*N* wall function momentum equations involves gradients of pressure in all three coordinate directions.

[7]The location of the reference pressure was not specified by Ahmed *et al*.

Case	Pressure Coefficient			Skin
	Nose	Slant	Base	Friction
Ahmed *et al.* [137]	0.020	0.140	0.070	0.055
Lienhart *et al*. [138]	-	0.158	0.116	-
linear $k-\varepsilon$, SCL	0.055	0.140	0.095	0.004
linear $k-\varepsilon$, UMIST-*N*	0.055	0.141	0.092	0.004
realizable $k-\varepsilon$, SCL (*)	0.048	0.139	0.103	0.004
realizable $k-\varepsilon$, UMIST-*A* (*)	0.049	0.139	0.100	0.005
non-linear $k-\varepsilon$, SCL (*)	0.047	0.105	0.111	0.004
non-linear $k-\varepsilon$, UMIST-*A* (*)	0.051	0.083	0.114	0.004

Table 7.4: Drag breakdown for the 25° Ahmed body. Realizable and non-linear $k-\varepsilon$ model results, marked with an asterisk (*), are taken from Robinson [35].

For example, the pressure-gradient term for the subgrid U-momentum equation is given by:

$$\sqrt{g_{11}}\left(g^{11}\frac{\partial P}{\partial \xi}+g^{12}\frac{\partial P}{\partial \eta}+g^{13}\frac{\partial P}{\partial \zeta}\right) \tag{7.2}$$

where ξ and η are the two wall-parallel coordinates, ζ is not parallel to the wall (but is not necessarily wall-normal) and g^{ij} is the contravariant metric tensor. The pressure distribution across the near-wall cell is determined by solving the following equation:

$$\nabla P\cdot\hat{\mathbf{n}}+(\nabla\cdot\rho\overline{\mathbf{u}\otimes\mathbf{u}})\cdot\hat{\mathbf{n}}=0 \tag{7.3}$$

where $\hat{\mathbf{n}}$ is the unit wall-normal vector, $\overline{\mathbf{u}\otimes\mathbf{u}}$ is the Reynolds stress in vector form. It is recognized that Equation (7.3) only provides an approximation of $\partial P/\partial\zeta$. To resolve accurately the pressure distribution in the near-wall region would entail the solution of a pressure-correction equation across the subgrid domain which would drastically increase the computational time (in effect one would be performing a full low-Reynolds-number model simulation).

To examine whether $\partial P/\partial\zeta$ is a significant term in the subgrid momentum equations and whether the above approximation is satisfactory, profiles have been plotted of the near-wall velocity in a region of the Ahmed body flow where the grid is highly skewed. Figure 7.35 shows the wall-parallel velocity in five locations around the 90° rear corner of the Ahmed body on the centreline (shown in Figure 7.36). The grid in this region has skewed cells of angle 45°. One can see that the velocity on the underside of the Ahmed body (profiles *A* and *B* on the left of Figure 7.35) increases smoothly from zero on the wall surface up to a maximum of around 0.8 (where 1.0 is the free-stream velocity). The velocity in profile *C*, just around the corner on the base surface, is lower near the wall and further up the base surface (profiles *D* and *E*) the wall-parallel velocity changes sign. Figure 7.37 shows the distribution of three subgrid pressure-gradient terms: $\left(\sqrt{g_{11}}g^{11}\partial P/\partial\xi\right)$, $\left(\sqrt{g_{11}}g^{12}\partial P/\partial\eta\right)$ and $\left(\sqrt{g_{11}}g^{13}\partial P/\partial\zeta\right)$, for the corner cell *C* (for this cell the ξ-direction is aligned to the main Ahmed body *z*-axis, the η-direction is aligned to the *y*-axis and the ζ-direction at angle of 45° to the base

surface, as shown in Figure 7.36). The two wall-parallel components, involving $\partial P/\partial\xi$ and $\partial P/\partial\eta$, are assumed constant across the subgrid and, as would be expected, the ξ-direction component is far greater than the transverse η-direction component. The calculated $\left(\sqrt{g_{11}}g^{13}\partial P/\partial\zeta\right)$ profile is non-uniform, having a maximum near the outer edge of the subgrid domain and decreasing to a quarter of that value near the wall. Near the outer edge of the cell, the term involving $\partial P/\partial\zeta$ is nearly three times as large as the $\partial P/\partial\xi$ term.

If the $\partial P/\partial\zeta$ term is removed from the Ahmed body calculation (by simply setting the term to zero) and the calculation run on from a pre-converged state for 500 iterations, the velocity profiles shown in Figure 7.38 are obtained. The principal effect of switching off $\partial P/\partial\zeta$ is in profile *C* where there is a marked increase in the subgrid velocity leading to a large strain-rate at the outer edge of the subgrid. Interestingly, the main-grid velocity field is practically unchanged by switching off the subgrid $\partial P/\partial\zeta$ even though the wall shear stress calculated from the subgrid solution is increased by approximately 86%. Plots of the overall main-grid flow behaviour, such as those shown in Figures 7.28 and 7.33, are also indistinguishable, meaning that the main-grid domain is little affected by the $\partial P/\partial\zeta$ term in the subgrid. The reason that the calculation was run for only 500 iterations, rather than until a fully-converged solution was reached, was that the calculation became unstable when the $\partial P/\partial\zeta$ term was removed from the subgrid momentum equations[8]. This instability was likely to have been due to the large strain-rate observed at the outer edge of the subgrid domain which caused large production and dissipation source terms in the subgrid k and $\tilde{\varepsilon}$ equations which, in turn, affected the main-grid solution.

To summarize the above discussion, the subgrid $\partial P/\partial\zeta$ term has been shown to have a significant effect on the subgrid velocity profile in a region of the flow where the cells are highly skewed and there are large pressure gradients. In the particular region of the Ahmed flow which has been examined, the calculated subgrid velocity profile has little effect on the near-wall main-grid velocity. This would indicate that the approximation of the subgrid $\partial P/\partial\zeta$ has little influence upon the overall flow field, although an inaccurate estimation of the subgrid pressure distribution may lead to large subgrid strain-rates which compromise the stability of the calculation.

7.5 Discussion & Conclusions

It has been shown that it is possible to apply the UMIST-*N* wall function to a complex three-dimensional flow involving a non-orthogonal multiblock grid arrangement. The prediction of the 25° Ahmed body flow using the new wall function was shown to be similar to that obtained using a standard log-law based wall function. This is surprising since the new wall function did predict skewing of the velocity vector across the near-wall cell, which was anticipated to be influential in the formation of the side-

[8]Momentum and turbulent kinetic energy residuals oscillated at a level around order-of-magnitude greater than that previously achieved when the $\partial P/\partial\zeta$ term was included. The dissipation-rate residuals also increased by approximately four orders-of-magnitude. Analysis of the velocity and turbulence parameters in the regions of maximum residual (located near the 90° rear corner of the Ahmed body) showed small changes in the profiles between successive iterations.

edge vortices over the rear slant. Although the results are therefore slightly disappointing the linear $k-\varepsilon$ model predictions with the UMIST-*N* wall function are broadly in agreement with the low-*Re* linear $k-\varepsilon$ model predictions of Leonard *et al*.[9] (both approaches predicted a fully-attached boundary layer over the rear slant). It appears, following the workshop comparisons, that the turbulence model used in the main-grid region of the flow domain has a greater influence on mode of the flow on the rear slant than the particular near-wall treatment employed. It would be interesting to examine this issue further, perhaps by making direct comparisons between a low-*Re* $k-\omega$ model (which predicted the separation bubble on the rear slant in almost perfect agreement with the experiments) and a $k-\omega$ model with different wall functions.

In the impinging-jet and spinning-disc flows considered in earlier chapters, the computing times of the UMIST-*N* wall function calculations were compared against the times for full low-*Re* model and standard log-law-based wall function calculations. A low-*Re* model simulation of the Ahmed body flow was not undertaken as part of the present study due to the computing requirements. Both the SCL and UMIST-*N* wall function calculations have been started from previous simulations, rather than from scratch, making it difficult to compare total CPU requirements. One can, however, compare computing times for the SCL and UMIST-*N* treatments on a per-iteration basis, as shown in Table 7.5. Ahmed body calculations with the UMIST-*N* wall function took around 24% greater time per iteration than those with the SCL wall function. This compares to an increase of around 60% for the impinging-jet flow and 100% for the spinning-disc flow.

Wall Function	CPU Time for 100 Iterations (s)	Relative CPU time
SCL	1022	1
UMIST-*N*	1268	1.24

Table 7.5: Computing times for 100 iterations of the Ahmed body calculation using the linear $k-\varepsilon$ model with the log-law-based Simplified Chieng & Launder (SCL) wall function and the new UMIST-*N* wall function. Computations were carried out on a 2.2GHz Pentium 4 processor with the same levels of compiler optimization.

One of the features of the new wall function which only becomes significant in a non-orthogonal grid arrangement, namely the appearance $\partial P/\partial\zeta$ in the subgrid momentum equations, has been shown to be an important term in the subgrid momentum equations in regions where the cells are highly skewed and there are large pressure gradients. The term was shown to have little or no effect on the overall main-grid solution although stability of the calculation was compromised if the term was neglected from the subgrid momentum equations. This indicates that the safest strategy is to use a grid which does not contain highly skewed subgrid cells.

In future simulations of the Ahmed body flow it would be interesting to examine the effect of using entrainment conditions on the top and side edges of the flow domain where, in the present calculations, symmetry conditions have been imposed. Menter noted at the 2002 ERCOFTAC workshop

[9]The results of Leonard *et al*. were presented at the 2002 ERCOFTAC Workshop on Refined Turbulence Modelling (see Footnote 3 on Page 132).

that specifying symmetry conditions instead of the more realistic entrainment conditions caused an increase in the velocity of the flow around the body due to the blockage effect which led to an increase in the predicted drag coefficient (an effect which was proportional to the square of the blockage ratio). The choice of boundary conditions was not however reported to affect the flow structure on the rear slant.

Chapter 8

Discussion and Conclusions

8.1 Preliminary Remarks

The aim of this thesis was to develop a computationally efficient wall function which can predict complex turbulent flows with an accuracy similar to full low-Reynolds-number model treatments, which involve the costly integration of transport equations all the way across the viscous sublayer to the wall. To assess the performance of the new wall function, three challenging test-cases were selected: an impinging jet, a spinning disc and a three-dimensional "Ahmed" car body flow. Each of these test cases provides challenges for the wall treatment. Near the stagnation point in the impinging jet flow, the turbulence energy is generated primarily by normal stresses and convection both normal and parallel to the wall are significant. The spinning-disc flow involves "natural" transition and the velocity vector undergoes significant skewing across the near-wall sublayer (a feature which cannot be captured accurately by standard log-law-based wall functions). The 25° Ahmed car body flow was chosen as an industrially-relevant three-dimensional flow which involves elements of the other two cases: flow impingement on the nose and strong near-wall skewing of the flow over the rear slant, whilst introducing additional complexities such as the use of a non-orthogonal multiblock grid.

The new wall function, UMIST-*N*, was presented in detail in Chapter 4. In summary, the wall function solves boundary-layer-type transport equations for wall-parallel velocity, turbulence parameters (such as k and $\tilde{\varepsilon}$), and temperature across an embedded grid situated within the near-wall cell. The wall function transport equations include terms for convection both parallel and normal to the wall, diffusion normal to the wall, pressure gradient and sources. The wall-normal velocity is obtained from continuity, with some additional scaling to allow for consistent boundary conditions. Since the wall function decouples the solution of the near-wall flow from that in the main-grid domain and a pressure-correction equation is not solved across the subgrid, the new wall function does not suffer from the slow convergence problems of a full low-Reynolds-number model treatment. Subgrid values of velocity, turbulence parameters and temperature are saved at each iteration so the overall storage requirements of the new wall function are roughly equal to those of a full low-*Re* model (although there are some savings since subgrid pressure is not stored and due to the grid arrangement).

The three test-cases were each examined using full low-*Re* models[1], the UMIST-*N* wall function and at least one standard log-law-based wall function. Linear and non-linear $k-\varepsilon$ models were used in the impinging jet and spinning-disc flows whilst only linear $k-\varepsilon$ results were presented for the Ahmed body flow. Discussions have already been presented on a case-by-case basis at the end of each of the flow calculation chapter. It is not intended to go through the same discussions again, but to highlight the salient points and draw some overall conclusions.

8.2 Conclusions

Impinging Jet Flow

Overall, the UMIST-*N* wall function predictions of the impinging jet flow were in excellent agreement with the low-*Re* model predictions using both linear and non-linear $k-\varepsilon$ models. Different wall-function grid arrangements were tested to assess the sensitivity of the models to the size of the near-wall cell. The UMIST-*N* wall function showed practically no sensitivity to the near-wall cell size, in contrast to the log-law-based wall functions. There was a small discrepancy between the heat transfer predictions of the low-*Re* linear $k-\varepsilon$ model and the UMIST-*N* wall function near the stagnation point in the impinging jet flow, but it was shown that this was due to the coarse wall-function grid providing an insufficient resolution of the near-wall variation of turbulence parameters. Computing times for the UMIST-*N* wall function were approximately 60% higher than those of the log-law-based Chieng & Launder wall function but an order-of-magnitude less than the low-*Re* NLEVM calculations.

Spinning "Free" Disc Flow

The near-wall tangential velocity exhibits a logarithmic profile in the fully-turbulent region of the spinning disc flow whilst the radial velocity increases from zero at the wall to a peak and then decays with distance from the disc. Standard wall functions which assume a logarithmic velocity profile in both directions therefore adequately approximate the tangential velocity profile but do not capture the radial velocity distribution. Traditionally, in order to predict accurately the flow and heat transfer over the disc, one has been forced to use full low-*Re* model treatments. The UMIST-*N* wall function showed excellent agreement with low-*Re* model predictions of both the radial and tangential velocity profiles.

The location of transition from laminar to turbulent flow was not specified in the calculations. Instead, an initial level of turbulence was left to decay in regions where there was insufficient straining of the flow field, near the disc axis. It was found that the predicted location of transition was slightly sensitive to the size of the near-wall cell with the UMIST-*N* wall function, although the results were close to those obtained with low-*Re* models. This sensitivity was shown to be significantly worse with

[1] with the exception that a low-*Re* model calculation of the Ahmed body flow was not undertaken due to the large computing time required.

standard wall functions, which use a criterion based on the local y^+-value to switch from assumed laminar to turbulent profiles.

Computing times with the UMIST-*N* wall function were approximately double those of the Chieng & Launder wall function but still an order-of-magnitude less than low-*Re* computations.

"Ahmed" Body Flow

The flow around the Ahmed body with a rear slant angle of 25° was examined. Experimental measurements have shown that the flow separates at the top edge of the rear slant, reattaches roughly half-way down the slant and thereafter remains attached due to the presence of strong side-edge vortices. Capturing this behaviour over the rear slant is crucial in obtaining the correct drag predictions.

Using a linear $k-\varepsilon$ model, the UMIST-*N* wall function was shown to give similar flow predictions to those obtained using a standard log-law-based wall function. This was surprising since the earlier spinning-disc calculations showed that the new wall function was better able to predict highly-skewed boundary layers and it had been anticipated that this would influence the formation of the side-edge vortices. Although the results are therefore slightly disappointing, this behaviour is broadly in agreement with low-*Re* linear $k-\varepsilon$ model predictions presented by other researchers at a recent ERCOFTAC workshop on the Ahmed body flow. Computing times with the UMIST-*N* wall function were around 24% higher per iteration than those of the standard wall function.

General Comments

In terms of the aims of this thesis, it has been demonstrated that the new wall function provides flow predictions in good agreement with full low-Reynolds-number model simulations. There is a modest computational overhead in switching from a standard log-law-based wall functions to the UMIST-*N* but in both the impinging jet and spinning disc cases it was shown that computing times were still an order-of-magnitude less than a full low-*Re* calculation. In the Introduction a number of features of the "ideal" wall function were discussed under the headings of flexibility, validation and robustness. The UMIST-*N* wall function has been applied with two turbulence models, a linear and a non-linear $k-\varepsilon$ model. In principle, it can be used with any turbulence closure and a step-by-step derivation has been included for both Cartesian and non-orthogonal grid arrangements to aid further developments. The wall function can be modified relatively easily to work as a stand-alone parabolic solver and various other means of testing and validating the code were discussed in Section 4.4. In the impinging jet and spinning disc flows, the UMIST-*N* wall function was found to converge in slightly fewer iterations than the Chieng & Launder wall function and was not found to cause problems with robustness of the overall flow calculation. However, there were some unresolved issues with the use of the NLEVM and UMIST-*N* wall function in the Ahmed body flow which are discussed below.

8.3 Further Work

Ahmed Body Simulations

Simulations of the Ahmed body flow using the UMIST-*N* wall function with the non-linear $k-\varepsilon$ model were numerical unstable. Various possible causes were investigated. Using the NLEVM across the wall-function region and a linear $k-\varepsilon$ model throughout the main-grid flow domain gave a stable solution; similarly, using a linear model across the subgrid and in a few cells near the wall whilst using the NLEVM elsewhere gave a stable solution. It was only when the NLEVM was used in the subgrid and the main-grid region close to the wall that stability problems arose.

In previous simulations of the Ahmed body flow using the NLEVM, Robinson [35] found that there was some transient motion in the wake of the Ahmed body which prevented the steady-state solution converging. Some preliminary time-dependent calculations were carried out with the UMIST-*N* wall function which seemed to indicate that this was not the cause of the stability problems.

There are known stability issues with the NLEVM in flows involving strong strain-rates. A feedback loop exists due to the strain-dependent c_μ term: an overpredicted strain-rate leads to a reduced c_μ, which in turn reduces the eddy-viscosity and leads to an increased strain-rate, which then reduces c_μ etc. A number of recent modifications by Craft *et al*. [67] have improved the stability of the model. These were tested but did not provide any improvement for the present test case. It seems unlikely that this is the root cause of the stability problems, however, since Robinson was able to obtain stable solutions for the Ahmed body flow using the same model with a log-law-based wall function.

It was remarked earlier that an incorrect prediction of the pressure distribution across the subgrid with the linear $k-\varepsilon$ model could cause numerical instability, due to large strain-rates arising at the outer boundary of the subgrid. The calculation for the subgrid pressure gradient $(\partial P/\partial\zeta)$ is based on local gradients of the Reynolds stress. It is therefore possible that there was some feedback between the subgrid Reynolds stress distribution generated by the NLEVM and the calculation for $\partial P/\partial\zeta$ which introduced numerical instability. However, a stable solution could be obtained using the NLEVM across the subgrid and linear model in the main-grid, which would indicate that this too was not the cause of the stability problem.

Clearly, it is necessary to investigate the possible causes of the numerical instability and find a solution. The Ahmed body flow is large and complex and it would be easier to investigate the causes of the problem in simpler geometries which contain similar flow features. Backward facing step and diffuser flows could be examined using grids with cells skewed at 45° to emulate the flow over the rear of the Ahmed body.

Internal Corners

The Parabolic Sub-Layer (PSL) treatment of Iacovides & Launder [59] shares some common features with the UMIST-*N* wall function. Neither of the approaches solves a pressure-correction equation within the near-wall region and instead the wall-normal velocity is determined from continuity. The

PSL treatment was found to be numerically unstable in flows involving internal corners where the wall-normal velocity in the corner cell was calculated from the wall-parallel velocity, which was itself calculated from continuity. These problems are not expected to occur with the UMIST-*N* wall function, since it does not directly calculate the main-grid velocities from continuity. However, this should be confirmed by tests with the UMIST-*N* wall function in flows involving internal corners.

Appendix A

RANS Equations for Axisymmetric Swirling Flow

The RANS equations for steady, incompressible flow are presented below in cylindrical-polar coordinates, using a stationary reference frame. The velocity components in the radial (r), axial (y) and tangential (ϕ) directions are denoted U, V and W respectively. Convection terms are shown in conservative form. For confirmation of these equations see Owen & Wilson [112] or Morse [124].

Continuity

$$\frac{1}{r}\frac{\partial}{\partial r}(rU)+\frac{\partial V}{\partial y}=0 \tag{A.1}$$

Radial Momentum, U

$$\begin{aligned}\frac{\partial}{\partial r}(\rho rUU)+\frac{\partial}{\partial y}(\rho rUV)-\rho W^2 &= -r\frac{\partial P}{\partial r}+\frac{\partial}{\partial r}\left(2r\mu\frac{\partial U}{\partial r}-\rho r\overline{u^2}\right)\\ &\quad+\frac{\partial}{\partial y}\left[r\mu\left(\frac{\partial U}{\partial y}+\frac{\partial V}{\partial r}\right)-\rho r\overline{uv}\right]\\ &\quad-\left(2\mu\frac{U}{r}-\rho\overline{w^2}\right)\end{aligned} \tag{A.2}$$

Axial Momentum, V

$$\begin{aligned}\frac{\partial}{\partial r}(\rho rUV)+\frac{\partial}{\partial y}(\rho rVV) &= -r\frac{\partial P}{\partial y}+\frac{\partial}{\partial r}\left[r\mu\left(\frac{\partial V}{\partial r}+\frac{\partial U}{\partial y}\right)-\rho r\overline{uv}\right]\\ &\quad+\frac{\partial}{\partial y}\left(2r\mu\frac{\partial V}{\partial y}-\rho r\overline{v^2}\right)\end{aligned} \tag{A.3}$$

Tangential Momentum, W

$$\begin{aligned}\frac{\partial}{\partial r}(\rho r UW)+\frac{\partial}{\partial y}(\rho r VW)+\rho UW &= \frac{\partial}{\partial r}\left(r\mu\frac{\partial W}{\partial r}-\rho r\overline{uw}\right)+\frac{\partial}{\partial y}\left(r\mu\frac{\partial W}{\partial y}-\rho r\overline{vw}\right)\\ &\quad -\left(\frac{\mu W}{r}+W\frac{\partial\mu}{\partial r}+\rho\overline{uw}\right)\end{aligned} \tag{A.4}$$

A.1 Linear $k-\varepsilon$ Model

Reynolds Stress, $\overline{u_i u_j}$

In a linear $k-\varepsilon$ model the Reynolds stresses, $\overline{u_i u_j}$, are as follows:

$$-\rho\overline{u^2}=2\mu_t\frac{\partial U}{\partial r}-\frac{2}{3}\rho k \tag{A.5}$$

$$-\rho\overline{v^2}=2\mu_t\frac{\partial V}{\partial y}-\frac{2}{3}\rho k \tag{A.6}$$

$$-\rho\overline{w^2}=2\mu_t\frac{U}{r}-\frac{2}{3}\rho k \tag{A.7}$$

$$-\rho\overline{uv}=\mu_t\left(\frac{\partial U}{\partial y}+\frac{\partial V}{\partial r}\right) \tag{A.8}$$

$$-\rho\overline{uw}=\mu_t r\frac{\partial}{\partial r}\left(\frac{W}{r}\right)=\mu_t\left(\frac{\partial W}{\partial r}-\frac{W}{r}\right) \tag{A.9}$$

$$-\rho\overline{vw}=\mu_t\frac{\partial W}{\partial y} \tag{A.10}$$

Substituting these into the above RANS equations:

Radial Momentum, U

$$\begin{aligned}\frac{\partial}{\partial r}(\rho r UU)+\frac{\partial}{\partial y}(\rho r UV)-\rho W^2 &= -r\frac{\partial P}{\partial r}-\frac{\partial}{\partial r}\left(\frac{2}{3}r\rho k\right)+\frac{\partial}{\partial r}\left[2r(\mu+\mu_t)\frac{\partial U}{\partial r}\right]\\ &\quad +\frac{\partial}{\partial y}\left[r(\mu+\mu_t)\left(\frac{\partial U}{\partial y}+\frac{\partial V}{\partial r}\right)\right]\\ &\quad -2(\mu+\mu_t)\frac{U}{r}+\frac{2}{3}\rho k\end{aligned} \tag{A.11}$$

Here the $2k/3$ term resulting from the $\overline{w^2}$ Reynolds stress cancels with part of the expanded $\overline{u^2}$ term:

$$\begin{aligned}-\frac{\partial}{\partial r}\left(\frac{2}{3}r\rho k\right)+\frac{2}{3}\rho k &= -r\frac{\partial}{\partial r}\left(\frac{2}{3}\rho k\right)-\frac{2}{3}\rho k\frac{\partial r}{\partial r}+\frac{2}{3}\rho k\\ &= -r\frac{\partial}{\partial r}\left(\frac{2}{3}\rho k\right)\end{aligned} \tag{A.12}$$

The remaining gradient of $2k/3$ is included in the pressure gradient term when the transport equations are coded. The final form of the radial-momentum transport equation is then:

$$\begin{aligned}\frac{\partial}{\partial r}(\rho rUU)+\frac{\partial}{\partial y}(\rho rUV) &= -r\frac{\partial P'}{\partial r}+\frac{\partial}{\partial r}\left(2r\mu_{eff}\frac{\partial U}{\partial r}\right)\\ &\quad+\frac{\partial}{\partial y}\left[r\mu_{eff}\left(\frac{\partial U}{\partial y}+\frac{\partial V}{\partial r}\right)\right]-2\mu_{eff}\frac{U}{r}+\rho W^2 \qquad \text{(A.13)}\end{aligned}$$

where $\mu_{eff}=\mu+\mu_t$ and $P'=P+2\rho k/3$.

Axial Momentum, V

Following a similar approach outlined above, the axial momentum expression can be written:

$$\begin{aligned}\frac{\partial}{\partial r}(\rho rUV)+\frac{\partial}{\partial y}(\rho rVV) &= -r\frac{\partial P'}{\partial y}+\frac{\partial}{\partial r}\left[r\mu_{eff}\left(\frac{\partial V}{\partial r}+\frac{\partial U}{\partial y}\right)\right]\\ &\quad+\frac{\partial}{\partial y}\left(2r\mu_{eff}\frac{\partial V}{\partial y}\right) \qquad \text{(A.14)}\end{aligned}$$

Tangential Momentum, W

$$\begin{aligned}\frac{\partial}{\partial r}(\rho rUW)+\frac{\partial}{\partial y}(\rho rVW)+\rho UW &= \frac{\partial}{\partial r}\left(r\mu\frac{\partial W}{\partial r}+r\mu_t\left(\frac{\partial W}{\partial r}-\frac{W}{r}\right)\right)+\frac{\partial}{\partial y}\left(r\mu_{eff}\frac{\partial W}{\partial y}\right)\\ &\quad-\left(\mu\frac{W}{r}+W\frac{\partial\mu}{\partial r}-\mu_t\left(\frac{\partial W}{\partial r}-\frac{W}{r}\right)\right) \qquad \text{(A.15)}\end{aligned}$$

This can be rearranged as follows:

$$\begin{aligned}\frac{\partial}{\partial r}(\rho rUW)+\frac{\partial}{\partial y}(\rho rVW) &= \frac{\partial}{\partial r}\left(r\mu_{eff}\frac{\partial W}{\partial r}\right)+\frac{\partial}{\partial y}\left(r\mu_{eff}\frac{\partial W}{\partial y}\right)\\ &\quad-\mu_{eff}\frac{W}{r}-W\frac{\partial\mu_{eff}}{\partial r}-\rho UW \qquad \text{(A.16)}\end{aligned}$$

Kinetic energy, k

$$\begin{aligned}\frac{\partial}{\partial r}(\rho rUk)+\frac{\partial}{\partial y}(\rho rVk) &= \frac{\partial}{\partial r}\left[r\left(\mu+\frac{\mu_t}{\sigma_k}\right)\frac{\partial k}{\partial r}\right]+\frac{\partial}{\partial y}\left[r\left(\mu+\frac{\mu_t}{\sigma_k}\right)\frac{\partial k}{\partial y}\right]\\ &\quad+rP_k-r\rho\varepsilon \qquad \text{(A.17)}\end{aligned}$$

where the production rate, P_k, is given by:

$$\begin{aligned} P_k &= \mu_t S_{ij} \frac{\partial U_i}{\partial x_j} \\ &= \mu_t \left\{ 2\left(\frac{\partial U}{\partial r}\right)^2 + 2\left(\frac{\partial V}{\partial y}\right)^2 + 2\left(\frac{U}{r}\right)^2 \right. \\ &\quad \left. + \left(\frac{\partial U}{\partial y} + \frac{\partial V}{\partial r}\right)^2 + \left(\frac{\partial W}{\partial r} - \frac{W}{r}\right)^2 + \left(\frac{\partial W}{\partial y}\right)^2 \right\} \end{aligned} \tag{A.18}$$

and the total dissipation rate, ε, comprising of isotropic dissipation rate ($\tilde{\varepsilon}$) and the value of dissipation rate at the wall, is given by:

$$\begin{aligned} \varepsilon &= \tilde{\varepsilon} + 2\nu \left(\frac{\partial \sqrt{k}}{\partial x_j}\right)^2 \\ &= \tilde{\varepsilon} + 2\nu \left[\left(\frac{\partial \sqrt{k}}{\partial r}\right)^2 + \left(\frac{\partial \sqrt{k}}{\partial y}\right)^2 \right] \end{aligned} \tag{A.19}$$

Dissipation Rate, $\tilde{\varepsilon}$

$$\begin{aligned} \frac{\partial}{\partial r}(r\rho U\tilde{\varepsilon}) + \frac{\partial}{\partial y}(\rho r V\tilde{\varepsilon}) &= \frac{\partial}{\partial r}\left[r\left(\mu + \frac{\mu_t}{\sigma_\varepsilon}\right)\frac{\partial \tilde{\varepsilon}}{\partial r}\right] + \frac{\partial}{\partial y}\left[r\left(\mu + \frac{\mu_t}{\sigma_\varepsilon}\right)\frac{\partial \tilde{\varepsilon}}{\partial y}\right] \\ &\quad + r\left(c_{\varepsilon 1} f_1 P_k - c_{\varepsilon 2} f_2 \rho\tilde{\varepsilon}\right)\frac{\tilde{\varepsilon}}{k} + rP_{\varepsilon 3} + r\rho Y_c \end{aligned} \tag{A.20}$$

where the gradient production term, $P_{\varepsilon 3}$, is given by:

$$\begin{aligned} P_{\varepsilon 3} &= 2\mu\nu_t \left(\frac{\partial^2 U_i}{\partial x_j \partial x_k}\right)^2 \\ &= 2\mu\nu_t \left\{ \left(\frac{\partial^2 U}{\partial r^2}\right)^2 + 3\left[\frac{1}{r^2}\left(r\frac{\partial U}{\partial r} - U\right)\right]^2 + \left(\frac{\partial^2 U}{\partial y^2}\right)^2 \right. \\ &\quad + 2\left(\frac{\partial^2 U}{\partial y \partial r}\right)^2 + 2\left(\frac{1}{r}\frac{\partial W}{\partial y}\right)^2 \\ &\quad + \left(\frac{\partial^2 W}{\partial r^2}\right)^2 + 3\left[\frac{1}{r^2}\left(r\frac{\partial W}{\partial r} - W\right)\right]^2 + \left(\frac{\partial^2 W}{\partial y^2}\right)^2 \\ &\quad + 2\left(\frac{\partial^2 W}{\partial y \partial r}\right)^2 + 2\left(\frac{1}{r}\frac{\partial U}{\partial y}\right)^2 \\ &\quad + \left(\frac{\partial^2 V}{\partial r^2}\right)^2 + \left(\frac{1}{r}\frac{\partial V}{\partial r}\right)^2 + \left(\frac{\partial^2 V}{\partial y^2}\right)^2 \\ &\quad \left. + 2\left(\frac{\partial^2 V}{\partial y \partial r}\right)^2 \right\} \end{aligned} \tag{A.21}$$

The whole of the above expression has been used for the work included in this thesis. Morse [124] and Launder & Sharma [13] used a simplified form of the above $P_{\varepsilon 3}$ expression.

A.2 Non-Linear $k-\varepsilon$ Model

In axisymmetric swirling flows the strain-rate and vorticity tensors appearing in the NLEVM are given by:

$$\begin{aligned} S_{ij} &= \frac{\partial U_i}{\partial x_j}+\frac{\partial U_j}{\partial x_i} \\ &= \begin{bmatrix} S_{11} & S_{12} & S_{13} \\ S_{21} & S_{22} & S_{23} \\ S_{31} & S_{32} & S_{33} \end{bmatrix} \\ &= \begin{bmatrix} \left(2\frac{\partial U}{\partial r}\right) & \left(\frac{\partial U}{\partial y}+\frac{\partial V}{\partial r}\right) & \left(\frac{\partial W}{\partial r}-\frac{W}{r}\right) \\ \left(\frac{\partial U}{\partial y}+\frac{\partial V}{\partial r}\right) & \left(2\frac{\partial V}{\partial y}\right) & \left(\frac{\partial W}{\partial y}\right) \\ \left(\frac{\partial W}{\partial r}-\frac{W}{r}\right) & \left(\frac{\partial W}{\partial y}\right) & \left(2\frac{U}{r}\right) \end{bmatrix} \end{aligned} \tag{A.22}$$

and:

$$\begin{aligned} \Omega_{ij} &= \frac{\partial U_i}{\partial x_j}-\frac{\partial U_j}{\partial x_i} \\ &= \begin{bmatrix} \Omega_{11} & \Omega_{12} & \Omega_{13} \\ \Omega_{21} & \Omega_{22} & \Omega_{23} \\ \Omega_{31} & \Omega_{32} & \Omega_{33} \end{bmatrix} \\ &= \begin{bmatrix} 0 & \left(\frac{\partial U}{\partial y}-\frac{\partial V}{\partial r}\right) & -\left(\frac{\partial W}{\partial r}+\frac{W}{r}\right) \\ -\left(\frac{\partial U}{\partial y}-\frac{\partial V}{\partial r}\right) & 0 & -\left(\frac{\partial W}{\partial y}\right) \\ \left(\frac{\partial W}{\partial r}+\frac{W}{r}\right) & \left(\frac{\partial W}{\partial y}\right) & 0 \end{bmatrix} \end{aligned} \tag{A.23}$$

Appendix B

Introduction to Curvilinear Coordinates

B.1 Definition of a Vector

A vector, **v**, in three-dimensional space is represented in the most general form as the summation of three components, v^1, v^2 and v^3, aligned with three "base" vectors, as follows:

$$\mathbf{v} = v^1\mathbf{g}_1 + v^2\mathbf{g}_2 + v^3\mathbf{g}_3 = \sum_{i=1}^{3} v^i\mathbf{g}_i \tag{B.1}$$

where bold typeface denotes vector quantities and the base vectors, $\mathbf{g}_i$, can be non-orthogonal and do not have to be unit vectors as long as they are non-coplanar. The subscript i indicates a *covariant* quantity and the superscript i indicates a *contravariant* quantity, hence the above formula describes vector **v** as three contravariant components of the covariant base vectors. The Einstein summation convention only applies where one dummy index i is subscript and the other is superscript (summation does not apply over a repeated subscript i, so that for instance the metric tensor g_{ii}, discussed later, has 3 separate components).

B.2 Transformation Properties of Covariant and Contravariant Tensors

The subject of covariant and contravariant tensors is often introduced in tensor analysis text books by defining the behaviour of the two under transformation. The gradient of a scalar, ϕ, is given by the following expression in general non-orthogonal coordinates (ξ, η, ζ):

$$\nabla\phi = \frac{\partial\phi}{\partial\xi}\mathbf{g}^1 + \frac{\partial\phi}{\partial\eta}\mathbf{g}^2 + \frac{\partial\phi}{\partial\zeta}\mathbf{g}^2 = \frac{\partial\phi}{\partial\xi^i}\mathbf{g}^i \tag{B.2}$$

If one defines another coordinate system $\left(\overline{\xi},\overline{\eta},\overline{\zeta}\right)$ then components of the gradient can be expressed using the chain-rule:

$$\frac{\partial\phi}{\partial\overline{\xi^i}}=\frac{\partial\xi^j}{\partial\overline{\xi^i}}\frac{\partial\phi}{\partial\xi^j} \tag{B.3}$$

which can be written:

$$\overline{A_i}=a_i^jA_j \tag{B.4}$$

where:

$$\overline{A_i}=\frac{\partial\phi}{\partial\overline{\xi^j}} \qquad a_i^j=\frac{\partial\xi^j}{\partial\overline{\xi^i}} \qquad A_j=\frac{\partial\phi}{\partial\xi^j} \tag{B.5}$$

Tensors that satisfy this transformation are called covariant tensors and have lowered subscripts, as in A_i.

To examine the transformation properties of a contravariant tensor, the vector d$\mathbf{r}$ is considered, as follows:

$$\mathrm{d}\mathbf{r}=\mathrm{d}\xi\mathbf{g}_1+\mathrm{d}\eta\mathbf{g}_2+\mathrm{d}\zeta\mathbf{g}_3 \tag{B.6}$$

As before, if one defines another coordinate system $\left(\overline{\xi},\overline{\eta},\overline{\zeta}\right)$ then components of the vector can be expressed using the chain-rule:

$$\mathrm{d}\overline{\xi^i}=\frac{\partial\overline{\xi^i}}{\partial\xi^j}\mathrm{d}\xi^j \tag{B.7}$$

This can be written:

$$\overline{A^i}=b_j^iA^j \tag{B.8}$$

where:

$$\overline{A^i}\equiv\mathrm{d}\overline{\xi^i} \qquad b_j^i=\frac{\partial\overline{\xi^i}}{\partial\xi^j} \qquad A^j=\mathrm{d}\xi^j \tag{B.9}$$

Tensors that transform according to Equation (B.8) are termed contravariant, and have raised indices.

B.3 Covariant and Contravariant Base Vectors, $\mathbf{g}_i$ and $\mathbf{g}^i$

One can define a point in space by the position vector, $\mathbf{r}$, using the familiar Cartesian coordinates, as follows:

$$\begin{aligned}\mathbf{r} &= x\hat{\mathbf{i}}+y\hat{\mathbf{j}}+z\hat{\mathbf{k}}\\ &= x^1\mathbf{e}_1+x^2\mathbf{e}_2+x^3\mathbf{e}_3\\ &= x^i\mathbf{e}_i\end{aligned} \tag{B.10}$$

and, equally, one can define the unit vector in the x-direction, $\hat{\mathbf{i}}$, as follows:

$$\hat{\mathbf{i}}=\frac{\partial\mathbf{r}}{\partial x} \tag{B.11}$$

or, more generally:

$$\mathbf{e}_i = \frac{\partial \mathbf{r}}{\partial x^i} \tag{B.12}$$

The same point in space can be defined using a more general coordinate system:

$$\begin{aligned} \mathbf{r} &= \xi \mathbf{g}_1 + \eta \mathbf{g}_2 + \zeta \mathbf{g}_3 \\ &= \xi^1 \mathbf{g}_1 + \xi^2 \mathbf{g}_2 + \xi^3 \mathbf{g}_3 \\ &= \xi^i \mathbf{g}_i \end{aligned} \tag{B.13}$$

where:

$$\mathbf{g}_i = \frac{\partial \mathbf{r}}{\partial \xi^i} \tag{B.14}$$

Equations (B.10) and (B.13) are equivalent. Using the chain rule, one can therefore express the covariant general base vectors $\mathbf{g}_i$ in terms of the covariant Cartesian base vectors, $\mathbf{e}_i$, as follows:

$$\begin{aligned} \frac{\partial \mathbf{r}}{\partial x^i} &= \frac{\partial \mathbf{r}}{\partial \xi^j} \frac{\partial \xi^j}{\partial x^i} \\ \mathbf{e}_i &= \frac{\partial \xi^j}{\partial x^i} \mathbf{g}_j \end{aligned} \tag{B.15}$$

and likewise:

$$\begin{aligned} \frac{\partial \mathbf{r}}{\partial \xi^i} &= \frac{\partial \mathbf{r}}{\partial x^j} \frac{\partial x^j}{\partial \xi^i} \\ \mathbf{g}_i &= \frac{\partial x^j}{\partial \xi^i} \mathbf{e}_j \end{aligned} \tag{B.16}$$

The covariant and contravariant base vectors are defined such that the scalar product of the covariant and contravariant base vectors is unity, i.e.:

$$\begin{aligned} \mathbf{g}_i \cdot \mathbf{g}^j &= 1 \text{ if } i = j \\ &= 0 \text{ if } i \neq j \end{aligned}$$

or:

$$\mathbf{g}_i \cdot \mathbf{g}^j = \delta_i^j \tag{B.17}$$

where $\delta_i^j \left(\equiv \delta^{ij} \equiv \delta_{ij} \right)$ is the Kronecker delta.

In Equation (B.13), the vector $\mathbf{r}$ was expressed in terms of the covariant base vector $\mathbf{g}_i$. In a similar way, vector $\mathbf{r}$ can be written in terms of the contravariant base vector $\mathbf{g}^i$:

$$\mathbf{r} = \xi_i \mathbf{g}^i \tag{B.18}$$

where, following a similar analysis to that given for Equation (B.16):

$$\frac{\partial \mathbf{r}}{\partial \xi_i} = \frac{\partial \mathbf{r}}{\partial x_j}\frac{\partial x_j}{\partial \xi_i} \tag{B.19}$$

and since $\mathbf{g}^i = \partial \mathbf{r}/\partial \xi_i$ and $\mathbf{e}^j = \partial \mathbf{r}/\partial x_j$, the contravariant base vector is given by:

$$\mathbf{g}^i = \frac{\partial x_j}{\partial \xi_i}\mathbf{e}^j \tag{B.20}$$

One can obtain the covariant and contravariant components from the scalar product of the vector, $\mathbf{r}$, and the corresponding base vectors ($\mathbf{g}_i$ or $\mathbf{g}^i$), as follows:

$$\mathbf{r}\cdot\mathbf{g}_i = \xi_j \mathbf{g}^j \cdot \mathbf{g}_i = \xi_j \delta_i^j = \xi_i \tag{B.21}$$

$$\mathbf{r}\cdot\mathbf{g}^i = \xi^j \mathbf{g}_j \cdot \mathbf{g}^i = \xi^j \delta_j^i = \xi^i \tag{B.22}$$

where δ_i^j has substitution operator properties (i.e. it changes the component ξ_j to ξ_i, or from ξ^j to ξ^i). Comparing Equations (B.18) and (B.21) one can also see that if the base vector is taken from the right-hand-side to the left-hand-side of Equation (B.18), the superscript $\mathbf{g}^i$ becomes subscript $\mathbf{g}_i$.

There is an alternative method to obtaining the contravariant base vector $\mathbf{g}^i$ as a function of $\mathbf{e}^j$ to that shown above. Returning to Equation (B.15), it was shown that:

$$\mathbf{e}_k = \frac{\partial \xi^j}{\partial x^k}\mathbf{g}_j \tag{B.23}$$

Taking the scalar product of both sides of this equation with $\mathbf{g}^i$:

$$\mathbf{e}_k \cdot \mathbf{g}^i = \frac{\partial \xi^j}{\partial x^k}\mathbf{g}_j \cdot \mathbf{g}^i = \frac{\partial \xi^j}{\partial x^k}\delta_j^i = \frac{\partial \xi^i}{\partial x^k} \tag{B.24}$$

Now, assuming that the contravariant base vector $\mathbf{g}^i$ can be obtained from $\mathbf{e}^j$ using a linear combination of factors α_j^i:

$$\mathbf{g}^i = \alpha_1^i \mathbf{e}^1 + \alpha_2^i \mathbf{e}^2 + \alpha_3^i \mathbf{e}^3 = \alpha_j^i \mathbf{e}^j \tag{B.25}$$

and taking the scalar product of both sides of this with $\mathbf{e}_k$:

$$\mathbf{g}^i \cdot \mathbf{e}_k = \alpha_j^i \mathbf{e}^j \cdot \mathbf{e}_k = \alpha_j^i \delta_k^j = \alpha_k^i \tag{B.26}$$

where $\left(\mathbf{g}^i \cdot \mathbf{e}_k = \partial \xi^i/\partial x^k\right)$ from Equation (B.24) and:

$$\alpha_j^i = \frac{\partial \xi^i}{\partial x^j} \tag{B.27}$$

Finally, from Equation (B.25), one obtains:

$$\mathbf{g}^i = \frac{\partial \xi^i}{\partial x^j}\mathbf{e}^j \tag{B.28}$$

which is the same result as Equation (B.20).

The vector product $(\mathbf{g}_2 \times \mathbf{g}_3)$ has magnitude equal to the area of the rectangle[1] with sides $\mathbf{g}_2$ and $\mathbf{g}_3$, with direction $\hat{\mathbf{n}}$ normal to both $\mathbf{g}_2$ and $\mathbf{g}_3$. The scalar product $(\mathbf{g}_1 \cdot \hat{\mathbf{n}})$ is equivalent to a distance in the normal direction, thus the volume of the parallelepiped spanned by vectors $\mathbf{g}_1$, $\mathbf{g}_2$ and $\mathbf{g}_3$ is given by:

$$\Delta Vol = \mathbf{g}_1 \cdot (\mathbf{g}_2 \times \mathbf{g}_3) \tag{B.30}$$

The contravariant base vectors also satisfy:

$$\mathbf{g}^1 = \frac{1}{\Delta Vol}(\mathbf{g}_2 \times \mathbf{g}_3) \quad \mathbf{g}^2 = \frac{1}{\Delta Vol}(\mathbf{g}_3 \times \mathbf{g}_1) \quad \mathbf{g}^3 = \frac{1}{\Delta Vol}(\mathbf{g}_1 \times \mathbf{g}_2) \tag{B.31}$$

and similarly the covariant base vectors satisfy:

$$\mathbf{g}_1 = \frac{1}{\Delta Vol'}\left(\mathbf{g}^2 \times \mathbf{g}^3\right) \quad \mathbf{g}_2 = \frac{1}{\Delta Vol'}\left(\mathbf{g}^3 \times \mathbf{g}^1\right) \quad \mathbf{g}_3 = \frac{1}{\Delta Vol'}\left(\mathbf{g}^1 \times \mathbf{g}^2\right) \tag{B.32}$$

where $\Delta Vol' = \mathbf{g}^1 \cdot \left(\mathbf{g}^2 \times \mathbf{g}^3\right)$ represents the volume of the parallelepiped spanned by the contravariant base vectors $\mathbf{g}^1$, $\mathbf{g}^2$and $\mathbf{g}^3$.

It is useful to note at this point that the covariant and contravariant rectangular Cartesian base vectors are identical, $\mathbf{e}^m \equiv \mathbf{e}_m$. This is partly why covariant and contravariant tensors are not mentioned in most fluid mechanics text books which only deal with Cartesian tensors. The equivalence of covariant and contravariant Cartesian tensors is demonstrated by:

$$\mathbf{g}^1 = \frac{1}{\Delta Vol}(\mathbf{g}_2 \times \mathbf{g}_3) \tag{B.33}$$

which states that the contravariant $\mathbf{g}^1$ vector is perpendicular to the plane defined by the two covariant vectors, $\mathbf{g}_2$ and $\mathbf{g}_3$. In Cartesian coordinates there is no distinction between $\mathbf{g}^1$ and $\mathbf{g}_1$ since the $\hat{\mathbf{k}}$ vector is orthogonal to the plane defined by the $\hat{\mathbf{i}}$ and $\hat{\mathbf{j}}$ vectors (i.e. the $\mathbf{g}_1$ vector is perpendicular to the plane defined by $\mathbf{g}_2$ and $\mathbf{g}_3$).

[1]The vector product is defined as:

$$(\mathbf{g}_2 \times \mathbf{g}_3) = (|\mathbf{g}_2||\mathbf{g}_3|\sin\theta)\hat{\mathbf{n}} \tag{B.29}$$

where $\hat{\mathbf{n}}$ is the unit normal to vectors $\mathbf{g}_2$ and $\mathbf{g}_3$ and θ is the angle between the two $\mathbf{g}_2$ and $\mathbf{g}_3$ vectors. Since the area of a triangle with sides $\mathbf{g}_2$ and $\mathbf{g}_3$ is determined from $(1/2 \times base \times height)$ which is equivalent to $(1/2 \times |\mathbf{g}_2| \times |\mathbf{g}_3|\sin\theta)$, the magnitude of the cross product must be equal to the area of the rectangle with sides $\mathbf{g}_2$ and $\mathbf{g}_3$ (i.e. two triangles).

B.4 The Jacobian Matrix, $[J]$

It has previously been shown (Equations B.16 and B.28) that the covariant and contravariant base vectors, $\mathbf{g}_i$ and $\mathbf{g}^i$, can be expressed in terms of the Cartesian base vectors, $\mathbf{e}_j$ or $\mathbf{e}^j$, as follows:

$$\mathbf{g}_i = \frac{\partial x^j}{\partial \xi^i}\mathbf{e}_j \tag{B.34}$$

$$\mathbf{g}^i = \frac{\partial \xi^i}{\partial x^j}\mathbf{e}^j \tag{B.35}$$

The Jacobian matrix, $[J]$, is defined as the matrix of coefficients appearing in Equation (B.34):

$$[J] = \frac{\partial x^j}{\partial \xi^i} = \begin{bmatrix} x_\xi & x_\eta & x_\zeta \\ y_\xi & y_\eta & y_\zeta \\ z_\xi & z_\eta & z_\zeta \end{bmatrix} \tag{B.36}$$

where, for example, $x_\xi \equiv \partial x/\partial \xi$ and all components are contravariant, i.e.:

$$\begin{aligned} x &\equiv x^1 \\ y &\equiv x^2 \\ z &\equiv x^3 \\ \xi &\equiv \xi^1 \\ \eta &\equiv \xi^2 \\ \zeta &\equiv \xi^3 \end{aligned}$$

B.5 Determinant of the Jacobian Matrix, J

The Jacobian, J, is defined as the determinant of the Jacobian matrix:

$$J = \det[J] = x_\xi\left(y_\eta z_\zeta - y_\zeta z_\eta\right) - x_\eta\left(y_\xi z_\zeta - y_\zeta z_\xi\right) + x_\zeta\left(y_\xi z_\eta - y_\eta z_\xi\right) \tag{B.37}$$

It was noted earlier that the base vectors used to describe vector $\mathbf{r}$ in three-dimensional space should not be coplanar. It was also shown that the volume of the parallelepiped spanned by the base vectors $\mathbf{g}_1$, $\mathbf{g}_2$ and $\mathbf{g}_3$ is given by:

$$\Delta Vol = \mathbf{g}_1 \cdot (\mathbf{g}_2 \times \mathbf{g}_3) \tag{B.38}$$

Using Equation (B.16), the vector product of $\mathbf{g}_2$ and $\mathbf{g}_3$ at a point in space is given by:

$$\begin{aligned}\mathbf{g}_2 \times \mathbf{g}_3 &= \begin{vmatrix} \hat{\mathbf{i}} & \hat{\mathbf{j}} & \hat{\mathbf{k}} \\ x_\eta & y_\eta & z_\eta \\ x_\zeta & y_\zeta & z_\zeta \end{vmatrix} \\ &= \hat{\mathbf{i}}\left(y_\eta z_\zeta - z_\eta y_\zeta\right) - \hat{\mathbf{j}}\left(x_\eta z_\zeta - z_\eta x_\zeta\right) + \hat{\mathbf{k}}\left(x_\eta y_\zeta - y_\eta x_\zeta\right) \end{aligned} \tag{B.39}$$

and the volume is given by:

$$\begin{aligned}\Delta Vol &= \mathbf{g}_1 \cdot (\mathbf{g}_2 \times \mathbf{g}_3) \\ &= x_\xi\left(y_\eta z_\zeta - z_\eta y_\zeta\right) - y_\xi\left(x_\eta z_\zeta - z_\eta x_\zeta\right) + z_\xi\left(x_\eta y_\zeta - y_\eta x_\zeta\right) \end{aligned} \tag{B.40}$$

This can be rearranged to give:

$$\Delta Vol = x_\xi\left(y_\eta z_\zeta - y_\zeta z_\eta\right) - x_\eta\left(y_\xi z_\zeta - y_\zeta z_\xi\right) + x_\zeta\left(y_\xi z_\eta - y_\eta z_\xi\right) \tag{B.41}$$

Since Equations (B.37) and (B.41) are identical, the Jacobian, J, is equivalent to the cell volume, ΔVol. Therefore, if the three base vectors are non-coplanar, $J \neq 0$.

B.6 Inverse of the Jacobian Matrix, $[J]^{-1}$

Taking the scalar product of Equation (B.34) and (B.35):

$$\mathbf{g}_i \cdot \mathbf{g}^k = \frac{\partial x^j}{\partial \xi^i}\mathbf{e}_j \cdot \frac{\partial \xi^k}{\partial x^m}\mathbf{e}^m \tag{B.42}$$

and since $\left(\mathbf{g}_i \cdot \mathbf{g}^k = \delta_i^k\right)$ and $\left(\mathbf{e}_j \cdot \mathbf{e}^m = \delta_j^m\right)$:

$$\begin{aligned}\delta_i^k &= \frac{\partial x^j}{\partial \xi^i}\frac{\partial \xi^k}{\partial x^m}\delta_j^m \\ 1 &= \frac{\partial x^j}{\partial \xi^i}\frac{\partial \xi^i}{\partial x^j} \end{aligned} \tag{B.43}$$

Therefore, if the Jacobian matrix is represented by $\left(\partial x^j/\partial \xi^i\right)$ then the inverse of the Jacobian must be given by $\left(\partial \xi^i/\partial x^j\right)$.

The inverse of the Jacobian matrix is found from:

$$[J]^{-1} = \frac{\partial \xi^i}{\partial x^j} = \begin{bmatrix} \xi_x & \xi_y & \xi_z \\ \eta_x & \eta_y & \eta_z \\ \zeta_x & \zeta_y & \zeta_z \end{bmatrix} = \frac{1}{J}\left[\text{cof}\,(J)\right]^T \tag{B.44}$$

$$= \frac{1}{J}\begin{bmatrix} \left(y_\eta z_\zeta - y_\zeta z_\eta\right) & -\left(x_\eta z_\zeta - x_\zeta z_\eta\right) & \left(x_\eta y_\zeta - x_\zeta y_\eta\right) \\ -\left(y_\xi z_\zeta - y_\zeta z_\xi\right) & \left(x_\xi z_\zeta - x_\zeta z_\xi\right) & -\left(x_\xi y_\zeta - x_\zeta y_\xi\right) \\ \left(y_\xi z_\eta - y_\eta z_\xi\right) & -\left(x_\xi z_\eta - x_\eta z_\xi\right) & \left(x_\xi y_\eta - x_\eta y_\xi\right) \end{bmatrix} \tag{B.45}$$

where, from the definition of the inverse of a matrix, $\left[\text{cof}\,(J)\right]^T$ is the transpose of the matrix of cofactors of the Jacobian matrix (or adjoint matrix, adj $[J]$).

B.7 Covariant Metric Tensor, g_{ij}

The scalar product of vector $\mathbf{r} = \xi^j \mathbf{g}_j$ with covariant base vector $\mathbf{g}_i$ is as follows:

$$\mathbf{r} \cdot \mathbf{g}_i = \left(\xi^j \mathbf{g}_j\right) \cdot \mathbf{g}_i = \xi^j \left(\mathbf{g}_j \cdot \mathbf{g}_i\right) \tag{B.46}$$

The scalar product of two covariant base vectors $(\mathbf{g}_i \cdot \mathbf{g}_j)$ is termed the covariant "metric tensor", g_{ij}. Due to the symmetry of the scalar product, the metric tensor is symmetrical:

$$g_{ij} = \mathbf{g}_i \cdot \mathbf{g}_j = \mathbf{g}_j \cdot \mathbf{g}_i = g_{ji} \tag{B.47}$$

The action of the covariant metric tensor g_{ij} is often referred to as "lowering the index", where scaling a contravariant component ξ^j with the metric tensor g_{ij} effectively lowers the index to give a covariant component ξ_i:

$$\xi_i = g_{ij}\xi^j \tag{B.48}$$

The above equation can be derived by considering the scalar product of vector $\mathbf{r}$ and $\mathbf{g}_i$, assuming the vector $\mathbf{r}$ to be given by $\xi_j \mathbf{g}^j$:

$$\mathbf{r} \cdot \mathbf{g}_i = \left(\xi_j \mathbf{g}^j\right) \cdot \mathbf{g}_i = \xi_j \delta_i^j = \xi_i \tag{B.49}$$

which is equivalent to Equation (B.46):

$$\mathbf{r} \cdot \mathbf{g}_i = \xi^j g_{ij} \tag{B.50}$$

Using Equation (B.34), the metric tensor can be written:

$$g_{ij} = \mathbf{g}_i \cdot \mathbf{g}_j = \frac{\partial x^k}{\partial \xi^i}\mathbf{e}_k \cdot \frac{\partial x^m}{\partial \xi^j}\mathbf{e}_m \tag{B.51}$$

and, since $\mathbf{e}_k$ and $\mathbf{e}_m$ are Cartesian base vectors ($\mathbf{e}_k \cdot \mathbf{e}_m = \delta_{km}$):

$$\begin{aligned} g_{ij} &= \frac{\partial x^k}{\partial \xi^i}\frac{\partial x^m}{\partial \xi^j}\delta_{km} \\ &= \sum_{k=1}^{3}\frac{\partial x^k}{\partial \xi^i}\frac{\partial x^k}{\partial \xi^j} \\ &= \frac{\partial x}{\partial \xi^i}\frac{\partial x}{\partial \xi^j} + \frac{\partial y}{\partial \xi^i}\frac{\partial y}{\partial \xi^j} + \frac{\partial z}{\partial \xi^i}\frac{\partial z}{\partial \xi^j} \end{aligned} \tag{B.52}$$

Using this definition of the covariant metric tensor, and Equation (B.28), one can also show that g_{ij} is capable of lowering the index of a vector. The product of the metric g_{ij} and the contravariant base vector $\mathbf{g}^j$ can be expanded as follows:

$$g_{ij}\mathbf{g}^j = \left(\frac{\partial x^k}{\partial \xi^i}\frac{\partial x^k}{\partial \xi^j}\right)\left(\frac{\partial \xi^j}{\partial x^m}\mathbf{e}^m\right) \tag{B.53}$$

Simplifying, using the chain-rule:

$$\begin{aligned} g_{ij}\mathbf{g}^j &= \frac{\partial x^k}{\partial \xi^i}\frac{\partial x^k}{\partial x^m}\mathbf{e}^m \\ &= \frac{\partial x^k}{\partial \xi^i}\delta^k_m\mathbf{e}^m \end{aligned} \tag{B.54}$$

and, since the covariant and contravariant rectangular Cartesian base vectors are identical, $\mathbf{e}^m = \mathbf{e}_m$, then from Equation (B.16):

$$g_{ij}\mathbf{g}^j = \frac{\partial x^k}{\partial \xi^i}\mathbf{e}_k = \mathbf{g}_i \tag{B.55}$$

B.8 Determinant of the Covariant Metric Tensor Matrix, g

Using Equation (B.52), the covariant metric tensor matrix can be written:

$$\begin{aligned} [g_{ij}] &= \begin{bmatrix} g_{11} & g_{12} & g_{13} \\ g_{21} & g_{22} & g_{23} \\ g_{31} & g_{32} & g_{33} \end{bmatrix} \\ &= \begin{bmatrix} (x_\xi x_\xi + y_\xi y_\xi + z_\xi z_\xi) & (x_\xi x_\eta + y_\xi y_\eta + z_\xi z_\eta) & (x_\xi x_\zeta + y_\xi y_\zeta + z_\xi z_\zeta) \\ (x_\eta x_\xi + y_\eta y_\xi + z_\eta z_\xi) & (x_\eta x_\eta + y_\eta y_\eta + z_\eta z_\eta) & (x_\eta x_\zeta + y_\eta y_\zeta + z_\eta z_\zeta) \\ (x_\zeta x_\xi + y_\zeta y_\xi + z_\zeta z_\xi) & (x_\zeta x_\eta + y_\zeta y_\eta + z_\zeta z_\eta) & (x_\zeta x_\zeta + y_\zeta y_\zeta + z_\zeta z_\zeta) \end{bmatrix} \end{aligned} \tag{B.56}$$

This is equivalent to the product of the Jacobian matrix and the transpose of the Jacobian matrix:

$$\begin{aligned}
[g_{ij}] &= [J]^T [J] \\
&= \begin{bmatrix} x_\xi & x_\eta & x_\zeta \\ y_\xi & y_\eta & y_\zeta \\ z_\xi & z_\eta & z_\zeta \end{bmatrix}^T \begin{bmatrix} x_\xi & x_\eta & x_\zeta \\ y_\xi & y_\eta & y_\zeta \\ z_\xi & z_\eta & z_\zeta \end{bmatrix} \\
&= \begin{bmatrix} x_\xi & y_\xi & z_\xi \\ x_\eta & y_\eta & z_\eta \\ x_\zeta & y_\zeta & z_\zeta \end{bmatrix} \begin{bmatrix} x_\xi & x_\eta & x_\zeta \\ y_\xi & y_\eta & y_\zeta \\ z_\xi & z_\eta & z_\zeta \end{bmatrix}
\end{aligned} \tag{B.57}$$

Using g to denote the determinant of matrix $[g_{ij}]$ one therefore finds that:

$$g = \det(g_{ij}) = \det\left([J]^T [J]\right) = \det[J] \det[J] = J^2 \tag{B.58}$$

where the determinant of a matrix is identical to the determinant of the transpose of the matrix $\left(\det[J] \equiv \det[J]^T\right)$. The above equation can also be written:

$$J = \sqrt{g} \tag{B.59}$$

B.9 Contravariant Metric Tensor, g^{ij}

Following a similar approach to that adopted in Section B.7, one can take the scalar product of vector $\mathbf{r}$ and contravariant base vector $\mathbf{g}^i$, as follows:

$$\mathbf{r} \cdot \mathbf{g}^i = \left(\xi_j \mathbf{g}^j\right) \cdot \mathbf{g}^i = \xi_j \left(\mathbf{g}^j \cdot \mathbf{g}^i\right) = \xi_j g^{ij} \tag{B.60}$$

where g^{ij} is the contravariant metric tensor. Since the scalar product $\mathbf{r} \cdot \mathbf{g}^i$ can also be written:

$$\mathbf{r} \cdot \mathbf{g}^i = \xi^j \mathbf{g}_j \cdot \mathbf{g}^i = \xi^j \delta^i_j = \xi^i \tag{B.61}$$

the actions of the contravariant metric tensor, g^{ij}, is often referred to as "raising the index":

$$\xi^i = g^{ij} \xi_j \tag{B.62}$$

where ξ_j and ξ^i are covariant and contravariant components, respectively.

One can show that the product of the covariant and contravariant metric tensors, g_{ik} and g^{jk}, gives the Kronecker delta, δ^j_i, as follows:

$$g_{ik} g^{jk} = (\mathbf{g}_i \cdot \mathbf{g}_k) \left(\mathbf{g}^j \cdot \mathbf{g}^k\right) \tag{B.63}$$

Using the definition:

$$\mathbf{g}_k = \frac{\partial \mathbf{r}}{\partial \xi^k} = \frac{\partial x^m}{\partial \xi^k}\mathbf{e}_m \tag{B.64}$$

and from Equation (B.28):

$$\mathbf{g}^k = \frac{\partial \xi^k}{\partial x^n}\mathbf{e}^n \tag{B.65}$$

one can write the product as:

$$g_{ik}g^{jk} = \left(\frac{\partial x^m}{\partial \xi^i}\frac{\partial x^m}{\partial \xi^k}\right)\left(\frac{\partial \xi^j}{\partial x^n}\frac{\partial \xi^k}{\partial x^n}\right) \tag{B.66}$$

Rearranging these terms:

$$g_{ik}g^{jk} = \left(\frac{\partial x^m}{\partial \xi^i}\frac{\partial \xi^j}{\partial x^n}\right)\left(\frac{\partial x^m}{\partial \xi^k}\frac{\partial \xi^k}{\partial x^n}\right) \tag{B.67}$$

and applying the chain-rule, one obtains:

$$\begin{aligned} g_{ik}g^{jk} &= \left(\frac{\partial x^m}{\partial \xi^i}\frac{\partial \xi^j}{\partial x^n}\right)\left(\frac{\partial x^m}{\partial x^n}\right) \\ &= \left(\frac{\partial x^m}{\partial \xi^i}\frac{\partial \xi^j}{\partial x^n}\right)\delta_n^m \end{aligned} \tag{B.68}$$

Using the substitution operator properties of δ_n^m and applying once more the chain-rule:

$$\begin{aligned} g_{ik}g^{jk} &= \left(\frac{\partial x^m}{\partial \xi^i}\frac{\partial \xi^j}{\partial x^m}\right) \\ &= \frac{\partial \xi^j}{\partial \xi^i} \end{aligned} \tag{B.69}$$

From the definition of the contravariant metric base vector, $\mathbf{g}_i \cdot \mathbf{g}^j = \delta_i^j$, one obtains:

$$\mathbf{g}_i \cdot \mathbf{g}^j = \frac{\partial x^k}{\partial \xi^i}\mathbf{e}_k \cdot \frac{\partial \xi^j}{\partial x^m}\mathbf{e}^m = \frac{\partial x^k}{\partial \xi^i}\frac{\partial \xi^j}{\partial x^m}\delta_k^m = \frac{\partial \xi^j}{\partial \xi^i} = \delta_i^j \tag{B.70}$$

and therefore:

$$g_{ik}g^{jk} = \delta_i^j \tag{B.71}$$

The matrix of the contravariant metric tensor, g^{ij}, is therefore the inverse of the covariant metric tensor, g_{ij}, or in terms of matrix manipulation:

$$g^{ij} = \frac{1}{g}G_{ij} \tag{B.72}$$

where g is the determinant and the and G_{ij} is the adjoint of the g_{ij} matrix, given by:

$$\begin{aligned} G_{ij} &= [\text{cof}\,(g_{ij})]^T \\ &= \begin{bmatrix} (g_{22}g_{33}-g_{23}g_{32}) & -(g_{12}g_{33}-g_{13}g_{32}) & (g_{12}g_{23}-g_{13}g_{22}) \\ -(g_{21}g_{33}-g_{23}g_{31}) & (g_{11}g_{33}-g_{13}g_{31}) & -(g_{11}g_{23}-g_{13}g_{21}) \\ (g_{21}g_{32}-g_{22}g_{31}) & -(g_{11}g_{32}-g_{12}g_{31}) & (g_{11}g_{22}-g_{12}g_{21}) \end{bmatrix} \end{aligned} \tag{B.73}$$

Since the metric tensor is symmetric ($g_{ij} = g_{ji}$), the adjoint and the matrix of cofactors of the g_{ij} matrix are equivalent, i.e. $[\text{cof}\,(g_{ij})]^T = \text{cof}\,(g_{ij})$.

B.10 Second Order Tensors, T

Second order tensors are represented in general coordinates as follows:

$$\mathbf{T} = T^{ij}\mathbf{g}_i \otimes \mathbf{g}_j = T_{ij}\mathbf{g}^i \otimes \mathbf{g}^j \tag{B.74}$$

where $\mathbf{g}_i \otimes \mathbf{g}_j$ and $\mathbf{g}^i \otimes \mathbf{g}^j$ are, respectively, the tensor product (or dyadic) of the covariant and contravariant base vectors, and T^{ij} and T_{ij} are, respectively, the contravariant and covariant tensor components.

B.11 Christoffel Symbols of the First Kind, Γ_{ijk}

Since the base vectors are generally not constant except in the case of the Cartesian coordinate system, the derivatives of the base vectors also form vectors which characterize the curvature of the curvilinear coordinate system. The vector $\partial\mathbf{g}_i/\partial\xi^j$ is expressed as a linear combination of the contravariant base vectors as follows:

$$\frac{\partial \mathbf{g}_i}{\partial \xi^j} = \Gamma_{ij1}\mathbf{g}^1 + \Gamma_{ij2}\mathbf{g}^2 + \Gamma_{ij3}\mathbf{g}^3 = \Gamma_{ijk}\mathbf{g}^k \tag{B.75}$$

where Γ_{ijk} are the "Christoffel symbols of the first kind". Equation (B.75) can be rearranged to give:

$$\Gamma_{ijk} = \frac{\partial \mathbf{g}_i}{\partial \xi^j} \cdot \mathbf{g}_k \tag{B.76}$$

If the base vector is given by:

$$\mathbf{g}_i = \frac{\partial \mathbf{r}}{\partial \xi^i} \tag{B.77}$$

then:

$$\frac{\partial \mathbf{g}_i}{\partial \xi^j} = \frac{\partial^2 \mathbf{r}}{\partial \xi^i \partial \xi^j} = \frac{\partial^2 \mathbf{r}}{\partial \xi^j \partial \xi^i} \tag{B.78}$$

and hence the i and j subscripts of the Christoffel symbol of the first kind, Γ_{ijk}, are interchangeable:

$$\Gamma_{ijk} = \Gamma_{jik} \tag{B.79}$$

Differentiating the covariant metric tensor, g_{ij}, using the product rule and Equations (B.47) and (B.76), gives:

$$\frac{\partial g_{ij}}{\partial \xi^k} = \mathbf{g}_i \cdot \frac{\partial \mathbf{g}_j}{\partial \xi^k} + \frac{\partial \mathbf{g}_i}{\partial \xi^k} \cdot \mathbf{g}_j = \Gamma_{jki} + \Gamma_{ikj} \tag{B.80}$$

Since i, j and k are free indices, one can also write this as:

$$\frac{\partial g_{jk}}{\partial \xi^i} = \Gamma_{kij} + \Gamma_{jik} \tag{B.81}$$

$$\frac{\partial g_{ik}}{\partial \xi^j} = \Gamma_{kji} + \Gamma_{ijk} \tag{B.82}$$

Adding the two equations above, one obtains:

$$2\Gamma_{ijk} + \Gamma_{ikj} + \Gamma_{jki} = \frac{\partial g_{jk}}{\partial \xi^i} + \frac{\partial g_{ik}}{\partial \xi^j} \tag{B.83}$$

and, rearranging this, using Equation (B.80):

$$\Gamma_{ijk} = \frac{1}{2}\left(\frac{\partial g_{jk}}{\partial \xi^i} + \frac{\partial g_{ik}}{\partial \xi^j} - \frac{\partial g_{ij}}{\partial \xi^k}\right) \tag{B.84}$$

The above equation expresses the Christoffel symbol of the first kind as a function of the derivatives of the metric tensor.

B.12 Christoffel Symbols of the Second Kind, Γ^k_{ij}

The vector $\partial \mathbf{g}_i / \partial \xi^j$ can also be expressed as a linear combination of the covariant base vectors as follows:

$$\frac{\partial \mathbf{g}_i}{\partial \xi^j} = \Gamma^1_{ij}\mathbf{g}_1 + \Gamma^2_{ij}\mathbf{g}_2 + \Gamma^3_{ij}\mathbf{g}_3 = \Gamma^k_{ij}\mathbf{g}_k \tag{B.85}$$

where the coefficients, Γ^k_{ij}, are the "Christoffel symbols of the second kind"[2]. Equation (B.85) can be rearranged in terms of the Christoffel symbol:

$$\Gamma^k_{ij} = \frac{\partial \mathbf{g}_i}{\partial \xi^j} \cdot \mathbf{g}^k \tag{B.86}$$

Following a similar method to that used above to derive Equation (B.79), it can be shown that the subscripts of the Christoffel symbol of the second kind are interchangeable, i.e.:

$$\Gamma^k_{ij} = \Gamma^k_{ji} \tag{B.87}$$

[2] In some texts, the Christoffel symbol of the second kind is written:

$$\Gamma^k_{ij} \equiv \left\{ \begin{array}{cc} & k \\ i & \\ & j \end{array} \right\}$$

Using the product rule to differentiating Equation (B.17), one obtains:

$$\frac{\partial \mathbf{g}_i}{\partial \xi^k} \cdot \mathbf{g}^j + \mathbf{g}_i \cdot \frac{\partial \mathbf{g}^j}{\partial \xi^k} = 0 \tag{B.88}$$

and hence from the definition of the Christoffel symbol of the second kind, Equation (B.86):

$$\Gamma^j_{ik} = -\frac{\partial \mathbf{g}^j}{\partial \xi^k} \cdot \mathbf{g}_i \tag{B.89}$$

Previously it was described how the covariant metric tensor, g_{ij}, can lower the index of a tensor. The raised index of the Christoffel symbol of the second kind can also be lowered by the covariant metric tensor, as follows:

$$\Gamma^k_{ij} g_{km} = \frac{\partial \mathbf{g}_i}{\partial \xi^j} \cdot \mathbf{g}^k g_{km} \tag{B.90}$$

From Equation (B.55):

$$\Gamma^k_{ij} g_{km} = \frac{\partial \mathbf{g}_i}{\partial \xi^j} \cdot \mathbf{g}_m \tag{B.91}$$

and from the definition of the Christoffel symbol of the first kind (Equation B.76):

$$\Gamma^k_{ij} g_{km} = \Gamma_{ijm} \tag{B.92}$$

Christoffel symbols of the second kind can therefore be calculated from the metric tensors, using Equation (B.84), as follows:

$$\Gamma^k_{ij} = \frac{1}{2} g^{kl} \left(\frac{\partial g_{jl}}{\partial \xi^i} + \frac{\partial g_{il}}{\partial \xi^j} - \frac{\partial g_{ij}}{\partial \xi^l} \right) \tag{B.93}$$

If this expression is contracted, by setting $k = i$, and has its dummy indices i and l switched around in the last term, one obtains:

$$\begin{aligned} \Gamma^i_{ij} &= \frac{1}{2} g^{il} \frac{\partial g_{jl}}{\partial \xi^i} + \frac{1}{2} g^{il} \frac{\partial g_{il}}{\partial \xi^j} - \frac{1}{2} g^{li} \frac{\partial g_{lj}}{\partial \xi^i} \\ &= \frac{1}{2} g^{il} \frac{\partial g_{il}}{\partial \xi^j} \end{aligned} \tag{B.94}$$

where the first and last terms cancel since the metric tensor is symmetric ($g^{il} = g^{li}$ and $g_{jl} = g_{lj}$).

It is also possible to express Equation (B.94) in terms of the Jacobian J of the metric tensor. The determinant of the metric tensor matrix $[g_{ij}]$ is given by:

$$\det[g_{ij}] = g = g_{11}G_{11} + g_{12}G_{12} + g_{13}G_{13} = g_{11}G_{11} + g_{21}G_{21} + g_{31}G_{31} \tag{B.95}$$

where G_{ij} is the cofactor matrix. Assuming that the determinant g is a function of the nine components

of g_{ij}, one can obtain the following partial derivatives:

$$\frac{\partial g}{\partial g_{ij}} = G_{ij} \tag{B.96}$$

Using the definition of the inverse of a matrix, Equation (B.72), the above expression can be written:

$$\frac{\partial g}{\partial g_{ij}} = g g^{ij} \tag{B.97}$$

where g and g^{ij} are, respectively, the determinant and the inverse of the matrix of g_{ij}. Since the metric tensor is symmetric, the transpose of the metric tensor $\left(g^{ij}\right)^T = g^{ij}$. The term gg^{ij} therefore represents the matrix of cofactors $\left(gg^{ij} = G_{ij}\right)$. The derivative of the determinant, g, with respect to the curvilinear coordinates can be written, using the chain rule:

$$\frac{\partial g}{\partial \xi^j} = \frac{\partial g}{\partial g_{il}} \frac{\partial g_{il}}{\partial \xi^j} \tag{B.98}$$

and substituting Equation (B.97):

$$\frac{\partial g}{\partial \xi^j} = g g^{il} \frac{\partial g_{il}}{\partial \xi^j} \tag{B.99}$$

Equation (B.94) can therefore be written:

$$\Gamma^i_{ij} = \frac{1}{2} g^{il} \frac{\partial g_{il}}{\partial \xi^j} = \frac{1}{2} \frac{1}{g} \frac{\partial g}{\partial \xi^j} \tag{B.100}$$

By treating the derivative in Equation (B.100) as a "function of a function" and using the definition of the Jacobian $\left(J^2 = g\right)$, the Christoffel can be expressed as:

$$\Gamma^i_{ij} = \frac{1}{J} \frac{\partial J}{\partial \xi^j} = \frac{\partial}{\partial \xi^j} \left(\log J\right) \tag{B.101}$$

In Cartesian coordinates the base vectors do not vary with position and therefore all components of the Christoffel symbols are zero. It follows then that the Christoffel symbols do not constitute third-order tensors since, if the Christoffel symbols transformed like tensors, their components would remain zero with respect to any coordinate system, which is not the case.

B.13 Gradient of a Scalar, $\nabla\phi$

The gradient of scalar, ϕ, is written in curvilinear coordinates:

$$\nabla\phi \;=\; \mathbf{g}^j \frac{\partial \phi}{\partial \xi^j} \tag{B.102}$$

The contravariant base vector, $\mathbf{g}^j$, can also be written $g^{jk}\mathbf{g}_k$, using the "raising of the index" property of the contravariant metric, g^{jk}. Therefore, the gradient of the scalar can also be written:

$$\nabla\phi = \frac{\partial\phi}{\partial\xi^j}g^{jk}\mathbf{g}_k \tag{B.103}$$

B.14 Covariant Derivatives of Vectors and Tensors

The covariant derivative of a vector $\left(\mathbf{v} = v^i\mathbf{g}_i\right)$ can be written, using the product rule:

$$\begin{aligned}\frac{\partial\mathbf{v}}{\partial\xi^j} &= \frac{\partial\left(v^i\mathbf{g}_i\right)}{\partial\xi^j} \\ &= \frac{\partial v^i}{\partial\xi^j}\mathbf{g}_i + v^i\frac{\partial\mathbf{g}_i}{\partial\xi^j}\end{aligned} \tag{B.104}$$

and from the definition of the Christoffel symbol (Equation B.86):

$$\begin{aligned}\frac{\partial\mathbf{v}}{\partial\xi^j} &= \frac{\partial v^i}{\partial\xi^j}\mathbf{g}_i + v^i\frac{\partial\mathbf{g}_i}{\partial\xi^j} \\ &= \frac{\partial v^i}{\partial\xi^j}\mathbf{g}_i + v^i\Gamma^k_{ij}\mathbf{g}_k\end{aligned} \tag{B.105}$$

The above derivative is often denoted:

$$\frac{\partial\mathbf{v}}{\partial\xi^j} = \nabla_j v^i\mathbf{g}_i \tag{B.106}$$

or simply:

$$\frac{\partial\mathbf{v}}{\partial\xi^j} = v^i_{,j}\mathbf{g}_i \tag{B.107}$$

where:

$$\nabla_j v^i = v^i_{,j} = \left(\frac{\partial v^i}{\partial\xi^j} + v^k\Gamma^i_{kj}\right) \tag{B.108}$$

The covariant derivative of a second-order tensor $\left(\mathbf{T} = T^{ij}\mathbf{g}_i\otimes\mathbf{g}_j\right)$ is similarly given by:

$$\begin{aligned}\frac{\partial\mathbf{T}}{\partial\xi^k} &= \frac{\partial T^{ij}}{\partial\xi^k}\mathbf{g}_i\otimes\mathbf{g}_j + T^{ij}\frac{\partial\mathbf{g}_i}{\partial\xi^k}\otimes\mathbf{g}_j + T^{ij}\mathbf{g}_i\otimes\frac{\partial\mathbf{g}_j}{\partial\xi^k} \\ &= \frac{\partial T^{ij}}{\partial\xi^k}\mathbf{g}_i\otimes\mathbf{g}_j + T^{ij}\Gamma^m_{ik}\mathbf{g}_m\otimes\mathbf{g}_j + T^{ij}\mathbf{g}_i\otimes\Gamma^m_{jk}\mathbf{g}_m \\ &= \left(\frac{\partial T^{ij}}{\partial\xi^k} + T^{mj}\Gamma^i_{mk} + T^{im}\Gamma^j_{mk}\right)\mathbf{g}_i\otimes\mathbf{g}_j\end{aligned} \tag{B.109}$$

This is often denoted:

$$\frac{\partial\mathbf{T}}{\partial\xi^k} = \nabla_k T^{ij}\mathbf{g}_i\otimes\mathbf{g}_j \tag{B.110}$$

or:

$$\frac{\partial \mathbf{T}}{\partial \xi^k} = T^{ij}_{,k} \mathbf{g}_i \otimes \mathbf{g}_j \tag{B.111}$$

An alternative approach to obtaining the covariant derivative of a second-order tensor is to compare the covariant derivative a scalar which is created from a tensor invariant with the set of its partial derivatives. For example, to find an expression for the covariant derivative of the covariant tensor T_{ij}, if one considers first the covariant derivative of scalar $\left(T_{ij}u^i v^j\right)$:

$$\left(T_{ij}u^i v^j\right)_{,k} = T_{ij,k}u^i v^i + T_{ij}\left(\frac{\partial u^i}{\partial \xi^k} + \Gamma^i_{km}u^m\right)v^j + T_{ij}u^i\left(\frac{\partial v^j}{\partial \xi^k} + \Gamma^j_{km}v^m\right) \tag{B.112}$$

The partial derivatives of $\left(T_{ij}u^i v^j\right)$ are given by:

$$\frac{\partial}{\partial \xi^k}\left(T_{ij}u^i v^j\right) = \frac{\partial T_{ij}}{\partial \xi^k}u^i v^j + T_{ij}\frac{\partial u^i}{\partial \xi^k}v^j + T_{ij}u^i\frac{\partial v^j}{\partial \xi^k} \tag{B.113}$$

For a scalar, the above covariant derivative and the set of partial derivatives are identical. Therefore, canceling terms and rearranging:

$$\left(T_{ij,k} + \Gamma^m_{ik}T_{mj} + \Gamma^m_{jk}T_{im} - \frac{\partial T_{ij}}{\partial \xi^k}\right)u^i v^j = 0 \tag{B.114}$$

Finally, canceling the arbitrary terms u^i and v^j and rearranging once more, one obtains:

$$T_{ij,k} = \frac{\partial T_{ij}}{\partial \xi^k} - \Gamma^m_{ik}T_{mj} - \Gamma^m_{jk}T_{im} \tag{B.115}$$

B.15 Covariant Derivative of the Metric Tensor

The covariant derivative of the Kronecker delta $\left(\delta_{ij,k}\right)$ is zero. Since δ_{ij} is equivalent to the metric tensor, g_{ij}, in Cartesian coordinates, the covariant derivative of the metric tensor must also be zero:

$$g_{ij,k} = 0 \tag{B.116}$$

This result can be confirmed using the above expression for the covariant derivative of a second-order tensor (Equation B.115):

$$g_{ij,k} = \frac{\partial g_{ij}}{\partial \xi^k} - \Gamma^m_{ik}g_{mj} - \Gamma^m_{jk}g_{im} \tag{B.117}$$

which can also be written using Equation (B.92):

$$g_{ij,k} = \frac{\partial g_{ij}}{\partial \xi^k} - \Gamma_{ikj} - \Gamma_{jki} \tag{B.118}$$

Earlier it was shown that the derivative of the covariant metric tensor g_{ij} with respect to ξ^k is as follows:

$$\begin{aligned} \frac{\partial g_{ij}}{\partial \xi^k} &= \mathbf{g}_i \cdot \frac{\partial \mathbf{g}_j}{\partial \xi^k} + \frac{\partial \mathbf{g}_i}{\partial \xi^k} \cdot \mathbf{g}_j \\ &= \Gamma_{jki} + \Gamma_{ikj} \end{aligned} \tag{B.119}$$

Substituting this expression into Equation (B.118), one obtains:

$$g_{ij,k} = \Gamma_{jki} + \Gamma_{ikj} - \Gamma_{ikj} - \Gamma_{jki} = 0 \tag{B.120}$$

For the special case where $i = j$ one can also write:

$$g_{ii,k} = \frac{\partial g_{ii}}{\partial \xi^k} - 2\Gamma^m_{ik} g_{im} = 0 \tag{B.121}$$

where, following the summation convention, there is no summation on i.

One can also show that $g^{ij}_{,k} = 0$, following the same method as described above. The covariant derivative of g^{ij} is expanded:

$$g^{ij}_{,k} = \frac{\partial g^{ij}}{\partial \xi^k} + g^{mj}\Gamma^i_{mk} + g^{im}\Gamma^j_{mk} \tag{B.122}$$

and the set of partial derivatives of g^{ij} :

$$\frac{\partial g^{ij}}{\partial \xi^k} = \mathbf{g}^i \cdot \frac{\partial \mathbf{g}^j}{\partial \xi^k} + \mathbf{g}^j \cdot \frac{\partial \mathbf{g}^i}{\partial \xi^k} \tag{B.123}$$

Using Equation (B.89), the partial derivatives can be expressed in terms of Christoffel symbols of the second kind, as follows:

$$\begin{aligned} \frac{\partial g^{ij}}{\partial \xi^k} &= -\mathbf{g}^i \cdot \mathbf{g}^m \Gamma^j_{mk} - \mathbf{g}^j \cdot \mathbf{g}^m \Gamma^i_{mk} \\ &= -g^{im}\Gamma^j_{mk} - g^{jm}\Gamma^i_{mk} \end{aligned} \tag{B.124}$$

Finally, substituting Equation (B.124) into (B.122):

$$g^{ij}_{,k} = g^{mj}\Gamma^i_{mk} + g^{im}\Gamma^j_{mk} - g^{im}\Gamma^j_{mk} - g^{jm}\Gamma^i_{mk} = 0 \tag{B.125}$$

B.16 Gradient of a Vector, $\nabla \mathbf{v}$

The gradient of a vector, $\mathbf{v}$, is written:

$$\text{grad}\,\mathbf{v} = \nabla \mathbf{v} = \mathbf{g}^j \frac{\partial \mathbf{v}}{\partial \xi^j} \tag{B.126}$$

Expanding the derivative term using Equation (B.108):

$$\nabla \mathbf{v} = \left(\frac{\partial v^i}{\partial \xi^j} + v^k \Gamma^i_{kj} \right) \mathbf{g}_i \otimes \mathbf{g}^j \tag{B.127}$$

and using the contravariant metric tensor, g^{jm}, to write the gradient in terms of two covariant base vectors, one obtains:

$$\nabla \mathbf{v} = \left(\frac{\partial v^i}{\partial \xi^j} + v^k \Gamma^i_{kj} \right) g^{jm} \mathbf{g}_i \otimes \mathbf{g}_m \tag{B.128}$$

B.17 Divergence of a Vector, $\nabla \cdot \mathbf{v}$

The divergence of a vector $\mathbf{v}$ is the derivative of the components of vector $\mathbf{v}$ in each of the respective component directions. This is calculated from the scalar (or inner) product of the *grad* operator (∇) and the vector $\mathbf{v}$, which can be expressed as:

$$\mathrm{div}\, \mathbf{v} = \nabla \cdot \mathbf{v} = \mathbf{g}^j \cdot \frac{\partial \mathbf{v}}{\partial \xi^j} = \mathbf{g}^j \cdot \mathbf{v}_{,j} \tag{B.129}$$

Since $\nabla \cdot \mathbf{v}$ consists of a scalar product between two vectors, the resulting expression is a scalar quantity. In Cartesian coordinates, where $\mathbf{v} = u^i \mathbf{e}_i$, the divergence is simply:

$$\begin{aligned} \nabla \cdot \mathbf{v} &= \mathbf{e}^j \cdot \frac{\partial \left(u^i \mathbf{e}_i \right)}{\partial x^j} \\ &= \mathbf{e}^j \cdot \left(\mathbf{e}_i \frac{\partial u^i}{\partial x^j} + u^i \frac{\partial \mathbf{e}_i}{\partial x^j} \right) \\ &= \delta^j_i \frac{\partial u^i}{\partial x^j} \\ &= \frac{\partial u^i}{\partial x^i} = \frac{\partial u}{\partial x} + \frac{\partial v}{\partial y} + \frac{\partial w}{\partial z} \end{aligned} \tag{B.130}$$

where the derivative $\partial \mathbf{e}_i / \partial x^j$ is zero, since the Cartesian base vectors do not vary with position.

In general non-orthogonal curvilinear coordinates, where $\mathbf{v} = v^i \mathbf{g}_i$, the divergence is given by (see also Section B.14):

$$\begin{aligned} \nabla \cdot \mathbf{v} &= \mathbf{g}^j \cdot \frac{\partial \left(v^i \mathbf{g}_i \right)}{\partial \xi^j} \\ &= \mathbf{g}^j \cdot \left(\frac{\partial v^i}{\partial \xi^j} \mathbf{g}_i + v^i \Gamma^k_{ij} \mathbf{g}_k \right) \\ &= \delta^j_i \frac{\partial v^i}{\partial \xi^j} + \delta^j_k v^i \Gamma^k_{ij} \\ &= \frac{\partial v^j}{\partial \xi^j} + v^k \Gamma^j_{kj} \end{aligned} \tag{B.131}$$

Using Equation (B.101) this becomes:

$$\nabla \cdot \mathbf{v} = \frac{\partial v^j}{\partial \xi^j} + \frac{v^j}{J}\frac{\partial J}{\partial \xi^j} \tag{B.132}$$

and applying the product rule:

$$\nabla \cdot \mathbf{v} = \frac{\Delta v^j}{\Delta \xi^j} = \frac{1}{J}\frac{\partial}{\partial \xi^j}\left(J v^j\right) \tag{B.133}$$

B.18 Divergence of a Tensor, $\nabla \cdot \mathbf{T}$

The divergence of the second-order tensor $\mathbf{T}$, where $\mathbf{T} = T^{ij}\mathbf{g}_i \otimes \mathbf{g}_j$, can be written as follows:

$$\operatorname{div}\mathbf{T} = \nabla \cdot \mathbf{T} = \mathbf{g}^k \cdot \frac{\partial \mathbf{T}}{\partial \xi^k} = \mathbf{g}^k \cdot \mathbf{T}_{,k} \tag{B.134}$$

From Equation (B.109), this can be expanded:

$$\nabla \cdot \mathbf{T} = \mathbf{g}^k \cdot \left(\frac{\partial T^{ij}}{\partial \xi^k} + T^{mj}\Gamma^i_{mk} + T^{im}\Gamma^j_{mk}\right)\mathbf{g}_i \otimes \mathbf{g}_j \tag{B.135}$$

$$= \delta^k_j\left(\frac{\partial T^{ij}}{\partial \xi^k} + T^{mj}\Gamma^i_{mk} + T^{im}\Gamma^j_{mk}\right)\mathbf{g}_i \tag{B.136}$$

$$= \left(\frac{\partial T^{ij}}{\partial \xi^j} + T^{mj}\Gamma^i_{mj} + T^{im}\Gamma^j_{mj}\right)\mathbf{g}_i \tag{B.137}$$

and simplified, using Equation (B.101):

$$\nabla \cdot \mathbf{T} = \left(\frac{\partial T^{ij}}{\partial \xi^j} + T^{mj}\Gamma^i_{mj} + \frac{T^{ij}}{J}\frac{\partial J}{\partial \xi^j}\right)\mathbf{g}_i \tag{B.138}$$

$$= \left[\frac{1}{J}\frac{\partial}{\partial \xi^j}\left(JT^{ij}\right) + T^{mj}\Gamma^i_{mj}\right]\mathbf{g}_i \tag{B.139}$$

$$= \left(\frac{\Delta T^{ij}}{\Delta \xi^j} + T^{mj}\Gamma^i_{mj}\right)\mathbf{g}_i \tag{B.140}$$

$$= \nabla_j T^{ij}\mathbf{g}_i \tag{B.141}$$

Note that the divergence of a second-order tensor results in a vector quantity. In going from Equation (B.135) to Equation (B.136) the base vectors $\mathbf{g}^k$ and $\mathbf{g}_i$ were combined into the Kronecker delta $\left(\mathbf{g}^k \cdot \mathbf{g}_i = \delta^k_i\right)$. One could equally have combined $\mathbf{g}^k$ and $\mathbf{g}_j$ which would give exactly the same result with different dummy indices.

B.19 Summation Convention

It was shown earlier that the divergence of a vector, **v**, is given by:

$$\nabla \cdot \mathbf{v} = v^j_{,j} = \frac{\partial v^j}{\partial \xi^j} + v^k \Gamma^j_{kj} \tag{B.142}$$

If the vector **v** is assumed to be obtained from the gradient of a scalar field ($\mathbf{v} = \text{grad}\,\phi$), then the divergence of vector **v** is given by:

$$\text{div}\,(\text{grad}\,\phi) = \nabla \cdot (\nabla \phi) = \nabla^2 \phi \tag{B.143}$$

where ∇^2 is the Laplacian operator. The covariant derivative of the scalar field is given by:

$$\frac{\partial \phi}{\partial \xi^j} = \phi_{,j} \tag{B.144}$$

however, in general coordinate systems, one cannot write:

$$\nabla \cdot (\nabla \phi) = (\phi_{,j})_{,j} \tag{B.145}$$

since summation can only be applied with indices on different levels. Instead, one needs to first calculate the contravariant component of $\text{grad}\,\phi$, by multiplying with the metric tensor g^{ij}, before taking the divergence, as follows:

$$\begin{aligned} \nabla \cdot (\nabla \phi) &= \left(g^{ij} \phi_{,j}\right)_{,i} \\ &= \frac{\partial}{\partial \xi^i}\left(g^{ij} \frac{\partial \phi}{\partial \xi^j}\right) + \Gamma^i_{ki} g^{kj} \frac{\partial \phi}{\partial \xi^j} \end{aligned} \tag{B.146}$$

This now satisfies the summation convention as indices i, j and k are repeated in upper and lower positions.

B.20 Physical Components

In the preceding analysis, tensor calculus has been used to express the divergence of first- and second-order tensors in terms of the covariant and contravariant base vectors, $\mathbf{g}_i$ and $\mathbf{g}^i$. In some coordinate systems the dimensions of the components of the base vectors are different to those of their parents (e.g. in cylindrical-polar coordinates (r, y, ϕ) the velocity component in the direction of the angular coordinate ϕ does not have dimensions of length/time). To overcome this shortcoming, unit base

vectors are used, which are obtained by dividing each base vector by its magnitude[3], i.e.:

$$\mathbf{g}_{(i)} = \frac{1}{\sqrt{g_{ii}}}\mathbf{g}_i \tag{B.148}$$

which can be rearranged to give:

$$\mathbf{g}_i = \sqrt{g_{ii}}\mathbf{g}_{(i)} \tag{B.149}$$

where there is no summation over the repeated i index in the above equations. A vector $\mathbf{v}$ can therefore be expressed as follows:

$$\mathbf{v} = v^i\mathbf{g}_i = v^i\sqrt{g_{ii}}\mathbf{g}_{(i)} \tag{B.150}$$

Since the vector $\mathbf{g}_{(i)}$ is a unit vector, the components $\left(v^i\sqrt{g_{ii}}\right)$ must have the same dimensions as the parent vector $\mathbf{v}$. These components are therefore called the "physical" components, denoted $v^{(i)}$. First- and second-order tensors can be expressed in terms of the physical components as follows:

$$\mathbf{v} = v^{(i)}\mathbf{g}_{(i)} = v_{(i)}\mathbf{g}^{(i)} \tag{B.151}$$

$$\mathbf{T} = T^{(ij)}\mathbf{g}_{(i)} \otimes \mathbf{g}_{(j)} \tag{B.152}$$

where:

$$v^{(i)} = \sqrt{g_{ii}}v^i \quad \text{(no summation)} \tag{B.153}$$

$$T^{(ij)} = \sqrt{g_{ii}}\sqrt{g_{jj}}T^{ij} \quad \text{(no summation)} \tag{B.154}$$

B.21 Key Formulae

A summary of equations derived in the preceding sections is given below:

- Covariant Metric Tensor, g_{ij}:

$$g_{ij} = \sum_{k=1}^{3}\frac{\partial x^k}{\partial \xi^i}\frac{\partial x^k}{\partial \xi^j} = \frac{\partial x}{\partial \xi^i}\frac{\partial x}{\partial \xi^j} + \frac{\partial y}{\partial \xi^i}\frac{\partial y}{\partial \xi^j} + \frac{\partial z}{\partial \xi^i}\frac{\partial z}{\partial \xi^j} \tag{B.155}$$

- Jacobian Matrix, $[J]$:

$$[J] = \frac{\partial x^j}{\partial \xi^i} = \begin{bmatrix} x_\xi & x_\eta & x_\zeta \\ y_\xi & y_\eta & y_\zeta \\ z_\xi & z_\eta & z_\zeta \end{bmatrix} \tag{B.156}$$

[3]The magnitude of a vector can be found from the scalar product ($\mathbf{a}\cdot\mathbf{b} = |\mathbf{a}|\,|\mathbf{b}|\cos\theta$), so for the covariant base vector the magnitude is given by:

$$\sqrt{g_{ii}} = \sqrt{\mathbf{g}_i\cdot\mathbf{g}_i} = \sqrt{|\mathbf{g}_i|\,|\mathbf{g}_i|\cos 0} = |\mathbf{g}_i| \tag{B.147}$$

- Jacobian, J:

$$J = \det[J] = x_\xi \left(y_\eta z_\zeta - y_\zeta z_\eta\right) - x_\eta \left(y_\xi z_\zeta - y_\zeta z_\xi\right) + x_\zeta \left(y_\xi z_\eta - y_\eta z_\xi\right) \tag{B.157}$$

- Inverse Jacobian Matrix, $[J]^{-1}$:

$$[J]^{-1} = \frac{\partial \xi^i}{\partial x^j} = \begin{bmatrix} \xi_x & \xi_y & \xi_z \\ \eta_x & \eta_y & \eta_z \\ \zeta_x & \zeta_y & \zeta_z \end{bmatrix} = \frac{1}{J}\left[\text{cof}\,(J)\right]^T \tag{B.158}$$

$$= \frac{1}{J}\begin{bmatrix} \left(y_\eta z_\zeta - y_\zeta z_\eta\right) & -\left(x_\eta z_\zeta - x_\zeta z_\eta\right) & \left(x_\eta y_\zeta - x_\zeta y_\eta\right) \\ -\left(y_\xi z_\zeta - y_\zeta z_\xi\right) & \left(x_\xi z_\zeta - x_\zeta z_\xi\right) & -\left(x_\xi y_\zeta - x_\zeta y_\xi\right) \\ \left(y_\xi z_\eta - y_\eta z_\xi\right) & -\left(x_\xi z_\eta - x_\eta z_\xi\right) & \left(x_\xi y_\eta - x_\eta y_\xi\right) \end{bmatrix} \tag{B.159}$$

- Contravariant Metric Tensor, g^{ij}:

$$g^{ij} = \frac{1}{g} G_{ij} \tag{B.160}$$

- Determinant of Covariant Metric Tensor Matrix, g:

$$g = J^2 \tag{B.161}$$

- Adjoint of the Covariant Metric Tensor Matrix, G_{ij}:

$$\begin{aligned} G_{ij} &= \left[\text{cof}\,(g_{ij})\right]^T \\ &= \begin{bmatrix} (g_{22}g_{33} - g_{23}g_{32}) & -(g_{12}g_{33} - g_{13}g_{32}) & (g_{12}g_{23} - g_{13}g_{22}) \\ -(g_{21}g_{33} - g_{23}g_{31}) & (g_{11}g_{33} - g_{13}g_{31}) & -(g_{11}g_{23} - g_{13}g_{21}) \\ (g_{21}g_{32} - g_{22}g_{31}) & -(g_{11}g_{32} - g_{12}g_{31}) & (g_{11}g_{22} - g_{12}g_{21}) \end{bmatrix} \end{aligned} \tag{B.162}$$

- Christoffel Symbol of the Second Kind, Γ^k_{ij}:

$$\Gamma^k_{ij} = \frac{1}{2} g^{kl}\left(\frac{\partial g_{jl}}{\partial \xi^i} + \frac{\partial g_{il}}{\partial \xi^j} - \frac{\partial g_{ij}}{\partial \xi^l}\right) \tag{B.163}$$

- Covariant Derivative, $\nabla_j v^i$:

$$\nabla_j v^i = \left(\frac{\partial v^i}{\partial \xi^j} + v^k \Gamma^i_{kj}\right) \tag{B.164}$$

- Gradient of a Scalar, $\nabla\phi$:

$$\nabla\phi = \frac{\partial \phi}{\partial \xi^j} g^{jk} \mathbf{g}_k \tag{B.165}$$

- Divergence of a Vector, $\nabla \cdot \mathbf{v}$:

$$\nabla \cdot \mathbf{v} = \frac{\Delta v^j}{\Delta \xi^j} = \frac{1}{J} \frac{\partial}{\partial \xi^j} \left(J v^j \right) \tag{B.166}$$

- Divergence of a Tensor, $\nabla \cdot \mathbf{T}$:

$$\begin{aligned} \nabla \cdot \mathbf{T} &= \nabla_j T^{ij} \mathbf{g}_i \\ &= \left(\frac{\Delta T^{ij}}{\Delta \xi^j} + T^{mj} \Gamma^i_{mj} \right) \mathbf{g}_i \\ &= \left[\frac{1}{J} \frac{\partial}{\partial \xi^j} \left(J T^{ij} \right) + T^{mj} \Gamma^i_{mj} \right] \mathbf{g}_i \end{aligned} \tag{B.167}$$

- Physical Vector Component, $v^{(i)}$:

$$v^{(i)} = \sqrt{g_{ii}} v^i \quad \text{(no summation)} \tag{B.168}$$

- Physical Tensor Component, $T^{(ij)}$:

$$T^{(ij)} = \sqrt{g_{ii}} \sqrt{g_{jj}} T^{ij} \quad \text{(no summation)} \tag{B.169}$$

Appendix C

RANS Equations in Curvilinear Coordinates

To begin with, the Reynolds-averaged Navier-Stokes (RANS) equations are presented in the familiar vector and Cartesian tensor forms. Each term in the transport equations is examined to see whether it complies with the Einstein summation convention for curvilinear coordinates. Then, according to the rules outlined in Appendix B, the equations are re-written in non-orthogonal curvilinear coordinates in which velocity vectors follow the coordinate directions. Those equations which are used in the derivation of the UMIST-*N* wall function transport equations are shown in boxes to highlight their significance.

C.1 Vector Form

Continuity

$$\frac{\partial \rho}{\partial t} + \nabla \cdot (\rho \mathbf{U}) = 0 \tag{C.1}$$

Momentum

$$\frac{\partial}{\partial t}(\rho \mathbf{U}) + \nabla \cdot (\rho \mathbf{U} \otimes \mathbf{U} - \mathbf{T}) = -\nabla P \tag{C.2}$$

Scalar, ϕ

$$\frac{\partial}{\partial t}(\rho \phi) + \nabla \cdot (\rho \mathbf{U} \phi - \mathbf{q}) \quad = \quad S_\phi \tag{C.3}$$

where $\mathbf{U}$ and $\mathbf{q}$ are, respectively, the mean velocity and scalar-flux vectors, $\mathbf{T}$ is the second-order stress tensor $\left(\mathbf{T} = \tau^{ij}\mathbf{g}_i \otimes \mathbf{g}_j\right)$ and P is the mean pressure. The divergence of a vector quantity is a scalar whilst the divergence of a second-order tensor results in a vector quantity and, therefore, in

3-*D* space the momentum equation consists of three component equations each multiplied by a base vector.

C.2 Cartesian Coordinates

The continuity, momentum and scalar transport equations can be written in Cartesian tensors as follows:

Continuity

$$\frac{\partial \rho}{\partial t} + \frac{\partial}{\partial x^j}\left(\rho U^j\right) = 0 \tag{C.4}$$

Momentum

$$\frac{\partial}{\partial t}\left(\rho U^i\right) + \frac{\partial}{\partial x^j}\left(\rho U^i U^j - \tau^{ij}\right) = -\frac{\partial P}{\partial x^i} \tag{C.5}$$

Scalar, ϕ

$$\frac{\partial}{\partial t}\left(\rho\phi\right) + \frac{\partial}{\partial x^j}\left(\rho\phi U^j - J_\phi^j\right) = S_\phi^i \tag{C.6}$$

Turbulent Kinetic Energy, k

$$\frac{\partial}{\partial t}\left(\rho k\right) + \frac{\partial}{\partial x^j}\left(\rho k U^j - \frac{\mu_t}{\sigma_k}\frac{\partial k}{\partial x^j}\right) = G - \rho\varepsilon \tag{C.7}$$

Isotropic Dissipation Rate, $\tilde{\varepsilon}$

$$\frac{\partial}{\partial t}\left(\rho\tilde{\varepsilon}\right) + \frac{\partial}{\partial x^j}\left(\rho\tilde{\varepsilon}U^j - \frac{\mu_t}{\sigma_\varepsilon}\frac{\partial\tilde{\varepsilon}}{\partial x^j}\right) = c_{\varepsilon 1} f_1 G\frac{\tilde{\varepsilon}}{k} - c_{\varepsilon 2} f_2 \rho\frac{\tilde{\varepsilon}^2}{k} + \rho Y_c + P_{\varepsilon 3} \tag{C.8}$$

where the stress tensor, τ^{ij}, is given by:

$$\tau^{ij} = \mu\left(\frac{\partial U^i}{\partial x^j} + \frac{\partial U^j}{\partial x^i} - \underbrace{\frac{2}{3}\delta^{ij}\frac{\partial U^m}{\partial x^m}}\right) - \rho\overline{u^i u^j} \tag{C.9}$$

In an incompressible flow, the underbraced terms in the above equations disappears since, from continuity, $(\partial U^m/\partial x^m = 0)$. The Reynolds stress $\left(-\rho\overline{u^i u^j}\right)$, is expressed, using a linear eddy-viscosity model:

$$-\rho\overline{u^i u^j} = \mu_t\left(\frac{\partial U^i}{\partial x^j} + \frac{\partial U^j}{\partial x^i} - \underbrace{\frac{2}{3}\delta^{ij}\frac{\partial U^m}{\partial x^m}}\right) - \underbrace{\frac{2}{3}\delta^{ij}\rho k} \tag{C.10}$$

where the two underbraced terms in the above equation arise from the trace condition (where, by definition, $\overline{u^i u^i} = 2k$). The term, J_ϕ^j, representing molecular and turbulent diffusive flux of the time-

averaged scalar, ϕ, is given by:

$$J_\phi^j = \Gamma_\phi \frac{\partial \phi}{\partial x^j} - \rho \overline{u^j \phi} \tag{C.11}$$

where Γ_ϕ is the molecular diffusivity (not to be confused with the Christoffel symbol, Γ^i_{jk}, which has three indices). The turbulent scalar flux $\left(-\rho \overline{u^j \phi}\right)$ is calculated using an eddy-diffusivity model:

$$-\rho \overline{u^j \phi} = \frac{\mu_t}{\sigma_\phi} \frac{\partial \phi}{\partial x^j} \tag{C.12}$$

The eddy-viscosity, μ_t, using a $k-\varepsilon$ turbulence model, is given by:

$$\mu_t = \rho c_\mu f_\mu \frac{k^2}{\tilde{\varepsilon}} \tag{C.13}$$

the production rate of turbulent kinetic energy, G:

$$G = -\rho \overline{u^i u^j} \frac{\partial U^i}{\partial x^j} \tag{C.14}$$

the total dissipation rate, ε:

$$\varepsilon = \tilde{\varepsilon} + 2\nu \left(\frac{\partial k^{1/2}}{\partial x^j} \right)^2 \tag{C.15}$$

the Yap correction, Y_c:

$$Y_c = \max \left\{ \left[0.83 \left(\frac{k^{3/2}/\tilde{\varepsilon}}{2.55y} - 1 \right) \left(\frac{k^{3/2}/\tilde{\varepsilon}}{2.55y} \right)^2 \frac{\tilde{\varepsilon}^2}{k} \right], 0 \right\} \tag{C.16}$$

and the gradient production term, $P_{\varepsilon 3}$:

$$P_{\varepsilon 3} = 2\mu\nu_t \left(\frac{\partial^2 U^i}{\partial x^j \partial x^k} \right)^2 \tag{C.17}$$

C.3 Summation Convention

The derivatives appearing in the above transport equations in Cartesian coordinates are *covariant*, in which case the derivative of, say, ϕ with respect to x^j can be written, $\partial\phi/\partial x^j = \phi_{,j}$, which in itself is a covariant tensor. Recalling Section B.19, the summation convention in general coordinates is defined such that summation only occurs where one dummy index is subscript and the other is superscript (i.e. summation only applies between covariant and contravariant terms). The second covariant derivative of ϕ cannot be written $\left(\phi_{,j}\right)_{,j}$ since this would violate the summation convention as both dummy indices are subscript. In order to change $\phi_{,j}$ into a contravariant tensor (effectively raising index j from subscript to superscript), the product is taken with the contravariant metric tensor g^{ij}

(which in Cartesian coordinates is equivalent to the Kronecker delta, δ^{ij}). As was shown in Section B.19, the correct form of the second derivative of ϕ is thus $\left(\delta^{jm}\phi_{,m}\right)_{,j}$ where dummy indices j and m are now repeated as subscript and superscript. Additionally, all of the terms in the each equation should be consistently covariant or contravariant, for instance, one cannot have a contravariant component on one side of the equation equal to a covariant component on the other. In the following sections, each of the terms in the momentum, kinetic energy and dissipation rate equations are examined to see whether they comply with the summation convention.

Convection

In the conservative form of convection of momentum, given by:

$$\frac{\partial\left(\rho U^i U^j\right)}{\partial x^j} = \left(\rho U^i U^j\right)_{,j} \tag{C.18}$$

the suffix j appears in the contravariant velocity component and the covariant derivative and therefore complies with the convention. Likewise, in the non-conservative form of convection:

$$\rho U^j \frac{\partial U^i}{\partial x^j} = \rho U^j \left(U^i\right)_{,j} \tag{C.19}$$

index j is repeated in subscript and superscript. Convection of a scalar quantity (ϕ, k or $\tilde{\varepsilon}$) can also be shown to agree with the summation convection.

Diffusion

The covariant gradient of the contravariant stress, τ^{ij}, is written:

$$\frac{\partial \tau^{ij}}{\partial x^j} = \left(\tau^{ij}\right)_{,j} \tag{C.20}$$

where j is repeated in subscript and superscript, in agreement with the summation convention.

Stress Tensor, τ^{ij}

In the contravariant stress tensor:

$$\tau^{ij} = \mu\left(\frac{\partial U^i}{\partial x^j} + \frac{\partial U^j}{\partial x^i} - \frac{2}{3}\delta^{ij}\frac{\partial U^m}{\partial x^m}\right) - \rho\overline{u^i u^j} \tag{C.21}$$

the strain-rate $\left(\partial U^i/\partial x^j\right) = U^i_{,j}$ involves a superscript i and subscript j. Since both i and j must be contravariant (since τ^{ij} is fully contravariant), the Kronecker delta, δ^{jm}, is introduced as follows:

$$\frac{\partial U^i}{\partial x^j} = U^i_{,j} = \delta^{jm} U^i_{,m} \tag{C.22}$$

where i and j now appear as superscripts. Likewise the second strain-rate term in Equation (C.21) is written:

$$\frac{\partial U^j}{\partial x^i} = U^j_{,i} = \delta^{im} U^j_{,m} \tag{C.23}$$

The remaining terms in Equation (C.21) agree with the summation convention. The contravariant stress tensor, τ^{ij}, is therefore given by:

$$\tau^{ij} = \mu\left(\delta^{jm}\frac{\partial U^i}{\partial x^m} + \delta^{im}\frac{\partial U^j}{\partial x^m} - \frac{2}{3}\delta^{ij}\frac{\partial U^m}{\partial x^m}\right) - \rho\overline{u^i u^j} \tag{C.24}$$

Scalar Flux Vector

Following a similar reasoning to that used with the stress tensor, the scalar flux J^j_ϕ, which is modelled using the eddy-diffusivity hypothesis, is given by:

$$\begin{aligned} J^j_\phi &= \Gamma_\phi \frac{\partial \phi}{\partial x^j} - \rho\overline{u^j\phi} \\ &= \left(\Gamma_\phi + \frac{\mu_t}{\sigma_\phi}\right)\frac{\partial \phi}{\partial x^j} \\ &= \left(\Gamma_\phi + \frac{\mu_t}{\sigma_\phi}\right)\phi_{,j} \end{aligned} \tag{C.25}$$

Since the scalar flux should be a contravariant vector, the subscript j must be raised by multiplying the above expression with δ^{jm}:

$$J^j_\phi = \left(\Gamma_\phi + \frac{\mu_t}{\sigma_\phi}\right)\delta^{jm}\frac{\partial \phi}{\partial x^m} = \left(\Gamma_\phi + \frac{\mu_t}{\sigma_\phi}\right)\delta^{jm}\phi_{,m} \tag{C.26}$$

Pressure Gradient

The pressure gradient in Equation (C.5) is expressed as the covariant derivative of the scalar parameter P and is therefore itself a covariant tensor, $\left(\partial P/\partial x^i = P_{,i}\right)$. However, the convection and diffusion terms, discussed above, both yield contravariant components once summation has been applied over the dummy indices (i.e. both convection and diffusion terms have superscript i). Therefore, to obtain agreement with all the components in the momentum equation, it is necessary to to raise the index i in the pressure gradient:

$$\frac{\partial P}{\partial x^i} = P_{,i} = \delta^{ij} P_{,j} \tag{C.27}$$

Turbulent Kinetic Energy Production, G

The production source term G in the k- and $\tilde{\varepsilon}$-equations is given by:

$$G = -\rho\overline{u^i u^j}\frac{\partial U^i}{\partial x^j} = -\rho\overline{u^i u^j}U^i_{,j} \tag{C.28}$$

Here the dummy index j is repeated in the subscript and superscript, in agreement with the summation convention, but index i appears superscript in both instances. Therefore, to satisfy the summation convention for index i, the covariant Kronecker delta (δ_{im}) is introduced, as follows:

$$G = -\rho\delta_{im}\overline{u^m u^j}U^i_{,j} \tag{C.29}$$

where the dummy indices (i, j and m) are all repeated in subscript and superscript.

Total Dissipation Rate, ε

The total dissipation rate, ε, is given by:

$$\varepsilon = \tilde{\varepsilon} + 2\nu\left(\frac{\partial k^{1/2}}{\partial x^j}\right)^2 = \tilde{\varepsilon} + 2\nu\left(k^{1/2}\right)_{,j}\left(k^{1/2}\right)_{,j} \tag{C.30}$$

This does not agree with the summation convention in general coordinates since both derivatives of $k^{1/2}$ are covariant tensors. To make one of the tensors contravariant, the contravariant Kronecker delta $\left(\delta^{jm}\right)$ is introduced, as follows:

$$\varepsilon = \tilde{\varepsilon} + 2\nu\delta^{jm}\left(k^{1/2}\right)_{,m}\left(k^{1/2}\right)_{,j} \tag{C.31}$$

Gradient Production of Dissipation Rate, $P_{\varepsilon 3}$

In the low-Reynolds-number model $\tilde{\varepsilon}$-equation, the near-wall damping term $(P_{\varepsilon 3})$ is given by:

$$P_{\varepsilon 3} = 2\mu\nu_t\left(\frac{\partial^2 U^i}{\partial x^j \partial x^k}\right)^2 = 2\mu\nu_t\left(U^i_{,j}\right)_{,k}\left(U^i_{,j}\right)_{,k} \tag{C.32}$$

In order to obtain the second covariant derivative one must first raise the index of the first derivative to satisfy the summation convention. The second derivative of the velocity is therefore written:

$$\left(\delta^{jk}U^i_{,k}\right)_{,l} \tag{C.33}$$

where k is a dummy index. The square of this term requires the introduction of three Kronecker deltas to comply with the need for repeated raised and lowered indices:

$$P_{\varepsilon 3} = 2\mu\nu_t\delta_{im}\delta_{jn}\delta^{lp}\left(\delta^{no}U^m_{,o}\right)_{,p}\left(\delta^{jk}U^i_{,k}\right)_{,l} \tag{C.34}$$

Unfortunately, to agree with the summation convention, $P_{\varepsilon 3}$ now contains eight dummy indices (i, j, k, l, m, n, o and p).

To summarize the preceding sections, the momentum and scalar transport equations are re-written below in Cartesian coordinates, where the general coordinate summation convention is observed:

Momentum

$$\frac{\partial}{\partial t}\left(\rho U^i\right)+\frac{\partial}{\partial x^j}\left(\rho U^i U^j-\tau^{ij}\right)=-\delta^{ij}\frac{\partial P}{\partial x^j} \tag{C.35}$$

where the stress tensor is given by:

$$\tau^{ij}=\mu\left(\delta^{jm}\frac{\partial U^i}{\partial x^m}+\delta^{im}\frac{\partial U^j}{\partial x^m}-\frac{2}{3}\delta^{ij}\frac{\partial U^m}{\partial x^m}\right)-\rho\overline{u^i u^j} \tag{C.36}$$

and the Reynolds stress:

$$-\rho\overline{u^i u^j}=\mu_t\left(\delta^{jm}\frac{\partial U^i}{\partial x^m}+\delta^{im}\frac{\partial U^j}{\partial x^m}-\frac{2}{3}\delta^{ij}\frac{\partial U^m}{\partial x^m}\right)-\frac{2}{3}\delta^{ij}\rho k \tag{C.37}$$

Scalar

$$\frac{\partial}{\partial t}\left(\rho\phi\right)+\frac{\partial}{\partial x^j}\left[\rho\phi U^j-\left(\Gamma_\phi+\frac{\mu_t}{\sigma_\phi}\right)\delta^{jm}\frac{\partial\phi}{\partial x^m}\right]=S_\phi^i \tag{C.38}$$

Alternative Approach to Summation Convention

An alternative way of examining the summation convention in the above equations is to start from the vector form of transport equations and convert each term into non-orthogonal curvilinear coordinates directly (omitting the in-between step of Cartesian tensors). For instance, the velocity gradient component of the stress tensor can be written in vector form:

$$\mathbf{T}=\text{grad}\,\mathbf{v}=\nabla\mathbf{v} \tag{C.39}$$

This can be converted into generalized tensor form as follows (see also Section B.18)

$$\mathbf{T} \quad = \quad \mathbf{g}^j\frac{\partial\left(v^i\mathbf{g}_i\right)}{\partial\xi^j} \tag{C.40}$$

The covariant derivative of vector **v** was shown in Section B.14 to be given by:

$$\frac{\partial\left(v^i\mathbf{g}_i\right)}{\partial\xi^j}=\left(\frac{\partial v^i}{\partial\xi^j}+v^m\Gamma^i_{mj}\right)\mathbf{g}_i=v^i_{,j}\mathbf{g}_i \tag{C.41}$$

hence the expression for the stress tensor becomes:

$$\mathbf{T}=v^i_{,j}\mathbf{g}_i\otimes\mathbf{g}^j \tag{C.42}$$

In the above equation, the stress tensor is expressed in terms of mixed covariant and contravariant base vectors, $\mathbf{g}_i$ and $\mathbf{g}^j$. In order to obtain agreement with the remaining terms in the momentum equation one needs to express the stress tensor in terms of the covariant base vectors $\mathbf{g}_i$ and $\mathbf{g}_j$. To do so, the

contravariant metric g^{jk} is introduced to lower the base vector $\mathbf{g}^j$ to $\mathbf{g}_k$:

$$\mathbf{T} = g^{jk} v^i_{,j} \mathbf{g}_i \otimes \mathbf{g}_k \tag{C.43}$$

Switching around the indices j and k so that the stress tensor is in terms of the base vectors $\mathbf{g}_i$ and $\mathbf{g}_j$, one obtains:

$$\mathbf{T} = g^{jk} v^i_{,k} \mathbf{g}_i \otimes \mathbf{g}_j \tag{C.44}$$

The components of the above expression are identical to the first term in the strain-rate tensor obtained in Equation (C.24).

C.4 Transformation Rules

To convert the RANS equations from Cartesian to curvilinear non-orthogonal coordinates, the following set of transformations are applied. These rules are identical to those adopted by Demirdžić *et al*. [86] with the exception that here the transformations are to non-physical parameters[1]. Expressions in Cartesian coordinates are shown on the left and equivalent expressions in non-orthogonal curvilinear coordinates on the right. The use of ∇_j and Δ/Δ_j symbols is to allow direct comparison with the equations given by Demirdžić *et al*. [86].

Scalars

$$\phi \rightarrow \phi \tag{C.45}$$

$$\frac{\partial \phi}{\partial x^j} \rightarrow \frac{\partial \phi}{\partial \xi^j} \tag{C.46}$$

Vectors

$$v^i \rightarrow v^i \tag{C.47}$$

$$\frac{\partial v^i}{\partial x^j} \rightarrow \nabla_j v^i = v^i_{,j} = \frac{\partial v^i}{\partial \xi^j} + v^m \Gamma^i_{mj} \tag{C.48}$$

$$\frac{\partial v^j}{\partial x^j} \rightarrow \nabla_j v^j = v^j_{,j} = \frac{\Delta v^j}{\Delta \xi^j} \tag{C.49}$$

$$= \frac{1}{J} \frac{\partial}{\partial \xi^j} \left(J v^j \right) \tag{C.50}$$

[1] Demirdžić *et al*. [86] expressed the transformed equations in physical curvilinear coordinates and subsequently integrated the transport equations in physical space (i.e. over the cell dimensions in terms of x^i rather than ξ^i) - for details see [85]. In the treatment outlined in this document, the integration takes place in ξ^i-space and therefore the equations are expressed in terms of the non-physical ξ^i components.

Tensors

$$T^{ij} \rightarrow T^{i} \tag{C.51}$$

$$\delta^{ij} \rightarrow g^{ij} \quad \delta_{ij} \rightarrow g_{ij} \tag{C.52}$$

$$\frac{\partial T^{ij}}{\partial x^{j}} \rightarrow \nabla_{j} T^{ij} = T^{ij}_{,j} = \frac{\Delta T^{ij}}{\Delta \xi^{j}} + T^{mj}\Gamma^{i}_{mj} \tag{C.53}$$

$$= \frac{\partial T^{ij}}{\partial \xi^{j}} + T^{im}\Gamma^{j}_{mj} + T^{mj}\Gamma^{i}_{mj} \tag{C.54}$$

$$= \frac{1}{J}\frac{\partial}{\partial \xi^{j}}\left(JT^{ij}\right) + T^{mj}\Gamma^{i}_{mj} \tag{C.55}$$

C.5 Non-Orthogonal Curvilinear Coordinates

Following the transformation rules summarized in Section C.4, the Navier-Stokes equations described in the preceding section are given below in non-physical non-orthogonal curvilinear coordinates.

Continuity

$$\frac{\partial \rho}{\partial t} + \frac{\Delta}{\Delta \xi^{j}}\left(\rho U^{j}\right) = 0 \tag{C.56}$$

Momentum

$$\frac{\partial}{\partial t}\left(\rho U^{i}\right) + \nabla_{j}\left(\rho U^{i}U^{j} - \tau^{ij}\right) = -g^{ij}\frac{\partial P}{\partial \xi^{j}} \tag{C.57}$$

where the non-physical stress tensor, τ^{ij}, is given by:

$$\tau^{ij} = \mu\left(g^{jm}\nabla_{m}U^{i} + g^{im}\nabla_{m}U^{j} - \frac{2}{3}g^{ij}\frac{\Delta U^{m}}{\Delta \xi^{m}}\right) - \rho\overline{u^{i}u^{j}} \tag{C.58}$$

and the non-physical Reynolds stress $\left(-\rho\overline{u^{i}u^{j}}\right)$:

$$-\rho\overline{u^{i}u^{j}} = \mu_{t}\left(g^{jm}\nabla_{m}U^{i} + g^{im}\nabla_{m}U^{j} - \frac{2}{3}g^{ij}\frac{\Delta U^{m}}{\Delta \xi^{m}}\right) - \frac{2}{3}g^{ij}\rho k \tag{C.59}$$

Scalar

$$\frac{\partial}{\partial t}\left(\rho\phi\right) + \frac{\Delta}{\Delta \xi^{j}}\left[\rho\phi U^{j} - \left(\Gamma_{\phi} + \frac{\mu_{t}}{\sigma_{\phi}}\right)g^{jm}\frac{\partial \phi}{\partial \xi^{m}}\right] = S_{\phi} \tag{C.60}$$

Turbulent Kinetic Energy

$$\frac{\partial}{\partial t}\left(\rho k\right) + \frac{\Delta}{\Delta \xi^{j}}\left[\rho k U^{j} - \left(\mu + \frac{\mu_{t}}{\sigma_{k}}\right)g^{jm}\frac{\partial k}{\partial \xi^{m}}\right] = G - \rho\varepsilon \tag{C.61}$$

Isotropic Dissipation Rate

$$\frac{\partial}{\partial t}(\rho\tilde{\varepsilon}) + \frac{\Delta}{\Delta\xi^j}\left[\rho\tilde{\varepsilon}U^j - \left(\mu + \frac{\mu_t}{\sigma_\varepsilon}\right) g^{jm}\frac{\partial\tilde{\varepsilon}}{\partial\xi^m}\right] = c_{\varepsilon 1} f_1 G\frac{\tilde{\varepsilon}}{k} - c_{\varepsilon 2} f_2 \rho\frac{\tilde{\varepsilon}^2}{k} + \rho Y_c + P_{\varepsilon 3} \tag{C.62}$$

where the generation rate of turbulent kinetic energy, G, is given by:

$$G = -\rho g_{im}\overline{u^j u^m}\nabla_j U^i \tag{C.63}$$

the total dissipation rate at the wall, ε:

$$\varepsilon = \tilde{\varepsilon} + 2\nu g^{jm}\left(\frac{\partial k^{1/2}}{\partial\xi^m}\right)\left(\frac{\partial k^{1/2}}{\partial\xi^j}\right) \tag{C.64}$$

and the gradient production of dissipation rate, $P_{\varepsilon 3}$:

$$P_{\varepsilon 3} = 2\mu\nu_t g_{im} g_{jn} g^{lp}\left[\nabla_p\left(g^{no}\nabla_o U^m\right)\right]\left[\nabla_l\left(g^{jk}\nabla_k U^i\right)\right] \tag{C.65}$$

C.5.1 Physical Velocity Components

The notion of "physical" components was introduced in Section B.20. If one considers the simple case of a constant velocity field in plane polar coordinates $(r-\theta)$, one can show that the radial and circumferential velocity components, v_r and v_θ, are given by:

$$v_r = \frac{\partial r}{\partial t} = v^1 = \text{constant} \tag{C.66}$$

$$v_\theta = r\frac{\partial\theta}{\partial t} = rv^2 = \text{constant} \tag{C.67}$$

where v^1 and v^2 are the non-physical velocity components in the radial and circumferential directions, respectively. As one approaches the axis of the polar coordinate system $(r \to 0)$ the circumferential non-physical velocity component tends to infinity $\left(v^2 \to \infty\right)$. This can introduce serious errors in numerical calculations and, therefore, one must solve for the physical velocity components (in this case, v_r and v_θ) [85]. In general curvilinear coordinates, the physical contravariant velocity component, $U^{(i)}$, is obtained from:

$$U^i = \frac{U^{(i)}}{\sqrt{g_{ii}}} \quad \text{(no summation)} \tag{C.68}$$

C.5.2 RANS Equations Using Physical Velocity Vectors

Continuity

The continuity equation can be written with the velocity components in physical form, using Equations (C.56) and (B.133) :

$$\frac{\partial\rho}{\partial t} + \frac{1}{J}\frac{\partial}{\partial\xi^j}\left(\frac{J}{\sqrt{g_{jj}}}\rho U^{(j)}\right) = 0 \tag{C.69}$$

which is expanded:

$$\frac{\partial \rho}{\partial t}+\frac{1}{J}\frac{\partial}{\partial \xi}\left(\frac{J}{\sqrt{g_{11}}}\rho U\right)+\frac{1}{J}\frac{\partial}{\partial \eta}\left(\frac{J}{\sqrt{g_{22}}}\rho V\right)+\frac{1}{J}\frac{\partial}{\partial \zeta}\left(\frac{J}{\sqrt{g_{33}}}\rho W\right)=0 \tag{C.70}$$

where, as above, U, V and W denote the physical velocity components in the direction of the non-physical base vector components ξ, η and ζ respectively.

Scalar

Using Equations (C.50), (C.60) and (C.68), the scalar transport equation in nonorthogonal curvilinear coordinates can be written using physical velocity components as follows:

$$\boxed{\frac{\partial}{\partial t}(\rho\phi)+\frac{1}{J}\frac{\partial}{\partial \xi^j}\left(\frac{J}{\sqrt{g_{jj}}}\rho\phi U^{(j)}\right)=\frac{1}{J}\frac{\partial}{\partial \xi^j}\left[J\left(\Gamma_\phi+\frac{\mu_t}{\sigma_\phi}\right)g^{jm}\frac{\partial \phi}{\partial \xi^m}\right]+S_\phi} \tag{C.71}$$

Momentum

An important difference with the scalar equation is that the divergence of a second-order tensor $(\rho\mathbf{U}\otimes\mathbf{U}-\mathbf{T})$ results in a vector, whereas in the scalar equation the divergence of $(\rho\mathbf{U}\phi-\mathbf{q})$ resulted in a scalar quantity. Therefore, the momentum equation can be written:

$$\left[\frac{\partial}{\partial t}\left(\rho U^i\right)+\nabla_j\left(\rho U^iU^j-\tau^{ij}\right)+g^{ij}\frac{\partial P}{\partial \xi^j}\right]\mathbf{g}_i=0 \tag{C.72}$$

The base vector, $\mathbf{g}_i$, is written in "physical" form (i.e. as a unit vector) as follows:

$$\mathbf{g}_i=\sqrt{g_{ii}}\mathbf{g}_{(i)} \tag{C.73}$$

and the momentum equation becomes:

$$\left[\frac{\partial}{\partial t}\left(\rho U^i\right)+\nabla_j\left(\rho U^iU^j-\tau^{ij}\right)+g^{ij}\frac{\partial P}{\partial \xi^j}\right]\sqrt{g_{ii}}\mathbf{g}_{(i)}=0 \tag{C.74}$$

It is important to keep the $\sqrt{g_{ii}}$ term in this expression so that the components are in terms of the physical base vectors. Without the $\sqrt{g_{ii}}$ term if one converts the equation into cylindrical polar coordinates, the axial, radial and *angular* (rather than tangential) momentum equations are obtained. Expanding the covariant derivative term $\left[\nabla_j\left(\rho U^iU^j-\tau^{ij}\right)\right]$ in the above expression using Equation (C.55) and writing the velocity components in physical form, $\left(U^i=U^{(i)}/\sqrt{g_{ii}}\right)$, the components of

the momentum equation are given by:

$$\frac{\partial}{\partial t}\left(\rho U^{(i)}\right) + \underbrace{\sqrt{g_{ii}}\frac{1}{J}\frac{\partial}{\partial \xi^j}\left(\frac{J}{\sqrt{g_{ii}g_{jj}}}\rho U^{(i)}U^{(j)}\right)}_{convection} + \rho U^{(j)}U^{(m)}\frac{\Gamma^i_{mj}\sqrt{g_{ii}}}{\sqrt{g_{jj}g_{mm}}}$$
$$= \left[-g^{ij}\frac{\partial P}{\partial \xi^j} + \underbrace{\frac{1}{J}\frac{\partial}{\partial \xi^j}\left(J\tau^{ij}\right)}_{diffusion} + \tau^{mj}\Gamma^i_{mj}\right]\sqrt{g_{ii}} \tag{C.75}$$

where there is no summation on the i index and it is assumed that the grid is not changing over time $\left(\partial\sqrt{g_{ii}}/\partial t = 0\right)$. The first underbraced term, denoted "convection", in the above expression can be written in a similar form to that given above for the ϕ-equation convection, using the quotient rule:

$$\sqrt{g_{ii}}\frac{1}{J}\frac{\partial}{\partial \xi^j}\left(\frac{J}{\sqrt{g_{ii}g_{jj}}}\rho U^{(i)}U^{(j)}\right) = \frac{1}{J}\frac{\partial}{\partial \xi^j}\left(\frac{J}{\sqrt{g_{jj}}}\rho U^{(i)}U^{(j)}\right) - \frac{\rho U^{(i)}U^{(j)}}{\sqrt{g_{ii}g_{jj}}}\frac{\partial\sqrt{g_{ii}}}{\partial \xi^j} \tag{C.76}$$

where, from Equation (B.121), the expression involving the derivative of the metric tensor can be written:

$$\frac{\partial\sqrt{g_{ii}}}{\partial \xi^j} = \frac{1}{2}\frac{1}{\sqrt{g_{ii}}}\frac{\partial g_{ii}}{\partial \xi^j} = \frac{1}{2}\frac{1}{\sqrt{g_{ii}}}\left(2\Gamma^m_{ij}g_{im}\right) = \frac{\Gamma^m_{ij}g_{im}}{\sqrt{g_{ii}}} \quad \text{(no summation on } i\text{)} \tag{C.77}$$

The second underbraced term in Equation (C.75) can also be expanded, as follows:

$$\begin{aligned}\sqrt{g_{ii}}\frac{1}{J}\frac{\partial}{\partial \xi^j}\left(J\tau^{ij}\right) &= \frac{1}{J}\frac{\partial}{\partial \xi^j}\left(\sqrt{g_{ii}}J\tau^{ij}\right) - \tau^{ij}\frac{\partial\sqrt{g_{ii}}}{\partial \xi^j} \\ &= \frac{1}{J}\frac{\partial}{\partial \xi^j}\left(\sqrt{g_{ii}}J\tau^{ij}\right) - \tau^{ij}\frac{\Gamma^m_{ij}g_{im}}{\sqrt{g_{ii}}}\end{aligned} \tag{C.78}$$

Finally, substituting Equations (C.76), (C.77) and (C.78) into Equation (C.75):

$$\boxed{\frac{\partial}{\partial t}\left(\rho U^{(i)}\right) + \frac{1}{J}\frac{\partial}{\partial \xi^j}\left(\frac{J}{\sqrt{g_{jj}}}\rho U^{(i)}U^{(j)}\right) = \frac{1}{J}\frac{\partial}{\partial \xi^j}\left(\sqrt{g_{ii}}J\tau^{ij}\right) + S^i_U} \tag{C.79}$$

where:

$$\begin{aligned}S^i_U &= \rho U^{(i)}U^{(j)}\frac{\Gamma^m_{ij}g_{im}}{g_{ii}\sqrt{g_{jj}}} - \rho U^{(j)}U^{(m)}\frac{\Gamma^i_{mj}\sqrt{g_{ii}}}{\sqrt{g_{jj}g_{mm}}} - g^{ij}\sqrt{g_{ii}}\frac{\partial P}{\partial \xi^j} \\ &\quad -\tau^{ij}\frac{\Gamma^m_{ij}g_{im}}{\sqrt{g_{ii}}} + \tau^{mj}\Gamma^i_{mj}\sqrt{g_{ii}}\end{aligned} \tag{C.80}$$

There is no summation on index i in the above equations.

Stress Tensor, τ^{ij}

The non-physical stress tensor, τ^{ij}, for incompressible flow is given by:

$$\tau^{ij} = \mu\left(g^{jm}U^{i}_{,m} + g^{im}U^{j}_{,m}\right) - \rho\overline{u^i u^j} \tag{C.81}$$

The six independent stress components are expanded as follows:

$$\tau^{11} = 2\mu\left(g^{11}U_{,1} + g^{12}U_{,2} + g^{13}U_{,3}\right) - \rho\overline{uu} \tag{C.82}$$

$$\tau^{22} = 2\mu\left(g^{21}V_{,1} + g^{22}V_{,2} + g^{23}V_{,3}\right) - \rho\overline{vv} \tag{C.83}$$

$$\tau^{33} = 2\mu\left(g^{31}W_{,1} + g^{32}W_{,2} + g^{33}W_{,3}\right) - \rho\overline{ww} \tag{C.84}$$

$$\begin{aligned}\tau^{12} = \tau^{21} = \mu\big(&g^{21}U_{,1} + g^{22}U_{,2} + g^{23}U_{,3} \\ &+ g^{11}V_{,1} + g^{12}V_{,2} + g^{13}V_{,3}\big) - \rho\overline{uv}\end{aligned} \tag{C.85}$$

$$\begin{aligned}\tau^{13} = \tau^{31} = \mu\big(&g^{31}U_{,1} + g^{32}U_{,2} + g^{33}U_{,3} \\ &+ g^{11}W_{,1} + g^{12}W_{,2} + g^{13}W_{,3}\big) - \rho\overline{uw}\end{aligned} \tag{C.86}$$

$$\begin{aligned}\tau^{23} = \tau^{32} = \mu\big(&g^{31}V_{,1} + g^{32}V_{,2} + g^{33}V_{,3} \\ &+ g^{21}W_{,1} + g^{22}W_{,2} + g^{23}W_{,3}\big) - \rho\overline{vw}\end{aligned} \tag{C.87}$$

where strain rates $U_{,i}$, $V_{,i}$ and $W_{,i}$ are expanded in Section C.5.2. The non-physical components of the Reynolds stress $\left(-\rho\overline{u^i u^j}\right)$ are obtained from Equation (C.59) for an incompressible flow, as follows:

$$-\rho\overline{u^i u^j} = \mu_t\left(g^{jm}U^{i}_{,m} + g^{im}U^{j}_{,m}\right) - \frac{2}{3}g^{ij}\rho k \tag{C.88}$$

which is expanded:

$$-\rho\overline{uu} = 2\mu_t\left(g^{11}U_{,1} + g^{12}U_{,2} + g^{13}U_{,3}\right) - \frac{2}{3}g^{11}\rho k \tag{C.89}$$

$$-\rho\overline{vv} = 2\mu_t\left(g^{21}V_{,1} + g^{22}V_{,2} + g^{23}V_{,3}\right) - \frac{2}{3}g^{22}\rho k \tag{C.90}$$

$$-\rho\overline{ww} = 2\mu_t\left(g^{31}W_{,1} + g^{32}W_{,2} + g^{33}W_{,3}\right) - \frac{2}{3}g^{33}\rho k \tag{C.91}$$

$$-\rho\overline{uv} = -\rho\overline{vu} = \mu_t \left(g^{21}U_{,1} + g^{22}U_{,2} + g^{23}U_{,3} + g^{11}V_{,1} + g^{12}V_{,2} + g^{13}V_{,3}\right) - \frac{2}{3}g^{12}\rho k \tag{C.92}$$

$$-\rho\overline{uw} = -\rho\overline{wu} = \mu_t \left(g^{31}U_{,1} + g^{32}U_{,2} + g^{33}U_{,3} + g^{11}W_{,1} + g^{12}W_{,2} + g^{13}W_{,3}\right) - \frac{2}{3}g^{13}\rho k \tag{C.93}$$

$$-\rho\overline{vw} = -\rho\overline{wv} = \mu_t \left(g^{31}V_{,1} + g^{32}V_{,2} + g^{33}V_{,3} + g^{21}W_{,1} + g^{22}W_{,2} + g^{23}W_{,3}\right) - \frac{2}{3}g^{23}\rho k \tag{C.94}$$

Velocity Gradient, $U^i_{,j}$

It was shown above that the strain-rate in Cartesian coordinates $\left(\partial U^i/\partial x^j\right)$ transforms into the following expression in non-orthogonal curvilinear coordinates:

$$\frac{\partial U^i}{\partial x^j} \rightarrow \nabla_j U^i \equiv U^i_{,j} = \frac{\partial U^i}{\partial \xi^j} + U^m \Gamma^i_{mj} \tag{C.95}$$

which is expressed in terms of the physical velocity component $U^{(i)}$:

$$U^i_{,j} = \frac{\partial}{\partial \xi^j}\left(\frac{U^{(i)}}{\sqrt{g_{ii}}}\right) + \frac{U^{(m)}}{\sqrt{g_{mm}}}\Gamma^i_{mj} \tag{C.96}$$

The strain-rate is expanded in 3-*D* curvilinear coordinates, as follows:

$$U_{,1} = \frac{\partial}{\partial \xi}\left(\frac{U}{\sqrt{g_{11}}}\right) + \frac{U}{\sqrt{g_{11}}}\Gamma^1_{11} + \frac{V}{\sqrt{g_{22}}}\Gamma^1_{21} + \frac{W}{\sqrt{g_{33}}}\Gamma^1_{31} \tag{C.97}$$

$$U_{,2} = \frac{\partial}{\partial \eta}\left(\frac{U}{\sqrt{g_{11}}}\right) + \frac{U}{\sqrt{g_{11}}}\Gamma^1_{12} + \frac{V}{\sqrt{g_{22}}}\Gamma^1_{22} + \frac{W}{\sqrt{g_{33}}}\Gamma^1_{32} \tag{C.98}$$

$$U_{,3} = \frac{\partial}{\partial \zeta}\left(\frac{U}{\sqrt{g_{11}}}\right) + \frac{U}{\sqrt{g_{11}}}\Gamma^1_{13} + \frac{V}{\sqrt{g_{22}}}\Gamma^1_{23} + \frac{W}{\sqrt{g_{33}}}\Gamma^1_{33} \tag{C.99}$$

$$V_{,1} = \frac{\partial}{\partial \xi}\left(\frac{V}{\sqrt{g_{22}}}\right) + \frac{U}{\sqrt{g_{11}}}\Gamma^2_{11} + \frac{V}{\sqrt{g_{22}}}\Gamma^2_{21} + \frac{W}{\sqrt{g_{33}}}\Gamma^2_{31} \tag{C.100}$$

$$V_{,2} = \frac{\partial}{\partial \eta}\left(\frac{V}{\sqrt{g_{22}}}\right) + \frac{U}{\sqrt{g_{11}}}\Gamma^2_{12} + \frac{V}{\sqrt{g_{22}}}\Gamma^2_{22} + \frac{W}{\sqrt{g_{33}}}\Gamma^2_{32} \tag{C.101}$$

$$V_{,3} = \frac{\partial}{\partial \zeta}\left(\frac{V}{\sqrt{g_{22}}}\right) + \frac{U}{\sqrt{g_{11}}}\Gamma^2_{13} + \frac{V}{\sqrt{g_{22}}}\Gamma^2_{23} + \frac{W}{\sqrt{g_{33}}}\Gamma^2_{33} \tag{C.102}$$

$$W_{,1} = \frac{\partial}{\partial \xi}\left(\frac{W}{\sqrt{g_{33}}}\right) + \frac{U}{\sqrt{g_{11}}}\Gamma^3_{11} + \frac{V}{\sqrt{g_{22}}}\Gamma^3_{21} + \frac{W}{\sqrt{g_{33}}}\Gamma^3_{31} \tag{C.103}$$

$$W_{,(2)} = \frac{\partial}{\partial \eta}\left(\frac{W}{\sqrt{g_{33}}}\right) + \frac{U}{\sqrt{g_{11}}}\Gamma^3_{12} + \frac{V}{\sqrt{g_{22}}}\Gamma^3_{22} + \frac{W}{\sqrt{g_{33}}}\Gamma^3_{32} \tag{C.104}$$

$$W_{,(3)} = \frac{\partial}{\partial \zeta}\left(\frac{W}{\sqrt{g_{33}}}\right) + \frac{U}{\sqrt{g_{11}}}\Gamma^3_{13} + \frac{V}{\sqrt{g_{22}}}\Gamma^3_{23} + \frac{W}{\sqrt{g_{33}}}\Gamma^3_{33} \tag{C.105}$$

where $U^{(i)} = (U,V,W)$ denote the physical velocity components and $\xi^i = (\xi,\eta,\zeta)$ the non-physical contravariant components of the covariant base vectors $\mathbf{g}_i = (\mathbf{g}_1,\mathbf{g}_2,\mathbf{g}_3)$.

C.5.3 Examination of Curvilinear Transport Equations

The momentum equation in curvilinear coordinates is given by:

$$\frac{\partial}{\partial t}\left(\rho U^{(i)}\right) + \frac{1}{J}\frac{\partial}{\partial \xi^j}\left(\frac{J}{\sqrt{g_{jj}}}\rho U^{(i)}U^{(j)}\right) = \frac{1}{J}\frac{\partial}{\partial \xi^j}\left(\sqrt{g_{ii}}J\tau^{ij}\right) + S^i_U \tag{C.106}$$

where the source term, S^i_U, is given by Equation (C.80). The diffusion term in the above equation can be rearranged so that it follows the same format as the diffusion term in the scalar equation (Equation C.71). The stress tensor for an incompressible flow, using a linear eddy-viscosity model, can be written:

$$\begin{aligned}\tau^{ij} &= \mu_{eff}\left(g^{jm}\nabla_m U^i + g^{im}\nabla_m U^j\right) - \frac{2}{3}g^{ij}\rho k \\ &= \mu_{eff}\left[g^{jm}\left(\frac{\partial U^i}{\partial \xi^m} + \Gamma^i_{km}U^k\right) + g^{im}\left(\frac{\partial U^j}{\partial \xi^m} + \Gamma^j_{km}U^k\right)\right] - \frac{2}{3}g^{ij}\rho k\end{aligned} \tag{C.107}$$

Substituting the above equation into Equation (C.106), the first component of the diffusion term is given by:

$$\frac{1}{J}\frac{\partial}{\partial \xi^j}\left(\sqrt{g_{ii}}J\mu_{eff}g^{jm}\frac{\partial U^i}{\partial \xi^m}\right) \tag{C.108}$$

Writing the velocity component U^i in terms of the physical component $U^{(i)}$:

$$\frac{1}{J}\frac{\partial}{\partial \xi^j}\left[\sqrt{g_{ii}}J\mu_{eff}g^{jm}\frac{\partial}{\partial \xi^m}\left(\frac{U^{(i)}}{\sqrt{g_{ii}}}\right)\right] \tag{C.109}$$

and expanding the inner-derivative using the quotient rule, one obtains:

$$\frac{1}{J}\frac{\partial}{\partial \xi^j}\left(J\mu_{eff}g^{jm}\frac{\partial U^{(i)}}{\partial \xi^m} - \frac{J}{\sqrt{g_{ii}}}\mu_{eff}g^{jm}U^{(i)}\frac{\partial \sqrt{g_{ii}}}{\partial \xi^m}\right) \tag{C.110}$$

The first term in the above Equation is of a similar format to the diffusion term in the scalar equation diffusion term, which was given as (Equation C.71):

$$\frac{1}{J}\frac{\partial}{\partial\xi^j}\left[J\left(\Gamma_\phi+\frac{\mu_t}{\sigma_\phi}\right)g^{jm}\frac{\partial\phi}{\partial\xi^m}\right] \tag{C.111}$$

Checking the Formulation of Convection

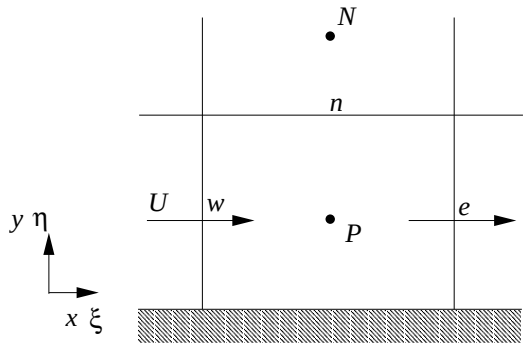

Figure C.1: Cartesian grid cell with mean velocity U parallel to the x-axis

In the preceding section it was shown that the transport equations for momentum and scalar can be expressed in the form:

$$\frac{\partial}{\partial t}(\rho\phi)+\frac{1}{J}\frac{\partial}{\partial\xi^j}\left(\frac{J}{\sqrt{g_{jj}}}\rho\phi U^{(j)}\right)=\frac{1}{J}\frac{\partial}{\partial\xi^j}\left(J\Gamma g^{jm}\frac{\partial\phi}{\partial\xi^m}\right)+S_\phi \tag{C.112}$$

where ϕ represents a scalar parameter or the physical velocity component, Γ denotes the relevant diffusivity and S_ϕ includes the pressure gradient and curvature source terms in the momentum equation. To confirm that the convection term in the above equation has been derived correctly, one can show that by integrating the convection term over a control volume one obtains an expression involving mass fluxes of parameter ϕ through the cell faces. The convection of scalar ϕ in the ξ-direction is discretized and integrated over a 2-*D* physical cell volume (see Figure C.1) as follows:

$$\begin{aligned}&\int\frac{1}{J}\frac{\partial}{\partial\xi^j}\left(\frac{J}{\sqrt{g_{jj}}}\rho\phi U^{(j)}\right)\mathrm{d}Vol\\&=\frac{1}{\Delta\xi_{ew}}\left[\left(\frac{J}{\sqrt{g_{11}}}\rho\phi U\right)_e-\left(\frac{J}{\sqrt{g_{11}}}\rho\phi U\right)_w\right]\Delta\xi_{ew}\Delta\eta_{ns}\end{aligned} \tag{C.113}$$

where U is the physical velocity component in the ξ-direction and $\Delta Vol = J\Delta\xi\Delta\eta$ is the cell volume (equivalent to an area in 2-*D*). Each of the dimensionless distances in computational space has unit magnitude:

$$\Delta\xi_{ew}=\Delta\eta_{ns}=1 \tag{C.114}$$

the Jacobian is therefore the cell volume:

$$J = \Delta Vol \tag{C.115}$$

The metric tensor $(g_{11})_e$ is equivalent to square of the physical distance between the nodes P and E:

$$\begin{aligned}(g_{11})_e &= \left(\frac{\partial x}{\partial \xi}\right)^2 + \left(\frac{\partial y}{\partial \xi}\right)^2 \\ &\approx \left(\frac{\Delta x_{EP}}{\Delta \xi_{EP}}\right)^2 + \left(\frac{\Delta y_{EP}}{\Delta \xi_{EP}}\right)^2 \\ &\approx (\Delta x_{EP})^2 \end{aligned} \tag{C.116}$$

and the convective flux through the eastern cell faces is therefore given by:

$$\left(\frac{J}{\sqrt{g_{11}}}\rho\phi U\right)_e = \left(\frac{\Delta Vol}{\Delta x_{EP}}\rho\phi U\right)_e = (\Delta y_{ns}\rho\phi U)_e \tag{C.117}$$

where the velocity U_e is normal to the eastern cell face which has area Δy_{ns}. Therefore, $(\Delta y_{ns}\rho\phi U)_e$ represents the mass flux of ϕ through the eastern cell face.

Checking the Formulation of Diffusion

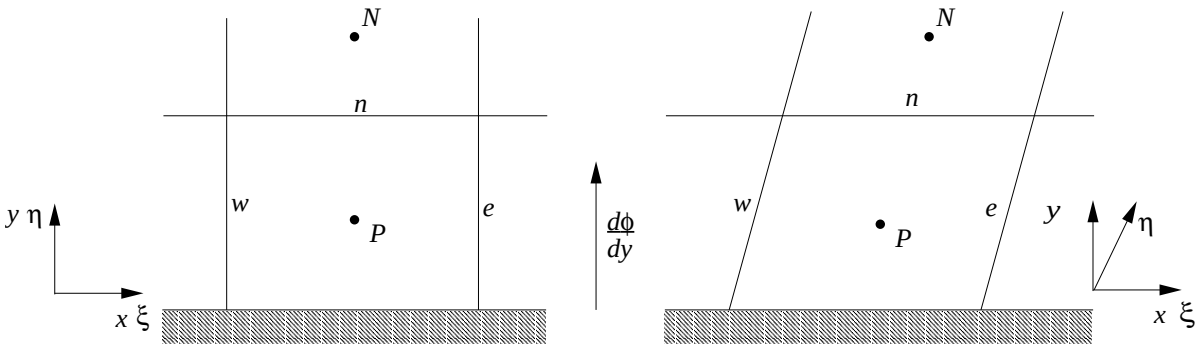

Figure C.2: Cartesian and skew grid arrangements with vertical gradient of ϕ

The second check on the derivation of the curvilinear transport equations involves the diffusion term. Figure C.2 shows two grid arrangements with equal spacing of grid-lines in both the vertical y-axis and the horizontal x-axis. In the first grid, the base vectors are aligned to a Cartesian grid (in which case $\xi = x$ and $\eta = y$) but in the second grid the η-axis is skewed from the vertical. A gradient in ϕ in the vertical y-direction is imposed and it should be demonstrated that equal diffusion of ϕ is obtained using the two different grids (assuming there to be no gradient of ϕ in the x-direction). The diffusion term is given by:

$$\frac{1}{J}\frac{\partial}{\partial \xi^j}\left(Jg^{jm}\Gamma\frac{\partial \phi}{\partial \xi^m}\right) \tag{C.118}$$

In the 2-*D* case considered here, the diffusion of ϕ in the vertical direction is calculated from:

$$\frac{1}{J}\frac{\partial}{\partial \eta}\left(Jg^{22}\Gamma\frac{\partial \phi}{\partial \eta}\right) \tag{C.119}$$

As before, the Jacobian in 2-*D* is equivalent to the cell area:

$$J = Area = \Delta x_{ew}\Delta y_{ns} = \Delta x_{ew}\Delta y_{NP} \tag{C.120}$$

The contravariant metric tensor, g^{22}, is obtained from matrix inversion:

$$\begin{aligned} g^{ij} = \frac{1}{g}G_{ij} &= \frac{1}{J^2}\left[cof\begin{pmatrix} g_{11} & g_{12} \\ g_{21} & g_{22} \end{pmatrix}\right]^T \\ &= \frac{1}{J^2}\begin{bmatrix} g_{22} & -g_{12} \\ -g_{21} & g_{11} \end{bmatrix} \end{aligned} \tag{C.121}$$

$$g^{22} = \frac{1}{J^2}g_{11} = \frac{1}{J^2}\left(\Delta x_{ew}\right)^2 \tag{C.122}$$

Substituting Equations (C.120) and (C.122) into (C.119):

$$\frac{1}{J}\frac{\partial}{\partial \eta}\left(Jg^{22}\Gamma\frac{\partial \phi}{\partial \eta}\right) = \frac{1}{J}\frac{\partial}{\partial \eta}\left(\frac{\left(\Delta x_{ew}\right)^2}{J}\Gamma\frac{\partial \phi}{\partial \eta}\right) \tag{C.123}$$

$$= \frac{1}{J}\frac{\partial}{\partial \eta}\left(\frac{\Delta x_{ew}}{\Delta y_{NP}}\Gamma\frac{\partial \phi}{\partial \eta}\right) \tag{C.124}$$

The diffusive fluxes obtained by discretizing and integrating the above equation are of the form:

$$\frac{\Gamma A}{L} \tag{C.125}$$

where where A is the cell-face area (equivalent in 2-*D* to Δx_{ew}) and L is the vertical distance between adjacent nodes (i.e. Δy_{TP}). The diffusion of ϕ in the vertical direction is therefore identical whether a Cartesian or skew grid is employed.

C.5.4 Non-Conservative Convection

Scalar

Convection of scalar ϕ in conservative form was shown earlier to be given by:

$$\frac{\partial}{\partial t}\left(\rho\phi\right) + \frac{1}{J}\frac{\partial}{\partial \xi^j}\left(\frac{J}{\sqrt{g_{jj}}}\rho\phi U^{(j)}\right) \tag{C.126}$$

Expanding this using the product rule:

$$\phi\frac{\partial\rho}{\partial t}+\rho\frac{\partial\phi}{\partial t}+\frac{\rho U^{(j)}}{\sqrt{g_{jj}}}\frac{\partial\phi}{\partial\xi^j}+\frac{\phi}{J}\frac{\partial}{\partial\xi^j}\left(\frac{J}{\sqrt{g_{jj}}}\rho U^{(j)}\right) \tag{C.127}$$

Continuity is expressed in curvilinear coordinates:

$$\frac{\partial\rho}{\partial t}+\frac{\Delta}{\Delta\xi^j}\left(\rho U^j\right) = 0 \tag{C.128}$$

$$\frac{\partial\rho}{\partial t}+\frac{1}{J}\frac{\partial}{\partial\xi^j}\left(\frac{J}{\sqrt{g_{jj}}}\rho U^{(j)}\right) = 0 \tag{C.129}$$

Therefore, Equation (C.127) simplifies to:

$$\boxed{\rho\frac{\partial\phi}{\partial t}+\frac{\rho U^{(j)}}{\sqrt{g_{jj}}}\frac{\partial\phi}{\partial\xi^j}} \tag{C.130}$$

Momentum

Convection of momentum can also be obtained in non-conservative form by expanding the conservative form and canceling terms using continuity. The conservative convection term was shown earlier to be given by:

$$\frac{\partial}{\partial t}\left(\rho U^{(i)}\right)+\frac{1}{J}\frac{\partial}{\partial\xi^j}\left(\frac{J}{\sqrt{g_{jj}}}\rho U^{(i)}U^{(j)}\right) \tag{C.131}$$

This can be rearranged to give the non-conservative form:

$$\boxed{\rho\frac{\partial U^{(i)}}{\partial t}+\frac{\rho U^{(j)}}{\sqrt{g_{jj}}}\frac{\partial U^{(i)}}{\partial\xi^j}} \tag{C.132}$$

C.5.5 Alternative Approach to Derivation

In the preceding analysis, it has been shown that the convection term in the momentum equations can be written in curvilinear coordinates, as follows:

$$\begin{aligned}(\mathbf{U}\cdot\nabla)\mathbf{U} &= \nabla_j\left(U^iU^j\right)\mathbf{g}_{(i)}\\ &= \left[\frac{U^{(j)}}{\sqrt{g_{jj}}}\frac{\partial U^{(i)}}{\partial\xi^j}-U^{(i)}U^{(j)}\frac{\Gamma^m_{ij}g_{im}}{g_{ii}\sqrt{g_{jj}}}+U^{(j)}U^{(m)}\frac{\Gamma^i_{mj}\sqrt{g_{ii}}}{\sqrt{g_{jj}g_{mm}}}\right]\mathbf{g}_{(i)}\end{aligned} \tag{C.133}$$

The above expression was obtained by converting the Cartesian convection term into curvilinear coordinates. To check that the derivation is correct, one can re-derive the convection term by starting

directly from the vector form, $(\mathbf{U}\cdot\nabla)\mathbf{U}$, as follows:

$$\begin{aligned}(\mathbf{U}\cdot\nabla)\mathbf{U} &= U^j\mathbf{g}_j\cdot\mathbf{g}^k\frac{\partial}{\partial\xi^k}\left(U^i\mathbf{g}_i\right)\\ &= U^j\delta^k_j\frac{\partial}{\partial\xi^k}\left(U^i\mathbf{g}_i\right)\\ &= U^j\frac{\partial}{\partial\xi^j}\left(U^i\mathbf{g}_i\right)\end{aligned} \tag{C.134}$$

The covariant derivative of a vector is given by:

$$\frac{\partial}{\partial\xi^j}\left(U^i\mathbf{g}_i\right)=\left(\frac{\partial U^i}{\partial\xi^j}+U^m\Gamma^i_{mj}\right)\mathbf{g}_i \tag{C.135}$$

and therefore we obtain:

$$(\mathbf{U}\cdot\nabla)\mathbf{U}=\left(U^j\frac{\partial U^i}{\partial\xi^j}+U^jU^m\Gamma^i_{mj}\right)\mathbf{g}_i \tag{C.136}$$

Using physical velocity components $U^{(i)}$, where $U^i=U^{(i)}/\sqrt{g_{ii}}$, and physical base vectors $\mathbf{g}_{(i)}$, where $\mathbf{g}_i=\sqrt{g_{ii}}\mathbf{g}_{(i)}$:

$$(\mathbf{U}\cdot\nabla)\mathbf{U}=\left[\underbrace{\sqrt{g_{ii}}\frac{U^{(j)}}{\sqrt{g_{jj}}}\frac{\partial}{\partial\xi^j}\left(\frac{U^{(i)}}{\sqrt{g_{ii}}}\right)}+U^{(j)}U^{(m)}\frac{\Gamma^i_{mj}\sqrt{g_{ii}}}{\sqrt{g_{jj}g_{mm}}}\right]\mathbf{g}_{(i)} \tag{C.137}$$

and using the quotient rule to rearrange the underbraced term:

$$\sqrt{g_{ii}}\frac{U^{(j)}}{\sqrt{g_{jj}}}\frac{\partial}{\partial\xi^j}\left(\frac{U^{(i)}}{\sqrt{g_{ii}}}\right)=\frac{U^{(j)}}{\sqrt{g_{jj}}}\frac{\partial U^{(i)}}{\partial\xi^j}-\frac{U^{(i)}U^{(j)}}{\sqrt{g_{ii}g_{jj}}}\frac{\partial\sqrt{g_{ii}}}{\partial\xi^j} \tag{C.138}$$

From Equation (C.77), the gradient term, $\partial\sqrt{g_{ii}}/\partial\xi^j$, can be expressed in terms of the Christoffel symbols and the convection term becomes:

$$(\mathbf{U}\cdot\nabla)\mathbf{U}=\left[\frac{U^{(j)}}{\sqrt{g_{jj}}}\frac{\partial U^{(i)}}{\partial\xi^j}-U^{(i)}U^{(j)}\frac{\Gamma^m_{ij}g_{im}}{g_{ii}\sqrt{g_{jj}}}+U^{(j)}U^{(m)}\frac{\Gamma^i_{mj}\sqrt{g_{ii}}}{\sqrt{g_{jj}g_{mm}}}\right]\mathbf{g}_{(i)} \tag{C.139}$$

This is identical to the expression which was derived earlier (Equation C.133).

Appendix D

Subgrid Wall Function Transport Equations

In the subgrid wall function a number of assumptions are made to obtain a set of simplified transport equations:

- Only the velocity components parallel to the wall are solved.
- Diffusion parallel to the wall is assumed to be negligible in comparison with diffusion normal to the wall.
- Convection is modelled in non-conservative form.
- The velocity component normal to the wall is obtained from continuity across the subgrid control volumes, with an additional scaling factor to ensure consistency in the boundary conditions.

For the present purposes of deriving transport equations in non-orthogonal curvilinear coordinates it is assumed that the wall is in the $\xi^1 - \xi^2$ (or $\xi - \eta$) plane, and $\xi^3 \equiv \zeta$ is the wall-normal direction[1]. In this reference frame, only the U- and V-momentum equations are solved across the subgrid and only diffusion terms involving gradients in the ζ-direction are significant.

D.1 Convection of Momentum

In Appendix C, the convection term in the momentum equation was derived as follows:

$$(\mathbf{U}\cdot\nabla)\,\mathbf{U} = \left(\frac{U^{(j)}}{\sqrt{g_{jj}}} \frac{\partial U^{(i)}}{\partial \xi^j} - U^{(i)} U^{(j)} \frac{\Gamma^m_{ij} g_{im}}{g_{ii}\sqrt{g_{jj}}} + U^{(j)} U^{(m)} \frac{\Gamma^i_{mj}\sqrt{g_{ii}}}{\sqrt{g_{jj} g_{mm}}} \right) \mathbf{g}_{(i)} \tag{D.1}$$

[1] In fact, if a skewed grid is employed, the ζ-direction may be at an angle to the wall other than 90^o.

where $U^{(i)}$ represents the physical velocity components aligned to the curvilinear base vectors and the last two terms, involving Christoffel symbols, arise from the use of a non-uniform grid. The UMIST-*N* wall function employs an upwind scheme for discretizing the convection term. However, rather than use the above expression for convection of momentum, the UMIST-*N* wall function transforms the velocity components in the upstream cell from the coordinate system used in the upstream cell into the coordinate system used in the current cell. To illustrate this, Figure D.1 shows a curved surface with a wall-parallel U-velocity in the positive ξ-direction and W-velocity in the ζ-direction. Using an upwind scheme, the wall-parallel convection term for node P is calculated by transforming the upstream velocity at node W from the coordinate frame used in cell W into the coordinate frame of cell P. Since the velocity components in the upstream and the current cells are expressed using identical base vectors (i.e. base vectors do not rotate between the adjacent cells), gradients of the metric tensors are zero. This means that the Christoffel symbols appearing in Equation D.1 are zero and the expression simplifies to:

$$(\mathbf{U}\cdot\nabla)\,\mathbf{U} = \frac{U^{(j)}}{\sqrt{g_{jj}}}\left(\frac{\partial U^{(i)}}{\partial \xi^j}\right)^{*}\mathbf{g}_{(i)} \tag{D.2}$$

The asterisk is introduced around the velocity gradient term to denote that upstream values of $U^{(i)}$ are transformed into the coordinate system used in the current cell. In the current version of the UMIST-*N* wall function, the upstream velocity is transformed from the upstream covariant base vectors into Cartesian base vectors and from there into the current cell covariant base vectors. Details of these transformations which involve the Jacobian and inverse Jacobian matrices are provided in Section E.8. Reasons for adopting this practice are discussed in Appendix G.

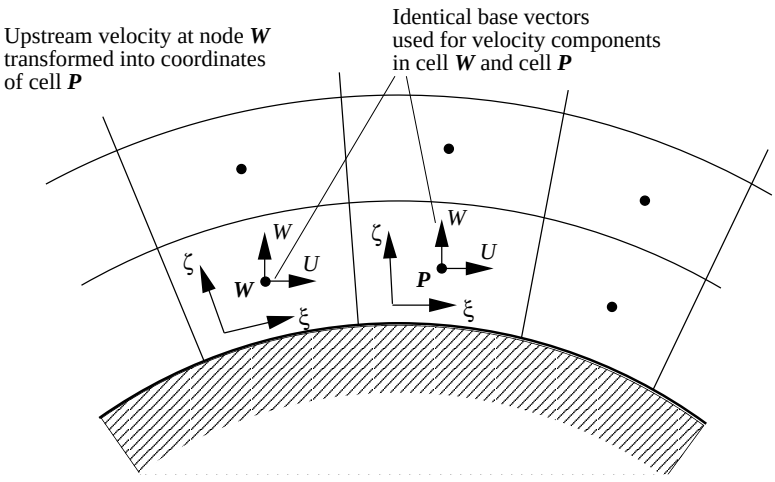

Figure D.1: Schematic of subgrid cells over a curved wall showing the transformation practice adopted for convection of momentum.

The subgrid momentum equations in non-orthogonal curvilinear coordinates can therefore be writ-

ten as follows:

$$\rho\frac{\partial U^{(i)}}{\partial t}+\frac{\rho U^{(j)}}{\sqrt{g_{jj}}}\left(\frac{\partial U^{(i)}}{\partial \xi^j}\right)^* = \frac{1}{J}\frac{\partial}{\partial \xi^j}\left(\sqrt{g_{ii}}J\tau^{ij}\right)+S_U^i \tag{D.3}$$

where the source term, S_U^i, is given by:

$$S_U^i = -g^{ij}\sqrt{g_{ii}}\frac{\partial P^{'}}{\partial \xi^j}-\tau^{ij}\frac{\Gamma_{ij}^m g_{im}}{\sqrt{g_{ii}}}+\tau^{mj}\Gamma_{mj}^i\sqrt{g_{ii}} \tag{D.4}$$

There is no summation on the i index in the above equations, the effective pressure is given by $P^{'}=P+2\rho k/3$ and the stress, τ^{ij}, is expanded in Section C.5.2.

D.2 U-Momentum

It is assumed that only the wall-normal (or ζ-direction) gradient of the stress tensor is significant across the subgrid. Writing convection in the form described above, the subgrid momentum equation becomes:

$$\rho\frac{\partial U^{(i)}}{\partial t}+\frac{\rho U^{(j)}}{\sqrt{g_{jj}}}\left(\frac{\partial U^{(i)}}{\partial \xi^j}\right)^* = \frac{1}{J}\frac{\partial}{\partial \zeta}\left(\sqrt{g_{ii}}J\tau^{i3}\right)+S_U^i \tag{D.5}$$

where the source term, S_U^i, is given by Equation (D.4). The subgrid stress tensor, τ^{i3} is obtained from Section C.5.2, where it is assumed that only the wall-normal gradient of the wall-parallel velocity is significant:

$$\tau^{i3} \;=\; \mu g^{33}U_{,3}^i-\rho\overline{u^i w} \tag{D.6}$$

Using a linear eddy-viscosity turbulence model, the Reynolds stress is given by:

$$-\rho\overline{u^i w}=\mu_t g^{33}U_{,3}^i-\frac{2}{3}g^{i3}\rho k \tag{D.7}$$

and the U-momentum diffusion term can then be written, using Equation (C.99):

$$\begin{aligned}
&\frac{1}{J}\frac{\partial}{\partial \zeta}\left(\sqrt{g_{ii}}J\tau^{i3}\right)\\
&=\frac{1}{J}\frac{\partial}{\partial \zeta}\left(J\sqrt{g_{11}}\mu_{eff}g^{33}\left[\underbrace{\frac{\partial}{\partial \zeta}\left(\frac{U}{\sqrt{g_{11}}}\right)}+\frac{U^{(m)}}{\sqrt{g_{mm}}}\Gamma_{m3}^1\right]\right)\\
&-\frac{1}{J}\frac{\partial}{\partial \zeta}\left(\frac{2}{3}\rho k g^{13}J\sqrt{g_{11}}\right)
\end{aligned} \tag{D.8}$$

where $(\mu_{eff} = \mu + \mu_t)$. Expanding the underbraced term using the quotient rule:

$$\begin{aligned}
&\frac{1}{J}\frac{\partial}{\partial\zeta}\left[J\sqrt{g_{11}}\mu_{eff}g^{33}\frac{\partial}{\partial\zeta}\left(\frac{U}{\sqrt{g_{11}}}\right)\right] \\
&= \frac{1}{J}\frac{\partial}{\partial\zeta}\left(J\mu_{eff}g^{33}\frac{\partial U}{\partial\zeta} - \frac{J}{\sqrt{g_{11}}}\mu_{eff}g^{33}U\frac{\partial\sqrt{g_{11}}}{\partial\zeta}\right)
\end{aligned} \tag{D.9}$$

where, from Equation (C.77):

$$\frac{\partial\sqrt{g_{11}}}{\partial\zeta} = \frac{g_{1m}}{\sqrt{g_{11}}}\Gamma^m_{13} \tag{D.10}$$

The diffusion term can, therefore, be written:

$$\frac{1}{J}\frac{\partial}{\partial\zeta}\left(J\mu_{eff}g^{33}\frac{\partial U}{\partial\zeta}\right) + S \tag{D.11}$$

where:

$$\begin{aligned}
S &= \frac{1}{J}\frac{\partial}{\partial\zeta}\left[J\mu_{eff}g^{33}\left(U^{(m)}\frac{\sqrt{g_{11}}}{\sqrt{g_{mm}}}\Gamma^1_{m3} - U\frac{g_{1m}}{g_{11}}\Gamma^m_{13}\right)\right] \\
&\quad -\frac{1}{J}\frac{\partial}{\partial\zeta}\left(\frac{2}{3}\rho k g^{13}J\sqrt{g_{11}}\right)
\end{aligned} \tag{D.12}$$

Finally, the subgrid U-momentum equation can be written:

$$\boxed{\frac{\rho U}{\sqrt{g_{11}}}\left(\frac{\partial U}{\partial\xi}\right)^* + \frac{\rho V}{\sqrt{g_{22}}}\left(\frac{\partial U}{\partial\eta}\right)^* + \frac{\rho W}{\sqrt{g_{33}}}\left(\frac{\partial U}{\partial\zeta}\right)^* = \frac{1}{J}\frac{\partial}{\partial\zeta}\left(J\mu_{eff}g^{33}\frac{\partial U}{\partial\zeta}\right) + S^1_U} \tag{D.13}$$

where the source term, S^1_U, is now given by:

$$\begin{aligned}
S^1_U &= -g^{1j}\sqrt{g_{11}}\frac{\partial P'}{\partial\xi^j} - \tau^{1j}\frac{\Gamma^m_{1j}g_{1m}}{\sqrt{g_{11}}} + \tau^{mj}\Gamma^1_{mj}\sqrt{g_{11}} \\
&\quad +\frac{1}{J}\frac{\partial}{\partial\zeta}\left[J\mu_{eff}g^{33}\left(U^{(m)}\frac{\sqrt{g_{11}}}{\sqrt{g_{mm}}}\Gamma^1_{m3} - U\frac{g_{1m}}{g_{11}}\Gamma^m_{13}\right)\right]
\end{aligned} \tag{D.14}$$

and the pressure term includes the isotropic component of the Reynolds stress $\left(P' = P + 2\rho k/3\right)$.

D.3 V-Momentum

The process described above to derive the subgrid U-momentum equation can be repeated to obtain the wall-parallel V-momentum equation:

$$\boxed{\frac{\rho U}{\sqrt{g_{11}}}\left(\frac{\partial V}{\partial\xi}\right)^* + \frac{\rho V}{\sqrt{g_{22}}}\left(\frac{\partial V}{\partial\eta}\right)^* + \frac{\rho W}{\sqrt{g_{33}}}\left(\frac{\partial V}{\partial\zeta}\right)^* = \frac{1}{J}\frac{\partial}{\partial\zeta}\left(J\mu_{eff}g^{33}\frac{\partial V}{\partial\zeta}\right) + S^2_U} \tag{D.15}$$

where:

$$\begin{aligned} S_U^2 &= -g^{2j}\sqrt{g_{22}}\frac{\partial P'}{\partial \xi^j} - \tau^{2j}\frac{\Gamma_{2j}^m g_{2m}}{\sqrt{g_{22}}} + \tau^{mj}\Gamma_{mj}^2\sqrt{g_{22}} \\ &\quad + \frac{1}{J}\frac{\partial}{\partial \zeta}\left[J\mu_{eff}g^{33}\left(U^{(m)}\frac{\sqrt{g_{22}}}{\sqrt{g_{mm}}}\Gamma_{m3}^2 - V\frac{g_{2m}}{g_{22}}\Gamma_{23}^m\right)\right] \end{aligned} \tag{D.16}$$

D.4 Scalar, ϕ

The subgrid steady-flow scalar equation is obtained from Equation (C.71) and (C.130) by neglecting diffusive fluxes parallel to the wall:

$$\boxed{\frac{\rho U}{\sqrt{g_{11}}}\frac{\partial \phi}{\partial \xi} + \frac{\rho V}{\sqrt{g_{22}}}\frac{\partial \phi}{\partial \eta} + \frac{\rho W}{\sqrt{g_{33}}}\frac{\partial \phi}{\partial \zeta} = \frac{1}{J}\frac{\partial}{\partial \zeta}\left(JJ_\phi^3\right) + S_\phi} \tag{D.17}$$

where the scalar flux, J_ϕ^3, is given by:

$$J_\phi^3 = \left(\Gamma_\phi + \frac{\mu_t}{\sigma_\phi}\right)g^{33}\frac{\partial \phi}{\partial \zeta} \tag{D.18}$$

D.5 Turbulent Kinetic Energy, k

The subgrid k-equation, obtained in a similar manner to that described above for the scalar equation, is given by:

$$\boxed{\frac{\rho U}{\sqrt{g_{11}}}\frac{\partial k}{\partial \xi} + \frac{\rho V}{\sqrt{g_{22}}}\frac{\partial k}{\partial \eta} + \frac{\rho W}{\sqrt{g_{33}}}\frac{\partial k}{\partial \zeta} = \frac{1}{J}\frac{\partial}{\partial \zeta}\left[Jg^{33}\left(\mu + \frac{\mu_t}{\sigma_k}\right)\frac{\partial k}{\partial \zeta}\right] + G - \rho\varepsilon} \tag{D.19}$$

where the production rate of turbulent kinetic energy, G, is as follows:

$$G = -\rho g_{im}\overline{u^j u^m}U_{,j}^i \tag{D.20}$$

All the components of the production term are included in the UMIST-N wall function to account for turbulence generation due to both normal and shear stress. Expressions for the Reynolds stress $\left(-\rho\overline{u^i u^j}\right)$ and strain-rate $\left(U_{,j}^i\right)$ are given above (see Equations C.89 to C.105). The expanded pro-

duction term, G, has three dummy indices and therefore expands to 27 terms, as follows:

$$\begin{aligned} G &= -\rho\overline{uu}(g_{11}U_{,1}+g_{21}V_{,1}+g_{31}W_{,1}) \\ &\quad -\rho\overline{uv}(g_{12}U_{,1}+g_{22}V_{,1}+g_{32}W_{,1}) \\ &\quad -\rho\overline{uw}(g_{13}U_{,1}+g_{23}V_{,1}+g_{33}W_{,1}) \\ &\quad -\rho\overline{uv}(g_{11}U_{,2}+g_{21}V_{,2}+g_{31}W_{,2}) \\ &\quad -\rho\overline{vv}(g_{12}U_{,2}+g_{22}V_{,2}+g_{32}W_{,2}) \\ &\quad -\rho\overline{vw}(g_{13}U_{,2}+g_{23}V_{,2}+g_{33}W_{,2}) \\ &\quad -\rho\overline{uw}(g_{11}U_{,3}+g_{21}V_{,3}+g_{31}W_{,3}) \\ &\quad -\rho\overline{vw}(g_{12}U_{,3}+g_{22}V_{,3}+g_{32}W_{,3}) \\ &\quad -\rho\overline{ww}(g_{13}U_{,3}+g_{23}V_{,3}+g_{33}W_{,3}) \end{aligned} \tag{D.21}$$

The expression for the total dissipation rate is simplified by only considering the gradient of $k^{1/2}$ normal to the wall (i.e. in the ζ-direction):

$$\begin{aligned} \varepsilon &= \tilde{\varepsilon}+2\nu g^{jm}\left(\frac{\partial k^{1/2}}{\partial \xi^m}\right)\left(\frac{\partial k^{1/2}}{\partial \xi^j}\right) \\ &\approx \tilde{\varepsilon}+2\nu g^{33}\left(\frac{\partial k^{1/2}}{\partial \zeta}\right)\left(\frac{\partial k^{1/2}}{\partial \zeta}\right) \end{aligned} \tag{D.22}$$

D.6 Dissipation Rate, $\tilde{\varepsilon}$

The subgrid $\tilde{\varepsilon}$-equation is given by:

$$\boxed{\begin{aligned} \frac{\rho U}{\sqrt{g_{11}}}\frac{\partial \tilde{\varepsilon}}{\partial \xi}+\frac{\rho V}{\sqrt{g_{22}}}\frac{\partial \tilde{\varepsilon}}{\partial \eta}+\frac{\rho W}{\sqrt{g_{33}}}\frac{\partial \tilde{\varepsilon}}{\partial \zeta} &= \frac{1}{J}\frac{\partial}{\partial \zeta}\left[Jg^{33}\left(\mu+\frac{\mu_t}{\sigma_\varepsilon}\right)\frac{\partial \tilde{\varepsilon}}{\partial \zeta}\right] \\ &\quad +c_{\varepsilon 1}f_1 G\frac{\tilde{\varepsilon}}{k}-c_{\varepsilon 2}f_2\rho\frac{\tilde{\varepsilon}^2}{k}+\rho Y_c+P_{\varepsilon 3} \end{aligned}} \tag{D.23}$$

The source terms appearing in the $\tilde{\varepsilon}$-equation include production $(c_{\varepsilon 1}G\tilde{\varepsilon}/k)$, dissipation $\left(c_{\varepsilon 2}\tilde{\varepsilon}^2/k\right)$, Yap correction (Y_c) and the near-wall gradient production source term $(P_{\varepsilon 3})$. The production term, G, is expanded as above, Equation (D.21). The full expansion of the gradient production source term, $P_{\varepsilon 3}$, is given by:

$$P_{\varepsilon 3}=2\mu\nu_t g_{im}g_{jn}g^{lp}\left(g^{no}U^m_{,o}\right)_{,p}\left(g^{jk}U^i_{,k}\right)_{,l} \tag{D.24}$$

where, from Equation (B.109), the double-derivative of the velocity component is given by:

$$\left(g^{jk}U^i_{,k}\right)_{,l} = \frac{\partial\left(g^{jk}U^i_{,k}\right)}{\partial\xi^l} + g^{jk}U^m_{,k}\Gamma^i_{ml} + g^{mk}U^i_{,k}\Gamma^j_{ml} \tag{D.25}$$

Clearly, the full expansion of $P_{\varepsilon 3}$ cannot be used within the UMIST-*N* wall function without considerable cost. To simplify this term, it is assumed that only the gradient of the wall-parallel U and V velocity components in the wall-normal ζ-direction are significant (i.e. $k = l = o = p = 3$ and $i = m = 1,2$):

$$\begin{aligned} P_{\varepsilon 3} &= 2\mu\nu_t\left[g_{11}g_{jn}g^{33}\left(g^{n3}U_{,3}\right)_{,3}\left(g^{j3}U_{,3}\right)_{,3} + g_{22}g_{jn}g^{33}\left(g^{n3}V_{,3}\right)_{,3}\left(g^{j3}V_{,3}\right)_{,3}\right] \qquad \text{(D.26)} \\ &= 2\mu\nu_t g_{11}g^{33}. \\ &\quad \left\{g_{11}\left[\left(g^{13}U_{,3}\right)_{,3}\right]^2 + g_{22}\left[\left(g^{23}U_{,3}\right)_{,3}\right]^2 + g_{33}\left[\left(g^{33}U_{,3}\right)_{,3}\right]^2\right. \\ &\quad \left. +2g_{12}\left(g^{13}U_{,3}\right)_{,3}\left(g^{23}U_{,3}\right)_{,3} + 2g_{13}\left(g^{13}U_{,3}\right)_{,3}\left(g^{33}U_{,3}\right)_{,3} + 2g_{23}\left(g^{23}U_{,3}\right)_{,3}\left(g^{33}U_{,3}\right)_{,3}\right\} \\ &\quad +2\mu\nu_t g_{22}g^{33}. \\ &\quad \left\{g_{11}\left[\left(g^{13}V_{,3}\right)_{,3}\right]^2 + g_{22}\left[\left(g^{23}V_{,3}\right)_{,3}\right]^2 + g_{33}\left[\left(g^{33}V_{,3}\right)_{,3}\right]^2\right. \\ &\quad \left. +2g_{12}\left(g^{13}V_{,3}\right)_{,3}\left(g^{23}V_{,3}\right)_{,3} + 2g_{13}\left(g^{13}V_{,3}\right)_{,3}\left(g^{33}V_{,3}\right)_{,3} + 2g_{23}\left(g^{23}V_{,3}\right)_{,3}\left(g^{33}V_{,3}\right)_{,3}\right\} \qquad \text{(D.27)} \end{aligned}$$

where the double-derivative term is obtained from:

$$\left(g^{j3}U^i_{,3}\right)_{,3} = \frac{\partial\left(g^{j3}U^i_{,3}\right)}{\partial\zeta} + g^{j3}\left(U_{,3}\Gamma^i_{13} + V_{,3}\Gamma^i_{23}\right) + U^i_{,3}\left(g^{13}\Gamma^j_{13} + g^{23}\Gamma^j_{23} + g^{33}\Gamma^j_{33}\right) \tag{D.28}$$

The above expressions require the cell boundary values of strain-rates $U_{,3}$ and $V_{,3}$ (given by Equations C.99 and C.102), the contravariant metric tensor g^{33} and the Jacobian, J.

D.7 Non-Linear EVM

In the non-linear eddy-viscosity model (NLEVM) of Craft *et al*. [30], the Reynolds stress is a function of linear, quadratic and cubic combinations of strain-rate and vorticity. The constitutive equation for the Reynolds stress anisotropy, a^{ij}, defined as the traceless ratio of the Reynolds stress to the turbulent kinetic energy is given in Equation (2.27) for Cartesian coordinates. In order to satisfy the summation convention in non-orthogonal curvilinear coordinates (i.e. summation between repeated upper and

lower pairs of indices) this becomes:

$$\begin{aligned}
a^{ij} &= \frac{\overline{u^i u^j}}{k} - \frac{2}{3}g^{ij} \\
&= -\frac{\nu_t}{k}S^{ij} \\
&\quad +c_1\frac{\nu_t}{\tilde{\varepsilon}}\left(g_{kl}S^{ik}S^{jl} - \frac{1}{3}g_{km}g_{ln}S^{kl}S^{mn}g^{ij}\right) \\
&\quad +c_2\frac{\nu_t}{\tilde{\varepsilon}}\left(g_{kl}\Omega^{ik}S^{jl} + g_{kl}\Omega^{jk}S^{il}\right) \\
&\quad +c_3\frac{\nu_t}{\tilde{\varepsilon}}\left(g_{kl}\Omega^{ik}\Omega^{jl} - \frac{1}{3}g_{km}g_{ln}\Omega^{kl}\Omega^{mn}g^{ij}\right) \\
&\quad +c_4\frac{\nu_t k}{\tilde{\varepsilon}^2}\left(S^{ki}\Omega^{lj} + S^{kj}\Omega^{li}\right)g_{lm}g_{kn}S^{mn} \\
&\quad +c_5\frac{\nu_t k}{\tilde{\varepsilon}^2}\left(g_{kl}g_{mn}\Omega^{ik}\Omega^{ln}S^{mj} + g_{kl}g_{mn}S^{ik}\Omega^{ln}\Omega^{mj} - \frac{2}{3}g_{kl}g_{mo}g_{np}S^{km}\Omega^{on}\Omega^{pl}g^{ij}\right) \\
&\quad +c_6\frac{\nu_t k}{\tilde{\varepsilon}^2}g_{km}g_{ln}S^{ij}S^{ml}S^{kn} \\
&\quad +c_7\frac{\nu_t k}{\tilde{\varepsilon}^2}g_{km}g_{ln}S^{ij}\Omega^{ml}\Omega^{kn}
\end{aligned} \tag{D.29}$$

with non-orthogonal curvilinear strain-rate and vorticity tensors:

$$S^{ij} = g^{jm}U^i_{,m} + g^{im}U^j_{,m} \qquad\qquad \Omega^{ij} = g^{jm}U^i_{,m} - g^{im}U^j_{,m} \tag{D.30}$$

The Craft *et al*. model also involves a c_μ function which is sensitized to the dimensionless strain-rate and vorticity invariants. In Cartesian coordinates these are given by:

$$\tilde{S} = \frac{k}{\tilde{\varepsilon}}\sqrt{\frac{1}{2}S_{ij}S_{ij}} \qquad\qquad \tilde{\Omega} = \frac{k}{\tilde{\varepsilon}}\sqrt{\frac{1}{2}\Omega_{ij}\Omega_{ij}} \tag{D.31}$$

In order to satisfy the summation convention in non-orthogonal curvilinear coordinates two additional contravariant metric tensors must be introduced into the above expression:

$$\tilde{S} = \frac{k}{\tilde{\varepsilon}}\sqrt{\frac{1}{2}g_{ik}g_{jl}S^{kj}S^{il}} \qquad\qquad \tilde{\Omega} = \frac{k}{\tilde{\varepsilon}}\sqrt{\frac{1}{2}g_{ik}g_{jl}\Omega^{kj}\Omega^{il}} \tag{D.32}$$

The recent Craft *et al*. paper [67] introduced an additional term in the c_μ function involving the dimensionless third invariant of the strain-rate tensor, S_I. In Cartesian coordinates this is given by:

$$S_I = \frac{S_{ij}S_{jk}S_{ki}}{\left(S_{nl}S_{nl}/2\right)^{3/2}} \tag{D.33}$$

and in curvilinear coordinates:

$$S_I = \frac{g_{il}g_{jm}g_{kn}S^{lj}S^{mk}S^{ni}}{\left(g_{oq}g_{pr}S^{qp}S^{or}/2\right)^{3/2}} \tag{D.34}$$

The S_I term in non-orthogonal curvilinear coordinates, with ten dummy indices (i,j,k,l,m,n,o,p,q,r), is extremely expensive to calculate fully and was not used in the non-orthogonal UMIST-*N* wall function implementation of the Craft *et al*. model. To improve the numerical stability of the model, the tensorially linear c_6 and c_7 terms in Equation D.29 are treated as effective viscosity terms when their sum is negative (see discussion in Section 2.3). The Reynolds stress is then given by:

$$-\rho\overline{u^i u^j} = \mu_t' S^{ij} - \rho\widehat{\overline{u^i u^j}} - \frac{2}{3}g^{ij}\rho k \tag{D.35}$$

where the modified eddy-viscosity, μ_t', and the remaining higher-order components of the Reynolds stress, $\widehat{\overline{u_i u_j}}$, are given by:

$$\mu_t' = \mu_t - \mu_t \frac{k^2}{\tilde{\varepsilon}^2}\min\left[\left(c_6 g_{km}g_{ln}S^{ml}S^{kn} + c_7 g_{km}g_{ln}\Omega^{ml}\Omega^{kn}\right),0\right] \tag{D.36}$$

$$\begin{aligned}
\widehat{\overline{u^i u^j}} &= c_1\frac{\nu_t k}{\tilde{\varepsilon}}\left(g_{kl}S^{ik}S^{jl} - \frac{1}{3}g_{km}g_{ln}S^{kl}S^{mn}g^{ij}\right) \\
&+c_2\frac{\nu_t k}{\tilde{\varepsilon}}\left(g_{kl}\Omega^{ik}S^{jl} + g_{kl}\Omega^{jk}S^{il}\right) \\
&+c_3\frac{\nu_t k}{\tilde{\varepsilon}}\left(g_{kl}\Omega^{ik}\Omega^{jl} - \frac{1}{3}g_{km}g_{ln}\Omega^{kl}\Omega^{mn}g^{ij}\right) \\
&+c_4\frac{\nu_t k^2}{\tilde{\varepsilon}^2}\left(S^{ki}\Omega^{lj} + S^{kj}\Omega^{li}\right)g_{lm}g_{kn}S^{mn} \\
&+c_5\frac{\nu_t k^2}{\tilde{\varepsilon}^2}\left(g_{kl}g_{mn}\Omega^{ik}\Omega^{ln}S^{mj} + g_{kl}g_{mn}S^{ik}\Omega^{ln}\Omega^{mj} - \frac{2}{3}g_{kl}g_{mo}g_{np}S^{km}\Omega^{on}\Omega^{pl}g^{ij}\right) \\
&+\nu_t\frac{k^2}{\tilde{\varepsilon}^2}\max\left[\left(c_6 g_{km}g_{ln}S^{ml}S^{kn} + c_7 g_{km}g_{ln}\Omega^{ml}\Omega^{kn}\right),0\right]
\end{aligned} \tag{D.37}$$

Using the NLEVM, the subgrid momentum equation becomes:

$$\boxed{\frac{\rho U}{\sqrt{g_{11}}}\left(\frac{\partial U^{(i)}}{\partial\xi}\right)^* + \frac{\rho V}{\sqrt{g_{22}}}\left(\frac{\partial U^{(i)}}{\partial\eta}\right)^* + \frac{\rho W}{\sqrt{g_{33}}}\left(\frac{\partial U^{(i)}}{\partial\zeta}\right)^* = \frac{1}{J}\frac{\partial}{\partial\zeta}\left(J\mu_{eff}' g^{33}\frac{\partial U^{(i)}}{\partial\zeta}\right) + S_U^i} \tag{D.38}$$

where $i=1$ and $i=2$ for the subgrid U- and V-momentum equations, respectively. The source term, S_U^i, is now given by:

$$\begin{aligned}
S_U^i &= -g^{ij}\sqrt{g_{ii}}\frac{\partial P'}{\partial\xi^j} - \tau^{ij}\frac{\Gamma_{ij}^m g_{im}}{\sqrt{g_{ii}}} + \tau^{mj}\Gamma_{mj}^i\sqrt{g_{ii}} \\
&+\frac{1}{J}\frac{\partial}{\partial\zeta}\left[J\mu_{eff}' g^{33}\left(U^{(m)}\frac{\sqrt{g_{ii}}}{\sqrt{g_{mm}}}\Gamma_{m3}^i - U\frac{g_{im}}{g_{ii}}\Gamma_{i3}^m\right)\right] \\
&\underbrace{\frac{1}{J}\frac{\partial}{\partial\zeta}\left(\sqrt{g_{ii}}J\rho\widehat{u^i w}\right)}
\end{aligned} \tag{D.39}$$

where the underbraced term in Equation (D.39) is a new term introduced by the NLEVM, the modified eddy-viscosity is given by $\mu_{eff}' = \mu + \mu_t'$, and the stress tensor terms in the above equations are now

calculated using:

$$\tau^{ij} = \mu'_{eff} S^{ij} - \rho\widehat{\overline{u^i u^j}} - \frac{2}{3} g^{ij} \rho k \tag{D.40}$$

D.8 Differential Yap Correction

The differential length-scale correction developed by Iacovides & Raisee [66] is given by:

$$Y_{dc} = c_w \frac{\tilde{\varepsilon}^2}{k} max\left[F\left(F+1\right)^2, 0\right] \tag{D.41}$$

where:

$$F = \frac{1}{c_l}\left[\left(\frac{\partial l}{\partial x_j}\frac{\partial l}{\partial x_j}\right)^{1/2} - dl_e dy\right] \tag{D.42}$$

The constants c_w and c_l and the function $dl_e dy$ are given in Section 2.2 and l is the turbulence length scale, calculated from $l = k^{3/2}/\varepsilon$. The gradient of the length scale in non-orthogonal curvilinear coordinates given by:

$$F = \frac{1}{c_l}\left[\left(g^{jk}\frac{\partial l}{\partial \xi^j}\frac{\partial l}{\partial \xi^k}\right)^{1/2} - dl_e dy\right] \tag{D.43}$$

In the UMIST-*N* wall function, this is simplified to:

$$F = \frac{1}{c_l}\left[\left(g^{33}\frac{\partial l}{\partial \zeta}\frac{\partial l}{\partial \zeta}\right)^{1/2} - dl_e dy\right] \tag{D.44}$$

where it is assumed that the gradient of the length scale parallel to the wall is negligible in comparison with the gradient normal to the wall.

Appendix E

Numerical Treatment of Subgrid Transport Equations

In the Appendix D, the subgrid momentum, scalar, turbulent kinetic energy and dissipation rate equations were derived. Each of the subgrid transport equations can be written in the following generic form:

$$\frac{\rho U}{\sqrt{g_{11}}}\left(\frac{\partial\phi}{\partial\xi}\right)^{*}+\frac{\rho V}{\sqrt{g_{22}}}\left(\frac{\partial\phi}{\partial\eta}\right)^{*}+\frac{\rho W}{\sqrt{g_{33}}}\left(\frac{\partial\phi}{\partial\zeta}\right)^{*}=\frac{1}{J}\frac{\partial}{\partial\zeta}\left(Jg^{33}\Gamma\frac{\partial\phi}{\partial\zeta}\right)+C \tag{E.1}$$

where ϕ denotes one of the subgrid parameters: U, V, k or $\tilde{\varepsilon}$, Γ is the diffusivity and the source term, C, includes all geometry-related source terms and the pressure gradient in the momentum equations. Following the finite-volume method, the subgrid transport equations are discretized and integrated over subgrid control volumes which have physical dimensions $(J\Delta\xi\Delta\eta\Delta\zeta)$ where, in the present treatment, it is assumed that the ξ-axis is parallel to east-west, η-axis north-south and ζ-axis top-bottom (the wall-normal direction). Using the same method as used previously for the UMIST-*N* wall function, gradients appearing in diffusion and source terms are calculated using central differencing while convective terms are discretized using upwind differencing.

E.1 1-*D* Diffusion

Considering only diffusion and the source term, the generic subgrid transport equation can be written:

$$\frac{1}{J}\frac{\partial}{\partial\zeta}\left(Jg^{33}\Gamma\frac{\partial\phi}{\partial\zeta}\right)+C=0 \tag{E.2}$$

which is discretized:

$$\frac{1}{\Delta\zeta_{tb}}\left(\frac{1}{J}\right)_{P}\left[\left(Jg^{33}\Gamma\frac{\partial\phi}{\partial\zeta}\right)_{t}-\left(Jg^{33}\Gamma\frac{\partial\phi}{\partial\zeta}\right)_{b}\right]+(C)_{P}=0 \tag{E.3}$$

and integrated over the control volume (where $\Delta Vol = J\Delta\xi_{ew}\Delta\eta_{ns}\Delta\zeta_{tb}$):

$$\left[\left(Jg^{33}\Gamma\right)_t \frac{(\phi_T - \phi_P)}{\Delta\zeta_{TP}} - \left(Jg^{33}\Gamma\right)_b \frac{(\phi_P - \phi_B)}{\Delta\zeta_{PB}}\right]\Delta\xi_{ew}\Delta\eta_{ns} + (C)_P \Delta Vol \tag{E.4}$$

where subscripts T, P, and B refer to the top, current and bottom nodes respectively, t and b denote values at the top and bottom boundaries of the subgrid cell, respectively. Equation (E.4) can be rearranged into:

$$D_t(\phi_T - \phi_P) - D_b(\phi_P - \phi_B) + (C)_P \Delta Vol = 0 \tag{E.5}$$

where:

$$D_t = \left(Jg^{33}\Gamma\right)_t \frac{\Delta\xi_{ew}\Delta\eta_{ew}}{\Delta\zeta_{TP}} \tag{E.6}$$

$$D_b = \left(Jg^{33}\Gamma\right)_b \frac{\Delta\xi_{ew}\Delta\eta_{ns}}{\Delta\zeta_{PB}} \tag{E.7}$$

Grouping coefficients of ϕ_P, Equation (E.5) becomes:

$$D_t\phi_T + D_b\phi_B + (C)_P \Delta Vol = (D_t + D_b)\phi_P \tag{E.8}$$

This can be expressed as:

$$a_P\phi_P = a_T\phi_T + a_B\phi_B + S \tag{E.9}$$

where:

$$a_T = D_t = \left(Jg^{33}\Gamma\right)_t \frac{\Delta\xi_{ew}\Delta\eta_{ew}}{\Delta\zeta_{TP}} \tag{E.10}$$

$$a_B = D_b = \left(Jg^{33}\Gamma\right)_b \frac{\Delta\xi_{ew}\Delta\eta_{ns}}{\Delta\zeta_{PB}} \tag{E.11}$$

$$a_P = a_T + a_B \tag{E.12}$$

$$S = (C)_P \Delta Vol \tag{E.13}$$

It is assumed that the cells have unit dimensions in curvilinear coordinates, i.e.:

$$\Delta\xi_{ew} = \Delta\eta_{ns} = \Delta\zeta_{tb} = 1 \tag{E.14}$$

Additionally, the distances between adjacent nodes are assumed to be unity so that, for example:

$$\Delta\xi_{EP} = 1 \tag{E.15}$$

In the subgrid cells adjacent to boundaries the distance from the node to the boundary is half a cell width. For example, the subgrid cell adjacent to bottom boundary shown in Figure E.1 has $\Delta\zeta_{PB} = 0.5$.

The covariant metric tensor $(g_{33})_b$ at the bottom boundary of the near-wall cell is given by:

$$(g_{33})_b = \frac{\partial z}{\partial \zeta}\frac{\partial z}{\partial \zeta} = \left(\frac{z_P - z_B}{\Delta\zeta_{PB}}\right)^2 = \left(\frac{\Delta z_{PB}}{0.5}\right)^2 \tag{E.16}$$

the Jacobian, J, at the bottom boundary is calculated from:

$$(J)_b = (\sqrt{g_{11}g_{22}g_{33}})_b = 2\Delta x_{ew}\Delta y_{ns}\Delta z_{PB} \tag{E.17}$$

and the contravariant metric tensor $\left(g^{33}\right)_b$ is given by:

$$\left(g^{33}\right)_b = \frac{1}{J^2}g_{11}g_{22} = \frac{\left(\Delta x_{ew}\Delta y_{ns}\right)^2}{4\left(\Delta x_{ew}\Delta y_{ns}\Delta z_{PB}\right)^2} = \frac{1}{4\left(\Delta z_{PB}\right)^2} \tag{E.18}$$

Substituting these expressions into Equation (E.11) for the diffusion coefficient at the bottom boundary:

$$\begin{aligned} a_B &= \left(Jg^{33}\Gamma\right)_b \frac{\Delta\xi_{ew}\Delta\eta_{ns}}{\Delta\zeta_{PB}} \\ &= 2\Delta x_{ew}\Delta y_{ns}\Delta z_{PB}\frac{1}{4\left(\Delta z_{PB}\right)^2}\Gamma_b\frac{1}{0.5} \\ &= \frac{\Delta x_{ew}\Delta y_{ns}\Gamma_b}{\Delta z_{PB}} \end{aligned} \tag{E.19}$$

This is exactly the same form as would be expected in a standard Cartesian discretization of the diffusion term. The coefficients are in the form $(a_B = \Gamma_b A/L)$, where A is the cross-sectional area of the cell and L is the distance between the near-wall node and the node on the boundary.

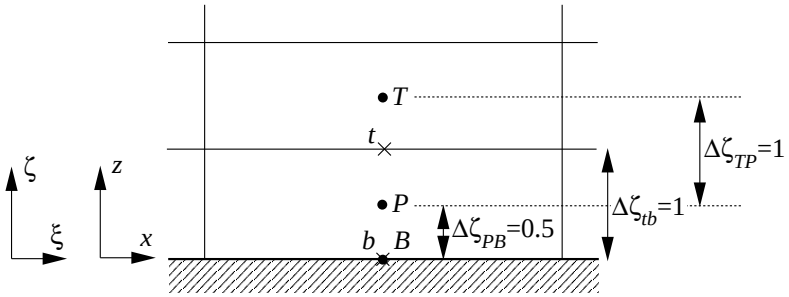

Figure E.1: Near-wall subgrid arrangement showing the location of the nodes and the computational cell widths.

E.2 Convection Parallel to the Wall

Convection of scalar ϕ in the ξ-direction is integrated over the subgrid cell volume (ΔVol) and added into the discretized equation source term, S, as follows:

$$S = -\int_{\Delta Vol} \frac{\rho U}{\sqrt{g_{11}}} \frac{\partial \phi}{\partial \xi} dVol \tag{E.20}$$

where the minus sign is introduced since the convection term is moved from the left- to the right-hand-side of the transport equation (Equation E.1). Using an upwind scheme, the convective ξ-direction source term is given by:

$$S = -\left(\frac{\rho U}{\sqrt{g_{11}}}\right)_P \frac{(\phi_P - \phi_W)}{\Delta\xi_{PW}} \Delta Vol \qquad \text{for} \quad U_P > 0 \tag{E.21}$$

$$S = -\left(\frac{\rho U}{\sqrt{g_{11}}}\right)_P \frac{(\phi_E - \phi_P)}{\Delta\xi_{EP}} \Delta Vol \qquad \text{for} \quad U_P < 0 \tag{E.22}$$

Rearranging these expressions in terms of coefficients of ϕ_P, ϕ_E and ϕ_W and splitting the source S into s_U and s_P terms (as described in Chapter 3) one obtains the following expressions:

$$\left.\begin{aligned} s_U &= \left(\frac{\rho U}{\sqrt{g_{11}}}\right)_P \frac{\phi_W}{\Delta\xi_{PW}} \Delta Vol \\ s_P &= -\left(\frac{\rho U}{\sqrt{g_{11}}}\right)_P \frac{1}{\Delta\xi_{PW}} \Delta Vol \end{aligned}\right\} \quad \text{for} \quad U_P > 0 \tag{E.23}$$

$$\left.\begin{aligned} s_U &= -\left(\frac{\rho U}{\sqrt{g_{11}}}\right)_P \frac{\phi_E}{\Delta\xi_{EP}} \Delta Vol \\ s_P &= \left(\frac{\rho U}{\sqrt{g_{11}}}\right)_P \frac{1}{\Delta\xi_{EP}} \Delta Vol \end{aligned}\right\} \quad \text{for} \quad U_P < 0 \tag{E.24}$$

where the discretized equation is given by:

$$(a_P - s_P)\,\phi_P = a_T \phi_T + a_B \phi_B + s_U \tag{E.25}$$

Using a similar approach one can show that the convective flux in the wall-parallel η-direction results in the following source terms:

$$\left.\begin{aligned} s_U &= \left(\frac{\rho V_P}{\sqrt{g_{22}}}\right)_P \frac{\phi_S}{\Delta\eta_{PS}} \Delta Vol \\ s_P &= -\left(\frac{\rho V_P}{\sqrt{g_{22}}}\right)_P \frac{1}{\Delta\eta_{PS}} \Delta Vol \end{aligned}\right\} \quad \text{for} \quad V_P > 0 \tag{E.26}$$

$$\left.\begin{aligned} s_U &= -\left(\frac{\rho V_P}{\sqrt{g_{22}}}\right)_P \frac{\phi_N}{\Delta\eta_{NP}}\Delta Vol \\ s_P &= \left(\frac{\rho V_P}{\sqrt{g_{22}}}\right)_P \frac{1}{\Delta\eta_{NP}}\Delta Vol \end{aligned}\right\} \quad \text{for} \quad V_P < 0 \tag{E.27}$$

E.3 Convection Normal to the Wall

Convection of scalar ϕ in the ζ-direction is integrated over the subgrid cell volume and added into the discretized equation source term, S, as follows:

$$S = -\int_{\Delta Vol} \frac{\rho W}{\sqrt{g_{33}}} \frac{\partial\phi}{\partial\zeta} \mathrm{d}Vol \tag{E.28}$$

where the W-velocity is obtained from subgrid continuity with additional scaling to satisfy the boundary conditions, as described in Section E.7. Using an upwind scheme, the convective ζ-direction source term is given by:

$$S = -\left(\frac{\rho W}{\sqrt{g_{33}}}\right)_P \frac{(\phi_P - \phi_B)}{\Delta\zeta_{PB}}\Delta Vol \qquad \text{for} \quad W_P > 0 \tag{E.29}$$

$$S = -\left(\frac{\rho W}{\sqrt{g_{33}}}\right)_P \frac{(\phi_T - \phi_P)}{\Delta\zeta_{TP}}\Delta Vol \qquad \text{for} \quad W_P < 0 \tag{E.30}$$

The above source terms can be rearranged in terms of coefficients of the nodal terms ϕ_N, ϕ_P and ϕ_S and then split into contributions for the source term s_P and the coefficients a_T and a_B, as follows:

$$\left.\begin{aligned} s_P &= -\left(\frac{\rho W}{\sqrt{g_{33}}}\right)_P \frac{1}{\Delta\zeta_{PB}}\Delta Vol \\ a_T &= 0 \\ a_B &= \left(\frac{\rho W}{\sqrt{g_{33}}}\right)_P \frac{1}{\Delta\zeta_{PB}}\Delta Vol \end{aligned}\right\} \quad \text{for} \quad W_P > 0 \tag{E.31}$$

$$\left.\begin{aligned} s_P &= \left(\frac{\rho W}{\sqrt{g_{33}}}\right)_P \frac{1}{\Delta\zeta_{TP}}\Delta Vol \\ a_T &= -\left(\frac{\rho W}{\sqrt{g_{33}}}\right)_P \frac{1}{\Delta\zeta_{TP}}\Delta Vol \\ a_B &= 0 \end{aligned}\right\} \quad \text{for} \quad W_P < 0 \tag{E.32}$$

E.4 Summary of Discretized Convection Terms

The following equations summarize the terms arising in the discretized subgrid transport equations due to convection parallel and normal to the wall:

$$\begin{aligned} s_U &= \left(\frac{\rho}{\sqrt{g_{11}}}\right)_P \frac{\max(U_P,0)\,\phi_W}{\Delta\xi_{PW}}\Delta Vol + \left(\frac{\rho}{\sqrt{g_{11}}}\right)_P \frac{\max(-U_P,0)\,\phi_E}{\Delta\xi_{EP}}\Delta Vol \\ &\quad + \left(\frac{\rho}{\sqrt{g_{22}}}\right)_P \frac{\max(V_P,0)\,\phi_S}{\Delta\eta_{PS}}\Delta Vol + \left(\frac{\rho}{\sqrt{g_{22}}}\right)_P \frac{\max(-V_P,0)\,\phi_N}{\Delta\eta_{NP}}\Delta Vol \end{aligned} \tag{E.33}$$

$$\begin{aligned} s_P &= \left(\frac{\rho}{\sqrt{g_{11}}}\right)_P \frac{\min(-U_P,0)}{\Delta\xi_{PW}}\Delta Vol + \left(\frac{\rho}{\sqrt{g_{11}}}\right)_P \frac{\min(U_P,0)}{\Delta\xi_{EP}}\Delta Vol \\ &\quad + \left(\frac{\rho}{\sqrt{g_{22}}}\right)_P \frac{\min(-V_P,0)}{\Delta\eta_{PS}}\Delta Vol + \left(\frac{\rho}{\sqrt{g_{22}}}\right)_P \frac{\min(V_P,0)}{\Delta\eta_{NP}}\Delta Vol \\ &\quad + \left(\frac{\rho}{\sqrt{g_{33}}}\right)_P \frac{\min(-W_P,0)}{\Delta\zeta_{PB}}\Delta Vol + \left(\frac{\rho}{\sqrt{g_{33}}}\right)_P \frac{\min(W_P,0)}{\Delta\zeta_{TP}}\Delta Vol \end{aligned} \tag{E.34}$$

$$a_T = \left(\frac{\rho}{\sqrt{g_{33}}}\right)_P \frac{\max(-W_P,0)}{\Delta\zeta_{TP}}\Delta Vol \tag{E.35}$$

$$a_B = \left(\frac{\rho}{\sqrt{g_{33}}}\right)_P \frac{\max(W_P,0)}{\Delta\zeta_{PB}}\Delta Vol \tag{E.36}$$

Convection of momentum follows the same approach as described above for scalar ϕ once the upstream velocity has been transformed from the coordinate system used in the upstream cell into the coordinate system of the current cell.

E.5 Source Terms

The following sections identify the source terms for the subgrid momentum, turbulent kinetic energy and dissipation rate equations in addition to those derived above from convection.

E.5.1 U-Momentum

Using the linear $k-\varepsilon$ model, the source term S_U^1 in the subgrid wall-parallel U-momentum equation is given by:

$$\begin{aligned} S_U^1 &= -g^{1j}\sqrt{g_{11}}\frac{\partial P'}{\partial \xi^j} - \tau^{1j}\frac{\Gamma_{1j}^m g_{1m}}{\sqrt{g_{11}}} + \tau^{mj}\Gamma_{mj}^1\sqrt{g_{11}} \\ &\quad + \frac{1}{J}\frac{\partial}{\partial\zeta}\left[J\mu_{eff}g^{33}\left(U^{(m)}\frac{\sqrt{g_{11}}}{\sqrt{g_{mm}}}\Gamma_{m3}^1 - U\frac{g_{1m}}{g_{11}}\Gamma_{13}^m\right)\right] \end{aligned} \tag{E.37}$$

The four terms in S_U^1 are expanded as follows:

$$-g^{1j}\sqrt{g_{11}}\frac{\partial P^{'}}{\partial \xi^j} = -\sqrt{g_{11}}\left(g^{11}\frac{\partial P^{'}}{\partial \xi}+g^{12}\frac{\partial P^{'}}{\partial \eta}+g^{13}\frac{\partial P^{'}}{\partial \zeta}\right) \tag{E.38}$$

$$\begin{aligned}-\tau^{1j}\frac{\Gamma^m_{1j}g_{1m}}{\sqrt{g_{11}}} &= -\frac{\tau^{11}}{\sqrt{g_{11}}}\left(\Gamma^1_{11}g_{11}+\Gamma^2_{11}g_{12}+\Gamma^3_{11}g_{13}\right)\\ &\quad -\frac{\tau^{12}}{\sqrt{g_{11}}}\left(\Gamma^1_{12}g_{11}+\Gamma^2_{12}g_{12}+\Gamma^3_{12}g_{13}\right)\\ &\quad -\frac{\tau^{13}}{\sqrt{g_{11}}}\left(\Gamma^1_{13}g_{11}+\Gamma^2_{13}g_{12}+\Gamma^3_{13}g_{13}\right)\end{aligned} \tag{E.39}$$

$$\begin{aligned}\tau^{mj}\Gamma^1_{mj}\sqrt{g_{11}} &= \sqrt{g_{11}}\left(\tau^{11}\Gamma^1_{11}+\tau^{21}\Gamma^1_{21}+\tau^{31}\Gamma^1_{31}\right)\\ &\quad +\sqrt{g_{11}}\left(\tau^{12}\Gamma^1_{12}+\tau^{22}\Gamma^1_{22}+\tau^{32}\Gamma^1_{32}\right)\\ &\quad +\sqrt{g_{11}}\left(\tau^{13}\Gamma^1_{13}+\tau^{23}\Gamma^1_{23}+\tau^{33}\Gamma^1_{33}\right)\end{aligned} \tag{E.40}$$

$$\begin{aligned}&\frac{1}{J}\frac{\partial}{\partial \zeta}\left[J\mu_{eff}g^{33}\left(U^{(m)}\frac{\sqrt{g_{11}}}{\sqrt{g_{mm}}}\Gamma^1_{m3}-U\frac{g_{1m}}{g_{11}}\Gamma^m_{13}\right)\right]\\ &=\frac{1}{J}\frac{\partial}{\partial \zeta}\left[J\mu_{eff}g^{33}\left(U\frac{\sqrt{g_{11}}}{\sqrt{g_{11}}}\Gamma^1_{13}+V\frac{\sqrt{g_{11}}}{\sqrt{g_{22}}}\Gamma^1_{23}+W\frac{\sqrt{g_{11}}}{\sqrt{g_{33}}}\Gamma^1_{33}\right)\right.\\ &\left.-\left(U\frac{g_{11}}{g_{11}}\Gamma^1_{13}+U\frac{g_{12}}{g_{11}}\Gamma^2_{13}+U\frac{g_{13}}{g_{11}}\Gamma^3_{13}\right)\right]\end{aligned} \tag{E.41}$$

The above source terms are integrated over the subgrid cell and included in the discretized U-momentum equation source term, s_U, as follows:

$$s_U = \int_{\Delta Vol}\left(S_U^1\right)_P \mathrm{d}Vol \tag{E.42}$$

where ($\Delta Vol = J\Delta\xi\Delta\eta\Delta\zeta$) is the volume of the subgrid cell and $()_P$ denotes the value obtained at the current node P. The wall-parallel components of the pressure-gradient term ($\partial P^{'}/\partial\xi$ and $\partial P^{'}/\partial\eta$) are calculated from the main-grid node pressure values. The calculation of the pressure profile across the subgrid in order to find $\partial P^{'}/\partial\zeta$ is discussed in Section E.9.

E.5.2 V-Momentum

The source term S_U^2 in the subgrid wall-parallel V-momentum equation is given by:

$$\begin{aligned} S_U^2 &= -g^{2j}\sqrt{g_{22}}\frac{\partial P'}{\partial \xi^j} - \tau^{2j}\frac{\Gamma_{2j}^m g_{2m}}{\sqrt{g_{22}}} + \tau^{mj}\Gamma_{mj}^2\sqrt{g_{22}} \\ &\quad + \frac{1}{J}\frac{\partial}{\partial \zeta}\left[J\mu_{eff}g^{33}\left(U^{(m)}\frac{\sqrt{g_{22}}}{\sqrt{g_{mm}}}\Gamma_{m3}^2 - V\frac{g_{2m}}{g_{22}}\Gamma_{23}^m\right)\right] \end{aligned} \tag{E.43}$$

The four terms in S_U^2 are expanded:

$$-g^{2j}\sqrt{g_{22}}\frac{\partial P}{\partial \xi^j} = -\sqrt{g_{22}}\left(g^{21}\frac{\partial P}{\partial \xi} + g^{22}\frac{\partial P}{\partial \eta} + g^{23}\frac{\partial P}{\partial \zeta}\right) \tag{E.44}$$

$$\begin{aligned} \tau^{2j}\frac{\Gamma_{2j}^m g_{2m}}{\sqrt{g_{22}}} &= -\frac{\tau^{21}}{\sqrt{g_{22}}}\left(\Gamma_{21}^1 g_{21} + \Gamma_{21}^2 g_{22} + \Gamma_{21}^3 g_{23}\right) \\ &\quad -\frac{\tau^{22}}{\sqrt{g_{22}}}\left(\Gamma_{22}^1 g_{21} + \Gamma_{22}^2 g_{22} + \Gamma_{22}^3 g_{23}\right) \\ &\quad -\frac{\tau^{23}}{\sqrt{g_{22}}}\left(\Gamma_{23}^1 g_{21} + \Gamma_{23}^2 g_{22} + \Gamma_{23}^3 g_{23}\right) \end{aligned} \tag{E.45}$$

$$\begin{aligned} \tau^{mj}\Gamma_{mj}^2\sqrt{g_{22}} &= \sqrt{g_{22}}\left(\tau^{11}\Gamma_{11}^2 + \tau^{21}\Gamma_{21}^2 + \tau^{31}\Gamma_{31}^2\right) \\ &\quad +\sqrt{g_{22}}\left(\tau^{12}\Gamma_{12}^2 + \tau^{22}\Gamma_{22}^2 + \tau^{32}\Gamma_{32}^2\right) \\ &\quad +\sqrt{g_{22}}\left(\tau^{13}\Gamma_{13}^2 + \tau^{23}\Gamma_{23}^2 + \tau^{33}\Gamma_{33}^2\right) \end{aligned} \tag{E.46}$$

$$\begin{aligned} &\frac{1}{J}\frac{\partial}{\partial \zeta}\left[J\mu_{eff}g^{33}\left(U^{(m)}\frac{\sqrt{g_{22}}}{\sqrt{g_{mm}}}\Gamma_{m3}^2 - V\frac{g_{2m}}{g_{22}}\Gamma_{23}^m\right)\right] \\ &= \frac{1}{J}\frac{\partial}{\partial \zeta}\left[J\mu_{eff}g^{33}\left(U\frac{\sqrt{g_{22}}}{\sqrt{g_{11}}}\Gamma_{13}^2 + V\frac{\sqrt{g_{22}}}{\sqrt{g_{22}}}\Gamma_{23}^2 + W\frac{\sqrt{g_{22}}}{\sqrt{g_{33}}}\Gamma_{33}^2\right)\right. \\ &\left. -\left(V\frac{g_{21}}{g_{22}}\Gamma_{23}^1 + V\frac{g_{22}}{g_{22}}\Gamma_{23}^2 + V\frac{g_{23}}{g_{22}}\Gamma_{23}^3\right)\right] \end{aligned} \tag{E.47}$$

These source terms are integrated over the subgrid cell and included in the discretized V-momentum equation source term in the same manner as described above for the U-momentum equation.

E.5.3 Turbulent Kinetic Energy, k

The kinetic energy equation in non-orthogonal curvilinear coordinates is given by:

$$\frac{\rho U}{\sqrt{g_{11}}}\frac{\partial k}{\partial \xi} + \frac{\rho V}{\sqrt{g_{22}}}\frac{\partial k}{\partial \eta} + \frac{\rho W}{\sqrt{g_{33}}}\frac{\partial k}{\partial \zeta} = \frac{1}{J}\frac{\partial}{\partial \zeta}\left[Jg^{33}\left(\mu + \frac{\mu_t}{\sigma_k}\right)\frac{\partial k}{\partial \zeta}\right] + G - \rho\varepsilon \tag{E.48}$$

where the production term, G (given by Equation D.21) and the dissipation term, ε (given by Equation D.22) are grouped together into the source term, S:

$$S = G - \rho\varepsilon \tag{E.49}$$

In order to maximize stability, the integrated source term split into components s_U and s_P as follows:

$$s_U = \max\left[(G - \rho\tilde{\varepsilon}), 0\right]_P \Delta Vol \tag{E.50}$$

$$s_P = \frac{1}{k_P}\left\{\max\left[(G - \rho\tilde{\varepsilon}), 0\right] - \rho\hat{\varepsilon}\right\}_P \Delta Vol \tag{E.51}$$

where:

$$\hat{\varepsilon} = 2\nu g^{33}\left(\frac{\partial k^{1/2}}{\partial\zeta}\right)\left(\frac{\partial k^{1/2}}{\partial\zeta}\right) \tag{E.52}$$

E.5.4 Dissipation Rate, $\tilde{\varepsilon}$

The dissipation rate equation in non-orthogonal curvilinear coordinates is given by:

$$\begin{aligned}\frac{\rho U}{\sqrt{g_{11}}}\frac{\partial\tilde{\varepsilon}}{\partial\xi} + \frac{\rho V}{\sqrt{g_{22}}}\frac{\partial\tilde{\varepsilon}}{\partial\eta} + \frac{\rho W}{\sqrt{g_{33}}}\frac{\partial\tilde{\varepsilon}}{\partial\zeta} = \frac{1}{J}\frac{\partial}{\partial\zeta}\left[Jg^{33}\left(\mu + \frac{\mu_t}{\sigma_\varepsilon}\right)\frac{\partial\tilde{\varepsilon}}{\partial\zeta}\right] \\ + c_{\varepsilon1}f_1 G\frac{\tilde{\varepsilon}}{k} - c_{\varepsilon2}f_2\rho\frac{\tilde{\varepsilon}^2}{k} + \rho Y_c + P_{\varepsilon3}\end{aligned} \tag{E.53}$$

where the gradient production term $P_{\varepsilon3}$ is given in Equation (D.27). The source term, S, is as follows:

$$S = c_{\varepsilon1}f_1 G\frac{\tilde{\varepsilon}}{k} - c_{\varepsilon2}f_2\rho\frac{\tilde{\varepsilon}^2}{k} + \rho Y_c + P_{\varepsilon3} \tag{E.54}$$

which is integrated over the subgrid control volume and split into components s_U and s_P, given by:

$$s_U = \left\{\max\left[\left(c_{\varepsilon1}f_1 G\frac{\tilde{\varepsilon}}{k} - c_{\varepsilon2}f_2\rho\frac{\tilde{\varepsilon}^2}{k}\right), 0\right] + \rho Y_c + P_{\varepsilon3}\right\}_P \Delta Vol \tag{E.55}$$

$$s_P = \frac{1}{\tilde{\varepsilon}_P}\left\{\min\left[\left(c_{\varepsilon1}f_1 G\frac{\tilde{\varepsilon}}{k} - c_{\varepsilon2}f_2\rho\frac{\tilde{\varepsilon}^2}{k}\right), 0\right]\right\}_P \Delta Vol \tag{E.56}$$

E.5.5 Main-Grid $P_{\varepsilon3}$ Source Term

A low-Reynolds-number turbulence model is used in the main-grid domain, when the UMIST-*N* wall function is used, so that arbitrarily small near-wall cells can be employed. In the low-*Re* Launder-Sharma and Craft *et al.* models, the main-grid $\tilde{\varepsilon}$-equation includes a damping term known as the gradient production, $P_{\varepsilon3}$. Care must be taken in evaluating the $P_{\varepsilon3}$ at the main-grid node adjacent to the near-wall node (node P in Figure E.2)[1]. The treatment of the main-grid $P_{\varepsilon3}$ term in the TEAM and

[1] In the near-wall main-grid cell (with node S in Figure E.2), the subgrid average $\overline{P_{\varepsilon3}}$ is used in the main-grid calculation.

STREAM codes is discussed below.

The gradient production term involves double-derivatives of the velocity components and is written in Cartesian coordinates as follows:

$$P_{\varepsilon 3} = 2\mu\nu_t \left(\frac{\partial^2 U_i}{\partial x_j \partial x_k} \right)^2 \tag{E.57}$$

To determine a double derivative, such as $\partial^2 U/\partial y^2$, the strain-rate at the cell faces are first calculated, $(\partial U/\partial y)_n$ and $(\partial U/\partial y)_s$, and then the gradient of the strain-rate across the cell are calculated as follows:

$$\frac{\partial^2 U}{\partial y^2} = \frac{[(\partial U/\partial y)_n - (\partial U/\partial y)_s]}{\Delta y_{ns}} \tag{E.58}$$

where n and s denote the north and south cell faces, respectively. In the TEAM code the strain-rate at cell faces is evaluated from the difference in velocity between neighbouring nodal values, e.g. $(\partial U/\partial y)_n = (U_N - U_P)/\Delta y_{NP}$. The STREAM code, however, evaluates the strain-rates at the cell face by interpolating between strain-rates evaluated at the cell centres, e.g. $(\partial U/\partial y)_n = 0.5[(\partial U/\partial y)_N + (\partial U/\partial y)_S]$. These two methods are shown in Figure E.2.

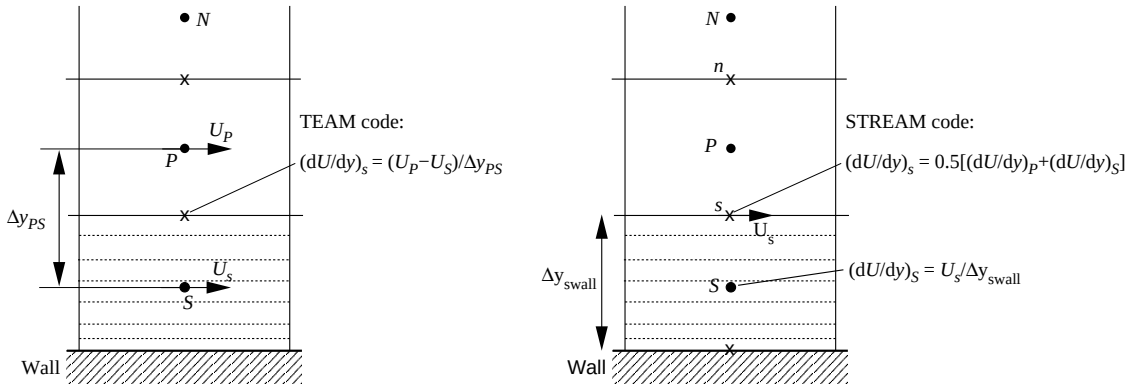

Figure E.2: Schematics of the near-wall grid arrangement showing the main-grid strain-rate $(\partial U/\partial y)_s$ as calculated by the TEAM code (left(and the STREAM code (right).

In the approach adopted by STREAM, the strain-rate at the southern cell boundary, s, shown in Figure E.2, is not calculated accurately when the near-wall node is outside the viscous sublayer (say $y^+ \approx 30$). This is because the main-grid strain-rate at the near wall node, $(\partial U/\partial y)_S$, is calculated assuming a linear velocity profile across the near-wall main-grid cell (whereas the actual velocity profile is closer to logarithmic for a plane channel flow). In the approach adopted by TEAM, this problem does not occur since it only uses the velocity at the main-grid nodes P and S to evaluate the gradient at the cell face.

To obtain a more accurate value for the main-grid strain-rate at the cell boundary with the STREAM code, one could use the strain-rate in the subgrid cell adjacent to the boundary (i.e. in the subgrid cell next to position s in Figure E.2). However, the transformation of the second-order strain-rate tensor

from contravariant subgrid components to Cartesian main-grid components is costly, as the tensor expression involves three dummy indices for each of the 9 independent strain-rate components (for details see Section E.8):

$$\underbrace{V^{p,q}}_{Cartesian} = g^{jk}\frac{\partial x^p}{\partial \xi^i}\frac{\partial x^q}{\partial \xi^k}\underbrace{U^i_{,j}}_{contravariant} \tag{E.59}$$

An alternative and more computationally efficient approach is simply to scale the main-grid $P_{\varepsilon 3}$ term so that it only becomes active when a relatively fine near-wall grid is used, in which case the assumed linear velocity profile across the main-grid near-wall cell is an adequate approximation. The following function was tested in the Ahmed body flow:

$$f_{P\varepsilon 3} = \exp\left(-\frac{\tilde{R}_t}{55}\right)^4 \tag{E.60}$$

where $\tilde{R}_t$ is the turbulence Reynolds number. The above $f_{P\varepsilon 3}$ function rapidly decreases from $f_{P\varepsilon 3} = 0.92$ at $\tilde{R}_t = 30$ to $f_{P\varepsilon 3} = 0.07$ at $\tilde{R}_t = 70$. Using this function, the linear $k-\varepsilon$ model main-grid $P_{\varepsilon 3}$ term becomes:

$$P_{\varepsilon 3} = 2 f_{P\varepsilon 3}\mu\nu_t\left(\frac{\partial^2 U_i}{\partial x_j \partial x_k}\right)^2 \tag{E.61}$$

E.6 Grid Generation and Geometric Parameters

A number of geometric parameters are involved in the subgrid transport equations in non-orthogonal curvilinear coordinates such as metric tensors (g_{ij}) and Christoffel symbols $\left(\Gamma^i_{jk}\right)$. Table E.1 gives a list of these parameters and where they are evaluated (at the subgrid node or at the subgrid cell face). To calculate and store each of these parameters at each subgrid node along the length of the wall would entail huge storage costs. Instead, efficient interpolation routines are employed. Values of the particular geometric parameter are stored at the top and bottom subgrid domain boundaries together with a few interpolation constants and, at each iteration, values of the parameter within the subgrid are interpolated.

The following sections firstly discuss grid generation and the calculation of grid parameters s and Δs, which denote the position and thickness of the subgrid cells, respectively. A description of the interpolation practices used for calculating the covariant metric tensors, g_{ij}, is then given. This is followed by a presentation of the equations used to calculate the Jacobian, the contravariant metric tensors and the Christoffel symbols.

E.6.1 Generating the Subgrid Mesh

Figure E.3 shows a typical curvilinear grid arrangement where the subgrid mesh is embedded within the near-wall cell which has corners *ABCD*. Subgrid vertices on the *AD* line are numbered from 1 to $(n-1)$ and subgrid nodes from 1 to n. The position of the main-grid vertex at corner *A* is denoted

Geometric Parameter	**Node/ Boundary**	**Term in which the parameter appears**	**See Equations**
J	Node	ΔVol in convection and source terms	(E.33–E.36), (E.50), (E.51), (E.42) etc.
	Boundary	$P_{\varepsilon 3}$ and Diffusion	(D.27), (E.4)
Γ^{i}_{jk}	Node	Momentum equation source terms, strain-rate for G	(D.21), (D.12)
	Boundary	Strain-rate for $P_{\varepsilon 3}$, $\left(\partial\tau^{13}/\partial\zeta\right)$	(D.27), (D.12)
g^{ij}	Node	Pressure gradient, ε, G	(D.21), (D.22), (D.12)
	Boundary	$P_{\varepsilon 3}$	(D.27)
g_{ij}	Node	Convection, source terms, G	(D.21), (E.33–E.36), (E.50), (E.51) etc.
	Boundary	$\left(\partial\tau^{13}/\partial\zeta\right)$	(D.12)

Table E.1: Geometric parameters employed in the subgrid transport equations in non-orthogonal curvilinear coordinates and where the parameter is required (at the node or boundary).

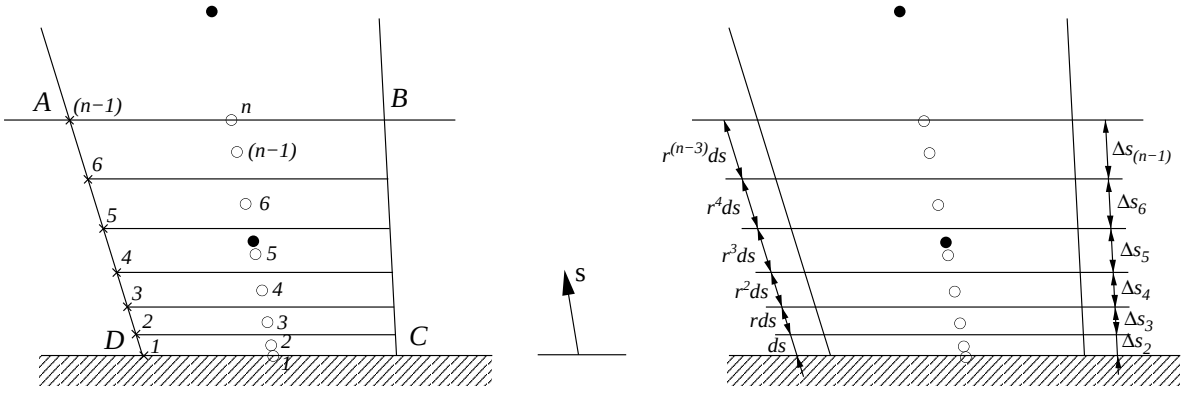

Figure E.3: Subgrid arrangement showing node and vertex notation and cell thicknesses. Distances indicated on the right are in the measured parallel to the s-axis (the physical equivalent of the ζ-axis).

with upper-case (XV_A, YV_A, ZV_A) and the position of the subgrid nodes with lower-case (x_i, y_i, z_i). The positions of the first and last subgrid nodes are given by:

$$x_1 = \frac{1}{2}(XV_C + XV_D) \; ; \; y_1 = \frac{1}{2}(YV_C + YV_D) \; ; \; z_1 = \frac{1}{2}(ZV_C + ZV_D) \tag{E.62}$$

$$x_n = \frac{1}{2}(XV_A + XV_B) \; ; \; y_n = \frac{1}{2}(YV_A + YV_B) \; ; \; z_n = \frac{1}{2}(ZV_A + ZV_B) \tag{E.63}$$

Between the first and last subgrid nodes the subgrid is algebraically generated, expanding with a given ratio from the wall to the outer edge of the domain, according to:

$$\Delta s_i = r \Delta s_{i-1} \tag{E.64}$$

where r is the expansion ratio and Δs_i is the cell width for node i, measured in the s-direction (parallel to the curvilinear ζ-axis). The distance between the bottom and top subgrid domain boundary locations, s_1 and s_n, consists of the sum of the control volume widths:

$$s_n - s_1 = t \, ds \tag{E.65}$$

where:

$$t = \sum_{m=0}^{(n-3)} r^m = \left(1 + r + r^2 + ... + r^{(n-3)}\right) \tag{E.66}$$

The thickness of the smallest control volume (adjacent to the wall) is then given by:

$$ds = \frac{(s_n - s_1)}{t} \tag{E.67}$$

The thickness of a subgrid cell, Δs_i, is as follows:

$$\begin{aligned} \Delta s_i &= r^{(i-2)} ds \\ &= \frac{r^{(i-2)}}{t}(s_n - s_1) \end{aligned} \tag{E.68}$$

This can also be expressed as:

$$c_i = \frac{\Delta s_i}{(s_n - s_1)} = \frac{r^{(i-2)}}{\sum_{m=0}^{(n-3)} r^m} \tag{E.69}$$

where c_i is the ratio of the size of the subgrid cell, Δs_i, to the thickness of the subgrid domain $(s_n - s_1)$. This ratio is only dependent upon the given expansion ratio, r, and the number of nodes, n. The ratio $\Delta s_i / (s_n - s_1)$ is stored for each wall (only requiring an array with n values, where n is the number of subgrid nodes across a given main-grid cell) and the thickness of a particular subgrid cell is obtained from the product of this ratio and the width of the main-grid near-wall cell $(s_n - s_1)$. One can calculate

the thickness of cell i in Cartesian coordinates as follows:

$$(\Delta x_{tb})_i = c_i (x_n - x_1) \tag{E.70}$$

$$(\Delta y_{tb})_i = c_i (y_n - y_1) \tag{E.71}$$

$$(\Delta z_{tb})_i = c_i (z_n - z_1) \tag{E.72}$$

where:

$$\Delta s_i^2 = (\Delta x_{tb})_i^2 + (\Delta y_{tb})_i^2 + (\Delta z_{tb})_i^2 \tag{E.73}$$

and:

$$(s_n - s_1)^2 = (x_n - x_1)^2 + (y_n - y_1)^2 + (z_n - z_1)^2 \tag{E.74}$$

Subscript tb refers to the distance from the top to the bottom of cell i (for cell notation see also Figure E.7). The location of the subgrid nodes in terms of distance s is determined from:

$$s_i = s_1 + \frac{1}{2}\Delta s_i + \sum_{j=2}^{(i-1)} \Delta s_j \tag{E.75}$$

so that, for instance, the location of node 4 in Figure E.3 is given by:

$$s_4 = s_1 + \Delta s_2 + \Delta s_3 + \frac{1}{2}\Delta s_4 \tag{E.76}$$

where s_1 is the location of the wall. Substituting Equation (E.69) into (E.75):

$$\begin{aligned} s_i - s_1 &= \frac{1}{2} c_i (s_n - s_1) + \sum_{j=2}^{(i-1)} [c_j (s_n - s_1)] \\ &= (s_n - s_1) \left(\frac{1}{2} c_i + \sum_{j=2}^{(i-1)} c_j \right) \\ &= (s_n - s_1) d_i \end{aligned} \tag{E.77}$$

which states that the position of the subgrid node relative to the wall $(s_i - s_1)$ is a function of the thickness of the main-grid cell $(s_n - s_1)$ and parameter d_i. Parameter d_i is only a function of c_i which was shown above to have storage requirements limited to a one-dimensional array with n entries.

The location of the top boundary of subgrid cell i, denoted s_i^t, is calculated as follows:

$$s_i^t = s_1 + \sum_{j=2}^{i} \Delta s_j \tag{E.78}$$

Rearranging this, using Equation (E.69), one obtains:

$$\begin{aligned} s_i^t - s_1 &= \sum_{j=2}^{i} \left[c_j \left(s_n - s_1 \right) \right] \\ &= \left(s_n - s_1 \right) \left(\sum_{j=2}^{i} c_j \right) \\ &= \left(s_n - s_1 \right) e_i \end{aligned} \tag{E.79}$$

where e_i depends only upon c_i and hence can be stored in a one-dimensional array with n entries. The parameter e_i is used to interpolate values to the top and bottom faces of the subgrid cells.

To summarize the above discussion, the subgrid is generated by specifying the number of subgrid nodes n (which includes nodes on the top and bottom boundaries) and the expansion ratio r, for which $(r > 1)$ leads to smaller cells near the wall than the outer boundary of the subgrid. The thickness each subgrid cell, Δs_i, is obtained from:

$$\boxed{\Delta s_i = c_i \left(s_n - s_1 \right)} \tag{E.80}$$

where:

$$c_i = \frac{r^{(i-2)}}{\sum_{m=0}^{(n-3)} r^m} \tag{E.81}$$

and the position of each subgrid node s_i relative to the wall boundary node, s_1, is given by:

$$\boxed{s_i - s_1 = \left(s_n - s_1 \right) d_i} \tag{E.82}$$

where:

$$d_i = \left(\frac{1}{2} c_i + \sum_{j=2}^{(i-1)} c_j \right) \tag{E.83}$$

The position of the subgrid top boundary for cell i is also calculated from

$$\boxed{s_i^t - s_1 = \left(s_n - s_1 \right) e_i} \tag{E.84}$$

where:

$$e_i = \sum_{j=2}^{i} c_j \tag{E.85}$$

E.6.2 Interpolation to Subgrid Cell Boundaries

In order to assemble the diffusion terms in the coefficient matrix it is necessary to interpolate to find the eddy-viscosity at subgrid cell boundaries. The subgrid nodes are positioned in the centre of the subgrid cells (as defined by the calculation of d_i, see Equation E.77), and linear interpolation of parameter ϕ to the top boundary (position t in Figure E.4) is achieved using the function f_i:

$$\boxed{\phi_t = \phi_i + f_i \left(\phi_{i+1} - \phi_i \right)} \tag{E.86}$$

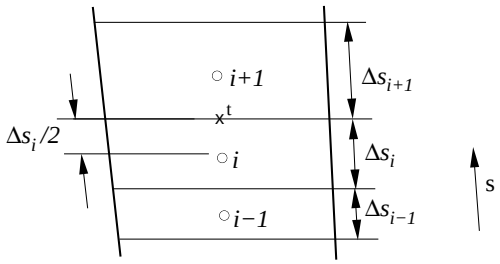

Figure E.4: Subgrid cells showing position of nodes within the cells

where:

$$f_i = \frac{\Delta s_i}{(\Delta s_{i+1} + \Delta s_i)} \tag{E.87}$$

Using Equation (E.80), this can be written:

$$f_i = \frac{c_i\,(s_n - s_1)}{[c_{i+1}\,(s_n - s_1) + c_i\,(s_n - s_1)]} = \frac{c_i}{(c_{i+1} + c_i)} \tag{E.88}$$

For an entire wall, the interpolation function can therefore be stored in a single one-dimensional array with n entries (where n is the number of subgrid cells in the wall-normal direction).

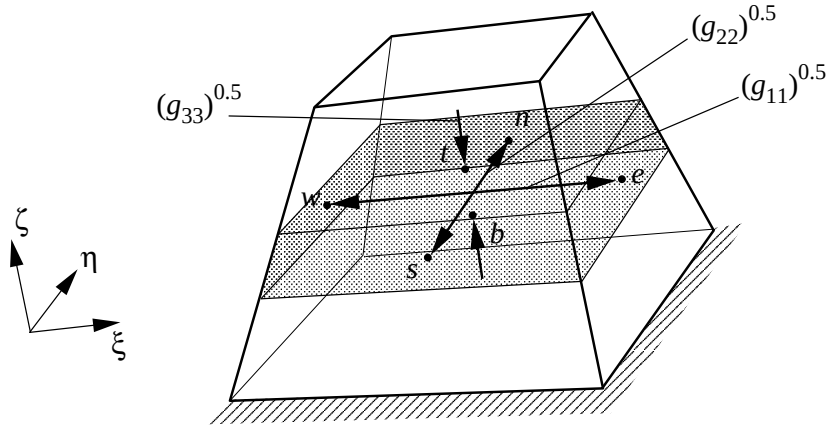

Figure E.5: Three-dimensional near-wall cell showing subgrid volume (shaded). The square-root of the metric tensors $\sqrt{g_{11}}$, $\sqrt{g_{22}}$ and $\sqrt{g_{33}}$ represent the physical distances between the east-west, north-south and top-bottom faces, respectively.

In addition to interpolating values at the top and bottom subgrid cell faces, it is necessary to find east, west, north and south subgrid cell face values. These are used, for example, in the calculation of the subgrid W-velocity. The value of ϕ at the eastern subgrid cell boundary is given by:

$$\phi_e = \phi_P + f_j^e\,(\phi_E - \phi_P) \tag{E.89}$$

where:

$$f_j^e = \frac{1}{2}\frac{\sqrt{(g_{11})_P}}{\sqrt{(g_{11})_e}} \tag{E.90}$$

and likewise:

$$\phi_w = \phi_W + f_j^w(\phi_P - \phi_W) \quad ; \quad f_j^w = \frac{1}{2}\frac{\sqrt{(g_{11})_W}}{\sqrt{(g_{11})_w}} \tag{E.91}$$

$$\phi_n = \phi_P + f_k^n(\phi_N - \phi_P) \quad ; \quad f_k^n = \frac{1}{2}\frac{\sqrt{(g_{22})_P}}{\sqrt{(g_{22})_n}} \tag{E.92}$$

$$\phi_s = \phi_S + f_j^s(\phi_P - \phi_S) \quad ; \quad f_k^s = \frac{1}{2}\frac{\sqrt{(g_{22})_S}}{\sqrt{(g_{22})_s}} \tag{E.93}$$

where upper case E, W, N, S refer to nodal values and lower case e, w, n, s refer for cell face values in the east, west, north and south directions respectively.

E.6.3 Covariant Metric Tensor, g_{ij}

The covariant metric tensor, g_{ij}, is calculated from:

$$g_{ij} = \sum_{k=1}^{3} \frac{\partial x^k}{\partial \xi^i}\frac{\partial x^k}{\partial \xi^j} = \frac{\partial x}{\partial \xi^i}\frac{\partial x}{\partial \xi^j} + \frac{\partial y}{\partial \xi^i}\frac{\partial y}{\partial \xi^j} + \frac{\partial z}{\partial \xi^i}\frac{\partial z}{\partial \xi^j} \tag{E.94}$$

So, for example, g_{12} is given by:

$$g_{12} = x_\xi x_\eta + y_\xi y_\eta + z_\xi z_\eta \tag{E.95}$$

where, for example:

$$x_\xi \equiv \frac{\partial x}{\partial \xi} = \frac{x_e - x_w}{\Delta \xi_{ew}} = x_e - x_w \tag{E.96}$$

The g_{ij} components are given by:

$$\begin{aligned}
[g_{ij}] &= \begin{bmatrix} g_{11} & g_{12} & g_{13} \\ g_{21} & g_{22} & g_{23} \\ g_{31} & g_{32} & g_{33} \end{bmatrix} \\
&= \begin{bmatrix} \left(x_\xi^2 + y_\xi^2 + z_\xi^2\right) & \left(x_\xi x_\eta + y_\xi y_\eta + z_\xi z_\eta\right) & \left(x_\xi x_\zeta + y_\xi y_\zeta + z_\xi z_\zeta\right) \\ \left(x_\xi x_\eta + y_\xi y_\eta + z_\xi z_\eta\right) & \left(x_\eta^2 + y_\eta^2 + z_\eta^2\right) & \left(x_\eta x_\zeta + y_\eta y_\zeta + z_\eta z_\zeta\right) \\ \left(x_\xi x_\zeta + y_\xi y_\zeta + z_\xi z_\zeta\right) & \left(x_\eta x_\zeta + y_\eta y_\zeta + z_\eta z_\zeta\right) & \left(x_\zeta^2 + y_\zeta^2 + z_\zeta^2\right) \end{bmatrix}
\end{aligned} \tag{E.97}$$

Since the metric tensor is symmetric ($g_{ij} = g_{ji}$), only 6 independent quantities need to be calculated.

In the UMIST-*N* wall function, rather than store all 6 components of the metric tensor for each of the subgrid cells all the way along the wall, values of the metric tensors are stored at the subgrid domain boundaries (top and bottom) together with a few interpolation constants. At the beginning

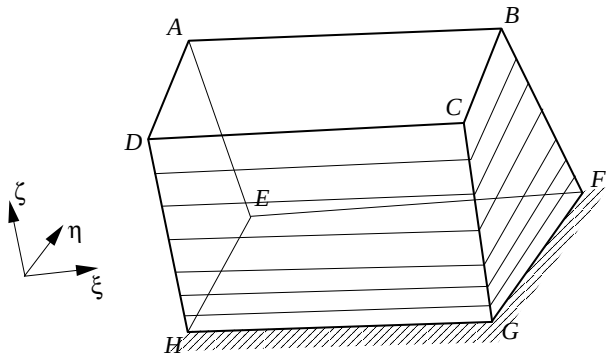

Figure E.6: Three-dimensional view of subgrid block. The top surface *ABCD* is assumed to be parallel to the wall surface $EFGH$. Both planes are parallel to the subgrid $\xi - \eta$ plane.

of each subgrid iteration, values of the metric tensor within the subgrid are interpolated. The interpolation functions are derived below for each of the metric tensors. Figure E.6 shows the general arrangement for a subgrid, where it is assumed that the top and bottom surfaces of the subgrid cells are parallel to the wall surface.

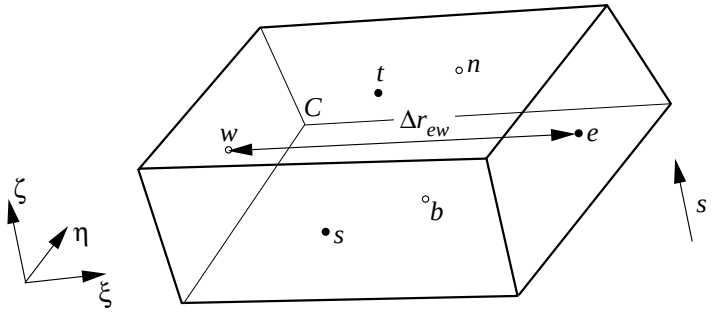

Figure E.7: Three-dimensional subgrid cell showing the distance from the east to the west face, Δr_{ew} . The physical wall-normal distance in the ζ-direction is denoted *s*.

The simplest interpolation functions are for the metric tensors g_{11} and g_{22}. Figure E.7 shows a typical subgrid cell and the distance between the east and west cell faces, Δr_{ew}. The metric tensor, g_{11} is given by:

$$\begin{aligned} g_{11} &= x_\xi^2 + y_\xi^2 + z_\xi^2 \\ &= (x_e - x_w)^2 + (y_e - y_w)^2 + (z_e - z_w)^2 \\ &= \Delta r_{ew}^2 \end{aligned} \tag{E.98}$$

Distance Δr_{ew} is a linear function of the physical wall-normal distance. The metric tensor g_{11} can therefore be interpolating from values at the top and bottom of the subgrid block, as follows:

$$\sqrt{g_{11}} = \frac{\left(\sqrt{(g_{11})_T} - \sqrt{(g_{11})_B}\right)}{(s_n - s_1)} (s - s_1) + \sqrt{(g_{11})_B} \tag{E.99}$$

where s_1 is the position of the subgrid node on the wall surface, $(s_n - s_1)$ is the total height of the subgrid domain, and upper-case T and B refer to values at the top and bottom of the subgrid domain (at the same positions as subgrid nodes 1 and n, shown in Figure E.3). Using Equation (E.82), this expression can be written:

$$\sqrt{g_{11}} = \sqrt{(g_{11})_B} + \left(\sqrt{(g_{11})_T} - \sqrt{(g_{11})_B} \right) d_i \tag{E.100}$$

A similar result can be obtained for the g_{22} metric, which is equivalent to the square of the distance from the north to the south faces of the subgrid cell, $(\Delta r_{ns})^2$. The metric tensor g_{33} is given by:

$$\begin{aligned} g_{33} &= x_\zeta^2 + y_\zeta^2 + z_\zeta^2 \\ &= (x_t - x_b)^2 + (y_t - y_b)^2 + (z_t - z_b)^2 \\ &= \Delta s^2 \end{aligned} \tag{E.101}$$

where Δs is the thickness of the subgrid cell, from top to bottom.

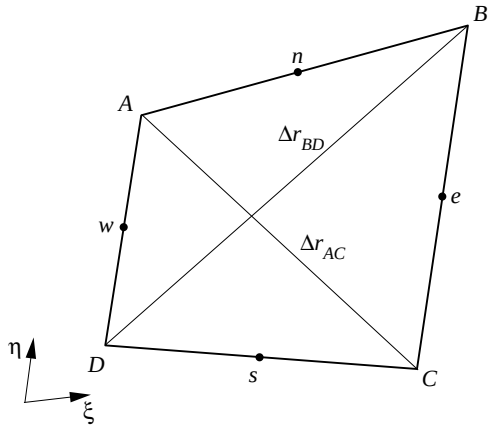

Figure E.8: 2-*D* plane in the $\xi - \eta$ axis used to calculate the metric tensor g_{12}. The four sides of the trapezoid *ABCD* are (in general) non-parallel and the lengths of the diagonal elements are denoted Δr_{BD} and Δr_{AC}.

The metric tensor g_{12} is given by:

$$\begin{aligned} g_{12} &= \left(x_\xi x_\eta + y_\xi y_\eta + z_\xi z_\eta \right) \\ &= (x_e - x_w)(x_n - x_s) + (y_e - y_w)(y_n - y_s) + (z_e - z_w)(z_n - z_s) \end{aligned} \tag{E.102}$$

The x-axis term can be expanded:

$$\begin{aligned}(x_e - x_w)(x_n - x_s) &= \frac{1}{4}(x_B + x_C - x_A - x_D)(x_A + x_B - x_C - x_D) \\ &= \frac{1}{4}\left[\left(x_B^2 - 2x_B x_D - x_D^2\right) - \left(x_A^2 - 2x_A x_C - x_C^2\right)\right] \\ &= \frac{1}{4}\left[(x_B - x_D)^2 - (x_A - x_C)^2\right] \end{aligned} \tag{E.103}$$

where subscripts A, B, C and D refer to corners of the quadrilateral element in the $\xi - \eta$ plane, as shown in Figure E.8. Performing similar manipulations of the y and z terms, the metric tensor g_{12} can be written:

$$\begin{aligned} g_{12} &= \frac{1}{4}\Big[(x_B - x_D)^2 - (x_A - x_C)^2 \\ &\quad + (y_B - y_D)^2 - (y_A - y_C)^2 \\ &\quad + (z_B - z_D)^2 - (z_A - z_C)^2\Big] \\ &= \frac{1}{4}\left(\Delta r_{BD}^2 - \Delta r_{AC}^2\right) \end{aligned} \tag{E.104}$$

where Δr_{BD} is the length of the diagonal from corners B to D, and Δr_{AC} from corners A to C. The two diagonals lie in the $\xi - \eta$ plane parallel to the wall[2]. Both Δr_{BD} and Δr_{AC} are linear functions of the distance along the ζ-axis, denoted s. The metric tensor g_{12} can therefore be interpolated from:

$$\Delta r_{BD} = \Delta r_{BD}^B + \left(\Delta r_{BD}^T - \Delta r_{BD}^B\right) d_i \tag{E.105}$$

$$\Delta r_{AC} = \Delta r_{AC}^B + \left(\Delta r_{AC}^T - \Delta r_{AC}^B\right) d_i \tag{E.106}$$

where:

$$g_{12} = \frac{1}{4}\left(\Delta r_{BD}^2 - \Delta r_{AC}^2\right) \tag{E.107}$$

The interpolation of the g_{13} and g_{23} covariant metric tensors is slightly more complex than g_{12} as the diagonal lengths (shown in Figure E.9 as Δr_{BD} and Δr_{AC}) are no longer a linear function of the distance from the wall since the subgrid cells have non-uniform thickness (assuming that cells are clustered towards the wall). The following derivation proves that the metric tensor g_{13} is proportional to $\sqrt{g_{11} g_{33}}$. Since expressions for the interpolation of g_{11} and g_{33} are already known, this proportionality expression provides an efficient route to interpolating g_{13}.

Using the cosine rule one can express the square of the length Δr_{BD} in terms of the lengths of the sides of the triangle *ABD* or triangle *BCD*:

$$\Delta r_{BD}^2 = \Delta r_{BC}^2 + \Delta r_{CD}^2 - \frac{1}{2}\Delta r_{BC}\Delta r_{CD}\cos\theta \tag{E.108}$$

[2]N.B. if the cell is orthogonal in the $\xi - \eta$ plane, the two diagonal lines Δr_{BD} and Δr_{AC} will be equal in length and hence g_{12} will be zero.

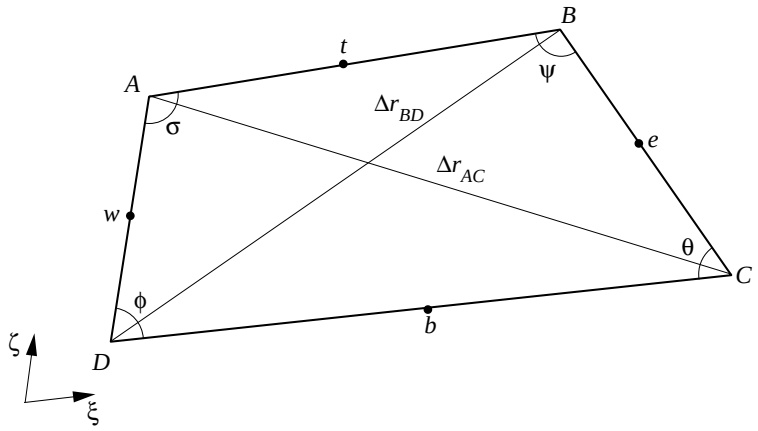

Figure E.9: 2-*D* plane parallel to the $\xi - \zeta$ axis used to calculate the metric tensor g_{13}. Sides *AB* and *CD* of the trapezoid *ABCD* are both parallel to the wall while sides *BC* and *DA* are (in general) non-parallel.

or:

$$\Delta r_{BD}^2 = \Delta r_{AB}^2 + \Delta r_{AD}^2 - \frac{1}{2}\Delta r_{AB}\Delta r_{AD}\cos\sigma \tag{E.109}$$

Combining these two expressions:

$$\Delta r_{BD}^2 = \frac{1}{2}\left(\Delta r_{BC}^2 + \Delta r_{CD}^2 + \Delta r_{AB}^2 + \Delta r_{AD}^2\right) - \frac{1}{4}\left(\Delta r_{BC}\Delta r_{CD}\cos\theta + \Delta r_{AB}\Delta r_{AD}\cos\sigma\right) \tag{E.110}$$

Similarly, for the diagonal length Δr_{AC} one can write:

$$\Delta r_{AC}^2 = \frac{1}{2}\left(\Delta r_{AB}^2 + \Delta r_{BC}^2 + \Delta r_{AD}^2 + \Delta r_{CD}^2\right) - \frac{1}{4}\left(\Delta r_{AB}\Delta r_{BC}\cos\psi + \Delta r_{AD}\Delta r_{CD}\cos\phi\right) \tag{E.111}$$

From Equation (E.104), the covariant metric g_{13} can be written:

$$\begin{aligned} g_{13} &= \frac{1}{4}\left(\Delta r_{BD}^2 - \Delta r_{AC}^2\right) \\ &= \frac{1}{16}\left(\Delta r_{AB}\Delta r_{BC}\cos\psi + \Delta r_{AD}\Delta r_{CD}\cos\phi\right. \\ &\quad \left. -\Delta r_{BC}\Delta r_{CD}\cos\theta - \Delta r_{AB}\Delta r_{AD}\cos\sigma\right) \end{aligned} \tag{E.112}$$

It is assumed that the top and bottom faces of the subgrid cell are parallel and therefore the sum of the internal angles $(\sigma + \phi) = 180^o$ and $(\psi + \theta) = 180^o$, hence:

$$\cos\sigma = \cos\left(180^o - \phi\right) = -\cos\phi \tag{E.113}$$

$$\cos\theta = \cos\left(180^o - \psi\right) = -\cos\psi \tag{E.114}$$

The metric tensor g_{13} can therefore be written:

$$\begin{aligned} g_{13} &= \frac{1}{16}\left(\Delta r_{AB}\Delta r_{BC}\cos\psi + \Delta r_{AD}\Delta r_{CD}\cos\phi + \Delta r_{BC}\Delta r_{CD}\cos\psi + \Delta r_{AB}\Delta r_{AD}\cos\phi\right) \\ &= \frac{1}{16}\left[\left(\Delta r_{AB}\Delta r_{BC} + \Delta r_{BC}\Delta r_{CD}\right)\cos\psi + \left(\Delta r_{AD}\Delta r_{CD} + \Delta r_{AB}\Delta r_{AD}\right)\cos\phi\right] \\ &= \frac{1}{16}\left[\left(\Delta r_{AB} + \Delta r_{CD}\right)\left(\Delta r_{BC}\cos\psi + \Delta r_{AD}\cos\phi\right)\right] \end{aligned} \tag{E.115}$$

Earlier it was shown that the covariant metric tensor g_{11} is given by:

$$g_{11} = \frac{1}{2}\left(\Delta r_{AB} + \Delta r_{CD}\right) \tag{E.116}$$

which is a linear function of the distance from the wall. The lengths of the sides Δr_{BC} and Δr_{AD} are also proportional to the thickness of the subgrid cell, Δs, and the angles ψ and ϕ are constant for a particular near-wall main-grid cell. Therefore, using Equation (E.101) one can write:

$$g_{13} \propto \sqrt{g_{11}g_{33}} \tag{E.117}$$

The metric g_{13} can then be linearly interpolated as follows,

$$g_{13} = (g_{13})_B + \frac{\left[(g_{13})_T - (g_{13})_B\right]}{\left[\sqrt{(g_{11}g_{33})_T} - \sqrt{(g_{11}g_{33})_B}\right]}\left[\sqrt{g_{11}g_{33}} - \sqrt{(g_{11}g_{33})_B}\right] \tag{E.118}$$

or, more simply:

$$g_{13} = a\sqrt{g_{11}g_{33}} + b \tag{E.119}$$

where the metric tensors g_{11} and g_{33} are evaluated using Equations (E.99) and (E.101) respectively, and constants a and b are given by:

$$a = \frac{\left[(g_{13})_T - (g_{13})_B\right]}{\left[\sqrt{(g_{11}g_{33})_T} - \sqrt{(g_{11}g_{33})_B}\right]} \;\; ; \;\; b = (g_{13})_B - \frac{\sqrt{(g_{11}g_{33})_B}\left[(g_{13})_T - (g_{13})_B\right]}{\left(\sqrt{(g_{11}g_{33})_T} - \sqrt{(g_{11}g_{33})_B}\right)} \tag{E.120}$$

Note that in Equations (E.118) and (E.120), subscripts T and B do not refer to values at the top and bottom of the subgrid domain. Instead these subscripts refer to values at the neighbouring cells $(n-1)$ and 2, shown in Figure E.3. This is because one needs to have a finite cell thickness ($\Delta s_i \neq 0$) in order to calculate g_{13}. Constants a and b are calculated once and stored in computer memory to reduce computing time. Values of $(g_{13})_T$ and $(g_{13})_B$ can be calculated from:

$$g_{13} = \left(x_e - x_w\right)\left(x_t - x_b\right) + \left(y_e - y_w\right)\left(y_t - y_b\right) + \left(z_e - z_w\right)\left(z_t - z_b\right) \tag{E.121}$$

An analogous solution can be obtained for the g_{23} metric tensor, where the trapezoid *ABCD* is located in the $\eta - \zeta$ plane.

E.6.4 Jacobian, J

The Jacobian, J, is evaluated from the determinant of the covariant metric tensor matrix, g. Once one has calculated all the g_{ij} components across the subgrid, one can evaluate J from Equations (B.58) and (B.95), as follows:

$$\begin{aligned} J &= \sqrt{g} \\ &= \left[g_{11}\left(g_{22}g_{33}-g_{23}g_{23}\right)-g_{12}\left(g_{21}g_{33}-g_{23}g_{31}\right)+g_{13}\left(g_{21}g_{32}-g_{22}g_{31}\right)\right]^{0.5} \end{aligned} \tag{E.122}$$

E.6.5 Contravariant Metric Tensor, g^{ij}

The contravariant metric tensor, g^{ij}, is evaluated by inverting of the covariant metric tensor matrix:

$$g^{ij} = \frac{1}{g} G_{ij} \tag{E.123}$$

where g is the determinant and G_{ij} is the matrix of cofactors of covariant metric tensor matrix. The contravariant metric tensor is thus given by:

$$\begin{aligned} g^{ij} &= \frac{1}{g}\begin{bmatrix} G_{11} & G_{12} & G_{13} \\ G_{21} & G_{22} & G_{23} \\ G_{31} & G_{32} & G_{33} \end{bmatrix} \\ &= \frac{1}{J^2}\begin{bmatrix} \left(g_{22}g_{33}-g_{23}g_{32}\right) & -\left(g_{12}g_{33}-g_{13}g_{32}\right) & \left(g_{12}g_{23}-g_{13}g_{22}\right) \\ -\left(g_{21}g_{33}-g_{23}g_{31}\right) & \left(g_{11}g_{33}-g_{13}g_{31}\right) & -\left(g_{11}g_{23}-g_{13}g_{21}\right) \\ \left(g_{21}g_{32}-g_{22}g_{31}\right) & -\left(g_{11}g_{32}-g_{12}g_{31}\right) & \left(g_{11}g_{22}-g_{12}g_{21}\right) \end{bmatrix} \end{aligned} \tag{E.124}$$

where $g_{ij} = g_{ji}$ and $G_{ij} = G_{ji}$, hence only 6 independent cofactors need to be calculated.

The leading diagonal terms in the cofactor matrix (G_{11}, G_{22} and G_{33}) are equivalent to the square of the ratio of the cell face areas to the cell volume. This can be deduced from the definition of the contravariant metric tensor (Equation B.31), as follows:

$$\begin{aligned} g^{33} &= \mathbf{g}^3 \cdot \mathbf{g}^3 \\ &= \frac{1}{\Delta Vol}\left(\mathbf{g}_1 \times \mathbf{g}_2\right) \cdot \frac{1}{\Delta Vol}\left(\mathbf{g}_1 \times \mathbf{g}_2\right) \\ &= \left(\frac{A_{12}}{\Delta Vol}\right)^2 \end{aligned} \tag{E.125}$$

where A_{12} is the area of the cell face in the $\xi-\eta$ plane and ΔVol is the cell volume. The above equation can be used to determine the wall-normal distance from $\Delta Vol/A_{12}$, where A_{12} is the area of the cell face on the wall.

Interpreting a physical meaning for the off-diagonal contravariant metric tensors is slightly more

difficult. The g^{12} metric tensor is expanded as follows:

$$g^{12} = \mathbf{g}^1 \cdot \mathbf{g}^2 = \frac{1}{\Delta Vol}(\mathbf{g}_2 \times \mathbf{g}_3) \cdot \frac{1}{\Delta Vol}(\mathbf{g}_1 \times \mathbf{g}_3) \equiv \frac{\mathbf{A}_{23} \cdot \mathbf{A}_{13}}{\Delta Vol^2} \tag{E.126}$$

where, from the definition of the cross-product, the vector $\mathbf{A}_{23}$ is the area formed by vectors $\mathbf{g}_2$ and $\mathbf{g}_3$ with direction normal to both $\mathbf{g}_2$ and $\mathbf{g}_3$ (i.e. in the direction of $\mathbf{g}^1$). If the base vectors $\mathbf{g}^1$ and $\mathbf{g}^2$ are orthogonal the g^{12} metric tensor will be zero.

E.6.6 Christoffel Symbol, Γ^i_{jk}

The Christoffel symbol of the second kind is calculated from:

$$\Gamma^k_{ij} = \frac{1}{2} g^{kl} \left(\frac{\partial g_{jl}}{\partial \xi^i} + \frac{\partial g_{il}}{\partial \xi^j} - \frac{\partial g_{ij}}{\partial \xi^l} \right) \tag{E.127}$$

For example, Γ^3_{12} is given by:

$$\begin{aligned} \Gamma^3_{12} = \frac{1}{2} \Bigg[& g^{31} \left(\frac{\partial g_{21}}{\partial \xi} + \frac{\partial g_{11}}{\partial \eta} - \frac{\partial g_{12}}{\partial \xi} \right) + g^{32} \left(\frac{\partial g_{22}}{\partial \xi} + \frac{\partial g_{12}}{\partial \eta} - \frac{\partial g_{12}}{\partial \eta} \right) \\ & + g^{33} \left(\frac{\partial g_{23}}{\partial \xi} + \frac{\partial g_{13}}{\partial \eta} - \frac{\partial g_{12}}{\partial \zeta} \right) \Bigg] \end{aligned} \tag{E.128}$$

where $\xi^1 \equiv \xi$, $\xi^2 \equiv \eta$ and $\xi^3 \equiv \zeta$. Since the metric tensor is symmetric ($g_{ij} = g_{ji}$), this can be simplified:

$$\Gamma^3_{12} = \frac{1}{2} \left[g^{31} \frac{\partial g_{11}}{\partial \eta} + g^{32} \frac{\partial g_{22}}{\partial \xi} + g^{33} \left(\frac{\partial g_{23}}{\partial \xi} + \frac{\partial g_{13}}{\partial \eta} - \frac{\partial g_{12}}{\partial \zeta} \right) \right] \tag{E.129}$$

To calculate the gradients of the covariant metric tensor, g_{ij}, it is necessary to evaluate g_{ij} at cell boundaries. The subscripts of the Christoffel symbol are interchangeable ($\Gamma^k_{ij} = \Gamma^k_{ji}$) and therefore there are only 18 independent terms, which are summarized below:

$$\begin{aligned} \Gamma^1_{11} &= \frac{1}{2} g^{1l} \left(2 \frac{\partial g_{1l}}{\partial \xi} - \frac{\partial g_{11}}{\partial \xi^l} \right) \\ &= \frac{1}{2} \left[g^{11} \left(\frac{\partial g_{11}}{\partial \xi} \right) + g^{12} \left(2 \frac{\partial g_{12}}{\partial \xi} - \frac{\partial g_{11}}{\partial \eta} \right) + g^{13} \left(2 \frac{\partial g_{13}}{\partial \xi} - \frac{\partial g_{11}}{\partial \zeta} \right) \right] \end{aligned} \tag{E.130}$$

$$\begin{aligned} \Gamma^1_{22} &= \frac{1}{2} g^{1l} \left(2 \frac{\partial g_{2l}}{\partial \eta} - \frac{\partial g_{22}}{\partial \xi^l} \right) \\ &= \frac{1}{2} \left[g^{11} \left(2 \frac{\partial g_{21}}{\partial \eta} - \frac{\partial g_{22}}{\partial \xi} \right) + g^{12} \left(\frac{\partial g_{22}}{\partial \eta} \right) + g^{13} \left(2 \frac{\partial g_{23}}{\partial \eta} - \frac{\partial g_{22}}{\partial \zeta} \right) \right] \end{aligned} \tag{E.131}$$

$$\begin{aligned}\Gamma^1_{33} &= \frac{1}{2}g^{1l}\left(2\frac{\partial g_{3l}}{\partial\zeta}-\frac{\partial g_{33}}{\partial\xi^l}\right)\\ &= \frac{1}{2}\left[g^{11}\left(2\frac{\partial g_{31}}{\partial\zeta}-\frac{\partial g_{33}}{\partial\xi}\right)+g^{12}\left(2\frac{\partial g_{32}}{\partial\zeta}-\frac{\partial g_{33}}{\partial\eta}\right)+g^{13}\left(\frac{\partial g_{33}}{\partial\zeta}\right)\right]\end{aligned} \tag{E.132}$$

$$\begin{aligned}\Gamma^1_{12}=\Gamma^1_{21} &= \frac{1}{2}g^{1l}\left(\frac{\partial g_{2l}}{\partial\xi}+\frac{\partial g_{1l}}{\partial\eta}-\frac{\partial g_{12}}{\partial\xi^l}\right)\\ &= \frac{1}{2}\left[g^{11}\left(\frac{\partial g_{11}}{\partial\eta}\right)+g^{12}\left(\frac{\partial g_{22}}{\partial\xi}\right)+g^{13}\left(\frac{\partial g_{23}}{\partial\xi}+\frac{\partial g_{13}}{\partial\eta}-\frac{\partial g_{12}}{\partial\zeta}\right)\right]\end{aligned} \tag{E.133}$$

$$\begin{aligned}\Gamma^1_{13}=\Gamma^1_{31} &= \frac{1}{2}g^{1l}\left(\frac{\partial g_{3l}}{\partial\xi}+\frac{\partial g_{1l}}{\partial\zeta}-\frac{\partial g_{13}}{\partial\xi^l}\right)\\ &= \frac{1}{2}\left[g^{11}\left(\frac{\partial g_{11}}{\partial\zeta}\right)+g^{12}\left(\frac{\partial g_{32}}{\partial\xi}+\frac{\partial g_{12}}{\partial\zeta}-\frac{\partial g_{13}}{\partial\eta}\right)+g^{13}\left(\frac{\partial g_{33}}{\partial\xi}\right)\right]\end{aligned} \tag{E.134}$$

$$\begin{aligned}\Gamma^1_{23}=\Gamma^1_{32} &= \frac{1}{2}g^{1l}\left(\frac{\partial g_{3l}}{\partial\eta}+\frac{\partial g_{2l}}{\partial\zeta}-\frac{\partial g_{23}}{\partial\xi^l}\right)\\ &= \frac{1}{2}\left[g^{11}\left(\frac{\partial g_{31}}{\partial\eta}+\frac{\partial g_{21}}{\partial\zeta}-\frac{\partial g_{23}}{\partial\xi}\right)+g^{12}\left(\frac{\partial g_{22}}{\partial\zeta}\right)+g^{13}\left(\frac{\partial g_{33}}{\partial\eta}\right)\right]\end{aligned} \tag{E.135}$$

$$\Gamma^2_{11} = \frac{1}{2}\left[g^{21}\left(\frac{\partial g_{11}}{\partial\xi}\right)+g^{22}\left(2\frac{\partial g_{12}}{\partial\xi}-\frac{\partial g_{11}}{\partial\eta}\right)+g^{23}\left(2\frac{\partial g_{13}}{\partial\xi}-\frac{\partial g_{11}}{\partial\zeta}\right)\right] \tag{E.136}$$

$$\Gamma^2_{22} = \frac{1}{2}\left[g^{21}\left(2\frac{\partial g_{21}}{\partial\eta}-\frac{\partial g_{22}}{\partial\xi}\right)+g^{22}\left(\frac{\partial g_{22}}{\partial\eta}\right)+g^{23}\left(2\frac{\partial g_{23}}{\partial\eta}-\frac{\partial g_{22}}{\partial\zeta}\right)\right] \tag{E.137}$$

$$\Gamma^2_{33} = \frac{1}{2}\left[g^{21}\left(2\frac{\partial g_{31}}{\partial\zeta}-\frac{\partial g_{33}}{\partial\xi}\right)+g^{22}\left(2\frac{\partial g_{32}}{\partial\zeta}-\frac{\partial g_{33}}{\partial\eta}\right)+g^{23}\left(\frac{\partial g_{33}}{\partial\zeta}\right)\right] \tag{E.138}$$

$$\Gamma^2_{12}=\Gamma^2_{21} = \frac{1}{2}\left[g^{21}\left(\frac{\partial g_{11}}{\partial\eta}\right)+g^{22}\left(\frac{\partial g_{22}}{\partial\xi}\right)+g^{23}\left(\frac{\partial g_{23}}{\partial\xi}+\frac{\partial g_{13}}{\partial\eta}-\frac{\partial g_{12}}{\partial\zeta}\right)\right] \tag{E.139}$$

$$\Gamma^2_{13}=\Gamma^2_{31} = \frac{1}{2}\left[g^{21}\left(\frac{\partial g_{11}}{\partial\zeta}\right)+g^{22}\left(\frac{\partial g_{32}}{\partial\xi}+\frac{\partial g_{12}}{\partial\zeta}-\frac{\partial g_{13}}{\partial\eta}\right)+g^{23}\left(\frac{\partial g_{33}}{\partial\xi}\right)\right] \tag{E.140}$$

$$\Gamma^2_{23}=\Gamma^2_{32} = \frac{1}{2}\left[g^{21}\left(\frac{\partial g_{31}}{\partial\eta}+\frac{\partial g_{21}}{\partial\zeta}-\frac{\partial g_{23}}{\partial\xi}\right)+g^{22}\left(\frac{\partial g_{22}}{\partial\zeta}\right)+g^{23}\left(\frac{\partial g_{33}}{\partial\eta}\right)\right] \tag{E.141}$$

$$\Gamma^3_{11} = \frac{1}{2}\left[g^{31}\left(\frac{\partial g_{11}}{\partial \xi}\right)+g^{32}\left(2\frac{\partial g_{12}}{\partial \xi}-\frac{\partial g_{11}}{\partial \eta}\right)+g^{33}\left(2\frac{\partial g_{13}}{\partial \xi}-\frac{\partial g_{11}}{\partial \zeta}\right)\right] \quad \text{(E.142)}$$

$$\Gamma^3_{22} = \frac{1}{2}\left[g^{31}\left(2\frac{\partial g_{21}}{\partial \eta}-\frac{\partial g_{22}}{\partial \xi}\right)+g^{32}\left(\frac{\partial g_{22}}{\partial \eta}\right)+g^{33}\left(2\frac{\partial g_{23}}{\partial \eta}-\frac{\partial g_{22}}{\partial \zeta}\right)\right] \quad \text{(E.143)}$$

$$\Gamma^3_{33} = \frac{1}{2}\left[g^{31}\left(2\frac{\partial g_{31}}{\partial \zeta}-\frac{\partial g_{33}}{\partial \xi}\right)+g^{32}\left(2\frac{\partial g_{32}}{\partial \zeta}-\frac{\partial g_{33}}{\partial \eta}\right)+g^{33}\left(\frac{\partial g_{33}}{\partial \zeta}\right)\right] \quad \text{(E.144)}$$

$$\Gamma^3_{12}=\Gamma^3_{21} = \frac{1}{2}\left[g^{31}\left(\frac{\partial g_{11}}{\partial \eta}\right)+g^{32}\left(\frac{\partial g_{22}}{\partial \xi}\right)+g^{33}\left(\frac{\partial g_{23}}{\partial \xi}+\frac{\partial g_{13}}{\partial \eta}-\frac{\partial g_{12}}{\partial \zeta}\right)\right] \quad \text{(E.145)}$$

$$\Gamma^3_{13}=\Gamma^3_{31} = \frac{1}{2}\left[g^{31}\left(\frac{\partial g_{11}}{\partial \zeta}\right)+g^{32}\left(\frac{\partial g_{32}}{\partial \xi}+\frac{\partial g_{12}}{\partial \zeta}-\frac{\partial g_{13}}{\partial \eta}\right)+g^{33}\left(\frac{\partial g_{33}}{\partial \xi}\right)\right] \quad \text{(E.146)}$$

$$\Gamma^3_{23}=\Gamma^3_{32} = \frac{1}{2}\left[g^{31}\left(\frac{\partial g_{31}}{\partial \eta}+\frac{\partial g_{21}}{\partial \zeta}-\frac{\partial g_{23}}{\partial \xi}\right)+g^{32}\left(\frac{\partial g_{22}}{\partial \zeta}\right)+g^{33}\left(\frac{\partial g_{33}}{\partial \eta}\right)\right] \quad \text{(E.147)}$$

E.7 Calculation of Wall-Normal Velocity

The subgrid velocity in the ζ-direction is calculated from continuity and scaled, as described in Section 4.3.1. The continuity equation in curvilinear coordinates is given by:

$$\frac{\partial \rho}{\partial t}+\frac{1}{J}\frac{\partial}{\partial \xi}\left(\frac{J}{\sqrt{g_{11}}}\rho U\right)+\frac{1}{J}\frac{\partial}{\partial \eta}\left(\frac{J}{\sqrt{g_{22}}}\rho V\right)+\frac{1}{J}\frac{\partial}{\partial \zeta}\left(\frac{J}{\sqrt{g_{33}}}\rho W\right)=0 \quad \text{(E.148)}$$

where, U, V and W denote the physical velocity components in the direction of the base vector components ξ, η and ζ respectively. For a steady, incompressible flow this expression integrated over a subgrid cell with volume ($\Delta Vol = J\Delta\xi_{ew}\Delta\eta_{ns}\Delta\zeta_{tb}$) gives:

$$\underbrace{\left(\frac{J}{\sqrt{g_{11}}}U\right)_e-\left(\frac{J}{\sqrt{g_{11}}}U\right)_w}_{flux_{ew}}+\underbrace{\left(\frac{J}{\sqrt{g_{22}}}V\right)_n-\left(\frac{J}{\sqrt{g_{22}}}V\right)_s}_{flux_{ns}}$$
$$+\left(\frac{J}{\sqrt{g_{33}}}W\right)_t-\underbrace{\left(\frac{J}{\sqrt{g_{33}}}W\right)_b}_{flux_b} = 0 \quad \text{(E.149)}$$

where, for instance, $flux_{ew}$ is the sum of the flux through the east and west subgrid cell faces. This can be rearranged in terms of the velocity at the top subgrid cell face, W_t, as follows:

$$W_t = (flux_b - flux_{ew} - flux_{ns}) \left(\frac{\sqrt{g_{33}}}{J} \right)_t \tag{E.150}$$

The calculation procedure for the subgrid W-velocity starts from the wall surface where, for a non-porous wall, it is assumed that the flux through the bottom wall is zero ($flux_b = 0$). In the wall-adjacent subgrid cell one can therefore calculate the W-velocity through the top cell face (W_t) from Equation (E.150). This calculation is repeated sequentially for each subgrid cell, moving steadily up the subgrid towards the top boundary. The W-velocity at the subgrid nodes (W_P) is then simply the mean of the top and bottom face values. Once all the W-velocity is known at all the subgrid nodes a scaling is applied as followed:

$$W = \alpha W_P^* \tag{E.151}$$

where:

$$\alpha = \frac{W_t'}{(W_t^* \pm tiny)} \quad -3 < \alpha < 3 \tag{E.152}$$

Subscript t denotes the position at outer edge of the subgrid domain (i.e. top of the main-grid cell), superscript $*$ denotes the value calculated from continuity and the prime $(')$ denotes the main-grid value or boundary condition (see also Section 4.3.1).

E.8 Conversion between Contravariant and Cartesian Components

E.8.1 Vector Quantities

The velocity vector, $\mathbf{v}$, can be expressed in terms of the Cartesian base vectors, $\mathbf{e}_i$, or the non-orthogonal curvilinear base vectors, $\mathbf{g}_j$, as follows:

$$\mathbf{v} = u^i \mathbf{e}_i = v^j \mathbf{g}_j \tag{E.153}$$

where u^i and v^j are the Cartesian and non-physical curvilinear components, respectively. One can similarly write an expression for the position vector $\mathbf{r}$:

$$\mathbf{r} = x^i \mathbf{e}_i = \xi^j \mathbf{g}_j \tag{E.154}$$

Rearranging this expression using the chain rule:

$$\mathbf{e}_i = \frac{\partial \mathbf{r}}{\partial x^i} = \frac{\partial \mathbf{r}}{\partial \xi^j} \frac{\partial \xi^j}{\partial x^i} = \mathbf{g}_j \frac{\partial \xi^j}{\partial x^i} \tag{E.155}$$

and substituting for the Cartesian base vector, one obtains:

$$\mathbf{v} = u^i \mathbf{e}_i = u^i \frac{\partial \xi^j}{\partial x^i} \mathbf{g}_j \tag{E.156}$$

Comparing Equations (E.153) and (E.156), the curvilinear velocity components $\left(v^j\right)$ must be equivalent to components $\left(u^i \partial \xi^j / \partial x^i\right)$:

$$v^j = u^i \frac{\partial \xi^j}{\partial x^i} \tag{E.157}$$

This can be expanded:

$$v^1 = u^1 \xi_x + u^2 \xi_y + u^3 \xi_z \tag{E.158}$$

$$v^2 = u^1 \eta_x + u^2 \eta_y + u^3 \eta_z \tag{E.159}$$

$$v^3 = u^1 \zeta_x + u^2 \zeta_y + u^3 \zeta_z \tag{E.160}$$

and written in matrix form, using the physical velocity components $v^{(j)}$, where $v^j = v^{(j)} / \sqrt{g_{jj}}$:

$$\underbrace{\begin{bmatrix} v^{(1)}/\sqrt{g_{11}} \\ v^{(2)}/\sqrt{g_{22}} \\ v^{(3)}/\sqrt{g_{33}} \end{bmatrix}}_{curvilinear} = \underbrace{\begin{bmatrix} \xi_x & \xi_y & \xi_z \\ \eta_x & \eta_y & \eta_z \\ \zeta_x & \zeta_y & \zeta_z \end{bmatrix}}_{[J]^{-1}} \underbrace{\begin{bmatrix} u^1 \\ u^2 \\ u^3 \end{bmatrix}}_{Cartesian} \tag{E.161}$$

where the 3×3 matrix in the above expression is equivalent to the inverse of the Jacobian matrix $[J]^{-1}$. The conversion factor $\partial \xi^j / \partial x^i$ is sometimes given the symbol β_i^j.

To reverse the above function and obtain Cartesian velocity components from the curvilinear one needs to express the curvilinear base vectors in terms of the Cartesian vectors, as follows:

$$\mathbf{g}_j = \frac{\partial \mathbf{r}}{\partial \xi^j} = \frac{\partial \mathbf{r}}{\partial x^i} \frac{\partial x^i}{\partial \xi^j} = \mathbf{e}_i \frac{\partial x^i}{\partial \xi^j} \tag{E.162}$$

The velocity vector can thus be written:

$$\mathbf{v} = u^i \mathbf{e}_i = v^j \mathbf{g}_j = v^j \frac{\partial x^i}{\partial \xi^j} \mathbf{e}_i \tag{E.163}$$

and so the in Cartesian velocity components $\left(u^i\right)$ are given by:

$$u^i = v^j \frac{\partial x^i}{\partial \xi^j} \tag{E.164}$$

In matrix form using physical contravariant velocity components, this can be written:

$$\underbrace{\begin{bmatrix} u^1 \\ u^2 \\ u^3 \end{bmatrix}}_{Cartesian} = \underbrace{\begin{bmatrix} x_\xi & x_\eta & x_\zeta \\ y_\xi & y_\eta & y_\zeta \\ z_\xi & z_\eta & z_\zeta \end{bmatrix}}_{[J]} \underbrace{\begin{bmatrix} v^{(1)}/\sqrt{g_{11}} \\ v^{(2)}/\sqrt{g_{22}} \\ v^{(3)}/\sqrt{g_{33}} \end{bmatrix}}_{curvilinear} \tag{E.165}$$

where the 3×3 matrix in the above expression is simply the Jacobian matrix, $[J]$.

The inverse Jacobian matrix $[J]^{-1}$ is found from:

$$[J]^{-1} = \frac{1}{J}[\mathrm{cof}\,(J)]^T \tag{E.166}$$

where J is the determinant, $\mathrm{cof}(J)$ is the matrix of cofactors and $[\mathrm{cof}\,(J)]^T$ is the adjoint of the $[J]$ matrix. This is expanded as follows:

$$\begin{aligned} [J]^{-1} &= \frac{1}{J}[\mathrm{cof}\,(J)]^T \\ &= \frac{1}{J}\begin{bmatrix} (y_\eta z_\zeta - y_\zeta z_\eta) & -(x_\eta z_\zeta - x_\zeta z_\eta) & (x_\eta y_\zeta - x_\zeta y_\eta) \\ -(y_\xi z_\zeta - z_\zeta y_\xi) & (x_\xi z_\zeta - x_\zeta z_\xi) & -(x_\xi y_\zeta - x_\zeta y_\xi) \\ (y_\xi z_\eta - y_\eta z_\xi) & -(x_\xi z_\eta - x_\eta z_\xi) & (x_\xi y_\eta - x_\eta y_\xi) \end{bmatrix} \end{aligned} \tag{E.167}$$

where the Jacobian, J, is given by:

$$J = x_\xi (y_\eta z_\zeta - y_\zeta z_\eta) - x_\eta (y_\xi z_\zeta - z_\zeta y_\xi) + x_\zeta (y_\xi z_\eta - y_\eta z_\xi) \tag{E.168}$$

E.8.2 Second-Order Tensors

A second-order tensor, such as the Reynolds stress, is expressed in contravariant and Cartesian coordinates as follows:

$$\mathbf{T} = \tau^{ij}\mathbf{g}_i \otimes \mathbf{g}_j = t_{ij}\mathbf{e}_i \otimes \mathbf{e}_j \tag{E.169}$$

Earlier it was show that the covariant base vector, $\mathbf{g}_j$, can be written in terms of the Cartesian unit vector $\mathbf{e}_i$:

$$\mathbf{g}_j = \frac{\partial \mathbf{r}}{\partial \xi^j} = \frac{\partial \mathbf{r}}{\partial x^i}\frac{\partial x^i}{\partial \xi^j} = \frac{\partial x^i}{\partial \xi^j}\mathbf{e}_i \tag{E.170}$$

Substituting this into Equation (E.169):

$$\mathbf{T} = \tau^{ij}\left(\frac{\partial x^p}{\partial \xi^i}\mathbf{e}_p\right) \otimes \left(\frac{\partial x^q}{\partial \xi^j}\mathbf{e}_q\right) \tag{E.171}$$

which can be rearranged:

$$\underbrace{t^{pq}}_{Cartesian} = \frac{\partial x^p}{\partial \xi^i}\frac{\partial x^q}{\partial \xi^j}\underbrace{\tau^{ij}}_{contravariant} \tag{E.172}$$

The above equation can be used to convert the Reynolds stress tensor, $\overline{u^i u^j}$ from contravariant to Cartesian coordinates.

The mean strain-rate tensor, $U^i_{,j}$, is a mixed contravariant and covariant tensor, having both a raised and a lowered index. To satisfy the summation convention of repeated upper and lower indices, the subgrid strain-rate tensor must be converted into a fully contravariant second-order tensor before it is transformed into into Cartesian coordinates, i.e.:

$$V^{p,q} = U^{i,k}\frac{\partial x^p}{\partial \xi^i}\frac{\partial x^q}{\partial \xi^k} = g^{jk}U^i_{,j}\frac{\partial x^p}{\partial \xi^i}\frac{\partial x^q}{\partial \xi^k} \tag{E.173}$$

where $V^{p,q}$ is the Cartesian strain-rate tensor and the contravariant strain-rate tensor is calculated from Equation (C.96):

$$U^i_{,j} = \frac{\partial}{\partial \xi^j}\left(\frac{U^{(i)}}{\sqrt{g_{ii}}}\right) + \frac{U^{(m)}}{\sqrt{g_{mm}}}\Gamma^i_{mj} \tag{E.174}$$

E.9 Calculation of Pressure Gradient, $\partial P/\partial \zeta$

In Section 4.2.2 it was discussed that the subgrid pressure gradient in the ζ-direction ($\partial P/\partial \zeta$) appears in the wall-parallel momentum equations when the near-wall grid is skewed in the plane normal to the wall. This is because the gradient of the pressure in the ζ-direction has a component which is parallel to the wall (since the ζ-axis is not perpendicular to the wall). The subgrid pressure gradient in the ζ-direction is calculated from the following expression:

$$\nabla P \cdot \hat{\mathbf{n}} + (\nabla \cdot \rho\overline{\mathbf{u}\otimes\mathbf{u}}) \cdot \hat{\mathbf{n}} = 0 \tag{E.175}$$

This states that the sum of the projection of the pressure gradient and the projection of the divergence of the Reynolds stress tensor in the wall-normal direction is zero. The ∇P and $(\nabla \cdot \overline{\mathbf{u}\otimes\mathbf{u}})$ terms are expanded as follows:

$$\nabla P = \frac{\partial P}{\partial \xi^j}\beta^j_i \mathbf{e}_i \tag{E.176}$$

$$\begin{aligned} \nabla \cdot \overline{\mathbf{u}\otimes\mathbf{u}} &= \mathbf{g}^k \cdot \frac{\partial}{\partial \xi^k}\left(\overline{u^i u^j}\mathbf{e}_i \otimes \mathbf{e}_j\right) \\ &= \frac{\partial \overline{u^i u^j}}{\partial \xi^k}\beta^k_j \mathbf{e}_i \end{aligned} \tag{E.177}$$

where the Reynolds stress components $\overline{u^i u^j}$ are in Cartesian coordinates. To convert from contravariant to Cartesian components, the conversion factor β^i_k is introduced which can be shown to be equiv-

alent to the inverse Jacobian matrix, $[J]^{-1}$, as follows:

$$\beta_j^k = \mathbf{e}_j \cdot \mathbf{g}^k = \frac{\partial \xi^m}{\partial x^j}\mathbf{g}_m \cdot \mathbf{g}^k = \frac{\partial \xi^m}{\partial x^j}\delta_m^k = \underbrace{\frac{\partial \xi^k}{\partial x^j}}_{[J]^{-1}} \tag{E.178}$$

The pressure gradient, ∇P, is expanded further as follows:

$$\begin{aligned}\nabla P = \frac{\partial P}{\partial \xi^j}\beta_i^j \mathbf{e}_i \quad = \quad & \left(\underbrace{\frac{\partial P}{\partial \xi}\beta_1^1 + \frac{\partial P}{\partial \eta}\beta_1^2}_{P_x^{\xi\eta}} + \frac{\partial P}{\partial \zeta}\beta_1^3 \right)\mathbf{e}_1 \\ & + \left(\underbrace{\frac{\partial P}{\partial \xi}\beta_2^1 + \frac{\partial P}{\partial \eta}\beta_2^2}_{P_y^{\xi\eta}} + \frac{\partial P}{\partial \zeta}\beta_2^3 \right)\mathbf{e}_2 \\ & + \left(\underbrace{\frac{\partial P}{\partial \xi}\beta_3^1 + \frac{\partial P}{\partial \eta}\beta_3^2}_{P_z^{\xi\eta}} + \frac{\partial P}{\partial \zeta}\beta_3^3 \right)\mathbf{e}_3\end{aligned} \tag{E.179}$$

and the projection of the pressure gradient in the wall-normal direction is given by:

$$\nabla P \cdot \hat{\mathbf{n}} = \left(P_x^{\xi\eta} + \frac{\partial P}{\partial \zeta}\beta_1^3 \right) n_x + \left(P_y^{\xi\eta} + \frac{\partial P}{\partial \zeta}\beta_2^3 \right) n_y + \left(P_z^{\xi\eta} + \frac{\partial P}{\partial \zeta}\beta_3^3 \right) n_z \tag{E.180}$$

where the wall-normal unit vector is given by:

$$\hat{\mathbf{n}} = n_x\mathbf{e}_1 + n_y\mathbf{e}_2 + n_z\mathbf{e}_3 \tag{E.181}$$

The divergence of the Reynolds stress tensor is expanded:

$$\begin{aligned}
\frac{\partial \overline{u^i u^j}}{\partial \xi^m}\beta_j^m \mathbf{e}_i &= \underbrace{\left(\frac{\partial \overline{uu}}{\partial \xi}\beta_1^1+\frac{\partial \overline{uu}}{\partial \eta}\beta_1^2+\frac{\partial \overline{uu}}{\partial \zeta}\beta_1^3 + \frac{\partial \overline{uv}}{\partial \xi}\beta_2^1+\frac{\partial \overline{uv}}{\partial \eta}\beta_2^2+\frac{\partial \overline{uv}}{\partial \zeta}\beta_2^3 + \frac{\partial \overline{uw}}{\partial \xi}\beta_3^1+\frac{\partial \overline{uw}}{\partial \eta}\beta_3^2+\frac{\partial \overline{uw}}{\partial \zeta}\beta_3^3\right)}_{S_x}\mathbf{e}_1 \\
&+ \underbrace{\left(\frac{\partial \overline{vu}}{\partial \xi}\beta_1^1+\frac{\partial \overline{vu}}{\partial \eta}\beta_1^2+\frac{\partial \overline{vu}}{\partial \zeta}\beta_1^3 + \frac{\partial \overline{vv}}{\partial \xi}\beta_2^1+\frac{\partial \overline{vv}}{\partial \eta}\beta_2^2+\frac{\partial \overline{vv}}{\partial \zeta}\beta_2^3 + \frac{\partial \overline{vw}}{\partial \xi}\beta_3^1+\frac{\partial \overline{vw}}{\partial \eta}\beta_3^2+\frac{\partial \overline{vw}}{\partial \zeta}\beta_3^3\right)}_{S_y}\mathbf{e}_2 \\
&+ \underbrace{\left(\frac{\partial \overline{wu}}{\partial \xi}\beta_1^1+\frac{\partial \overline{wu}}{\partial \eta}\beta_1^2+\frac{\partial \overline{wu}}{\partial \zeta}\beta_1^3 + \frac{\partial \overline{wv}}{\partial \xi}\beta_2^1+\frac{\partial \overline{wv}}{\partial \eta}\beta_2^2+\frac{\partial \overline{wv}}{\partial \zeta}\beta_2^3 + \frac{\partial \overline{ww}}{\partial \xi}\beta_3^1+\frac{\partial \overline{ww}}{\partial \eta}\beta_3^2+\frac{\partial \overline{ww}}{\partial \zeta}\beta_3^3\right)}_{S_z}\mathbf{e}_3
\end{aligned} \tag{E.182}$$

and its projection in the wall-normal direction is given by:

$$\begin{aligned}
(\nabla\cdot\overline{\mathbf{u}\otimes\mathbf{u}})\cdot\hat{\mathbf{n}} &= (S_x\mathbf{e}_1+S_y\mathbf{e}_2+S_z\mathbf{e}_3)\cdot(n_x\mathbf{e}_1+n_y\mathbf{e}_2+n_z\mathbf{e}_3) \\
&= S_x n_x + S_y n_y + S_z n_z
\end{aligned} \tag{E.183}$$

Finally, Equation (E.175) can be rearranged in terms of $\partial P/\partial\zeta$:

$$\frac{\partial P}{\partial \zeta} = -\left[\frac{(S_x n_x + S_y n_y + S_z n_z) + \left(P_x^{\xi\eta} n_x + P_y^{\xi\eta} n_y + P_z^{\xi\eta} n_z\right)}{\left(\beta_1^3 n_x + \beta_2^3 n_y + \beta_3^3 n_z\right)}\right] \tag{E.184}$$

Since one needs to find gradients of the Reynolds stress components across the subgrid cells, the above method requires the subgrid Reynolds stress in Cartesian coordinates to be stored. A similar method to that described above is used to determine the main-grid pressure on the wall surface in the STREAM code (see Section 3.3.5).

E.10 Calculation of Wall Shear Stress, τ_{wall}

The wall shear stress, τ_{wall}, is calculated using the non-physical contravariant subgrid velocity components and then transformed into Cartesian coordinates. The two wall shear stress components, τ^{ξ}_{wall} and τ^{η}_{wall}, in the grid-aligned ξ- and η-directions are calculated from:

$$\tau^{\xi}_{wall} = \mu\frac{\partial U}{\partial n} = \mu\frac{\left[\left(U/\sqrt{g_{11}}\right)_P - \left(U/\sqrt{g_{11}}\right)_{wall}\right]}{\Delta n} \tag{E.185}$$

$$\tau^{\eta}_{wall} = \mu\frac{\partial V}{\partial n} = \mu\frac{\left[\left(V/\sqrt{g_{22}}\right)_P - \left(V/\sqrt{g_{22}}\right)_{wall}\right]}{\Delta n} \tag{E.186}$$

where $\left(U/\sqrt{g_{11}}\right)_P$ and $\left(V/\sqrt{g_{22}}\right)_P$ are the non-physical contravariant velocity components at the near-wall subgrid node, U_{wall} and V_{wall} are assumed to be zero, and Δn is the perpendicular distance from the wall to the adjacent subgrid node[3]. This distance, Δn, is calculated from the contravariant metric tensor, g^{33}, in the near-wall control volume. It was shown in Section E.6.5 that this metric tensor has the physical meaning:

$$g^{33} = \left(\frac{A_{12}}{\Delta Vol}\right)^2 \tag{E.187}$$

where A_{12} is the cell face area in the $\xi-\eta$ plane through the midpoint of the cell, and Vol is the cell volume. Assuming that the top and bottom (wall) faces of the near-wall cell are parallel, the volume is given by the product of area A_{12} and the wall-normal distance. The distance from the node (halfway down the cell) to the wall is therefore given by:

$$\Delta n = \frac{1}{2}\frac{\Delta Vol}{A_{12}} = \frac{1}{2\sqrt{g^{33}}} \tag{E.188}$$

The wall shear stress is then transformed into Cartesian components using Equation (E.165):

$$\begin{bmatrix} \tau^{x}_{wall} \\ \tau^{y}_{wall} \\ \tau^{z}_{wall} \end{bmatrix} = \underbrace{\begin{bmatrix} x_\xi & x_\eta & x_\zeta \\ y_\xi & y_\eta & y_\zeta \\ z_\xi & z_\eta & z_\zeta \end{bmatrix}}_{[J]} \begin{bmatrix} \tau^{\xi}_{wall} \\ \tau^{\eta}_{wall} \\ 0 \end{bmatrix} \tag{E.189}$$

[3]Non-physical components must be used here since the wall shear stress is subsequently converted into Cartesian coordinates using the Jacobian matrix, $[J]$. It was shown in Section (E.8) that this Jacobian matrix converts from non-physical contravariant into Cartesian components.

Appendix F

Transport Equations used in STREAM

The STREAM code uses a nonorthogonal curvilinear grid arrangement but aligns velocity components to a Cartesian reference frame. The following sections briefly describe the derivation of the RANS equations in this coordinate system (see also Lien [73]).

F.1 Introduction to Hybrid Curvilinear-Cartesian Coordinates

F.1.1 Vector Components

The velocity vector, $\mathbf{v}$, can be represented as either a function of the covariant base vectors, $\mathbf{g}_j$, or as a function of the Cartesian base vectors, $\mathbf{e}_m$, as follows:

$$\mathbf{v} = v^j \mathbf{g}_j = u^m \mathbf{e}_m \tag{F.1}$$

This can be rearranged:

$$v^j = u^m \mathbf{e}_m \cdot \mathbf{g}^j = u^m \beta^j_m \tag{F.2}$$

where, from Section B.3:

$$\beta^i_k = \mathbf{e}_k \cdot \mathbf{g}^i = \frac{\partial \xi^j}{\partial x^k} \mathbf{g}_j \cdot \mathbf{g}^i = \frac{\partial \xi^j}{\partial x^k} \delta^i_j = \underbrace{\frac{\partial \xi^i}{\partial x^k}}_{[J]^{-1}} \tag{F.3}$$

The term δ^i_j is the Kronecker delta (which has substitution-operator properties) and $\partial \xi^j / \partial x^m$ are elements of the inverse Jacobian matrix, $[J]^{-1}$.

F.1.2 Covariant Derivative of Vector, v

The derivative of the Cartesian vector in Cartesian coordinates is expanded:

$$\frac{\partial}{\partial x^j}\left(u^i \mathbf{e}_i\right) = \frac{\partial u^i}{\partial x^j} \mathbf{e}_i + \underbrace{u^i \frac{\partial \mathbf{e}_i}{\partial x^j}} \tag{F.4}$$

where the underbraced term is zero since the Cartesian base vectors do not vary with position. Using the chain-rule this can also be expressed in terms of the derivative in the covariant coordinates:

$$\frac{\partial}{\partial x^j}\left(u^i\mathbf{e}_i\right) = \frac{\partial u^i}{\partial \xi^k}\frac{\partial \xi^k}{\partial x^j}\mathbf{e}_i = \frac{\partial u^i}{\partial \xi^k}\beta^k_j\mathbf{e}_i \tag{F.5}$$

F.1.3 Covariant Derivative of Tensor, T

The Cartesian derivative of the second-order tensor, $\mathbf{T} = \tau^{ij}\mathbf{e}_i \otimes \mathbf{e}_j$, is given by:

$$\begin{aligned}\frac{\partial \mathbf{T}}{\partial x^k} &= \frac{\partial}{\partial x^k}\left(\tau^{ij}\mathbf{e}_i \otimes \mathbf{e}_j\right) \\ &= \frac{\partial \tau^{ij}}{\partial x^k}\mathbf{e}_i \otimes \mathbf{e}_j\end{aligned} \tag{F.6}$$

This can be expressed in terms of the curvilinear components, ξ^m, using the chain-rule, as follows:

$$\begin{aligned}\frac{\partial \mathbf{T}}{\partial x^k} &= \frac{\partial \tau^{ij}}{\partial \xi^m}\frac{\partial \xi^m}{\partial x^k}\mathbf{e}_i \otimes \mathbf{e}_j \\ &= \frac{\partial \tau^{ij}}{\partial \xi^m}\beta^m_k\mathbf{e}_i \otimes \mathbf{e}_j\end{aligned} \tag{F.7}$$

F.1.4 Gradient of a Scalar, $\nabla\phi$

The gradient of the scalar, ϕ, can be expanded as follows:

$$\begin{aligned}\nabla\phi &= \frac{\partial \phi}{\partial x^j}\mathbf{e}^j \\ &= \frac{\partial \phi}{\partial \xi^j}\frac{\partial \xi^k}{\partial x^j}\mathbf{e}^j \\ &= \frac{\partial \phi}{\partial \xi^j}\beta^k_j\mathbf{e}_j\end{aligned} \tag{F.8}$$

where the covariant and contravariant Cartesian base vectors are equivalent $\mathbf{e}_j \equiv \mathbf{e}^j$.

F.1.5 Gradient of a Vector, $\nabla\mathbf{v}$

The gradient of the velocity vector in Cartesian coordinates is given by:

$$\nabla\mathbf{v} = \mathbf{e}^j\frac{\partial}{\partial x^j}\left(u^i\mathbf{e}_i\right) \tag{F.9}$$

In Equation (F.5) it was shown that the covariant derivative of a Cartesian vector is as follows:

$$\frac{\partial}{\partial x^j}\left(u^i\mathbf{e}_i\right) = \frac{\partial u^i}{\partial \xi^k}\beta^k_j\mathbf{e}_i \tag{F.10}$$

The gradient of **v** therefore becomes:

$$\nabla \mathbf{v} = \frac{\partial u^i}{\partial \xi^k} \beta_j^k \mathbf{e}_i \otimes \mathbf{e}_j \tag{F.11}$$

The components of the tensor $\nabla \mathbf{v} = \tau^{ij} \mathbf{e}_i \otimes \mathbf{e}_j$ are therefore:

$$\tau^{ij} = \beta_j^k \frac{\partial u^i}{\partial \xi^k} \tag{F.12}$$

F.1.6 Divergence of a Vector, $\nabla \cdot \mathbf{v}$

The divergence of vector $\mathbf{v} = u^i \mathbf{e}_i$ is given by:

$$\nabla \cdot \mathbf{v} = \mathbf{e}^k \cdot \frac{\partial}{\partial x^k} \left(u^i \mathbf{e}_i \right) \tag{F.13}$$

Substituting Equation (F.5) into the above expression and rearranging:

$$\begin{aligned} \nabla \cdot \mathbf{v} &= \frac{\partial u^i}{\partial \xi^j} \beta_k^j \mathbf{e}_i \cdot \mathbf{e}^k \\ &= \frac{\partial u^i}{\partial \xi^j} \beta_k^j \delta_i^k \\ &= \frac{\partial u^i}{\partial \xi^j} \beta_i^j \end{aligned} \tag{F.14}$$

An alternative expression for $\nabla \cdot \mathbf{v}$ can be obtained by considering the divergence of vector **v** in curvilinear coordinates, as given by Equation (B.133):

$$\nabla \cdot \mathbf{v} = \frac{1}{J} \frac{\partial}{\partial \xi^j} \left(J v^j \right) \tag{F.15}$$

Converting the curvilinear component v^j into Cartesian components, using Equation (F.2), one obtains:

$$\nabla \cdot \mathbf{v} = \frac{1}{J} \frac{\partial}{\partial \xi^j} \left(J u^i \beta_i^j \right) \tag{F.16}$$

Equations (F.14) and (F.16) are equivalent, therefore one can write:

$$\frac{\partial u^i}{\partial \xi^j} \beta_i^j = \frac{1}{J} \frac{\partial}{\partial \xi^j} \left(J u^i \beta_i^j \right) \tag{F.17}$$

Expanding the right-hand-side of the above equation using the product rule, one obtains:

$$\frac{\partial u^i}{\partial \xi^j} \beta_i^j = \frac{\partial u^i}{\partial \xi^j} \beta_i^j + \underbrace{\frac{u^i}{J} \frac{\partial}{\partial \xi^j} \left(J \beta_i^j \right)}_{zero} \tag{F.18}$$

where, in order for the two sides of the above equation to be equal, the underbraced term must be zero.

F.1.7 Divergence of a Tensor, $\nabla \cdot \mathbf{T}$

Divergence of the second-order tensor, $\mathbf{T} = \tau^{ij}\mathbf{e}_i \otimes \mathbf{e}_j$ in Cartesian coordinates is given by:

$$\nabla \cdot \mathbf{T} = \mathbf{e}^k \cdot \frac{\partial}{\partial x^k}\left(\tau^{ij}\mathbf{e}_i \otimes \mathbf{e}_j\right) \tag{F.19}$$

This can also be written, using Equation (F.7):

$$\begin{aligned} \nabla \cdot \mathbf{T} &= \mathbf{e}^k \cdot \frac{\partial \tau^{ij}}{\partial \xi^m}\beta_k^m \mathbf{e}_i \otimes \mathbf{e}_j \\ &= \frac{\partial \tau^{ij}}{\partial \xi^m}\beta_k^m \delta_j^k \mathbf{e}_i \\ &= \frac{\partial \tau^{ij}}{\partial \xi^m}\beta_j^m \mathbf{e}_i \end{aligned} \tag{F.20}$$

F.1.8 Summary of Transformation Rules

The following equations are used to derive the RANS equations in a coordinate system where derivatives are taken with respect to non-orthogonal curvilinear vectors $\mathbf{r} = \xi^i \mathbf{g}_i$, whilst vector and tensor parameters are aligned to a Cartesian coordinate system ($\mathbf{v} = u^i \mathbf{e}_i$ and $\mathbf{T} = \tau^{ij}\mathbf{e}_i \otimes \mathbf{e}_j$).

Scalars

$$\nabla\phi \rightarrow \frac{\partial \phi}{\partial \xi^j}\beta_i^j \mathbf{e}_i \tag{F.21}$$

Vectors

$$\nabla \mathbf{v} \rightarrow \beta_j^k \frac{\partial u^i}{\partial \xi^k}\mathbf{e}_i \otimes \mathbf{e}_j \tag{F.22}$$

$$\nabla \cdot \mathbf{v} \rightarrow \frac{\partial u^i}{\partial \xi^k}\beta_i^k \equiv \frac{1}{J}\frac{\partial}{\partial \xi^j}\left(J u^m \beta_m^j\right) \tag{F.23}$$

Tensors

$$\nabla \cdot \mathbf{T} \rightarrow \frac{\partial \tau^{ij}}{\partial \xi^m}\beta_j^m \mathbf{e}_i \tag{F.24}$$

F.2 Transport Equations in Hybrid Coordinates

F.2.1 Scalar

The transport equation for scalar, ϕ, in vector form is given by:

$$\nabla \cdot (\rho \mathbf{U} \phi - \mathbf{q}) = S_\phi \tag{F.25}$$

where the scalar flux vector is given by:

$$\mathbf{q} = \Gamma_\phi \nabla \phi \tag{F.26}$$

where Γ_ϕ is the diffusivity. Using the equations given in Section F.1.8, one obtains the following scalar transport equation:

$$\frac{\partial}{\partial \xi^j} \left(J \beta^j_m \rho U^m \phi - J \beta^j_m \beta^n_m \Gamma_\phi \frac{\partial \phi}{\partial \xi^n} \right) = J S_\phi \tag{F.27}$$

where the velocity components, U^m, are aligned to Cartesian base vectors and gradients are taken with respect to the curvilinear components, ξ^j. The term J is the Jacobian which is equivalent to the cell volume (see Section B.5).

F.2.2 Momentum

The Reynolds-averaged momentum equation can be written in vector form:

$$\nabla \cdot (\rho \mathbf{U} \otimes \mathbf{U} - \mathbf{T}) = -\nabla P \tag{F.28}$$

where $\mathbf{U}$ is the mean velocity vector, $\mathbf{T}$ is the second-order stress tensor and P is the mean pressure. The pressure gradient term is expanded:

$$-\nabla P = -\frac{\partial P}{\partial \xi^j} \beta^j_i \mathbf{e}_i \tag{F.29}$$

which can also be written, using Equation (F.18) and the product rule:

$$\begin{aligned} -\nabla P &= -\left[\frac{\partial P}{\partial \xi^j} \beta^j_i + \frac{P}{J} \frac{\partial}{\partial \xi^j} \left(J \beta^j_i \right) \right] \mathbf{e}_i \\ &= -\frac{1}{J} \frac{\partial}{\partial \xi^j} \left(J \beta^j_i P \right) \mathbf{e}_i \end{aligned} \tag{F.30}$$

The divergence of the convective flux is expanded:

$$\nabla \cdot (\rho \mathbf{U} \otimes \mathbf{U}) = \frac{\partial \left(\rho U^i U^m \right)}{\partial \xi^j} \beta^j_m \mathbf{e}_i \tag{F.31}$$

Following the same approach used above for the pressure gradient, Equation (F.31) can be written:

$$\nabla \cdot (\rho \mathbf{U} \otimes \mathbf{U}) = \frac{1}{J} \frac{\partial}{\partial \xi^j} \left(J \beta^j_m \rho U^i U^m \right) \mathbf{e}_i \tag{F.32}$$

The stress tensor is given by:

$$\mathbf{T} = \tau^{im} \mathbf{e}_i \otimes \mathbf{e}_m \tag{F.33}$$

with Cartesian components:

$$\tau^{im} = \mu \left(\frac{\partial U^i}{\partial x^m} + \frac{\partial U^m}{\partial x^i} \right) + \delta^{im} \lambda \frac{\partial U^k}{\partial x^k} - \rho \overline{u^i u^m} \tag{F.34}$$

where $\lambda = -2\mu/3$ is the bulk viscosity. The above equation can be rearranged, using the chain-rule to express gradients in curvilinear coordinates, as follows:

$$\tau^{im} = \mu \left(\frac{\partial U^i}{\partial \xi^n} \beta^n_m + \frac{\partial U^m}{\partial \xi^n} \beta^n_i \right) + \delta^{im} \lambda \frac{\partial U^k}{\partial \xi^n} \beta^n_k - \rho \overline{u^i u^m} \tag{F.35}$$

The divergence of the stress tensor is then:

$$\begin{aligned} \nabla \cdot \mathbf{T} &= \frac{1}{J} \frac{\partial}{\partial \xi^j} \left(J \beta^j_m \tau^{im} \right) \mathbf{e}_i \\ &= \frac{1}{J} \frac{\partial}{\partial \xi^j} \left[J \beta^j_m \mu \left(\frac{\partial U^i}{\partial \xi^n} \beta^n_m + \frac{\partial U^m}{\partial \xi^n} \beta^n_i \right) + \delta^{im} \lambda \frac{\partial U^k}{\partial \xi^n} \beta^n_k - J \beta^j_m \rho \overline{u^i u^m} \right] \mathbf{e}_i \end{aligned} \tag{F.36}$$

Finally, combining Equations (F.30), (F.32) and (F.36), one obtains the following expression for the momentum equation in hybrid Cartesian-curvilinear coordinates:

$$\begin{aligned} &\frac{\partial}{\partial \xi^j} \left(J \beta^j_m \rho U^i U^m - J \beta^j_m \beta^n_m \mu \frac{\partial U^i}{\partial \xi^n} \right) \\ &= \frac{\partial}{\partial \xi^j} \left(-J \beta^j_i P + J \beta^j_m \beta^n_i \mu \frac{\partial U^m}{\partial \xi^n} + J \beta^j_m \beta^n_k \delta^{im} \lambda \frac{\partial U^k}{\partial \xi^n} - J \beta^j_m \rho \overline{u^i u^m} \right) \end{aligned} \tag{F.37}$$

Appendix G

Other Wall Function Options Explored

G.1 Subgrid Storage Requirements

Storage requirements of the UMIST-*N* wall function are similar to those of a full low-*Re* model approach: values of velocity, turbulence parameters and temperature (if a thermal field is being solved) are stored in each subgrid cell along the length of the wall[1]. Clearly, it would be advantageous to reduce this storage demand. Saving subgrid values is necessary for convection parallel to the wall, calculation of the wall-normal W-velocity and initialization of the subgrid values at each iteration. These three components of the UMIST-*N* wall function are discussed below.

G.1.1 Wall-Parallel Convection

In the UMIST-*N* wall function, subgrid convection parallel to the wall is approximated using an upwind differencing scheme which uses upstream subgrid values. Therefore upstream values of velocity, turbulence parameters and temperature must be stored. For practical application of the wall function to complex flows in which one does not have prior knowledge of the flow direction, or in which there is separation and reattachment, this requires storage of subgrid values along the whole length of the wall. An alternative scheme was tested during the development of the UMIST-*N* wall function which involved using main-grid values for wall-parallel convection. For a wall which is parallel to the x-axis, in Cartesian coordinates, the wall-parallel convection of scalar, ϕ, was approximated as:

$$\rho U \frac{\partial \phi}{\partial x} = \rho U_P \frac{(\phi'_e - \phi'_w)}{\Delta x} \underbrace{\frac{\phi_o}{\overline{\phi}}} \tag{G.1}$$

where ϕ represents the wall-parallel velocity component (U), turbulence parameters (k or $\tilde{\varepsilon}$) or temperature (T), ϕ'_e is the main-grid value of ϕ at the eastern boundary of the subgrid, determined from a linear interpolation between main-grid nodes E and O, see Figure G.1, and subscript P refers to the

[1] In fact, the storage demands are likely to be slightly less than a full low-*Re* model approach since the subgrid pressure distribution does not need to be stored and there is effectively a discontinuity in the cell size due to the use of an embedded grid within the near-wall main-grid cell.

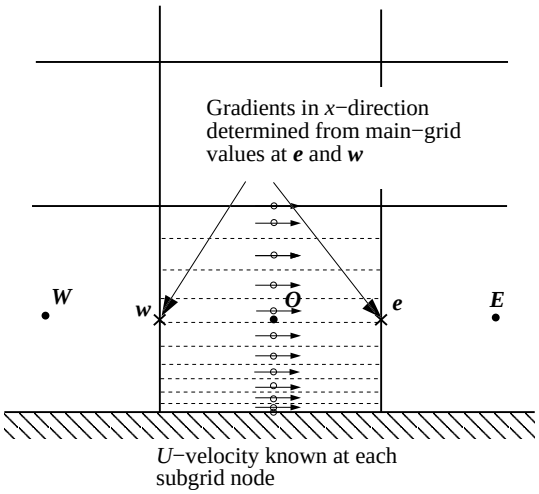

Figure G.1: Calculation of subgrid convection parallel to the wall using main-grid node values

current subgrid node. Rather than assume that the gradients of ϕ are constant across the whole subgrid region a scaling factor is introduced (the underbraced term in Equation G.1), based on the ratio of the main-grid nodal value (ϕ_o) to the average subgrid value ($\overline{\phi}$). This convection scheme was tested in the impinging jet flow in which the average subgrid value $\overline{\phi}$ was non-zero for all of the parameters: U, k, $\tilde{\varepsilon}$ and T. A modified scaling function or some limit would need to be introduced to prevent unrealistic values occurring when $\overline{\phi} \rightarrow 0$, for example in situations where flow reversal takes place across the subgrid (so that the average velocity, $\overline{U}$, is close to zero). The above wall-parallel convection term was integrated over the subgrid cell and placed in the discretized subgrid equation source term. The convection source term in the momentum equation and in the k and $\tilde{\varepsilon}$ equations was linearized (by splitting the source into $S = s_U + s_P\phi_P$) to maximize stability. Central differencing was used to discretize the main-grid gradient term in Equation (G.1). In tests with the impinging jet flow, there was no change in stability from switching to an upwind scheme and results using the two schemes were identical.

It was found in the impinging jet flow that using scaled main-grid-values for wall-parallel convection (Equation G.1) led to instabilities early in the solution process when there were abrupt changes in the mass flux between neighbouring cells. To obtain a stable solution with a linear $k-\varepsilon$ model, subgrid convection of momentum, and in some cases convection of k and $\tilde{\varepsilon}$, was only activated once the total mass residual fell below a threshold value (in the impinging jet case, this was when the normalized mass residual fell to approximately 5×10^{-4}, which was achieved in roughly one-third of the total computational time). In addition, it was found that for moderately large near-wall main-grid cell sizes ($y^+ > 250$) some under-relaxation of the subgrid momentum equations was required (typically, a factor of $\alpha = 0.9$ was used). When the cubic non-linear EVM of Craft *et al.* [67] was used the above convection treatment was found to be highly unstable. No amount of under-relaxation could stabilize

the numerical solution for large near-wall cells.

This behaviour contrasts to that observed using the recommended approach of saving subgrid values along the wall and using these to calculate convection (as described in Section 4). Using the recommended approach, it is not necessary to wait until the flow-field has settled down before activating subgrid convection. No under-relaxation of the subgrid momentum equations is required (even for large near-wall main-grid cells). One is also able to capture changes in the sign of the gradients across the subgrid, for instance where the k-gradient parallel to the wall ($\partial k/\partial x$) is positive at the outer edge of subgrid but negative near wall. In the scaled main-grid approach the sign of the gradient across the whole of the subgrid is determined by the main-grid gradient (i.e. $\partial k/\partial x$ would be the same sign across the whole subgrid). Whilst this, in itself, did not seem to be source of the instability problems encountered with the scaled main-grid convection scheme, it was observed to lead to "wiggles" in the wall shear stress and Nusselt number profiles in the impinging jet flow.

G.1.2 Calculation of the Subgrid Wall-Normal Velocity

In the UMIST-*N* wall function, the subgrid wall-normal V-velocity is calculated from continuity within each of the subgrid control volumes and then the resulting subgrid V-profile is scaled in order to match the main-grid boundary condition (as described in Chapter 4). In order to interpolate subgrid velocities to the cell faces, which are used in the discretized continuity equation, one needs to store the subgrid velocities in the neighbouring subgrid nodes (which, practically, involves storing the subgrid velocity in each subgrid cell along the length of the wall). An alternative approach is simply to prescribe a V-velocity profile across the subgrid. Low-Reynolds-number model results for the impinging jet flow showed that the V-velocity varies almost linearly across the subgrid region (see Figure 4.6 on Page 77). As a first approximation, one could use a linear V-velocity profile, with the boundary values of $V = 0$ at the wall (assuming the wall to be non-porous) and, at the opposite face, the main-grid V-velocity boundary condition (as shown in Figure G.2). However, the gradient of a linear V-velocity profile in the wall-normal direction would then be constant ($\partial V/\partial y = constant$), whereas continuity implies that $\partial V/\partial y \rightarrow 0$ at the wall, since $\partial U/\partial x = 0$. In order to satisfy this constraint one can either introduce near-wall damping of the V-velocity, or one can assume a non-linear profile across the whole subgrid. The latter approach was found to be more successful in the impinging jet flow, where the following power law was assumed:

$$V = a y^{1.1} \tag{G.2}$$

The term a is calculated from $a = V_n'/y_n^{1.1}$ in order to satisfy the boundary conditions, where V_n' is the main-grid velocity at the outer subgrid boundary $(y = y_n)$. This prescription was close enough to a linear profile to agree well with low-Reynolds-number model predictions in the impinging jet flow, whilst satisfying the condition that $\partial V/\partial y \rightarrow 0$ as $y \rightarrow 0$.

Nusselt number profiles for the impinging jet flow using the prescribed subgrid wall-normal V-velocity profile are shown in Figures G.3 and G.4, using the linear and non-linear $k-\varepsilon$ models,

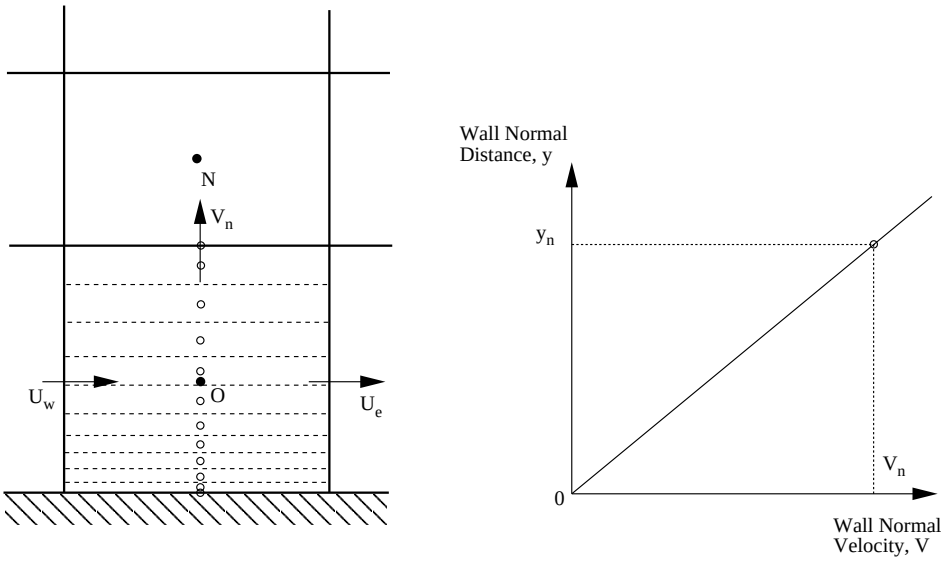

Figure G.2: Calculation of the subgrid wall-normal V-velocity

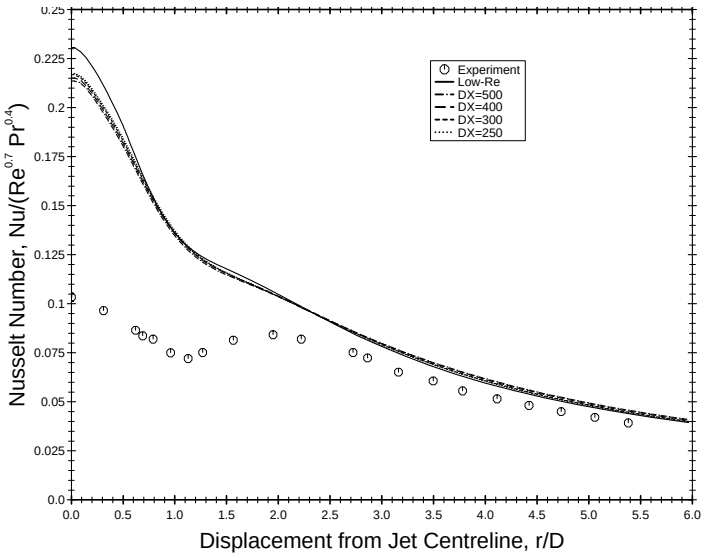

Figure G.3: Nusselt number profiles obtained for the impinging jet flow using the UMIST-*N* wall function with the saved-subgrid convection scheme parallel to the wall (Equation 4.62), prescribed wall-normal velocity profile (Equation G.2), linear $k-\varepsilon$ model and standard Yap correction. Solid line: low-*Re* Launder-Sharma model; broken lines: wall function results for different near-wall cell widths; symbols: experiments of Baughn *et al*. [94].

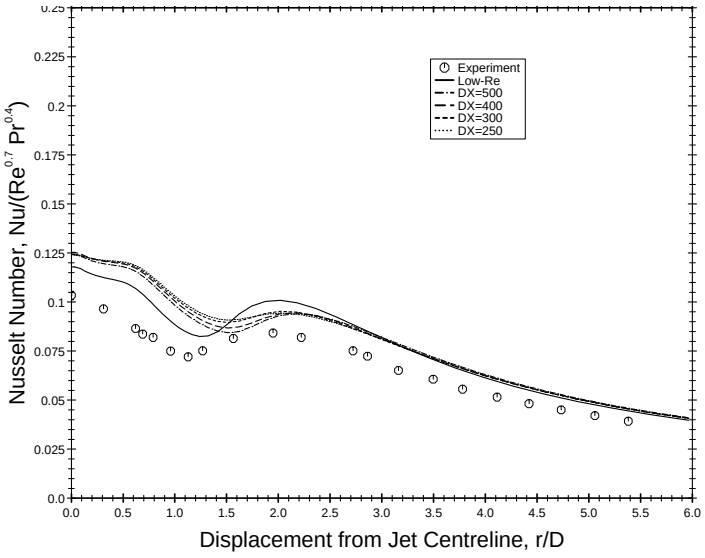

Figure G.4: Nusselt number profiles obtained using the subgrid wall function with the NLEVM of Craft *et al*. [67], differential Yap correction, saved-subgrid convection scheme parallel to the wall (Equation 4.62) and prescribed wall-normal velocity profile (Equation G.2). Solid line: low-Reynolds-number model; broken lines: wall function results for different near-wall cell widths; symbols: experiments of Baughn *et al*. [94].

respectively. These can be compared to Figures 5.20 and 5.46 which used the same models with the recommended scaled-continuity approach to calculate the subgrid V-velocity (as presented in Chapter 4). With the linear model, a slightly higher Nusselt number is predicted with the prescribed V-velocity approach near the stagnation point $(r/D < 2)$ than with the scaled-continuity approach. The prescribed velocity profile result is therefore in slightly better agreement with the low-*Re* model prediction. However, with the non-linear model, the prescribed V-velocity approach overpredicts the low-*Re* model Nusselt number near the stagnation point $(r/D < 2)$ by around 6% and shows some sensitivity to the near-wall cell size. In comparison, the scaled-continuity approach gave results in excellent agreement with the low-*Re* model and showed practically no sensitivity to the near-wall cell size. Modest changes in the prescribed subgrid V-profile were also found to lead to significant changes in the predicted Nusselt number in the impinging jet flow. Whilst prescribing a V-velocity profile is a conceptually simple approach which is easy to implement and does not require additional storage, the recommended practice of calculating V from subgrid continuity removes the reliance of the UMIST-*N* wall function on any assumed profiles, which should make the wall function applicable to a wider range of flows.

Another approach to finding the subgrid V-velocity which was tested in the impinging jet flow involved the solution of a simplified V-velocity transport equation, which was derived using the same assumptions that were used to obtain the wall-parallel U-velocity equation (see Chapter 4). This approach was found to be extremely sensitive to the assumed pressure profile within the subgrid. One cannot obtain a pressure profile across the subgrid by solving a pressure-correction equation as

this would introduce additional coupling and lead to computing times for the subgrid wall function approaching that of a full low-Reynolds-number model solution.

G.1.3 Initialization of Subgrid Values

In the UMIST-*N* wall function, all the subgrid values of velocity, turbulence parameters and temperature are stored along the length of the wall. This enables the values from the previous subgrid iteration to be used as initial conditions for the current iteration. If an alternative treatment is employed in which subgrid values are not stored, the initial conditions for a subgrid calculation can be taken from neighbouring subgrid values, since the subgrid calculation proceeds sequentially along the wall (see Figure G.5). One can also scale the adjoining subgrid cell values by a factor corresponding to the difference in neighbouring main-grid nodal values. This approach was tested in the impinging jet flow. The scaling factor applied to the subgrid profile at the previous location to provide initial conditions for the current subgrid solution was based on the difference between the previous and the current subgrid boundary conditions. In addition to starting from more realistic values, this scaling removed the possibility of a discontinuity at the outer edge of the subgrid, which may have otherwise occurred due to the updated boundary conditions. If the current nodal position is assumed to be node j and the previous position node $(j-1)$ then the factor with which the previous subgrid profile was scaled, is given by:

$$\frac{\phi_j^b}{\phi_{j-1}^b} \tag{G.3}$$

where the superscript b refers to the subgrid boundary condition for ϕ at the j or $(j-1)$ node. This scaling was applied to subgrid profiles for U, k, $\tilde{\varepsilon}$ and T in the impinging jet flow. The scaling factor may need to be modified in other flows if the denominator in the above expression, ϕ_{j-1}^b, was close to zero, for example in situations involving flow reversal (where velocity U_{j-1}^b may be zero).

The problem with starting the subgrid calculation using initial values scaled from a neighbouring subgrid cell is that one must perform a number of iterations of the subgrid calculation per main-grid iteration in order to obtain a converged solution. In the impinging jet flow, around 5 subgrid iterations were necessary for each main-grid iteration which led to an increase in the overall computing time of 42% compared to the saved-subgrid approach which used one subgrid iteration per main-grid iteration.

G.1.4 Summary

There are three main reasons why the UMIST-*N* wall function saves subgrid values of velocity, turbulence parameters and temperature (if a thermal field is being solved) at each subgrid node along the length of the wall. Firstly, the alternative convection treatment involving main-grid values is less numerically stable. Secondly, using a prescribed wall-normal velocity profile is likely to be less generally applicable and has been shown to give poorer results in the impinging jet flow with the NLEVM. Thirdly, the subgrid calculation cannot be initialized accurately without storing subgrid values. If sub-

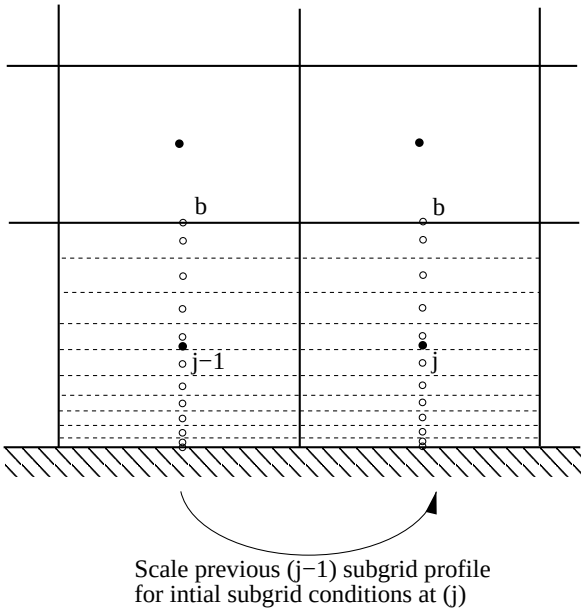

Figure G.5: Updating subgrid nodal values for initial conditions

grid values are not stored a number of subgrid iterations must be performed per main-grid iteration, which leads to prolonged computing times.

In addition to these considerations, if one is storing the subgrid parameters at each subgrid node, one is able to calculate all the components of the production term in the turbulent kinetic energy equation (which requires velocity gradients parallel to the wall). When a non-orthogonal grid arrangement is used, one is also able to calculate the subgrid pressure gradient $\partial P/\partial\zeta$ from gradients in the Reynolds stresses (as described in Chapter 4).

G.2 Convection Treatment in Curvilinear Coordinates

The convection term in the momentum equations for non-orthogonal curvilinear coordinates, derived in Appendix C, is given by:

$$(\mathbf{U}\cdot\nabla)\mathbf{U} = \left(\frac{U^{(j)}}{\sqrt{g_{jj}}}\frac{\partial U^{(i)}}{\partial\xi^j} - U^{(i)}U^{(j)}\frac{\Gamma^m_{ij}g_{im}}{g_{ii}\sqrt{g_{jj}}} + U^{(j)}U^{(m)}\frac{\Gamma^i_{mj}\sqrt{g_{ii}}}{\sqrt{g_{jj}g_{mm}}}\right)\mathbf{g}_{(i)} \tag{G.4}$$

In Appendix D, an alternative approach to calculating convection was recommended, rather than expand the lengthy expression given above. This involved the transformation of the velocity components in the upstream cell (assuming an upwind convection scheme is employed) from the coordinate system used in the upstream cell into the coordinate system used in the current cell. This gave the following

expression:

$$(\mathbf{U}\cdot\nabla)\mathbf{U} = \frac{U^{(j)}}{\sqrt{g_{jj}}}\left(\frac{\partial U^{(i)}}{\partial \xi^j}\right)^{*}\mathbf{g}_{(i)} \tag{G.5}$$

The asterisk is introduced around the velocity gradient term to denote that upstream values of $U^{(i)}$ are transformed into the coordinate system used in the current cell.

Both of the above convection treatments were tested in the Ahmed body flow, discussed in Chapter 7. Equation (G.4) was found to lead to numerical instability in regions where the grid was highly skewed, such as the 90° corner between the base and the underside of the car (where, at the apex of the corner, the grid was skewed at 45° to the wall). The alternative and considerably simpler convection treatment, given by Equation (G.5), was not found to cause stability problems. The precise cause of the convergence problem with Equation (G.4) was not traced. Analysis of the flow around the 90° rear corner of the Ahmed body becomes very complex once one has expanded all the geometric terms. It may be that problems were introduced by using an upwind scheme for the velocity gradient term in Equation (G.4) whilst using central differencing for the gradients of the metric tensors (used in the Christoffel symbols). Coding errors cannot be ruled out, especially when dealing with such lengthy expressions, although every effort was made to ensure that the equations were coded correctly[2]. In order to investigate the matter further it would be easier to study a simpler flow than the Ahmed body, such as a two-dimensional backward-facing step flow. In such a test-case, one could examine the effects of using a contoured grid as opposed to a Cartesian grid (as shown in Figure G.6), the code would run significantly faster and one would not have to consider the effects of the convection treatment upstream of the corner (as one does for the Ahmed car body). Whilst it would be useful to find out why the convection treatment of Equation (G.4) was numerically unstable, the alternative treatment given by Equation (G.5) is to be preferred since it is conceptually simpler, easier to code and has been shown to be more robust.

[2]Channel flows were examined using the same code with grids skewed in different planes to ensure that the geometric parameters were calculated correctly. In addition, the code was run using several different FORTRAN compilers using various debugging options to see if any array boundaries were exceeded or values used before they were initialized etc.

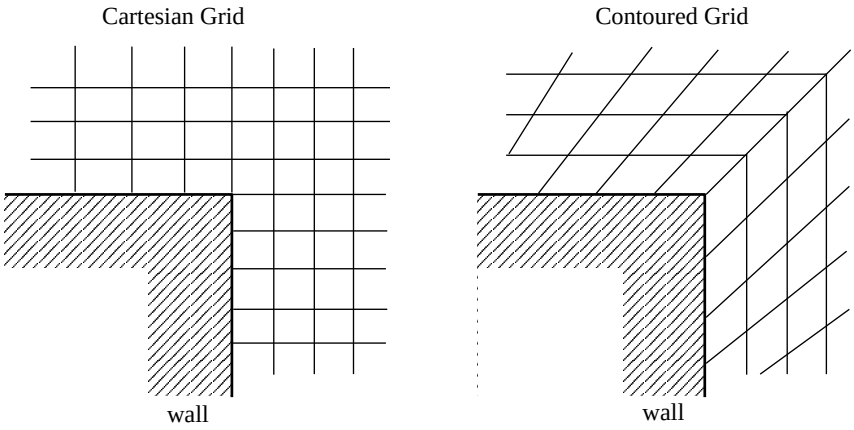

Figure G.6: Different grid arrangements for a 90° corner

Bibliography

[1] P. Bradshaw, editor. *Turbulence*. Topics in Applied Physics. Springer-Verlag, second edition, 1978.

[2] J. H. Ferziger. The physics and simulation of turbulence. ERCOFTAC Summer School, UMIST, Manchester, UK, 2002.

[3] P. Moin and K. Mahesh. Direct numerical simulation: a tool in turbulence research. *Annu. Rev. Fluid Mech.*, 30:539–578, 1998.

[4] H. Tennekes and J. L. Lumley. *A first course in turbulence*. MIT Press, Massachusetts, USA, 1972.

[5] S. B. Pope. *Turbulent Flows*. Cambridge University Press, 2000.

[6] P. R. Spalart. Strategies for turbulence modelling and simulations. *Int. J. Heat Fluid Flow*, 21:252–263, 2000.

[7] G. I. Taylor. Eddy motion in the atmosphere. *Philosophical Transactions of the Royal Society of London*, Series A:215, 1915.

[8] L. Prandtl. Über die ausgebildete turbulenz. *ZAMM*, 5:136–139, 1925. also Intern. Congr. Appl. Mech. Zürich 1926, 62-75 and Coll. Works II, 736-751.

[9] L. Prandtl. Über ein neues formelsystem der ausgebildeten turbulenz. *Nachr. Akad. Wiss. Göttingen*, pages 6–19, 1945. also Coll. Works II, 874-888.

[10] P. R. Spalart and S. R. Allmaras. A one-equation turbulence model for aerodynamic flows. *AIAA Paper 92-439, Reno, Nevada, USA*, 1992.

[11] P. Godin, D. W. Zingg, and T. E. Nelson. High-lift aerodynamic computations with one and two-equation turbulence models. *AIAA Paper 96-0567*, 1996.

[12] W. P. Jones and B. E. Launder. The prediction of laminarization with a two-equation model of turbulence. *Int. J. Heat Mass Transfer*, 15:301–314, 1972.

[13] B. E. Launder and B. I. Sharma. Application of the energy-dissipation model of turbulence to the calculation of flow near a spinning disc. *Lett. in Heat Mass Transfer*, 1:131–138, 1974.

[14] D. C. Wilcox. *Turbulence modeling for CFD*. DCW Industries Inc., La Cañada, California, 1993.

[15] P-Y. Chou. On velocity correlations and the solution of the equations of turbulent fluctuations. *Quarterly of Applied Mathematics*, 3:38, 1945.

[16] B. I. Davidov. On the statistical dynamics of an incompressible turbulent fluid. *Dokl. Akad. Nauk S.S.S.R*, 136:47–50, 1961.

[17] F. H. Harlow and P. I. Nakayama. Transport of turbulence energy decay rate. *Los Alamos Sci. Lab., University of California Report LA-3854*, 1968.

[18] A. N. Kolmogorov. Equations of turbulent motion of an incompressible fluid. *Izvestia Academy of Sciences, USSR; Physics*, 6(1 and 2):56–58, 1942.

[19] V. C. Patel, W. Rodi, and G. Scheuerer. Turbulence models for near-wall and low Reynolds number flows: a review. *AIAA Journal*, 23(9):1308–1319, 1985.

[20] F. R. Menter. Two-equation eddy-viscosity turbulence models for engineering applications. *AIAA Journal*, 32(8):1598–1605, 1994.

[21] P. Spalart. Direct simulation of a turbulent boundary layer up to $R_\theta = 1410$. *J. Fluid Mech.*, 187:61–98, 1988.

[22] E. Brundrett and W. D. Baines. The production and diffusion of vorticity in duct flow. *J. Fluid Mech.*, 19:375–392, 1964.

[23] S. C. Cheah, L. Cheng, D. Cooper, and B. E. Launder. On the structure of turbulent flow in spirally fluted tubes. In *Proc. 5th International Symposium on Refined Flow Modelling and Turbulence Measurements*, Paris, 1993.

[24] B. E. Launder, C. H. Priddin, and B. I. Sharma. The calculation of turbulent boundary layers on spinning and curved surfaces. *Journal of Fluids Engineering*, pages 231–239, March 1977.

[25] B. E. Launder and N. D. Sandham, editors. *Closure strategies for turbulent and transitional flows*. Cambridge Univ. Press, 2002.

[26] W. Rodi. *The prediction of free turbulent boundary layers using a two-equation model of turbulence*. PhD thesis, Imperial College, London, 1972.

[27] T. B. Gatski and C. G. Speziale. On explicit algebraic stress models for complex turbulent flows. *J. Fluid Mech.*, 254:59–78, 1993.

[28] D. D. Apsley and M. A. Leschziner. A new low-Reynolds-number nonlinear two-equation turbulence model for complex flows. *Int. J. Heat Fluid Flow*, 19:209–222, 1998.

[29] S. B. Pope. A more general effective-viscosity hypothesis. *J. Fluid Mech.*, 72:331–340, 1975.

[30] T. J. Craft, B. E. Launder, and K. Suga. Development and application of a cubic eddy-viscosity model of turbulence. *Int. J. Heat and Fluid Flow*, 17:108–115, 1996.

[31] C. G. Speziale. On nonlinear $k-l$ and $k-\varepsilon$ models of turbulence. *J. Fluid Mech.*, 178:459, 1987.

[32] R. Rubinstein and M. Barton. Nonlinear Reynolds stress models and the renormalization group. *Phys. Fluids A*, 2:1472–1476, 1990.

[33] A. Yoshizawa. Statistical analysis of the deviation of the Reynolds stress from its eddy viscosity representation. *Phys. Fluids*, 27:1377–1387, 1984.

[34] K. Suga. *Development & application of a non-linear eddy viscosity model sensitized to stress and strain invariants*. PhD thesis, Dept. of Mechanical Engineering, Faculty of Technology, University of Manchester, 1995.

[35] C. M. E. Robinson. *Advanced CFD modelling of road-vehicle aerodynamics*. PhD thesis, Dept. of Mechanical Engineering, UMIST, Manchester, UK, 2001.

[36] H. Iacovides and Launder B. E. The computation of momentum and heat transport in turbulent flow around pipe bends. In *Proc. First UK National Conference on Heat Transfer*, IChemE Symposium Series No.86, pages 1097–1113, Leeds, UK, 1984.

[37] C. M. Millikan. A critical discussion of turbulent flows in channels and circular tubes. In *Proc. 5th Int. Congr. Appl. Mech.*, pages 386–392, Cambridge, Mass. USA, 1938. Wiley.

[38] S. Nazarenko. On exact solutions for near-wall turbulence theory. *Physics Letters A*, 264:444–448, 2000.

[39] J. Kim, P. Moin, and R. Moser. Turbulence statistics in fully developed channel flow at low Reynolds number. *J. Fluid Mech.*, 177:133–166, 1987.

[40] R. D. Moser, J. Kim, and N. N. Mansour. Direct numerical simulation of turbulent channel flow up to $Re_\tau = 590$. *Physics of Fluids*, 11(4):943–945, 1999.

[41] G. I. Barenblatt and A. J. Chorin. Turbulence: an old challenge and new perspectives. *Meccanica*, 33:445–468, 1998.

[42] P. Bradshaw and G. P. Huang. The law of the wall in turbulent flow. *Proc. R. Soc. Lond. A*, 451:165–188, 1995.

[43] T. Cebeci and P. Bradshaw. *Physical and computational aspects of convective heat transfer*. Springer-Verlag, New York, USA, 1984.

[44] C. L. V. Jayatilleke. The influence of Prandtl number and surface roughness on the resistance of the laminar sublayer to momentum and heat transfer. *Prog. Heat Mass Transfer*, 1:193, 1969.

[45] N. N. Mansour, J. Kim, and P. Moin. Reynolds stress and dissipation-rate budgets in a turbulent channel flow. *J. Fluid Mech.*, 194:15–44, 1988.

[46] P. Rautaheimo and T. Siikonen. Improved solid-wall boundary treatments in low-Reynolds number turbulence models. Technical Report 122, Laboratory of Applied Thermodynamics, Helsinki Univ. Tech., Espoo, Finland, 1999.

[47] H. Grotjans and F. R. Menter. Wall function for general application CFD codes. In *Computational Fluid Dynamics 1998, Proceedings of the Fourth European CFD Conference, ECCOMAS*. John Wiley & Sons, 1998.

[48] B. E. Launder and D. B. Spalding. The numerical computation of turbulent flows. *Computer Methods in Applied Mechanics and Engineering*, 3:269–289, 1974.

[49] C. C. Chieng and B. E. Launder. On the calculation of turbulent heat transport downstream from an abrupt pipe expansion. *Numerical Heat Transfer*, 3:189–207, 1980.

[50] R.W. Johnson and B.E. Launder. Discussion of "On the calculation of turbulent heat transport downstream from an abrupt pipe expansion". *Numerical Heat Transfer*, 5:493–496, 1982.

[51] M. Ciofalo and M. W. Collins. k-ε predictions of heat transfer in turbulent recirculating flows using an improved wall treatment. *Numerical Heat Transfer*, B 15:21–47, 1989.

[52] S. Acharya, S. Dutta, and T. A. Myrum. Heat transfer in turbulent flow past a surface-mounted two-dimensional rib. *ASME Journal of Heat Transfer*, 120:724–734, 1998.

[53] R. S. Amano. Development of a turbulence near-wall model and its application to separated and reattached flows. *Numerical Heat Transfer*, 7:59–75, 1984.

[54] D. C. Wilcox. Wall matching, a rational alternative to wall functions. *AIAA Paper 89-611*, 1989.

[55] J. R. Viegas and M. W. Rubesin. Wall-function boundary conditions in the solution of the Navier-Stokes equations for complex compressible flows. In *AIAA 16th Fluid & Plasma Dynamics Conference*, Massachusetts, 1983.

[56] J. R. Viegas, M. W. Rubesin, and C. C. Horstman. On the use of wall functions as boundary conditions for 2-dimensional separated compressible flow. In *AIAA 23rd Aerospace Sciences Meeting*, Reno, Nevada, 1985.

[57] B. R. Smith. The $k-kl$ turbulence model and wall layer model for compressible flows. *AIAA Paper 90-1483, Seattle, WA*, 1990.

[58] V. Boyer and D. Laurence. A shape function wall function approach for high and low Reynolds near-wall turbulence models. *Int. J. Numer. Meth. Fluids*, 40:241–251, 2002.

[59] H. Iacovides and B. E. Launder. PSL - an economical approach to the numerical analysis of near-wall elliptic flows. *ASME J. Fluids Eng.*, 106:245, 1984.

[60] B. E. Launder. Numerical computation of convective heat transfer in complex turbulent flows: time to abandon wall functions? *Int. J. Heat Mass Transfer*, 27:2485–1491, 1984.

[61] T. J. Craft, A. V. Gerasimov, H. Iacovides, and Launder B. E. Progress in the generalization of wall-function treatments. *Int. J. Heat and Fluid Flow*, 23:148–160, 2002.

[62] U. Piomelli, J. Ferziger, P. Moin, and J. Kim. New approximate boundary conditions for large eddy simulations of wall-bounded flows. *Physics of Fluids, A.*, 1(6):1061–1068, 1989.

[63] E. Balaras, C. Benocci, and U. Piomelli. Two-layer approximate boundary condition large-eddy simulations. *AIAA J.*, 34:1111–1119, 1996.

[64] C.R. Yap. *Turbulent heat and momentum transfer in recirculating and impinging flows*. PhD thesis, Dept. of Mechanical Engineering, Faculty of Technology, University of Manchester, 1987.

[65] T. J. Craft, L. J. W. Graham, and B. E. Launder. Impinging jet studies for turbulence model assessment. Part 2: An examination of the performance of four turbulence models. *Int. J. Heat Mass Transfer*, 36(10):2685–2697, 1993.

[66] H. Iacovides and M. Raisee. Computation of flow and heat transfer in 2-D rib roughened passages. *2nd Int. Symposium on Turbulence, Heat & Mass Transfer, Delft*, pages 21–29, 1997.

[67] T. J. Craft, H. Iacovides, and J. H. Yoon. Progress in the use of non-linear two-equation models in the computation of convective heat-transfer in impinging and separated flows. *Flow, Turbulence and Combustion*, 63:59–80, 1999.

[68] M. Raisee. *Computation of flow and heat transfer through two- and three-dimensional rib-roughened passages*. PhD thesis, Dept. of Mechanical Engineering, UMIST, Manchester, UK, 1999.

[69] T. J. Craft, B. E. Launder, and N. I. Ince. Recent developments in second-moment closure for buoyancy-affected flows. *Dynamics of Atmospheres and Oceans*, 23:99, 1996.

[70] P.G. Huang and M.A. Leschziner. *TEAM, an introduction and guide to the computer code*. Dept. of Mechanical Engineering, Faculty of Technology, University of Manchester, 1984.

[71] P. G. Huang. *The computation of elliptic turbulent flows with second-moment closure models*. PhD thesis, Dept. of Mechanical Engineering, Faculty of Technology, University of Manchester, 1986.

[72] F. S. Lien and M. A. Leschziner. A general non-orthogonal finite-volume algorithm for turbulent flow at all speeds incorporating second-moment turbulence-transport closure. *Comp. Meth. Appl. Mech. Eng.*, 114:123–167, 1994.

[73] F. S. Lien. *Computational modelling of 3D flow in complex ducts and passages*. PhD thesis, Dept. of Mechanical Engineering, Faculty of Technology, University of Manchester, 1992.

[74] S. V. Patankar. *Numerical heat transfer and fluid flow*. Series in Computational Methods in Mechanics and Thermal Sciences. Hemisphere Publ. Corp., McGraw-Hill, 1980.

[75] H. K. Versteeg and W. Malalasekera. *An introduction to computational fluid dynamics*. Longman Scientific & Technical, 1995.

[76] J. H. Ferziger and M. Perić. *Computational Methods for Fluid Dynamics*. Springer-Verlag, Berlin, 1999.

[77] D. A. Anderson, Jr. *Computational fluid dynamics: the basics with applications*. Mechanical Engineering Series. McGraw-Hill, 1995.

[78] S. V. Patankar and D. B. Spalding. A calculation procedure for heat, mass and momentum transfer in three-dimensional parabolic flows. *Int. J. Heat Mass Transfer*, 15:1787, 1972.

[79] B. P. Leonard. A stable and accurate convective modelling procedure based on quadratic upstream interpolation. *Comput. Methods Appl. Mech. Eng.*, 19:59–98, 1979.

[80] R. Courant, E. Isaacson, and M. Rees. On the solution of nonlinear hyperbolic differential equations by finite differences. *Comm. Pure Appl. Math.*, 5:243, 1952.

[81] F. S. Lien and M. A. Leschziner. Upstream monotonic interpolation for scalar transport with application to complex turbulent flows. *Int. J. Num. Meth. Fluids*, 19:527–548, 1994.

[82] C. M. Rhie and W. L. Chow. Numerical study of the turbulent flow past an airfoil with trailing edge separation. *AIAA J.*, 21:1525–1532, 1983.

[83] M. C. Richmond, H. C. Chen, and V. C. Patel. Equations of laminar and turbulent flows in general curvilinear coordinates. IIHR report no. 300, Iowa Institute of Hydraulic Research, Univ. of Iowa, 1986.

[84] S. B. Pope. The calculation of turbulent recirculating flows in general orthogonal coordinates. *J. Comp. Phys.*, 26:197–217, 1977.

[85] I. A. Demirdžić. *A finite volume method for computation of fluid flow in complex geometries*. PhD thesis, University of London, 1982.

[86] I. A. Demirdžić, A. D. Gosman, R. I. Issa, and M. Perić. A calculation procedure for turbulent flow in complex geometries. *Computers & Fluids*, 15:251–273, 1987.

[87] T. Gal-Chen and R. C. J. Somerville. On the use of a coordinate transformation for the solution of the Navier-Stokes equations. *J. Comp. Phys.*, 17:209–228, 1975.

[88] A. E. Mynett, P. Wesseling, A. Segal, and C. G. M. Kassels. The ISNaS incompressible Navier-Stokes solver: invariant discretization. *Applied Scientific Research*, 48:175–191, 1991.

[89] S. Lee and B. K. Soni. Governing equations of fluid mechanics in physical curvilinear coordinate system. In J. Graef, R. Shivaji, B. Soni, and J. Zhu, editors, *Differential Equations and Computational Simulations III*, pages 149–157, 1997.

[90] M. Farrashkhalvat and J. P. Miles. *Tensor methods for engineers and scientists*. Ellis Horwood Series in Mathematics and its Applications. Ellis Horwood, 1990.

[91] R. Aris. *Vectors, tensors and the basic equations of fluid mechanics*. Dover Publications, New York, USA, 1989.

[92] J. G. Simmonds. *A brief on tensor analysis*. Undergraduate Texts in Mathematics. Springer-Verlag, 1982.

[93] A. J. McConnell. *Applications of tensor analysis*. Dover Publications Inc., 1982.

[94] J. W. Baughn, X. J. Yan, and M. Mesbah. The effect of Reyolds number on the heat transfer distribution from a flat plate to a turbulent impinging jet. *ASME Winter Annual Meeting*, November 1992.

[95] D. Cooper, D. C. Jackson, B. E. Launder, and G. X. Liao. Impinging jet studies for turbulence model assessment. Part 1: Flow field experiments. *Int. J. Heat Mass Transfer*, 36(10):2675–2684, 1993.

[96] P. Bradshaw. Effects of streamline curvature on turbulent flow. *AGARDograph*, Vol. 169, (distributed through NATO National Distribution Centres), 1973.

[97] M. Kato and B. E. Launder. The modelling of turbulent flow around stationary and vibrating cylinders. In *Proc. 9th Symposium on Turbulent Shear Flows*, Kyoto, Japan, 1993.

[98] P.A. Durbin. On the k-ε stagnation point anomaly. *Int. J. Heat Fluid Flow*, 17:89–90, 1996.

[99] A. Abdon and B. Sundén. Numerical simulation of turbulent impingement cooling. In *Proceedings of ASME Turbo Expo 2001, Paper 2001-GT-0150*, New Orleans, USA, 2001.

[100] M. Behnia, S. Parneix, and P. A. Durbin. Prediction of heat transfer in an axisymmetric turbulent jet impinging on a flat plate. *Int. J. Heat Mass Transfer*, 41(12):1845–1855, 1998.

[101] M. Behnia, S. Parneix, Y. Shabany, and P. A. Durbin. Numerical study of turbulent heat transfer in confined and unconfined impinging jets. *Int. J. Heat Fluid Flow*, 20:1–9, 1999.

[102] K. Heyerichs and A. Pollard. Heat transfer in separated and impinging turbulent flows. *Int. J. Heat Mass Transfer*, 39(12):2385–2400, 1996.

[103] R. S. Amano and H. Brandt. Numerical study of turbulent axisymmetric jets impinging on a flat plate and flowing into an axisymmetric cavity. *ASME Journal of Fluids Engineering*, 106(4):410–417, 1984.

[104] R. S. Amano and M. K. Jensen. Turbulent heat transfer of impinging jet on a flat plate. In *ASME Paper No. 82-WA/HT-55*, Winter Annual Meeting, Phoenix, 1982.

[105] R. Amano and S. Sugiyama. Investigation on turbulent heat transfer of an axisymmetric jet impinging on a flat plate. *Bulletin of the JSME*, 28(235):74–79, 1985.

[106] S. Ashforth-Frost and K. Jambunathan. Numerical prediction of semi-confined jet impingement and comparison with experimental data. *Int. J. Num. Meth. Fluids*, 23:295–306, 1996.

[107] M. Bouainouche, N. Bourabaa, and B. Desmet. Numerical study of the wall shear stress produced by the impingement of a plane turbulent jet on a plate. *Int. J. Num. Meth. Heat Fluid Flow*, 7(5-6):548–564, 1997.

[108] W. Vieser, T. Esch, and F. Menter. Heat transfer predictions using advanced two-equation turbulence models. CFX Validation Report, CFX-VAL10/0602, 2002.

[109] K. Jambunathan, E. Lai, M. A. Moss, and B. L. Button. A review of heat transfer for single circular jet impingement. *Int. J. Heat and Fluid Flow*, 13:106–115, 1992.

[110] E. Goncalves and R. Houdeville. Reassessment of the wall function approach for RANS computations. *Aerosp. Sci. Technol.*, 5:1–14, 2001.

[111] G. Wickern, K. Zwicker, and M. Pfadenhauer. Rotating wheels - their impact on wind tunnel test techniques and on vehicle drag results. Technical Report 970133, SAE, 1997.

[112] J. M. Owen and M. Wilson. Heat transfer and cooling in gas turbines. *von Karman Institute for Fluid Dynamics Lecture Series*, May 1995.

[113] N. Gregory, J. T. Stuart, and W. S. Walker. On the stability of three-dimensional boundary layers with application to the flow due to a rotating disk. *Phil. Trans. A*, 248:155–199, 1955.

[114] T. Theodorsen and A. Regier. Experiments on drag of revolving disks, cylinders and streamline rods at high speeds. Technical Report 793, NACA, 1944.

[115] J. M. Owen, Haynes C. M., and F. J. Bayley. Heat transfer from an air-cooled rotating disk. *Proc. Roy. Soc. Lond. A*, 336:453–473, 1974.

[116] T-S. Cham and M. R. Head. Turbulent boundary-layer flow on a rotating disk. *J. Fluid Mech.*, 37:129–147, 1969.

[117] R. E. Mayle. The role of laminar-turbulent transition in gas turbine engines. *ASME Journal of Turbomachinery*, 113:509–537, 1991.

[118] H. Schlichting. *Boundary-Layer Theory*. McGraw-Hill, seventh edition, 1979.

[119] N. Gregory, J. T. Stuart, and W. S. Walker. On the stability of three-dimensional boundary layers with application to the flow due to a rotating disk. *Phil. Trans. Roy. Soc. London A*, 248:155–199, 1955.

[120] A. M. Savill. Some recent progress in the turbulence modelling of by-pass transition. In R. M. C. So, C. G. Speziale, and B. E. Launder, editors, *Near-Wall Turbulent Flows*. Elsevier Science, 1993.

[121] G. P. Virr, J. W. Chew, and J. Coupland. Application of computational fluid dynamics to turbine disk cavities. *Journal of Turbomachinery, Trans. ASME*, 116(4):701–708, 1994.

[122] J. W. Chew. Prediction of flow in rotating disc systems using the $k-\varepsilon$ turbulence model. In *ASME Gas Turbine and Fluids, Paper 84-GT-229*, 1984.

[123] A. D. Gosman, M. L. Koosinlin, F. C. Lockwood, and D. B. Spalding. Transfer of heat in rotating systems. In *ASME Gas Turbine and Fluids Eng. Conf., Paper 76-GT-25*, New Orleans, 1976.

[124] A. P. Morse. Numerical prediction of turbulent flow in rotating cavities. *ASME Journal of Turbomachinery*, 110:202–212, 1988.

[125] M. Williams, W.C. Chen, G. Bache, and A. Eastland. An analysis methodology for internal swirling flow systems with a rotating wall. In *ASME Gas Turbine and Fluids, Paper 89-GT-185*, 1989.

[126] A. P. Morse. Assessment of laminar-turbulent transition in closed disk geometries. *ASME Journal of Turbomachinery*, 113:131–138, 1991.

[127] C. L. Ong. Computation of fluid flow and heat transfer in rotating disk systems. D. Phil thesis, University of Sussex, 1988.

[128] M. Kiliç. *Flow between contra-rotating discs*. PhD thesis, University of Bath, 1993.

[129] Th. von Kármán. Über laminare und turbulente reibung. *Z. angew. Math. Mech.*, 1:233–252, 1921.

[130] E. C. Cobb and O. A. Saunders. Heat transfer from a rotating disk. *Proc. Roy. Soc. Lond. A*, 236:343–351, 1956.

[131] W. G. Cochran. The flow due to a rotating disk. *Proc. Camb. Phil. Soc.*, 30:365–375, 1934.

[132] J. M. Owen and R. H. Rogers. *Flow and heat transfer in rotating disc systems: Vol. 1, Rotor-stator systems*. Research Studies Press, Taunton, U.K. and John Wiley, New York, USA, 1989.

[133] A. Harun. Application of eddy viscosity models to the swirling impinging jet. MSc Thesis, Dept. of Mechanical Engineering, UMIST, Manchester, UK, 2000.

[134] T. J. Craft, B. E. Launder, and K. Suga. Prediction of turbulent transitional phenomena with a nonlinear eddy-viscosity model. *Int. J. Heat Fluid Flow*, 18:15–28, 1997.

[135] L. Janssen and W-H. Hucho. Aerodynamische entwicklung von VW-Golf und VW-Scirocco. *Automobiltech. Z.*, 77:1–5, 1975.

[136] S. R. Ahmed. Influence of base slant on the wake structure and drag of road vehicles. *ASME J. Fluids Eng.*, 105:429–434, 1983.

[137] S. R. Ahmed, G. Ramm, and G. Faltin. Some salient features of the time-averaged ground vehicle wake. *SAE*, 93(840300:2):473–503, 1984.

[138] H. Lienhart, C. Stoots, and S. Becker. Flow and turbulence structures in the wake of a simplified car model (Ahmed model). In *DGLR Fach Symp. der AG STAB*, Stuttgart University, November 2000.

[139] A. Spohn and P. Gilliéron. Flow separations generated by a simplified geometry of an automotive vehicle. *IUTAM Symposium on Unsteady Separated Flows*, April 2002.

[140] T. Han. Computational analysis of three-dimensional turbulent flow around a bluff body in ground proximity. *AIAA J.*, 27(9):1213–1219, 1989.

[141] K. Suga, M. Nagaoka, N. Horinouchi, K. Abe, and Y. Kondo. Application of a three-equation cubic eddy-viscosity model to 3-D turbulent flows by the unstructured grid method. *Int. J. Heat and Fluid Flow*, 22:252–258, 2001.

[142] K. Maeda, N. Kobayashi, and S. Katsumata. Analysis of air flow behaviour around a vehicle to improve aerodynamic characteristic. *Trans. JSAE*, 45:54–59, 1990.

[143] B. E. Launder and D. B. Spalding. *Mathematical models of turbulence*. London: Academic Press, 1972.

[144] N. E. May. Efficient implementation of two-equation and differential Reynolds stress turbulence models into a cell-vertex, explicit, time-marching, Navier-Stokes flow code. Technical Report M345/1, Aircraft Research Assoc., Bedford, UK, 1998.

Figures

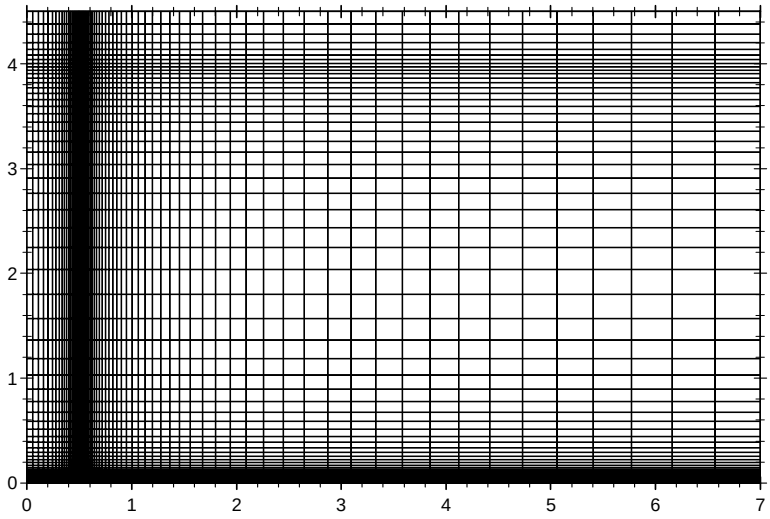

Figure 5.4: Low-Reynolds-number 90×70 (axial $\times$ radial) grid used in the impinging jet flow calculations.

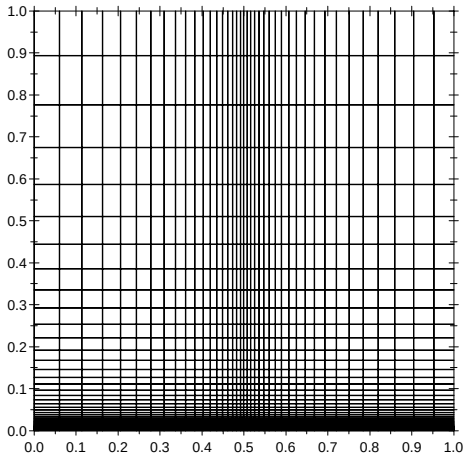

Figure 5.5: Close-up of wall-bounded region, low-Reynolds-number 90×70 (axial $\times$ radial) grid used in the impinging jet flow calculations.

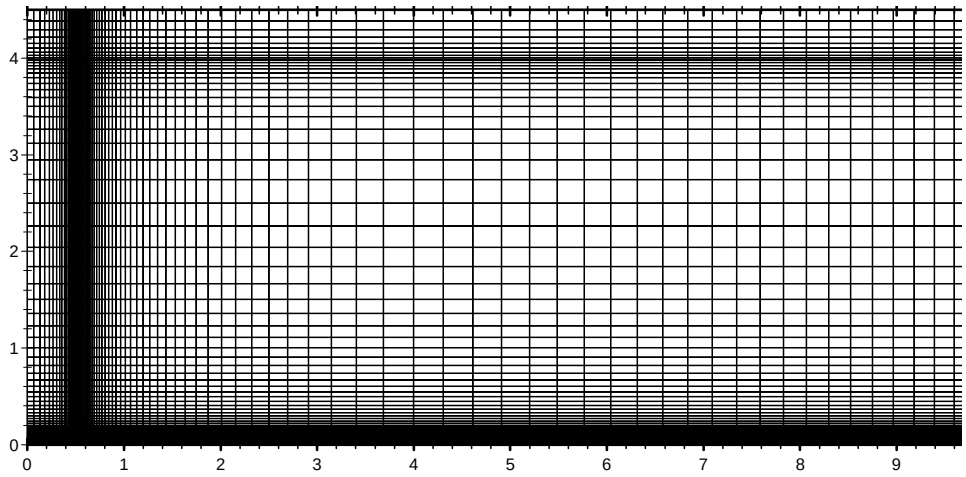

Figure 5.6: Low-Reynolds-number 120×90 grid used in the impinging jet flow calculations.

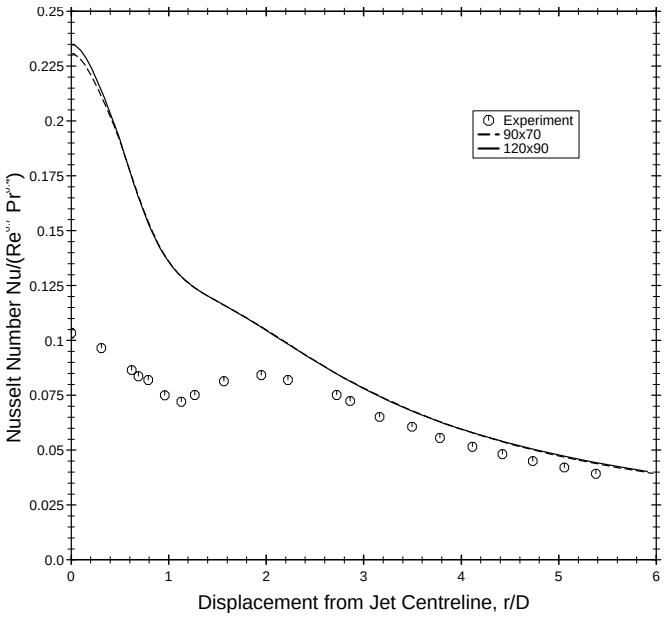

Figure 5.7: Comparison of Nusselt number predictions for the impinging jet flow with the 90×70 and 120×70 grids, using a linear $k - \varepsilon$ model with the standard Yap correction.

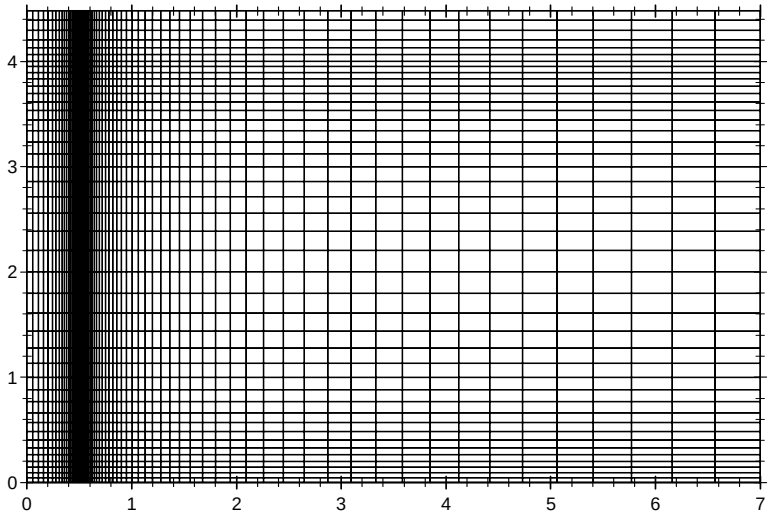

Figure 5.8: High-Reynolds-number 45×70 (axial $\times$ radial) grid used in the impinging jet flow with a near-wall cell size $DX = 250$.

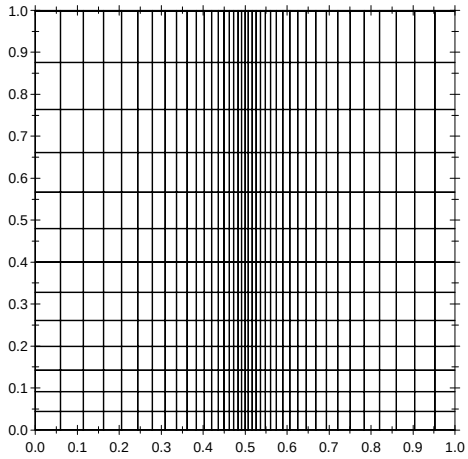

Figure 5.9: Close-up of wall-bounded region in the high-Reynolds-number 45×70 (axial $\times$ radial) grid used in the impinging jet flow with a near-wall cell size $DX = 250$.

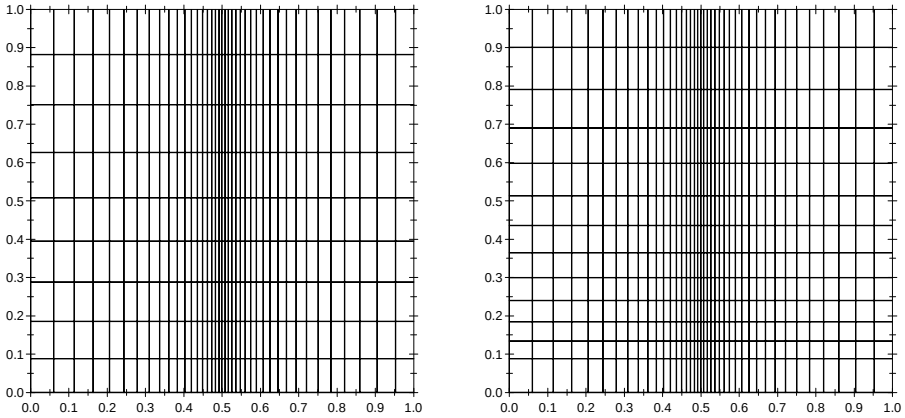

Figure 5.10: Comparison of near-wall region in the impinging jet flow for $DX = 500$ cells with continuous near-wall grid size (left) and 2:1 step change in grid size (right).

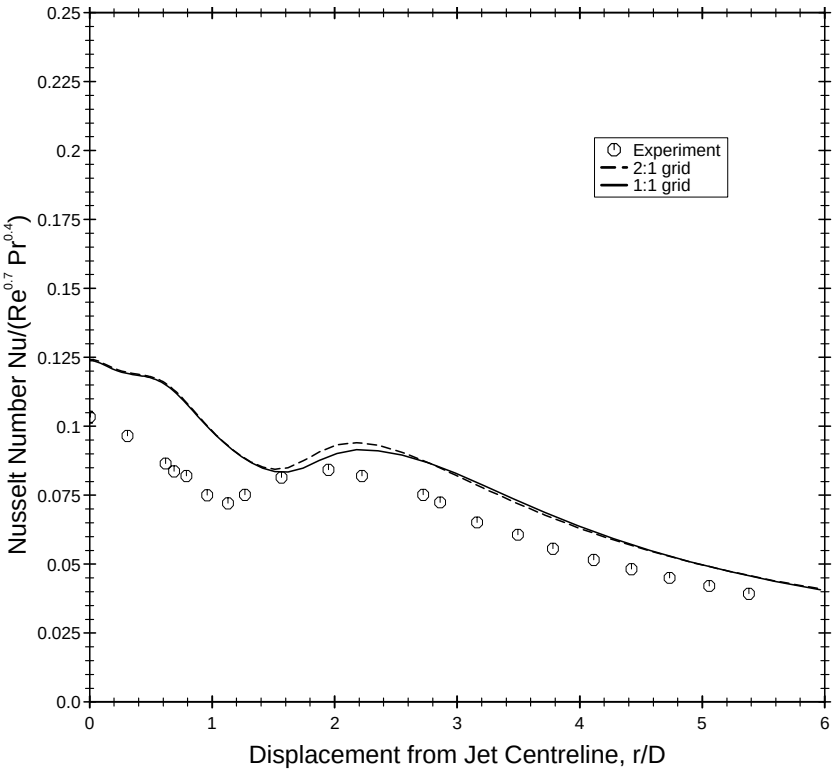

Figure 5.11: Comparison of Nusselt number predictions for the impinging jet flow with the $DX = 500$ continuous (1:1) grid and discontinuous (2:1) grids as shown in Figure 5.10, with the UMIST-*N* wall function, NLEVM of Craft *et al*. [67] and differential Yap correction.

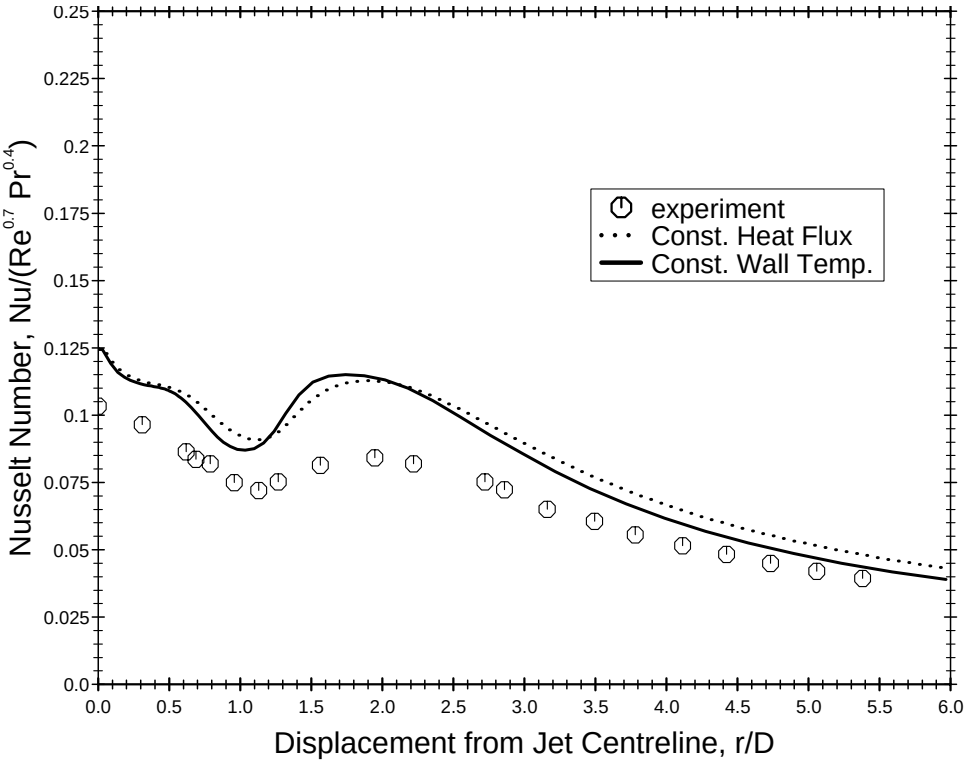

Figure 5.12: Comparison of Nusselt number predictions for the impinging jet flow using constant heat flux and constant wall temperature boundary conditions (broken and solid lines respectively). Both calculations used the low-*Re* non-linear $k-\varepsilon$ model of Craft *et al.* with the "standard" Yap correction. Symbols show the data points of the Baughn *et al*. [94] experiments which used constant wall temperature boundary conditions.

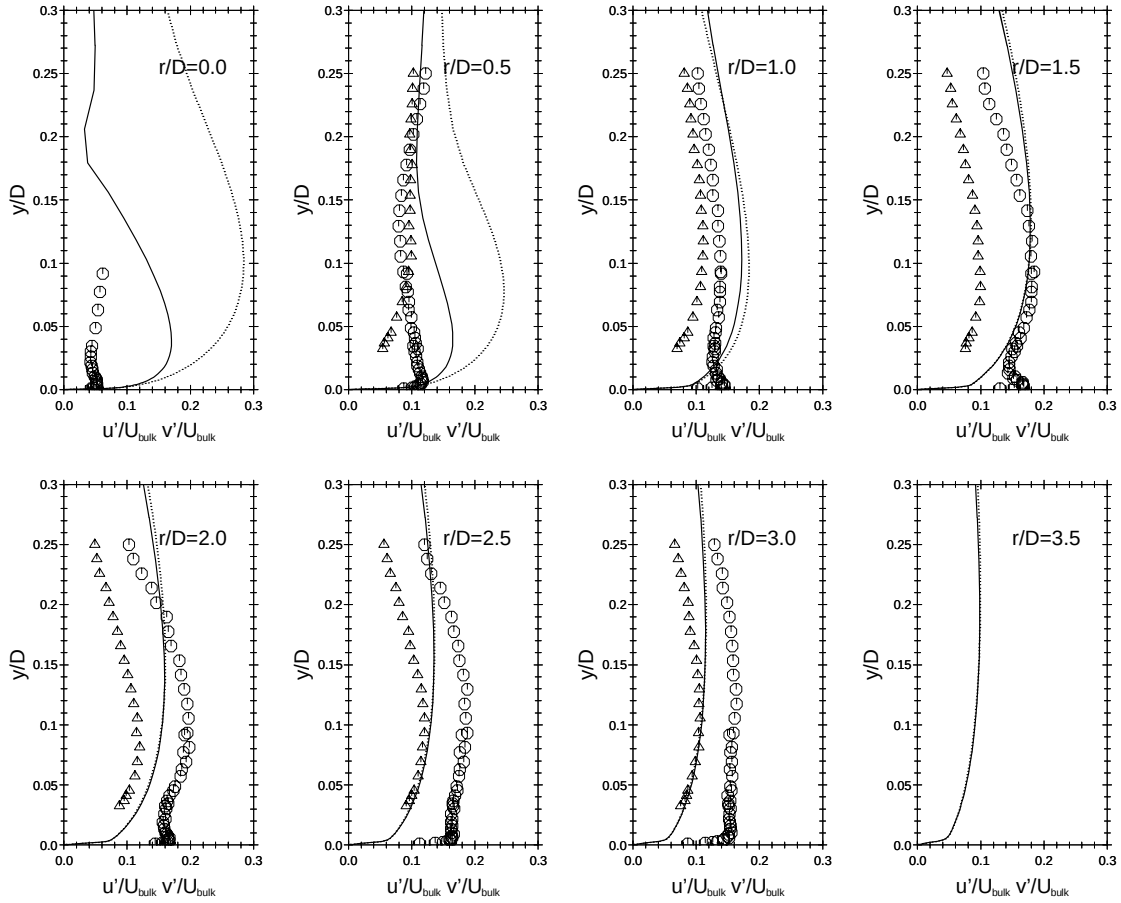

Figure 5.13: Radial (wall-parallel) and axial (wall-normal) RMS velocity components for the impinging jet flow at 8 radial positions using the low-*Re* linear $k-\varepsilon$ model with standard Yap correction. Lines represent the low-*Re* model predictions and symbols the experimental data of Cooper *et al*. [95]. —- and $\ominus$: radial u' component; ..... and $\triangle$: axial v' component.

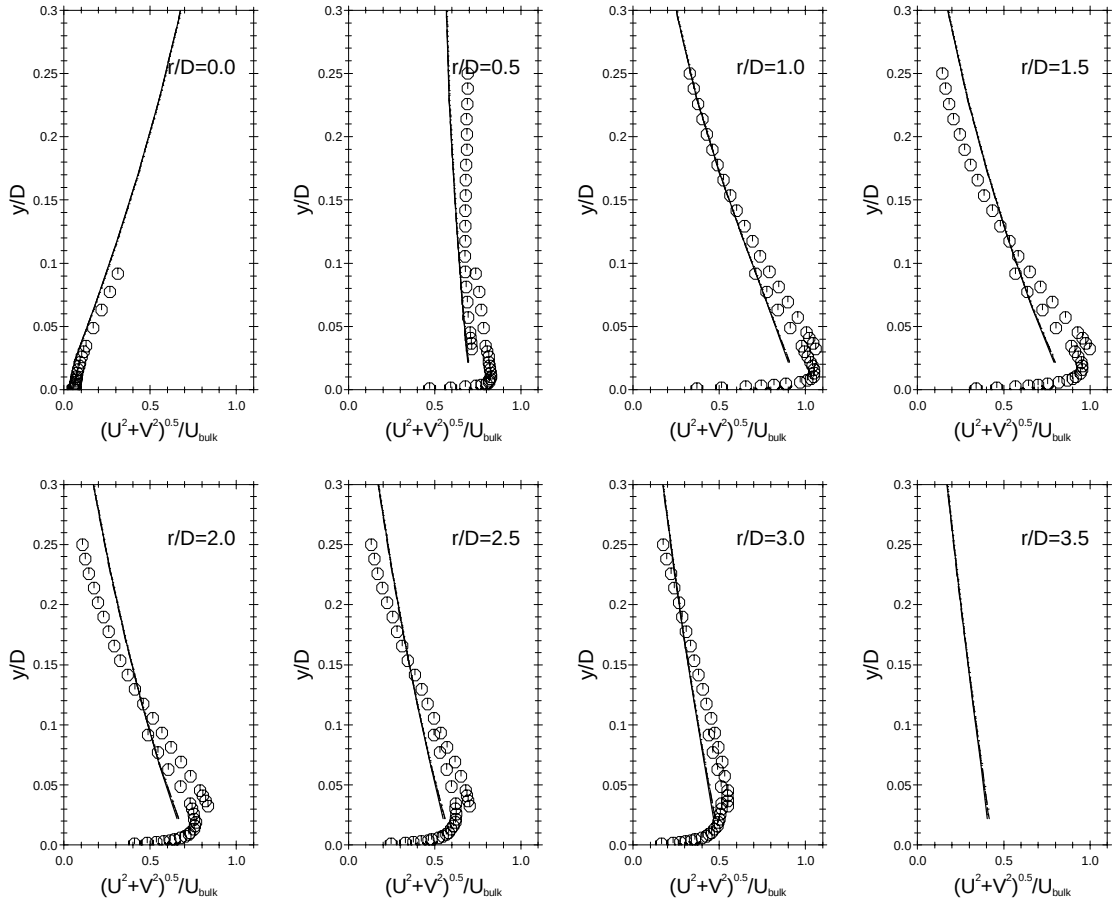

Figure 5.14: Resultant velocity profiles for the impinging jet flow at 6 radial positions using four "standard" wall functions with the linear $k-\varepsilon$ model, standard Yap correction and near-wall cell size $DX = 250$. ——: TEAM; - - -: SCL; – . –: CL; .....: JL; $\ominus$: experimental data of Cooper *et al*. [95]. Lines from the four wall function calculations lie on top of each other and have been shown up to the position of the near-wall node.

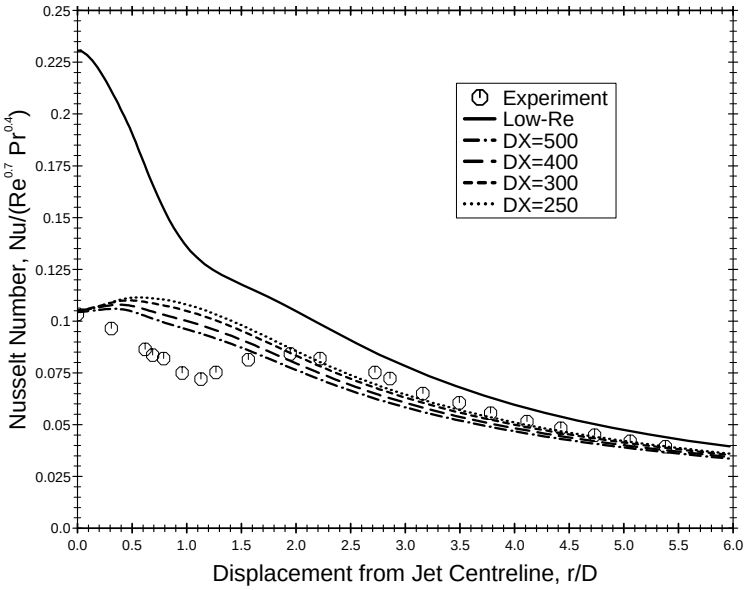

Figure 5.15: Nusselt number profiles obtained for the impinging jet flow using the Launder & Spalding (TEAM) wall function with the linear $k-\varepsilon$ model and standard Yap correction. Solid line: low-Reynolds-number model; broken lines: wall function results for different near-wall cell widths; symbols: experiments of Baughn *et al*. [94]. Normal stress components are included in the cell-averaged production term, $\overline{P_k}$, of the wall function (see Equation 2.49).

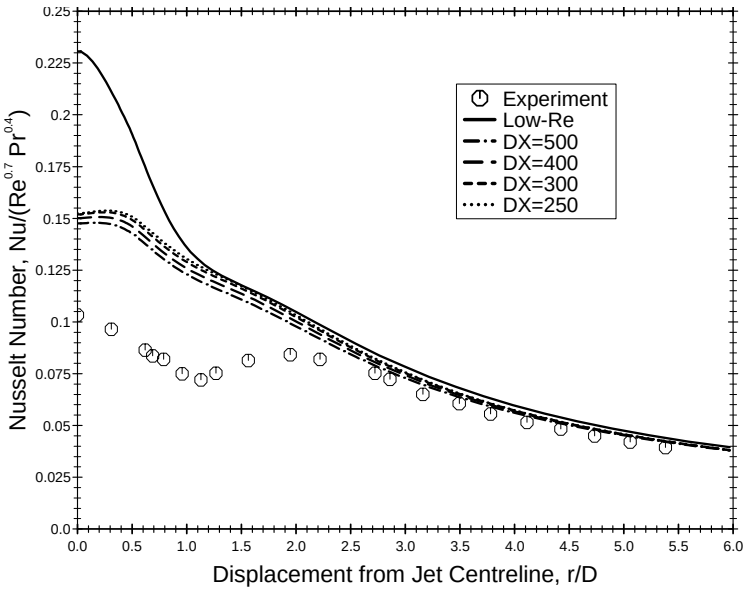

Figure 5.16: Nusselt number profiles obtained for the impinging jet flow using the simplified Chieng & Launder wall function with the linear $k-\varepsilon$ model and standard Yap correction. Solid line: low-Reynolds-number model; broken lines: wall function results for different near-wall cell widths; symbols: experiments of Baughn *et al*. [94]. Normal stress components are included in the cell-averaged production term, $\overline{P_k}$, of the wall function (see Equation 2.49).

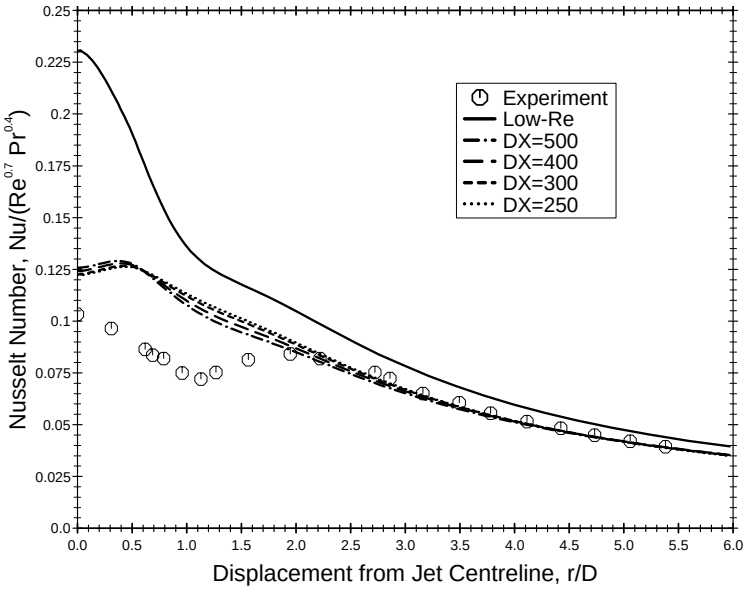

Figure 5.17: Nusselt number profiles obtained for the impinging jet flow using the Chieng & Launder wall function with the linear $k-\varepsilon$ model and standard Yap correction. Solid line: low-Reynolds-number model; broken lines: wall function results for different near-wall cell widths; symbols: experiments of Baughn *et al*. [94]. Normal stress components are included in the cell-averaged production term, $\overline{P_k}$, of the wall function (see Equation 2.49).

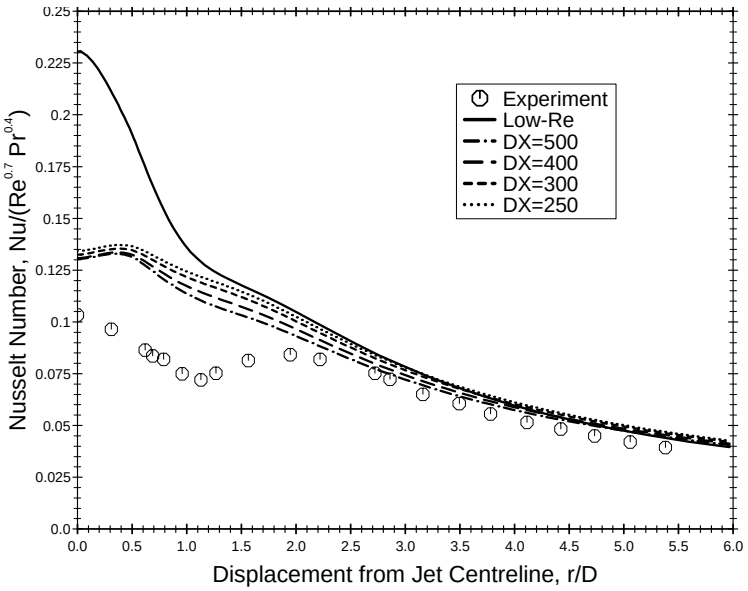

Figure 5.18: Nusselt number profiles obtained for the impinging jet flow using the Johnson & Launder wall function with the linear $k-\varepsilon$ model and standard Yap correction. Solid line: low-Reynolds-number model; broken lines: wall function results for different near-wall cell widths; symbols: experiments of Baughn *et al*. [94]. Normal stress components are included in the cell-averaged production term, $\overline{P_k}$, of the wall function (see Equation 2.49).

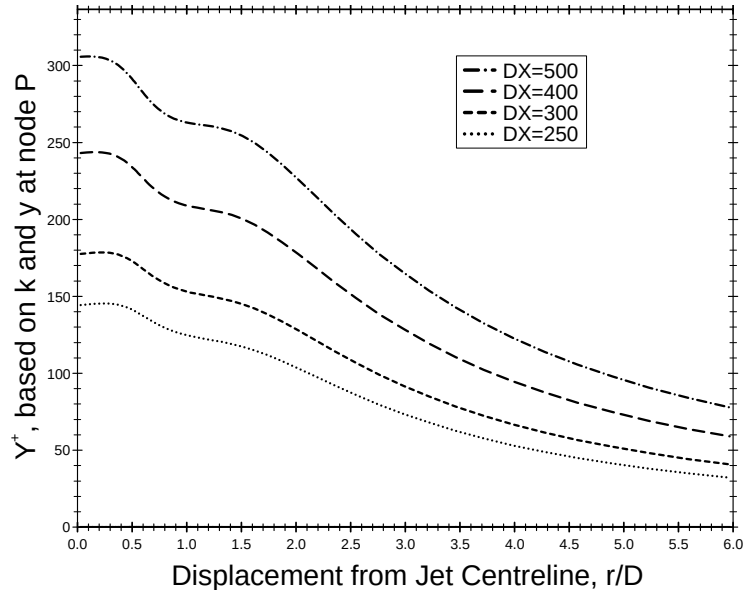

Figure 5.19: Calculated $y^+ \left(= c_\mu^{1/4} k_P^{1/2} y_P / \nu\right)$ profiles obtained for the impinging jet flow using the Chieng & Launder wall function with the linear $k-\varepsilon$ model and standard Yap correction, corresponding to the Nusselt number profiles shown in Figure 5.17. Broken lines show wall function results for different near-wall cell widths.

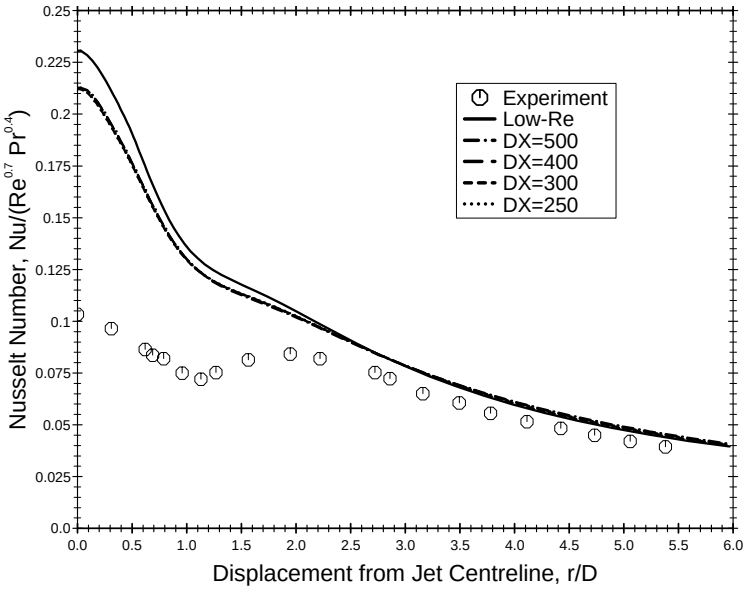

Figure 5.20: Nusselt number profiles obtained for the impinging jet flow using the UMIST-*N* wall function with the linear $k-\varepsilon$ model and standard Yap correction. Solid line: low-Reynolds-number model; broken lines: wall function results for different near-wall cell widths; symbols: experiments of Baughn *et al*. [94].

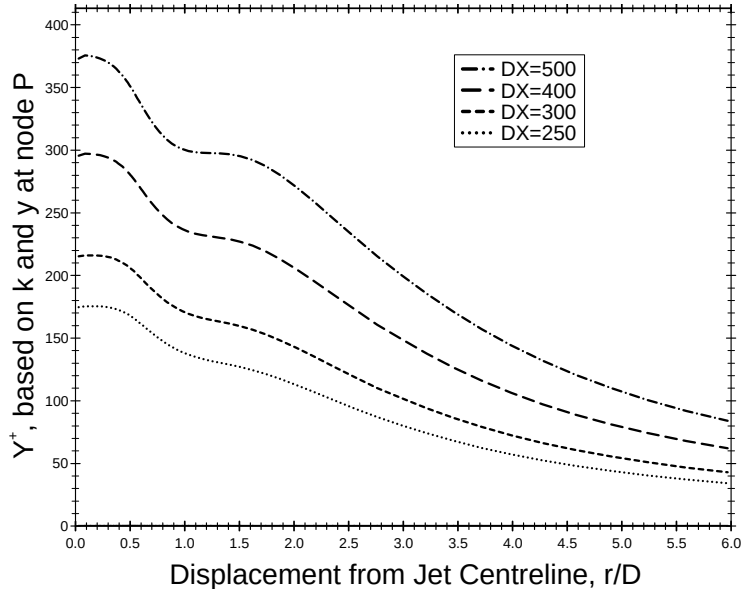

Figure 5.21: Calculated $y^+ \left(= c_\mu^{1/4} k_P^{1/2} y_P / \nu\right)$ profiles obtained for the impinging jet flow using the UMIST-*N* wall function with the linear $k-\varepsilon$ model and standard Yap correction, corresponding to the Nusselt number profiles shown in Figure 5.20. Broken lines show wall function results for different near-wall cell widths.

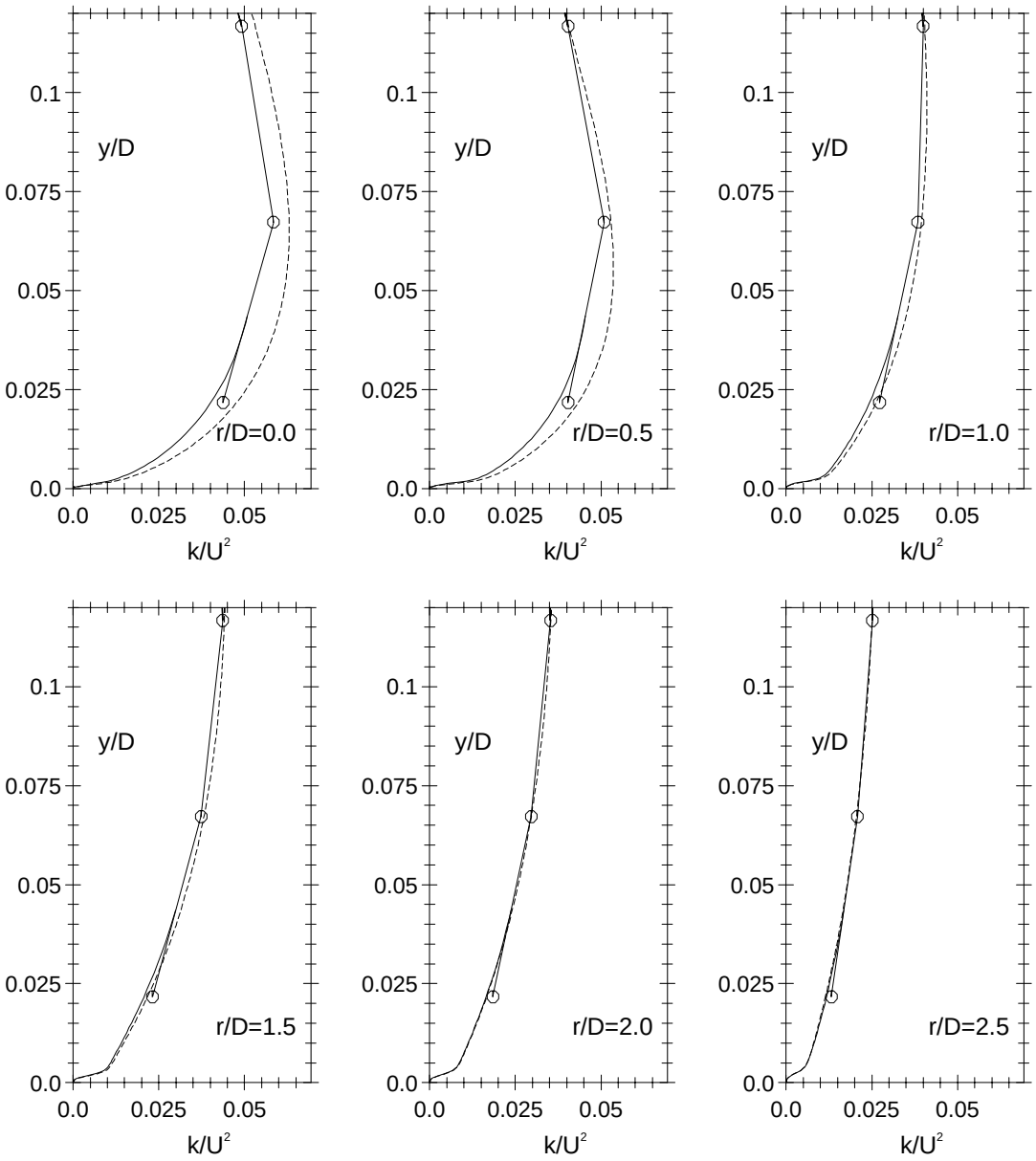

Figure 5.22: Turbulent kinetic energy profiles in the near-wall region (including the subgrid) at 6 different radial positions measured from the axis of the impinging jet, obtained using the linear $k-\varepsilon$ model and standard Yap correction. —-: UMIST-*N* wall function with near wall cell size $DX = 250$ and grid arrangement as shown in Figure 5.9; - - -: low-Reynolds-number model; symbols: main-grid node values in the wall-function calculation.

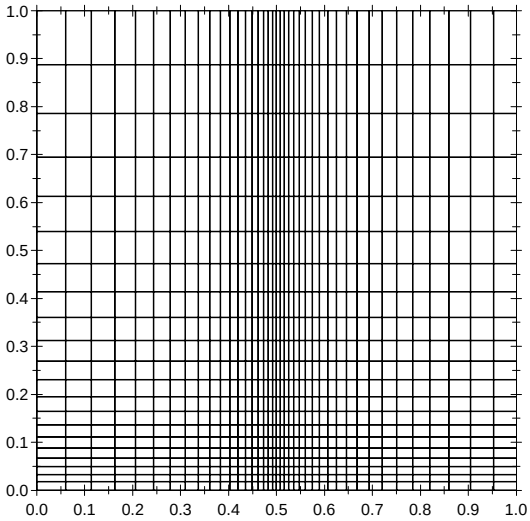

Figure 5.23: Close-up of the wall-bounded region of the impinging jet flow using the high-Reynolds-number 51×70 grid with near-wall cell size $DX = 100$.

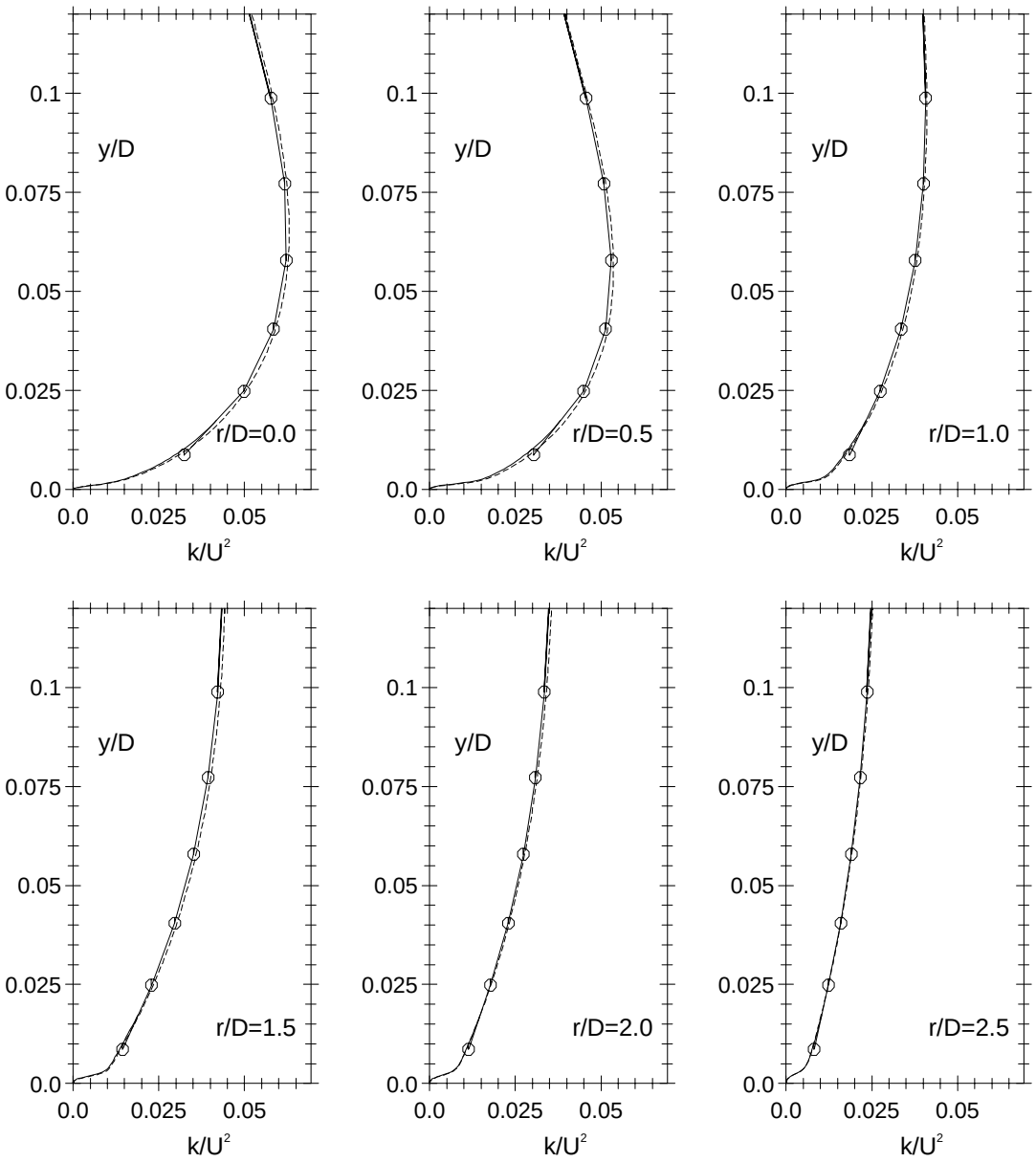

Figure 5.24: Turbulent kinetic energy profiles in the near-wall region (including the subgrid) at 6 different radial positions measured from the axis of the impinging jet, obtained using the linear $k-\varepsilon$ model and standard Yap correction. —-: UMIST-*N* wall function with near wall cell size $DX = 100$ and grid arrangement as shown in Figure 5.23; - - -: low-Reynolds-number model; symbols: main-grid node values in the wall-function calculation.

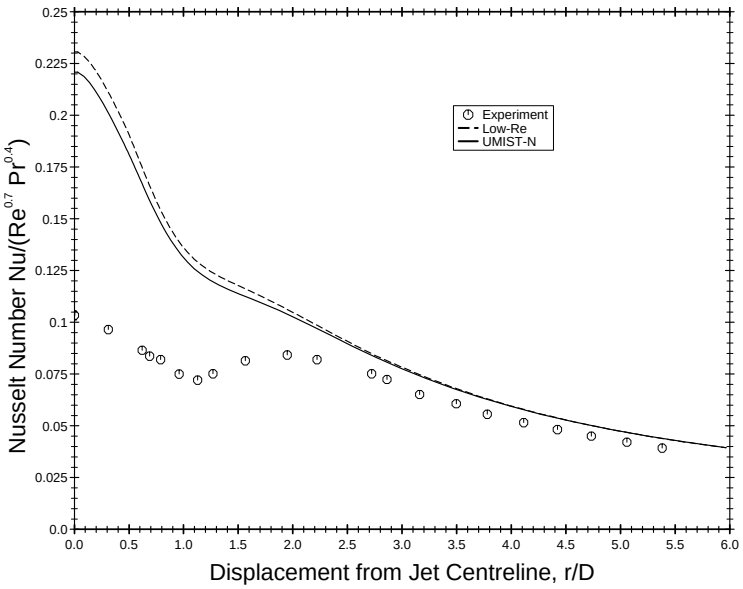

Figure 5.25: Nusselt number profiles obtained for the impinging jet flow with the linear $k-\varepsilon$ model and standard Yap correction. Dashed line: low-Reynolds-number model; solid line: UMIST-*N* wall function result obtained with near wall cell size $DX = 100$ and grid arrangement as shown in Figure 5.23. Symbols: experiments of Baughn *et al*. [94].

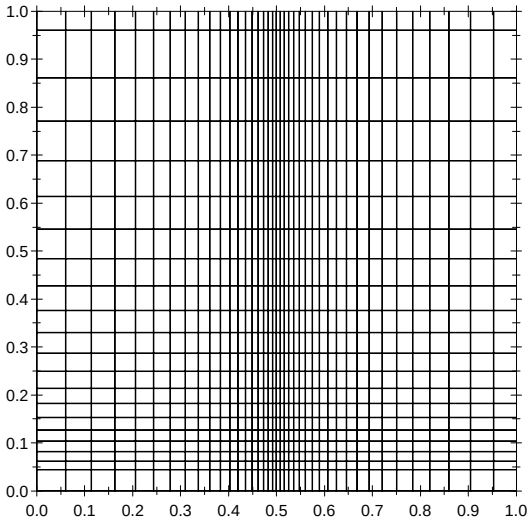

Figure 5.26: Close-up of the wall-bounded region in the impinging jet flow using the high-Reynolds-number 51×70 grid with near-wall cell size $DX = 250$.

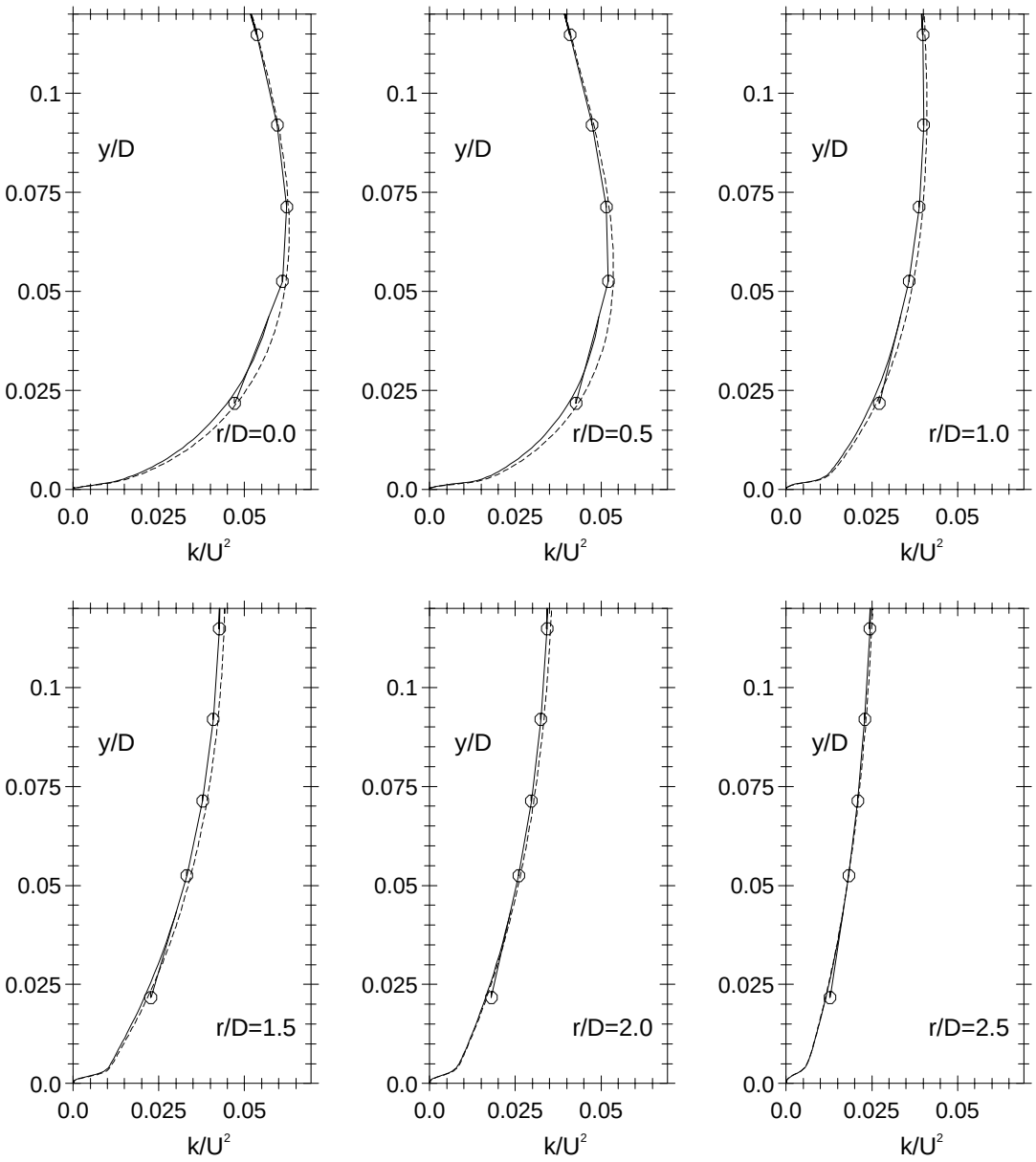

Figure 5.27: Turbulent kinetic energy profiles in the near-wall region (including the subgrid) at 6 different radial positions measured from the axis of the impinging jet, obtained using the linear $k-\varepsilon$ model and standard Yap correction. —-: UMIST-*N* wall function with near wall cell size $DX = 250$ and grid arrangement as shown in Figure 5.26; - - -: low-Reynolds-number model; symbols: main-grid node values in the wall-function calculation.

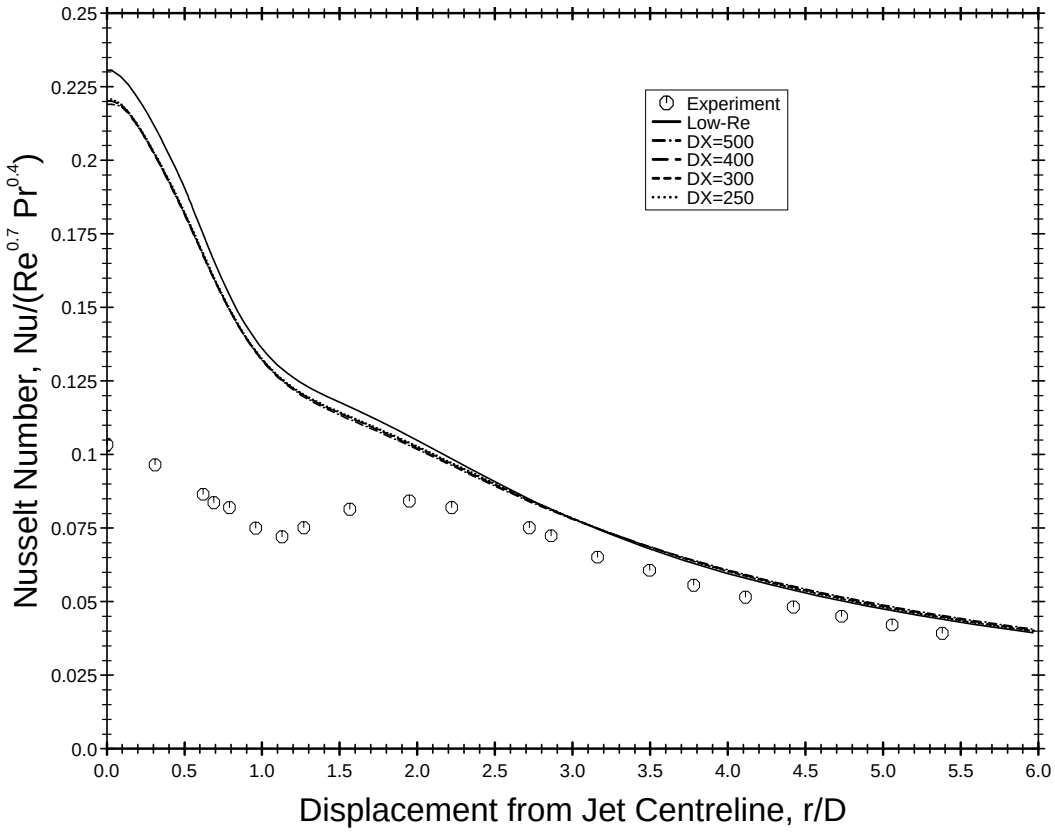

Figure 5.28: Nusselt number profiles obtained for the impinging jet flow using the linear $k-\varepsilon$ model and standard Yap correction. Solid line: low-Reynolds-number model; broken lines: UMIST-*N* wall function results for different near-wall cell widths with the grid arrangement outside the near-wall cell as shown in Figure 5.26 for $DX = 250$; symbols: experiments of Baughn *et al*. [94].

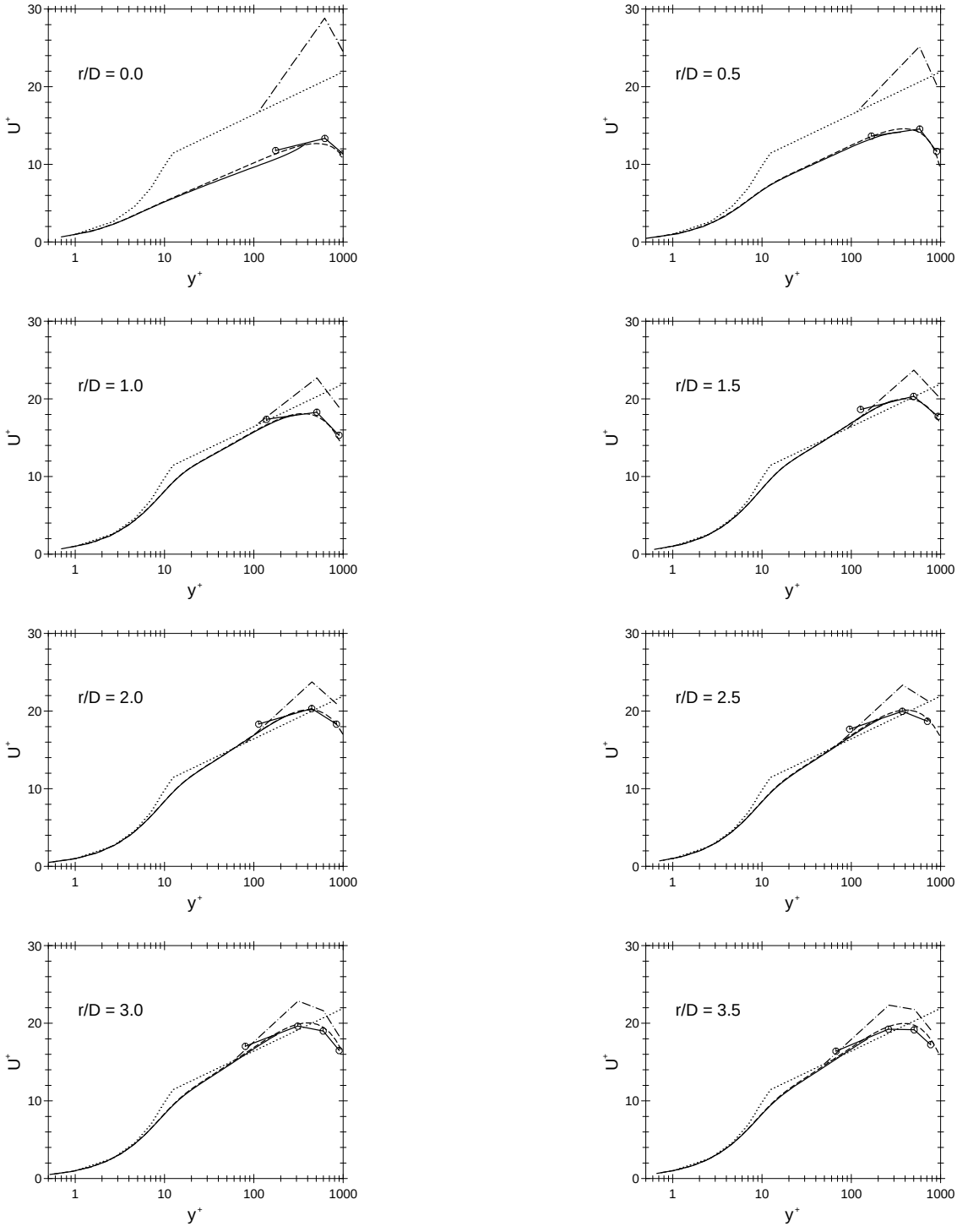

Figure 5.29: Semi-logarithmic velocity profiles for the impinging jet flow at 8 radial locations. —⊖—: UMIST-*N* wall function (circles indicate the position of main-grid nodes); – – –: low-*Re* model; – . –: Chieng & Launder wall function; ....: "universal" log-law. All results shown used the linear $k-\varepsilon$ model and standard Yap correction. Wall function calculations used the $DX = 250$ grid shown in Figure 5.9. Results shown for $r/D = 0$ are taken at the node adjacent to the axis of symmetry. Equation (2.44) is used to define U^+ and y^+.

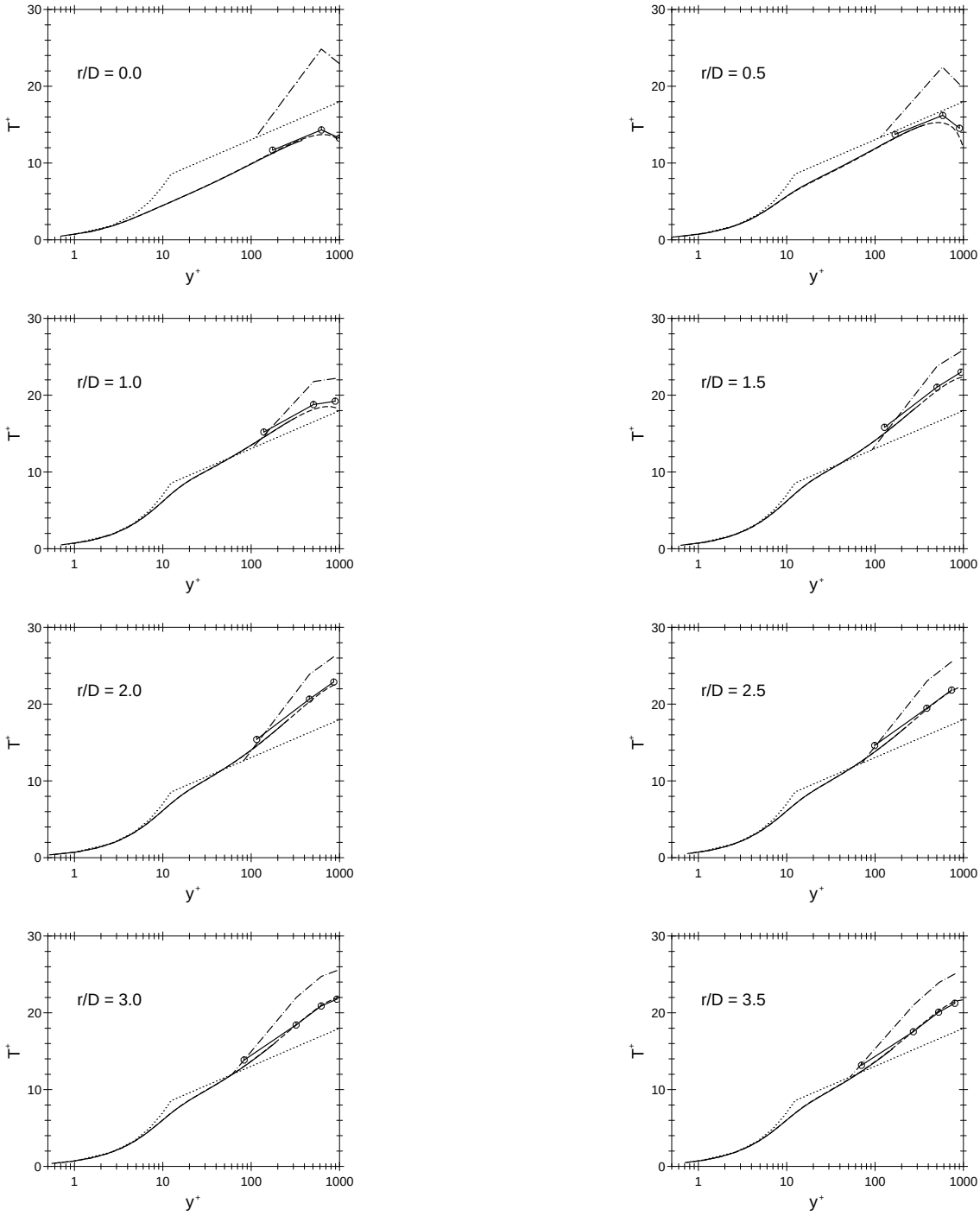

Figure 5.30: Semi-logarithmic temperature profiles for the impinging jet flow at 8 radial locations. —○—: UMIST-*N* wall function (circles indicate the position of main-grid nodes); – – –: low-*Re* model; – . –: Chieng & Launder wall function; ....: "universal" log-law. All results shown used the linear $k-\varepsilon$ model and standard Yap correction. Wall function calculations were performed using the $DX = 250$ grid shown in Figure 5.9. Results shown for $r/D = 0$ are taken at the node adjacent to the axis of symmetry. The friction velocity used to define y^+ was found from $U_\tau = c_\mu^{1/4} k^{1/2}$.

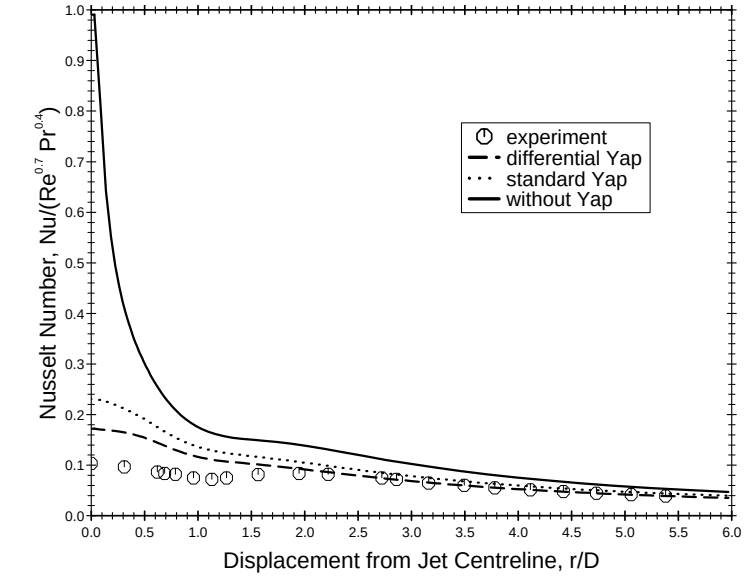

Figure 5.31: Nusselt number profiles for the impinging jet flow obtained using the low-*Re* linear $k-\varepsilon$ model without any Yap correction, with the standard Yap correction (Equation 2.16) and with the differential Yap correction (Equation 2.17). Symbols: experiments of Baughn *et al*. [94].

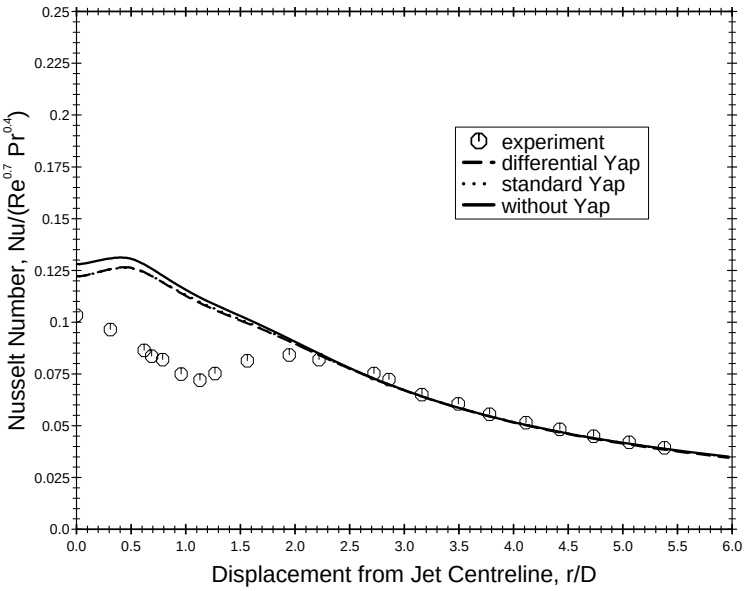

Figure 5.32: Nusselt number profiles for the impinging jet flow obtained using the linear $k-\varepsilon$ model and the Chieng & Launder wall function without any Yap correction, with the standard Yap correction (Equation 2.16) and with the differential Yap correction (Equation 2.17). The standard and differential Yap correction results are practically identical. The wall function grid used a near-wall cell size $DX = 250$. Experimental data points are from of Baughn *et al*. [94].

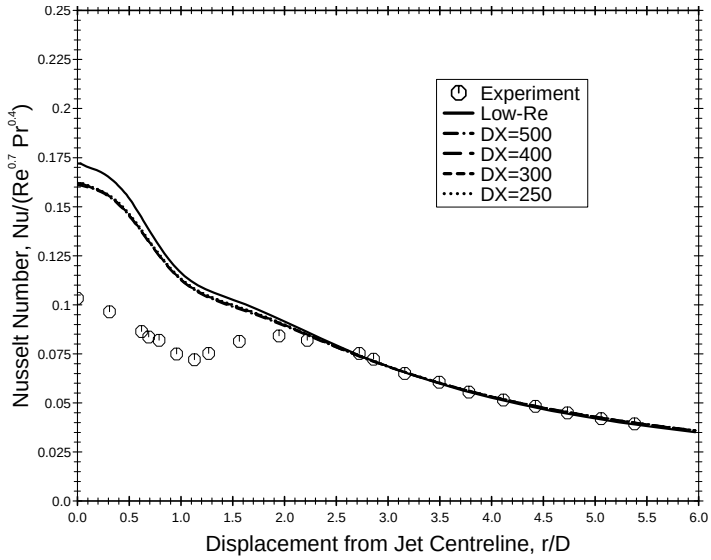

Figure 5.33: Nusselt number profiles for the impinging jet obtained using the linear $k-\varepsilon$ model and the differential Yap correction (Equation 2.17). Solid line: low-Reynolds-number model; broken lines: UMIST-*N* wall function results for different near-wall cell widths; symbols: experiments of Baughn *et al*. [94].

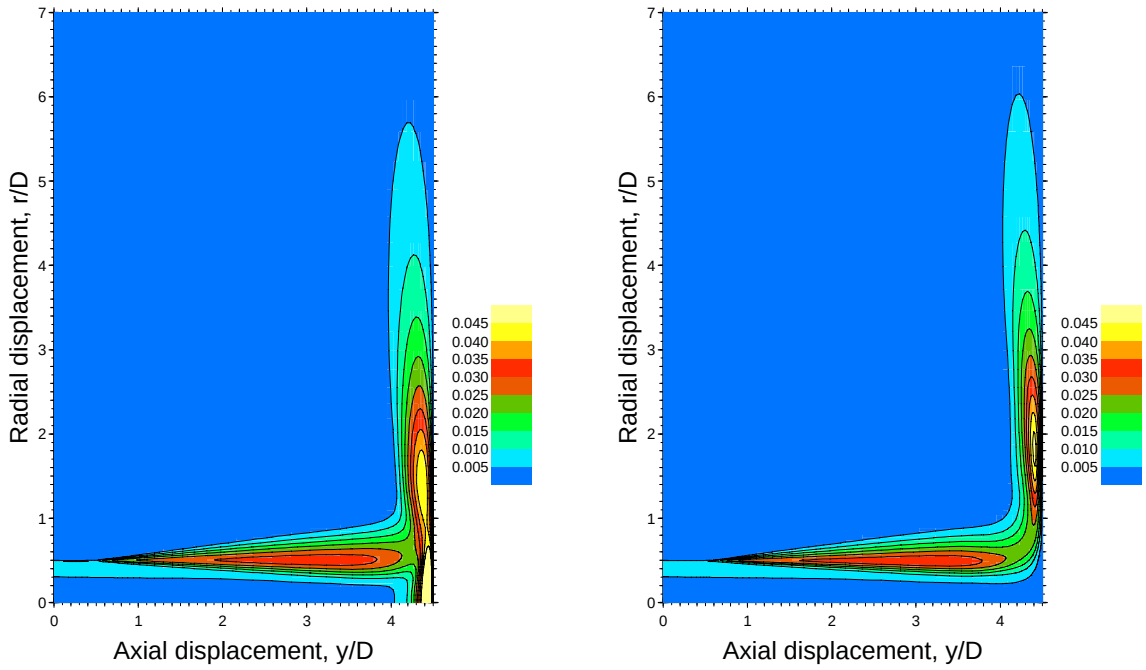

Figure 5.34: Contour plots of the dimensionless turbulent kinetic energy $\left(k/U_{bulk}^2\right)$ for the impinging jet flow obtained using the low-*Re* linear $k-\varepsilon$ model (left) and the low-*Re* NLEVM (right). Axial displacement is measured from the entrainment boundary, i.e. the wall is located at $y/D = 4.5$.

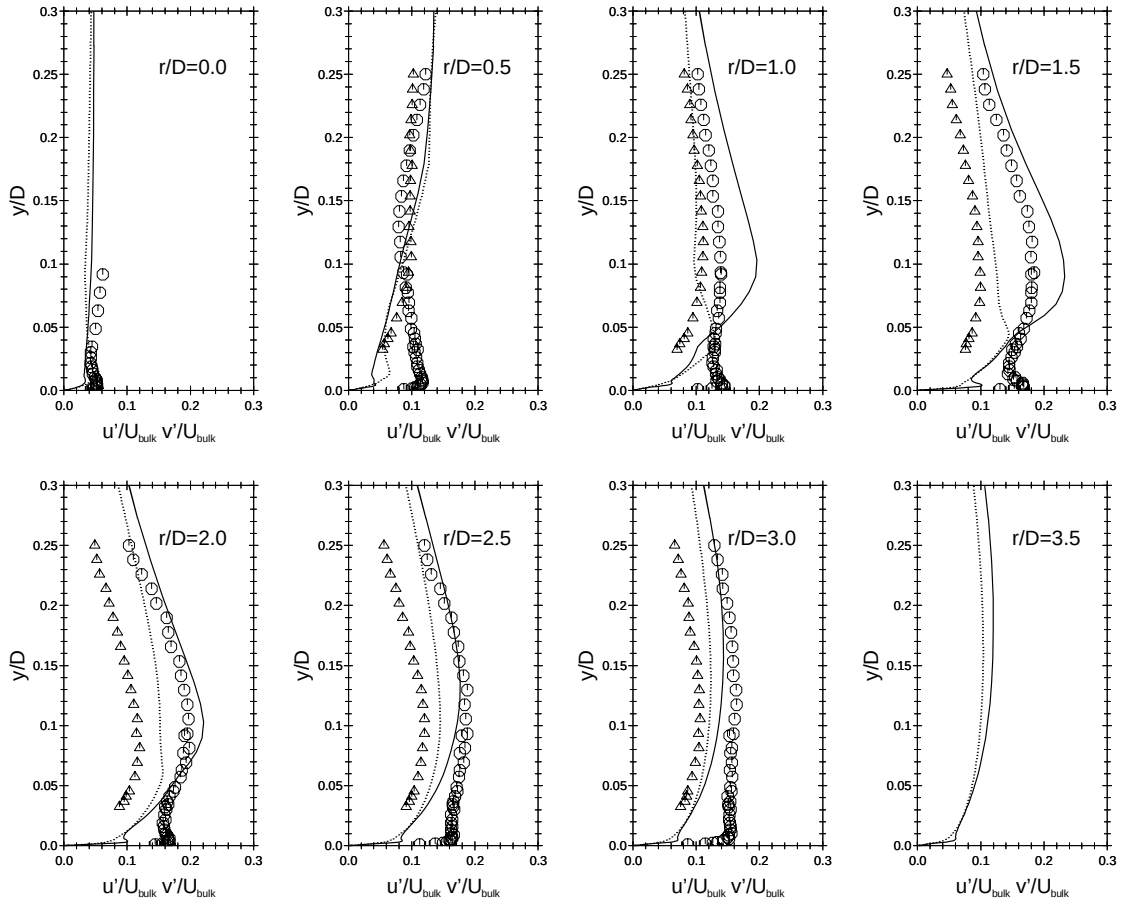

Figure 5.35: Radial (wall-parallel) and axial (wall-normal) RMS velocity components for the impinging jet flow at 8 radial positions using the NLEVM with the differential Yap correction and the c_μ function of Equation (2.36). Lines represent the low-*Re* model predictions and symbols the experimental data of Cooper *et al*. [95]. —- and $\ominus$: radial u' component; ..... and $\triangle$: axial v' component.

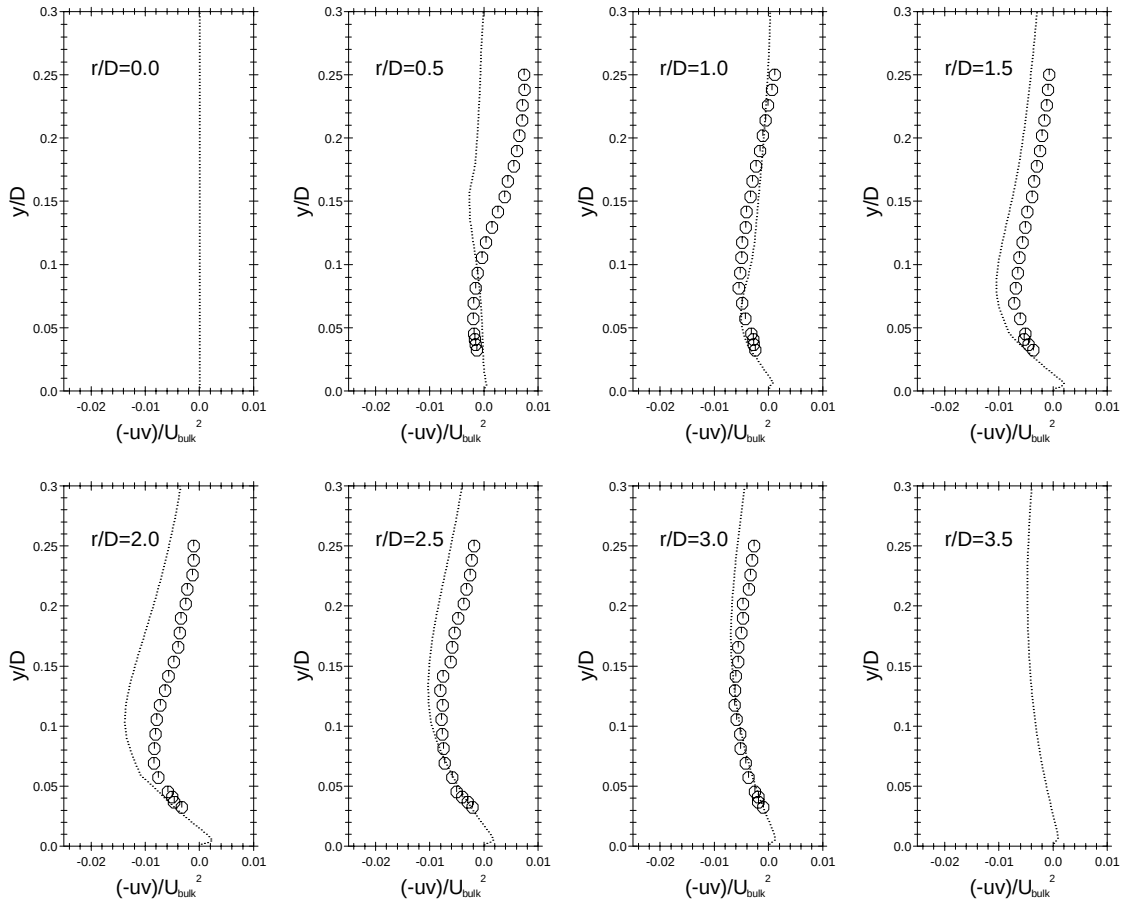

Figure 5.36: Turbulent shear stress (in the axial-radial plane) for the impinging jet flow at 8 radial positions using the NLEVM with the differential Yap correction and the c_μ function of Equation (2.36). Lines represent the low-*Re* model predictions and symbols the experimental data of Cooper *et al*. [95].

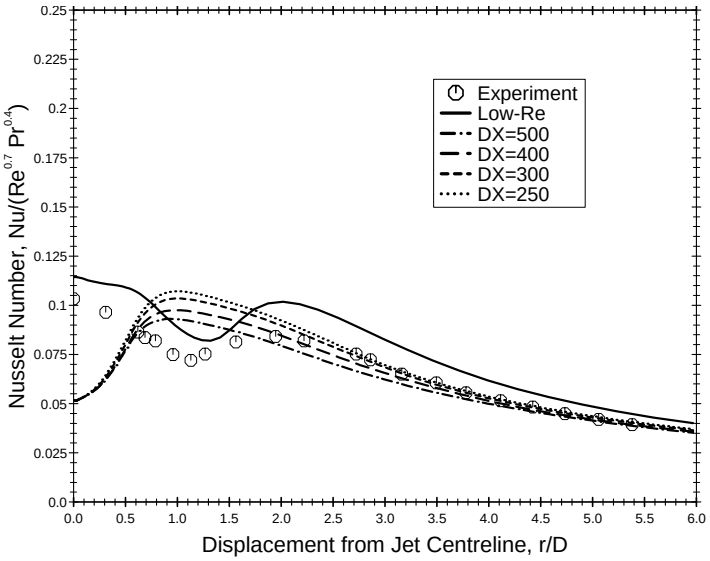

Figure 5.37: Nusselt number profiles obtained for the impinging jet flow using the Launder & Spalding (TEAM) wall function with the non-linear $k-\varepsilon$ model, the c_μ function of Equation (2.36) and differential Yap correction. Solid line: low-Reynolds-number model; broken lines: wall function results for different near-wall cell widths; symbols: experiments of Baughn *et al.* [94]. Normal stress components are included in the cell-averaged production term, $\overline{P_k}$, of the wall function (see Equation 2.49).

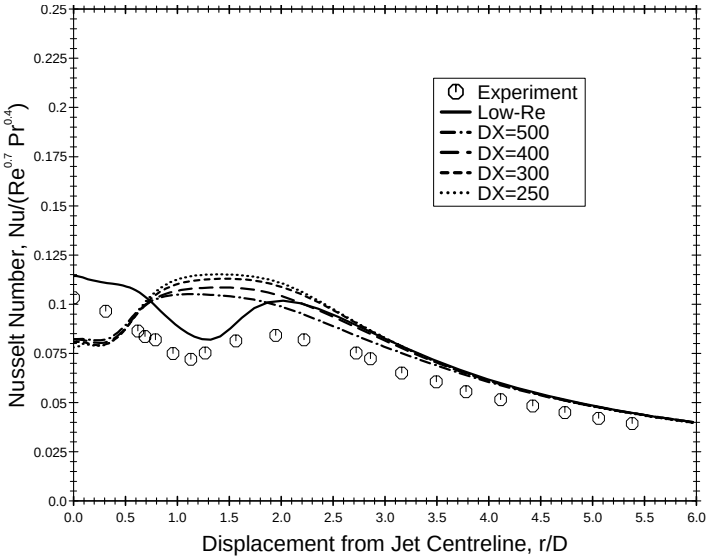

Figure 5.38: Nusselt number profiles obtained for the impinging jet flow using the simplified Chieng & Launder wall function with the non-linear $k-\varepsilon$ model, the c_μ function of Equation (2.36) and differential Yap correction. Solid line: low-Reynolds-number model; broken lines: wall function results for different near-wall cell widths; symbols: experiments of Baughn *et al*. [94]. Normal stress components are included in the cell-averaged production term, $\overline{P_k}$, of the wall function (see Equation 2.49).

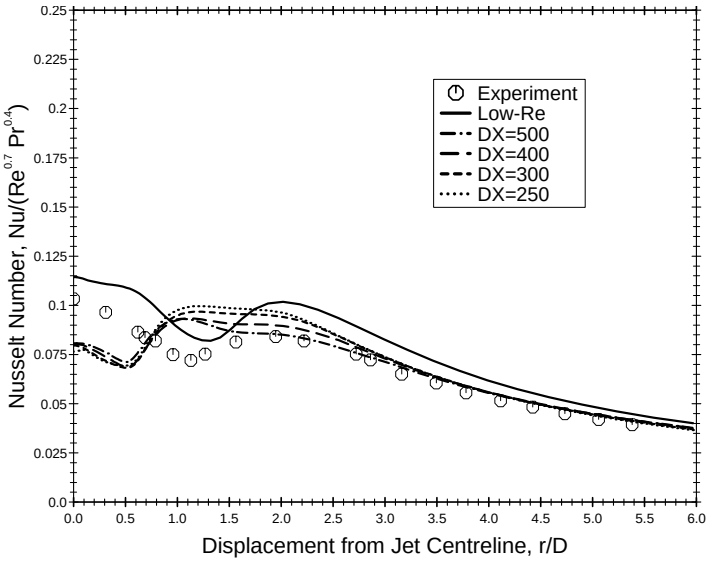

Figure 5.39: Nusselt number profiles obtained for the impinging jet flow using the Chieng & Launder wall function with the non-linear $k-\varepsilon$ model, the c_μ function of Equation (2.36) and differential Yap correction. Solid line: low-Reynolds-number model; broken lines: wall function results for different near-wall cell widths; symbols: experiments of Baughn *et al*. [94]. Normal stress components are included in the cell-averaged production term, $\overline{P_k}$, of the wall function (see Equation 2.49).

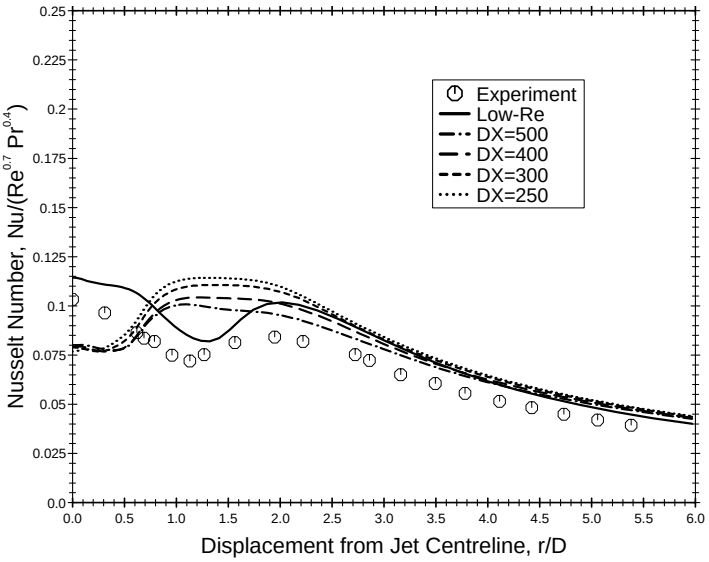

Figure 5.40: Nusselt number profiles obtained for the impinging jet flow using the Johnson & Launder wall function with the non-linear $k-\varepsilon$ model, the c_μ function of Equation (2.36) and differential Yap correction. Solid line: low-Reynolds-number model; broken lines: wall function results for different near-wall cell widths; symbols: experiments of Baughn *et al*. [94]. Normal stress components are included in the cell-averaged production term, $\overline{P_k}$, of the wall function (see Equation 2.49).

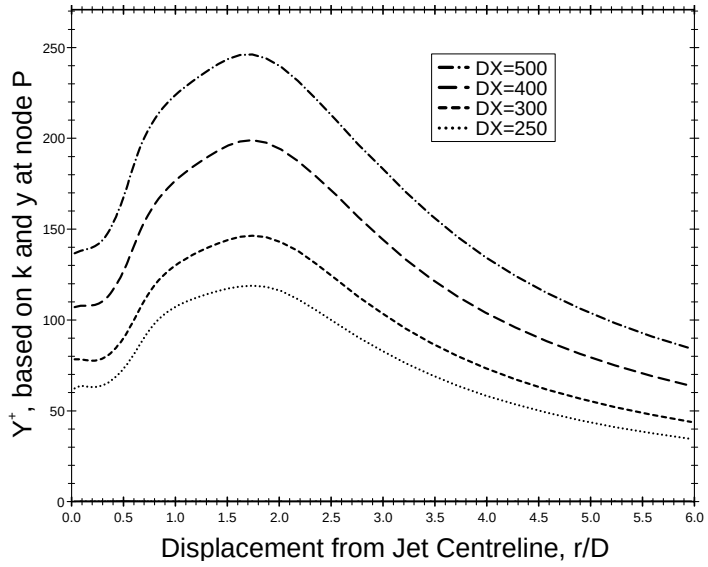

Figure 5.41: Calculated $y^+\left(=c_\mu^{1/4}k_P^{1/2}y_P/\nu\right)$ profiles obtained for the impinging jet flow using the Chieng & Launder wall function with the non-linear $k-\varepsilon$ model, the c_μ function of Equation (2.36) and differential Yap correction, corresponding to the Nusselt number profiles shown in Figure 5.39. Broken lines show wall function results for different near-wall cell widths.

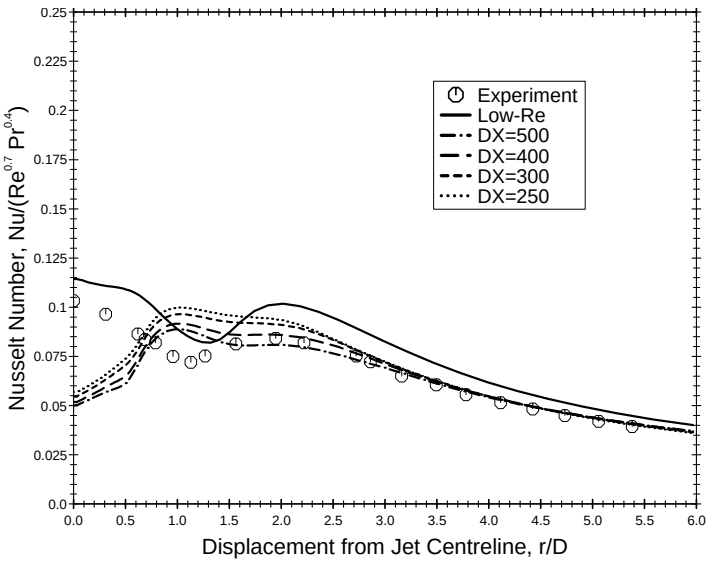

Figure 5.42: Nusselt number profiles obtained for the impinging jet flow using the Chieng & Launder wall function with the NLEVM of Craft *et al*. [67], the c_μ-function given by Equation (2.36) and the differential Yap correction. Solid line: low-Reynolds-number model; broken lines: wall function results for different near-wall cell widths; symbols: experiments of Baughn *et al*. [94]. Normal stress components are *not* included in the cell-averaged production term, $\overline{P_k}$, of the wall function.

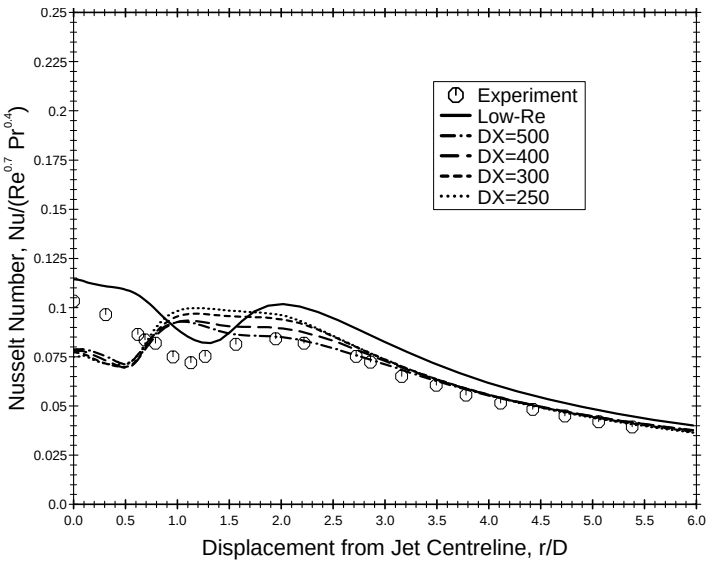

Figure 5.43: Nusselt number profiles obtained for the impinging jet flow using the Chieng & Launder wall function with the NLEVM of Craft *et al*. [67], the c_μ-function given by Equation (2.36) and the differential Yap correction. Solid line: low-Reynolds-number model; broken lines: wall function results for different near-wall cell widths; symbols: experiments of Baughn *et al*. [94]. The cell-averaged production term, $\overline{P_k}$, of the wall function is modified by assuming that the normal stresses vary linearly across the fully-turbulent region of the near-wall cell.

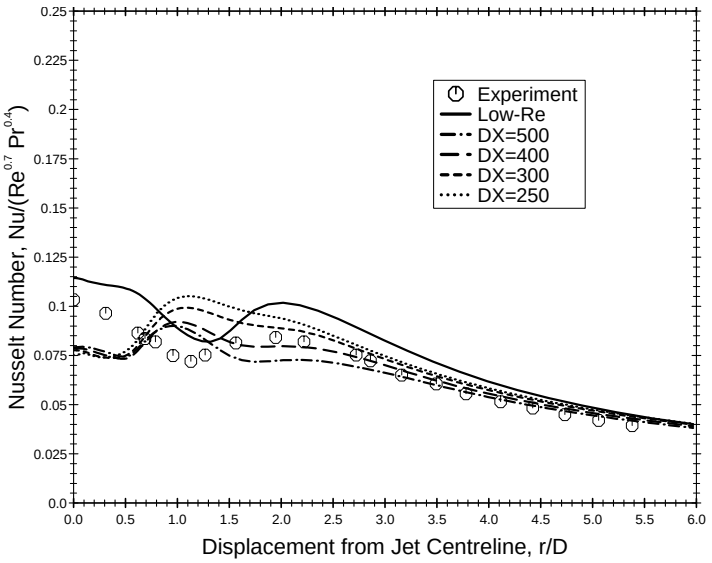

Figure 5.44: Nusselt number profiles obtained for the impinging jet flow using the Chieng & Launder wall function with the NLEVM of Craft *et al*. [67], the c_μ-function given by Equation (2.36) and the differential Yap correction. Solid line: low-Reynolds-number model; broken lines: wall function results for different near-wall cell widths; symbols: experiments of Baughn *et al*. [94]. The cell-averaged production term, $\overline{P_k}$, of the wall function is modified by assuming that the normal stresses vary linearly across the fully-turbulent region of the near-wall cell and that the Reynolds stresses vary according to their wall-limiting behaviour across the viscous sublayer.

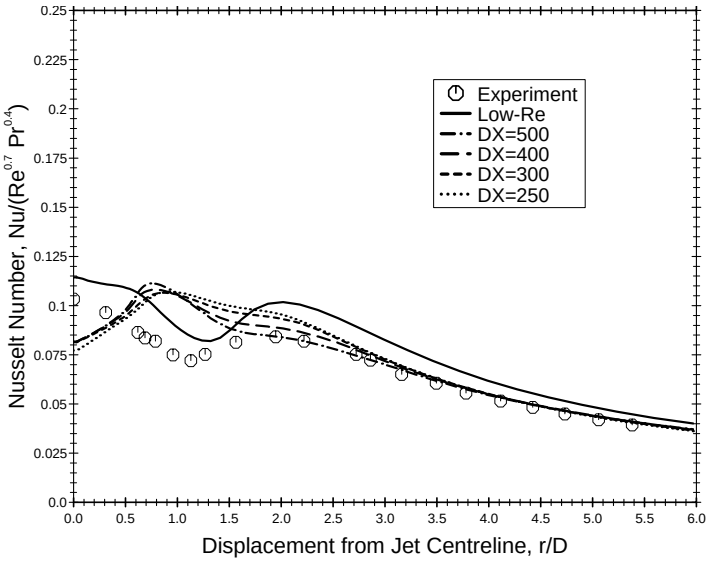

Figure 5.45: Nusselt number profiles obtained for the impinging jet flow using the Chieng & Launder wall function with the NLEVM of Craft *et al*. [67], the c_μ-function given by Equation (2.36) and the differential Yap correction. Solid line: low-Reynolds-number model; broken lines: wall function results for different near-wall cell widths; symbols: experiments of Baughn *et al*. [94]. Wall function results obtained using $\partial U/\partial y$ calculated from the derivative of the log-law in the near-wall cell for the non-linear stress terms and c_μ function.

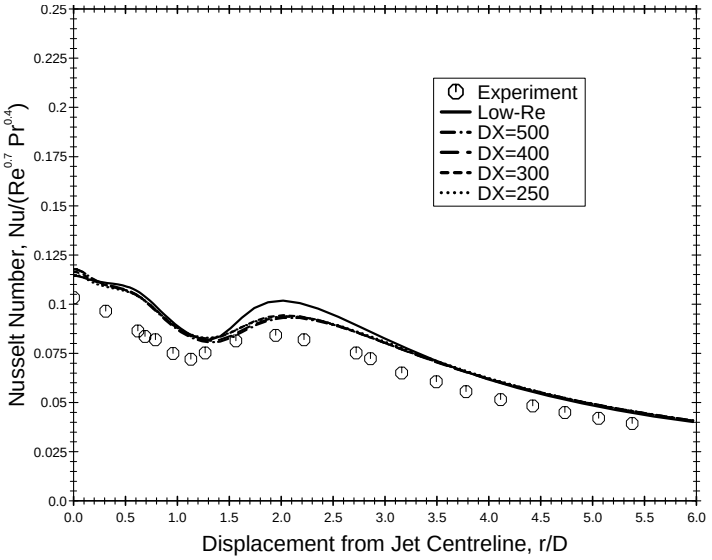

Figure 5.46: Nusselt number profiles obtained for the impinging jet flow using the UMIST-*N* wall function with the NLEVM of Craft *et al*. [67], the c_μ-function given by Equation (2.36) and the differential Yap correction. Solid line: low-Reynolds-number model; broken lines: wall function results for different near-wall cell widths; symbols: experiments of Baughn *et al*. [94].

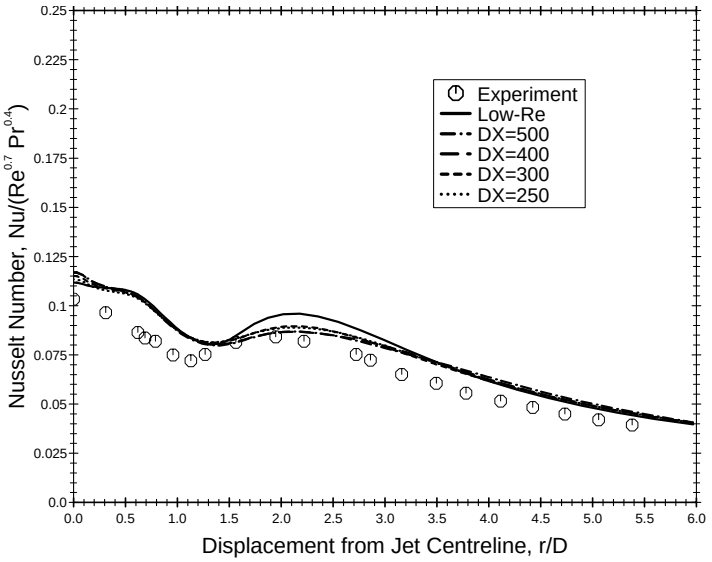

Figure 5.47: Nusselt number profiles obtained for the impinging jet flow using the UMIST-*N* wall function with the NLEVM of Craft *et al*. [30], the c_μ-function given by Equation (2.33) and the differential Yap correction. Solid line: low-Reynolds-number model; broken lines: wall function results for different near-wall cell widths; symbols: experiments of Baughn *et al*. [94].

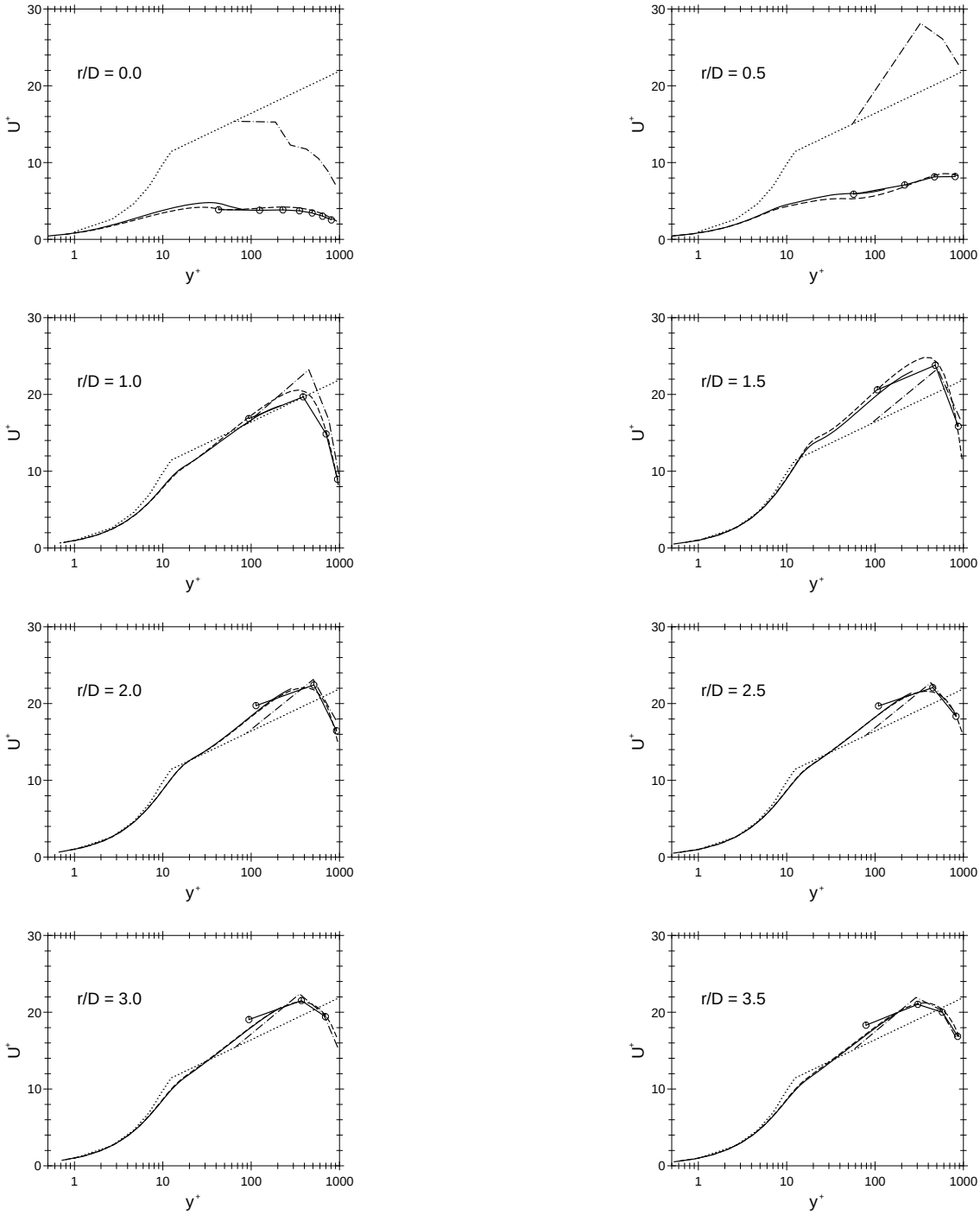

Figure 5.48: Semi-logarithmic velocity profiles for the impinging jet flow at 8 radial locations. —⊖—: UMIST-*N* wall function (circles indicate the position of main-grid nodes); – – –: low-*Re* model; – . –: Chieng & Launder wall function; ....: "universal" log-law. All results shown used the non-linear $k-\varepsilon$ model with the c_μ function given by Equation (2.36) and differential Yap correction. Wall function calculations used the $DX = 250$ grid shown in Figure 5.9. Results shown for $r/D = 0$ are taken at the node adjacent to the axis of symmetry. Equation (2.44) is used to define U^+ and y^+.

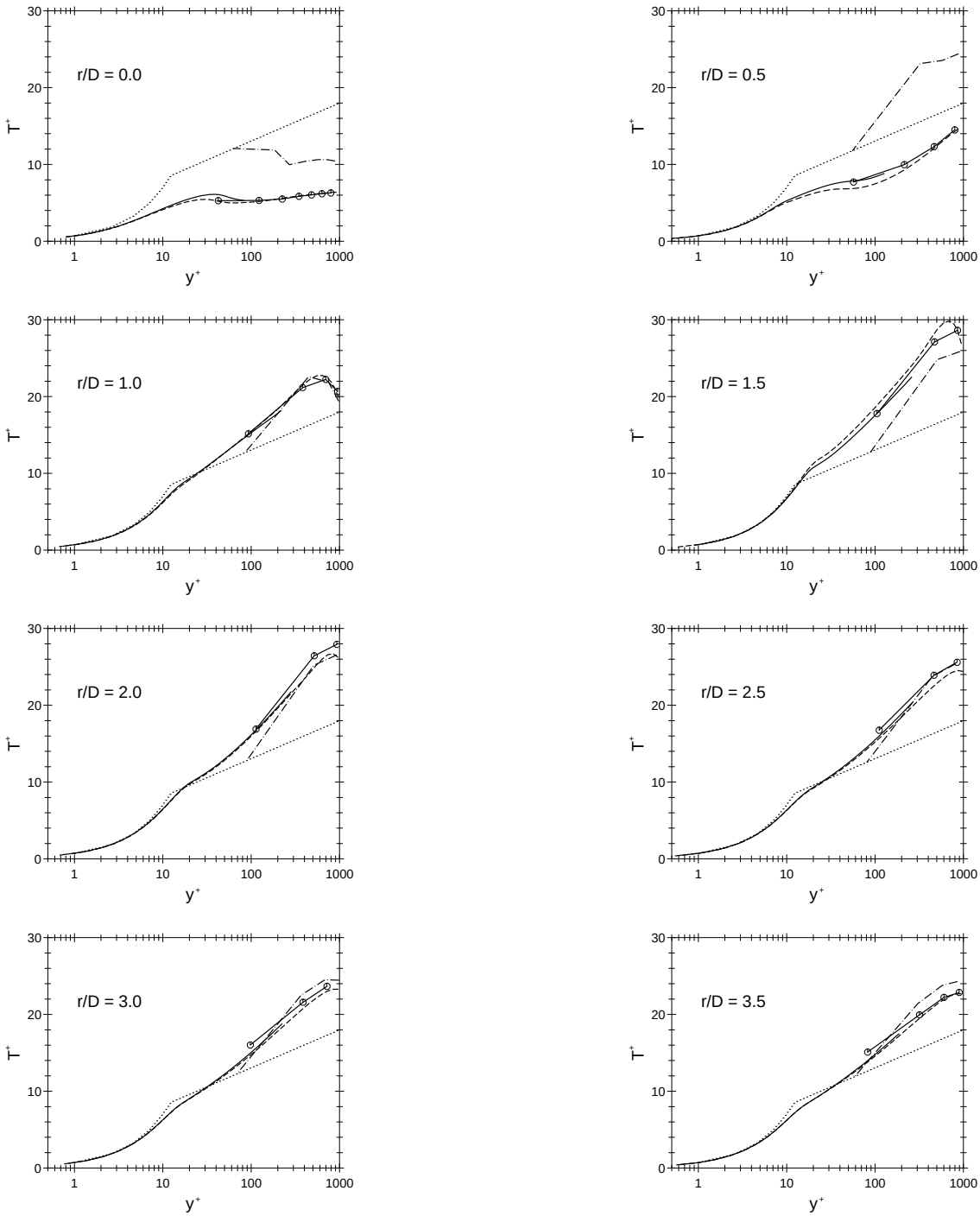

Figure 5.49: Semi-logarithmic temperature profiles for the impinging jet flow at 8 radial locations. —○—: UMIST-*N* wall function (circles indicate the position of main-grid nodes); – – –: low-*Re* model; – . –: Chieng & Launder wall function; .....: "universal" log-law. All results shown used the non-linear $k-\varepsilon$ model with the c_μ function given by Equation (2.36) and differential Yap correction. Wall function calculations were performed using the $DX = 250$ grid shown in Figure 5.9. Results shown for $r/D = 0$ are taken at the node adjacent to the axis of symmetry. The friction velocity used to define y^+ was found from $U_\tau = c_\mu^{1/4} k^{1/2}$.

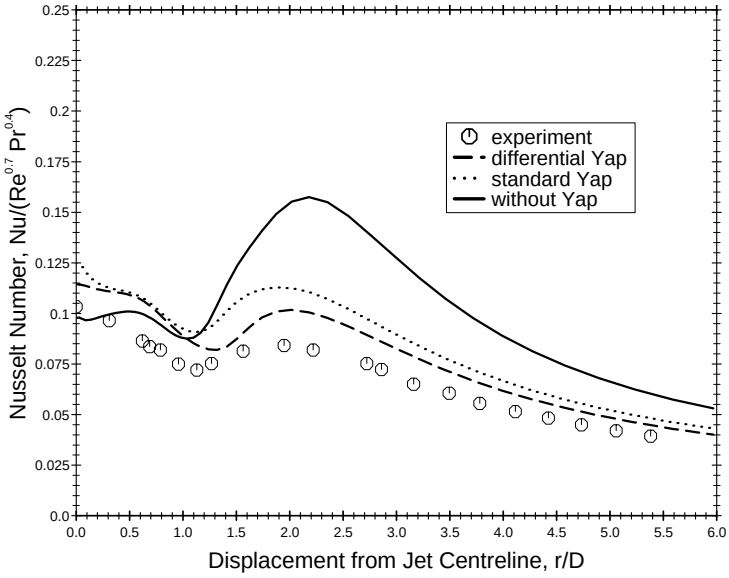

Figure 5.50: Nusselt number profiles for the impinging jet obtained using the low-*Re* NLEVM of Craft *et al*. [67] and the c_μ-function given by Equation (2.36) without any Yap correction, with the standard Yap correction (Equation 2.16) and with the differential Yap correction (Equation 2.17). Symbols: experiments of Baughn *et al*. [94].

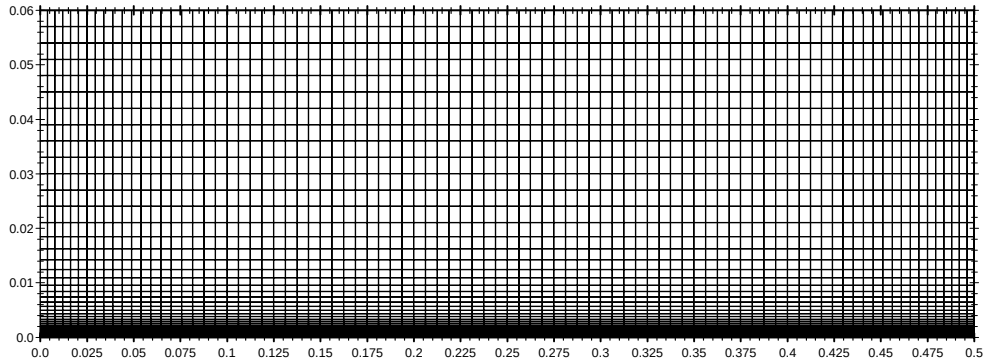

Figure 6.2: Low-Reynolds-number 90×70 (radial$\times$axial) grid used in the free-disc flow.

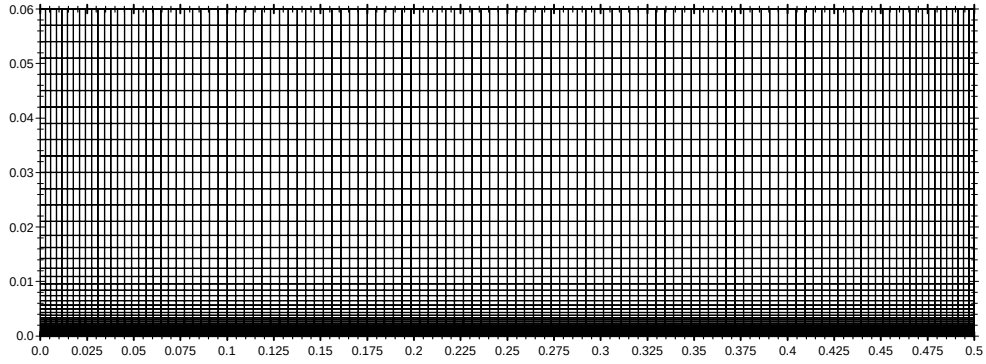

Figure 6.3: Low-Reynolds-number 120×70 (radial$\times$axial) grid used in the free-disc flow.

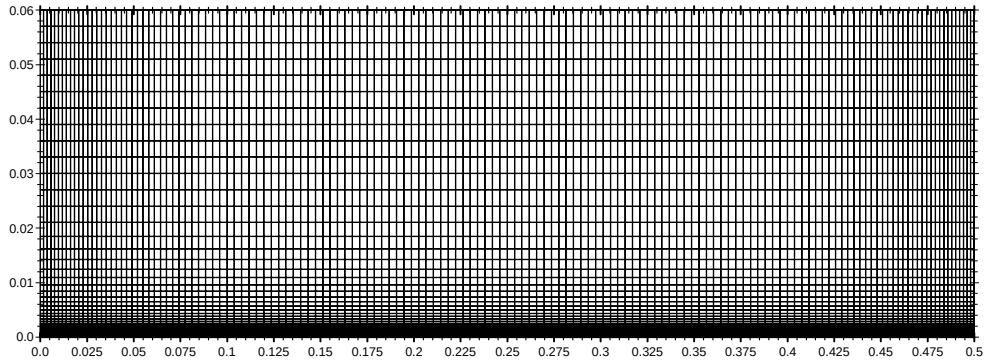

Figure 6.4: Low-Reynolds-number 150×70 (radial$\times$axial) grid used in the free-disc flow.

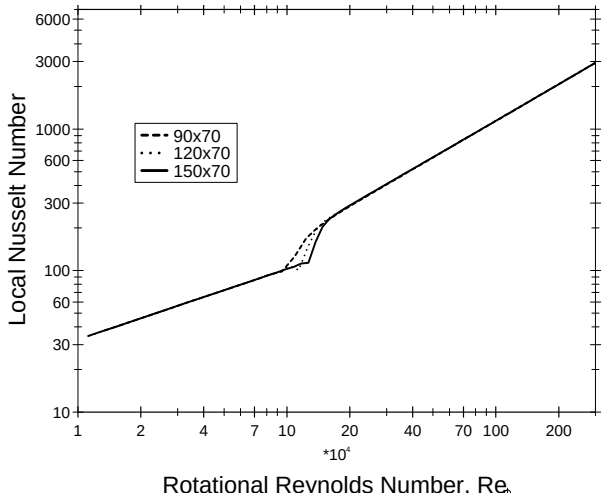

Figure 6.5: Predicted Nusselt number in the free-disc flow with the low-*Re* linear $k-\varepsilon$ model using three different radial grid densities; - - -: 90×70 grid; .....: 120×70 grid; ——: 150×70 grid.

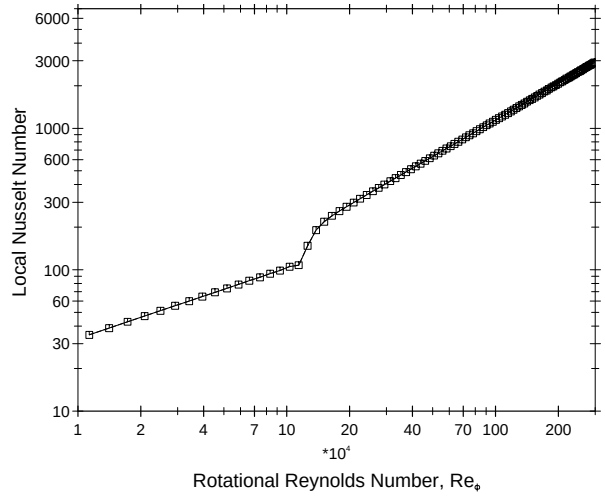

Figure 6.6: Predicted Nusselt number in the free-disc flow with the low-*Re* linear $k-\varepsilon$ model for the 120×70 grid; □: location of radial nodes.

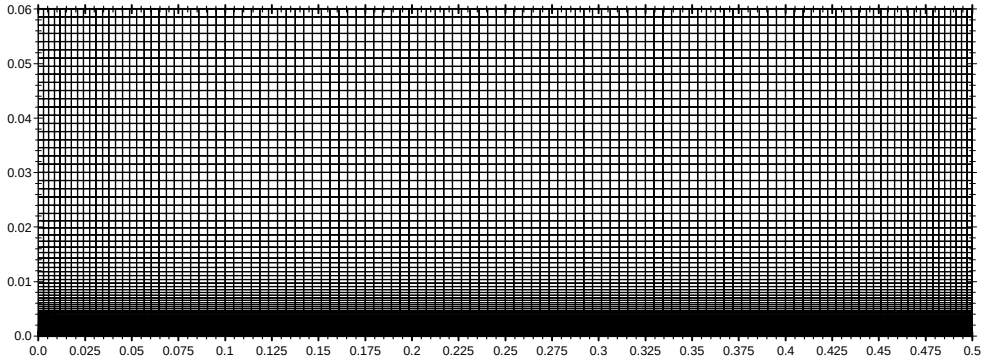

Figure 6.7: Low-Reynolds-number 120×120 grid used in the free-disc flow.

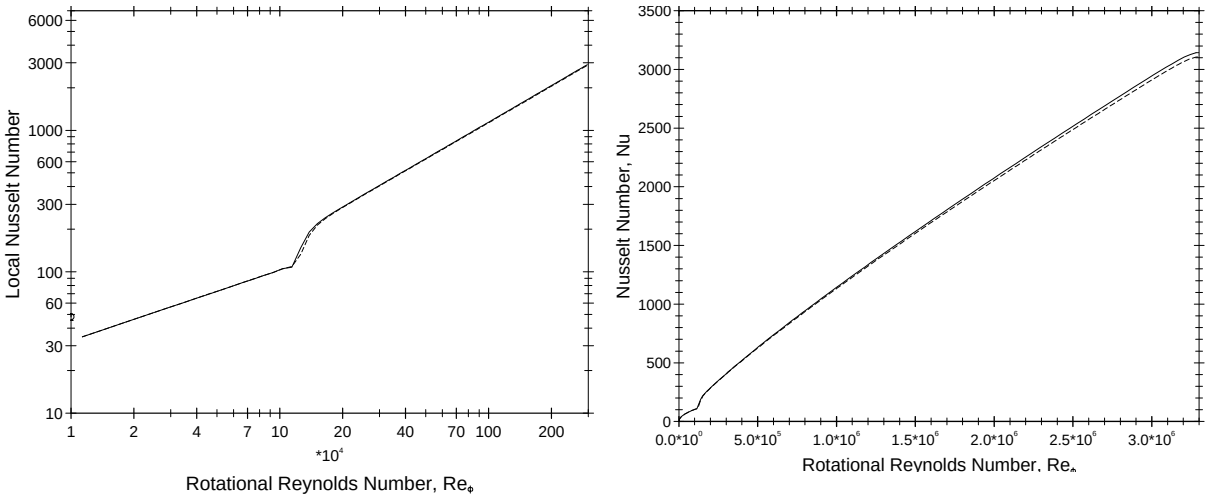

Figure 6.8: Predicted Nusselt number in the free-disc flow with axial refinement of the grid using the low-*Re* Launder & Sharma model; ——: 120×70 (radial$\times$axial) grid; - - -: 120×120 grid; *a*.) semi-log scale (left); *b*.) linear scale (right).

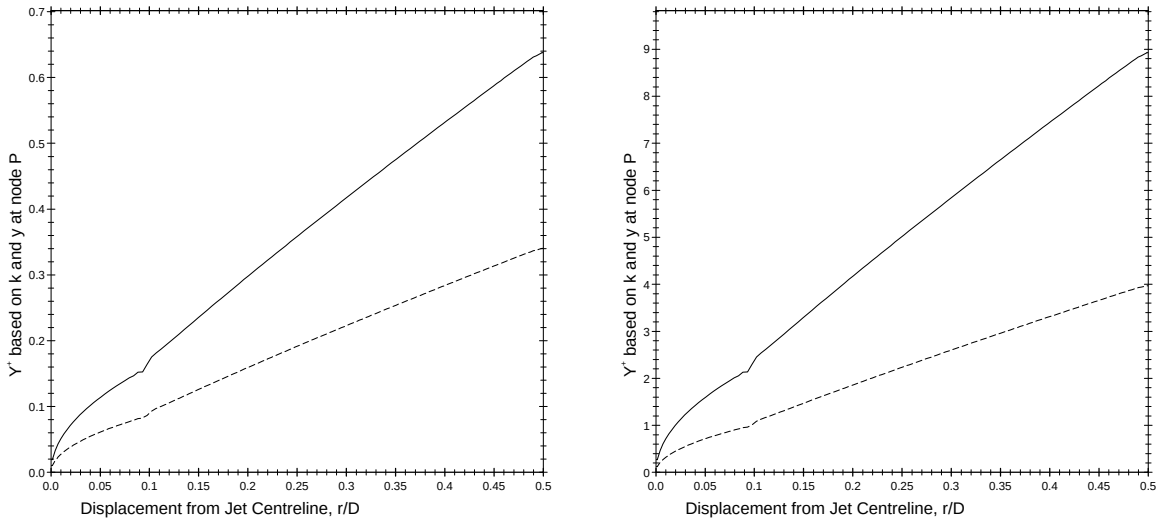

Figure 6.9: Predicted dimensionless wall distance, $y^+ = U_\tau y/\nu$ (where $U_\tau = \sqrt{\tau_{wall}/\rho}$ and τ_{wall} is the resultant wall shear stress), in the free-disc flow with axial refinement of the grid using the low-*Re* Launder & Sharma model; ——: 120×70 (radial$\times$axial) grid; - - -: 120×120 grid; *a*.) wall-adjacent node (left); *b*.) tenth node from the wall (right).

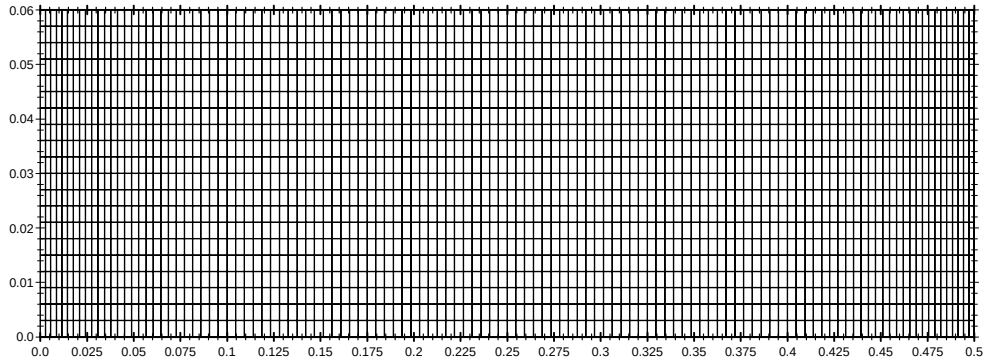

Figure 6.10: High-Reynolds-number 120×22 (radial$\times$axial) grid used in the free-disc flow.

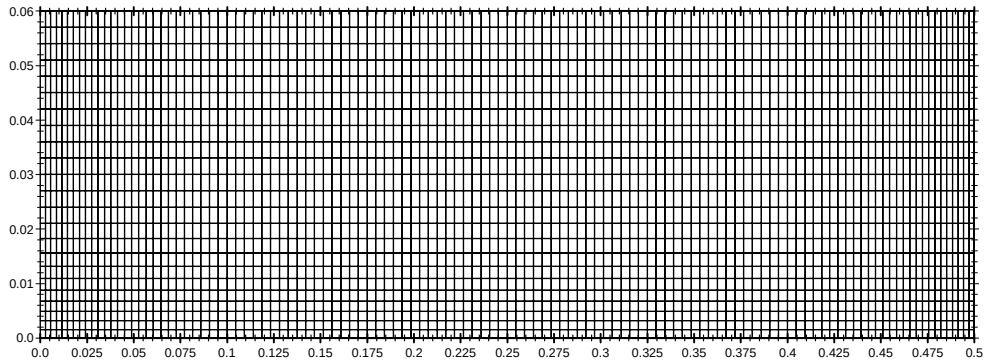

Figure 6.11: High-Reynolds-number 120×25 (radial$\times$axial) grid used in the free-disc flow.

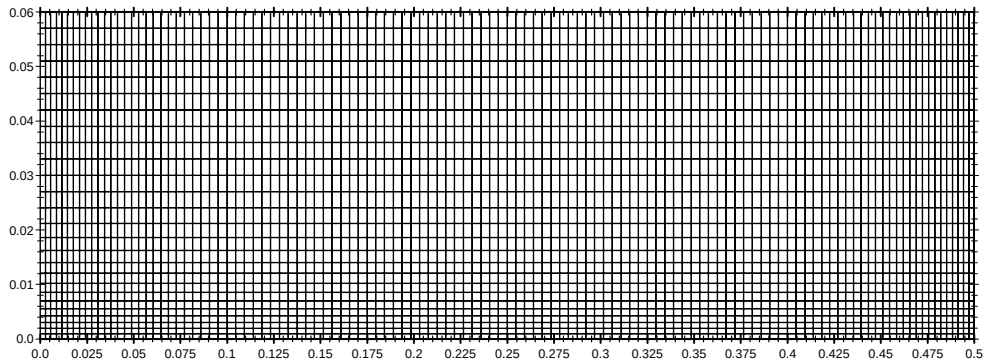

Figure 6.12: High-Reynolds-number 120×28 (radial$\times$axial) grid used in the free-disc flow.

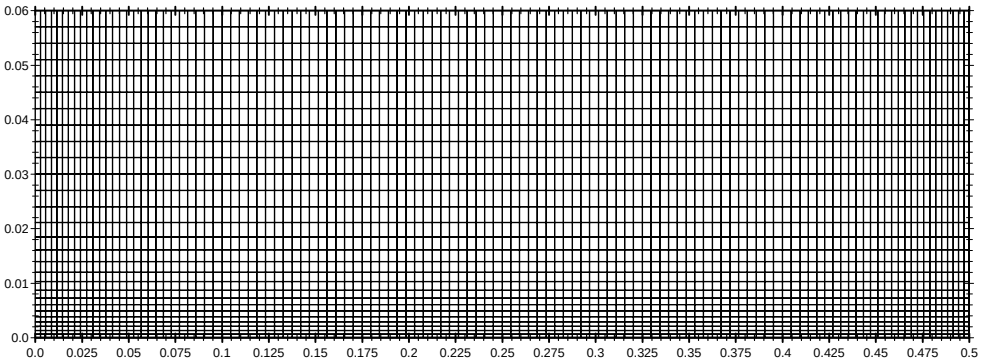

Figure 6.13: High-Reynolds-number 120×30 (radial$\times$axial) grid used in the free-disc flow.

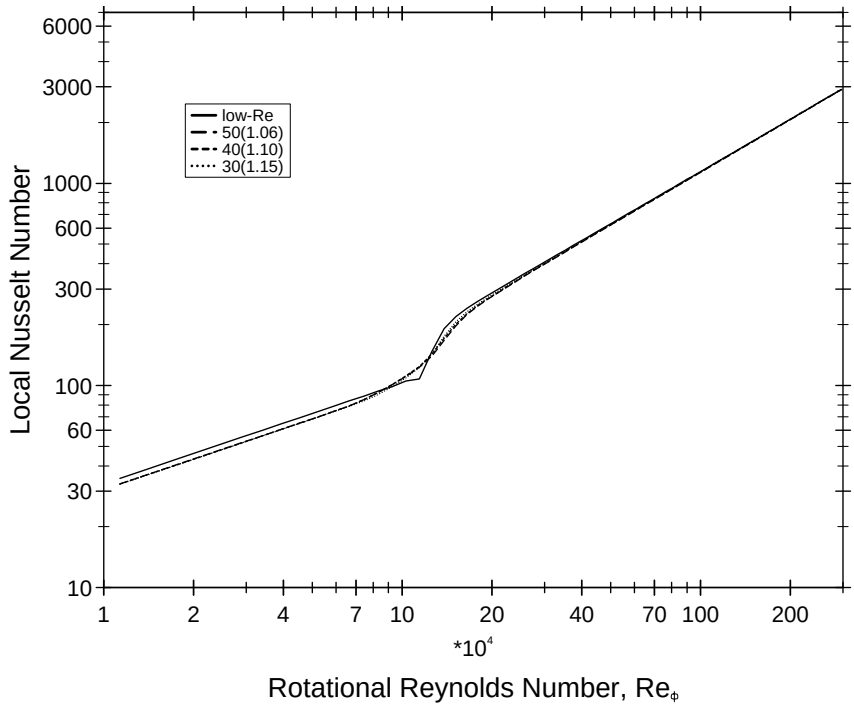

Figure 6.14: Predicted Nusselt number in the free-disc flow using the UMIST-*N* wall function and linear $k-\varepsilon$ model with different subgrid node density for the 120×28 main-grid (the key shows the number of subgrid nodes with the expansion ratio used to generate the subgrid mesh in parentheses).

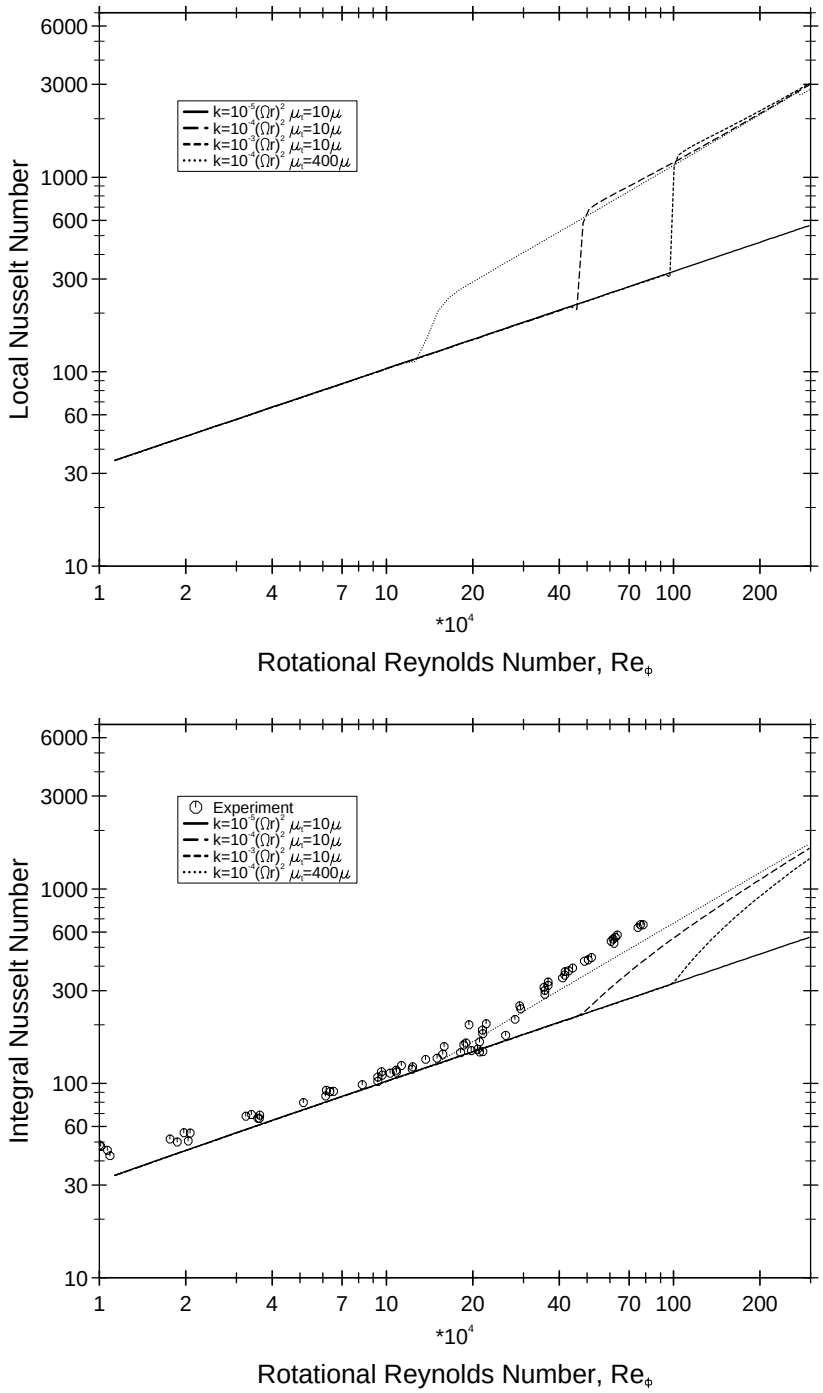

Figure 6.15: Predicted Nusselt number in the free-disc flow using the low-*Re* Launder & Sharma $k-\varepsilon$ model with different initial turbulence levels; ○: Cobb & Saunders experiments; *a*.) local Nusselt number (top); *b*.) integral Nusselt number (bottom).

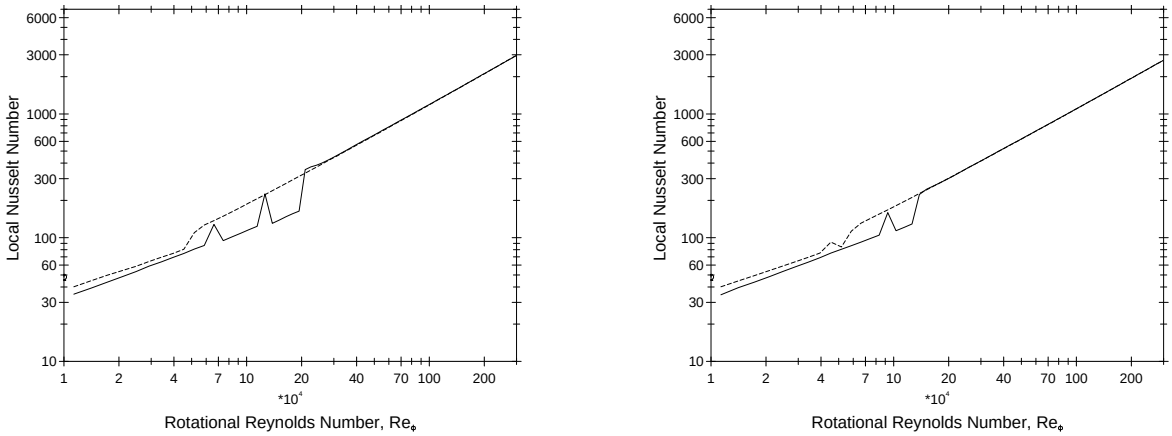

Figure 6.16: Predicted Nusselt number in the free-disc flow with two initial turbulence conditions, ——: $k = 10^{-5}\,(\Omega r_b)^2$ and $\mu_t = 10\mu$; - - -: $k = 10^{-5}\,(\Omega r_b)^2$ and $\mu_t = 400\mu$. Results obtained with the simplified Chieng & Launder (left) and Chieng & Launder wall function (right).

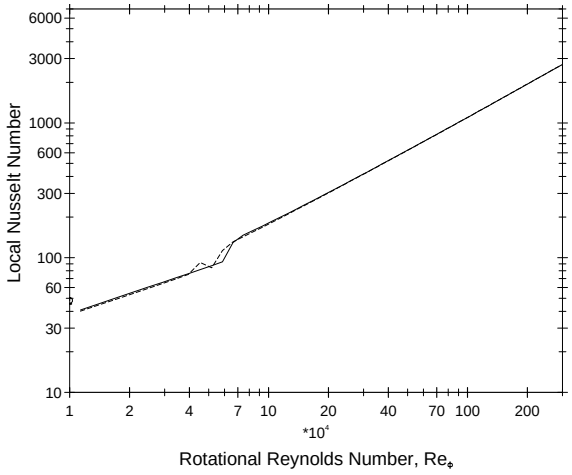

Figure 6.17: Predicted Nusselt number in the free-disc flow using the Chieng & Launder wall function with two different levels of under-relaxation; ——: $\alpha_{U,V,W} = 0.1$, $\alpha_P = 0.2$, $\alpha_{k,\varepsilon} = 0.1$ and $\alpha_T = 0.4$; - - -: $\alpha_{U,V,W} = 0.2$, $\alpha_P = 0.3$, $\alpha_{k,\varepsilon} = 0.1$ and $\alpha_T = 0.4$.

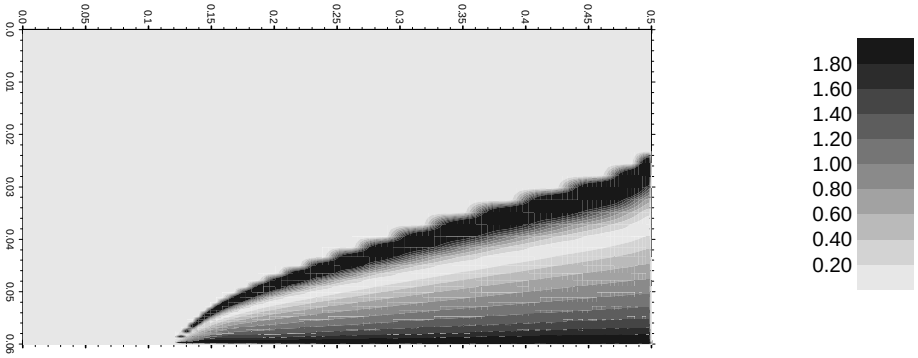

Figure 6.18: Predicted turbulent length scale gradient $\left(\left|\partial l/\partial x_j\right|\right)$ in the free-disc flow. Radial distance (r/D) is on the horizontal axis and axial distance (y/D) on the vertical axis. Transition from laminar to turbulent flow can be seen to occur at $r/D \approx 0.12$.

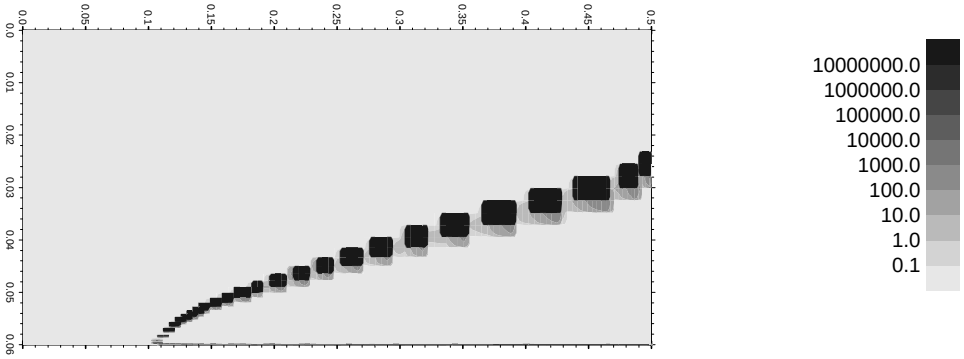

Figure 6.19: Predicted Yap correction using Equation (2.17) and $c_w = 0.83$ in the free-disc flow. Radial distance (r/D) is on the horizontal axis and axial distance (y/D) on the vertical axis.

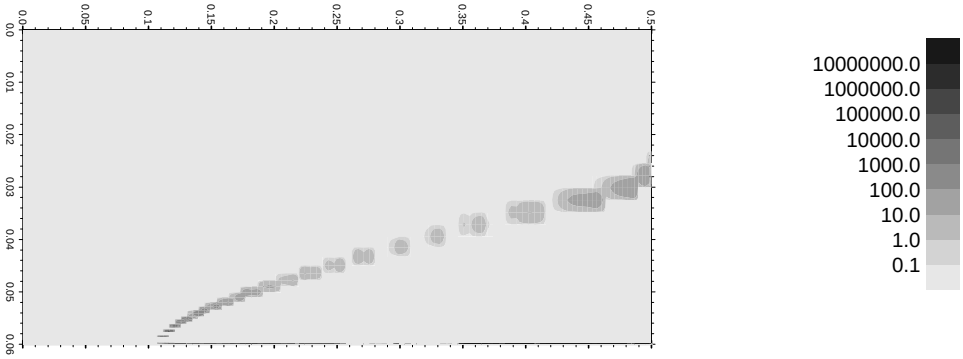

Figure 6.20: Predicted Yap correction in the free-disc flow using Equation (2.17) with c_w given by Equation (2.20). Radial distance (r/D) is on the horizontal axis and axial distance (y/D) on the vertical axis.

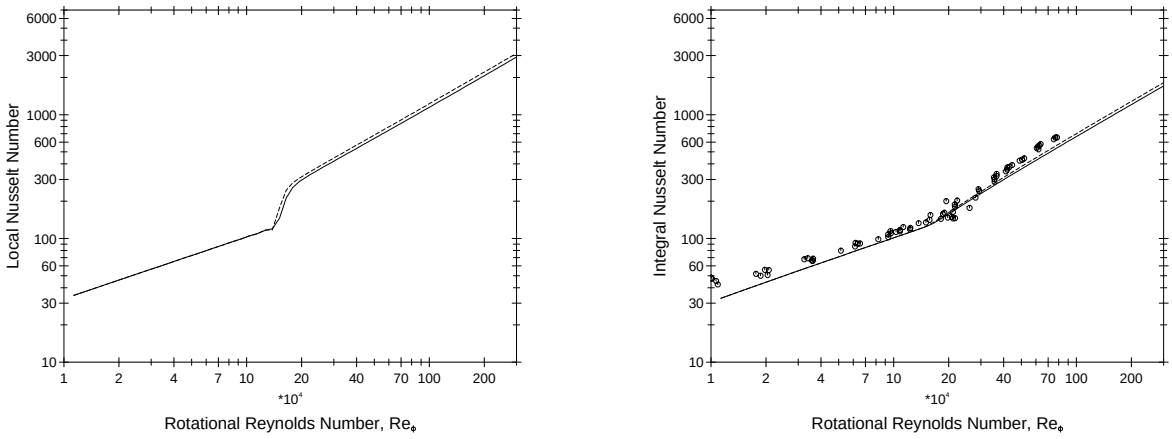

Figure 6.21: Predicted Nusselt number in the free-disc flow using the low-Reynolds-number NLEVM: ——: with differential Yap correction; - - -: without differential Yap correction; ○: experimental values from Cobb & Saunders [130]; *a*.) local Nusselt number (left); *b*.) integral Nusselt number (right).

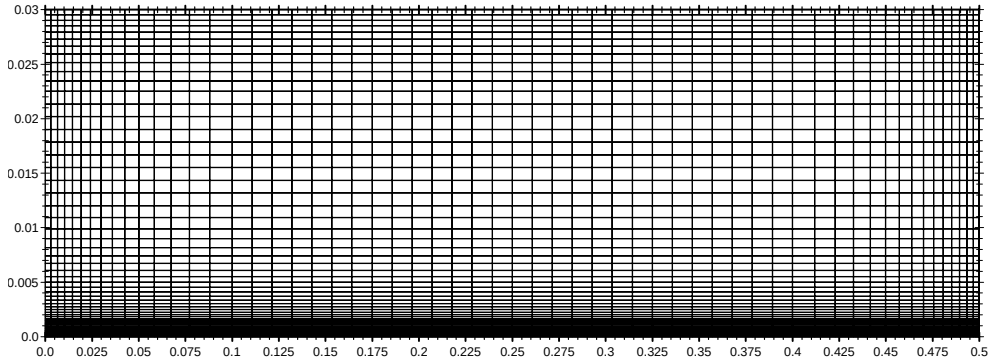

Figure 6.22: 60×60 grid used for laminar free-disc flow validation.

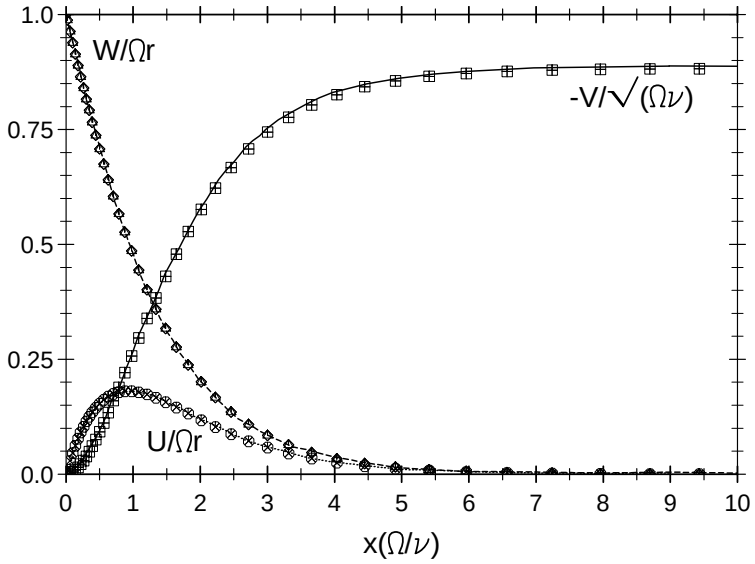

Figure 6.23: Velocity profiles for laminar free-disc flow; lines show the solution of the von Kármán equations by Owen & Rogers [132] ....: $U/\Omega r$; ——: $-V/\sqrt{\Omega\nu}$; - - -: $W/\Omega r$; (where U, V and W are respectively the radial, axial and tangential velocity); symbols indicate corresponding velocity predictions using the linear $k-\varepsilon$ model and the 60×60 grid shown in Figure 6.22 at three different rotational Reynolds numbers, $Re_\phi = 9000$, 25000 and 49000.

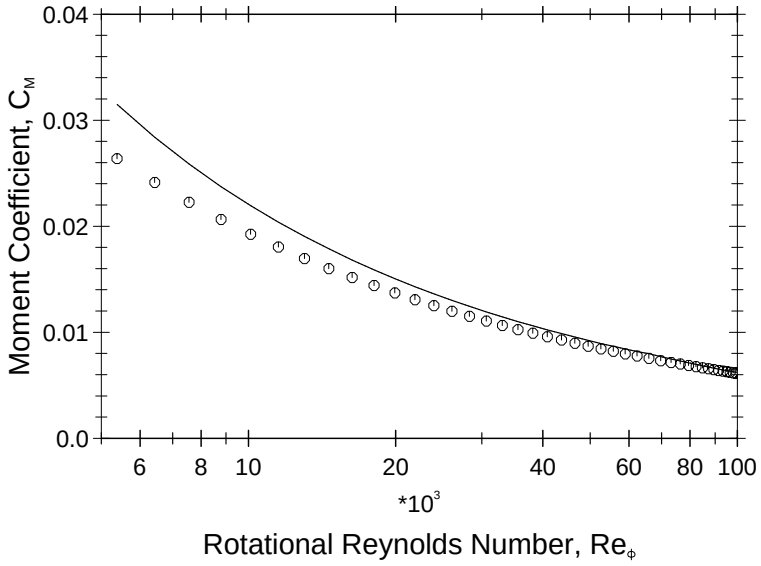

Figure 6.24: Predicted moment coefficient for laminar free-disc flow using the linear $k-\varepsilon$ model and the 60×60 grid shown in Figure 6.22. ○: Cochran's numerical solution of von Kármán's equations for laminar flow over the free-disc [131].

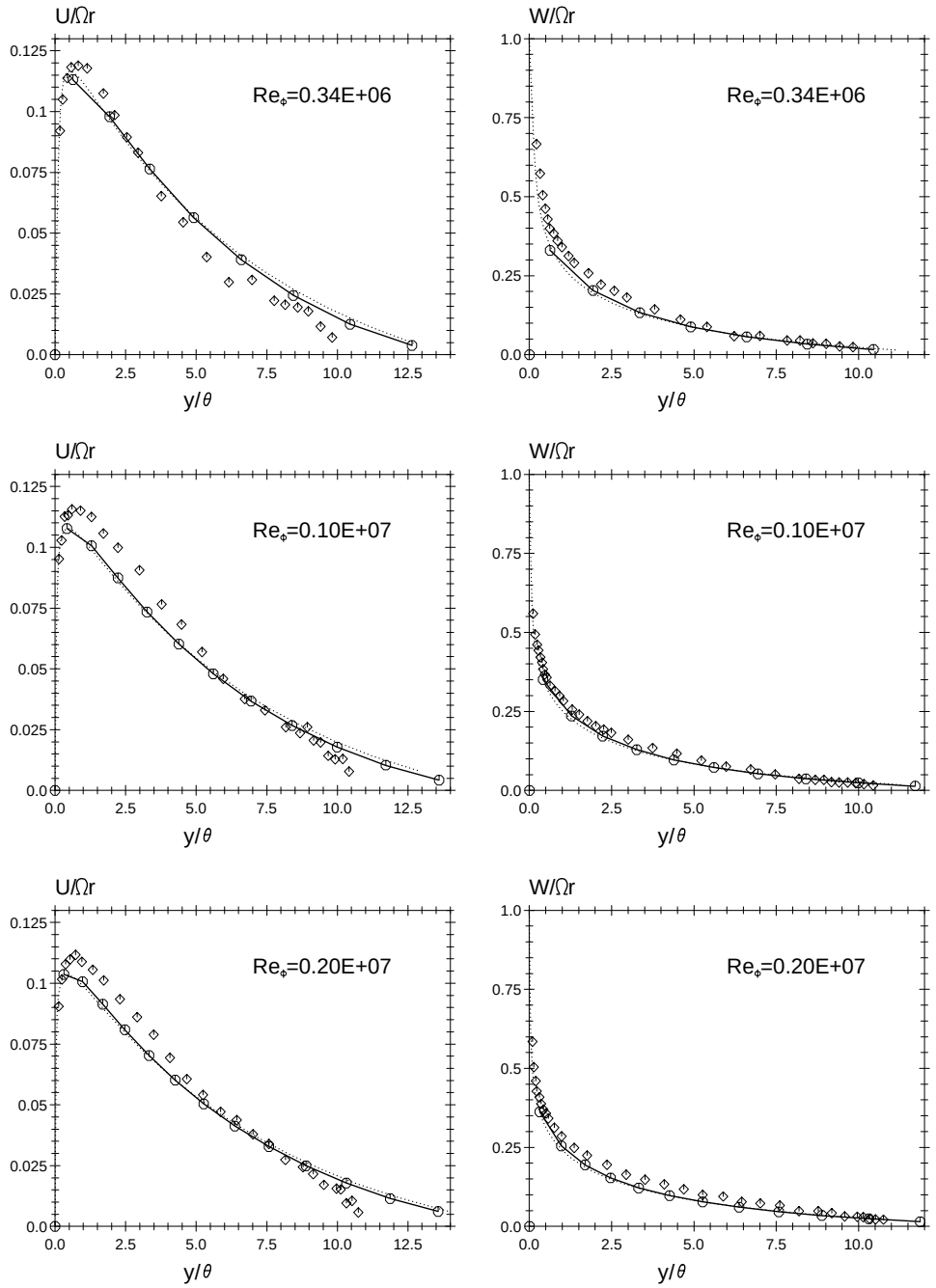

Figure 6.25: Radial and tangential velocity profiles in the free-disc flow using the TEAM wall function and linear $k-\varepsilon$ model with the 120×28 grid; —○—: high-*Re* model prediction (circles indicate the position of nodes); .....: low-*Re* model prediction; ◊: Cham & Head experiments.

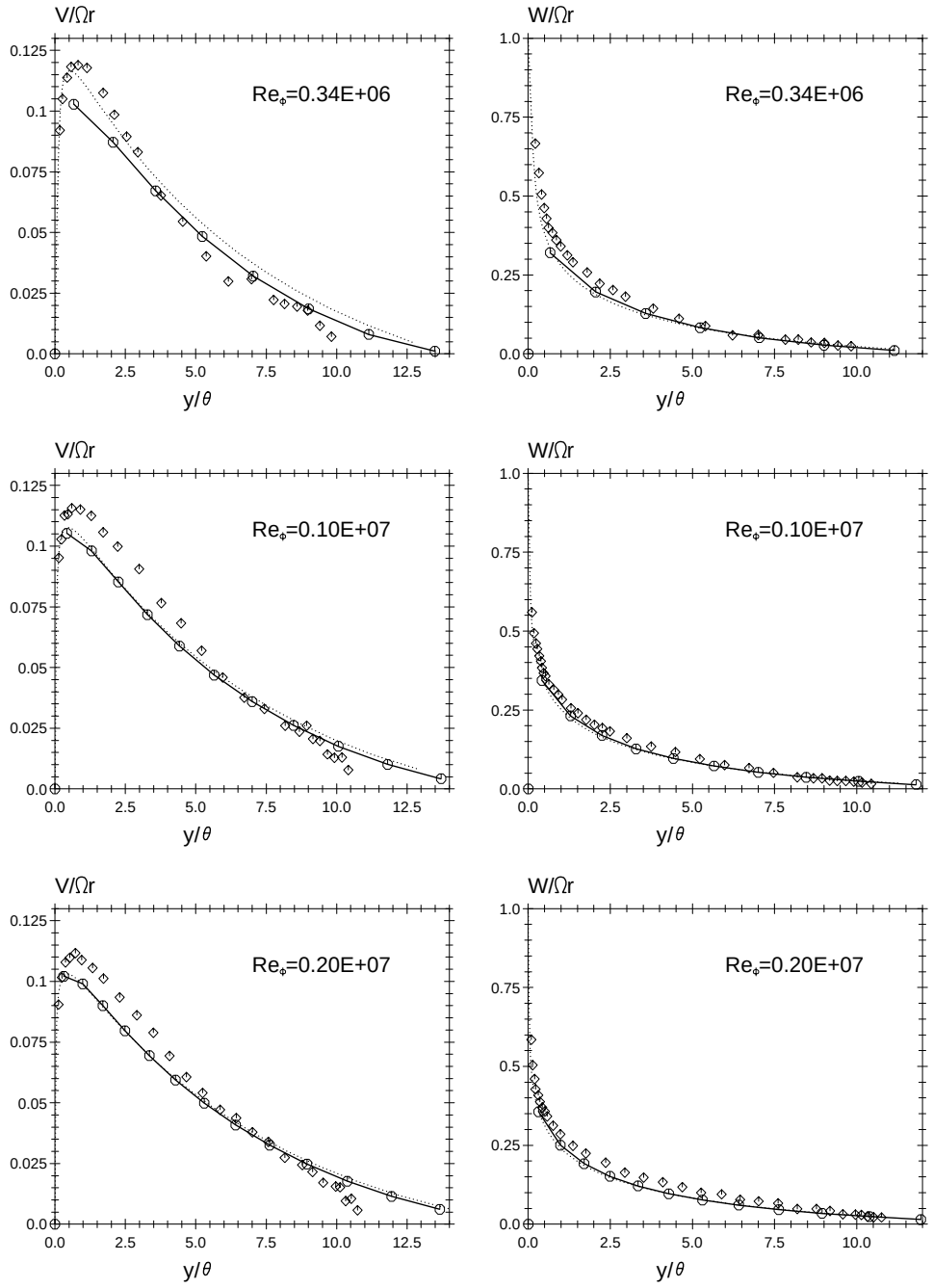

Figure 6.26: Radial and tangential velocity profiles in the free-disc flow using the simplified Chieng & Launder wall function and linear $k-\varepsilon$ model with the 120×28 grid; —○—: high-*Re* model prediction (circles indicate the position of nodes); .....: low-*Re* model prediction; ♢: Cham & Head experiments.

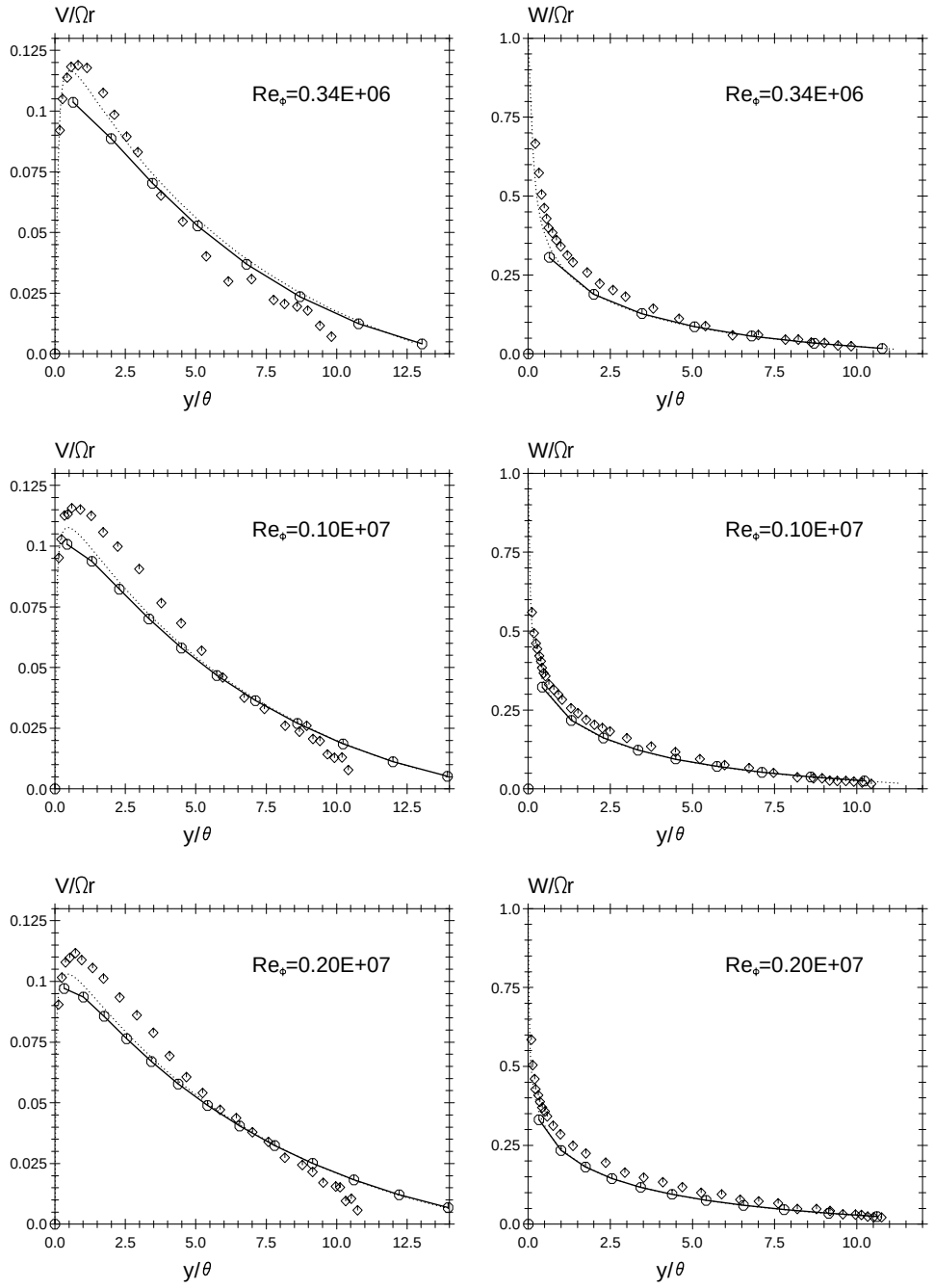

Figure 6.27: Radial and tangential velocity profiles in the free-disc flow using the Chieng & Launder wall function and linear $k-\varepsilon$ model with the 120×28 grid; —⊖—: high-*Re* model prediction (circles indicate the position of nodes); .....: low-*Re* model prediction; ♢: Cham & Head experiments.

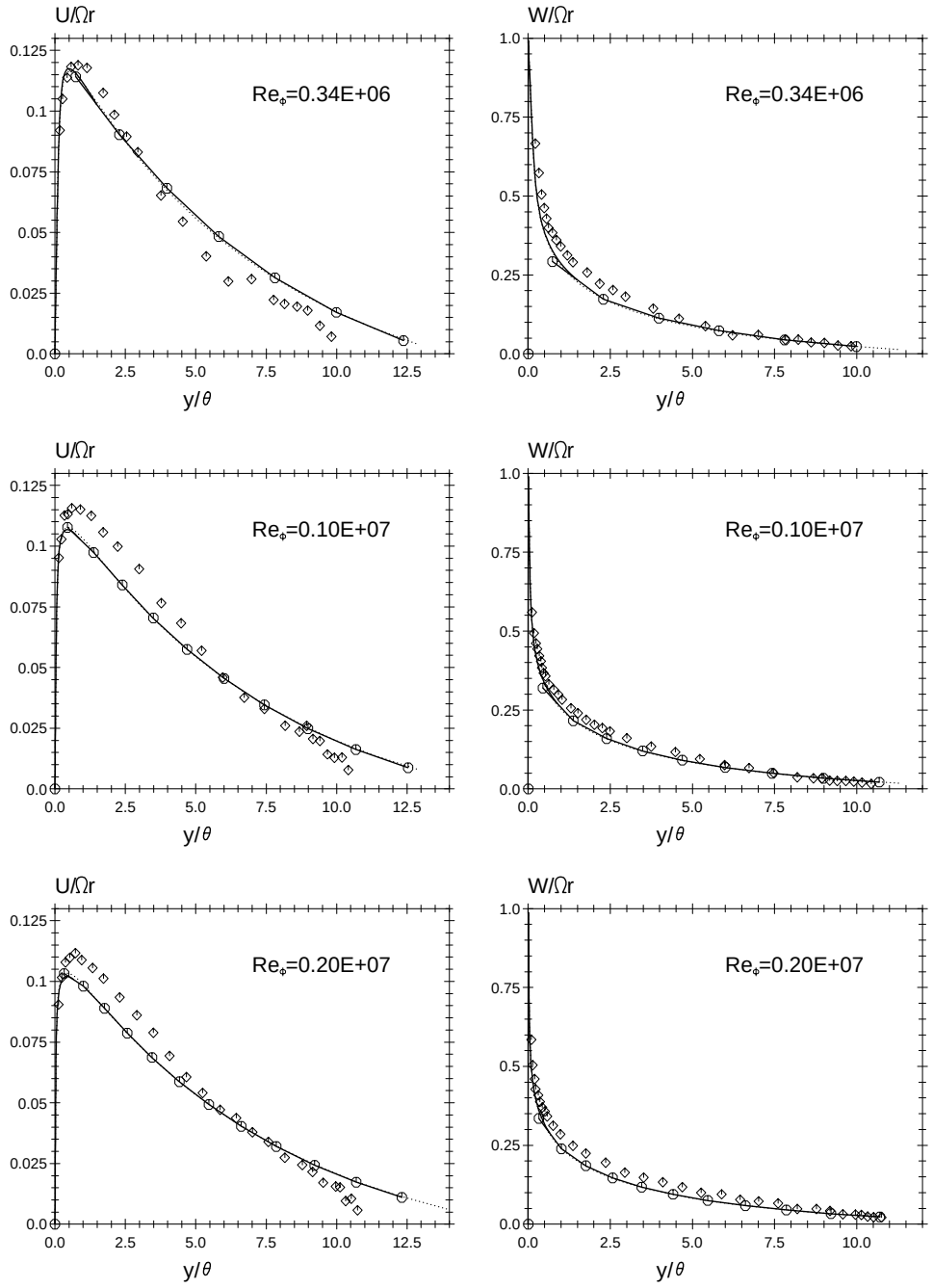

Figure 6.28: Radial and tangential velocity profiles in the free-disc flow using the UMIST-*N* wall function and linear $k-\varepsilon$ model with the 120×28 grid; —⊖—: high-*Re* model prediction (circles indicate the position of nodes); .....: low-*Re* model prediction; ♢: Cham & Head experiments.

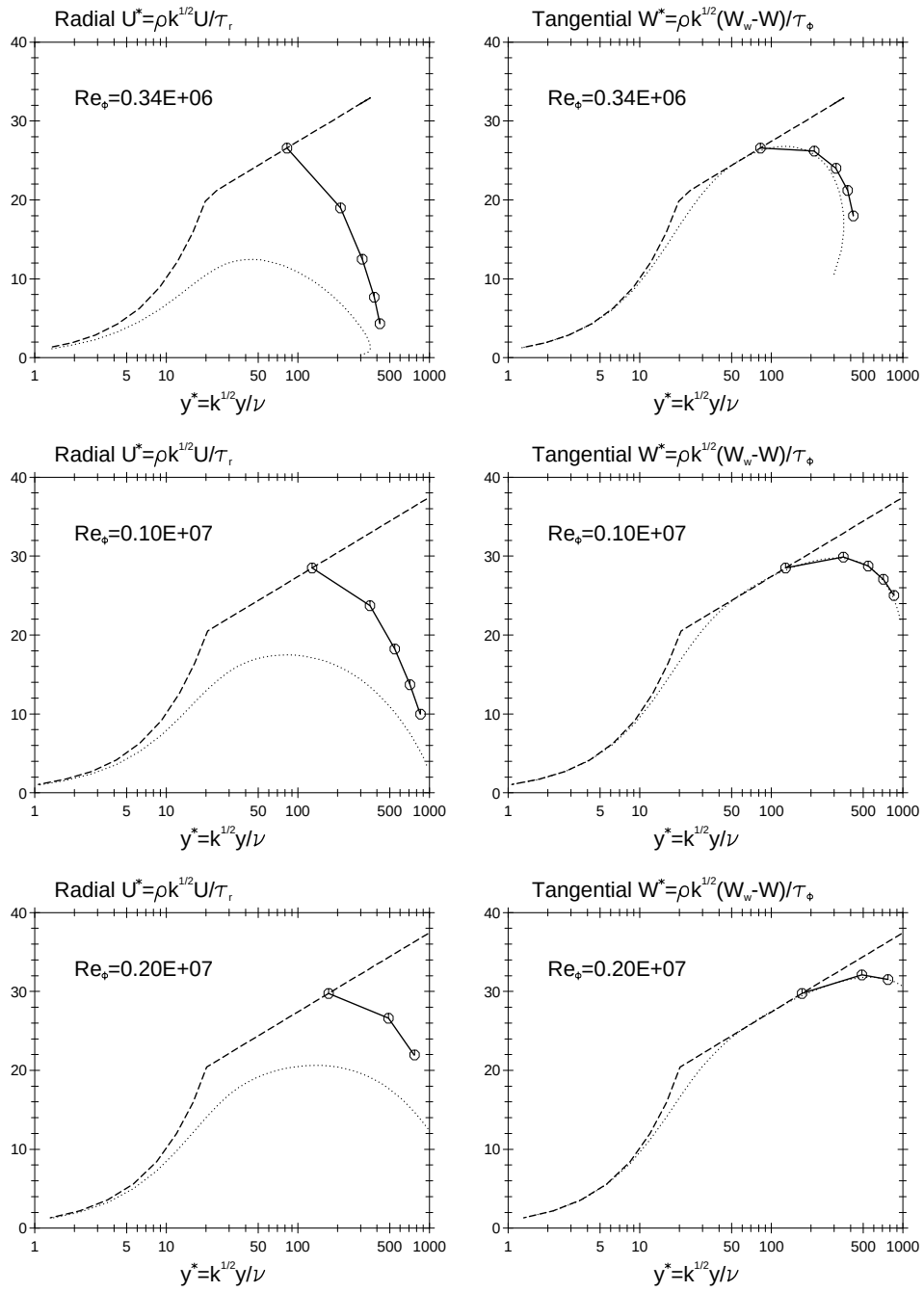

Figure 6.29: Radial and tangential velocity profiles in the free-disc flow using the TEAM wall function and linear $k-\varepsilon$ model with the 120×28 grid; —○—: high-*Re* model prediction (circles indicate the position of nodes); .....: low-*Re* model prediction; - - -: "universal" log-law.

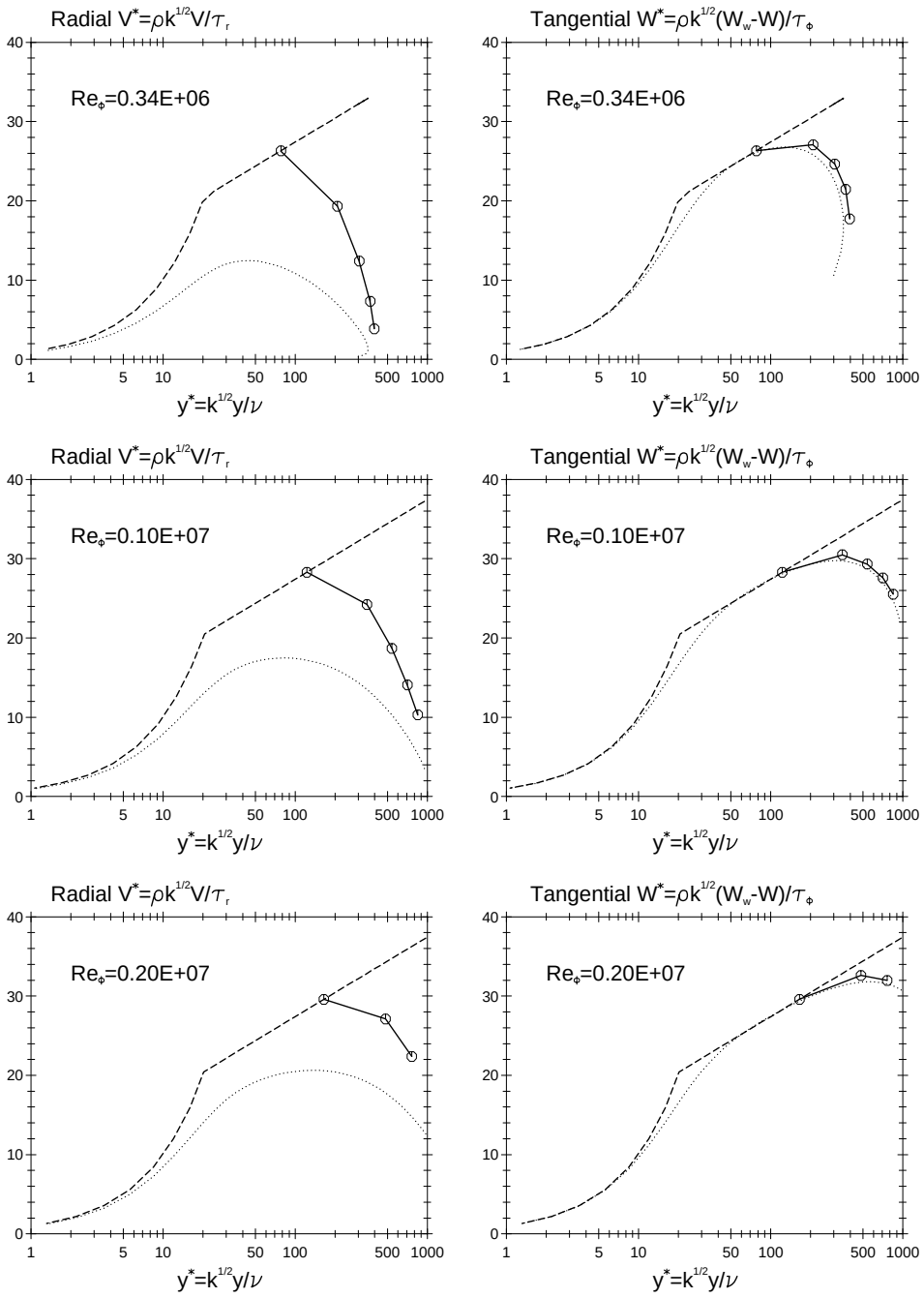

Figure 6.30: Radial and tangential velocity profiles in the free-disc flow using the simplified Chieng & Launder wall function and linear $k-\varepsilon$ model with the 120×28 grid; —○—: high-*Re* model prediction (circles indicate the position of nodes); .....: low-*Re* model prediction; - - -: "universal" log-law.

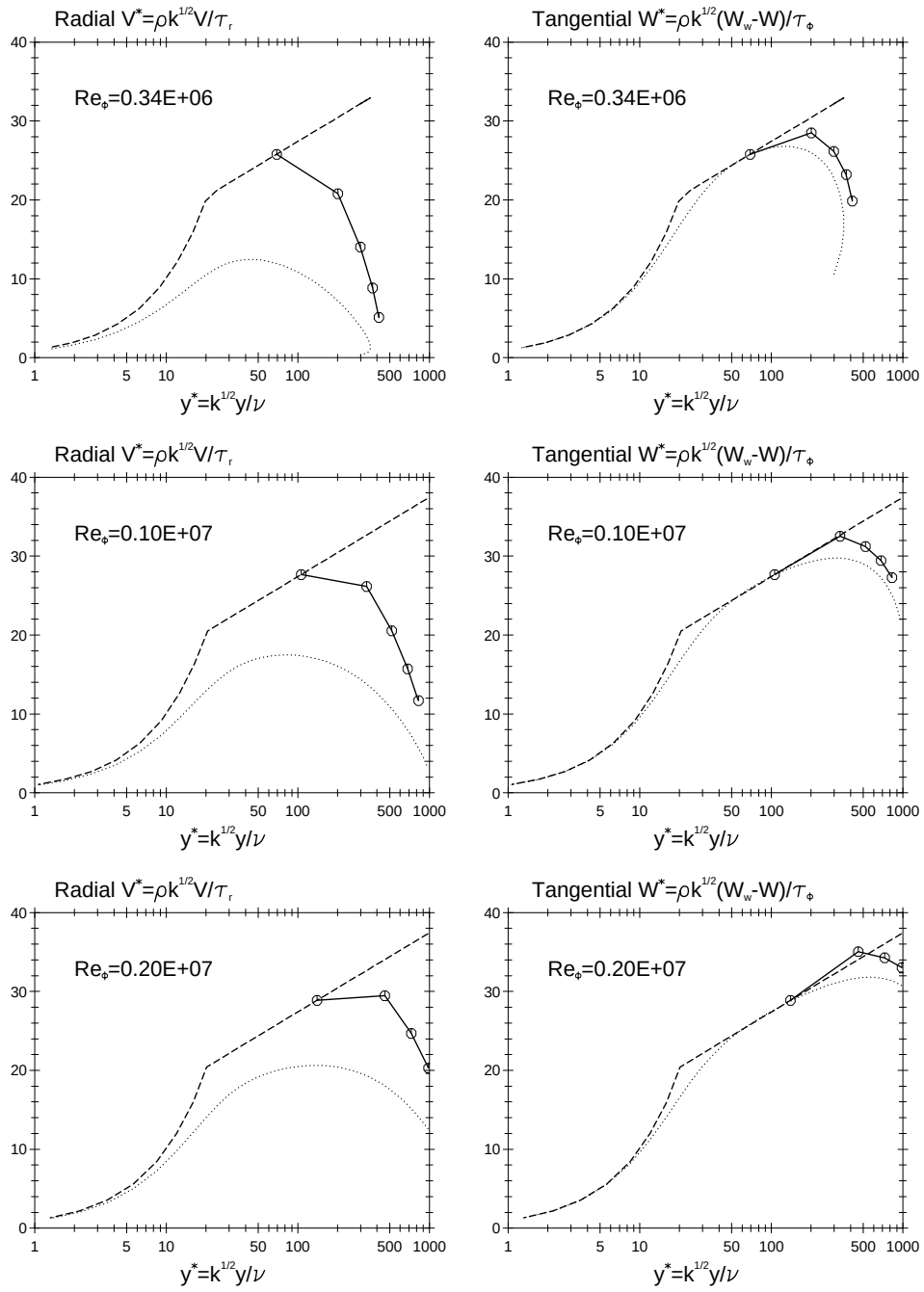

Figure 6.31: Radial and tangential velocity profiles in the free-disc flow using the Chieng & Launder wall function and linear $k-\varepsilon$ model with the 120×28 grid; —○—: high-*Re* model prediction (circles indicate the position of nodes); .....: low-*Re* model prediction; - - -: "universal" log-law.

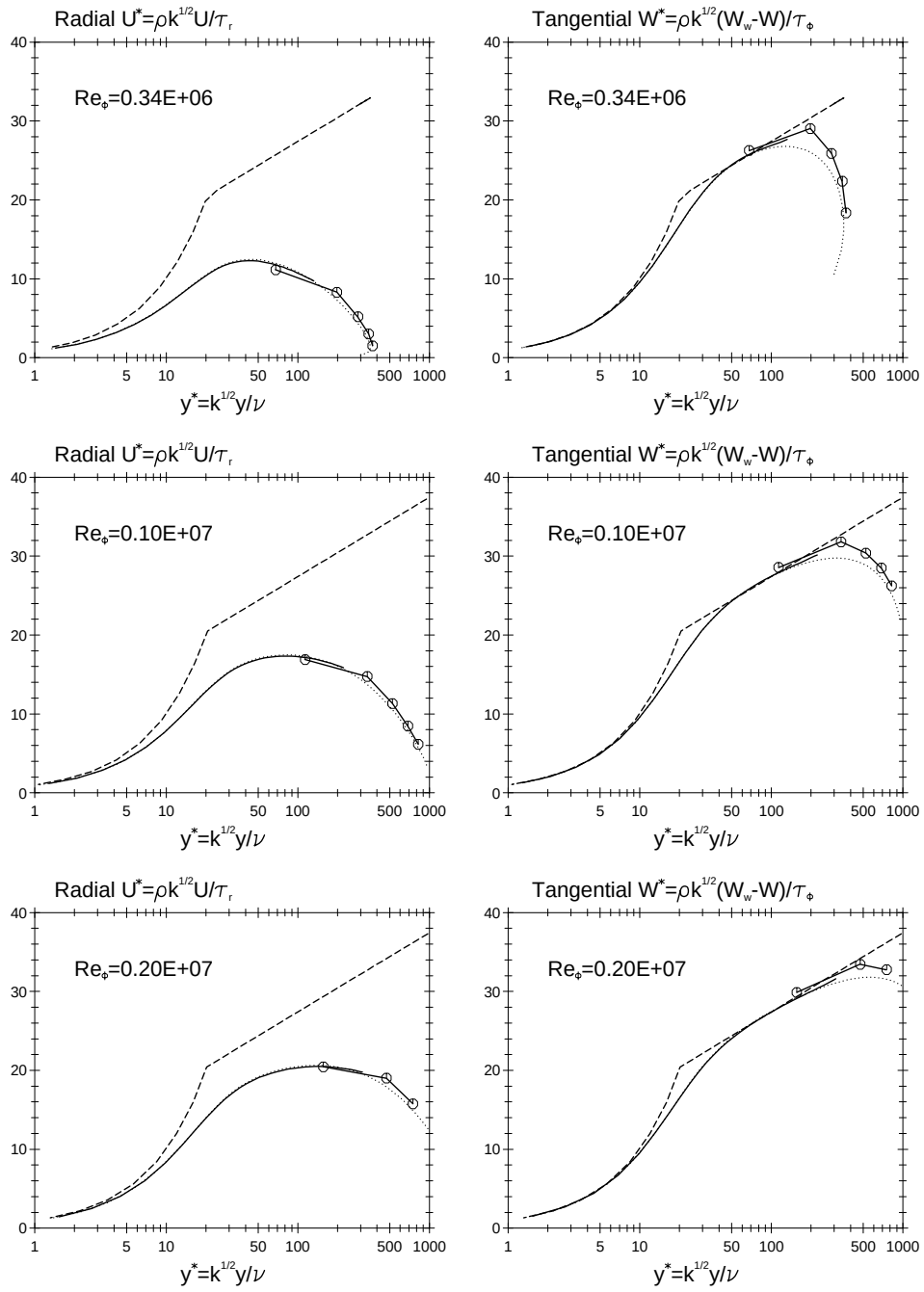

Figure 6.32: Radial and tangential velocity profiles in the free-disc flow using the UMIST-*N* wall function and linear $k-\varepsilon$ model with the 120×28 grid; —⊖—: high-*Re* model prediction (circles indicate the position of nodes); .....: low-*Re* model prediction; - - -: "universal" log-law.

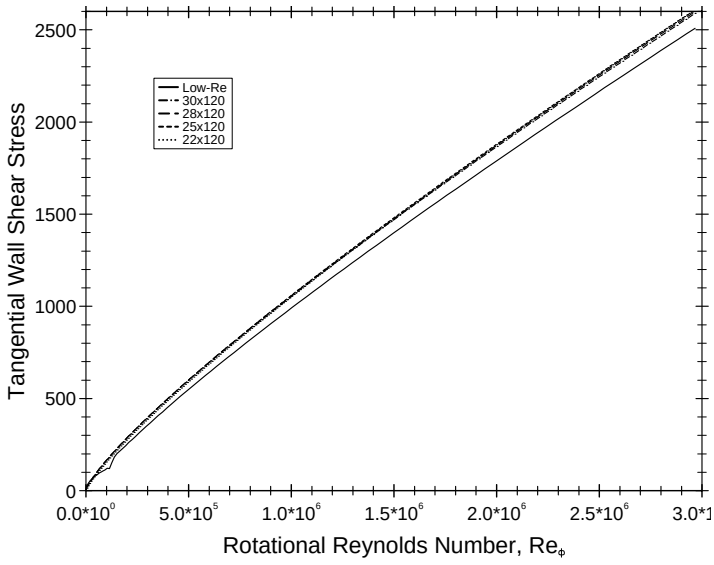

Figure 6.33: Predicted tangential wall shear stress, given by $\tau_{wall,\phi} / \left[0.5\rho\left(\Omega r_b\right)^2\right] \times 10^6$, in the free-disc flow using the TEAM wall function and linear $k-\varepsilon$ model. Solid line: low-*Re* model; broken lines: wall function results for different grid arrangements (for corresponding y^+ values for these grids see Figure 6.50).

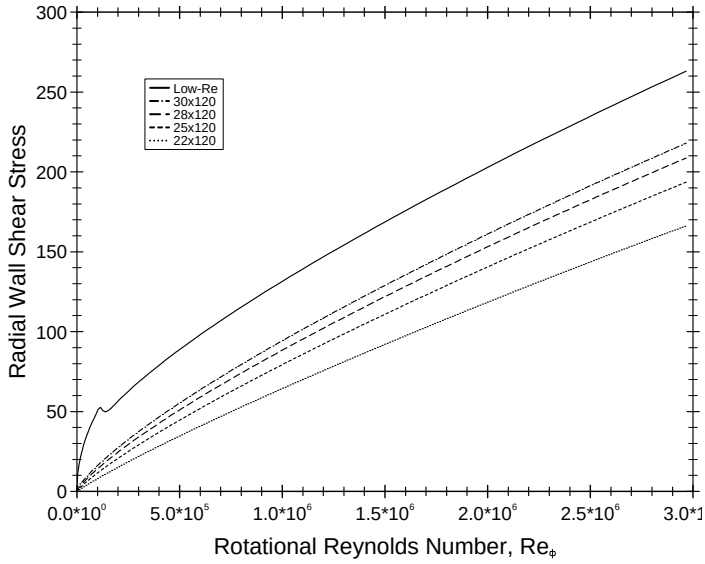

Figure 6.34: Predicted radial wall shear stress, given by $\tau_{wall,r} / \left[0.5\rho\left(\Omega r_b\right)^2\right] \times 10^6$, in the free-disc flow using the TEAM wall function and linear $k-\varepsilon$ model. Solid line: low-*Re* model; broken lines: wall function results for different grid arrangements (for corresponding y^+ values for these grids see Figure 6.50).

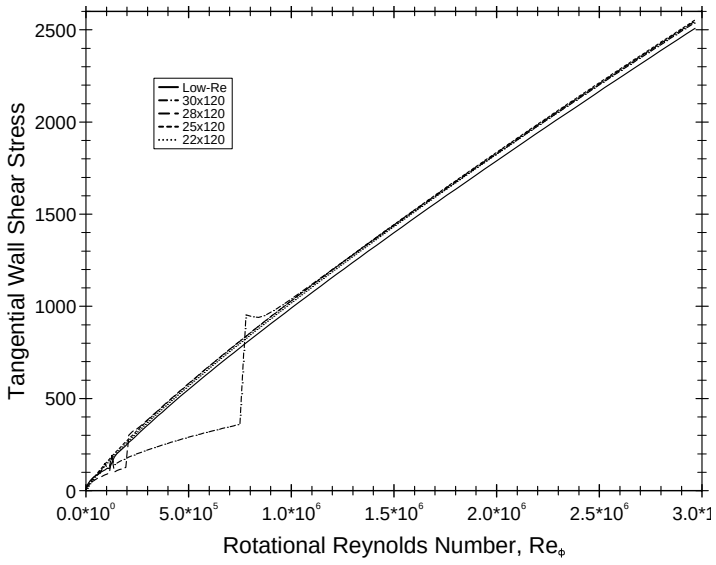

Figure 6.35: Predicted tangential wall shear stress, given by $\tau_{wall,\phi} / \left[0.5\rho\left(\Omega r_b\right)^2\right] \times 10^6$, in the free-disc flow using the simplified Chieng & Launder wall function and linear $k-\varepsilon$ model. Solid line: low-*Re* model; broken lines: wall function results for different grid arrangements (for corresponding y^+ values for these grids see Figure 6.51).

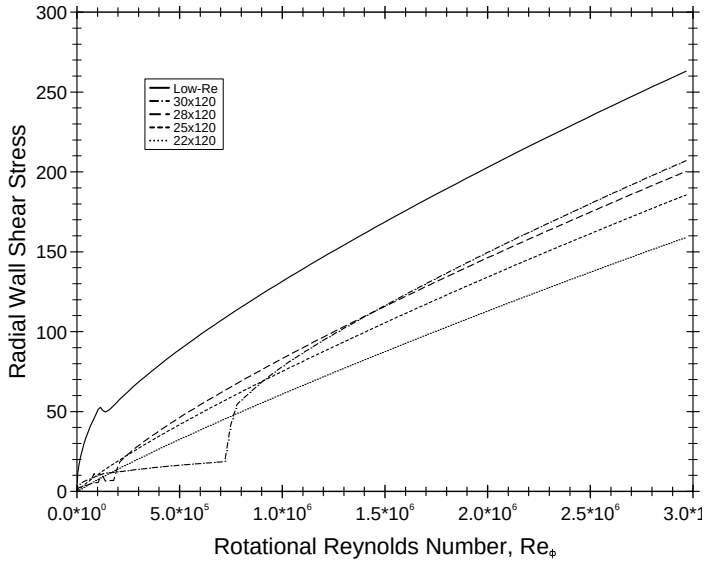

Figure 6.36: Predicted radial wall shear stress, given by $\tau_{wall,r} / \left[0.5\rho\left(\Omega r_b\right)^2\right] \times 10^6$, in the free-disc flow using the simplified Chieng & Launder wall function and linear $k-\varepsilon$ model. Solid line: low-*Re* model; broken lines: wall function results for different grid arrangements (for corresponding y^+ values for these grids see Figure 6.51).

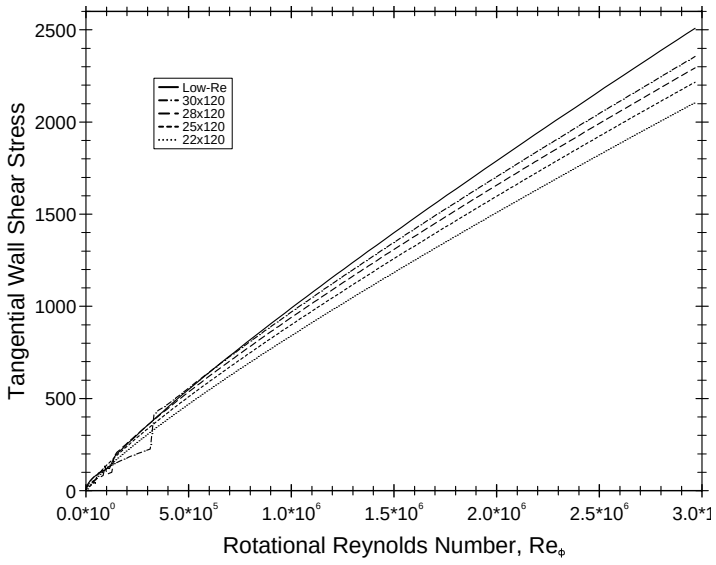

Figure 6.37: Predicted tangential wall shear stress, given by $\tau_{wall,\phi} / \left[0.5\rho\left(\Omega r_b\right)^2\right] \times 10^6$, in the free-disc flow using the Chieng & Launder wall function and linear $k-\varepsilon$ model. Solid line: low-*Re* model; broken lines: wall function results for different grid arrangements (for corresponding y^+ values for these grids see Figure 6.52).

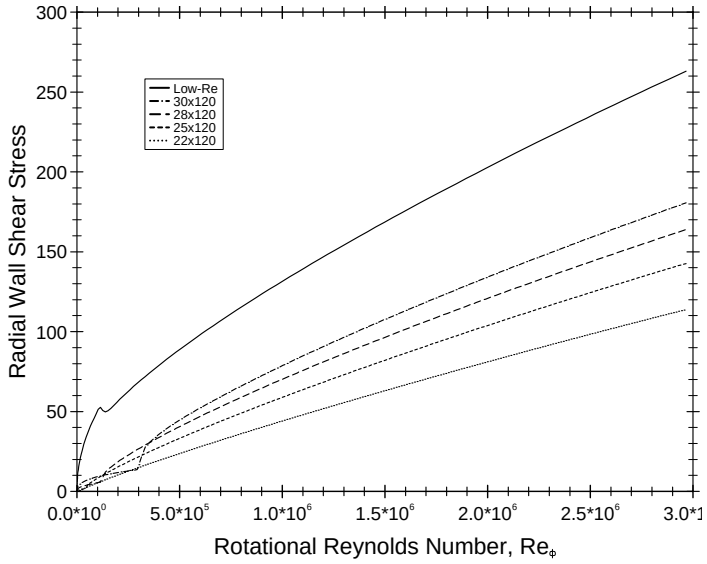

Figure 6.38: Predicted radial wall shear stress, given by $\tau_{wall,r} / \left[0.5\rho\left(\Omega r_b\right)^2\right] \times 10^6$, in the free-disc flow using the Chieng & Launder wall function and linear $k-\varepsilon$ model. Solid line: low-*Re* model; broken lines: wall function results for different grid arrangements (for corresponding y^+ values for these grids see Figure 6.52).

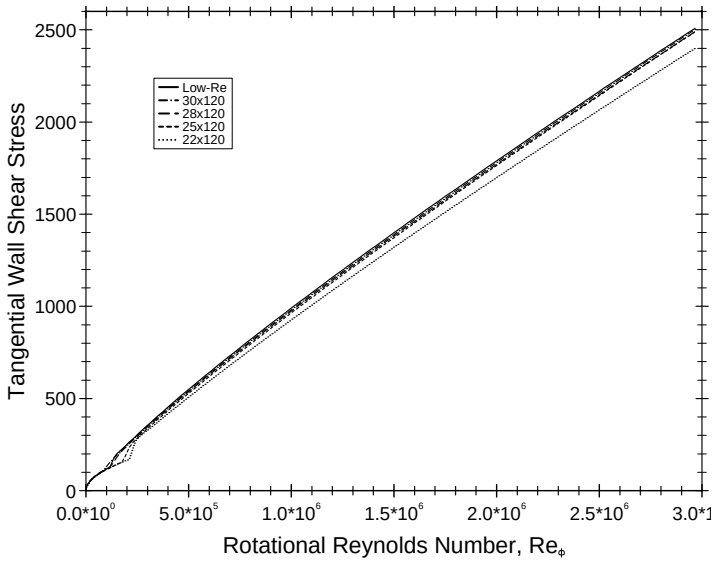

Figure 6.39: Predicted tangential wall shear stress, given by $\tau_{wall,\phi}/\left[0.5\rho\left(\Omega r_b\right)^2\right] \times 10^6$, in the free-disc flow using the UMIST-*N* wall function and linear $k-\varepsilon$ model. Solid line: low-*Re* model; broken lines: wall function results for different grid arrangements (for corresponding y^+ values for these grids see Figure 6.53).

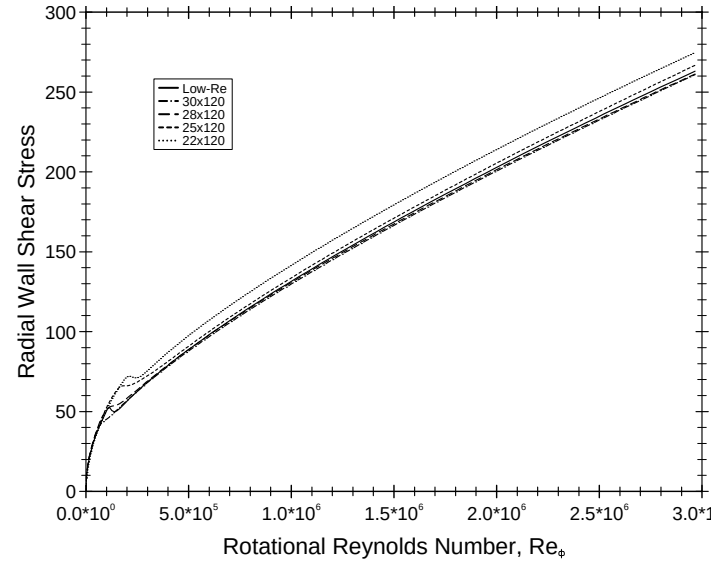

Figure 6.40: Predicted radial wall shear stress, given by $\tau_{wall,r}/\left[0.5\rho\left(\Omega r_b\right)^2\right] \times 10^6$, in the free-disc flow using the UMIST-*N* wall function and linear $k-\varepsilon$ model. Solid line: low-*Re* model; broken lines: wall function results for different grid arrangements (for corresponding y^+ values for these grids see Figure 6.53).

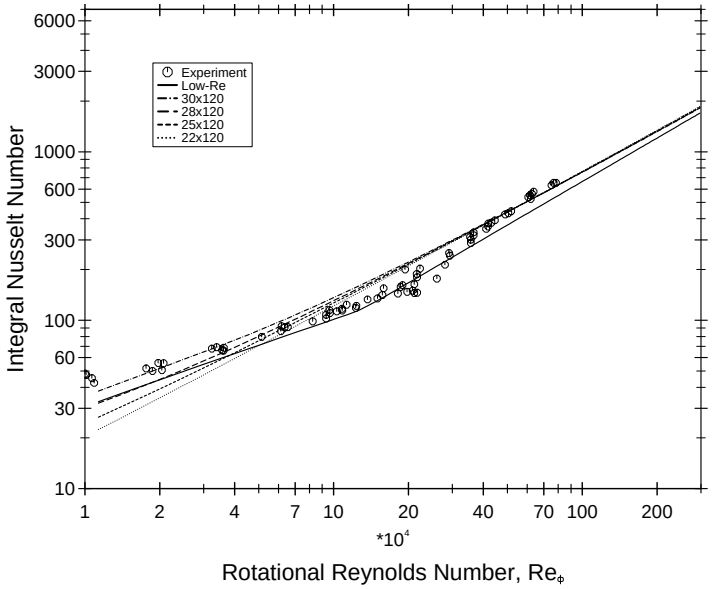

Figure 6.41: Predicted integral Nusselt number in the free-disc flow using the TEAM wall function and linear $k-\varepsilon$ model. Solid line: low-*Re* model; broken lines: wall function results for different grid arrangements (for corresponding y^+ values for these grids see Figure 6.50); ○: experimental values from Cobb & Saunders [130].

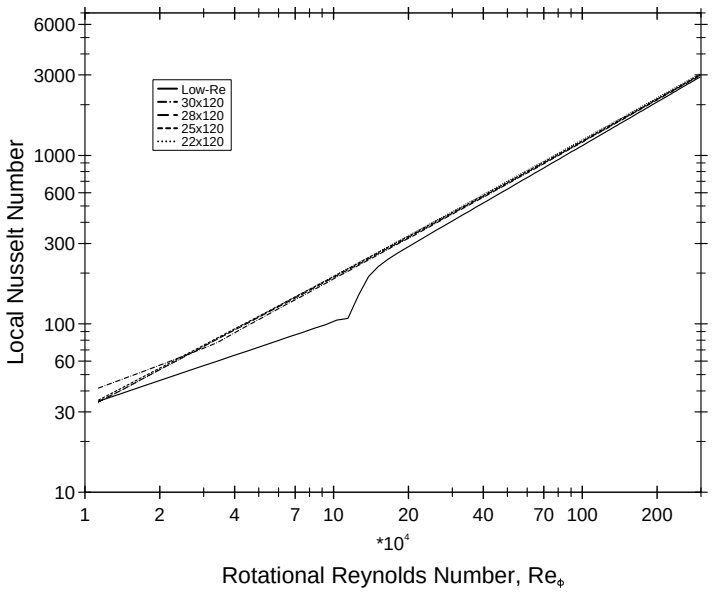

Figure 6.42: Predicted local Nusselt number in the free-disc flow using the TEAM wall function and linear $k-\varepsilon$ model. Solid line: low-*Re* model; broken lines: wall function results for different grid arrangements (for corresponding y^+ values for these grids see Figure 6.50).

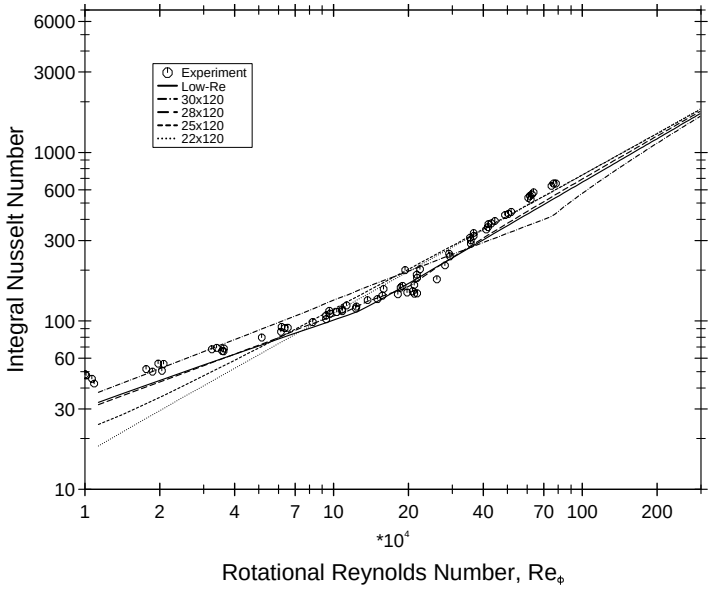

Figure 6.43: Predicted integral Nusselt number in the free-disc flow using the simplified Chieng & Launder wall function and linear $k-\varepsilon$ model. Solid line: low-*Re* model; broken lines: wall function results for different grid arrangements (for corresponding y^+ values for these grids see Figure 6.51); ○: experimental values from Cobb & Saunders [130].

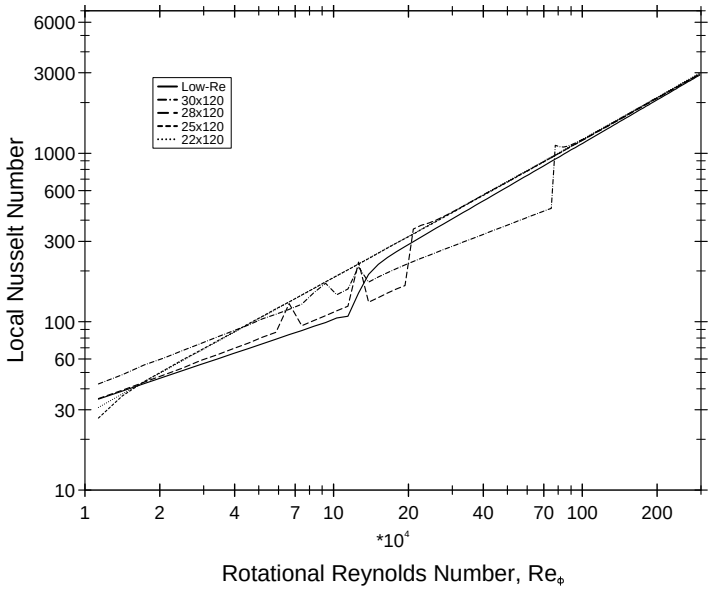

Figure 6.44: Predicted local Nusselt number in the free-disc flow using the simplified Chieng & Launder wall function and linear $k-\varepsilon$ model. Solid line: low-*Re* model; broken lines: wall function results for different grid arrangements (for corresponding y^+ values for these grids see Figure 6.51).

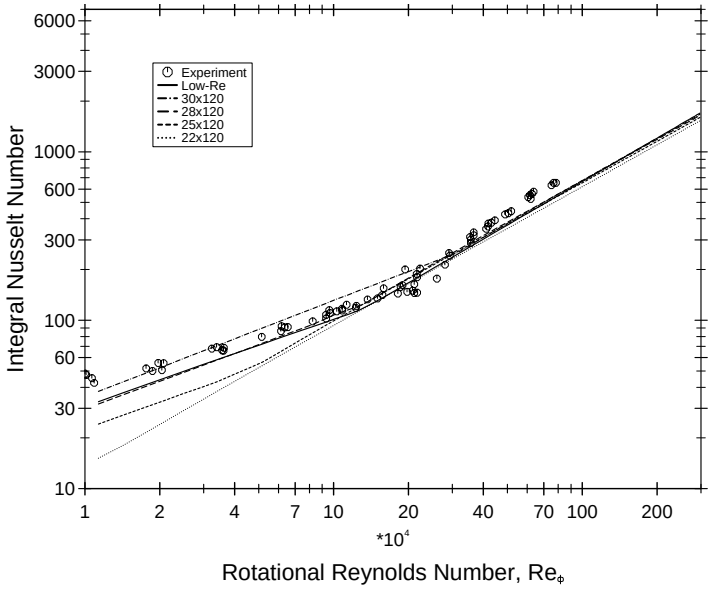

Figure 6.45: Predicted integral Nusselt number in the free-disc flow using the Chieng & Launder wall function and linear $k-\varepsilon$ model. Solid line: low-*Re* model; broken lines: wall function results for different grid arrangements (for corresponding y^+ values for these grids see Figure 6.52); ○: experimental values from Cobb & Saunders [130].

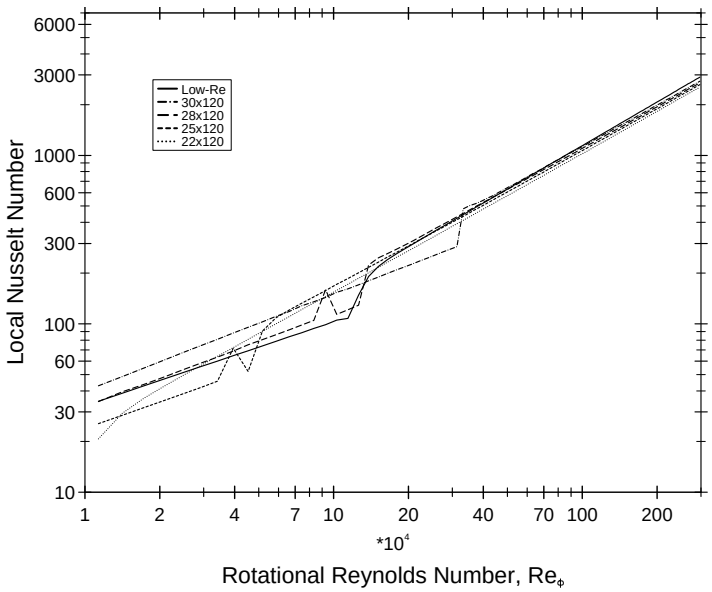

Figure 6.46: Predicted local Nusselt number in the free-disc flow using the Chieng & Launder wall function and linear $k-\varepsilon$ model. Solid line: low-*Re* model; broken lines: wall function results for different grid arrangements (for corresponding y^+ values for these grids see Figure 6.52).

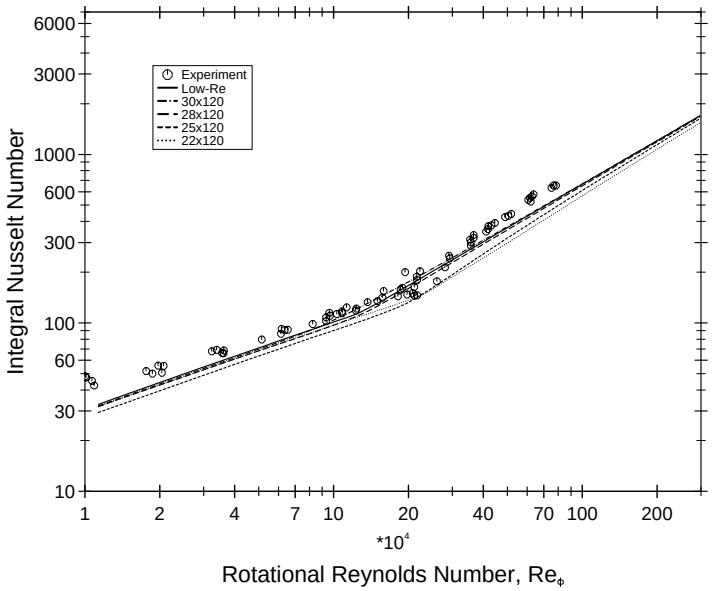

Figure 6.47: Predicted integral Nusselt number in the free-disc flow using the UMIST-*N* wall function and linear $k-\varepsilon$ model. Solid line: low-*Re* model; broken lines: wall function results for different main-grid arrangements (for corresponding y^+ values for these grids see Figure 6.53); ○: experimental values from Cobb & Saunders [130].

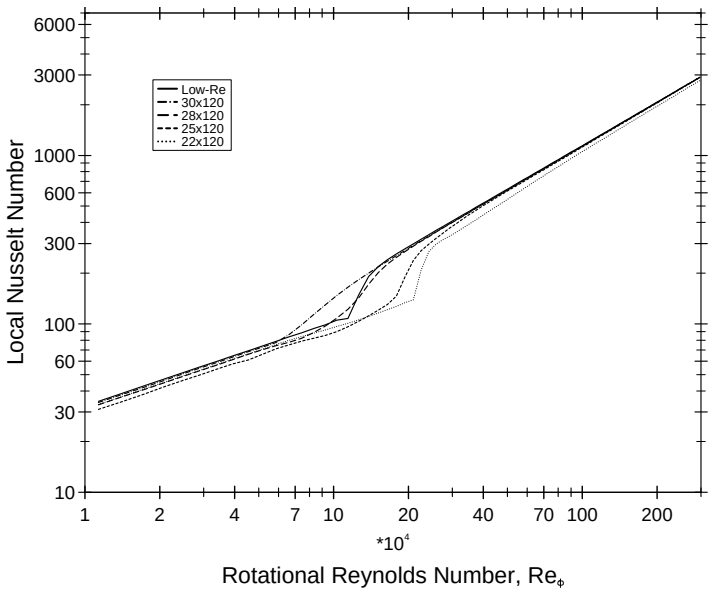

Figure 6.48: Predicted local Nusselt number in the free-disc flow using the UMIST-*N* wall function and linear $k-\varepsilon$ model. Solid line: low-*Re* model; broken lines: wall function results for different main-grid arrangements (also shown on linear axes in Figure 6.49). For corresponding y^+ values for these grids see Figure 6.53.

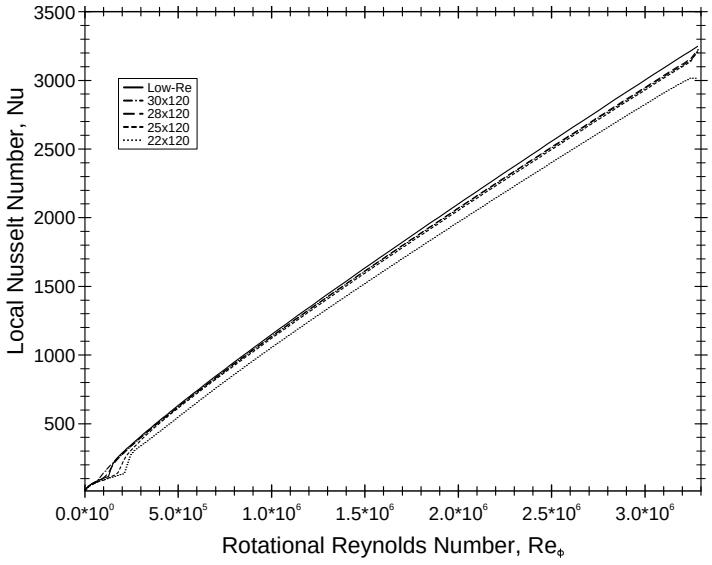

Figure 6.49: Predicted Nusselt number in the free-disc flow using the UMIST-*N* wall function and linear $k-\varepsilon$ model. Solid line: low-*Re* model; broken lines: wall function results for different main-grid arrangements (also shown on log-axes in Figure 6.48).

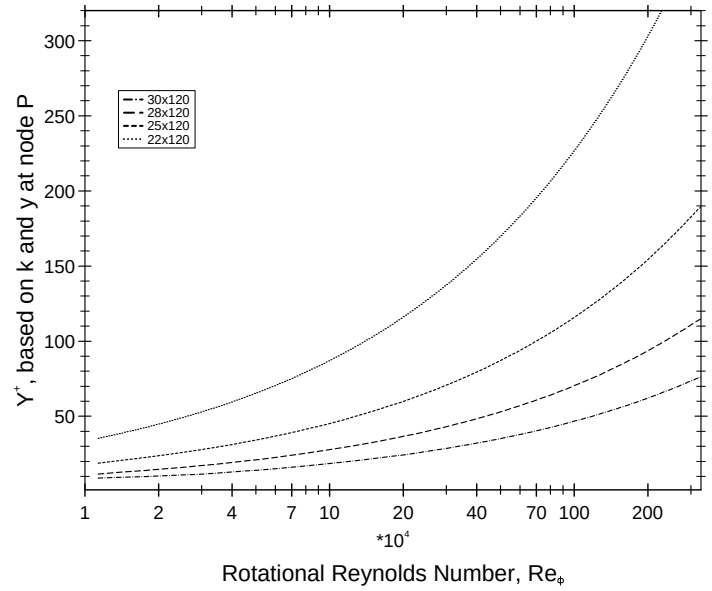

Figure 6.50: Dimensionless wall distance, $y^+ = c_\mu^{1/4} k^{1/2} y/\nu$, of the wall adjacent node in the free-disc flow using the TEAM wall function and linear $k-\varepsilon$ model with different grid arrangements, corresponding to the Nusselt number predictions shown in Figure 6.41 and 6.42.

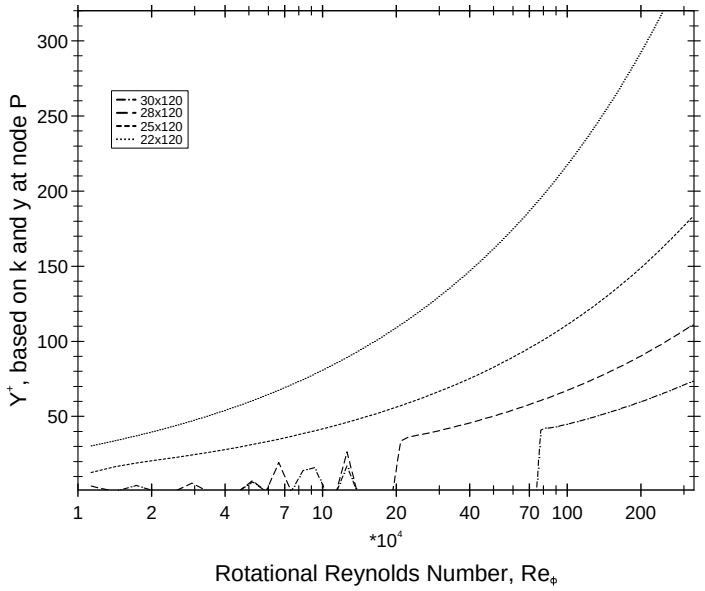

Figure 6.51: Dimensionless wall distance, $y^+ = c_\mu^{1/4} k^{1/2} y/\nu$, of the wall adjacent node in the free-disc flow using the simplified Chieng & Launder wall function and linear $k-\varepsilon$ model with different grid arrangements, corresponding to the Nusselt number predictions shown in Figure 6.43 and 6.44.

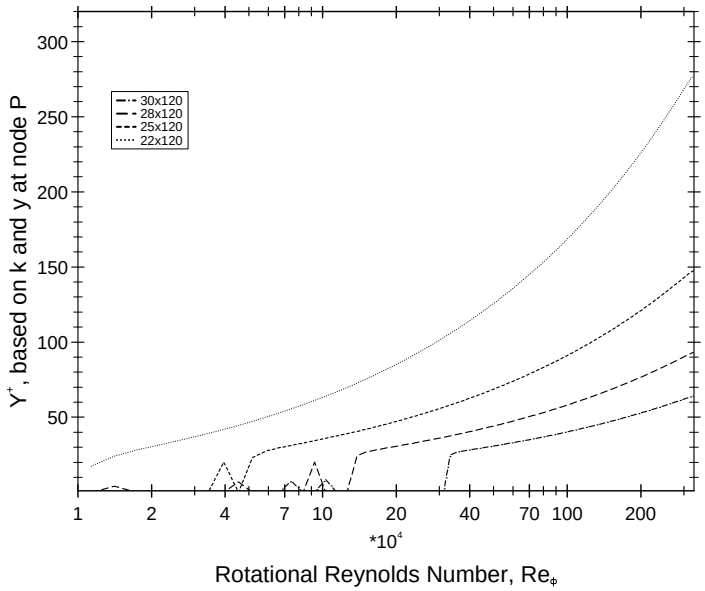

Figure 6.52: Dimensionless wall distance, $y^+ = c_\mu^{1/4} k^{1/2} y/\nu$, of the wall adjacent node in the free-disc flow using the Chieng & Launder wall function and linear $k-\varepsilon$ model with different grid arrangements, corresponding to the Nusselt number predictions shown in Figure 6.45 and 6.46.

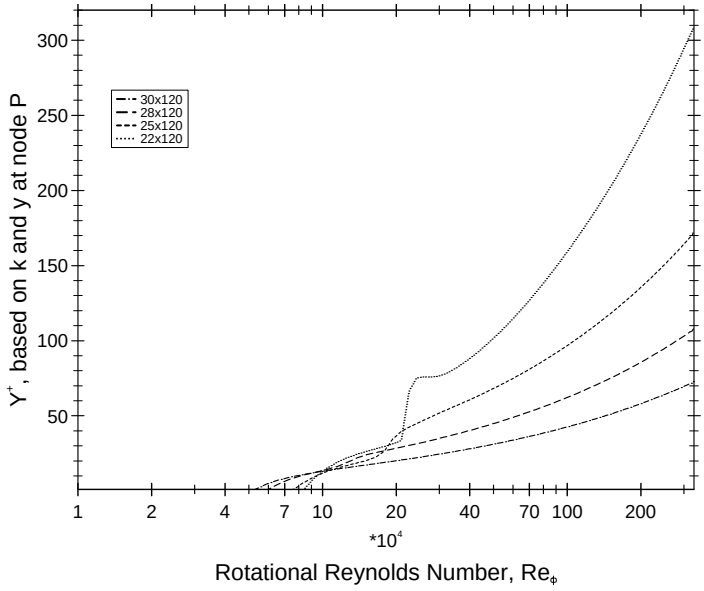

Figure 6.53: Dimensionless wall distance, $y^+ = c_\mu^{1/4} k^{1/2} y/\nu$, of the wall adjacent node in the free-disc flow using the UMIST-*N* wall function and linear $k-\varepsilon$ model with different main-grid arrangements corresponding to the Nusselt number predictions shown in Figures 6.47, 6.48 and 6.49.

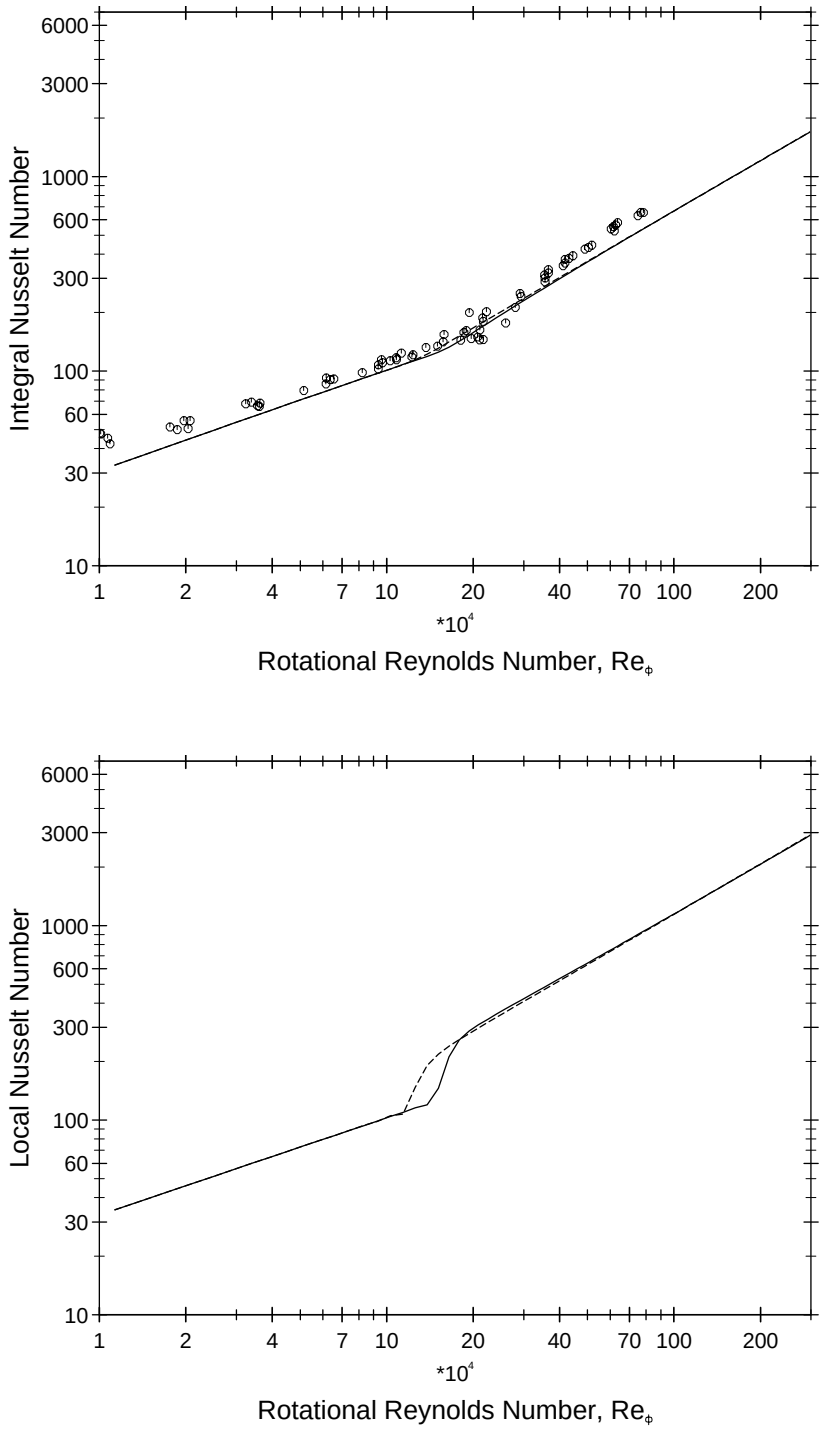

Figure 6.54: Predicted Nusselt number in the free-disc flow using the low-Reynolds-number linear $k-\varepsilon$ model of Launder & Sharma and the non-linear $k-\varepsilon$ model of Craft *et al.* [67]; ——: NLEVM; - - -: linear $k-\varepsilon$; ○: Cobb & Saunders experiments; *a.*) integral Nusselt number (top) *b.*) local Nusselt number (bottom).

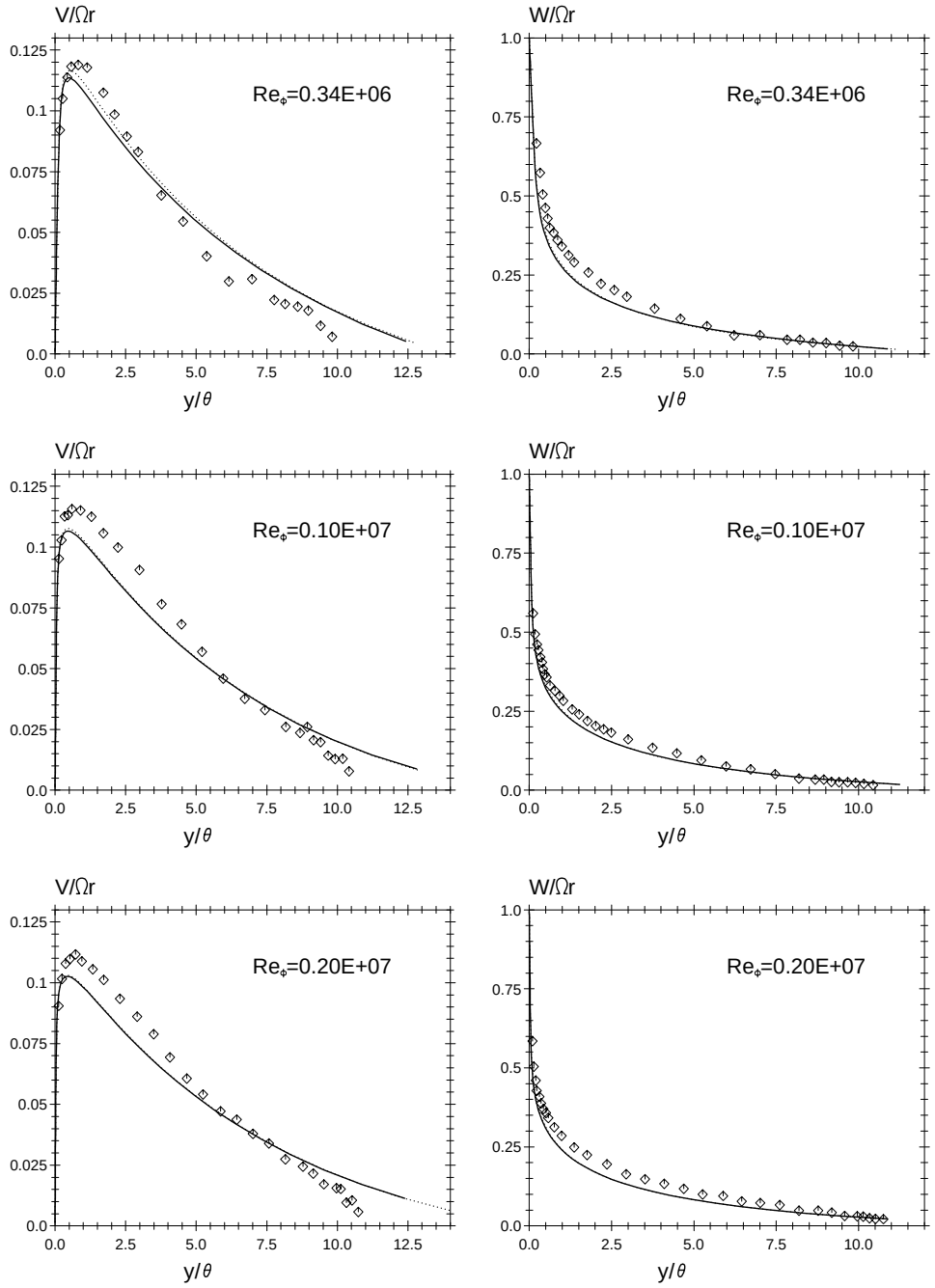

Figure 6.55: Radial and tangential velocity profiles in the free-disc flow using the low-Reynolds-number linear $k-\varepsilon$ model of Launder & Sharma and the non-linear $k-\varepsilon$ model of Craft *et al.* [67] at three different rotational Reynolds numbers; ——: NLEVM; .....: linear $k-\varepsilon$; ◊: Cham & Head experiments.

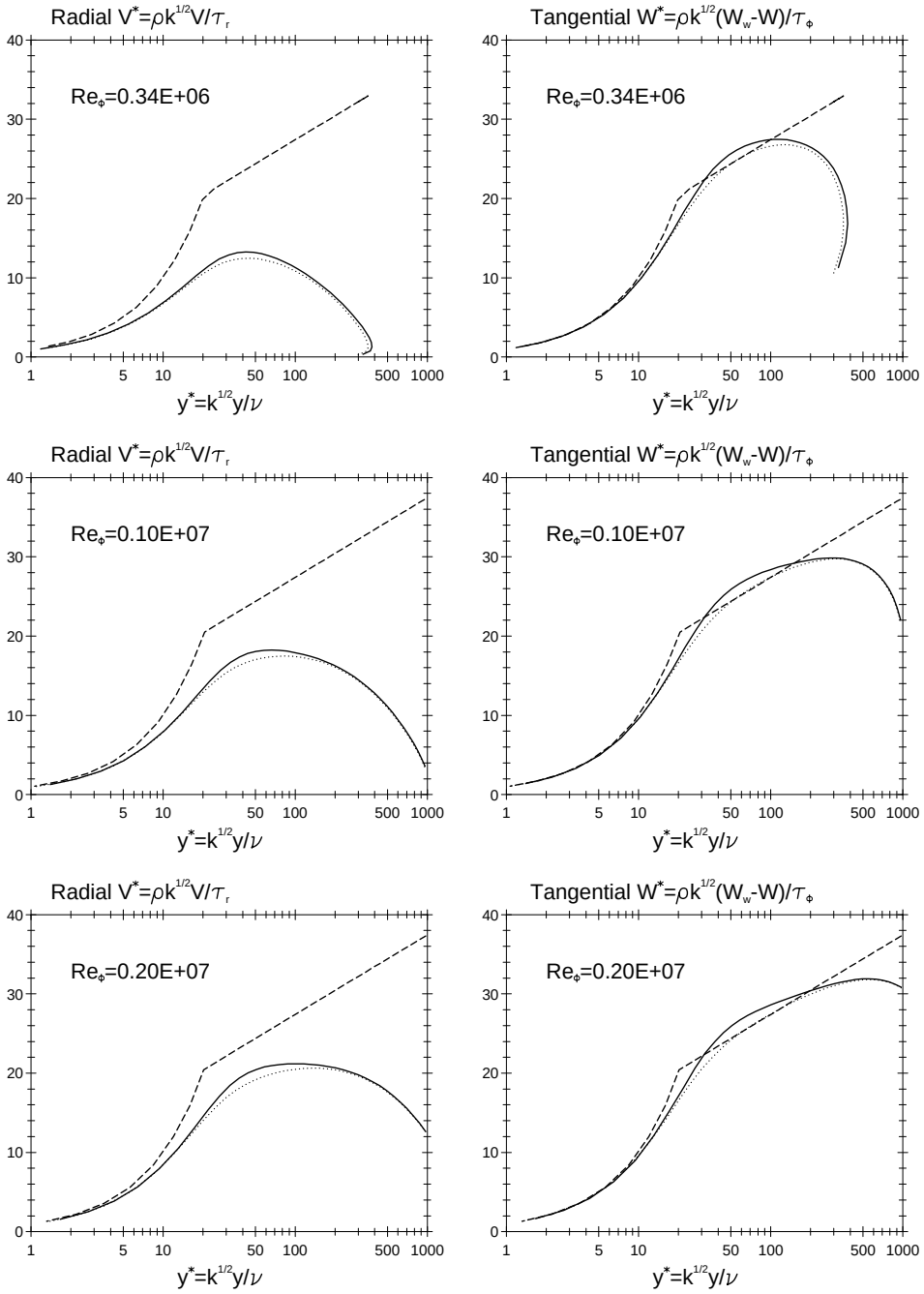

Figure 6.56: Radial and tangential velocity profiles in the free-disc flow using the low-Reynolds-number linear $k-\varepsilon$ model of Launder & Sharma and the non-linear $k-\varepsilon$ model of Craft *et al.* [67] at three different rotational Reynolds numbers; ——: NLEVM; .....: linear $k-\varepsilon$; - - -: "universal" log-law.

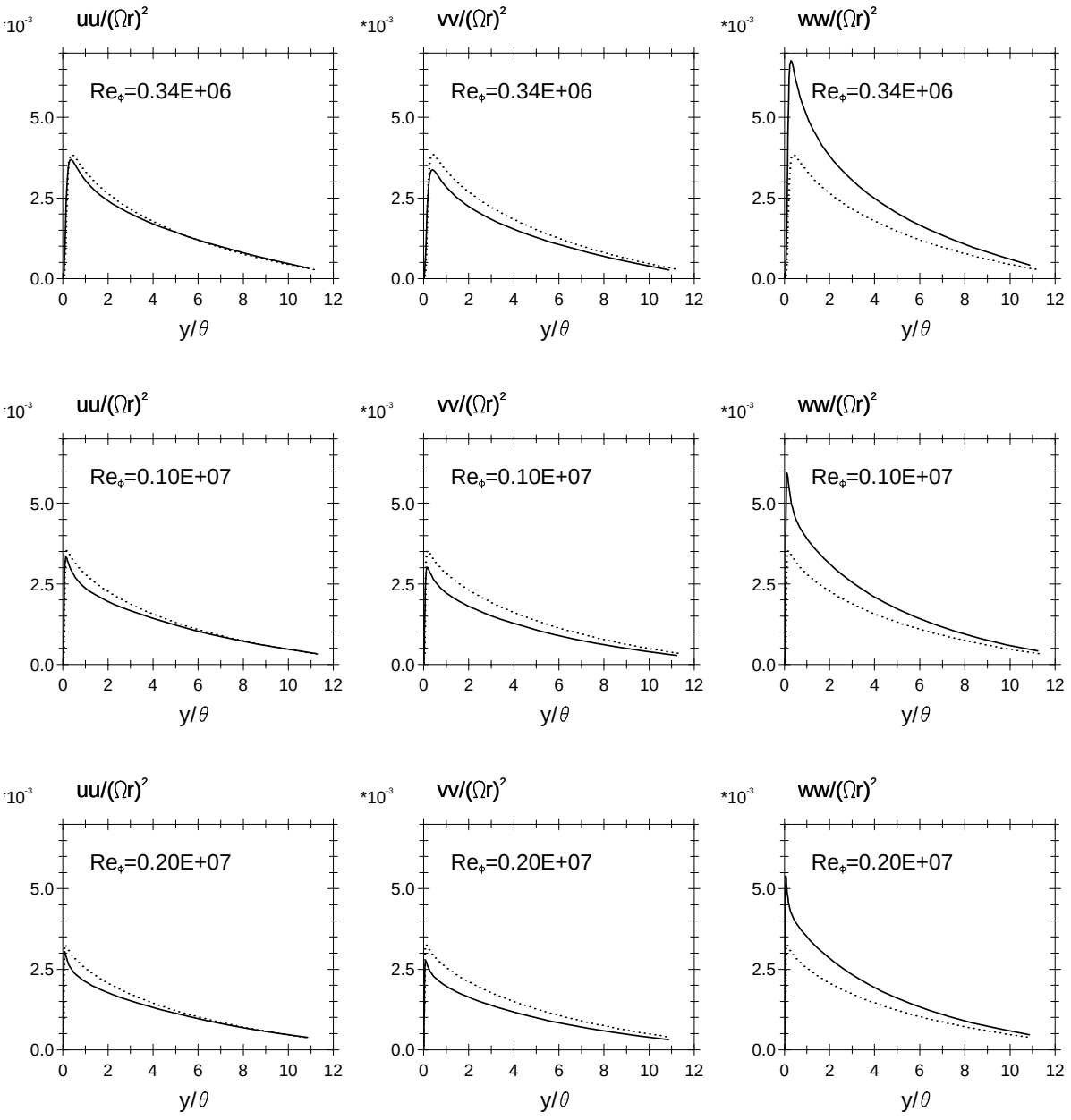

Figure 6.57: Predicted normal stresses (non-dimensionalized with the square of the local wall velocity) in the free-disc flow using the low-Reynolds-number linear $k-\varepsilon$ model of Launder & Sharma and the non-linear $k-\varepsilon$ model of Craft *et al*. [67] at three different rotational Reynolds numbers; ——: NLEVM; .....: linear $k-\varepsilon$.

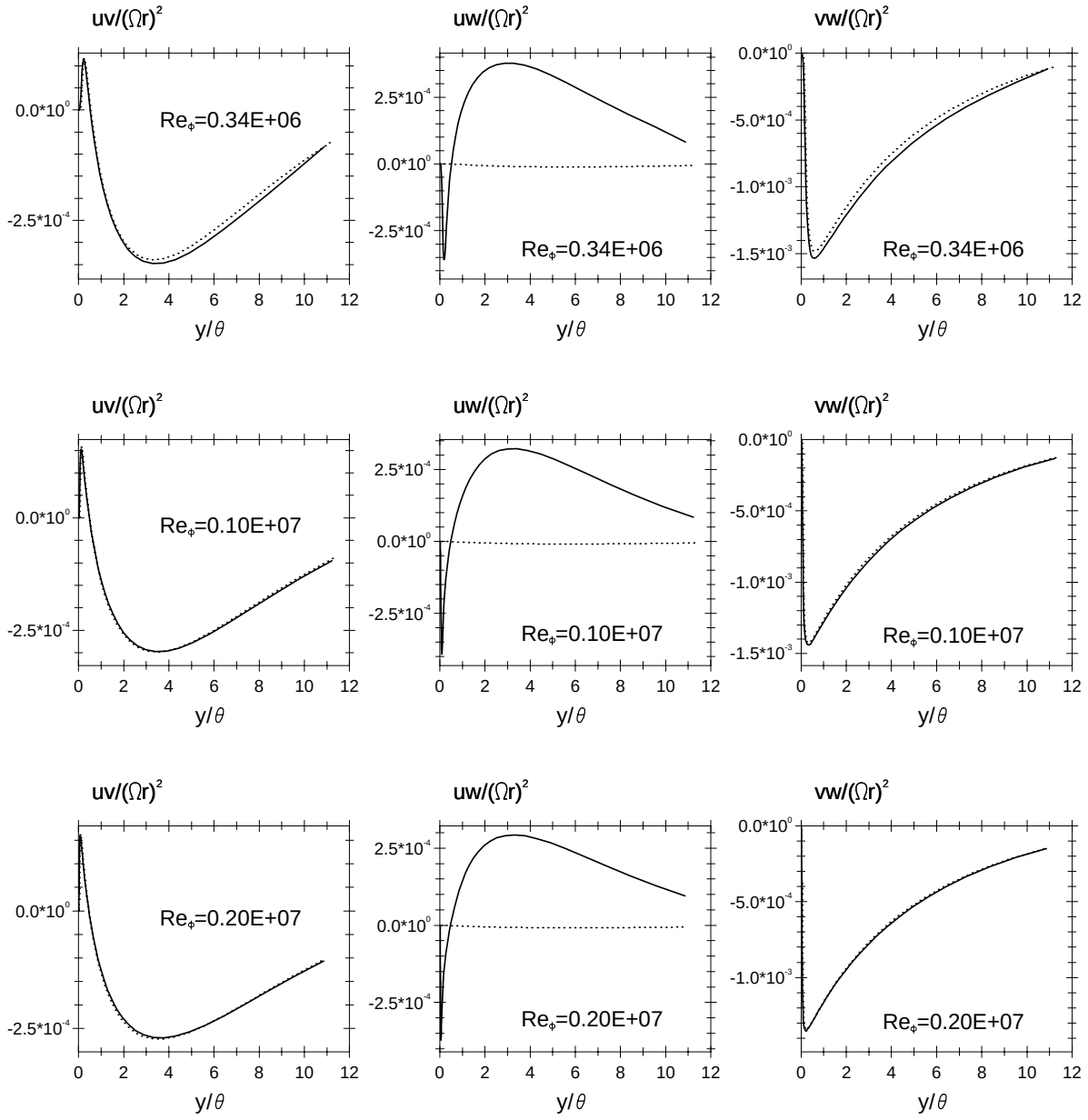

Figure 6.58: Predicted shear stresses (non-dimensionalized with the square of the local wall velocity) in the free-disc flow using the low-Reynolds-number linear $k-\varepsilon$ model of Launder & Sharma and the non-linear $k-\varepsilon$ model of Craft *et al.* [67] at three different rotational Reynolds numbers; ——: NLEVM; .....: linear $k-\varepsilon$.

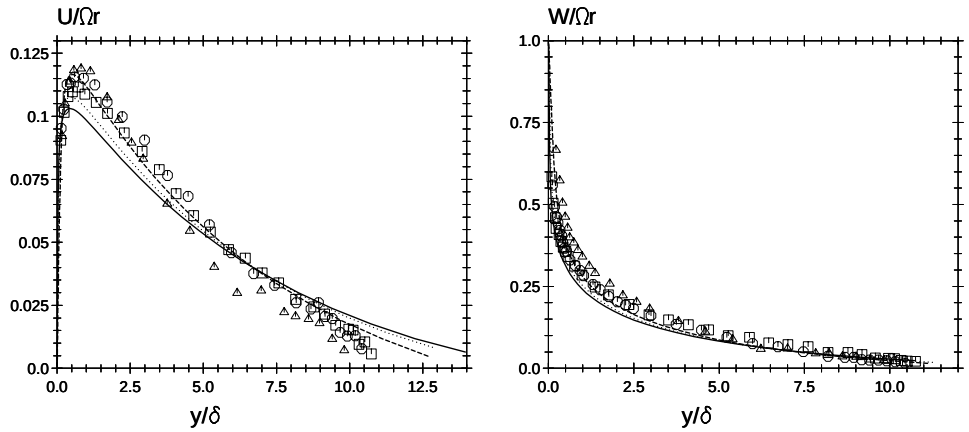

Figure 6.59: Radial and tangential velocity profiles in the free-disc flow using the low-Reynolds-number linear $k-\varepsilon$ model of Launder & Sharma at three different rotational Reynolds numbers, shown in Figure 6.55, overlaid on the same set of axes (lines indicate computational results and symbols are experimental measurements by Cham & Head); —— and □: $Re_\phi = 2\times10^6$; ..... and ○: $Re_\phi = 1\times10^6$; - - - and △: $Re_\phi = 3.4\times10^5$.

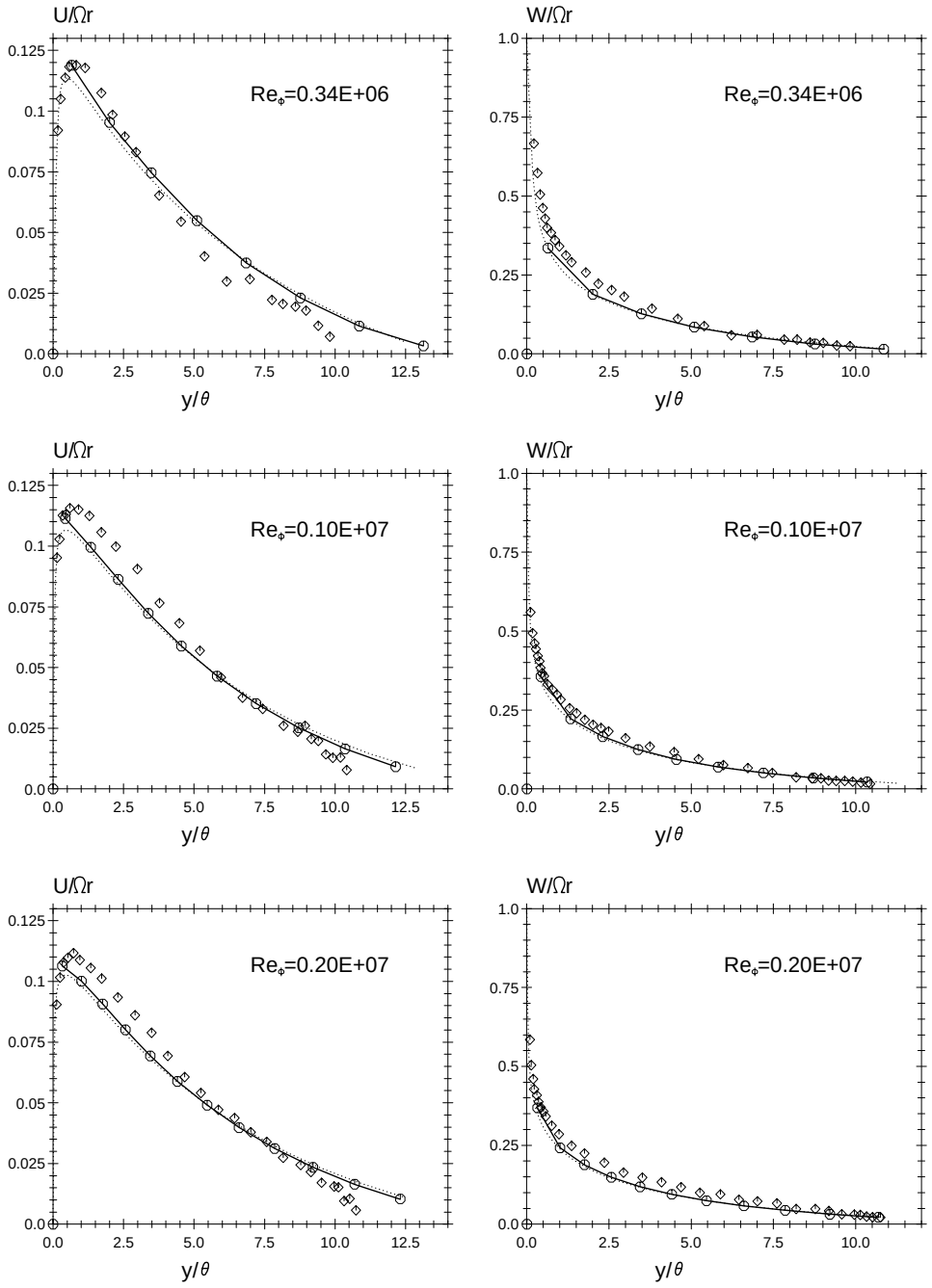

Figure 6.60: Radial and tangential velocity profiles in the free-disc flow using the TEAM wall function and non-linear $k-\varepsilon$ model with the 120×28 grid; —⊖—: high-*Re* model prediction (circles indicate the position of nodes); .....: low-*Re* model prediction; ♢: Cham & Head experiments.

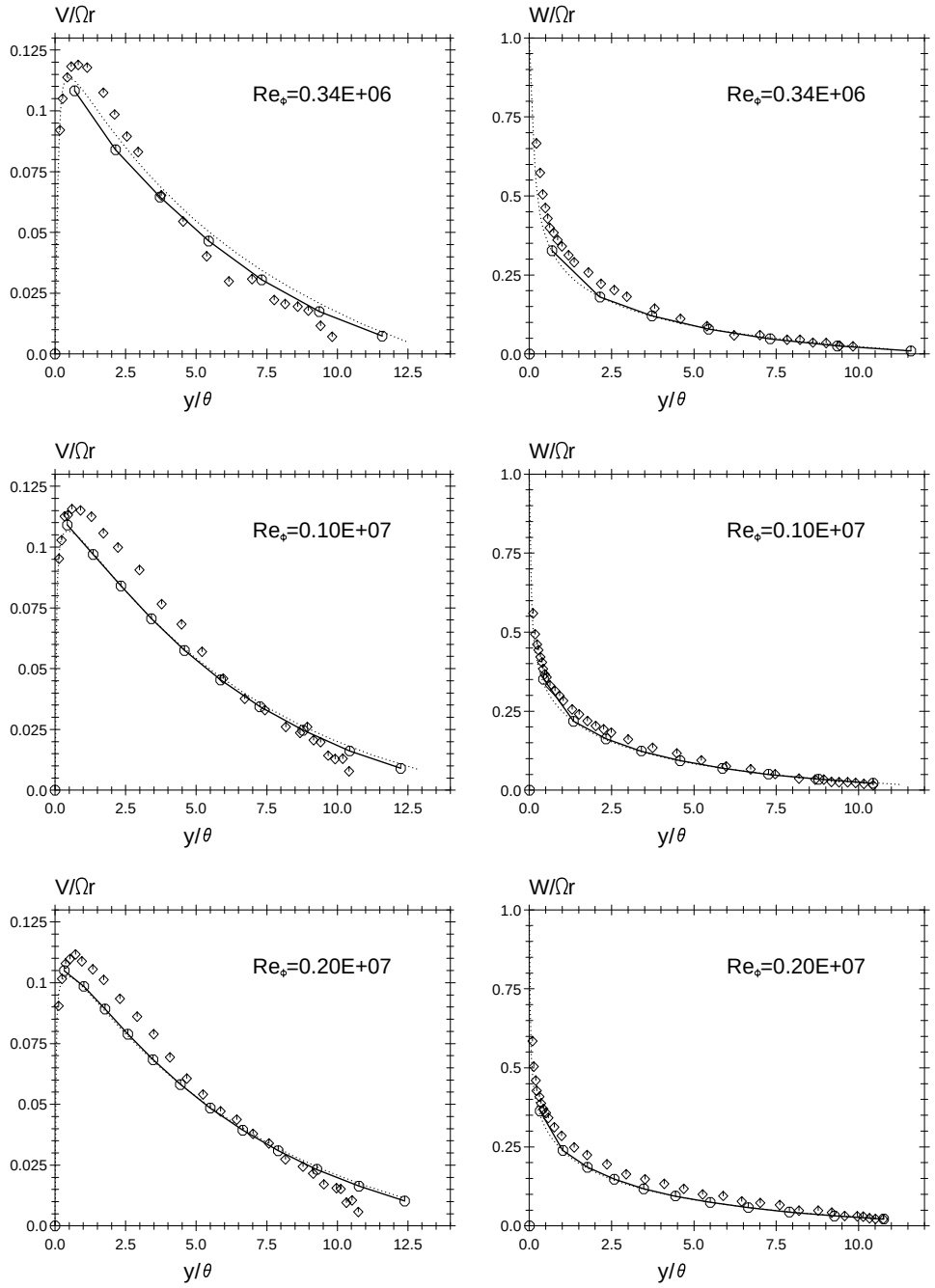

Figure 6.61: Radial and tangential velocity profiles in the free-disc flow using the simplified Chieng & Launder wall function and non-linear $k-\varepsilon$ model with the 120×28 grid; —⊖—: high-*Re* model prediction (circles indicate the position of nodes); .....: low-*Re* model prediction; ♢: Cham & Head experiments.

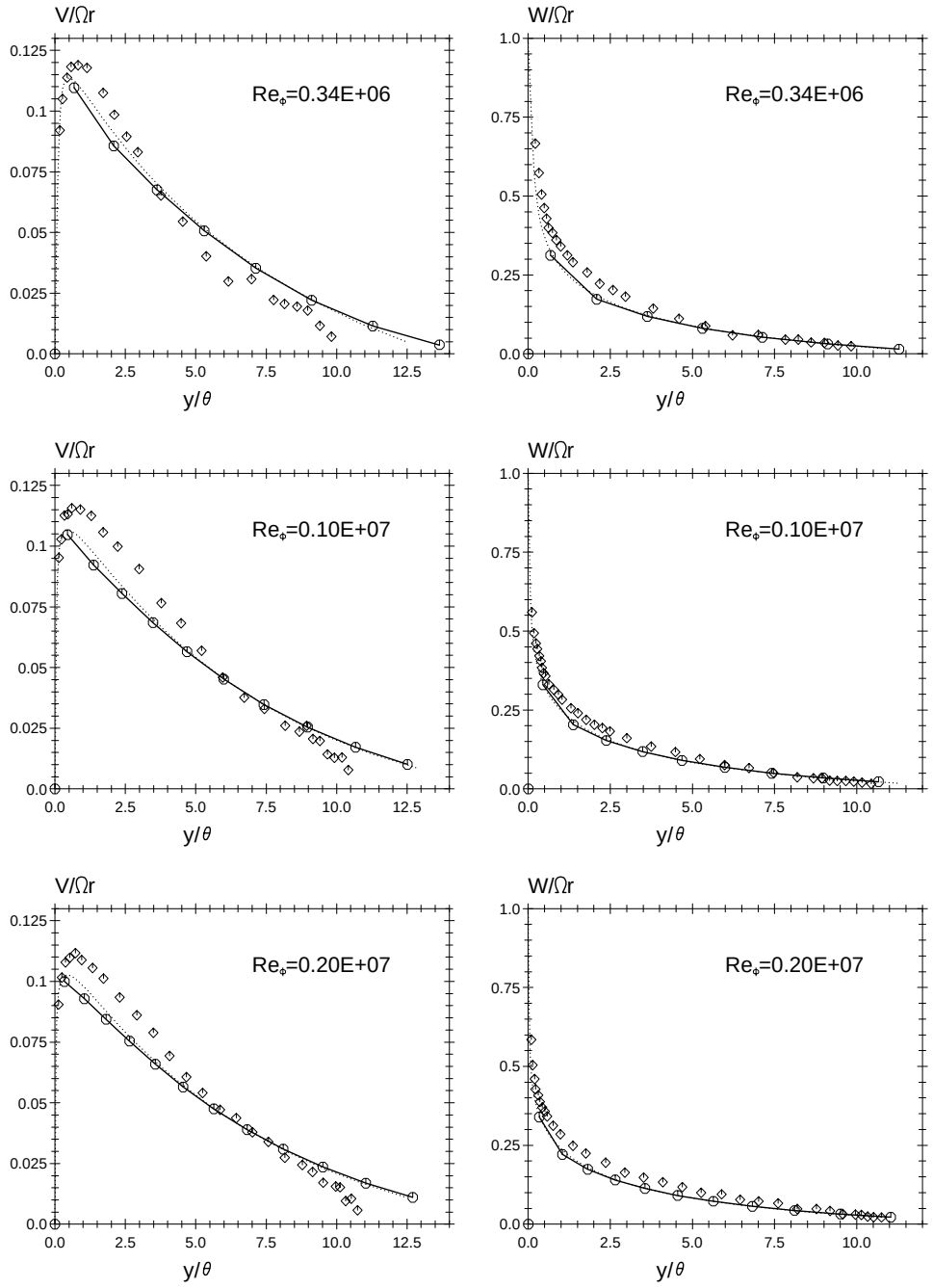

Figure 6.62: Radial and tangential velocity profiles in the free-disc flow using the Chieng & Launder wall function and non-linear $k-\varepsilon$ model with the 120×28 grid; —○—: high-*Re* model prediction (circles indicate the position of nodes); .....: low-*Re* model prediction; ♢: Cham & Head experiments.

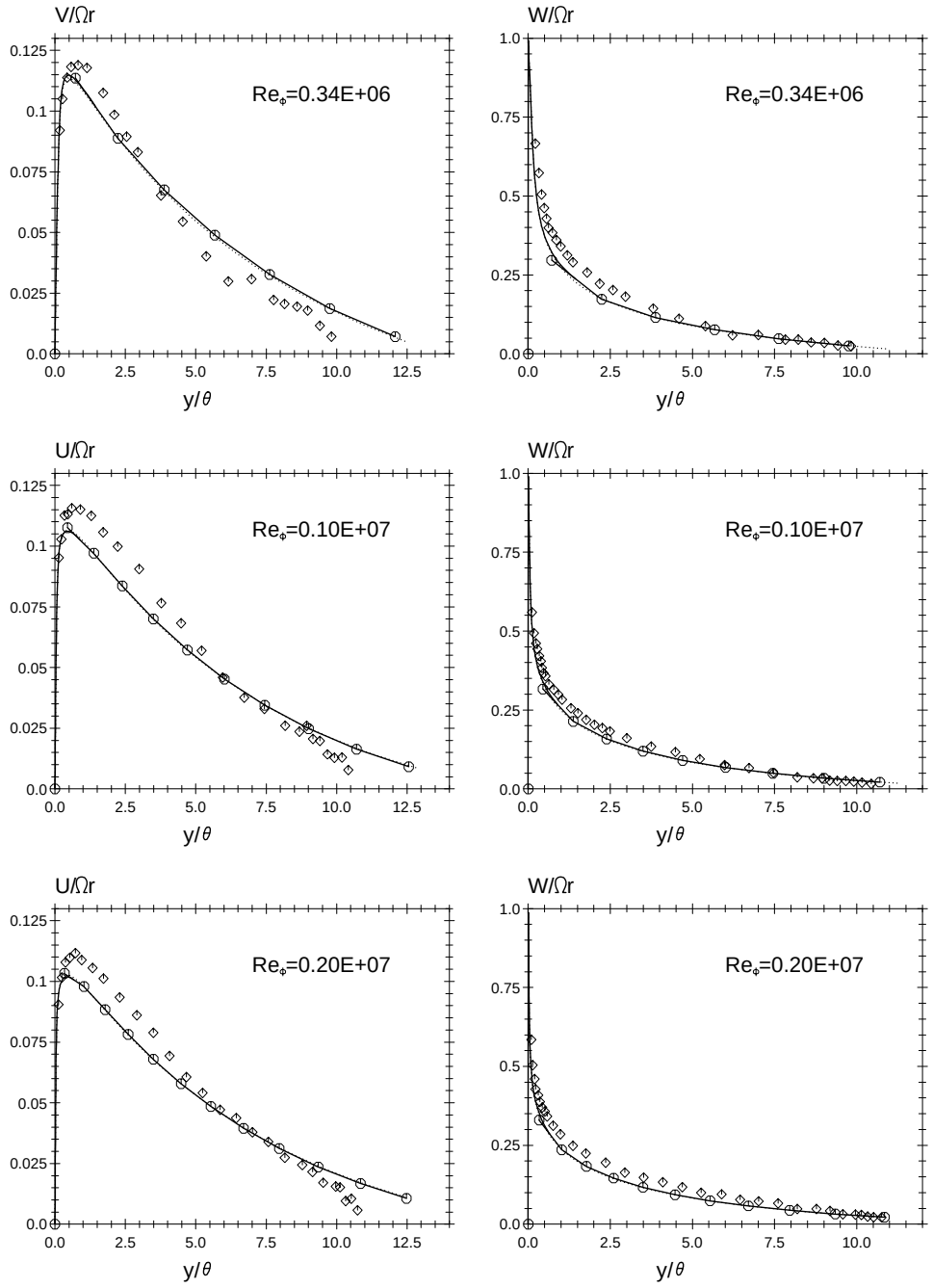

Figure 6.63: Radial and tangential velocity profiles in the free-disc flow using the UMIST-*N* wall function and non-linear $k-\varepsilon$ model with the 120×28 grid; —⊖—: high-*Re* model prediction (circles indicate the position of nodes); .....: low-*Re* model prediction; ♢: Cham & Head experiments.

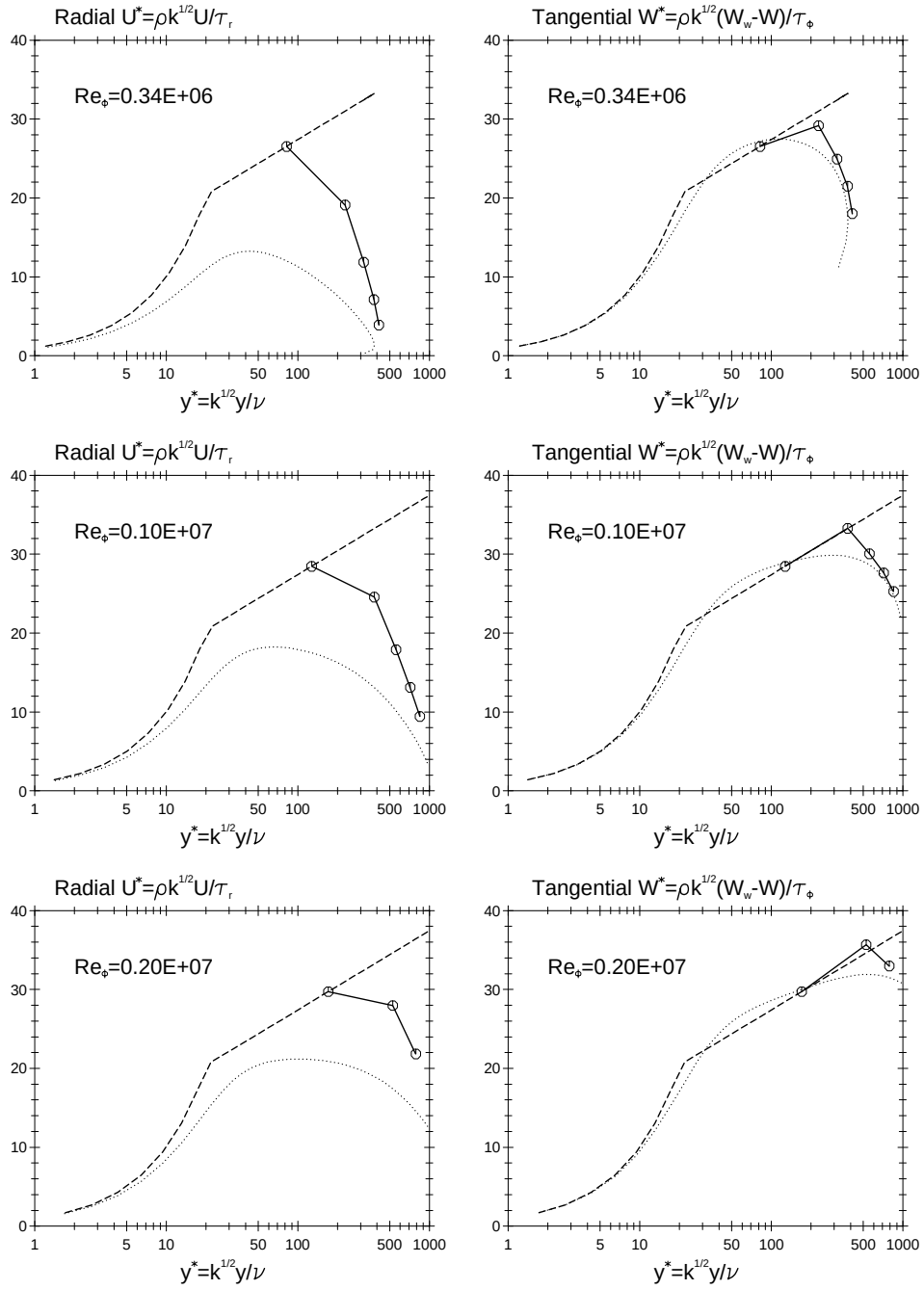

Figure 6.64: Radial and tangential velocity profiles in the free-disc flow using the TEAM wall function and non-linear $k-\varepsilon$ model with the 120×28 grid; —⊖—: high-*Re* model prediction (circles indicate the position of nodes); .....: low-*Re* model prediction; - - -: "universal" log-law.

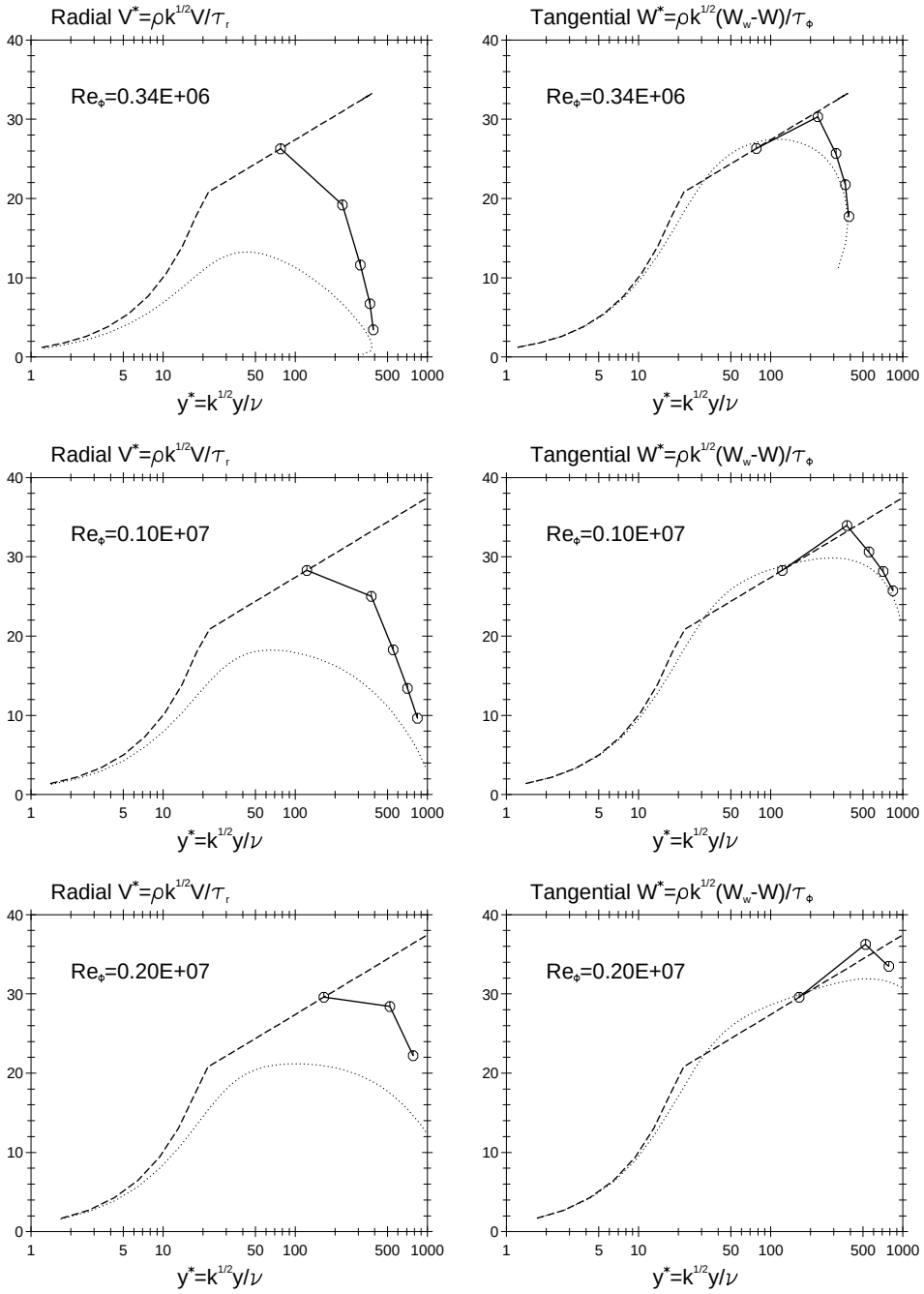

Figure 6.65: Radial and tangential velocity profiles in the free-disc flow using the simplified Chieng & Launder wall function and non-linear $k-\varepsilon$ model with the 120×28 grid; —○—: high-*Re* model prediction (circles indicate the position of nodes); .....: low-*Re* model prediction; - - -: "universal" log-law.

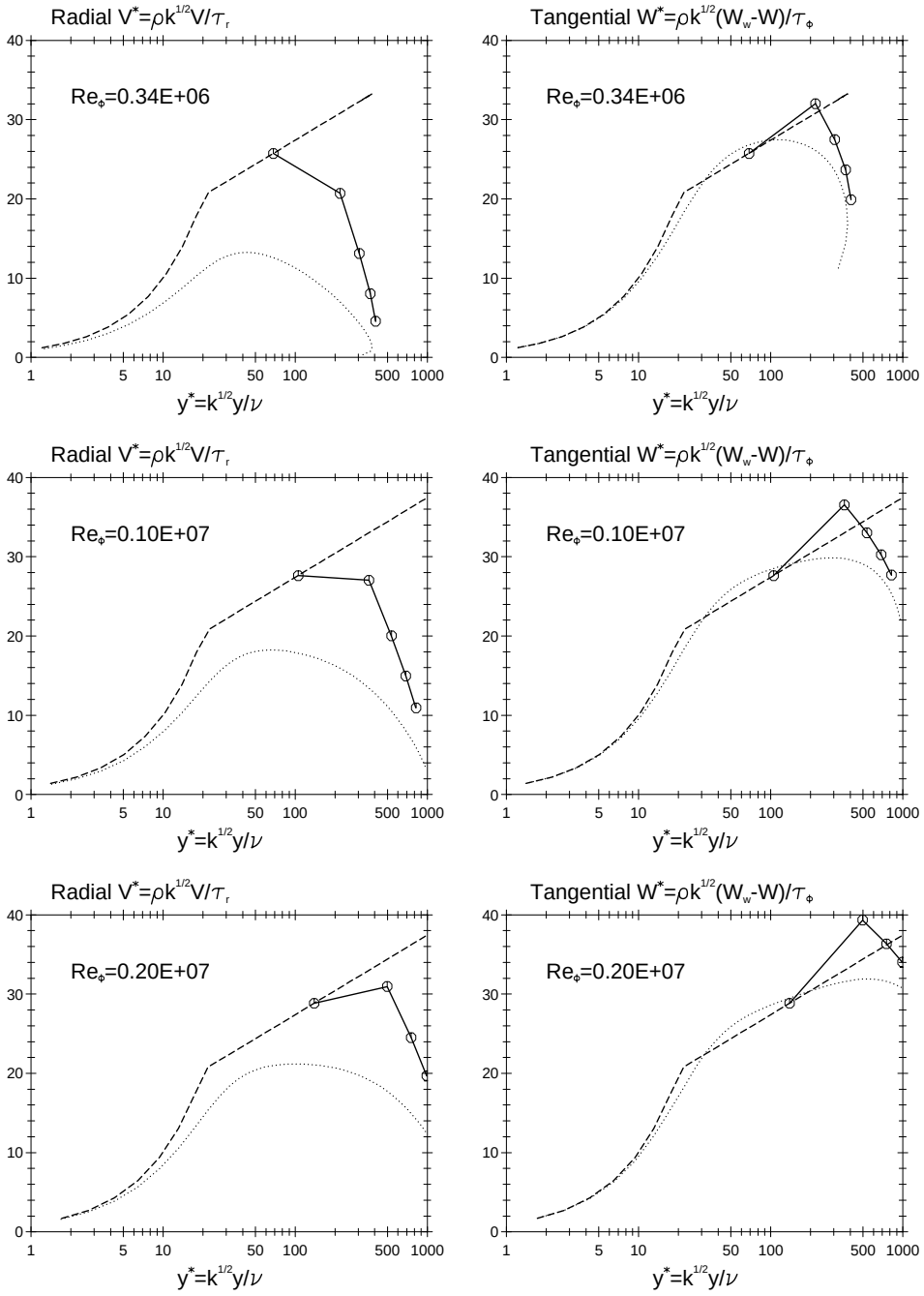

Figure 6.66: Radial and tangential velocity profiles in the free-disc flow using the Chieng & Launder wall function and non-linear $k-\varepsilon$ model with the 120×28 grid; —⊖—: high-*Re* model prediction (circles indicate the position of nodes); .....: low-*Re* model prediction; - - -: "universal" log-law.

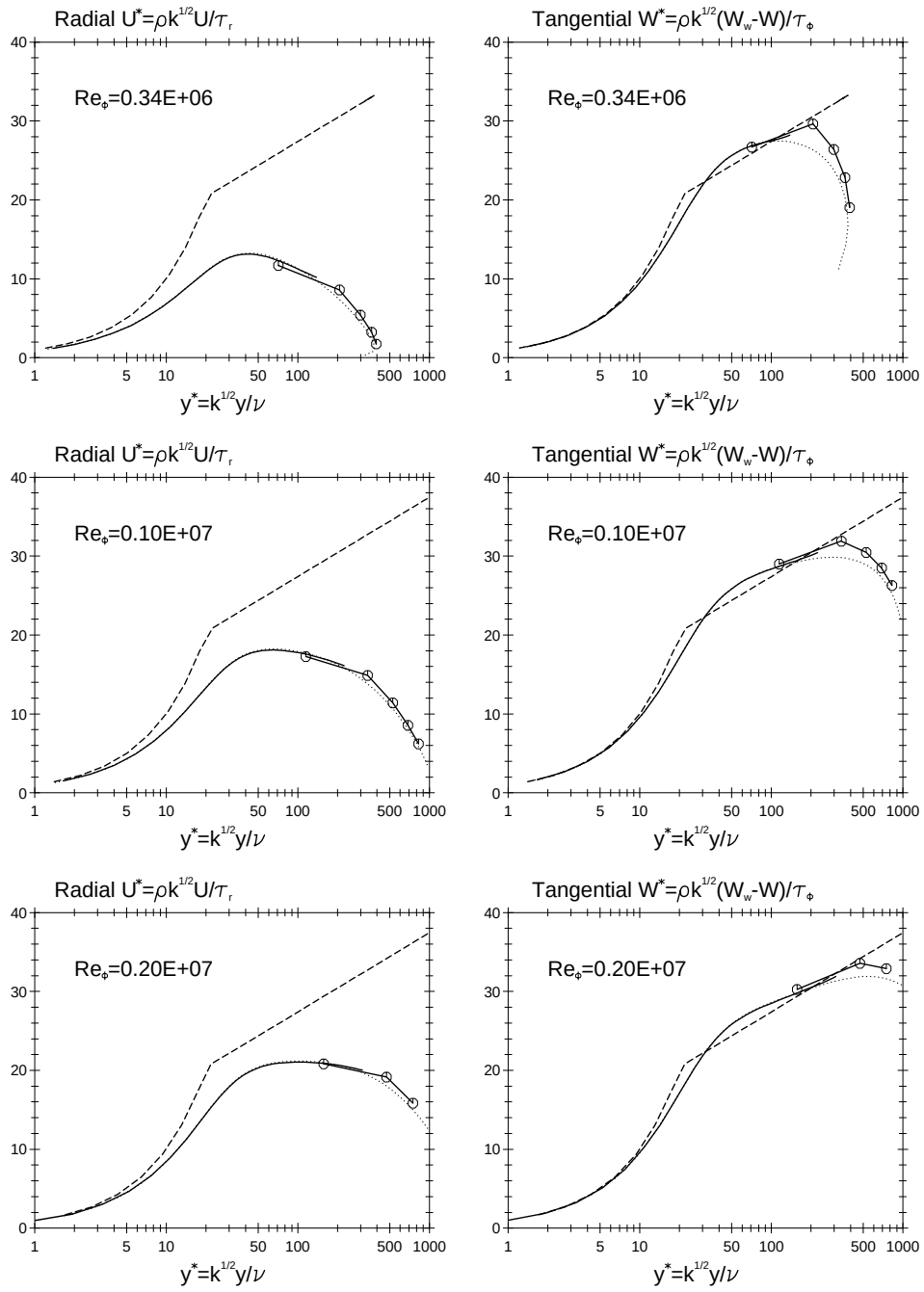

Figure 6.67: Radial and tangential velocity profiles in the free-disc flow using the UMIST-*N* wall function and non-linear $k-\varepsilon$ model with the 120×28 grid; —○—: high-*Re* model prediction (circles indicate the position of nodes); .....: low-*Re* model prediction; - - -: "universal" log-law.

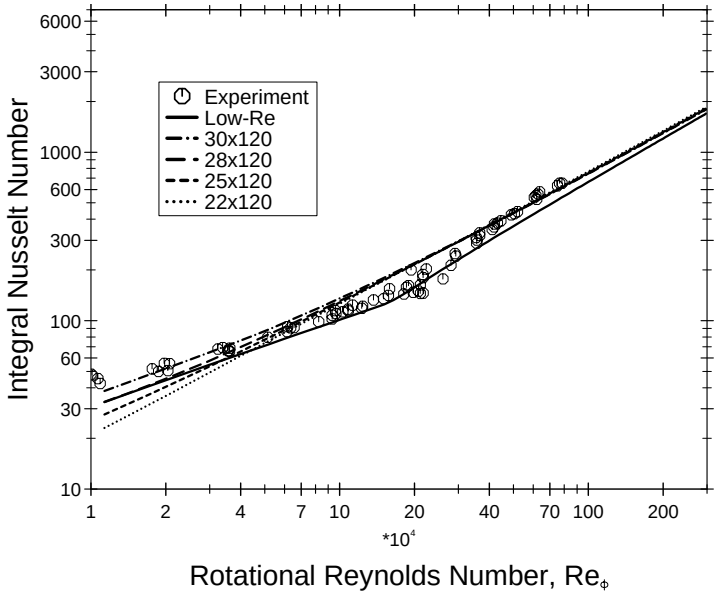

Figure 6.68: Predicted integral Nusselt number in the free-disc flow using the TEAM wall function and non-linear $k-\varepsilon$ model. Solid line: low-*Re* model; broken lines: wall function results for different grid arrangements; ○: experimental values from Cobb & Saunders [130].

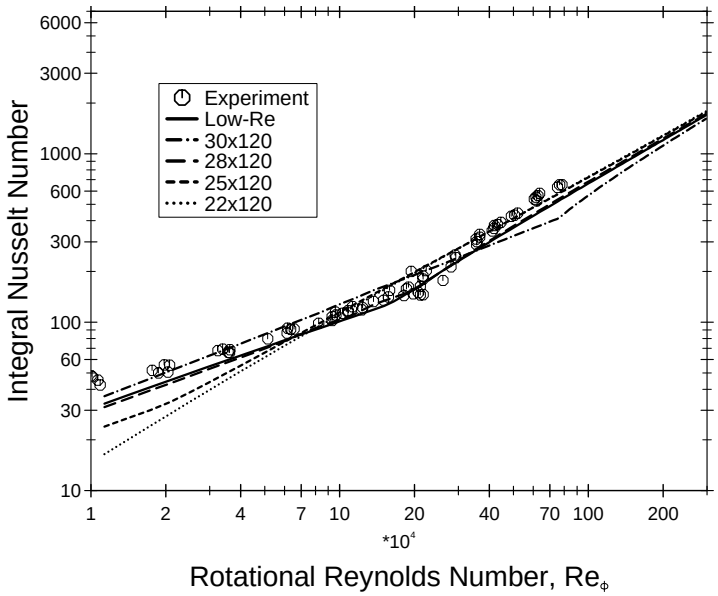

Figure 6.69: Predicted integral Nusselt number in the free-disc flow using the simplified Chieng & Launder wall function and non-linear $k-\varepsilon$ model. Solid line: low-*Re* model; broken lines: wall function results for different grid arrangements; ○: experimental values from Cobb & Saunders [130].

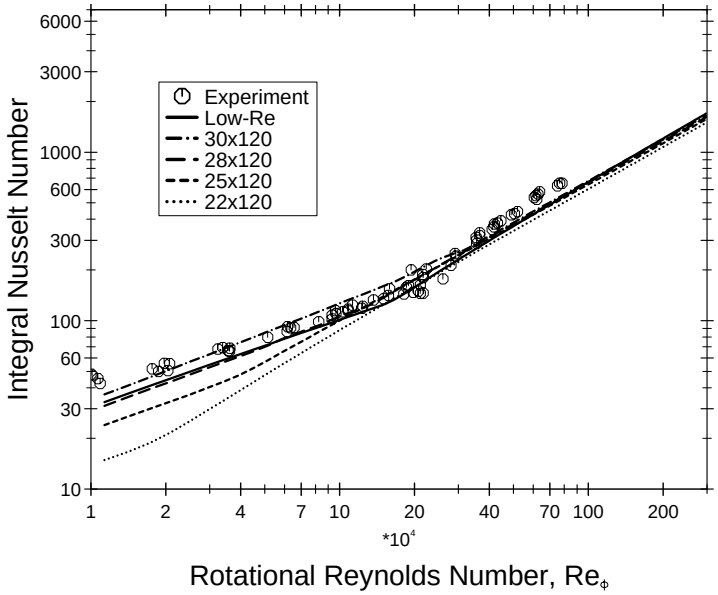

Figure 6.70: Predicted integral Nusselt number in the free-disc flow using the Chieng & Launder wall function and non-linear $k-\varepsilon$ model. Solid line: low-*Re* model; broken lines: wall function results for different grid arrangements; ○: experimental values from Cobb & Saunders [130].

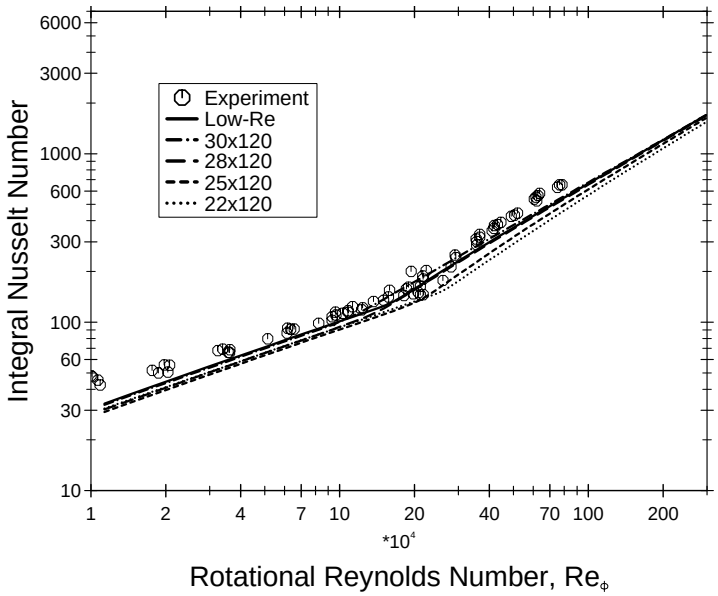

Figure 6.71: Predicted integral Nusselt number in the free-disc flow using the UMIST-*N* wall function and non-linear $k-\varepsilon$ model. Solid line: low-*Re* model; broken lines: wall function results for different grid arrangements; ○: experimental values from Cobb & Saunders [130].

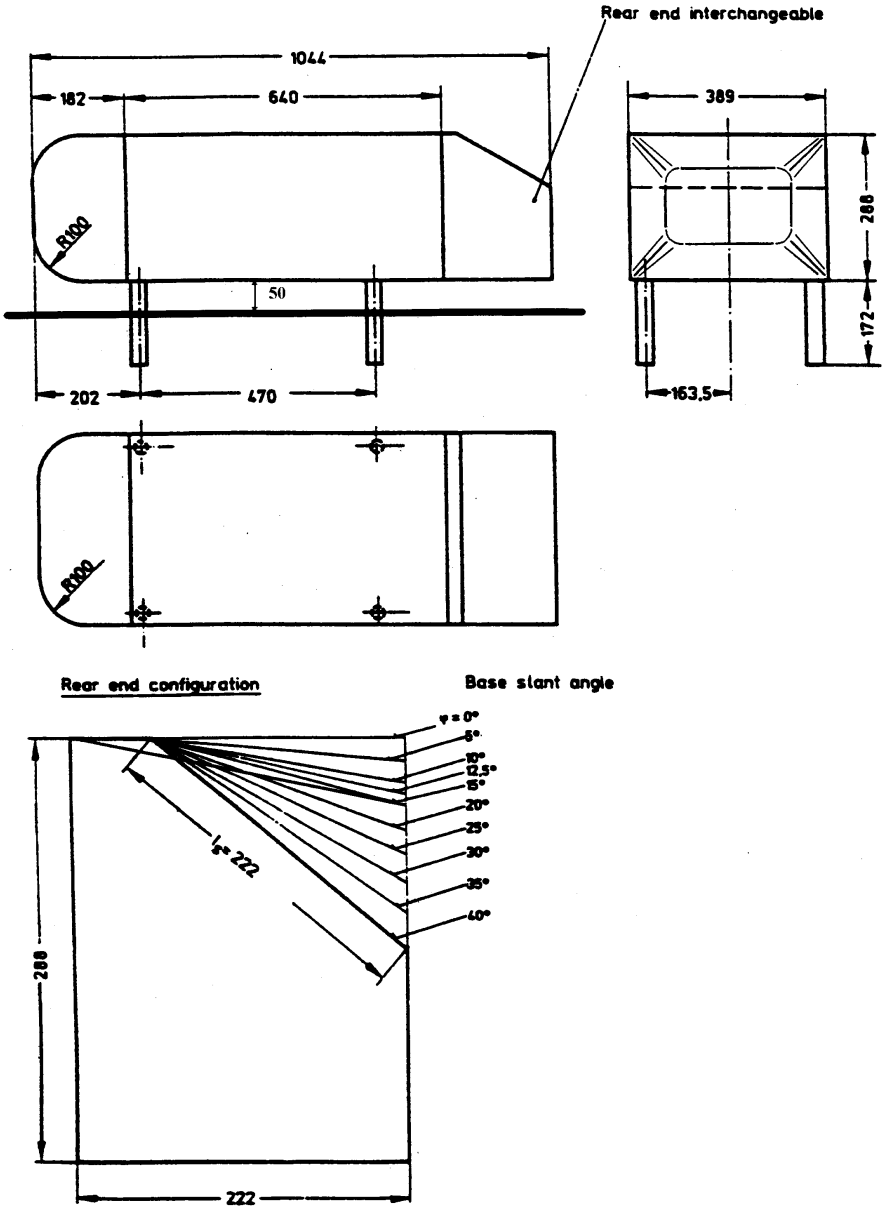

Figure 7.1: Ahmed body geometry (taken from Ahmed *et al*. [137]).

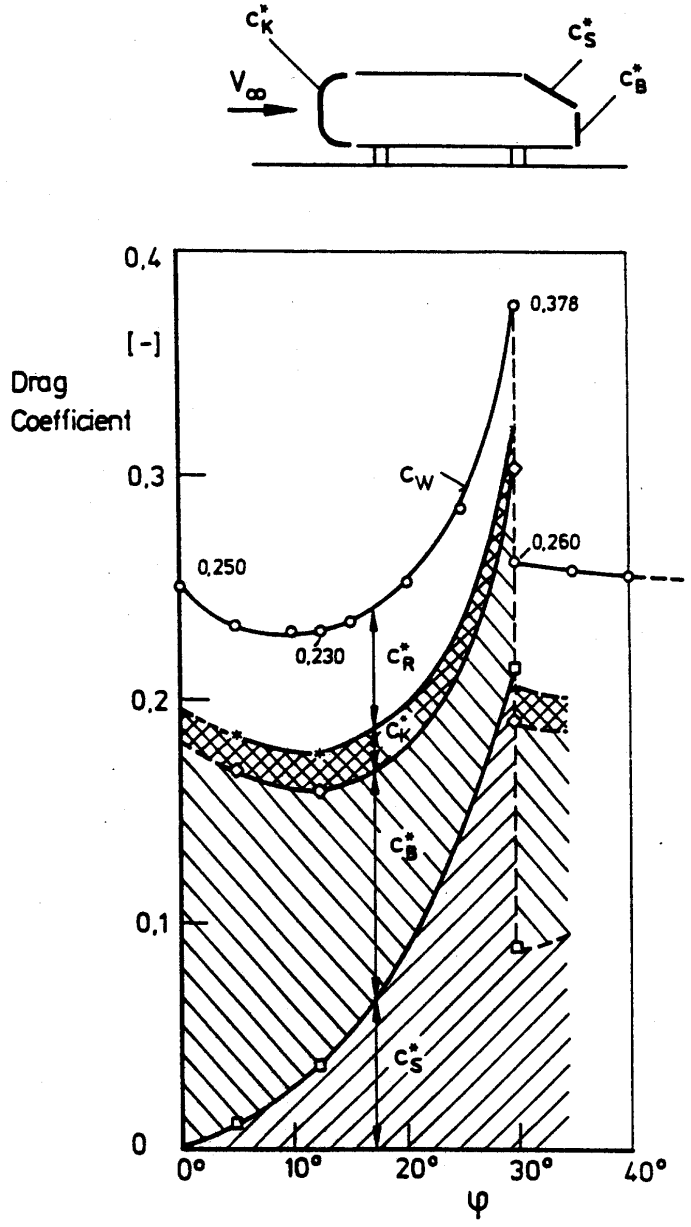

Figure 7.2: Drag breakdown measured by Ahmed *et al.* [137] for varying slant angle, φ.

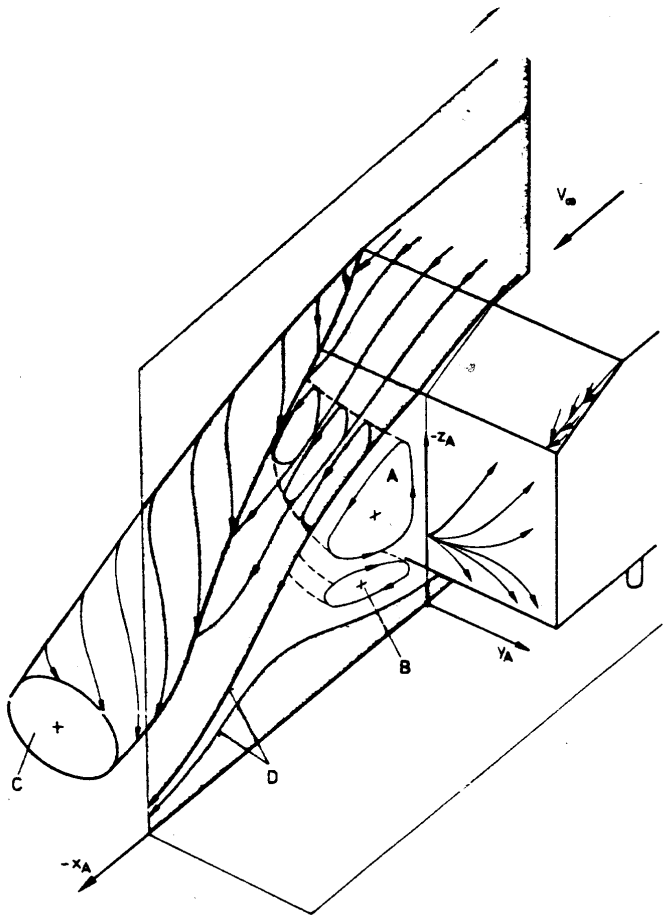

Figure 7.3: Schematic representation of the Ahmed body with low drag flow $\beta \approx 20^\circ$ (taken from Ahmed *et al*. [137]).

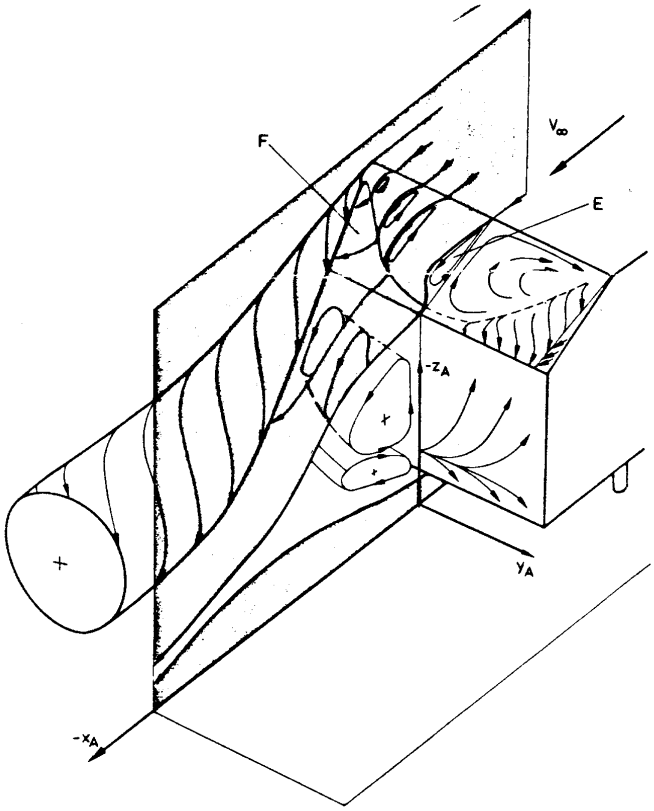

Figure 7.4: Schematic representation of the Ahmed body with high drag flow $\beta = 30^\circ$ (taken from Ahmed *et al*. [137]).

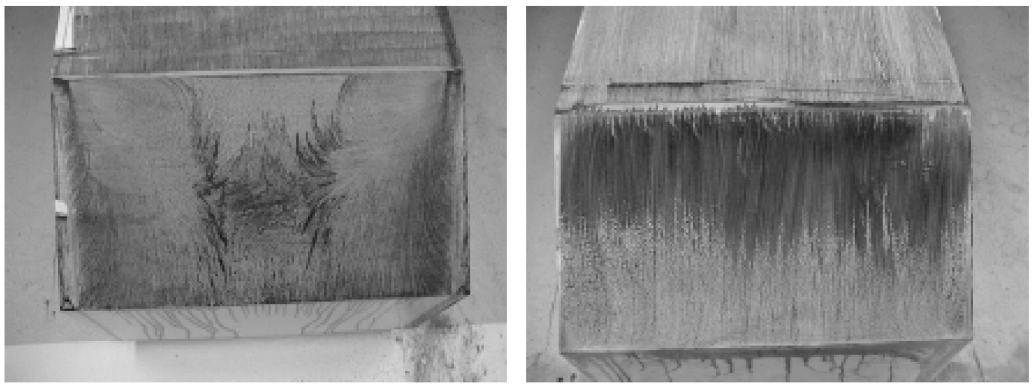

Figure 7.5: Oil/soot streakflow visualization on the rear of the Ahmed body with slant angles 25° (left) and 35° (right) (taken from Lienhart *et al*. [138]).

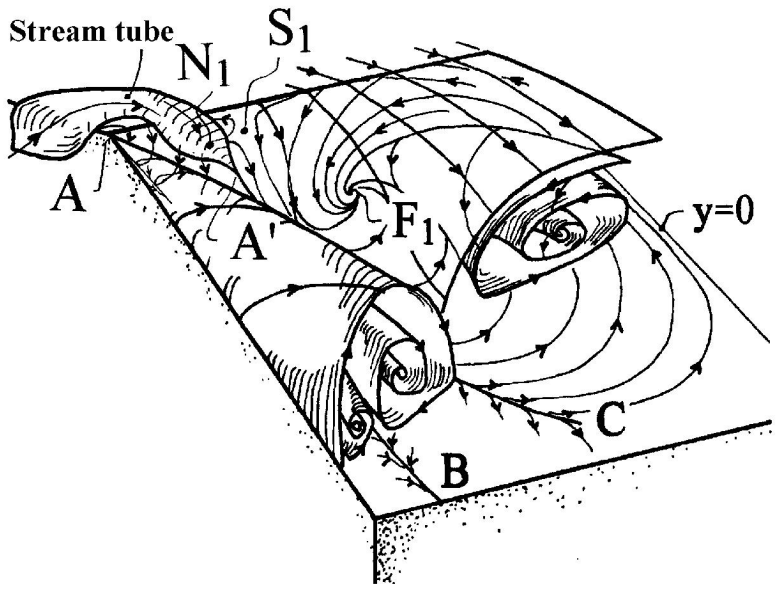

Figure 7.6: Schematic representation of the flow over the 25° rear slant of the Ahmed body (taken from from Spohn & Gilliéron. [139]).

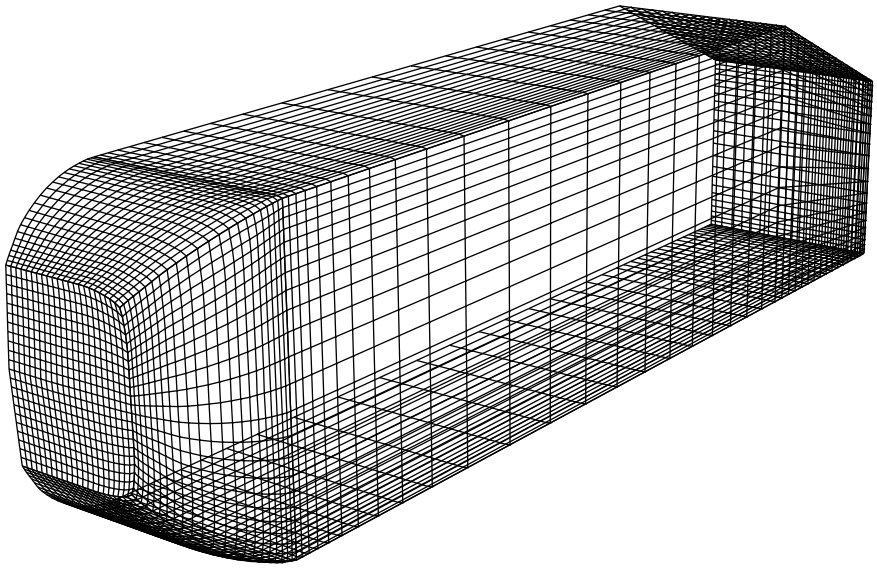

Figure 7.7: Grid on nose cone and front portion of Ahmed body (taken from Robinson [35]).

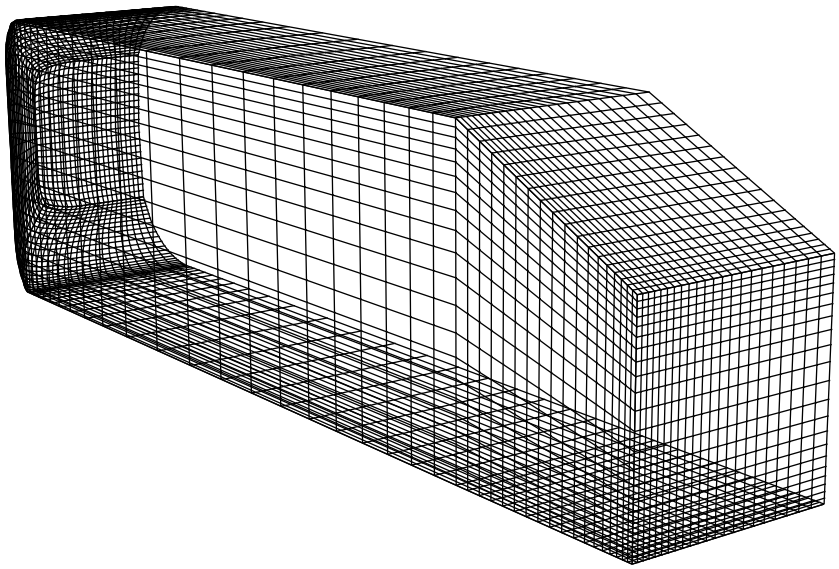

Figure 7.8: Grid used on rear section and slant of 25° Ahmed body (taken from Robinson [35]).

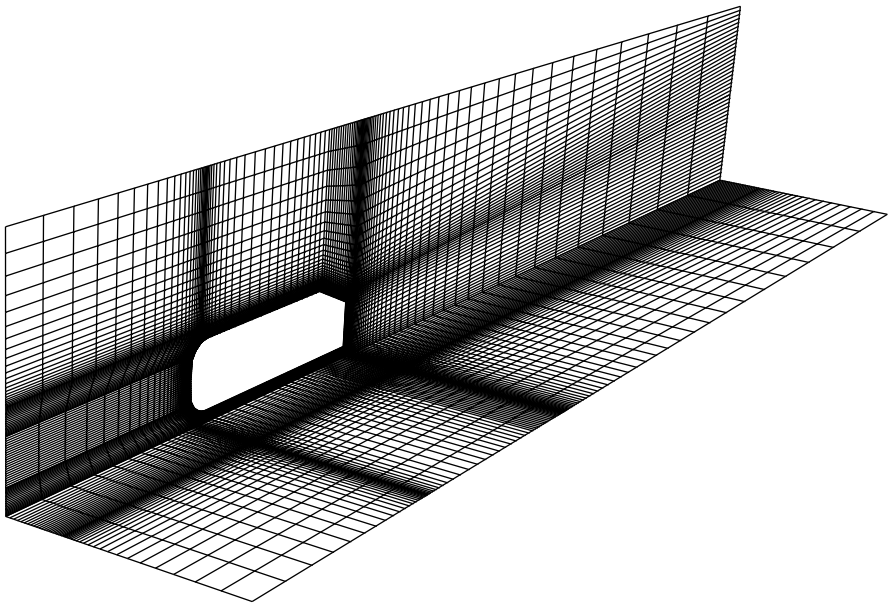

Figure 7.9: Grid on symmetry plane and floor showing some refinement propagated at block boundaries (taken from Robinson [35]).

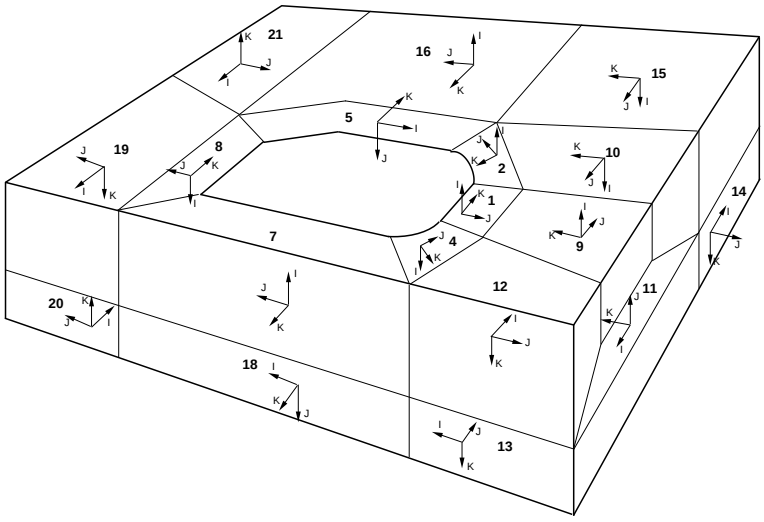

Figure 7.10: Block arrangement for the Ahmed body (25° slant angle) showing block numbers and coordinate frames.

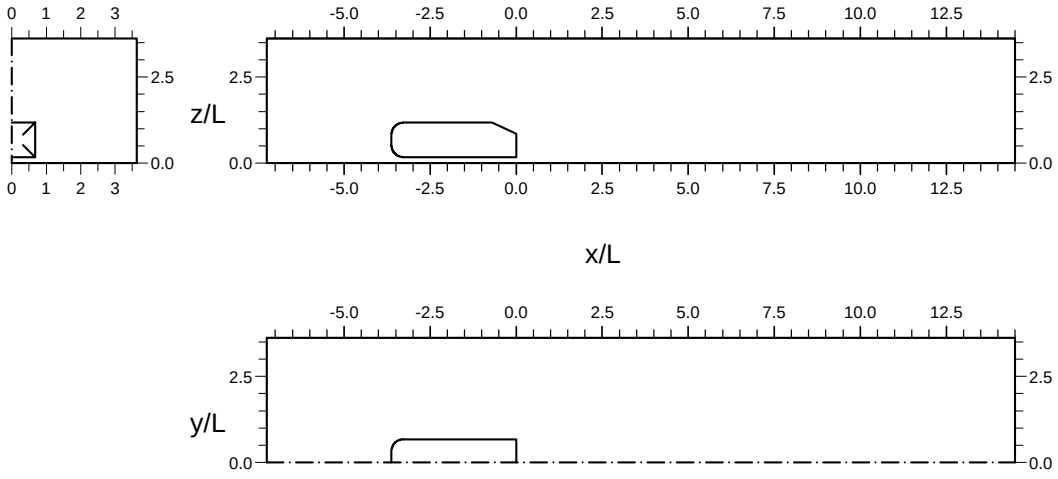

Figure 7.11: Sketch of domain in third angle projection used for Ahmed body calculations (taken from Robinson [35]). Lengths are non-dimensionalized with $L = 0.288$m, the height of the body.

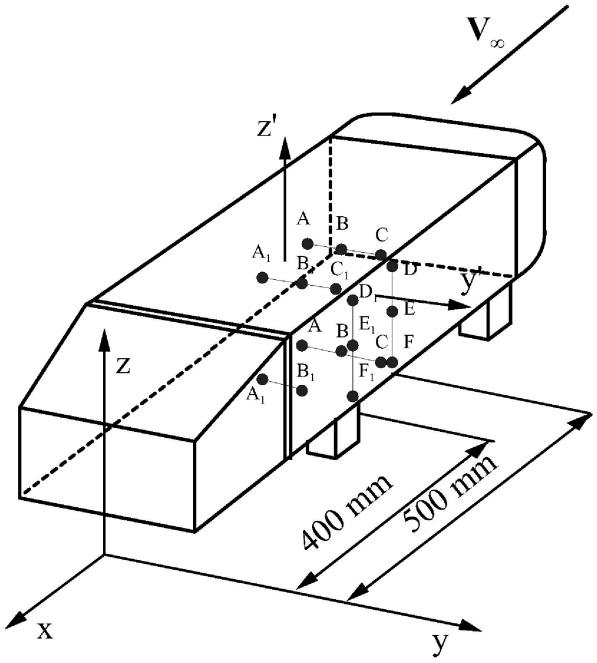

Top	x	y
A	-500	0
A_1	-400	0
B	-500	80
B_1	-400	80
C	-500	160
C_1	-400	160

Side	x	z
D	-500	294
D_1	-400	294
E	-500	194
E_1	-400	194
F	-500	94
F_1	-400	94

Down	x	y
A	-500	0
A_1	-400	0
B	-500	80
B_1	-400	80
C	-500	160

Figure 7.12: Sketch showing position of boundary layer measurements on the central part of the Ahmed body (taken from information supplied to participants of the 2002 ERCOFTAC Workshop on Refined Turbulence Modelling).

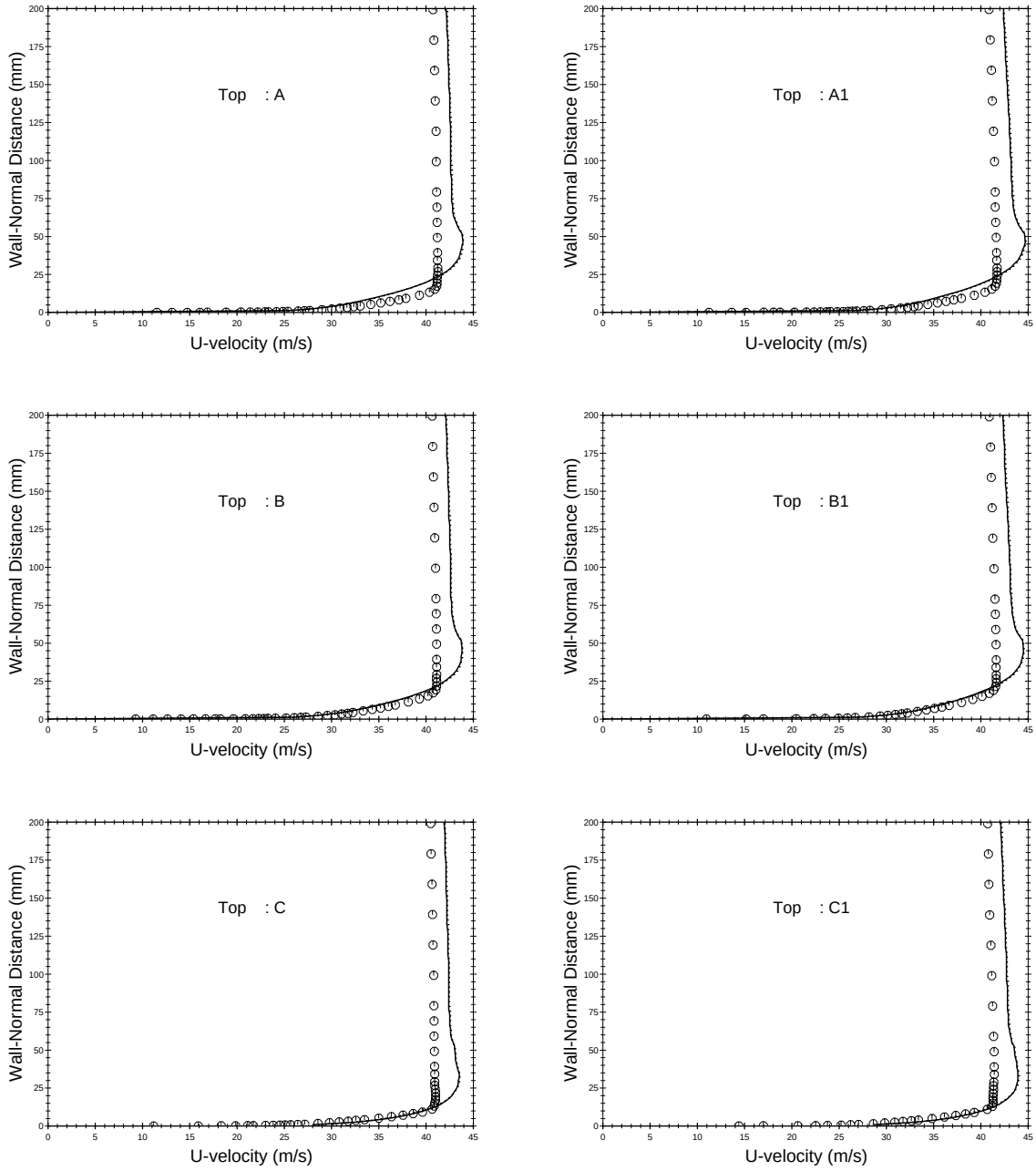

Figure 7.13: Streamwise mean U-velocity profiles at six positions on the top surface of the Ahmed body (for position of points see Figure 7.12), —-: linear $k-\varepsilon$ with SCL wall function; ....: linear $k-\varepsilon$ with UMIST-N wall function; ○: experimental measurements from Lienhart *et al*. [138].

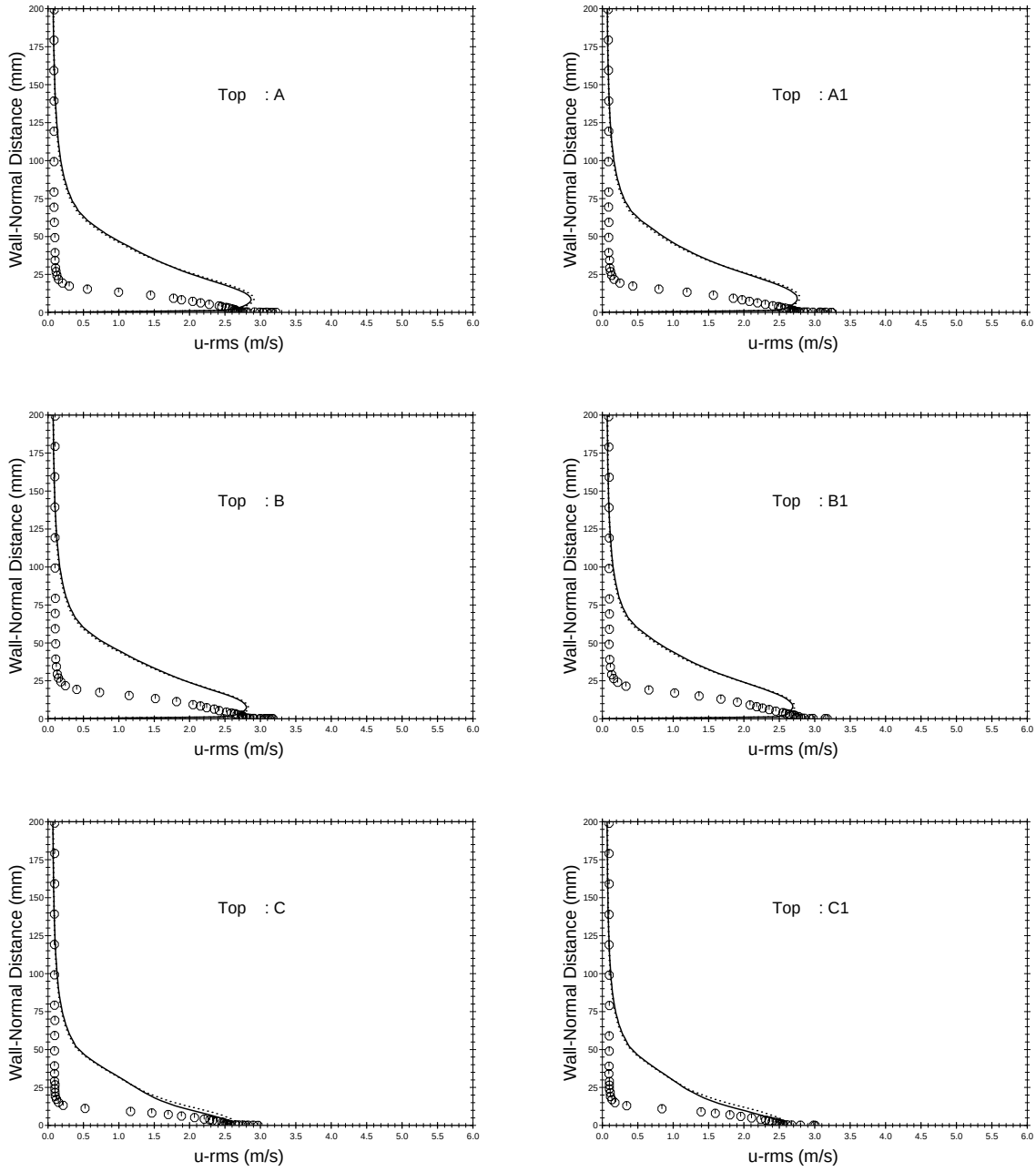

Figure 7.14: Streamwise RMS u'-profiles at six positions on the top surface of the Ahmed body (for position of points see Figure 7.12), —-: linear $k-\varepsilon$ with SCL wall function; ....: linear $k-\varepsilon$ with UMIST-*N* wall function; ○: experimental measurements from Lienhart *et al*. [138].

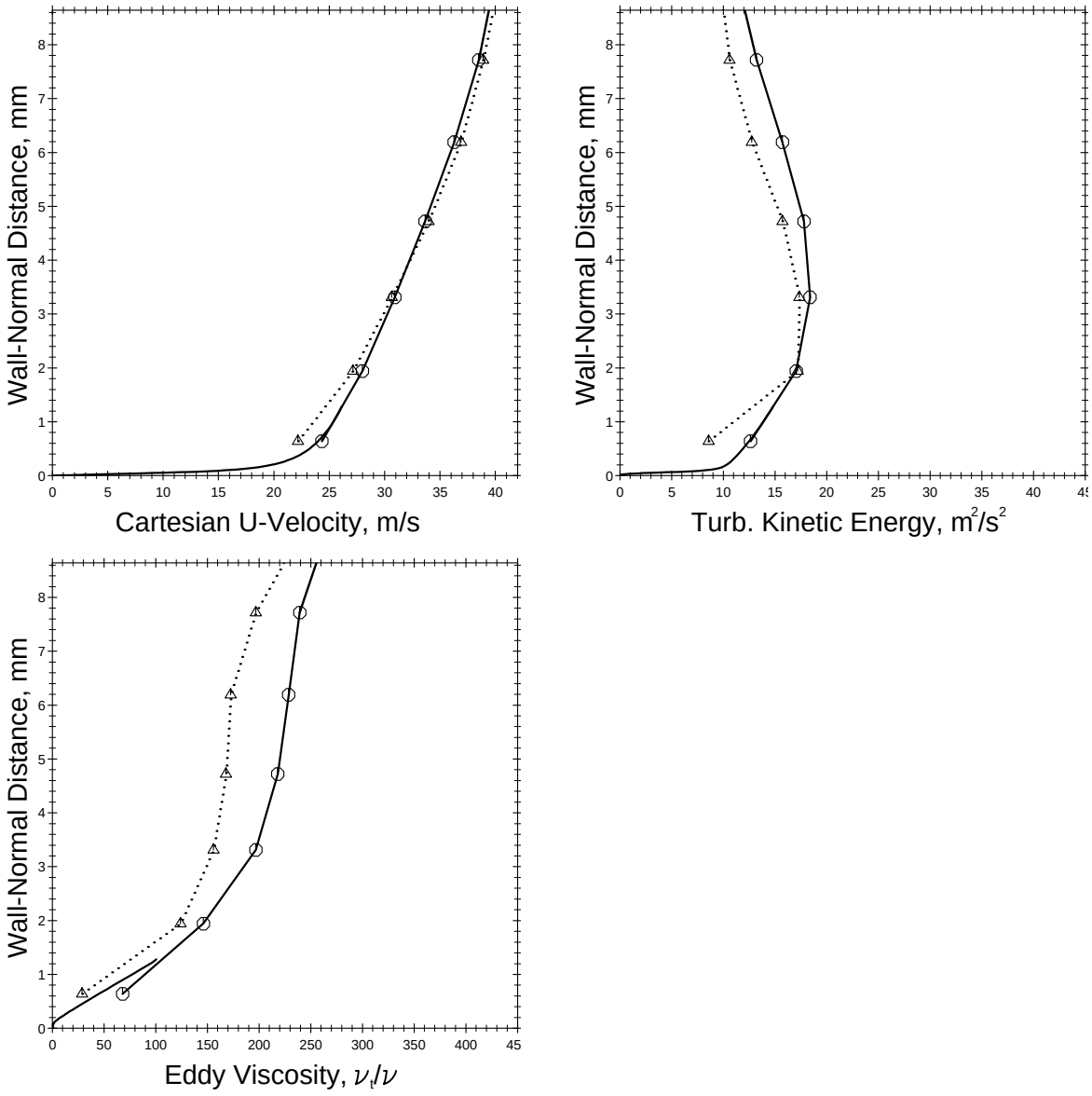

Figure 7.15: Streamwise mean U-velocity, turbulent kinetic energy and eddy-viscosity at $x \approx -831$mm on the top surface and on centreline of the Ahmed body, —○—: linear $k-\varepsilon$ with UMIST-N wall function; ....△....: linear $k-\varepsilon$ with SCL wall function; (symbols indicate position of grid nodes).

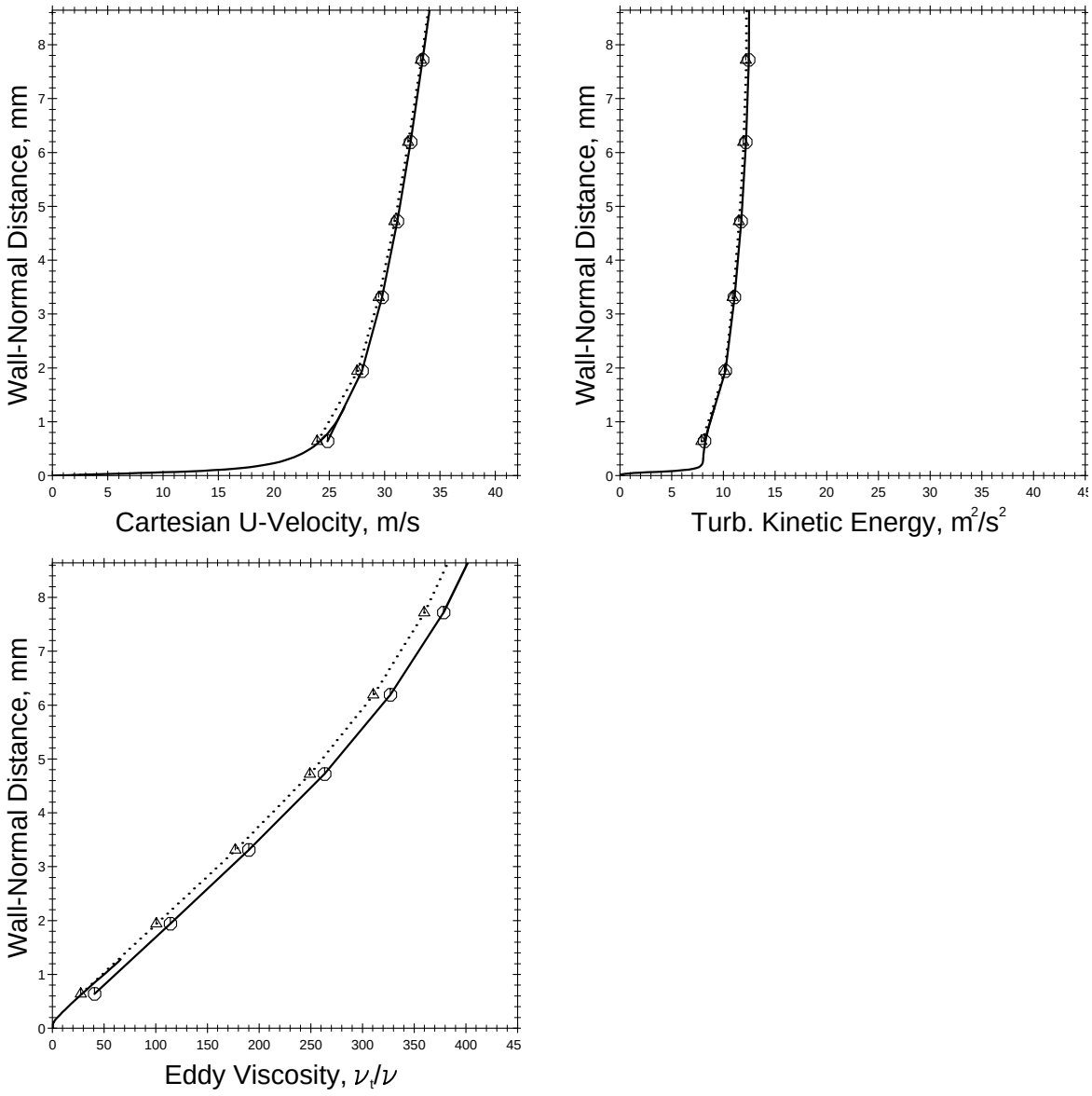

Figure 7.16: Streamwise mean U-velocity, turbulent kinetic energy and eddy-viscosity at $x \approx -475$mm on the top surface and on centreline of the Ahmed body, —○—: linear $k-\varepsilon$ with UMIST-N wall function; ....△....: linear $k-\varepsilon$ with SCL wall function; (symbols indicate position of grid nodes).

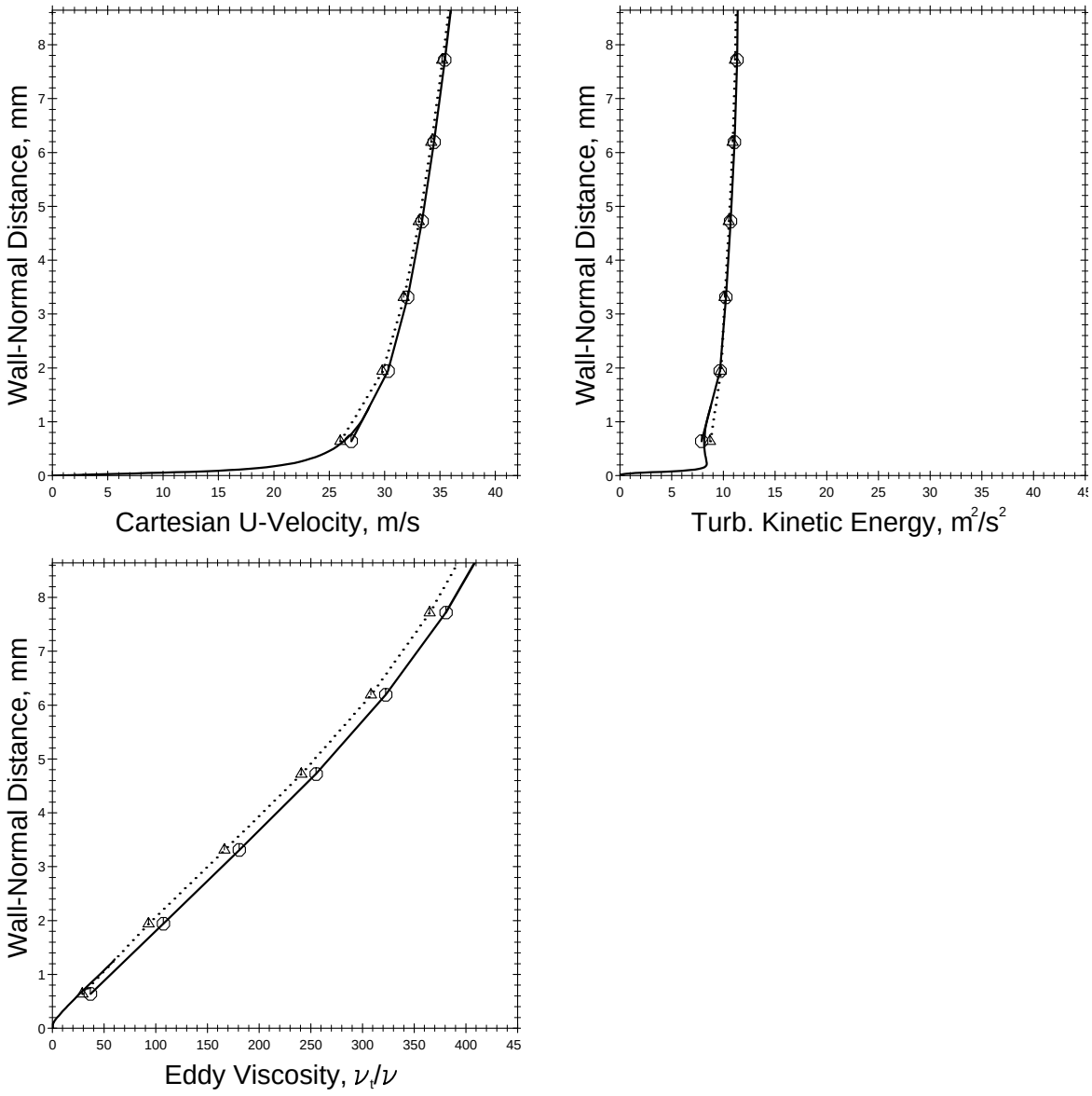

Figure 7.17: Streamwise mean U-velocity, turbulent kinetic energy and eddy-viscosity at $x \approx -346$mm on the top surface and on centreline of the Ahmed body, —○—: linear $k-\varepsilon$ with UMIST-N wall function; ....△....: linear $k-\varepsilon$ with SCL wall function; (symbols indicate position of grid nodes).

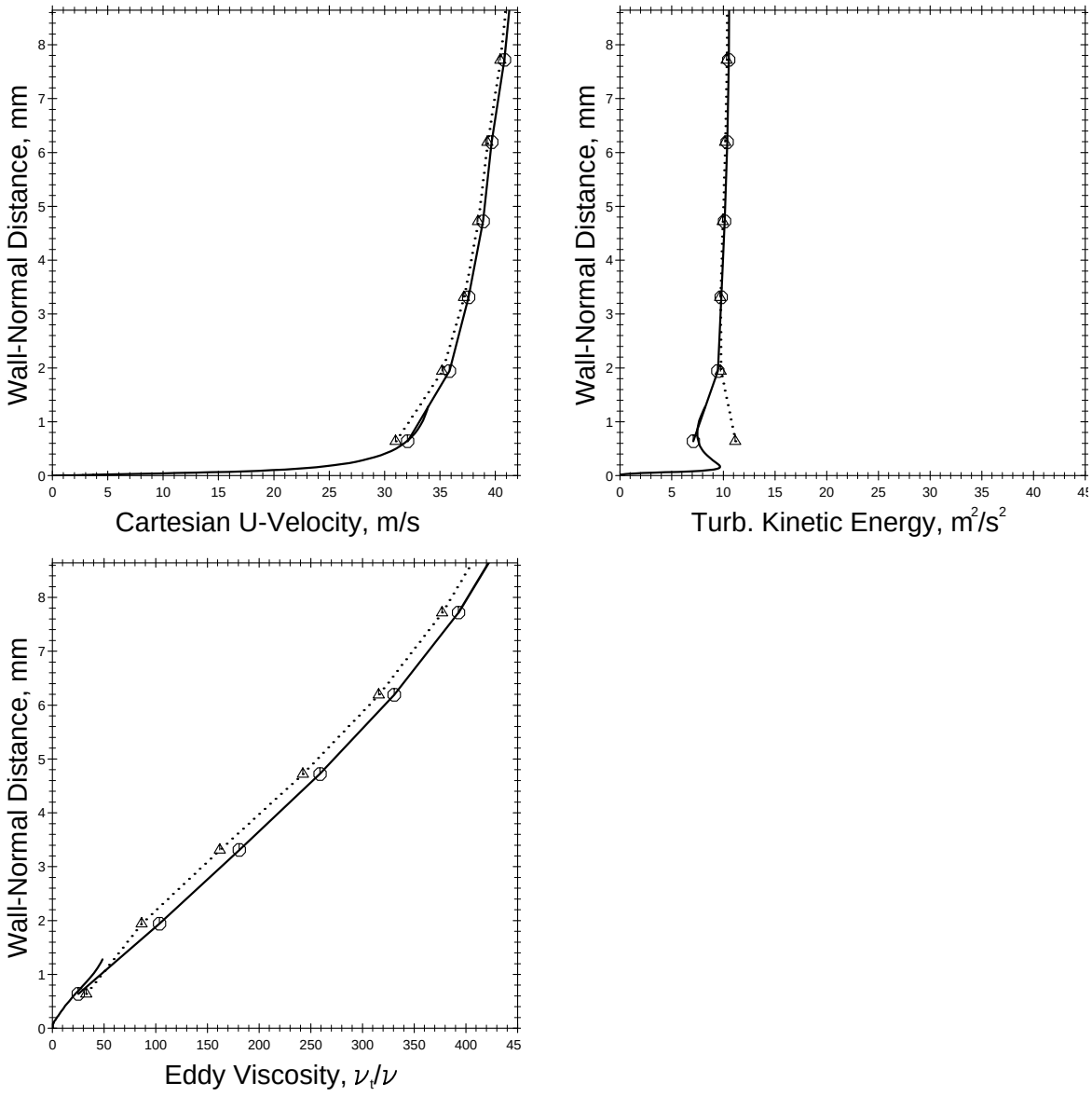

Figure 7.18: Streamwise mean U-velocity, turbulent kinetic energy and eddy-viscosity at $x \approx -244$mm on the top surface and on centreline of the Ahmed body, —○—: linear $k-\varepsilon$ with UMIST-N wall function; ....△....: linear $k-\varepsilon$ with SCL wall function; (symbols indicate position of grid nodes).

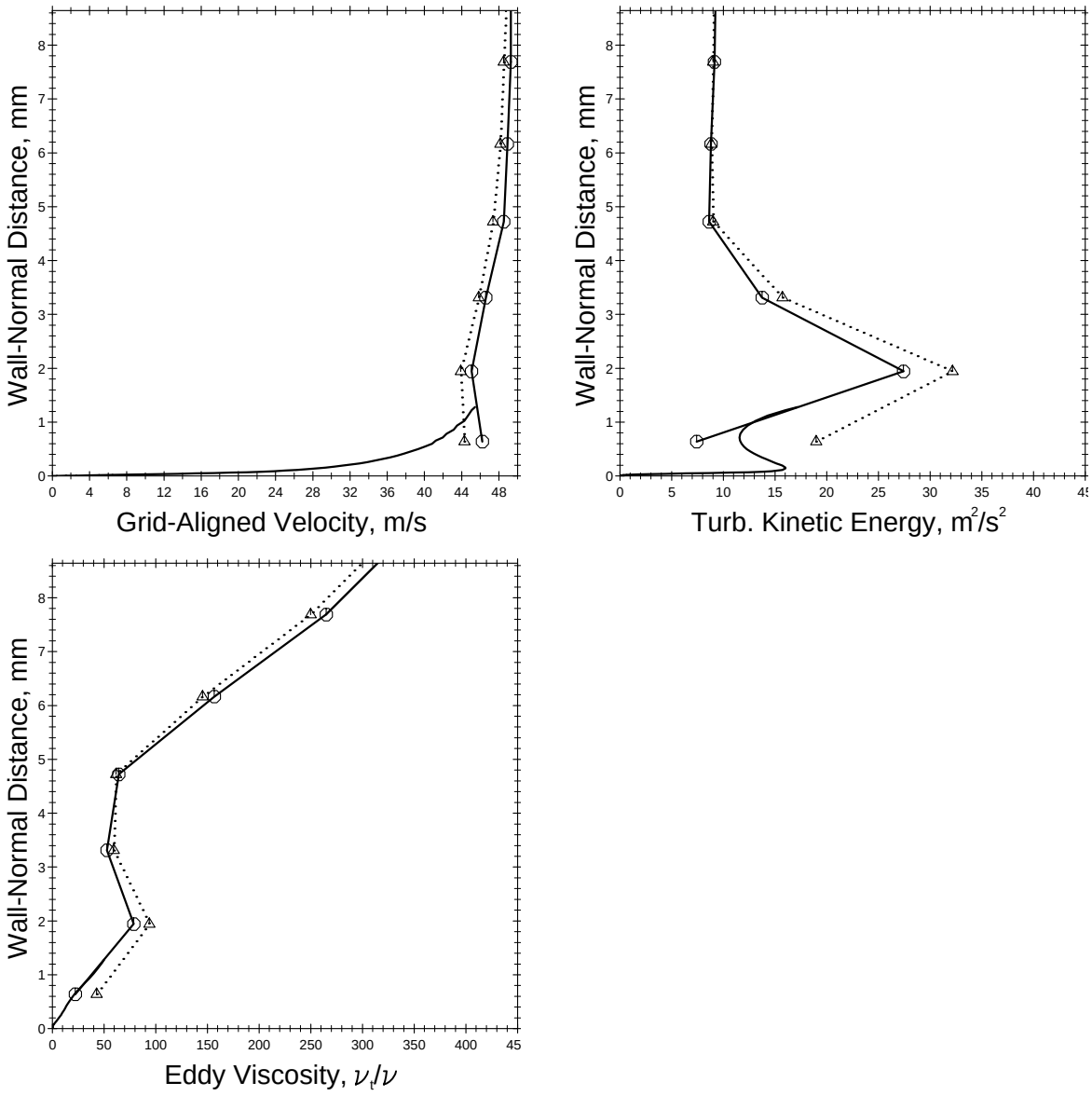

Figure 7.19: Wall-parallel mean velocity, turbulent kinetic energy and eddy-viscosity at $x \approx -194$mm on the slant surface and on centreline of the Ahmed body, —○—: linear $k-\varepsilon$ with UMIST-*N* wall function; ....△....: linear $k-\varepsilon$ with SCL wall function; (symbols indicate position of grid nodes).

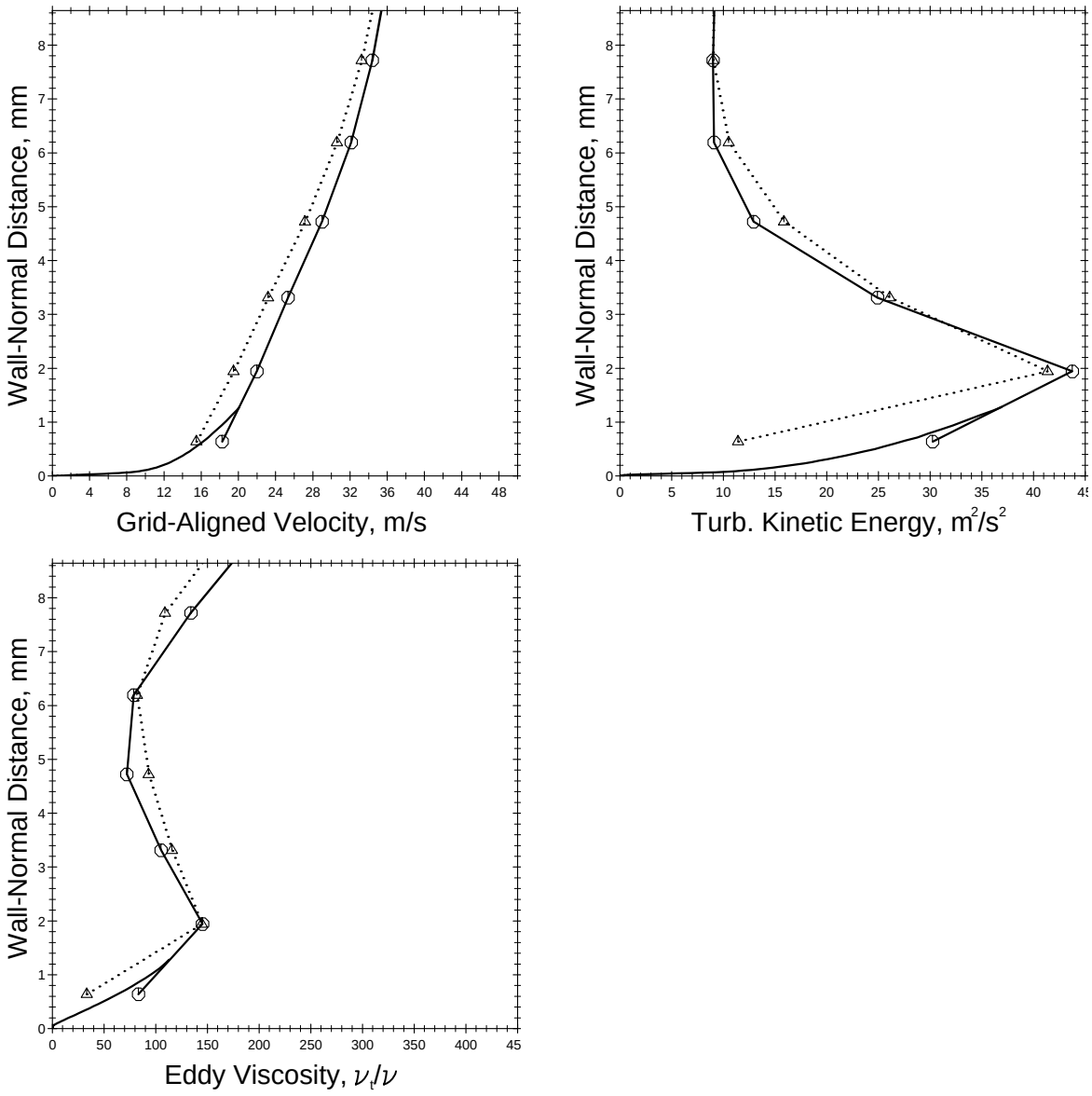

Figure 7.20: Wall-parallel mean velocity, turbulent kinetic energy and eddy-viscosity at $x \approx -165$mm on the slant surface and on centreline of the Ahmed body, —○—: linear $k-\varepsilon$ with UMIST-*N* wall function; ....△....: linear $k-\varepsilon$ with SCL wall function; (symbols indicate position of grid nodes).

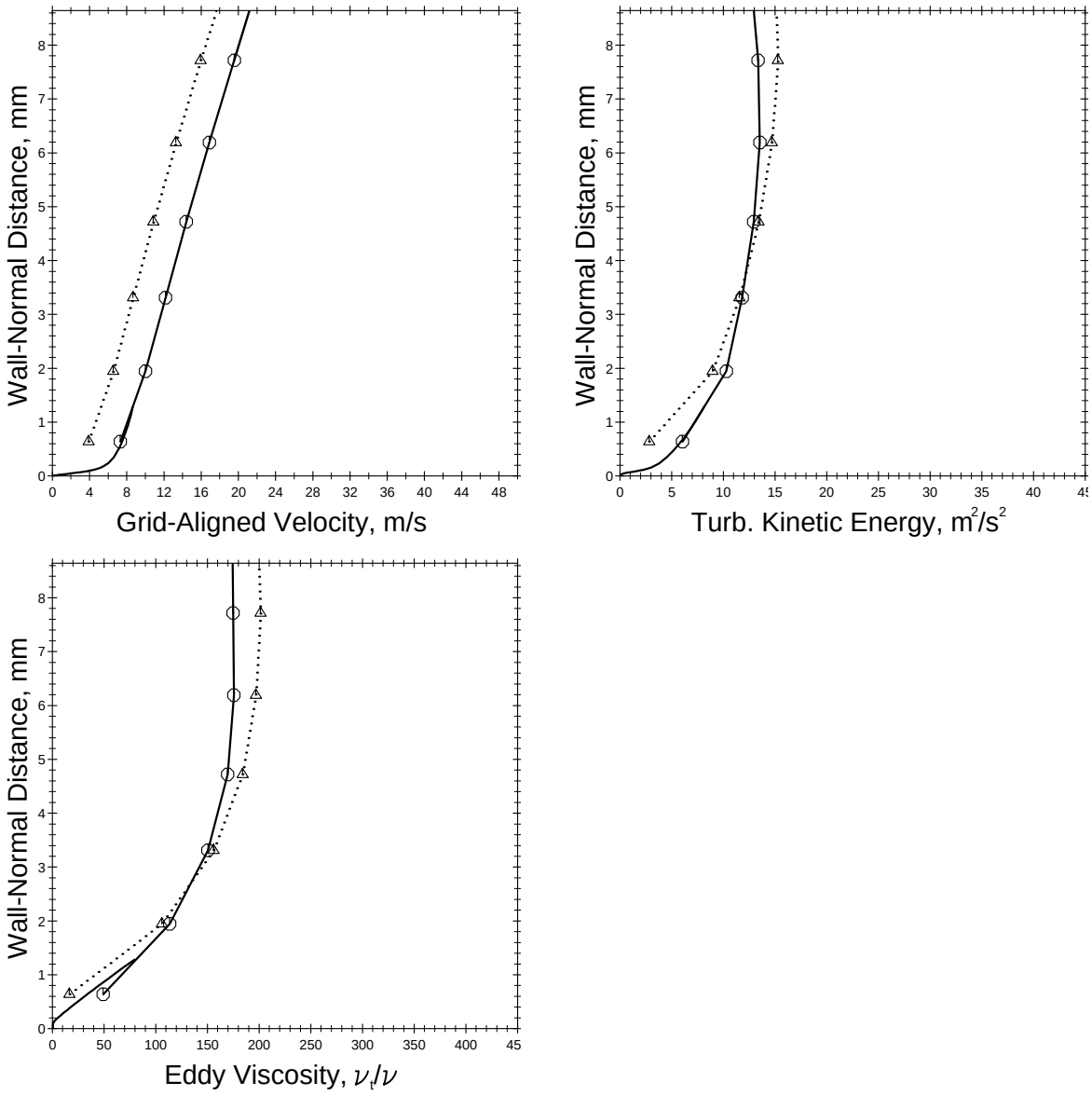

Figure 7.21: Wall-parallel mean velocity, turbulent kinetic energy and eddy-viscosity at $x \approx -109$mm on the slant surface and on centreline of the Ahmed body, —○—: linear $k-\varepsilon$ with UMIST-*N* wall function; ....△....: linear $k-\varepsilon$ with SCL wall function; (symbols indicate position of grid nodes).

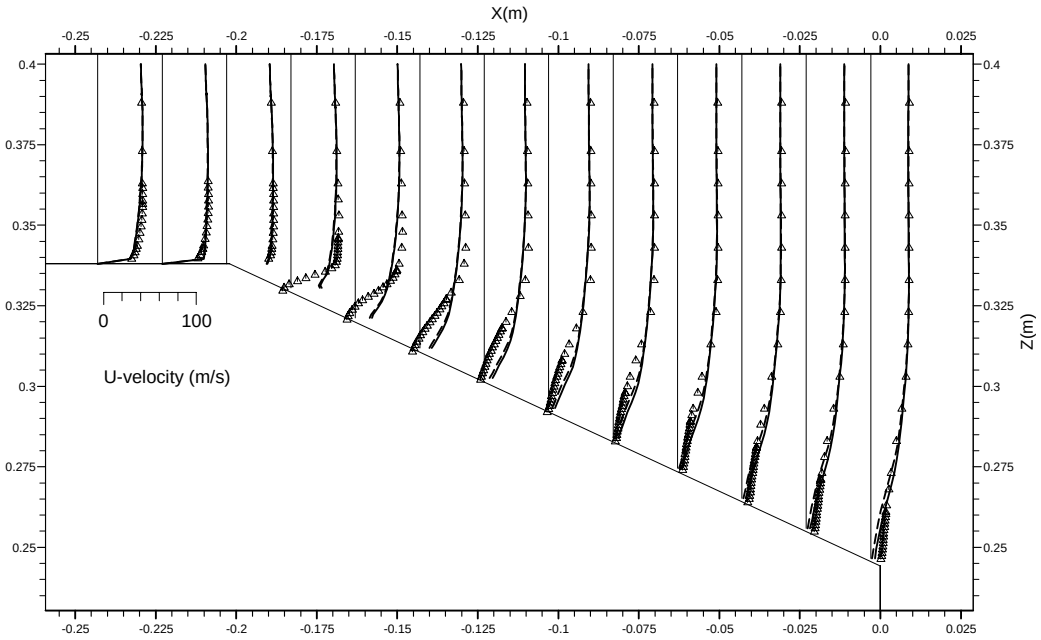

Figure 7.22: Mean U-velocity profiles over the Ahmed body 25° rear slant, ——: linear $k-\varepsilon$ with UMIST-N wall function; - - -: linear $k-\varepsilon$ with SCL wall function; △: experimental measurements of Lienhart *et al*. [138].

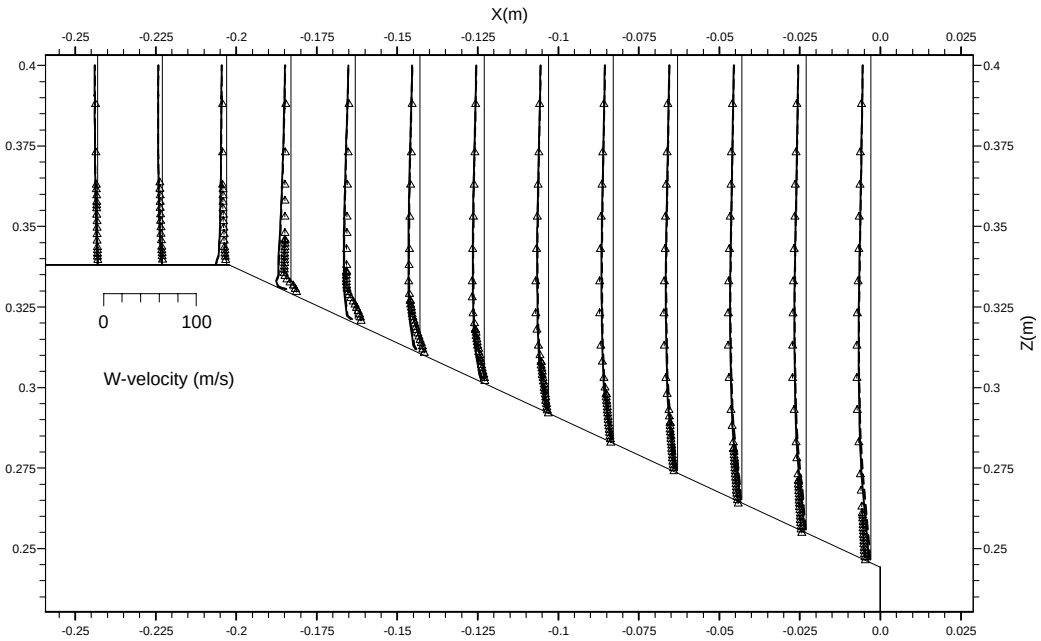

Figure 7.23: Mean W-velocity profiles over the Ahmed body 25° rear slant, ——: linear $k-\varepsilon$ with UMIST-N wall function; - - -: linear $k-\varepsilon$ with SCL wall function; △: experimental measurements of Lienhart *et al*. [138].

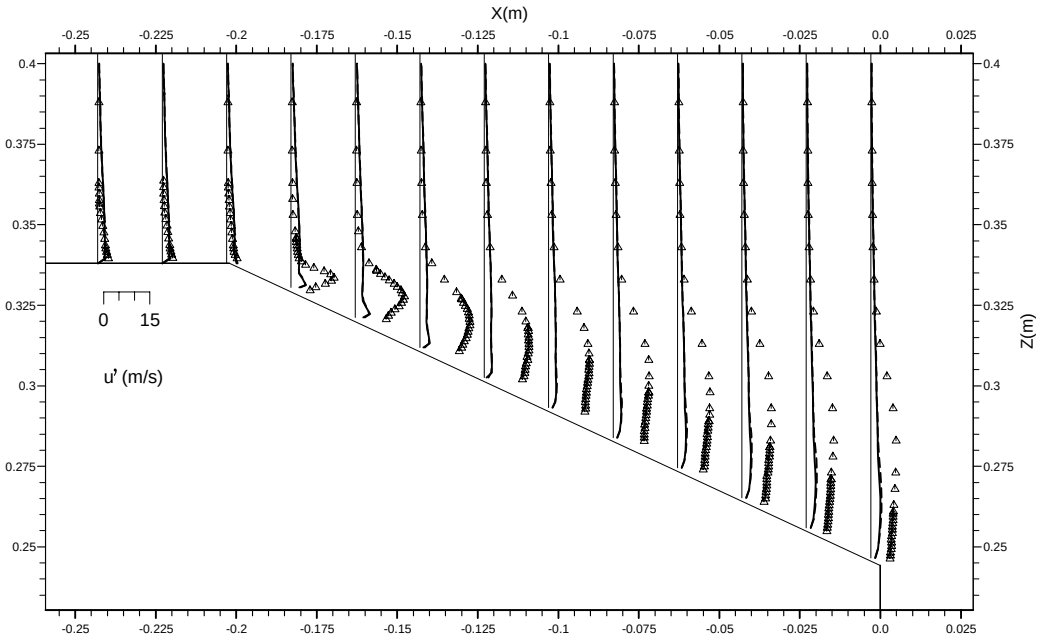

Figure 7.24: RMS u'-velocity profiles over the Ahmed body 25° rear slant, ——: linear $k-\varepsilon$ with UMIST-*N* wall function; - - -: linear $k-\varepsilon$ with SCL wall function; △: experimental measurements of Lienhart *et al*. [138].

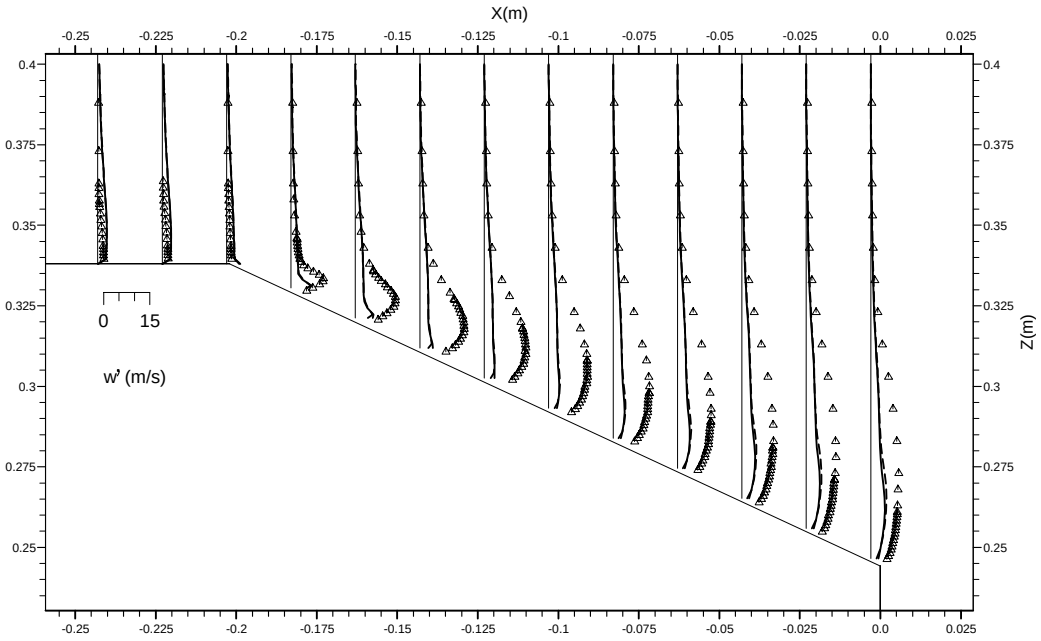

Figure 7.25: RMS w'-velocity profiles over the Ahmed body 25° rear slant, ——: linear $k-\varepsilon$ with UMIST-*N* wall function; - - -: linear $k-\varepsilon$ with SCL wall function; △: experimental measurements of Lienhart *et al*. [138].

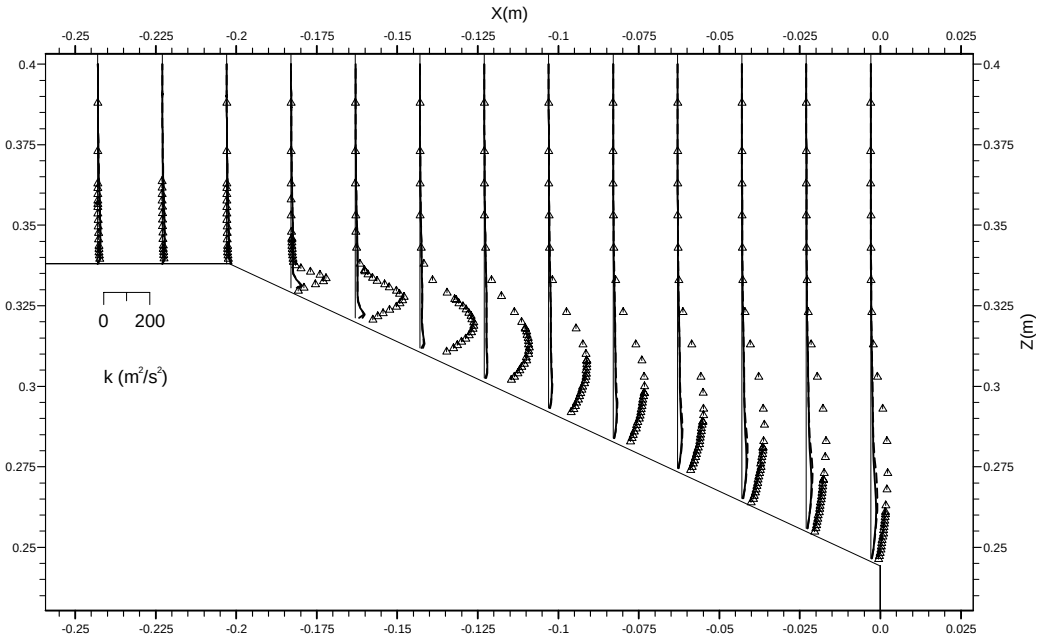

Figure 7.26: Turbulent kinetic energy profiles over the Ahmed body 25° rear slant, ——: linear $k-\varepsilon$ with UMIST-*N* wall function; - - -: linear $k-\varepsilon$ with SCL wall function; △: experimental measurements of Lienhart *et al*. [138].

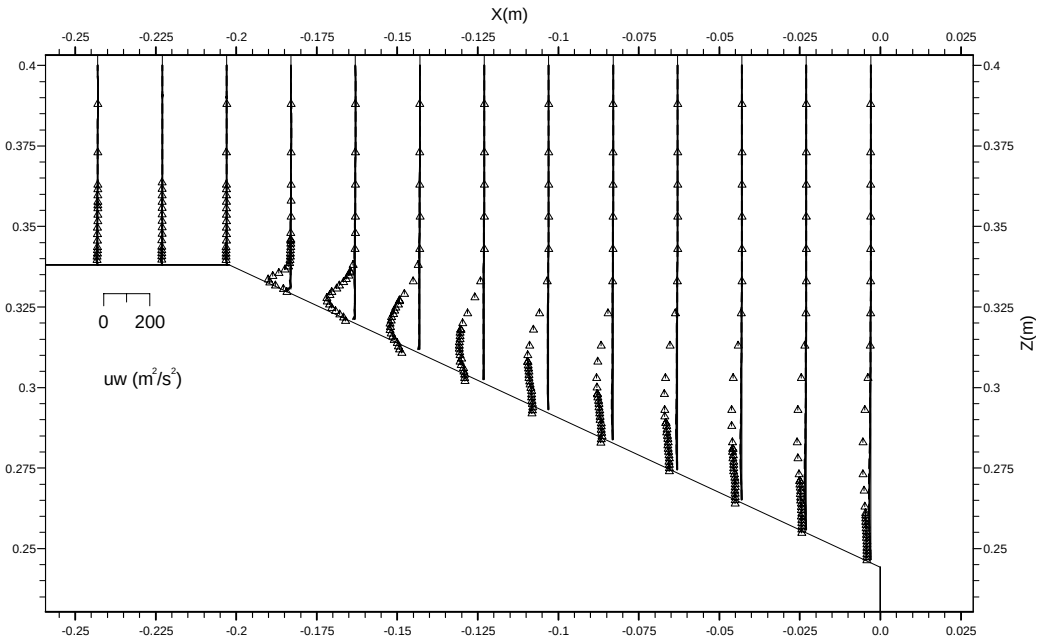

Figure 7.27: *uw*-stress profiles over the Ahmed body 25° rear slant, ——: linear $k-\varepsilon$ with UMIST-*N* wall function; - - -: linear $k-\varepsilon$ with SCL wall function; △: experimental measurements of Lienhart *et al*. [138].

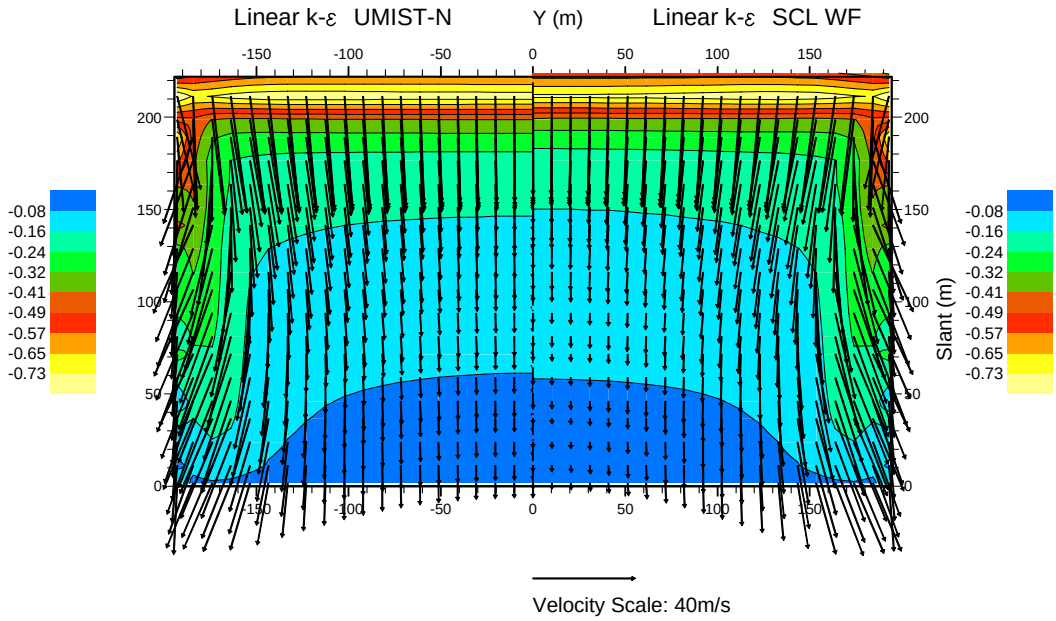

Figure 7.28: Velocity vectors and pressure coefficient contours on the Ahmed body 25° rear slant. The left half of the picture shows results from the linear $k-\varepsilon$ model with UMIST-*N* wall function and the right half the linear $k-\varepsilon$ model with SCL wall function. Velocity vectors shown are taken from values at the main-grid node adjacent to the wall surface.

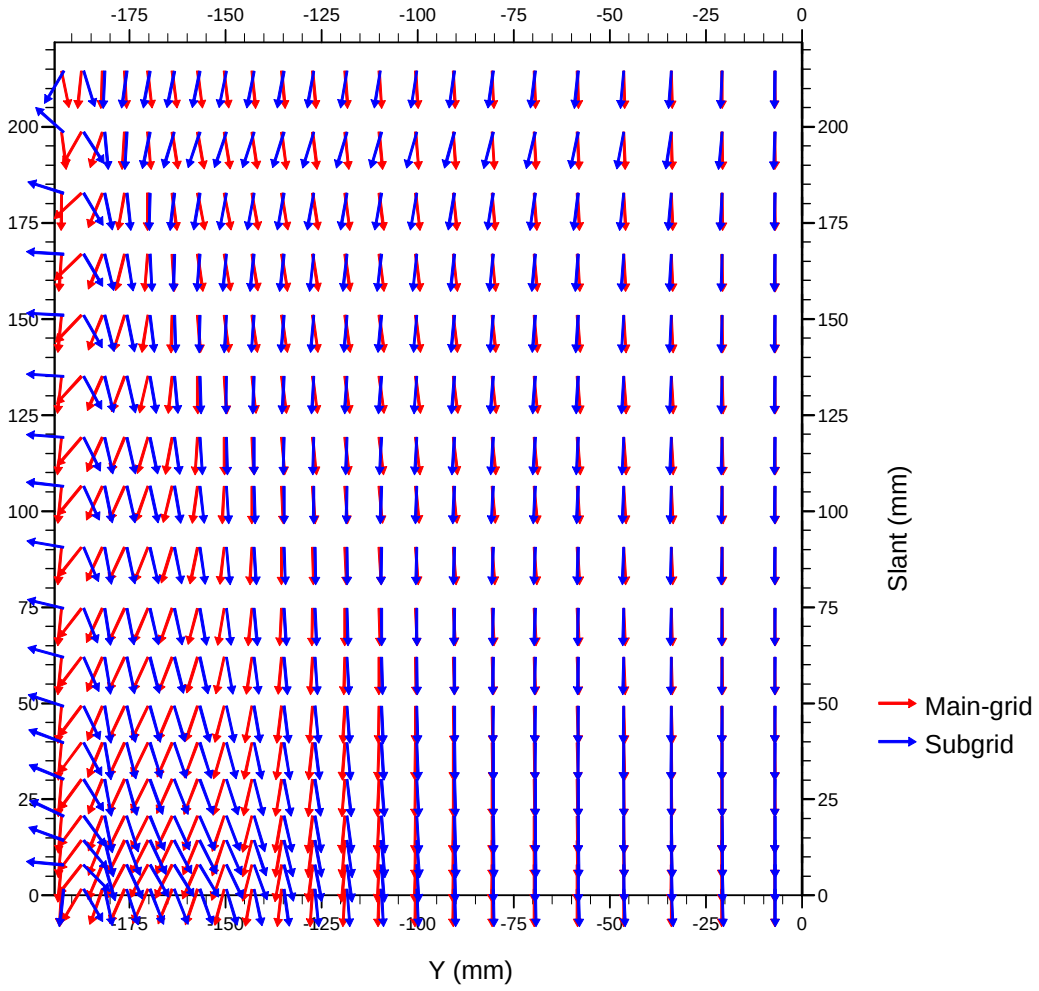

Figure 7.29: Velocity vectors on the Ahmed body 25° rear slant, as viewed from above (the axis of symmetry is on the right-hand *y*-axis). Results were obtained using the linear $k-\varepsilon$ model and UMIST-*N* wall function. Velocity vectors in red are the near-wall main-grid node values whilst vectors in blue are from the subgrid node which is closest to the wall (i.e. the subgrid node that is used to calculate the wall shear stress). Differences in the direction of the red and blue arrows therefore indicate skewing of the velocity vector between the main-grid node and the wall. The red vectors correspond to those shown on the left-hand-side of Figure 7.28. All vectors have been specified with unit length.

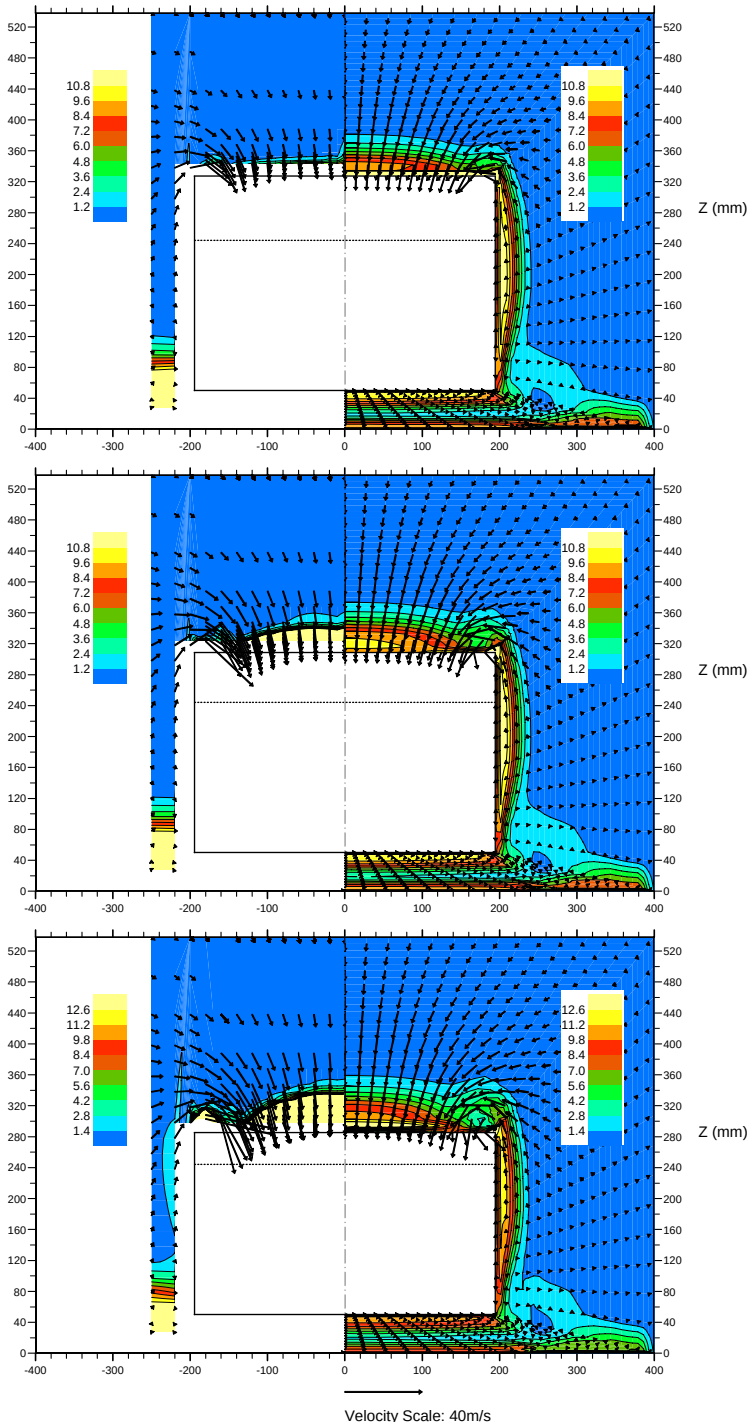

Figure 7.30: Velocity vectors and turbulent kinetic energy contours (in m^2s^{-2}) around the rear of the Ahmed body. The left half of the pictures show experimental data from Lienhart *et al.* [138] and the right half predictions using the linear $k-\varepsilon$ model with UMIST-*N* wall function. The outline of the Ahmed body is shown in solid lines and the slant edge in broken lines. The top picture is at $x=-178$mm, the middle at $x=-138$mm and bottom at $x=-88$mm.

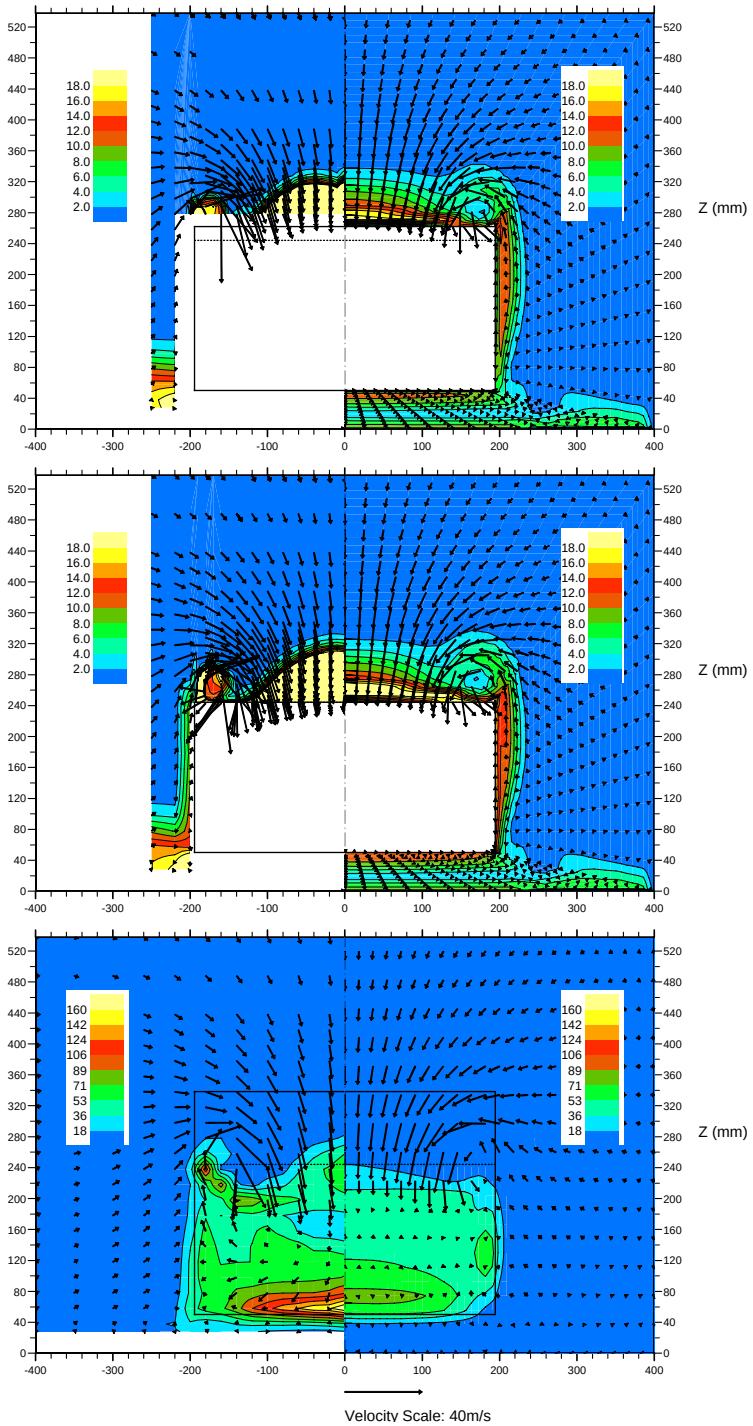

Figure 7.31: Velocity vectors and turbulent kinetic energy contours (in m^2s^{-2}) around the rear of the Ahmed body. The left half of the pictures show experimental data from Lienhart *et al.* [138] and the right half predictions using the linear $k-\varepsilon$ model with UMIST-*N* wall function. The outline of the Ahmed body is shown in solid lines and the slant edge in broken lines. The top picture is at $x=-38$mm, the middle at $x=0$mm and bottom at $x=80$mm.

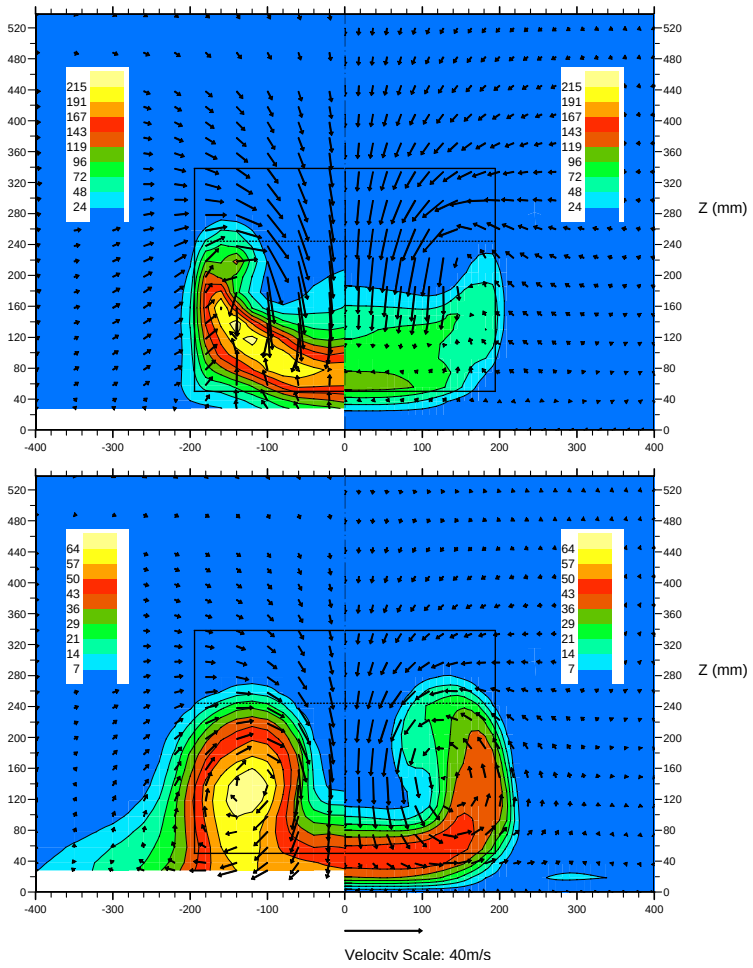

Figure 7.32: Velocity vectors and turbulent kinetic energy contours (in m^2/s^2) around the rear of the Ahmed body. The left half of the pictures show experimental data from Lienhart *et al.* [138] and the right half predictions using the linear $k-\varepsilon$ model with UMIST-*N* wall function. The outline of the Ahmed body is shown in solid lines and the slant edge in broken lines. The top picture is at $x = 200$mm and the bottom at $x = 500$mm.

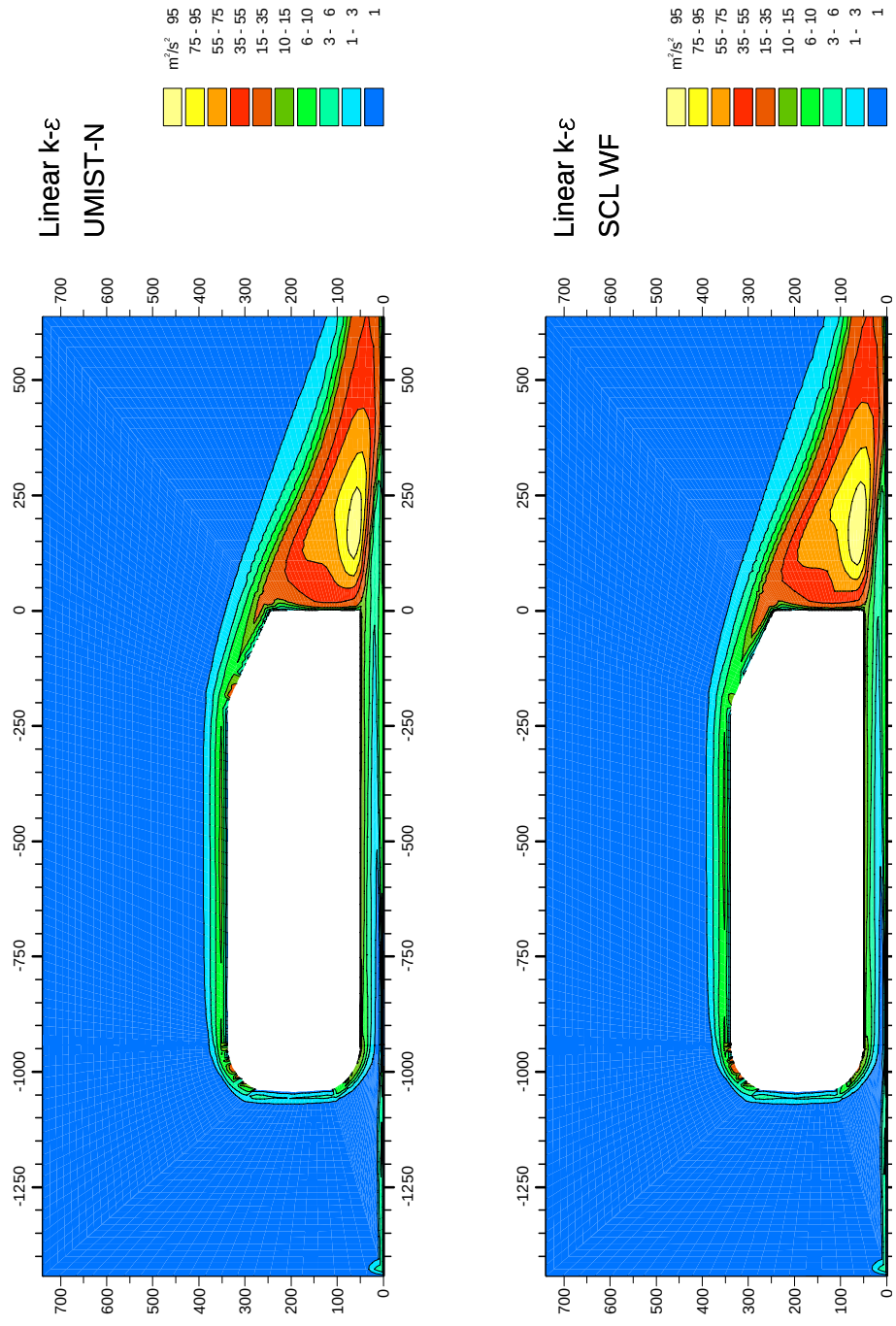

Figure 7.33: Turbulent kinetic energy contours around the Ahmed body at $y = 0$ using the linear $k - \varepsilon$ model with the UMIST-*N* wall function (top) and the linear $k - \varepsilon$ model with the Simplified Chieng & Launder wall function (bottom).

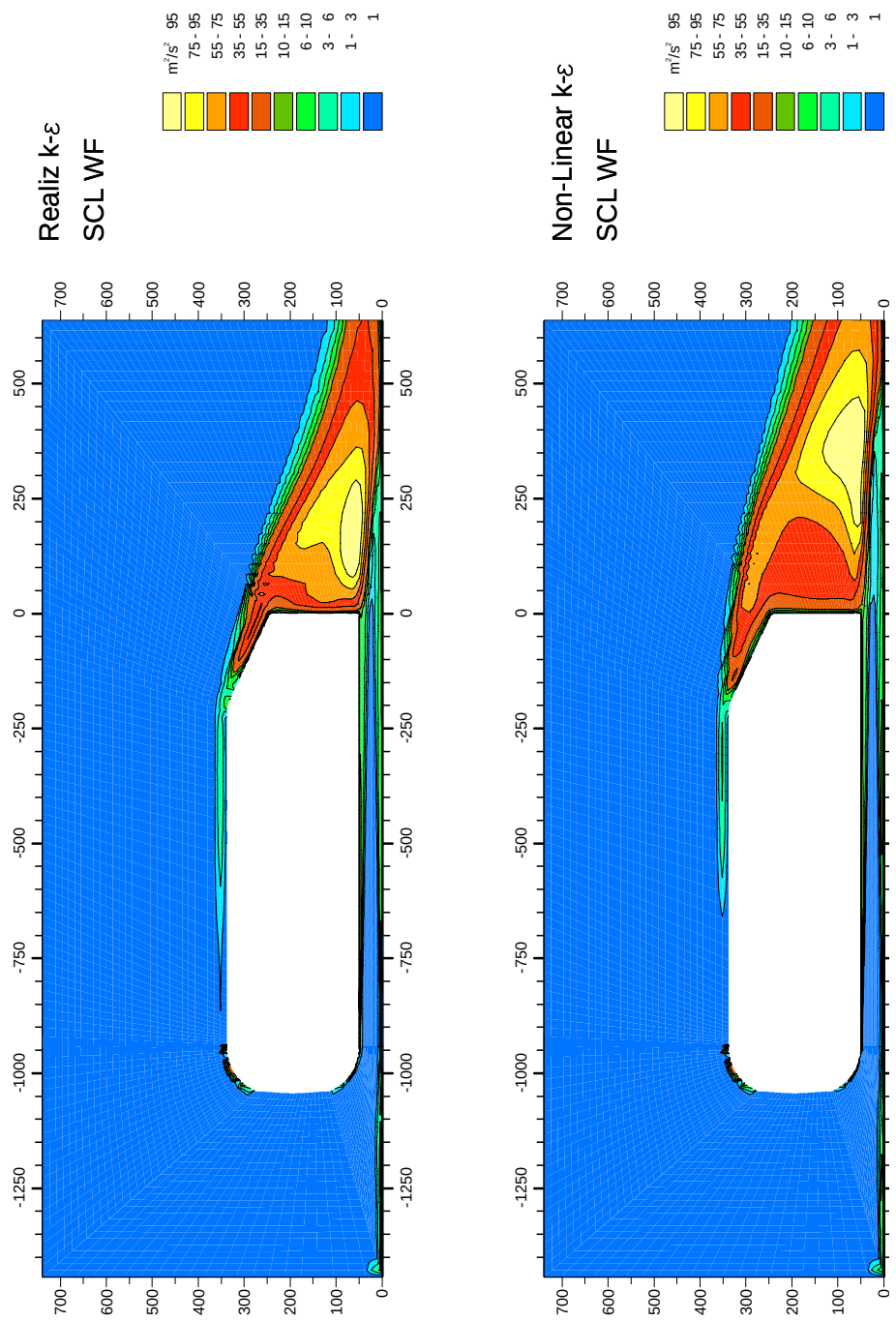

Figure 7.34: Turbulent kinetic energy contours around the Ahmed body at $y = 0$ using the realizable linear $k - \varepsilon$ model with the SCL wall function (top) and the non-linear $k - \varepsilon$ model with the SCL wall function (bottom). Both realizable and non-linear model computations were undertaken by Robinson [35].

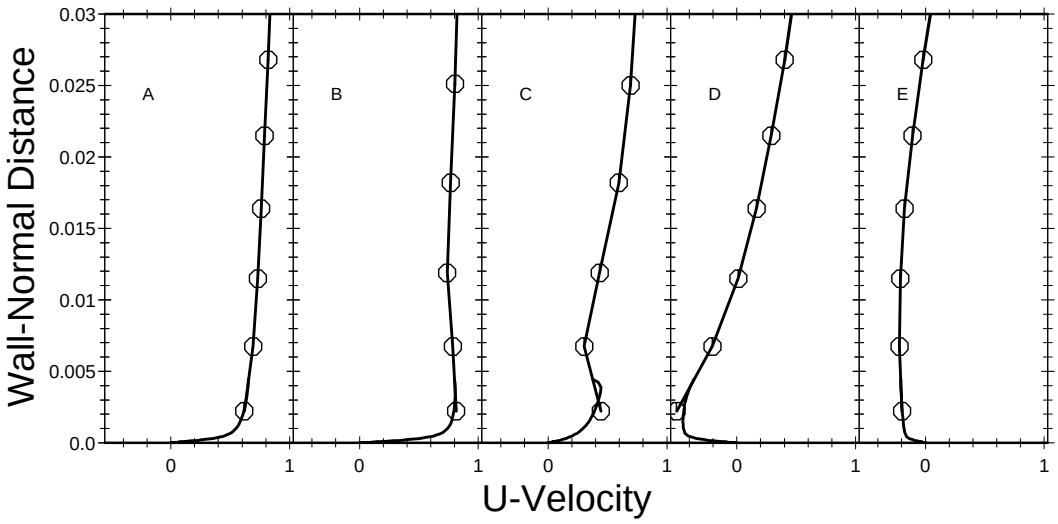

Figure 7.35: Profiles of the wall-parallel U-velocity at five positions around the 90° rear corner of the Ahmed body, *A*, *B*, *C*, *D* and *E*, shown in Figure 7.36. Results were obtained using the linear $k-\varepsilon$ model with the UMIST-*N* wall function (including the $\partial P/\partial\zeta$ term). Symbols indicate main-grid nodal values and the subgrid velocity distribution is also shown. The wall-normal distance is non-dimensionalized with the height of the car body $(L = 288\text{mm})$ and velocity with the free-stream value $\left(U_0 = 38.51\text{ms}^{-1}\right)$.

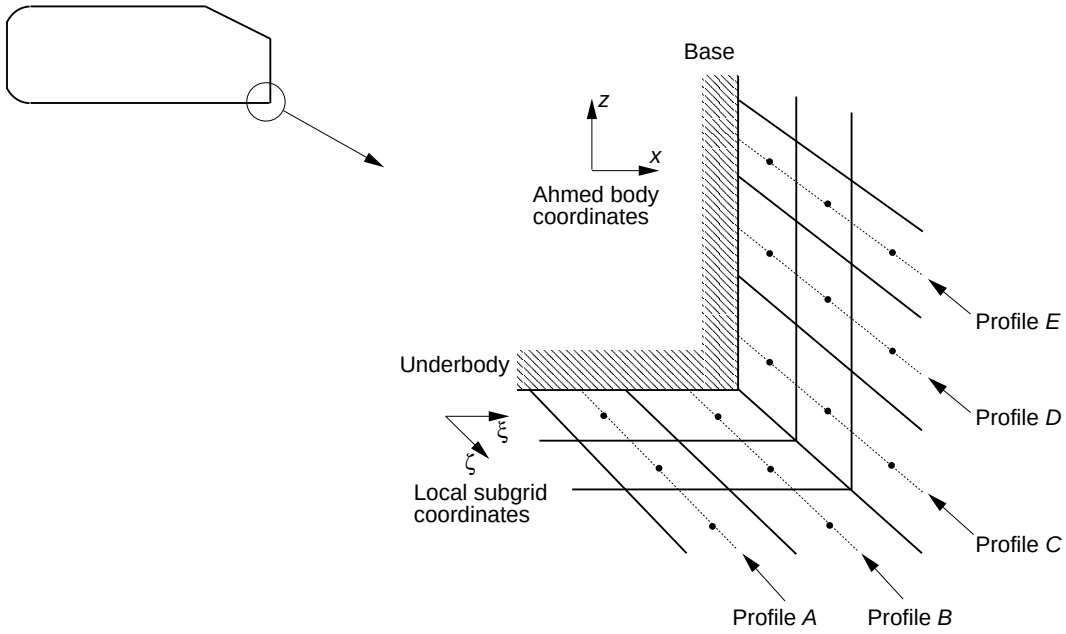

Figure 7.36: Sketch of the rear corner of the Ahmed body showing the local grid arrangement and the location of profiles used in Figures 7.35, 7.37 and 7.38.

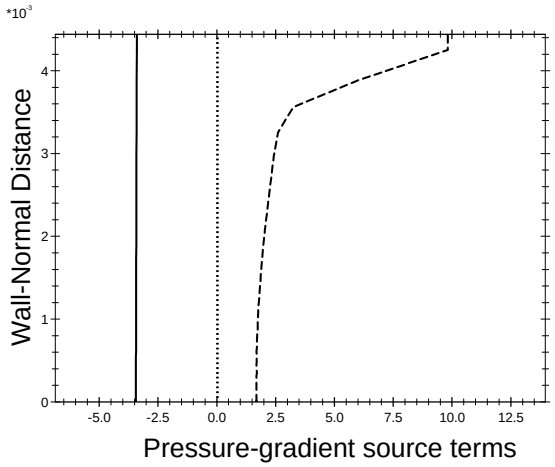

Figure 7.37: Profiles of the three pressure-gradient source terms appearing in the subgrid U-momentum equation at position C adjacent to the 90° rear corner of the Ahmed body, shown in Figure 7.36; —-: $\left(\sqrt{g_{11}}g^{11}\partial P/\partial\xi\right)$; ....: $\left(\sqrt{g_{11}}g^{12}\partial P/\partial\eta\right)$; - - -: $\left(\sqrt{g_{11}}g^{13}\partial P/\partial\zeta\right)$. Results were obtained using the linear $k-\varepsilon$ model with the UMIST-N wall function. The wall-normal distance is non-dimensionalized with the height of the car body $(L = 288\text{mm})$.

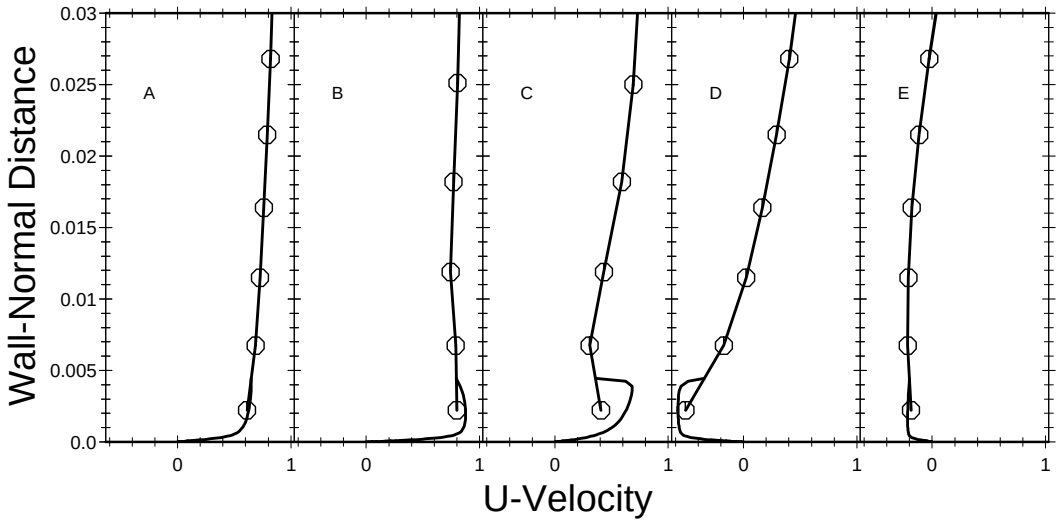

Figure 7.38: Profiles of the wall-parallel U-velocity at five positions around the 90° rear corner of the Ahmed body, shown in Figure 7.36. Results were obtained using the linear $k-\varepsilon$ model with the UMIST-N wall function (without the $\partial P/\partial\zeta$ term). Symbols indicate main-grid nodal values and the subgrid velocity distribution is also shown. The wall-normal distance is non-dimensionalized with the height of the car body $(L = 288\text{mm})$ and velocity with the free-stream value $\left(U_0 = 38.51\text{ms}^{-1}\right)$.